広島大学学位請求論文

Testing modified gravity models with multi-wavelength observations of galaxy clusters

（銀河団の多波長観測を用いた修正重力理論の検証）

2016年

広島大学大学院理学研究科物理科学専攻

照喜名 歩

目次

(4) The XMM Cluster Survey: Testing chameleon gravity using the profiles of clusters
H. Wilcox, D. Bacon, R.C Nichol, P.J.Rooney, A. Terukina, A.K Romer, K. Koyama, G-B, Zhao, R. Hood, R.G. Mann, M. Hilton, M. Manolopoulou, M. Sahlen, C.A. Collins, A.R. Liddle, J.A. Mayers, N. Mehrtens, C.J. Miller, J.P. Stott and P.T.P. Viana
Monthly Notices of the Royal Astronomical Society 452 (2015) 1171

主論文

THESIS

Testing modified gravity models with multi-wavelength observations of galaxy clusters

Ayumu Terukina

Graduate School of Science
Hiroshima University

January, 2016

Rerefences

A. Terukina and K. Yamamoto,
Gas Density Profile in Dark Matter Halo in Chameleon Cosmology,
Physical Review D 86 (2012) 103503.

A. Terukina, L. Lombriser, K. Yamamoto, D. Bacon, K. Koyama and R.C. Nichol,
Testing chameleon gravity with the Coma cluster,
Journal of Cosmology and Astroparticle Physics 04 (2014) 013.

A. Terukina, K. Yamamoto, N. Okabe, K. Matsushita and T. Sasaki,
Testing a generalized cubic Galileon gravity model with the Coma Cluster,
Journal of Cosmology and Astroparticle Physics 10 (2015) 064.

Abstract

Cosmological observations have revealed that our universe is in an accelerated expansion phase. This fact suggests that an extra energy component with negative pressure, which is called dark energy, is present in the universe. It is known that a cosmological constant best explains the cosmological observations, but there is a fundamental problem, called the cosmological constant problem.

On the other hand, modified gravity theories can serve as an alternative to dark energy models to explain the cosmic acceleration. There are many models of the modified gravity: for example, the $f(R)$ model, which introduces a nonlinear function of the Ricci scalar in addition to the Einstein–Hilbert term; the Dvali–Gabadaze–Porrati (DGP) model, motivated by the 5D brane world scenario; and the Galileon model, which introduces a scalar field with higher derivative terms in the Lagrangian, but keeps a second-order differential equation as the equation of motion. These models introduce additional degrees of freedom, which give rise to a fifth force. For example, the chameleon model, which is equivalent to the $f(R)$ model, modifies gravity by introducing a scalar field which is non-minimally coupled with the matter components and gives rise to a fifth force that can be of the same order as the standard gravitational force. The DGP model and the Galileon model also include a scalar field, which gives rise to a fifth force.

Any fifth forces are, however, severely constrained by experiments in the solar system. So viable models with modified gravity must employ screening mechanisms to evade these constraints. For example, the chameleon and $f(R)$ models are equipped with the chameleon mechanism, and the DGP and Galileon models are equipped with the Vainshtein mechanism. These mechanisms screen behavior of the fifth force depending on the matter density and the space-time curvature. The screening mechanisms work in high-density regions where the matter density contrast is nonlinear but do not work over large cosmological scales. In the context of screening mechanisms, galaxy clusters are a useful regime for testing modified gravity because they are objects on the transition between linear and nonlinear scales. Namely, standard

gravitational behavior is recovered thanks to the screening mechanism in the interior of a galaxy cluster, but the screening mechanism may not completely screen the fifth force in the outer region of the galaxy cluster.

In this thesis, we propose a novel method to test modified gravity models using galaxy clusters. When the scalar field is coupled with gas components in galaxy clusters, the fifth force due to the scalar field would affect the gas distribution because of an additional pressure gradient for the gas that balances with the fifth force. Thus, modified gravity models can be tested by combining gas measurements from galaxy clusters. Through various physical processes, galaxy clusters can be observed at multiple wavelengths, for example, the X-rays from thermal gas radiation, the Sunyaev–Zel'dovich effect due to inverse Compton scattering of cosmic microwave background photons and the gravitational weak-lensing effect due to the matter distribution in a galaxy cluster. This suggests that a gravity model can be tested using these observations by precisely modeling the matter distribution of a galaxy cluster.

We develop a theoretical model of galaxy clusters under the influence of modified gravity, and compare theoretical predictions with the observational data set of nearly galaxy clusters. With this approach we have obtained useful constraints on the chameleon model and a generalized cubic Galileon model using multi-wavelength observations. For the chameleon model, we obtained constraints on the model parameters, β and ϕ_∞, the coupling strength of the scalar field and the field value in the cosmological background. This result provides a powerful constraint on the $f(R)$ model, corresponding to a particular choice of the chameleon coupling constant $\beta = \sqrt{1/6}$, for which we obtained an upper bound for the parameter f_{R0}, which is equivalent to ϕ_∞: $|f_{R0}| \lesssim 6\times10^{-5}$ at the 95% CL. This bound is competitive with the current strongest cosmological constraints on the $f(R)$ model. For the generalized cubic Galileon model, which contains the DGP model and a Galileon model, we obtained constraints on the model parameters, ϵ, $\mu_{\rm G}$ and $\mu_{\rm L}$, which are the parameters characterizing the screening scale, and the amplitudes of modification of the gravitational potential and the lens potential, respectively. In these models, the fifth force affects not only the gas distribution characterized by $\mu_{\rm G}$ but also the weak-lensing profile characterized by $\mu_{\rm L}$. We showed that these features can be investigated by a combination of the observations of a galaxy cluster reflecting the gas distribution profiles and the weak-lensing signals. The multi-wavelength observations are complementary and can, therefore, put a constraint on the modified gravity model by breaking the degeneracy between the model parameters. We also carefully discuss systematic errors which may affect our method.

Acknowledgments

First of all, I would like to thank my supervisor, Associate Professor Kazuhiro Yamamoto who gave me constructive comments and encouragement during the course of my studies. Without his guidance and persistent help this thesis would not have been possible. I am grateful to Assistant Professor Nobuhiro Okabe, whose insightful comments and enormous support were very helpful for me. Special thanks is also due to Professor Kojima whose opinions and information were invaluable for my study. I want to thank Tatsuya Narikawa, Rampei Kimura, Lucas Lombriser, Yuichiro Takushima, Tatsuro Kanemaru, Takuya Hirakawa, and all of my collaborators for discussions and their cooperation when completing papers. I also wish to thank Jun Kakuwa, Yugo E. Kato, and all the members of the Astrophysics Group of Hiroshima University for useful comments and discussions. Finally, I would like to thank my family, who have supported me and given me warm encouragement throughout my studies.

Contents

Chapter 1

Introduction

That our universe is undergoing an accelerated expansion phase at the present time is indicated by many observations: for example, the Ia supernova [1, 2], the cosmic microwave background (CMB) radiation [3, 4], the large scale structure (LSS) [5, 6], and the number density of galaxies [7, 8]. Why the expansion of our universe is accelerating is one of the most fundamental mysteries in basic science. One basic interpretation of this fact is that our universe does not contain only matter and radiation energy components but also other extra energy components with negative pressure, which are called *dark energy*. Recently, it has been shown that the cosmological constant and cold dark matter (ΛCDM) model best describes our universe. However, this model has some theoretical problems, such as the cosmological constant problem, so it is still incomplete.

On the other hand, modifying gravity theory is an interesting approach to explaining the accelerated expansion of the universe. However, any covariant modification of general relativity introduces additional degrees of freedom, giving rise to a fifth force. This is strictly constrained by gravity tests in the solar system. Solar system experiments [9, 10] are in excellent agreement with general relativity, requiring that this additional degree of freedom be hidden on the scale of the solar system. Such a process is referred to as a *screening mechanism*, and is key for any viable modified gravity model. In general, this screening mechanism works in high-density regions where the matter density contrast is nonlinear. However, this does not work on large cosmological scales. This screening mechanism that characterizes viable modified gravity models is an important feature to be tested with observations.

The chameleon mechanism [11, 12] is a screening mechanism that works in an $f(R)$ gravity model and the chameleon gravity model [13–15]. In these models, a scalar degree of freedom that gives rise to the fifth force is screened in a high-

density region due to coupling with matter. The chameleon gravity model and an $f(R)$ model can be viable owing to the chameleon mechanism [16]. The Vainshtein mechanism [17] is another relevant screening mechanism, which is employed in the Dvali–Gabadaze–Porrati (DGP) model [18, 19], the simplest cubic Galileon model [20–23], and its generalized version [24,25]. The DGP model is an archetypal modified gravity model developed in the context of the brane-world scenario. There are two branches of solutions in the DGP model. The self-acceleration branch DGP (sDGP) model [26–28] includes a mechanism to explain self-acceleration in the late universe, while the normal branch DGP (nDGP) model [29–31] with a cosmological constant is a healthy modified gravity model avoiding the ghost problem [32, 33]. The simplest cubic Galileon model is also a typical modified gravity model that explains self-acceleration of the universe while avoiding the ghost problem. In these models, a scalar field giving rise to a fifth force is screened due to self-interaction on small scales where density perturbations become nonlinear.

Galaxy clusters provide a unique laboratory for testing modified gravity models with screening mechanisms, because they are objects on the borderline between linear and nonlinear scales. That is, they cover non-screened and screened scales: while the interior of a cluster may be screened, the screening mechanism may not completely screen the modifications of gravity in the outer regions of the cluster [34–46].

In this thesis, we investigate a cosmological constraint on modified gravity models focusing on use of gas distributions in galaxy clusters. The pressure gradient of gas in a galaxy cluster balances with the gravitational force. When the gas components feel the fifth force due to modifications of gravity, the balance will be changed, which creates a change of gas distribution in the cluster. We will review this idea and establish a method of testing modified gravity models by comparing observations of gas distribution with theoretical predictions of gas distributions in the presence of the fifth force.

This thesis is organized as follows. In Chapter 1, we briefly review the standard ΛCDM model and modified gravity models considered in this thesis. In Chapter 2, we review physical processes in galaxy clusters. In Chapter 3, we construct theoretical cluster profiles in the presence of a fifth force. In Chapter 4, we demonstrate the testing of modified gravity models using multi-wavelength observations of galaxy clusters and put useful constraints on modified gravity models. In Chapter 5, we present a summary and our conclusions.

1.1 Units and notation

First of all, let us mention the units and notation that we use throughout this thesis. Unless otherwise noted, we use units in which the speed of light, c, and the reduced Planck constant, $\hbar$, are unity, $c = \hbar = 1$, and we also use the reduced Planck mass, $M_{\rm Pl}$, which is defined by $M_{\rm Pl} = 1/\sqrt{8\pi G}$ with Newton's gravitational constant, G. We adopt a present Hubble parameter of $H_0 = 100\ h$km/s/Mpc with $h = 0.7$, and the present matter and dark energy density parameters of $\Omega_{\rm m0} = 0.3$ and $\Omega_{\Lambda 0} = 1 - \Omega_{\rm m0}$, respectively. Then we ignore the radiation and curvature in the universe ($\Omega_{\rm r0} = \Omega_{\rm K0} = 0$). We also follow the metric signature convention of $(-,+,+,+)$.

The Christoffel symbol is defined by

$$\Gamma^{\mu}_{\alpha\beta} = \frac{1}{2} g^{\mu\nu} (\partial_\beta g_{\alpha\mu} + \partial_\alpha g_{\beta\nu} - \partial_\nu g_{\alpha\beta}) \tag{1.1}$$

where $g_{\mu\nu}$ is the metric tensor. The Riemann tensor is given by

$$R^{\mu}_{\nu\alpha\beta} = \partial_\alpha \Gamma^{\mu}_{\nu\beta} - \partial_\beta \Gamma^{\mu}_{\nu\alpha} + \Gamma^{\mu}_{\sigma\alpha}\Gamma^{\sigma}_{\nu\beta} - \Gamma^{\mu}_{\sigma\beta}\Gamma^{\sigma}_{\nu\alpha}, \tag{1.2}$$

and the Einstein tensor is given by

$$G_{\mu\nu} = R_{\mu\nu} - \frac{1}{2} g_{\mu\nu} R, \tag{1.3}$$

where $R_{\mu\nu} \equiv R^{\alpha}_{\mu\alpha\nu}$ is the Ricci tensor and $R \equiv g^{\mu\nu} R_{\mu\nu}$ is the Ricci scalar.

The energy momentum tensor is defined by

$$T_{\mu\nu} \equiv -\frac{2}{\sqrt{-g}} \frac{\partial \mathcal{L}_{\rm m}}{\partial g_{\mu\nu}}, \tag{1.4}$$

where g is the determinant of the metric, $g_{\mu\nu}$, and $\mathcal{L}_{\rm m}$ is the matter Lagrangian.

We denote the derivative operator with respect to the physical time t by

$$\dot{} \equiv \frac{d}{dt} \tag{1.5}$$

1.2 ΛCDM model

Historically, the cosmological constant, Λ, was introduced by Einstein to explain a static universe. However, it has been found that this idea well describes the observed accelerating expansion of the universe. The action is given by the Einstein–Hilbert

term with cosmological constant,

$$S = \int d^4x\sqrt{-g}\left[\frac{M_{\rm Pl}}{2}(R-2\Lambda)+\mathcal{L}_{\rm m}\right], \tag{1.6}$$

Variation of the action (1.6) with respect to the metric, $g_{\mu\nu}$, yields the Einstein equations

$$M_{\rm Pl}^2 G_{\mu\nu} = T_{\mu\nu} + T_{\mu\nu}^{(\Lambda)}, \tag{1.7}$$

where

$$T_{\mu\nu}^{(\Lambda)} \equiv M_{\rm Pl}^2 \Lambda g_{\mu\nu} \tag{1.8}$$

is the energy momentum tensor coming from the cosmological constant.

For a homogeneous, isotropic and spatially flat universe, with the Friedmann–Lemaitre–Robertson–Walker (FLRW) metric,

$$ds^2 = -dt^2 + a(t)^2\delta_{ij}dx^i dx^j, \tag{1.9}$$

where a is the scale factor, the Einstein equations (1.7) are reduced to the following equations,

$$3M_{\rm Pl}^2 H^2 = \rho_{\rm m} + \rho_\Lambda, \tag{1.10}$$

$$-M_{\rm Pl}^2(2\dot{H}+3H^2) = p_\Lambda \tag{1.11}$$

where $H \equiv \dot{a}/a$ is the Hubble parameter, and ρ_i and p_i are the energy density and pressure, respectively, and the subscript $i = {\rm m}, \Lambda$ denotes contributions from the matter and cosmological constant, respectively. The energy density of matter evolves[1] as $\rho_{\rm m}(z) = \rho_{\rm m0}(1+z)^3$. On the other hand, we obtain the energy density of the cosmological constant as $\rho_\Lambda = -p_\Lambda \equiv M_{\rm Pl}^2\Lambda_{\rm cos}$, which means that the cosmological constant causes repulsive pressure and leads to the accelerated expansion of the universe.

Here we introduce the critical density, $\rho_{\rm c}$, and density parameters, Ω_i, as

$$\rho_{\rm c}(z) = 3M_{\rm Pl}H^2(z), \tag{1.12}$$

[1]The densities of radiation and curvature evolve as $\rho_{\rm r}(z) = \rho_{\rm r0}(1+z)^4$ and $\rho_K(z) = 3M_{\rm Pl}^2K(1+z)^2$, respectively.

$$\Omega_i(z) = \frac{\rho_i(z)}{\rho_{\rm c}(z)}. \tag{1.13}$$

The Friedmann equation (1.10) normalized by the Hubble parameter at the present time, H_0, is given by

$$\frac{H^2(z)}{H_0^2} = \Omega_{\rm m0}(1+z)^3 + \Omega_{\Lambda 0}, \tag{1.14}$$

where we define $\Omega_i(0) \equiv \Omega_{i0}$ with $i = {\rm m}, \Lambda$. Then we find that $1 = \Omega_{\rm m}(z) + \Omega_\Lambda(z)$ is satisfied.

Distances

Here, we introduce the definitions of distance between our solar system and an object at redshift z.

When we know the actual size of the object, x, and the angular size of the object θ, the *angular diameter distance* is defined by $D_{\rm A} = x/\theta$. Using cosmological parameters, the angular diameter distance is given by

$$D_{\rm A} = \frac{1}{(1+z)H_0}\int_0^z \frac{dz}{\sqrt{\Omega_{\rm m0}(1+z)^3 + \Omega_{\Lambda 0}}} \tag{1.15}$$

When we know the luminosity and flux of the object, L and F, the *luminosity distance* is defined by $D_{\rm L} = (L/4\pi F)^{1/2}$. The luminosity distance is related to the angular diameter distance by $D_{\rm L} = (1+z)^2 D_{\rm A}$.

1.3 Modified gravity theories

We now briefly review modified gravity models used in this thesis.

1.3.1 Chameleon model

We consider an action in which a scalar field is non-minimally coupled with the matter field:

$$S = \int d^4x\sqrt{-g}\left[\frac{M_{\rm Pl}^2}{2}R - \frac{1}{2}g^{\mu\nu}\partial_\mu\phi\partial_\nu\phi - V(\phi)\right] - \int d^4x \mathcal{L}_{\rm m}(\Psi, e^{2\beta\phi/M_{\rm Pl}}g_{\mu\nu}), \tag{1.16}$$

where ϕ is the scalar field, $V(\phi)$ is the potential of the scalar field, β is the coupling constant and Ψ is the potential of the matter field. The action (1.16) can be transformed into an action in which the scalar field is minimally coupled with the matter field, but is non-minimally coupled with gravity. The frame for the action (1.16) is called the *Einstein frame*, and the frame for the transformed action in which the scalar field is minimally coupled with matter field is called the *Jordan frame*. These frames are related by a *conformal transformation*. The detail of the transformation is summarized in Appendix (A.1.2). It is interesting to study this model because this model includes the $f(R)$ model (see the next subsection) in the Jordan frame, and the screening mechanism to pass local gravity tests is easy to understand.

First, we review the cosmology in the chameleon model. For the spatially flat FLRW metric (1.9), we obtain the modified Friedmann equation

$$3H^2 M_{\rm Pl}^2 = \frac{1}{2}\dot{\phi}^2 + V(\phi) + \rho_{\rm m} e^{\beta\phi/M_{\rm Pl}}, \tag{1.17}$$

where $\rho_{\rm m}$ is the matter density *conserved in the Einstein frame* (Appendix A.1.2). Then, we obtain the critical density $\rho_{\rm c}$ and matter density parameter $\Omega_{\rm m}$ as

$$\rho_{\rm c}(z) = \frac{1}{2}\dot{\phi}^2 + V(\phi) + \rho_{\rm m}(z) e^{\beta\phi/M_{\rm Pl}} \tag{1.18}$$

$$\Omega_{\rm m}(z) = \frac{\rho_{\rm m}(z) e^{\beta\phi/M_{\rm Pl}}}{\rho_{\rm c}(z)} \tag{1.19}$$

On the other hand, the variation of the action (1.16) with respect to the scalar field (chameleon field) gives the equation of motion for the chameleon field as

$$\ddot{\phi} + 3H\dot{\phi} = V_{,\phi} + \frac{\beta}{M_{\rm Pl}}\rho_{\rm m} e^{\beta\phi/M_{\rm Pl}} \tag{1.20}$$

$$= -V_{{\rm eff},\phi}(\phi), \tag{1.21}$$

where we assume that the chameleon field is homogeneous and $V_{\rm eff}$ is the effective potential defined by

$$V_{\rm eff}(\phi) \equiv V(\phi) + \rho_{\rm m} e^{\beta\phi/M_{\rm Pl}}. \tag{1.22}$$

Chameleon Force

Since the chameleon field is coupled with the matter field, particles feel not only the gravitational force but also the *fifth force* coming from chameleon field, which is

called the *chameleon force*.

The geodesic equation in the Jordan frame is given by

$$\ddot{x}^\lambda + \tilde{\Gamma}^\lambda_{\mu\nu}\dot{x}^\mu\dot{x}^\nu = 0, \tag{1.23}$$

where $\dot{} \equiv d/d\tilde{\tau}$ means the derivative with respect to proper time in the Jordan frame, $\tilde{\tau}$. Using the relation between the metrics of the Jordan and Einstein frames,

$$\tilde{g}_{\mu\nu} = e^{2\beta\phi/M_{\rm Pl}}g_{\mu\nu}, \tag{1.24}$$

Eq. (1.23) can be transformed into the geodesic equation in the Einstein frame as

$$\ddot{x}^\lambda + \tilde{\Gamma}^\lambda_{\mu\nu}\dot{x}^\mu\dot{x}^\nu + \frac{\beta}{M_{\rm Pl}}(2\phi_{,\mu}\dot{x}^\mu\dot{x}^\lambda + g^{\lambda\nu}\phi_{,\nu}) = 0 \tag{1.25}$$

The third term of the left-hand side of Eq. (1.25) gives the chameleon force. In the non-relativistic limit, a test particle feels the chameleon force represented by

$$F_\phi = -\frac{\beta}{M_{\rm Pl}}\nabla\phi. \tag{1.26}$$

Chameleon mechanism

The chameleon field equation is given by the variation of the action (1.16) with respect to the chameleon field, ϕ:

$$\Box\phi = V_{,\phi} - \frac{\beta}{M_{\rm Pl}}e^{4\beta\phi/M_{\rm Pl}}g^{\mu\nu}T_{\mu\nu}, \tag{1.27}$$

where $\Box \equiv g^{\mu\nu}\nabla_\mu\nabla_\nu$ is the d'Alembertian and

$$\tilde{T}_{\mu\nu} \equiv \frac{2}{\sqrt{-\tilde{g}}}\frac{\delta\mathcal{L}_{\rm m}}{\delta\tilde{g}^{\mu\nu}} \tag{1.28}$$

is the energy-momentum tensor in the Jordan frame which satisfies the energy and momentum conservation laws

$$\tilde{\nabla}_\nu\tilde{T}_{\mu\nu} = 0. \tag{1.29}$$

Under the assumption of a perfect fluid, using the mater energy density $\tilde{\rho}$ and the pressure $\tilde{p}$, we have

$$\tilde{T}^{\mu\nu}\tilde{g}_{\mu\nu} = -(1-3w)\tilde{\rho} \tag{1.30}$$

where we assume $\tilde{p} = w\tilde{\rho}$ with a parameter w. The energy density conserved in the Einstein frame is given by

$$\rho \equiv e^{3(1+w)\beta\phi/M_{\rm Pl}}\tilde{\rho} \tag{1.31}$$

Using Eq. (1.31), the chameleon field equation is reduced to

$$\Box\phi = V_{,\phi} + \frac{\beta}{M_{\rm Pl}}\rho e^{\beta\phi/M_{\rm Pl}} \tag{1.32}$$

$$= \frac{dV_{\rm eff}}{d\phi}, \tag{1.33}$$

where $V_{\rm eff}$ is the effective potential defined by Eq. (1.22). Because the effective potential depends on the matter density, the chameleon field also depends on the matter density. When the effective potential reaches a minimum with $\phi = \phi_{\rm min}$, the mass of the chameleon field $m_{\rm min}$ is given by the second derivative of the effective potential with respect to ϕ

$$m_{\rm min}^2 = V_{,\phi\phi}(\phi_{\rm min}) + \frac{\beta^2}{M_{\rm Pl}^2}\rho e^{\beta\phi_{\rm mim}/M_{\rm Pl}}, \tag{1.34}$$

where the first derivative of the effective potential satisfies

$$\frac{dV_{\rm eff}}{d\phi} = V_{,\phi}(\phi_{\rm min}) + \frac{\beta}{M_{\rm Pl}}\rho e^{\beta\phi_{\rm mim}/M_{\rm Pl}} = 0. \tag{1.35}$$

Figure 1.1 shows the effective potential as a function of ϕ (red curve) in the case that the matter density is high (left panel) and in the case of the matter density is low (right panel). This figure shows that the curvature of the effective potential, which is equivalent to the mass of the chameleon field (1.34), in a high density region is larger than that in a low density region. Since the Compton wave length of the chameleon field is inversely proportional to the mass, $\propto 1/m_{\rm min}$, we find that the Compton wave length in a high density region is shorter, which means the interaction between the matter field and the chameleon field becomes weak. Therefore, in a high density region, the chameleon force effectively does not appear.

1.3.2 $f(R)$ model

We consider the action

$$S = \int d^4x\sqrt{-g}\left[\frac{M_{\rm Pl}^2}{2}(R + f(R)) + \mathcal{L}_{\rm m}\right], \tag{1.36}$$

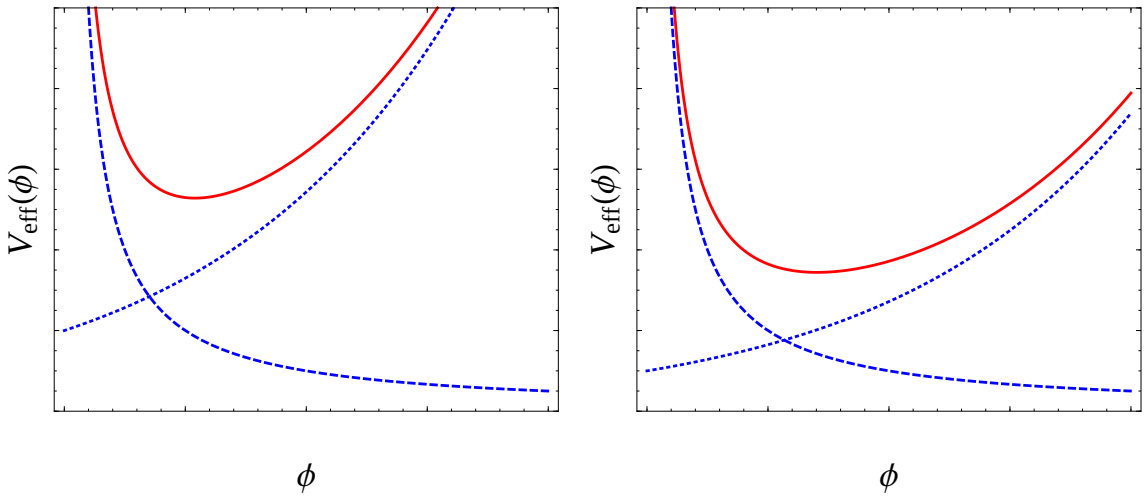

Figure 1.1: The effective potential as a function of ϕ (red curve) in a high density region (left panel) and in a low density region (right panel). Blue dashed and dotted curves show $V(\phi)$ and $\rho e^{\beta\phi/M_{\rm Pl}}$ as a function of ϕ, respectively.

where $f(R)$ is an arbitrary nonlinear function of the Ricci scalar.

Variation of the action (1.36) with respect to the metric $g_{\mu\nu}$ yields the modified Einstein equations

$$R_{\mu\nu} = R_{\mu\nu} - \frac{1}{2}g_{\mu\nu}R + f_R R_{\mu\nu} - \left(\frac{f}{2} - \Box f_R\right) g_{\mu\nu} - \nabla_\mu\nabla_\nu f_R = 8\pi G T_{\mu\nu}. \quad (1.37)$$

This model contains an additional degree of freedom, $f_R \equiv df(R)/dR$. The equation of motion for f_R is given by the trace of Eq. (1.37) as

$$\Box f_R = \frac{1}{3}\left[R - f_R R + 2f - 8\pi G(\rho - 3p)\right]. \quad (1.38)$$

Assuming the spatially flat FLRW metric, the $(0,0)$ component of the modified Einstein equation (1.37) gives the modified Friedmann equation

$$H^2 - f_R(HH' + H^2) + \frac{f}{6} + H^2 f_{RR}R' = \frac{8\pi G}{3}(\rho - 3p), \quad (1.39)$$

where $' = d/d\ln a$.

The $f(R)$ model can be written in the form of the chameleon model by a conformal

transformation. The detail of the equivalence between the $f(R)$ model and the chameleon model is given in Appendix (A.1).

A viable $f(R)$ model for an alternative dark energy has to satisfy several conditions, for example, avoid a ghost state and negative mass squared of the scalar field, be consistent with local gravity constraints, be stable and include a late-time de Sitter solution, which are summarized in Ref. [47].

The viable nonlinear $f(R)$ functions in an $f(R)$ model satisfying the above conditions are

$$f(R) = -\lambda R_{\rm c} \left(\frac{R}{R_{\rm c}}\right)^{p} \tag{1.40}$$

$$f(R) = -\lambda R_{\rm c} \frac{(R/R_{\rm c})^{2n}}{(R/R_{\rm c})^{2n}+1} \tag{1.41}$$

$$f(R) = -\lambda R_{\rm c} \left[1 - \left(1 + \frac{R^2}{R_{\rm c}^2}\right)^{-n}\right] \tag{1.42}$$

$$f(R) = -\lambda R_{\rm c} \tanh\left(\frac{R}{R_{\rm c}}\right) \tag{1.43}$$

where the parameters satisfy $0 < p < 1$ and $n, \lambda, R_{\rm c} > 0$. The models (1.40), (1.41), (1.42) and (1.43) were proposed in Refs. [13–15, 48], respectively.

In this thesis, we adopt the Hu-Sawiki model (1.41). The function $f(R)$ of the Hu-Sawiki model can be re-expressed as

$$f(R) = -m^2 \frac{c_1 (R/m^2)^n}{c_2 (R/m^2)^2 + 1}, \tag{1.44}$$

where n, m, c_1 and c_2 are constant model parameters. Eq. (1.44) has an asymptotic form with $R \ll m^2$ ($|f_R| \ll 1$), which is given by

$$f(R) = -m^2 \frac{c_1}{c_2} + \frac{m^2 c_1}{c_2^2} \left(\frac{R}{m^2}\right)^{-n}. \tag{1.45}$$

Note that $m^2 c_1/c_2/2$ can be chosen such that the modification exhibits an effective cosmological constant and mimics the expansion history of the concordance model. Hence, we specify $m^2 = \Omega_{\rm m} H_0^2$ and $c_1/c_2 = 6\Omega_\Lambda/\Omega_m$. Furthermore, we have $n c_1/c_2^2 = -f_{R0}[3(1 + 4\Omega_\Lambda/\Omega_m)]^{n+1}$, where we introduced the model parameter, f_{R0}, which is the value of f_R at the present time and at the background. In this case, only the parameters f_{R0} and n are needed to describe the model.

The mass of f_R, m_{f_R}, is given by

$$m_{f_R}^2 \simeq \frac{1}{3f_{RR}}, \tag{1.46}$$

where

$$f_R = -\frac{4n\lambda}{R_{\rm c}}\left(\frac{R}{R_{\rm c}}\right)^{-(2n+1)}, \tag{1.47}$$

$$f_{RR} = \frac{4n(2n+1)\lambda}{R_{\rm c}^2}\left(\frac{R}{R_{\rm c}}\right)^{-(2n+2)}. \tag{1.48}$$

Here we use Eq. (1.41) (or Eq. (1.42)) with $R \gg R_{\rm c}$ to give the asymptotic form

$$f(R) \simeq \lambda R_{\rm c}\left[1 - \left(\frac{R}{R_{\rm c}}\right)^{-2n}\right] \tag{1.49}$$

As mentioned in the previous subsection, the Compton wavelength of the additional degree of freedom characterizes the scale at which particles feel the fifth force. Here, we define the wavenumber $k_{\rm C}$ of f_R which is related to the Compton wavelength by

$$\frac{1}{3f_{RR}} = k_{\rm C}^2\left(\frac{\Omega_{\rm m0}(1+z)^3 + 4(1-\Omega_{\rm m0})}{\Omega_{\rm m0} + 4(1-\Omega_{\rm m0})}\right)^{2n+2} \tag{1.50}$$

where we use $2\Lambda = \lambda R_{\rm c} = 6(1-\Omega_{\rm m0})H_0^2$. Then the wavenumber is given by

$$k_{\rm C}^2 = \frac{\Omega_{\rm m0}H_0^2}{4n(2n+1)}\left(\frac{\lambda}{2}\right)^{2n}\left(\frac{\Omega_{\rm m0}}{1-\Omega_{\rm m0}}\right)^{2n+1}\left(1 + \frac{4(1-\Omega_{\rm m0})}{\Omega_{\rm m0}}\right). \tag{1.51}$$

1.3.3 DGP model

The Dvali-Gabadadze-Porrati (DGP) model is motivated in the context of the braneworld scenario. The action is given by

$$S = \frac{M_{(5)}^3}{2}\int d^5X\sqrt{-g_{(5)}}R_{(5)} + \frac{M_{\rm Pl}^2}{2}\int d^4x\sqrt{-g}R + \int d^4x\sqrt{-g}\mathcal{L}_{\rm m}^{\rm brane}, \tag{1.52}$$

where $g_{(5)}$ is the determinant of the metric in the 5D bulk, $g_{\mu\nu} = \partial_\mu X^A \partial_\nu B^B g_{AB}$ is the induced metric on the brane with $X^A(x^c)$ being the coordinates of an event on the brane labeled by x^c, $M_{(5)}$ is the 5D Planck mass and R_5 is the Ricci scalar of the

5D metric. The first and second terms in the action (1.52) are the Einstein-Hilbert action in the 5D bulk and on the brane, respectively. $\mathcal{L}_{\rm m}^{\rm brane}$ is the matter Lagrangian localized on the 3-brane.

When we consider a spatially flat FLRW brane, the modified Friedmann equation is given by

$$H^2 - \frac{\epsilon}{r_{\rm c}} H = \frac{\rho_{\rm m}}{3M_{\rm Pl}^2}. \tag{1.53}$$

Here, $\epsilon = \pm 1$, so the DGP model has two branches. When we chose $\epsilon = 1$, which corresponds to a *self-accelerating branch* DGP (sDGP) model [2], the modified Friedmann equation (1.53) can be rewritten as

$$\frac{H(a)}{H_0} = \frac{1-\Omega_{\rm m0}}{2} + \sqrt{\frac{\Omega_{\rm m0}}{a^3} + \frac{(1-\Omega_{\rm m0})^2}{4}}, \tag{1.54}$$

where the matter density parameter is related to the crossover scale by $r_{\rm c} = 1/(1 - \Omega_{\rm m0} H_0)$.

On the other hand, when we chose $\epsilon = -1$, which corresponds to a *normal branch* DGP (nDGP) model, there is no self-accelerating solution unless a cosmological constant is introduced [19,21]. Here we consider the nDGP model with a dynamical dark energy component on the brane, which is tuned such that the background evolves as in the lambda cold dark matter model [31].

1.3.4 Galileon model

Galileon action in Minkowski spacetime

Inspired by the decoupling limit of the DGP model (Section 1.3.3), Galileon model was originally developed by letting $M_{\rm Pl}$ and $r_{\rm c} \to \infty$ while keeping a fixed strong coupling scale, $(r_{\rm c}^{-2} M_{\rm Pl}^{1/3})$.

The action is represented by

$$S = \int d^4x \sqrt{-g} \left[\mathcal{L}_{\rm GR} + \mathcal{L}_\pi \right], \tag{1.55}$$

where $\mathcal{L}_{\rm GR}$ is the Lagrangian for a linearized general relativity and $\mathcal{L}_\pi = \mathcal{L}_{\rm gal}(\pi, \partial\pi, \partial\partial\pi) + \pi T$ represents the generalization of the π-Lagrangian coming from the decoupling

[2] However, the sDGP model suffers from a ghost instability and inconsistencies with cosmological observations.

limit of the DGP model. The vacuum part, $\mathcal{L}_{\rm gal}(\pi, \partial\pi, \partial\partial\pi)$, is invariant under the Minkowski spacetime transformation

$$\pi \to \pi + b_\mu x^\mu + c, \tag{1.56}$$

in the sense that $\mathcal{L}_{\rm gal} \to \mathcal{L}_{\rm gal} + (\text{total derivative})$, where b_μ and c are constants. This invariant is called the *Galileon shift symmetry*.

The Lagrangian satisfying above invariance can be written as

$$\mathcal{L}_{\rm gal}(\pi, \partial\pi, \partial\partial\pi) = \sum_{i=1}^{5} c_i \mathcal{L}_i(\pi, \partial\pi, \partial\partial\pi), \tag{1.57}$$

where c_i are constants, and

$$\mathcal{L}_1 = \pi, \tag{1.58}$$

$$\mathcal{L}_2 = -\frac{1}{2}(\partial\pi)^2, \tag{1.59}$$

$$\mathcal{L}_3 = -\frac{1}{2}\partial^2\pi(\partial\pi)^2, \tag{1.60}$$

$$\mathcal{L}_4 = -\frac{1}{2}\left[(\partial^2\pi)^2 - (\partial\partial\pi)^2\right](\partial\pi)^2 + (\partial^2\pi)\partial_\mu\pi\partial_\nu\pi\partial^\mu\partial^\nu\pi - \partial_\mu\pi\partial^\mu\partial^\nu\pi\partial_\nu\partial_\rho\pi\partial^\rho\pi, \tag{1.61}$$

$$\begin{aligned}\mathcal{L}_5 = &-\frac{1}{2}\left[(\partial^2\pi)^3 - 3(\partial^2\pi)(\partial\partial\pi)^2 + 2(\partial\partial\pi)^3\right](\partial\pi)^2 \\ &+ \frac{3}{2}\left[(\partial^2\pi)^2 - 2(\partial^2\pi) - (\partial\partial\pi)^2\right]\partial_\mu\pi\partial_\nu\pi\partial^\mu\partial^\nu\pi \\ &+ 3\partial_\mu\pi\partial^\mu\partial^\nu\pi\partial_\nu\partial_\rho\pi\partial^\rho\partial^\sigma\pi\partial_\sigma\pi.\end{aligned} \tag{1.62}$$

Here $\partial^2 = \partial_\mu\partial^\mu$, $(\partial\pi)^2 = \partial_\mu\pi\partial^\mu\pi$ and $(\partial\partial\pi)^n = (\partial_{\alpha_1}\partial^{\alpha_1}\pi)(\partial_{\alpha_2}\partial^{\alpha_2}\pi)\cdots(\partial_{\alpha_n}\partial^{\alpha_n}\pi)$. Even though the Lagrangian contains higher derivative terms, the equation of motion for gravity and the Galileon field, π, remains a second-order differential equation owing to the Galileon shift symmetry. The variation of action (1.55) gives an equation of motion which can be written in total derivative form as

$$\partial_\mu J^\mu(\pi, \partial\pi, \partial^2\pi) = 0, \tag{1.63}$$

in the absence of matter.

Covariant Galileon

Because the Lagrangian (1.57) is invariant under the Galileon shift symmetry only in Minkowski spacetime, it does not represent a curved spacetime. Nonetheless, the covariant derivative version of the Lagrangian (1.57) gives the equations of motion for gravity and the Galileon field as second-order differential equations. So, we can write the covariant theory of the Galileon model as

$$S = \int d^4x\sqrt{-g}\left[\frac{M_{\rm Pl}^2}{2}R + \mathcal{L}_{\rm gal}^{\rm cov} + \mathcal{L}_{\rm m}\right], \tag{1.64}$$

where

$$\mathcal{L}_{\rm gal}^{\rm cov}(\phi, \partial\phi, \partial\partial\phi) = \sum_{i=2}^{5} c_i \mathcal{L}_i^{\rm cov}(\phi, \nabla\phi, \nabla\nabla\phi), \tag{1.65}$$

with

$$\mathcal{L}_1 = \phi, \tag{1.66}$$

$$\mathcal{L}_2 = -\frac{1}{2}(\nabla\phi)^2, \tag{1.67}$$

$$\mathcal{L}_3 = -\frac{1}{2}\Box\phi(\nabla\phi)^2, \tag{1.68}$$

$$\mathcal{L}_4 = -\frac{1}{4}\left[4(\Box\phi)^2 - 4\nabla_\mu\nabla_\nu\phi\nabla^\mu\nabla^\nu\phi - R(\nabla\phi)^2\right](\nabla\phi)^2, \tag{1.69}$$

$$\begin{aligned}\mathcal{L}_5 = -\frac{1}{2}\big[&(\nabla^2\phi)^3 - 3(\Box\phi)\nabla_\mu\nabla_\nu\phi\nabla^\mu\nabla^\nu\phi \\ &+2\nabla_\mu\nabla^\nu\phi\nabla_\nu\nabla^\rho\phi\nabla_\rho\nabla^\nu\phi - 6G_{\mu\nu}(\nabla^\mu\phi)(\nabla^\nu\nabla_\lambda\phi)\nabla^\lambda\phi\big](\nabla\phi)^2.\end{aligned} \tag{1.70}$$

Simplest cubic Galileon model

We consider the Galileon model in a curved spacetime with minimal coupling to gravity. The action is given by

$$S = \int d^4x\sqrt{-g}\left[\frac{M_{\rm Pl}^2}{2}R - X - \left(\frac{r_{\rm c}^2}{M_{\rm Pl}}\right)X\Box\phi + \mathcal{L}_{\rm m}\right]. \tag{1.71}$$

As explained in the next subsection, this model is a specific case of the covariant Galileon model. When we adopt the late time de Sitter attractor solution [49], the

modified Friedmann equation in the spatially flat FLRW metric is given by

$$\left(\frac{H(a)}{H_0}\right)^2 = \frac{1}{2}\left[\frac{\Omega_{\rm m0}}{a^3} + \sqrt{\left(\frac{\Omega_{m0}}{a^3}\right)^3 + 4(1-\Omega_{\rm m0})}\right]. \tag{1.72}$$

1.3.5 A generalized cubic Galileon model

The most general scalar-tensor theory

First, we introduce the most general scalar-tensor theory. The theory is the most general non-canonical and non-minimally coupled single-field scalar-tensor theory which gives equations of motion for gravity and the scalar field as second-order differential equations. The expression was first derived by Horndeski [50], so the theory is often called *Horndeski* theory. The action is given by [50–52]

$$S = \int d^4x\sqrt{-g}\left[\sum_{i=2}^{5}\mathcal{L}_i + \mathcal{L}_{\rm m}\right], \tag{1.73}$$

where

$$\mathcal{L}_2 = K(\phi, X), \tag{1.74}$$
$$\mathcal{L}_3 = -G_3(\phi, X)\Box\phi, \tag{1.75}$$
$$\mathcal{L}_4 = G_4(\phi, X)R + G_{4X}\left[(\Box\phi)^2 - (\nabla_\mu\nabla_\nu\phi)^2\right], \tag{1.76}$$
$$\mathcal{L}_5 = G_5(\phi, X)G_{\mu\nu}\nabla^\mu\nabla^\nu\phi - \frac{G_{5X}}{6}\left[(\Box\phi)^3 - 3(\Box\phi)(\nabla_\mu\nabla_\nu\phi)^2 + 2(\nabla_\mu\nabla_\nu\phi)^3\right], \tag{1.77}$$

Note that the covariant Galileon can be reproduced by setting $K = c_1\phi - c_2X$, $G_3 = c_3X/M^3$, $G_4 = M_{\rm Pl}^2/2 - c_4X^2/M^6$ and $G_5 = c_5X^2/M^9$ where c_i are dimensionless parameters and M is a mass-dimension constant.

A subclass of the most general scalar-tensor theory

Here, we consider a subclass of the most general scalar-tensor theory with an action given by [53]

$$S = \int d^4x\sqrt{-g}\Big[G_4(\phi)R + K(\phi, X) - G_3(\phi, X)\Box\phi + \mathcal{L}_{\rm m}\Big], \tag{1.78}$$

which is produced by setting $G_{4X} = G_5 = 0$ in action (1.73). This model is a non-minimal coupling version of the kinetic gravity braiding model [54]. This model contains the simplest cubic Galileon and DGP models. The simplest cubic Galileon model is defined by $G_4 = M_{\rm Pl}^2/2$, $K = -X$ and $G_3 = (r_{\rm c}^2/M_{\rm Pl})X$, which corresponds to taking $c_1 = -1$ in Ref. [55]. The DGP model is originally a 5-dimensional brane-world model, however, it can be effectively described as a Galileon model. So, here we call this model the generalized cubic Galileon model. Note that the DGP model has two branches of cosmological solutions, the self-accelerating branch (sDGP) model [26,27] and the normal branch DGP (nDGP) model [29]. The relations between the generalized Galileon model and these specific models are summarized in Appendix (A.2).

The background solutions are given by

$$2XK_X - K + 6X\dot{\phi}HG_{3X} - 2XG_{3\phi} - 6H^2G_4 - 6H\dot{\phi}G_\phi = \rho_{\rm m}, \tag{1.79}$$

$$K - 2X\left(G_{3\phi} + \ddot{\phi}G_{3X}\right) + 2\left(3H^2 + 2\dot{H}\right)G_4 + 2\left(\ddot{\phi} + 2H\dot{\phi}\right)G_{4\phi} + 4XG_{4\phi\phi} = 0, \tag{1.80}$$

where $\rho_{\rm m}$ is the non-relativistic matter energy density and $H = \dot{a}/a$ is the Hubble parameter. The background equation for the scalar field can be written as

$$\dot{J} + 3HJ - P = 0, \tag{1.81}$$

with

$$J \equiv \dot{\phi}K_X + 6HXG_{3X} - 2\dot{\phi}G_{3\phi}, \tag{1.82}$$

$$P \equiv K_\phi - 2X\left(G_{3\phi\phi} + \ddot{\phi}G_{3\phi X}\right) + 6\left(2H^2 + \dot{H}\right)G_{4\phi}. \tag{1.83}$$

Vainshtein mechanism

The DGP model in the decoupling limit, the simplest cubic Galileon model and the covariant Galileon model include a self-interaction term for the Galileon field, $\mathcal{L} \propto (\nabla\phi)^2\Box\phi$. This term causes screening. To understand the screening mechanism, we consider the Lagrangian of the DGP model in the decoupling limit, whose action is given by

$$\mathcal{L} = -\frac{M_{\rm Pl}^2}{4}h^{\mu\nu}(\mathcal{E}h)_{\mu\nu} - 3(\partial\pi)^2 - \frac{r_{\rm c}^2}{M_{\rm Pl}}(\partial\pi)^2\Box\pi + \frac{1}{2}h^{\mu\nu}T_{\mu\nu} + \frac{1}{\rm Pl}\pi T, \tag{1.84}$$

where $\mathcal{E}^{\alpha\beta}_{\mu\nu}h_{\alpha\beta}$ is the linearized Einstein tensor. To understand the effect of the Galileon field around a point source, we consider the equation of motion of the scalar field, which is given by

$$\partial^\mu[6M_{\rm Pl}\partial_\mu\pi + 2r_{\rm c}^2\partial_\mu\pi\Box\pi - r_{\rm c}^2\partial_\mu(\partial\pi)^2] = -T. \tag{1.85}$$

Note that the energy density of a point source is given by $T = -M\delta^3(r)$. For the spherically symmetric and static case, Eq. (1.85) can be integrated once, which reduces it to

$$\frac{\pi'(r)}{M_{\rm Pl}} = \frac{3r}{4r_{\rm c}^2}\left(-1 + \sqrt{1 + \frac{4}{9}\frac{r_{\rm V}^3}{r^3}}\right). \tag{1.86}$$

Here, $r_{\rm V} = (r_{\rm c}^2 r_{\rm g})^{1/3}$ is called the *Vainshtein radius* and $r_{\rm g}$ is the Schwarzschild radius. Since $r_{\rm c}$ is of the order of the Hubble horizon ($\sim H_0^{-1}$), $r_{\rm V}$ is much larger than the Schwarzschild radius. Note that two solutions can be obtained by solving for π', and we choose the solution for which $\pi' \to 0$ at $r \to \infty$. The other solution corresponds to the sDGP model. At very small scales $r \ll r_{\rm V}$, the ratio of the scalar force to Newton's force can be written as

$$\frac{F_\pi}{F_{\rm g}} = \frac{|\boldsymbol{\nabla}\pi|}{M_{\rm Pl}|\boldsymbol{\nabla}\Psi|} = \left(\frac{r}{r_{\rm V}}\right)^{3/2} \ll 1 \tag{1.87}$$

Therefore, the Galileon field is screened inside the Vainshtein radius, and general relativity behavior is recovered through nonlinear effects. This is called the *Vainshtein mechanism*.

1.4 Constraints on modified gravity theories

Any gravity theory has to pass stringent constraints from the Solar System. There are several methods to test gravity theories. For example, the fifth force is tested by considering a modification of Newton's inverse-square law with a Yukawa-like potential parametrization [9, 56, 57] and the Parametrized Post-Newtonian (PPN) formalism gives a constraint on the time-space curvature [58]. As described in previous sections, the chameleon model and the $f(R)$ model pass these tests thanks to the chameleon mechanism, while the Galileon model and the DGP model also pass thanks to the Vainshtein mechanism.

Lots of cosmological observations also give constraints on modifications of grav-

ity [59]: for example, the CMB, the large scale structure and cluster abundance.

To obtain tighter constraints on modifications of gravity, many unique methods of testing are being investigated: for example, the gravitational weak-lensing effect of galaxy clusters [41, 60], redshift-space distortions [61], the peculiar velocity dispersion of satellite galaxies in halos [62], and higher order cosmological density perturbations [63, 64]. Their approaches commonly focus on exploring the screening scale of the fifth force depending on the matter density. In this sense, galaxy clusters are a unique laboratory for exploring the screening scale, because they are objects on the borderline between linear and nonlinear scales of the matter density perturbation. That is, they cover non-screened and screened scales: while the interior of a cluster may be screened, the screening mechanism may not completely screen the modifications of gravity in the outer regions of the cluster.

We provide a novel method of testing gravity using gas distributions in galaxy clusters in the following chapters. To illustrate the effectiveness of our approach, in Fig. 1.2, we compare our result to current constraints from cosmological, astrophysical, and local tests in the well-studied case that the chameleon model reduces to an $f(R)$ model. The parameter f_{R0} characterizes the $f(R)$ model. Our Coma Cluster constraint is currently the tightest constraint on cosmological scales (see Section 4.2). In Ref. [44] a tighter constraint is obtained by using a technique developed from our approach which also shows its usefulness.

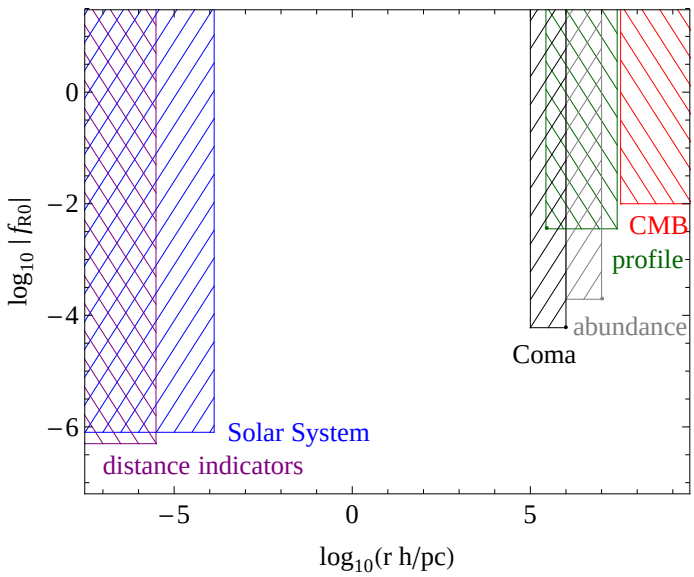

Figure 1.2: Comparison of our Coma Cluster constraint to current constraints on $f(R)$ gravity from the Solar System [14,65], distance indicators in unscreened dwarf galaxies [66], the cosmic microwave background (CMB) [67, 68], cluster density profiles [37] and abundance [34, 69]. The figure is adapted from [37]. Also compare to Fig. 2 (resp. 3) of [70, 71] for prospective constraints on $f(R)$ gravity.

Chapter 2

Galaxy clusters

2.1 Introduction to galaxy clusters

Galaxy clusters are the largest gravitationally bound systems in the universe. The orders of magnitude of physical quantities in a cluster are summarized in Table 2.1 The number density of galaxy clusters in the present universe is 10^{-5} Mpc^{-3}. Clusters contain more than 10 galaxies, but it is hard to know the exact number of galaxies in a cluster because of uncertainty in estimates of the number of dark galaxies. The system smaller than a cluster is called a galaxy group, but the boundary between clusters and groups is unclear because they are continuous objects. The matter density of a cluster is a few hundred times higher than that of the universe. The clusters are strictly not isolated systems because the environmental gas and galaxies are falling. The clusters are composed of dark matter, intracluster medium (ICM, hot baryon, gas) and galaxies (cold baryon). Their abundance ratios are summarized in Table. 2.2.

Table 2.1: Orders of magnitude in a galaxy cluster.

Scale	Order
$r_{\rm vir}$	$\sim$ Mpc
$M_{\rm vir}$	$\sim 10^{14} M_\odot$
$n_{\rm gas}$	$\sim 10^{-3}$cm^{-3}
$T_{\rm gas}$	$\sim 10^8$K ($\sim$ keV)

The dark matter is dominant and determines the gravitational behavior of galaxy clusters; its mass is roughly $M_{\rm vir} \sim 10^{14} M_\odot$. The dynamical time, $t_{\rm dyn}$, characterizes the time scale of the gravitational structure formation and is given by

$$t_{\rm dyn} \sim \frac{r_{\rm vir}}{\sigma_{\rm 1D}} \sim \sqrt{\frac{1}{G\bar{\rho}}} \tag{2.1}$$

$$\sim 4 \times 10^9 \left(\frac{\bar{\rho}}{10^{-24} {\rm g/cm^3}} \right)^{-1/2} \ {\rm yr} \tag{2.2}$$

for galaxy clusters, where $r_{\rm vir}$ is the size of a cluster, $\sigma_{\rm 1D} \sim \sqrt{GM_{\rm vir}/r_{\rm vir}}$ is the 1-dimensional velocity dispersion of the matter and $\bar{\rho} \sim 3M_{\rm vir}/4\pi r_{\rm vir}^3$ is the mean matter density. On the other hand, the age of the universe is given by

$$t_0 \sim 1.4 \times 10^{10} \ {\rm yr}. \tag{2.3}$$

Thus we have $t_{\rm dyn} \lesssim t_0$, which means that galaxy clusters contain information about the history of cosmological evolution because they evolve with the universe, while being roughly in dynamical equilibrium. So, galaxy clusters are important for investigating cosmological evolution, structure formation and the screening scale of modified gravity (see Section 1.4).

The ICM is mainly composed of electrons, protons, and helium gas, which are faint and smoothly distributed in clusters. The mean interval between each gas particle in a cluster is

$$d_{\rm mean} \sim n_{\rm gas}^{-1/3} \sim 10 \left(\frac{n_{\rm gas}}{10^{-3} {\rm cm^{-3}}} \right) \ {\rm cm}. \tag{2.4}$$

On the other hand, the mean free path determined by the Coulomb scattering of

Table 2.2: Components of a galaxy cluster.

Components	Mass ratio
Dark matter	$\sim 85\%$
ICM	$\sim 15\%$
Galaxies	$\sim 5\%$

electron or proton pairs is given by

$$\lambda_{\rm gas} \sim 20 \left(\frac{n_{\rm gas}}{10^{-3}{\rm cm}^{-3}}\right)^{-3} \left(\frac{T}{10^8{\rm K}}\right) \ {\rm kpc}. \tag{2.5}$$

Thus we have $d_{\rm mean} \ll \lambda_{\rm gas}$, which allows us to treat gases as fluids. In addition, the ratio of the energy of the electromagnetic interaction to the kinetic energy for each gas component is given by

$$\frac{e^2 n_{\rm gas}^{1/3}}{kT_{\rm gas}} \sim 10^{-12} \left(\frac{n_{\rm gas}}{10^{-3}{\rm cm}^3}\right) \left(\frac{T_{\rm gas}}{10^8{\rm K}}\right), \tag{2.6}$$

which is very small. Therefore, gas in clusters can be treated as perfect fluid, so the equation of motion for gas is given by

$$\dot{\boldsymbol{v}} + (\boldsymbol{v}\cdot\boldsymbol{\nabla})\boldsymbol{v} = -\frac{\boldsymbol{\nabla} P_{\rm gas}}{\rho_{\rm gas}} - \boldsymbol{\nabla}\Psi, \tag{2.7}$$

where $\boldsymbol{v}$ is the velocity of gas, $P_{\rm gas}$ is the gas pressure and Ψ is the gravitational potential. The sound crossing time which characterizes the time scale of structure formation by gas is given by

$$t_{\rm sound} = \frac{r_{\rm vir}}{c_{\rm s}} \sim 7 \times 10^8 \left(\frac{T_{\rm gas}}{10^8{\rm K}}\right)^{-1/2} \left(\frac{r_{\rm vir}}{\rm Mpc}\right) \ {\rm yr}, \tag{2.8}$$

where $c_{\rm s}$ is sound speed for monatomic gas. On the other hand, the free fall time which characterizes the time scale of the variation of the gravitational potential is given by

$$t_{\rm ff} = \sqrt{\frac{3\pi}{32G\bar{\rho}}} \sim 4 \times 10^9 \left(\frac{\rho}{100\rho_{\rm c0}}\right)^{-1/2} \ {\rm yr}. \tag{2.9}$$

Thus we have $t_{\rm sound} < t_{\rm ff}$, which means that the galaxy clusters are roughly in hydrostatic equilibrium. In this case, the velocity of gas can be set to $\boldsymbol{v} \sim \boldsymbol{0}$ in Eq. (2.7), which then reduces to

$$\frac{\boldsymbol{\nabla} P_{\rm gas}}{\rho_{\rm gas}} = -\boldsymbol{\nabla}\Psi. \tag{2.10}$$

Thus the gas distribution in a cluster is in balance with the gravitational force, which is important for our strategy to test modified gravity.

Dark matter and the ICM cause various physical phenomena, which allow us to observe galaxy clusters in a variety of different ways. In this chapter, we review the physical processes caused by a cluster's components: the physics of the ICM in Section 2.2 and the physics of dark matter in Section 2.3.

Throughout this chapter, we explicitly include the speed of light, c, and the reduced Planck constant, $\hbar$.

2.2 Intracluster medium

Because of ultraviolet rays emitted during the process of galaxy formation, the ICM is hot, which causes the ionization of gas. The ionized gas causes thermal radiation and the scattering of cosmic microwave background (CMB) photons. In this section, we review the thermal physical processes caused by the thermally ionized gas.

2.2.1 X-ray emission

In galaxy clusters, the X-ray emission is dominated by the bremsstrahlung and line emissions from heavy elements, such as iron and oxygen. The emissivity of this radiation is dominated and characterized by one in the thermalized system. In this subsection, we review the emissivity for the thermal bremsstrahlung and the line emissions.

Thermal bremsstrahlung

The bremsstrahlung is typically electromagnetic radiation produced by the deceleration of an electron when deflected by a proton, a quasi-quantum process that is reviewed in Appendix B.1.

The emissivity per unit time and per unit volume from two-body scattering is given by Eq. (B.9) as

$$dP \equiv \int_{b_{\min}}^{b_{\max}} n_{\rm e} n_{\rm i} \eta \hbar \omega d\omega 2\pi v b db = \frac{16\pi}{3\sqrt{3}} \frac{e^6 Z^2 n_{\rm e} n_{\rm i}}{v m_{\rm e}^2 c^3} g_{\rm ff} d\omega, \tag{2.11}$$

where

$$g_{\rm ff} \equiv \frac{\sqrt{3}}{\pi} \ln\left(\frac{b_{\max}}{b_{\min}}\right) \tag{2.12}$$

is the Gaunt factor for free-free emission. Here, for the ICM, the maximum value of

the integral interval is given by

$$b_{\max} \equiv \frac{v}{\omega} \tag{2.13}$$

and the minimum value of the integral interval is determined by the uncertainty relation $\Delta x \Delta p \lesssim \hbar$, with $\Delta x \sim b_{\min}$ and $\Delta p \sim m_{\rm e} v$, which gives

$$b_{\min} \equiv \frac{\hbar}{m_{\rm e} v}. \tag{2.14}$$

Using Eqs. (B.9), the emissivity of the frequency between ν and $\nu + d\nu$, per unit time and per unit volume from the thermal electron gas is given by

$$\epsilon_\nu^{\rm ff} d\nu \equiv \frac{\displaystyle\int_{v_{\min}}^{\infty} dv dP v^2 \exp\left(-\frac{m_{\rm e} v^2}{2kT}\right)}{\displaystyle\int_0^{\infty} dv v^2 \exp\left(-\frac{m_{\rm e} v^2}{2kT}\right)} \tag{2.15}$$

$$= \frac{2^5 \pi e^6}{3 m_{\rm e} c^3} \left(\frac{2\pi}{2m_{\rm e}}\right)^{1/2} n_{\rm e} \sum_j Z_j^2 n_{\rm i} \bar{g}_{\rm ff}(Z, T, \nu) \times (kT)^{-1/2} \exp\left(-\frac{h\nu}{kT}\right) d\nu, \tag{2.16}$$

where $\bar{g}_{\rm ff}$ is the Maxwell distribution weighted mean Gaunt factor, and we use that fact that electrons in thermal equilibrium satisfy

$$h\nu \leq \frac{1}{2} m_{\rm e} v^2, \tag{2.17}$$

when there is emission of photons with the energy $\hbar\omega = h\nu$, which gives the minimum value of the incident velocity, $v_{\min}$, as

$$v_{\min} = \sqrt{\frac{2\hbar\omega}{m_{\rm e}}}. \tag{2.18}$$

For X-ray observations, the emissivity is given by integrating Eq. (2.15) with respect to the frequency ν within the observable frequency range $[\nu_{\min}, \nu_{\max}]$,

$$\epsilon_{\rm ff} = \int_{\nu_{\min}(1+z)}^{\nu_{\max}(1+z)} \epsilon_\nu^{\rm ff} d\nu = \lambda_{\rm ff}(E_{\max}, E_{\min}, T, Z) n_{\rm e}^2. \tag{2.19}$$

in units of [ergs cm^{-3} s^{-1}], or

$$\epsilon_{\rm ff} = \int_{\nu_{\rm min}(1+z)}^{\nu_{\rm max}(1+z)} \frac{\epsilon_\nu^{\rm ff}}{h\nu} d\nu = \lambda_{\rm ff}(E_{\rm max}, E_{\rm min}, T, Z) n_{\rm e}^2 \tag{2.20}$$

in units of [counts cm^{-3} s^{-1}], where z is the redshift of the cluster and $\lambda_{\rm ff}$, in units of [ergs cm^3 s^{-1}] or [counts cm^3 s^{-1}], is the cooling function, which depends on the observable energy range, the electron temperature and the abundance of heavy elements.

Line emission

X-ray emissions from thermal gas in clusters include line emissions from heavy elements. For example, the energy levels of an ion having a single electron is given by

$$E_n = -13.6 \frac{Z_i^2}{n^2} \text{ eV}, \tag{2.21}$$

where Z_i is the charge of the ion and n is the principal quantum number. Thus the line emissions from the Ly-α ($n = 2 \rightarrow 1$) transitions of the ions listed in Table 2.3 are X-rays. The K-α ($n = 2 \rightarrow 1$) transition of Fe XXV having two electrons also emits an X-ray. The emissivity per unit time and per unit volume of the $n = k \rightarrow l$ transition of ion X_i is represented by

$$\epsilon_{\rm line} = \Gamma_{\rm line} n_{X_{i,k}}, \tag{2.22}$$

where $\Gamma_{\rm line}$ is the spontaneous transition rate per unit time and $n_{X_{i,k}}$ is the number density of ion, X_i, with energy level, k. Because the energy density of the photon in clusters is lower than that from blackbody radiation with the same temperature, the

Table 2.3: Ly-α ($n = 2 \rightarrow 1$) transitions for heavy elements

Ion	O VIII	Ne X	Mg XII	Si XIV	S XVI	Fe XXVI
Z_i	8	10	12	14	16	26
$E_2 - E_1$ [keV]	0.65	1.0	1.5	2.0	2.6	6.9

stimulated radiation can be neglected. So $\Gamma_{\rm line}$ does not depend on the temperature of the ion. Even though $n_{X_{i,k}}$ is determined by the detailed balance between the energy levels, the main process of excitation is the collision with electrons in clusters. In this case, we have $n_{X_{i,k}} \propto n_{\rm e} n_{X_j}$. Then Eq. (2.22) reduces to

$$\epsilon_{\rm line} = f_{\rm line}(T) Z n_{\rm e}^2 = \lambda_{\rm line}(T, Z) n_{\rm e}^2, \tag{2.23}$$

where $f_{\rm line}$ is a function determined for each transition, which depends on the temperature of the ion in thermal and ionized equilibrium, and $\lambda_{\rm line}$ is the cooling function for the transition.

Surface brightness

Using Eqs. (2.19) and (2.23), the total emissivity of the X-ray emission for the ICM electron gas in thermal and ionized equilibrium can be represented as

$$\epsilon_{\rm X} = \epsilon_{\rm ff} + \epsilon_{\rm line} = (\lambda_{\rm ff} + \lambda_{\rm line}) n_{\rm e}^2 = \lambda_{\rm c} n_{\rm e}^2 \tag{2.24}$$

where $\lambda_{\rm c}$ is the cooling function for the thermal bremsstrahlung and line emission.

The observed X-ray flux is given by

$$F = \frac{1}{4\pi D_{\rm L}(z)^2} \int_{r<r_{\rm max}} \epsilon_{\rm X} dV, \tag{2.25}$$

where $D_{\rm L}$ is the luminosity distance and $r_{\rm max}$ is the observable maximum radius. Here, we decompose the volume element, dV, into the line of sight, dl, and the solid angle on the celestial sphere, $d\theta^2$,

$$dV = D_{\rm A}(z)^2 dl d\theta^2, \tag{2.26}$$

where $r^2 = l^2 + D_{\rm A}^2 \theta^2$, $D_{\rm A} = (1+z)^{-2} D_{\rm L}$ is the angular diameter distance, and $D_{\rm A} \gg r$. Using this relation, we obtain the observed surface brightness in units of [ergs/cm^2/s/rad^2] or [counts/cm^2/s/rad^2] by integrating the emissivity along the line of sight, l,

$$S(r_\perp) = \frac{D_{\rm A}^2}{4\pi D_{\rm L}^2} \int \epsilon_{\rm X}(r) dl \tag{2.27}$$

$$= \frac{1}{4\pi (1+z)^4} \int \lambda_{\rm c} n_{\rm e}(r)^2 dl, \tag{2.28}$$

where $r_\perp = \theta D_\mathrm{A}$ is the perpendicular radius with the apparent angle, θ, from the cluster center.

2.2.2 Sunyaev–Zel'dovich effect

The cosmic microwave background (CMB) is an evidence of the Big-Bang universe and its secondary anisotropy is important for galaxy clusters.

The intensity of the CMB follows a practically isotropic perfect blackbody distribution which is given by the Planck distribution,

$$I_\nu(\nu) = \frac{2h\nu^3}{c^2}\left[\exp\left(\frac{h\nu}{kT_\mathrm{CMB}(z)}\right) - 1\right]^{-1}, \tag{2.29}$$

where ν is the frequency of the CMB photon, $h = 2\pi\hbar$ is the Planck constant, k is the Boltzmann constant and $T_\mathrm{CMB}(z) = T_\mathrm{CMB,0}(1+z)$ is the CMB temperature at redshift z, with the present CMB temperature being $T_\mathrm{CMB,0} = 2.725$ K. Note that $I_\nu \propto (1+z)^3$ because $T_\mathrm{CMB} \propto (1+z)$ and $\nu \propto (1+z)$.

When the CMB photons pass through a galaxy cluster, their intensity is shifted by inverse Compton scattering caused by hot electrons in the cluster, which is called the Sunyaev–Zel'dovich (SZ) effect [72]. The process of inverse Compton scattering is reviewed in Appendix B.2. The radial intensity profile of inverse Compton scattering, given by Eq. (B.20), is

$$\frac{\Delta I_\nu^\mathrm{(SZ)}(\nu, r_\perp)}{I_\nu(\nu)} = \frac{1}{4\pi I_\nu(\nu)}\int n_\mathrm{e}(r)\frac{dW_\mathrm{SZ}(\nu, T_\mathrm{e}(r))}{dtd\nu}dl, \tag{2.30}$$

where $\Delta I_\nu^\mathrm{(SZ)}$ is the difference between the intensities after and before scattering, $dW_\mathrm{SZ}/dtd\nu$ is the emissivity per unit time and per unit frequency caused by an electron, and $r = \sqrt{r_\perp^2 + l^2}$. The lowest order of Eq. (B.29), which corresponds to the case of the Maxwell distribution

$$f_\mathrm{M}(v)dv = 4\pi\left(\frac{m_\mathrm{e}}{2\pi kT_\mathrm{e}}\right)^{3/2}\exp\left(-\frac{m_\mathrm{e}v^2}{2kT_\mathrm{e}}\right)v^2dv \tag{2.31}$$

for thermal electrons, gives the SZ spectrum as

$$\begin{aligned}\frac{dW_\mathrm{SZ}(\nu)}{dtd\nu} &= \int\frac{dW_\mathrm{IC}(\nu, v)}{dtd\nu}f_\mathrm{M}(v)dv/c \\ &\simeq 4\pi\sigma_\mathrm{T}I_\nu(\nu)\frac{xe^x}{e^x-1}\left[\theta_\mathrm{e}\left(-4 + x\coth\left(\frac{x}{2}\right)\right) + \beta_\mathrm{b}\mu\right],\end{aligned} \tag{2.32}$$

where $\beta_{\rm b}$ is the bulk velocity of the cluster electrons and μ is the angle of the bulk motion. The first term of Eq. (2.32) gives isotropic radiation which is called the *thermal SZ effect*, and the second term of Eq. (2.32) gives anisotropic radiation depending on the bulk motion of cluster electrons, which is called the *kinematic SZ effect*.

Thermal SZ effect

Assuming an isotropic distribution for electrons in the rest frame of CMB photons, the second term of Eq. (2.32) vanishes when integrating with respect to angle, μ, so we obtain

$$\frac{\Delta I_\nu^{(\rm TSZ)}(\nu, r_\perp)}{I_\nu(\nu)} = \frac{xe^x}{e^x - 1}\left(x\coth\frac{x}{2} - 4\right)y \tag{2.33}$$

where we define the Compton-y parameter as

$$y \equiv \int dl \sigma_{\rm T} n_{\rm e} \frac{k_{\rm B}T}{m_{\rm e}c^2} \tag{2.34}$$

Kinematic SZ effect

When the electrons in a cluster have bulk velocity, the second term of Eq. (2.32) is not negligible, which gives

$$\frac{\Delta I_\nu^{(\rm kSZ)}(\nu, r_\perp)}{I_\nu(\nu)} = \frac{1}{I_\nu(\nu)}\int n_{\rm e}\frac{dW_{\rm SZ}(\nu)}{dtd\nu\Omega}dz \tag{2.35}$$

$$= \frac{xe^x}{e^x - 1}\int dl\sigma_{\rm T} n_{\rm e}\mu\beta \tag{2.36}$$

$$= \frac{xe^x}{e^x - 1}\tau_{\rm e}\frac{\bar{v}_\parallel}{c} \tag{2.37}$$

where $\tau_{\rm e}$ is the optical depth for Thomson scattering and $\bar{v}_\parallel$ is the mean velocity toward the line of sight of the bulk motion of the electron gas.

2.3 Dark matter

The presence of dark matter is one of the fundamental mysteries of cosmology, and it is also important for galaxy clusters. Assuming that the gravitational potential,

galaxy kinematic energy, and gas temperature energy are of the same order,

$$\sigma_{\rm 1D}^2 \sim \frac{kT_{\rm gas}}{m_{\rm p}} \sim \frac{GM_{\rm vir}}{r_{\rm vir}}, \tag{2.38}$$

we can estimate the total cluster mass from optical and X-ray observations as

$$M_{\rm vir} \sim 3 \times 10^{14} \left(\frac{\sigma_{\rm 1D}}{1000 \text{ km/s}} \right)^2 \left(\frac{r_{\rm vir}}{\rm Mpc} \right) \ M_\odot, \tag{2.39}$$

and

$$M_{\rm vir} \sim 2 \times 10^{14} \left(\frac{kT_{\rm gas}}{10^8 \text{ K}} \right) \left(\frac{r_{\rm vir}}{\rm Mpc} \right) \ M_\odot. \tag{2.40}$$

Eqs. (2.39) and (2.40) are of the same order; however, the sum of the masses of a galaxy and its gas is only 20% of $M_{\rm vir}$. It is therefore suggested that there is a large amount of dark matter in galaxy clusters, which dominates their gravitational behavior. Many N-body simulations provide information about the nonlinear evolution of dark matter. These simulations suggest that the radial profile of dark matter in a galaxy cluster is the Navarro–Frenk–White (NFW) profile [73],

$$\rho(r) = \frac{\rho_{\rm s}}{r/r_{\rm s}(1 + r/r_{\rm s})^2}. \tag{2.41}$$

It is known that this profile roughly agrees with many observations.

Chapter 3

Modeling of cluster profiles

We review our model focusing on connecting gas distributions with observational quantities (the X-ray brightness, X-ray temperature and Sunyaev–Zel'dovich [SZ] effect profiles). Our gas distribution model is based on an assumption of hydrostatic equilibrium, which is a key assumption needed to connect with modifications of gravity. We also review the tangential shear profile due to weak- gravitational lensing. At the end of this chapter, we review analytic solutions for modifications of gravity in spherical symmetric systems, and construct the modified cluster profiles.

3.1 Matter distribution profile

We assume that the dark matter component dominates over the baryonic contribution in the cluster and that the matter density of the cluster, ρ, is well described by

$$\rho(r) = \rho_{\rm s} y_{\rm m}(r/r_{\rm s}), \tag{3.1}$$

where $\rho_{\rm s}$ and $r_{\rm s}$ are parameters, and the dimensionless profile, $y_{\rm m}$, is given by a generalized NFW profile [74],

$$y_{\rm m}(x) = \frac{1}{x(1+x)^b}. \tag{3.2}$$

Taking $b = 2$, Eq. (3.2) corresponds to the NFW profile (2.41) which is motivated by predictions from numerical simulations [73]. The mass enclosed within a radius

r, $M(<r)$, is given by a volume integral of Eq. (3.1):

$$M(<r) = 4\pi \int_0^r dr r^2 \rho(r) = 4\pi \rho_{\rm s} r_{\rm s}^3 m(r/r_{\rm s}), \tag{3.3}$$

where

$$m(x) \equiv \int_0^x du u^2 y_{\rm m}(u) = \begin{cases} \dfrac{-1+x^2-bx(1+x)+(1+x)^b}{(b-2)(b-1)(1+x)^b} & \text{for } b \neq 2 \\ \ln(1+x) - \dfrac{x}{1+x} & \text{for } b = 2 \end{cases}. \tag{3.4}$$

Note that the NFW proifle is based on N-body dark matter simulations of the concordance model. It is nontrivial to extend this assumption to modified gravity models. However, it was shown in [38] that the NFW profile provides equally good fits for $f(R)$ clusters as it does for the Newtonian scenario. This was shown using N-body simulations of the Hu-Sawicki $f(R)$ gravity model corresponding to $\beta = \sqrt{1/6}$, which characterizes only a subgroup of the more general chameleon model studied here. The effects of the modifications on observables are, however, qualitatively similar between different values of the coupling strength β and can even partially be mapped into each other, suggesting the applicability of the NFW profile. Its validity for the full range of the parameters considered in this paper may still be worthwhile checking using N-body simulations. From an observational perspective, recent work b [75, 76] supports the consistency of the NFW profile with measurements. Hence, even independent of the simulation results, the NFW profile could be used for the reconstruction of the lensing mass with the same motivation as introducing the gas profiles in the reconstruction of the hydrostatic mass in Chapter 4.

Here, we introduce the virial mass, $M_{\rm vir}$, and the concentration, c, instead of $r_{\rm s}$ and $\rho_{\rm s}$,

$$M_{\rm vir} \equiv M(<r_{\rm vir}) = \frac{4\pi}{3} r_{\rm vir}^3 \Delta_{\rm c}(z) \rho_c(z), \tag{3.5}$$

$$c \equiv \frac{r_{\rm vir}}{r_{\rm s}}, \tag{3.6}$$

where $r_{\rm vir}$ is the virial radius, which is defined by

$$r_{\rm vir} = \left[\frac{M_{\rm vir}}{(4\pi/3)\Delta_{\rm c}(z)\rho_{\rm c}(z)} \right]^{1/3}, \tag{3.7}$$

and $\Delta_{\rm c}(z)$ is the critical overdensity contrast, which is the ratio of the mean matter

density within the virial radius, $\bar{\rho}(< r_{\rm vir})$, to the critical density,

$$\Delta_{\rm c}(z) \equiv \frac{\bar{\rho}(< r_{\rm vir})}{\rho_{\rm c}(z)}, \tag{3.8}$$

given by spherical collapse models [77–80]. We adopt $\Delta_{\rm c} = 100$ based on Ref. [80] with $z \sim 0$. Note that the critical overdensity contrast, $\Delta_{\rm c}$, generally depends on the modified gravity parameters. For example, the authors in Ref. [81] found $\Delta_{\rm c} \sim 80$ in an $f(R)$ model, which is equivalent to $\Delta_{\rm vir} \sim 300$ at redshift $z \sim 0$. Nonetheless, our final conclusion is independent of this modification of $\Delta_{\rm c}$ because our analysis includes the parameters $M_{\rm vir}$ and c, which re degenerate with $\Delta_{\rm c}$. Therefore, the change of $\Delta_{\rm c}$ only introduces shifts in the values of $M_{\rm vir}$ and c.

The relations between $M_{\rm vir}$, c, $r_{\rm s}$ and $\rho_{\rm s}$ are

$$r_{\rm s} = \frac{1}{c}\left[\frac{M_{\rm vir}}{(4\pi/3)\Delta_{\rm c}(z)\rho_{\rm c}(z)}\right]^{1/3}, \tag{3.9}$$

$$\rho_{\rm s} = \frac{M_{\rm vir}}{4\pi r_{\rm s}^3 m(c)}. \tag{3.10}$$

In addition, we introduce the radius at which the mean matter density corresponds to the cosmological reference density, $r_{\Delta{\rm ref}}$, its concentration, $c_{\Delta{\rm ref}} = r_{\Delta{\rm ref}}/r_{\rm s}$), and the mass enclosed within this radius, $M_{\Delta{\rm ref}} \equiv M(< r_{\Delta{\rm ref}})$. Using Eqs. (3.5) and (3.6), the relations between $r_{\Delta{\rm ref}}$ and $M_{\Delta{\rm ref}}$ are

$$c_{\Delta{\rm ref}} = \frac{r_{\Delta{\rm ref}}}{r_{\rm s}} = \frac{1}{r_{\rm s}}\left[\frac{M_{\Delta{\rm ref}}}{(4\pi/3)\Delta\rho_{\rm ref}(z)}\right]^{1/3}, \tag{3.11}$$

and

$$M_{\Delta{\rm ref}} = \frac{m(r_{\Delta{\rm ref}}/r_{\rm s})}{m(c)} M_{\rm vir}, \tag{3.12}$$

where the reference density is $\rho_{\rm ref} = \rho_{\rm c}$ or $\rho_{\rm m}$. We note that $\rho_{\rm m}(z) = \Omega_{\rm m}(z)\rho_{\rm c}(z)$. From Eqs. (3.11) and (3.12), we can compute $r_{\Delta{\rm ref}}$ and $M_{\Delta{\rm ref}}$ when c and $M_{\rm vir}$ are given.

Gravitational potential

The gravitational potential is given by the Poisson equation,

$$\triangle\Psi = \frac{1}{2M_{\rm Pl}}\rho. \tag{3.13}$$

Assuming that the matter distribution of the cluster is given by Eq. (3.1), we can solve Eq. (3.13) to get

$$\Psi(r) = -\frac{GM(<r)}{r^2} = \begin{cases} -\Psi_0 \dfrac{1-(1+r/r_{\rm s})^{2-b}}{(b-2)r/r_{\rm s}} & \text{for } b \neq 2 \\ -\Psi_0 \dfrac{\ln(1+r/r_{\rm s})}{r/r_{\rm s}} & \text{for } b = 2 \end{cases}, \tag{3.14}$$

where $x = r/r_{\rm s}$ and

$$\Psi_0 \equiv \frac{\rho_{\rm s} r_{\rm s}^2}{2M_{\rm Pl}^2(b-1)} \tag{3.15}$$

is the gravitational potential at the center of the cluster.

3.2 Gas distribution profiles

In this section, we construct the radial distribution profiles of the thermal gas described by the gas pressure, $P_{\rm gas}$, the gas temperature, $T_{\rm gas}$, and the gas density, $\rho_{\rm gas}$.

3.2.1 Equation of state for gas components

First, we summarize the equation of state for gas components. The intracluster medium is dominated by ionized Hydrogen and Helium gas. In this section, assuming complete ionization of the gas, we review the equation of state for the gas components. In the following, n_i and m_i are the number density and mass, and their subscripts, $i =$ e, p, H, He, denote the electron, proton, hydrogen and helium, respectively.

We define the mean molecular weight μ as

$$(n_{\rm e} + n_{\rm H} + n_{\rm He})\mu m_{\rm p} = m_{\rm H} n_{\rm H} + m_{\rm He} n_{\rm He}, \tag{3.16}$$

where we neglect the electron mass. Assuming an electrically neutral intracluster gas, we then have

$$n_{\rm e} = n_{\rm H} + 2n_{\rm He}. \tag{3.17}$$

Using Eqs. (3.16) and (3.17), we obtain the mean molecular weight as

$$\mu = \frac{n_{\rm H} + 4n_{\rm He}}{2n_{\rm H} + 3n_{\rm He}} = \frac{4}{3 + 5X} \simeq 0.59, \tag{3.18}$$

where we use the approximations $m_{\rm H} \sim m_{\rm p}$ and $m_{\rm He} \sim 4m_{\rm p}$, and an abundance ratio between Hydrogen and Helium of $X = n_{\rm H}/(n_{\rm H} + 4n_{\rm He}) \simeq 0.75$.

Here we define the gas number density as $n_{\rm gas} = n_{\rm e} + n_{\rm H} + n_{\rm He}$. Assuming that the intracluster gas is an ideal fluid, the equation of motion for the intracluster gas can be written as

$$P_{\rm gas} = n_{\rm gas} k T_{\rm gas} = \frac{\rho_{\rm gas} k T_{\rm gas}}{\mu m_{\rm p}}, \tag{3.19}$$

where k is the Boltzmann constant, $P_{\rm gas}$ is the gas pressure, $T_{\rm gas}$ is the gas temperature, and $\rho_{\rm gas}$ is the gas density. Assuming the gas temperature is equal to the electron temperature, that is $T_{\rm gas} = T_{\rm e}$, the equation of state for the electron is

$$P_{\rm e} = n_{\rm e} k T_{\rm e} = \frac{2(X+1)}{5X+3} P_{\rm gas} = \frac{2+\mu}{5} P_{\rm gas}, \tag{3.20}$$

where $P_{\rm e}$ is the electron pressure, and we use the relation

$$n_{\rm e} = \frac{2(X+1)}{5X+3} n_{\rm gas} = \frac{2+\mu}{5} n_{\rm gas}. \tag{3.21}$$

Note that the assumption of $T_{\rm gas} = T_{\rm e}$ is nontrivial because the equipartition timescale between electrons and protons through Coulomb collisions is close to the dynamical timescale of the cluster (see, e.g., [82]).

3.2.2 Hydrostatic equilibrium

We first assume hydrostatic equilibrium in the spherically symmetric system as

$$\frac{1}{\rho_{\rm gas}} \frac{dP_{\rm gas}}{dr} = -\frac{d\Psi}{dr}. \tag{3.22}$$

Assuming the gas physics described in Section (3.2.1), we derive the solution of Eq. (3.22). We review some solutions of Eq. (3.22) to link with observations of gas distributions in the following subsections.

3.2.3 Polytropic model

Here we derive the gas distribution profiles based on [83–85]. We assume the polytropic equation of state for thermal gas:

$$P_{\rm gas} \propto \rho_{\rm gas} T_{\rm gas} \propto \rho_{\rm gas}^{\gamma}, \tag{3.23}$$

where γ is the polytropic index. Using the dimensionless gas profile $y_{\rm gas}$, we can write

$$\rho_{\rm gas}(r) = \rho_{\rm gas,0} y_{\rm gas}(r), \tag{3.24}$$
$$T_{\rm gas}(r) = T_{\rm gas,0} y_{\rm gas}^{\gamma-1}(r), \tag{3.25}$$
$$P_{\rm gas}(r) = P_{\rm gas,0} y_{\rm gas}^{\gamma}(r), \tag{3.26}$$

where $P_{\rm gas,0}$, $\rho_{\rm gas,0}$ and $T_{\rm gas,0}$ are the pressure, density and temperature at the cluster center, satisfying the equation of state

$$P_{\rm gas,0} = \frac{k T_{\rm gas,0} \rho_{\rm gas,0}}{\mu m_{\rm p}}, \tag{3.27}$$

and $y_{\rm gas}(0) = 1$. Under the assumption of hydrostatic equilibrium (Eq. (3.22)), we can obtain a differential equation for $y_{\rm gas}$,

$$\frac{d y_{\rm gas}^{\gamma-1}}{dr} = -\frac{\mu m_{\rm p}}{k T_{\rm gas,0}} \left(\frac{\gamma - 1}{\gamma} \right) \frac{d\Psi}{dr}, \tag{3.28}$$

which has the solution

$$y_{\rm gas} = \left\{ 1 - \frac{\mu m_{\rm p}}{k T_{\rm gas,0}} \left(\frac{\gamma - 1}{\gamma} \right) [\Psi(r) - \Psi(0)] \right\}^{1/(\gamma-1)} \tag{3.29}$$

for the dimensionless gas profile.

3.2.4 Non-polytropic model

Here, we consider two models as the solution of hydrostatic equilibrium (3.22) without the polytropic relation.

Model A ($n_{\rm e}$-based model)

For the electron number density profile, we assume the functional form of the so-called β-model [86]:

$$n_{\rm e} = n_0 \left[1 + \left(\frac{r}{r_1}\right)^2\right]^{-b_1} \tag{3.30}$$

where n_0 is the electron number density at the cluster center, and b_1 and r_1 are parameters. The β-model is well-established to represent the observed surface brightness of galaxy clusters with low angular resolution. Integrating Eq. (3.22) and using Eq. (3.30), we obtain the electron pressure profile

$$P_{\rm e} = n_0 T_0 + \mu m_{\rm p} \int_0^r dr n_{\rm e}(r) \left[-\frac{d\Psi}{dr}\right], \tag{3.31}$$

where T_0 is the electron temperature at the cluster center. Then, the electron temperature profile is given by $kT_{\rm e}(r) = P_{\rm e}(r)/n_{\rm e}(r)$ from Eqs. (3.30) and (3.31). Model A is thus characterized by 6 parameters: $M_{\rm vir}$, c, n_0, T_0, b_1, and r_1.

Model B ($T_{\rm e}$-based model)

For the electron temperature profile, we assume the functional form

$$T_{\rm e}(r) = T_0 \left[1 + \left(\frac{r}{r_1}\right)^{b_1}\right]^{-b_2/b_1}, \tag{3.32}$$

where T_0 is the electron temperature at the cluster center and b_1, b_2 and r_1 are parameters. Integrating Eq. (3.22) and using Eq. (3.32), we obtain the electron pressure profile

$$P_{\rm e}(r) = n_0 T_0 \exp\left(\int_0^r dr \frac{\mu m_{\rm p}}{kT_{\rm e}(r)} \left[-\frac{d\Psi}{dr}\right]\right), \tag{3.33}$$

where n_0 is the electron number density at the cluster center. Then, the electron number density profile is given by $n_{\rm e}(r) = P_{\rm e}(r)/kT_{\rm e}(r)$ from Eqs. (3.33) and (3.32). The model B is thus characterized by 7 parameters: $M_{\rm vir}$, c, n_0, T_0, b_1, b_2, and r_1.

3.2.5 Observables

Using our model of the 3-dimensional profiles, we construct the observables for X-rays and the cosmic microwave background (CMB) temperature distortion by the SZ effect.

X-ray surface brightness

The X-ray surface brightness, which reflects X-ray emission from thermal bremsstrahlung emission and line emission, is given by Eq. (2.27),

$$S_{\rm X}(r_\perp) = \frac{1}{4\pi(1+z)^4}\int_{-\infty}^{\infty} n_{\rm e}^2(r)\lambda_{\rm c}(r)dl, \tag{3.34}$$

where $r_\perp = \sqrt{r^2+l^2}$ is the radius perpendicular to the line-of-sight, l, and $\lambda_{\rm c}$ is the cooling function, which depends on the electron temperature, abundance of heavy elements and observable energy range (e.g., [87]). Here, to estimate the cooling function, we use XSPEC [88], adopting the thermal plasma emission spectra model with the APEC code [89]. The XSPEC software gives the X-ray flux based on the APEC model. The X-ray flux can be converted to the cooling function by the flux-luminosity relation.

We also define the X-ray brightness as $B_{\rm X} \equiv norm/area$, where *norm* is the spectrum normalization obtained from the XSPEC software [88] using the APEC emission spectrum [89], and *area* is the area of the spectrum. The spectrum normalization is given by $norm \propto \int n_{\rm e} n_{\rm H} dV$, where $n_{\rm H} = 0.86 n_{\rm e}$ is the hydrogen number density and V is the volume of the spectrum. Then, we write the X-ray brightness as

$$B_{\rm X}(r_\perp) = \frac{10^{-14}}{4\pi(1+z)^2}\int_{-\infty}^{\infty} n_{\rm e}(r) n_{\rm H}(r) dl \ [{\rm cm}^{-5}/{\rm arcmin}^2]. \tag{3.35}$$

X-ray temperature

The thermal gas temperature is given by a spectral fit of the observed X-ray spectrum, which is represented by a weighted temperature,

$$T_{\rm X}(r_\perp) = \frac{\displaystyle\int_{-\infty}^{\infty} W(r) T_{\rm gas}(r) dl}{\displaystyle\int_{-\infty}^{\infty} W(r) dl}, \tag{3.36}$$

where $r_\perp = \sqrt{r^2 + l^2}$ the radius perpendicular to the line-of-sight, l, and W is the weight factor which is given by $W = n_{\rm e}^2 T_{\rm gas}^{1/2}$ for the emission-weighted temperature and as $W = n_{\rm e}^2 T_{\rm gas}^{-3/4}$ for the spectroscopic-like temperature. Because the emission-weighted temperature is systematically higher than the actual measurement, the spectroscopic-like temperature was proposed by [90] to avoid this systematic error. In this thesis, we use the emission-weighted temperature to avoid numerical singularities.

Compton-y parameter

The CMB temperature distortion is caused by CMB photons passing through clusters and being scattered by electrons in the clusters, namely, the SZ effect. The difference between the averaged CMB temperature and the observed CMB temperature, $\Delta T_{\rm SZ}$, or y-parameter can be expressed as

$$y(r_\perp) = -\frac{\Delta T_{\rm SZ}}{2T_{\rm CMB}} = \frac{\sigma_{\rm T}}{m_{\rm e}} \int P_{\rm e}(r) dl, \tag{3.37}$$

where $r_\perp = \sqrt{r^2 + l^2}$ is the radius perpendicular to the line-of-sight, l, and $T_{\rm CMB} = 2.725$ K is the CMB temperature, $\sigma_{\rm T}$ is the Thomson cross section and $m_{\rm e}$ is the electron mass.

3.3 Tangential shear profile due to weak-gravitational lensing

We consider a spatially flat cosmological background, and work with the cosmological Newtonian gauge, in which a line element is written as

$$ds^2 = -(1 + 2\Psi(t, \mathbf{x}))dt^2 + a(t)^2(1 + 2\Phi(t, \mathbf{x}))d\mathbf{x}^2, \tag{3.38}$$

where a is the scale factor, and Ψ and Φ are the gravitational and curvature potentials, respectively. The propagation of light is determined by the lensing potential $(\Phi - \Psi)/2$, which means that the weak-lensing signal is determined by $(\Phi - \Psi)/2$. For example, the convergence is given by

$$\kappa = -\frac{1}{2} \int_0^\chi d\chi' \frac{(\chi - \chi')\chi'}{\chi} \triangle^{(\rm 2D)}(\Phi - \Psi), \tag{3.39}$$

where χ is the comoving distance and $\triangle^{(\rm 2D)}$ is the comoving two-dimensional Laplacian. For the case of general relativity, we set $\triangle\Psi = -\triangle\Phi = 4\pi G a^2 \rho$. Then, using

the thin lens approximation, (3.39) reduces to

$$\kappa = \frac{(\chi_{\rm S} - \chi_{\rm L})\chi_{\rm L}}{\chi_{\rm S}} \int_0^{\chi_{\rm S}} d\chi' \left[4\pi G\rho(r')\right] a_{\rm L}^2, \tag{3.40}$$

where $\chi_{\rm L}$ and $\chi_{\rm S}$ denote the comoving distance between the observer and lens and that between the observer and the source, respectively, and $a_{\rm L} = 1/(1+z_{\rm L})$ is the scale factor specified by the redshift of the lensing object, $z_{\rm L}$. For a spherically symmetric cluster, (3.40) is given by

$$\kappa(r_\perp) = \frac{2}{\Sigma_{\rm c}} \int_0^\infty dz \rho(r) \tag{3.41}$$

with the physical coordinate $r = \sqrt{r_\perp^2 + z^2}$. We define the critical surface mass density, $\Sigma_{\rm c} = \chi_{\rm S}/[4\pi G(\chi_{\rm S} - \chi_{\rm L})\chi_{\rm L} a_{\rm L}]$. We then define the reduced shear

$$g_+(r_\perp) \equiv \frac{\gamma_+(r_\perp)}{1 - \kappa(r_\perp)}, \tag{3.42}$$

where $\gamma_+(r_\perp)$ is the tangential shear, which is related to the convergence by

$$\gamma_+(r_\perp) = \bar{\kappa}(< r_\perp) - \kappa(r_\perp), \tag{3.43}$$

with

$$\bar{\kappa}(< r_\perp) \equiv \frac{2}{r_\perp^2} \int_0^{r_\perp} dr'_\perp r'_\perp \kappa(r'_\perp). \tag{3.44}$$

For the NFW profile, the convergence (3.40) can be integrated to obtain [91]

$$\kappa_{\rm nfw}(x) = \begin{cases} \dfrac{2r_{\rm s}\rho_{\rm s}}{\Sigma_{\rm c}(x^2-1)} \left[1 - \dfrac{2}{\sqrt{1-x^2}} \mathrm{arctanh}\sqrt{\dfrac{1-x}{1+x}}\right], & (x<1) \\ \dfrac{2r_{\rm s}\rho_{\rm s}}{3\Sigma_{\rm c}}, & (x=1) \\ \dfrac{2r_{\rm s}\rho_{\rm s}}{\Sigma_{\rm c}(x^2-1)} \left[1 - \dfrac{2}{\sqrt{x^2-1}} \arctan\sqrt{\dfrac{x-1}{1+x}}\right], & (x>1) \end{cases} \tag{3.45}$$

and Eq. (3.41) also can be integrated to obtain

$$\bar{\kappa}_{\rm nfw}(<x) = \begin{cases} \dfrac{4r_{\rm s}\rho_{\rm s}}{\Sigma_{\rm c}x^2}\left[\dfrac{2}{\sqrt{1-x^2}}{\rm arctanh}\sqrt{\dfrac{1-x}{1+x}} + \ln\left(\dfrac{x}{2}\right)\right], & (x<1) \\ \dfrac{4r_{\rm s}\rho_{\rm s}}{\Sigma_{\rm c}}\left[1+\ln\left(\dfrac{1}{2}\right)\right], & (x=1) \\ \dfrac{4r_{\rm s}\rho_{\rm s}}{\Sigma_{\rm c}x^2}\left[\dfrac{2}{\sqrt{x^2-1}}\arctan\sqrt{\dfrac{x-1}{1+x}} + \ln\left(\dfrac{x}{2}\right)\right], & (x>1) \end{cases} \tag{3.46}$$

with $x = r/r_{\rm s}$.

Here, we assume that the source galaxies have a random orientation of ellipticity, $\epsilon_{\rm S}$, the average of which is $\langle\epsilon_{\rm S}\rangle = 0$. Once the tangential ellipticity of the source galaxies, $\epsilon_{\rm obs}$ is averaged, we obtain an average lensing signal from galaxy clusters $g_+ = \langle\epsilon_{\rm obs.}\rangle$ due to the random orientations.

3.4 Modification of gravitational and lens potentials

3.4.1 Chameleon field

We first review an analytic solution for the chameleon field for a spherically symmetric galaxy cluster [42, 92, 93]. Next, we construct the gas distribution profile using the analytic solution assuming a polytropic gas distribution, and review how the modification of gravity affects the gas distribution.

The equation of motion for the chameleon field is given by Eq. (1.27):

$$\nabla^2\phi(r) = V_{,\phi} + \frac{\beta}{M_{\rm Pl}}\rho(r), \tag{3.47}$$

where we assume the potential $V(\phi) = \Lambda^{4+n}/\phi^n$, and use the approximation, $\beta\phi/M_{\rm Pl} \ll 1$. In the inner region of the cluster we assume the condition

$$\frac{M_{\rm Pl}\nabla^2\phi}{\beta\rho(r)} \ll 1. \tag{3.48}$$

In this case, Eq. (3.47) reduces to

$$0 \simeq V_{,\phi} + \frac{\beta}{M_{\rm Pl}}\rho(r). \tag{3.49}$$

Assuming the generalized NFW matter distribution profile given in Eq. (3.2), Eq. (3.49)

gives an inner solution for the chameleon field of

$$\phi_{\rm int}(x) = \phi_{\rm s}[x(1+x)^b]^{1/(n+1)}, \tag{3.50}$$

where $x = r/r_{\rm s}$ and

$$\phi_{\rm s} \equiv \left(\frac{n\Lambda^{n+4}M_{\rm Pl}}{\beta\rho_{\rm s}}\right)^{1/(n+1)}. \tag{3.51}$$

Next, for the outer region of the cluster, we assume the condition

$$V_{,\phi} \ll \nabla^2\phi. \tag{3.52}$$

In this case, Eq. (3.47) reduces to

$$\nabla^2\phi(r) \simeq \frac{\beta\rho(r)}{M_{\rm Pl}}. \tag{3.53}$$

Assuming the generalized NFW matter distribution profile in Eq. (3.2), Eq. (3.53) gives an outer solution for the chameleon field of

$$\phi_{\rm ext}(x) = \begin{cases} -2\beta\phi_0\dfrac{1-(1+x)^{2-b}}{(b-2)x} - \dfrac{C}{x} + \phi_\infty, & b \neq 2 \\ -2\beta\phi_0\dfrac{\log(1+x)}{x} - \dfrac{C}{x} + \phi_\infty, & b = 2 \end{cases} \tag{3.54}$$

where C and ϕ_∞ are the integration constants. The constant ϕ_∞, which defined by $\phi_\infty = \phi(r=\infty)$, is the background chameleon field.

C and ϕ_∞ are related by connecting the inner solution and the outer solution at the radius $x_{\rm c}$,

$$C = -2\beta\phi_0\frac{1-(1+x_{\rm c})^{2-b}}{b-2} + \phi_\infty x_c - \phi_{\rm s}[x_{\rm c}(1+x_{\rm c})^b]^{1/(n+1)}x_{\rm c}, \tag{3.55}$$

$$\phi_\infty - 2\beta\phi_0(1+x_{\rm c})^{1-b} = \phi_{\rm s}(x_{\rm c}(1+x_{\rm c})^b)^{1/(n+1)}\left(1 + \frac{(1+b)x_{\rm c}+1}{(n+1)(1+x_{\rm c})}\right), \tag{3.56}$$

for $b \neq 2$, and

$$C = -2\beta\phi_0\ln(1+x_{\rm c}) + \phi_\infty x_{\rm c} - \phi_{\rm s}[x_{\rm c}(1+x_{\rm c})^2]^{1/(n+1)}x_{\rm c}, \tag{3.57}$$

$$\phi_\infty - 2\beta\phi_0(1+x_{\rm c})^{-1} = \phi_{\rm s}[x_{\rm c}(1+x_{\rm c})^2]^{1/(n+1)}\frac{(n+4)x_{\rm c}+n+2}{(n+1)(1+x_{\rm c})}, \tag{3.58}$$

for $b = 2$.

Here, $\phi_{\rm s}$ is the typical chameleon field in the interior region where the matter density is high and the chameleon mechanism works, which gives $\phi_{\rm s} \ll \phi_\infty \sim \phi_0$. Therefore, we can use the approximation $\phi_{\rm s} \to 0$. Then Eqs. (3.55) and (3.56) can be approximated as

$$C \simeq -2\beta\phi_0 \frac{1-(1+x_{\rm c})^{2-b}}{b-2} + \phi_\infty x_{\rm c}, \tag{3.59}$$

$$\phi_\infty - 2\beta\phi_0(1+x_{\rm c})^{1-b} \simeq 0. \tag{3.60}$$

In this case, the solution for the chameleon field does not depend on the parameters of the potential, n and Λ, but is characterized by the NFW parameters and the background chameleon field, ϕ_∞.

By a conformal transformation, we can also construct the solution in the Jordan frame, obtaining the solution for f_R, which is the degree of freedom in the $f(R)$ model. This procedure is summarized in Appendix A.1.3.

Chameleon Force

The chameleon force is given by Eq. (1.26):

$$F_\phi = -\frac{\beta}{M_{\rm Pl}}\nabla\phi. \tag{3.61}$$

Using the analytic solution for the chameleon field, the chameleon force is given by

$$F(x) = \begin{cases} \dfrac{\phi_0}{M_{\rm Pl} r_{\rm s}} \left[\dfrac{1+(b-1)x-(1+x)^{b-1}}{(b-2)x^2(1+x)^{b-1}} \right. & \\ \qquad \left. - \dfrac{\beta\phi_{\rm s}}{(n+1)\phi_0} \dfrac{(1+(1+b)x)(x(1+x)^b)^{1/(n+1)}}{x(1+x)} \right], & x \le x_{\rm c} \\ \dfrac{\phi_0}{M_{\rm Pl} r_{\rm s}} \left[(1+2\beta^2) \dfrac{1+(b-1)x-(1+x)^{b-1}}{(b-2)x^2(1+x)^{b-1}} - \dfrac{\beta C}{\phi_0 x^2} \right], & x > x_{\rm x} \end{cases} \tag{3.62}$$

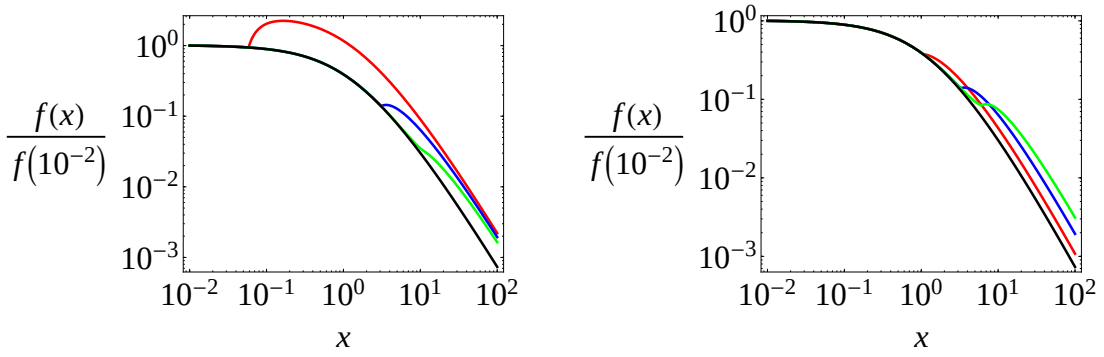

Figure 3.1: Total force as a function radius $x = r/r_{\rm s}$. In the left figure, the red, blue and green curves are for the chameleon field with the virial mass $M_{\rm vir} = 10^{13} M_\odot$, $10^{14} M_\odot$, and $4 \times 10^{14} M_\odot$, respectively. In the right figure, the colored curves are also for the chameleon field, but with the coupling constant $\beta = 0.5$ (red), 1 (blue), and 1.5 (red), where the virial mass is fixed at $M_{\rm vir} = 10^{14} M_\odot$. Black curves are the Newtonian case.

for $b \neq 2$, and

$$F(x) = \begin{cases} \dfrac{\phi_0}{M_{\rm Pl} r_{\rm s}} \left[\left(\dfrac{1}{x(1+x)} - \dfrac{\ln(1+x)}{x^2} \right) \right. \\ \qquad \left. - \dfrac{\beta \phi_{\rm s}}{(n+1)\phi_0} \dfrac{(1+(1+b)x)(x(1+x)^b)^{1/(n+1)}}{x(1+x)} \right], & x \leq x_{\rm c} \\ \dfrac{\phi_0}{M_{\rm Pl} r_{\rm s}} \left[(1+2\beta^2) \left(\dfrac{1}{x(1+x)} - \dfrac{\ln(1+x)}{x^2} \right) - \dfrac{\beta C}{\phi_0 x^2} \right], & x > x_{\rm c} \end{cases} \tag{3.63}$$

for $b = 2$.

Figure 3.1 shows the radial total force per unit mass acting on a test particle. The black line shows the Newtonian case, and the red, blue and green lines show the cases with the chameleon force assuming the NFW profile ($b = 2$) with virial masses $M_{\rm vir} = 10^{13} M_\odot$, $10^{14} M_\odot$ and $4 \times 10^{14} M_\odot$, respectively. In the inner region, the chameleon force is screened by the chameleon mechanism, but in the outer region, the chameleon force appears and depends on the virial mass.

Gas distribution with the chameleon field

In the presence of the fifth force, the gravitational potential (3.14) is effectively modified as

$$\Psi \to \Psi + \frac{\beta}{M_{\rm Pl}}\phi. \tag{3.64}$$

Then, the solutions for gas distributions are also modified to

$$y_{\rm gas} = \left\{1 - \frac{\mu m_{\rm p}}{kT_{\rm gas,0}}\left(\frac{\gamma-1}{\gamma}\right)\left[\Psi(r) - \Psi(0) + \frac{\beta}{M_{\rm Pl}}(\phi(r)-\phi_0)\right]\right\}^{1/(\gamma-1)}, \tag{3.65}$$

for the polytropic model,

$$P_{\rm gas}(r) = P_{\rm gas,0} + \mu m_{\rm p}\int_0^r n_{\rm e}(r)\left(-\frac{d\Psi}{dr} - \frac{\beta}{M_{\rm Pl}}\frac{d\phi(r)}{dr}\right)dr, \tag{3.66}$$

for Model A, and

$$P_{\rm e}(r) = P_0 \exp\left(\int_0^r \frac{\mu m_{\rm p}}{kT_{\rm e}(r)}\left[-\frac{d\Psi}{dr} - \frac{\beta}{M_{\rm Pl}}\frac{d\phi}{dr}\right]dr\right), \tag{3.67}$$

for Model B.

Here, we demonstrate how the modification of gravity affects gas distributions using the polytropic gas distribution. Using the solution for the chameleon field, the solution (3.65) can be explicitly written as

$$y_{\rm gas}(x) = \begin{cases} \left[1 - A\left(1 + \dfrac{(1+x)^{2-b}-1}{(b-2)x} - \dfrac{\beta\phi_{\rm s}}{\phi_0}(x(1+x)^b)^{1/(n+1)}\right)\right]^{1/(\gamma-1)}, & x \le x_{\rm c} \\ \left[1 - A\left(1 + (1+2\beta^2)\dfrac{(1+x)^{2-b}-1}{(b-2)x} - \dfrac{\beta}{\phi_0}\left(\phi_\infty - \dfrac{C}{x}\right)\right)\right]^{1/(\gamma-1)}, & x > x_{\rm c} \end{cases} \tag{3.68}$$

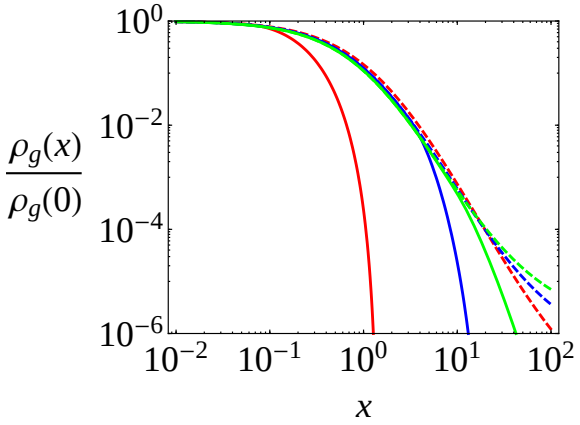

Figure 3.2: Gas density profile as a function of $x = r/r_s$. The solid lines are the cases with the chameleon force, and the dashed lines are the cases without the chameleon force. Green, blue and red lines shows the cases of $M_{\rm vir} = 4 \times 10^{14} M_\odot$, $10^{14} M_\odot$, $10^{13} M_\odot$, respectively, where we fix $\beta = 1$ and $\phi_\infty = 1.1 \times 10^{-5} M_{\rm Pl}$.

for $b \neq 2$, and

$$y_{\rm gas}(x) = \begin{cases} \left[1 - A\left(1 - \dfrac{\log(1+x)}{x} - \dfrac{\beta\phi_{\rm s}}{\phi_0}(x(1+x)^2)^{1/(n+1)}\right)\right]^{1/(\gamma-1)}, & x \leq x_{\rm c} \\ \left[1 - A\left(1 - (1+2\beta^2)\dfrac{\log(1+x)}{x} - \dfrac{\beta}{\phi_0}\left(\phi_\infty - \dfrac{C}{x}\right)\right)\right]^{1/(\gamma-1)}, & x > x_{\rm c} \end{cases} \tag{3.69}$$

for $b = 2$, where

$$A \equiv \frac{\mu m_{\rm p} \phi_0}{k T_{\rm gas,0} M_{\rm Pl}} \frac{\gamma - 1}{\gamma}. \tag{3.70}$$

Typically, we find $\phi_{\rm s}/\phi_0 \ll 1$. Then the inner solution can be represented by the solution for the Newtonian case,

$$y_{\rm gas}^{\rm (NG)}(x) = \begin{cases} \left[1 - A\left(1 + \dfrac{(1+x)^{2-b} - 1}{(b-2)x}\right)\right]^{1/(\gamma-1)}, & b \neq 2 \\ \left[1 - A\left(1 - \dfrac{\log(1+x)}{x}\right)\right]^{1/(\gamma-1)}, & b = 2. \end{cases} \tag{3.71}$$

Figure 3.2 shows radial density profiles. The solid curves show the Newtonian cases and the dashed curves show the cases with the chameleon field. The red, blue and green curvesare for virial masses of $M_{\rm vir} = 10^{13}M_\odot$, $10^{14}M_\odot$ and $4\times10^{14}M_\odot$, respectively. The gas density decreases rapidly in the outer region, where the chameleon force is influential. For a large mass cluster, the chameleon mechanism works out to large radii, because the density of the matter is high enough even outside the cluster. On the other hand, for a small mass cluster, the chameleon mechanism works only at small radii, because the matter density is high only in the central region. Because the chameleon force is an attractive force, a larger pressure gradient is necessary to balance it. This makes the gas distribution compact. This feature is more significant for smaller-mass clusters.

3.4.2 Galileon field

In this section, we review an analytic solution for the Galileon field of the generalized Galileon model. The solution was derived in [25], assuming spherical symmetry of the system within the sub-horizon scale, the quasi-static approximation and keeping the Vainshtein mechanism.

We consider perturbations of the space-time metric, the matter density and the Galileon field .

$$ds^2 = -(1+2\Psi(\mathbf{x}))dt^2 + a(t)^2(1+2\Phi(\mathbf{x}))d\mathbf{x}^2, \tag{3.72}$$

$$\rho(t,\mathbf{x}) = \rho(t)(1+\delta(\mathbf{x})) \tag{3.73}$$

$$\phi(t,\mathbf{x}) = \phi(t)(1+Q(\mathbf{x})) \tag{3.74}$$

where the perturbed values, Ψ, Φ, δ and Q are expressed in the comoving coordinate frame. Within the sub-horizon scale in the quasi-static approximation, the Einstein equation and the Galileon field equation yield the following perturbed equations.

$$\frac{\triangle}{a^2}\Phi = -4\pi G\delta\rho + \xi\frac{\triangle}{a^2}Q, \tag{3.75}$$

$$\Phi + \Psi = -\alpha Q, \tag{3.76}$$

$$\frac{\triangle}{a^2}Q + \lambda^2\left(\frac{Q_{,ij}}{a^2}\frac{Q^{,ij}}{a^2} + \left(\frac{\triangle}{a^2}Q\right)^2\right) = -4\pi G\xi\delta\rho \tag{3.77}$$

where $\triangle$ is the Laplacian in the comoving coordinate frame, and α, ξ, ζ and λ^2, are the model parameters, which are determined by the arbitrary functions $G_4(\phi)$,

$K(\phi, X)$ and $G_3(\phi, X)$. The expressions for α, ξ, ζ and λ^2 are summarized in Appendix A.2. In the spherically symmetric system, Eqs. (3.75), (3.76) and(3.77) reduce to

$$\frac{d\Psi}{dr} = \frac{GM(<r)}{r^2} - (\alpha+\xi)\frac{dQ}{dr}, \tag{3.78}$$

$$\frac{d\Phi}{dr} = -\frac{GM(<r)}{r^2} + \xi\frac{dQ}{dr}, \tag{3.79}$$

$$\frac{dQ}{dr} = \frac{r}{4\lambda^2}\left(1 - \sqrt{1 + \frac{8G\lambda^2\zeta M(<r)}{r^3}}\right), \tag{3.80}$$

where $M(<r) \equiv 4\pi\int_0^r dr' r'^2 \rho(r')$ is the mass of the halo enclosed within the physical radius r. Note that the perturbed values Ψ, Φ and Q in Eqs. (3.78)$\sim$(3.80) are written in the physical coordinate frame. The explicit expressions for the simplest cubic Galileon, the sDGP and the nDGP models were also presented in [25], and are summarized in Appendix A.2.

Here, we define the Vainshtein radius $r_{\rm V}$ as

$$r_{\rm V} \equiv [8G\lambda^2\zeta M_{\rm vir}]^{1/3} = \left[\frac{8G\epsilon^2 M_{\rm vir}}{H_0^2}\right]^{1/3}, \tag{3.81}$$

where we define $\epsilon = \sqrt{H_0^2\lambda^2\zeta}$ using the Hubble constant H_0. For $r \ll r_{\rm V}$, the scalar field is negligible compared with the Newton potential, so Newtonian gravity is recovered. For $r \gg r_{\rm V}$ the scalar field cannot be neglected, and we have

$$\frac{d\Psi}{dr} \simeq \frac{(1+\zeta(\alpha+\xi))GM(<r)}{r^2}, \tag{3.82}$$

$$\frac{d\Phi}{dr} \simeq -\frac{(1+\zeta\xi)GM(<r)}{r^2}. \tag{3.83}$$

Thus the gravitational and curvature potentials are modified at $r \gg r_{\rm V}$. These modifications affect both the gas and weak-lensing profiles. We next construct observational quantities for the gas and weak-lensing profiles, taking the scalar field into account.

Since gas components feel the gravitational force through the gravitational potential Ψ, the X-ray brightness and the SZ profiles are modified by the modification of Ψ. On the other hand, the gravitational lensing is characterized by the lensing potential $(\Phi - \Psi)/2$, so the modified lensing potential alters the observed lensing

profile. We, therefore, introduce the parameters

$$\mu_{\rm G} \equiv (\alpha + \xi)\zeta, \tag{3.84}$$

$$\mu_{\rm L} \equiv \frac{1}{2}(\alpha + 2\xi)\zeta, \tag{3.85}$$

with which we can write $d\Psi/dr \simeq (1+\mu_{\rm G})GM(<r)/r^2$ and $d(\Psi-\Phi)/dr/2 \simeq (1+\mu_{\rm L})GM(<r)/r^2$ at $r \gg r_{\rm V}$.

In the generalized Galileon model, with the use of parameters $\mu_{\rm G}$, $\mu_{\rm L}$ and ϵ our modeling for the electron pressure profiles in Eqs. (3.29), (3.31), and (3.33), and the weak-lensing profile in Eq. (3.41) are modified.

Chapter 4

Testing modified gravity models

As described in Section 3.4, the presence of a fifth force or the modification of the gravitational and lens potentials causes the modification of gas distribution and shear profiles. Using these characteristic features, we shall consider constraints on modified gravity models. This chapter is organized as follows. We first demonstrate that the presence of a fifth force affects the observations of X-ray temperature of the Hydra A cluster using the polytropic gas distribution model in Section 4.1. From that we can obtain a useful constraint on the chameleon model. In Section 4.2, we develop our method of testing the chameleon model used in 4.1 by joint fitting with multi-wavelength observations of the Coma Cluster. In Section 4.3, we apply the method used in Section 4.2 to the generalized Galileon model.

4.1 The chameleon field applied to the Hydra A cluster

4.1.1 Introduction

In this section, we compare the theoretical predictions of X-ray temperature with the Suzaku observation of the Hydra A cluster out to virial radius [94]. Because of the steep drop of the gas distribution in the presence of the attractive chameleon force, a similar drop in X-ray observations is expected to be found in the outer region. The Hydra A cluster is a medium-sized cluster located at a distance of 230 Mpc. Two different fields are observed [94]. One is the northwest offset from the X-ray peak of the cluster, and the other is the northeast offset. The former and latter fields are called the filament and void fields, respectively, because each field continues into the filament and void structures, respectively. In Fig. 4.1 the points with error bars show the data for the filament direction from Ref. [94].

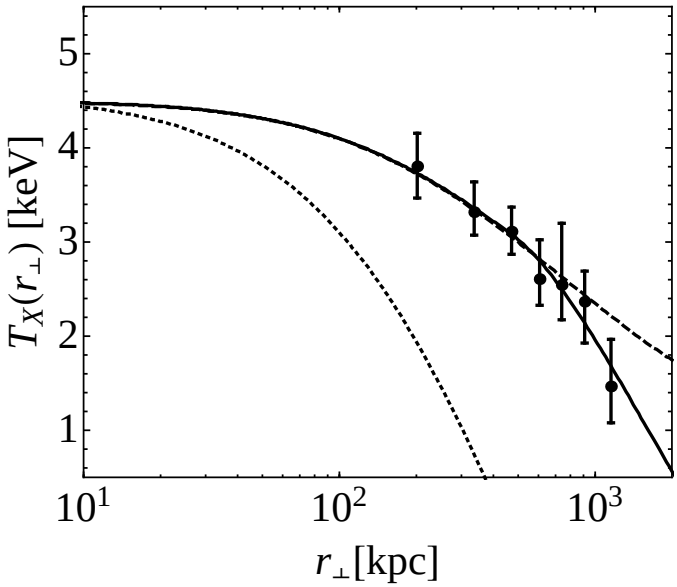

Figure 4.1: Temperature profiles as a function of the radius $r_\perp$. The points with error bars show the observation data of the filament direction [94]. The curves are the theoretical predictions of the chameleon model. The solid curve uses the best-fit parameters $(\phi_\infty, M_{\rm vir}, c, T_g(0)) = (5.4\times10^{-5}M_{\rm Pl}, 5.1\times10^{14}M_\odot, 5.8, 4.9{\rm keV})$. The dashed curve uses $\phi_\infty = 2\times10^{-5}M_{\rm Pl}$, while the dotted curve uses $\phi_\infty = 1.3\times10^{-4}M_{\rm Pl}$, where the other parameters are the same as those of the solid curve. Here we fixed $\beta = 1$ and $b = 2$. The dotted and dashed curves correspond to limits of the modified gravity in Eq. (4.2) and Newtonian gravity in Eq. (4.5), respectively.

4.1.2 Comparison with X-ray temperature

Here, we assume a generalized NFW profile and the polytropic equation of state for gas components. In this case, the gas distribution with an analytic solution for the chameleon field is described by the dimensionless gas profile, $y_{\rm gas}$, which is given by Eq. (3.65),

$$y_{\rm gas}(x) = \begin{cases} \left[1 - A\left(1 + \dfrac{(1+x)^{2-b}-1}{(b-2)x}\right)\right]^{1/(\gamma-1)}, & x \le x_{\rm c} \\ \left[1 - A\left(1 + (1+2\beta^2)\dfrac{(1+x)^{2-b}-1}{(b-2)x} - \dfrac{\beta}{\phi_0}\left(\phi_\infty - \dfrac{C}{x}\right)\right)\right]^{1/(\gamma-1)}, & x > x_{\rm c} \end{cases}$$

(4.1)

for $b \neq 2$, and

$$y_{\rm gas}(x) = \begin{cases} \left[1 - A\left(1 - \dfrac{\log(1+x)}{x}\right)\right]^{1/(\gamma-1)}, & x \leq x_{\rm c} \\ \left[1 - A\left(1 - (1+2\beta^2)\dfrac{\log(1+x)}{x} - \dfrac{\beta}{\phi_0}\left(\phi_\infty - \dfrac{C}{x}\right)\right)\right]^{1/(\gamma-1)}, & x > x_{\rm c} \end{cases} \tag{4.2}$$

for $b = 2$, where

$$A \equiv \frac{\mu m_{\rm p}\phi_0}{kT_{\rm gas,0}M_{\rm Pl}}\frac{\gamma-1}{\gamma}, \tag{4.3}$$

and $\phi_{\rm s}$ is neglected. Then the X-ray temperature, $T_{\rm X}$, is characterized by the parameters $M_{\rm vir}$, c, b, $T_{\rm gas,0}$, γ, β and ϕ_∞, but we determine the polytropic index γ by using Eq. (17) in Ref. [95]. The relation between the polytropic index, γ, and the concentration, c, asymptotically follows the equation [95])

$$\gamma = 1.137 + 8.94 \times 10^2 \ln(c/5) - 3.68 \times 10^3 (c-5). \tag{4.4}$$

Our conclusions are not altered qualitatively for $1.1 \leq \gamma \leq 1.3$. The curves in Fig. 4.1 show our theoretical model of the X-ray temperature. The solid curve is the best-fit curve, whose parameters are noted in the caption. The dashed curve and the dotted curve use $\phi_\infty = 2 \times 10^{-5} M_{\rm Pl}$ and $1.3 \times 10^{-4} M_{\rm Pl}$, respectively, where the other parameters are the same as those for the solid curve. The dotted curve, the solid curve, and the dashed curve in Fig. 4.1 represent the characteristic curves which appear when we vary ϕ_∞ from a sufficiently large value to a smaller one. First, the dotted curve represents the limit of the modified gravity. Namely, for the large value of $\phi_\infty \geq \phi_0$, x_c becomes negative from Eq. (3.60). This means that no interior region where the chameleon mechanism works to recover Newtonian gravity appears in a cluster. Thus, for the case $\phi_\infty \geq \phi_0$, we have $\phi(x) = \phi_{\rm out}(x)$ for the entire region and, therefore, the solution of Eqs. (4.1) and (4.2) should be replaced with

$$y_{\rm gas}^{(MG)}(x) = \begin{cases} \left[1 - A(1+2\beta^2)\left(1 + \dfrac{(1+x)^{2-b} - 1}{(b-2)x}\right)\right]^{1/(\gamma-1)}, & b \neq 2 \\ \left[1 - A(1+2\beta^2)\left(1 - \dfrac{\log(1+x)}{x}\right)\right]^{1/(\gamma-1)}, & b = 2 \end{cases} \tag{4.5}$$

On the other hand, the dashed curve represents the limit of Newtonian gravity,

$$y_{\rm gas}^{\rm (NG)}(x) = \begin{cases} \left[1 - A\left(1 + \dfrac{(1+x)^{2-b} - 1}{(b-2)x}\right)\right]^{1/(\gamma-1)}, & b \neq 2 \\ \left[1 - A\left(1 - \dfrac{\log(1+x)}{x}\right)\right]^{1/(\gamma-1)}, & b = 2 \end{cases} \tag{4.6}$$

From Eq. (3.60), the value of $x_{\rm c}$ becomes larger as ϕ_∞ becomes smaller. This means that the chameleon force is influential at only very large radii, so Newtonian behavior is recovered for the entire region of the cluster. Note that the interior solution $y_{\rm gas}(x)$, given by Eq. (4.2) for $x < x_c$, can be approximated by taking the limit of $\beta \to 0$ in Eq. (4.5), because, in order to screen the scalar field where the chameleon mechanism works, ϕ_s takes a very small value. In summary, the dotted curve and the dashed curve are the two opposite limits, and our theoretical curve is restricted by these two limits. Note that the modified gravity limit of Eq. (4.5) depends on the coupling constant β.

4.1.3 Constraint on chameleon model

Let us define χ^2 is by

$$\chi^2 = \sum_{i=1}^{7} \frac{(T_X(r_{\perp,i}) - T_i^{\rm obs.})^2}{(\Delta T_i^{\rm obs.})^2}, \tag{4.7}$$

where $T_i^{\rm obs.}$ and $\Delta T_i^{\rm obs.}$ are the observed data and the error of the filament direction, respectively, and $T_X(r_{\perp,i})$ is our theoretical model. Let $\chi^2_{\rm min}$ be the minimum value of χ^2. Figure 4.2 shows the contours of $\Delta\chi^2 = \chi^2 - \chi^2_{\rm min}$ on the parameter plane for ϕ_∞ and $M_{\rm vir}$. Here, we have fixed $\beta = 1$ and $b = 2$, but the parameters c and $T_{\rm gas,0}$ are varied so as to minimize χ^2. These parameters are varied within the ranges

	Upper limit for ϕ_∞ in unit of $[M_{\rm Pl}]$	
	Filament	Void
$b = 1.7$	1.4×10^{-4}	0.9×10^{-4}
$b = 2.0$	1.0×10^{-4}	0.8×10^{-4}
$b = 2.5$	0.8×10^{-4}	0.6×10^{-4}

Table 4.1: Upper bounds of ϕ_∞ at the 2-sigma level for different values of b and the data for the filament and void directions. Here we have fixed $\beta = 1$.

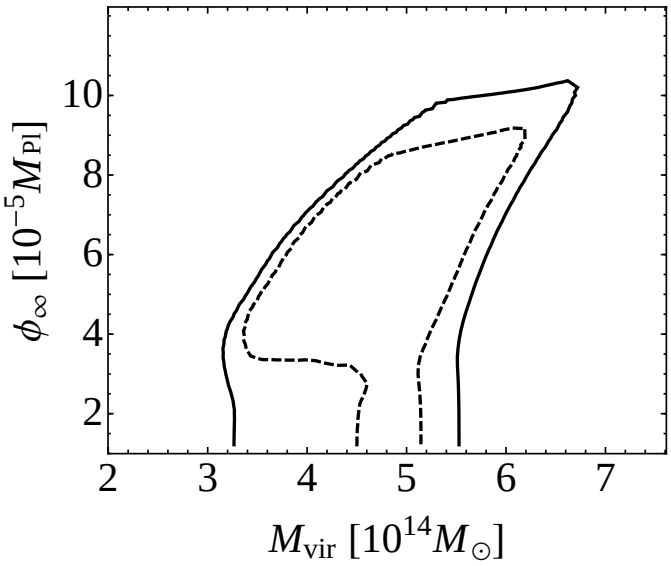

Figure 4.2: The contours of $\Delta\chi^2$ on the parameter plane ϕ_∞- $M_{\rm vir}$. Here we have fixed $\beta = 1$ and $b = 2$, but c and $T_{\rm gas,0}$ are varied as fitting parameters. The contour levels of the inner dashed curve and the outer solid curve are $\Delta\chi^2 = 2.7$ and 6.6, respectively.

$3 \leq c \leq 10$ and $T_0^*/\alpha \leq T_{\rm gas,0} \leq T_0^*\alpha$ with $\alpha = 1.1$, where T_0^* is given by Eq. (19) in Ref. [95]:

$$T_0^* = \eta_0 \frac{4}{3+5X} \frac{G m_p M_{\rm vir}}{3 r_{\rm vir}}, \tag{4.8}$$

with

$$\eta_0 = 2.235 + 0.202(c-5) - 1.16 \times 10^3 (c-5)^2. \tag{4.9}$$

When taking $T_{\rm gas,0}$ as a completely free parameter, it is difficult to obtain a useful constraint from the present data due to the degeneracy between $T_{\rm gas,0}$ and $M_{\rm vir}$. The minimum value of χ^2 is $\chi^2_{\rm min} = 1.0$, where the number of degrees of freedom (d.o.f.) is 3. The behavior of the contour is explained by the fact that the theoretical curve approaches that of Newtonian gravity as ϕ_∞ becomes small and that the steep drop becomes significant as ϕ_∞ increases. Figure 4.2 gives an upper bound of $\phi_\infty < 10^{-4} M_{\rm Pl}$ at the 2-sigma level for the case $b = 2$ and $\beta = 1$. We obtain a similar upper bound of ϕ_∞ for different values of b, which are summarized in Table 4.1. The

upper bound of ϕ_∞ becomes larger as b becomes smaller, but we conclude that the results do not significantly depend on b. Table 4.1 includes the results for the void direction. The upper bound of ϕ_∞ depends on the data, that is, whether we consider the filament direction or the void direction; however, our conclusion does not alter significantly.

Constraint on an $f(R)$ model

So far, we have considered the case $\beta = 1$; we shall now discuss the case $\beta = 1/\sqrt{6}$, which corresponds to an $f(R)$ model [13–15]. In this case, we could not obtain a useful constraint on ϕ_∞, which is explained as follows. The theoretical density profile is limited by two characteristic curves: Eq. (4.5) and Eq. (4.5) with $\beta = 0$. When β is small, the difference between these two characteristic curves is small, because the drop of the gas distribution is not steep. This is the reason why no useful constraint on the $f(R)$ model was obtained from the current X-ray data here.

4.1.4 Systematic effects

We cannot rule out the possibility that the assumption of hydrostatic equilibrium of the hot gas is crucial for constraints on the chameleon field. To estimate the effect, we consider the effect of the non-thermal pressure by simply introducing a constant parameter, ϵ,

$$\frac{1+\epsilon}{\rho_{\rm gas}}\frac{dP_{\rm gas}}{dr} = -\frac{d\Psi}{dr} - \frac{\beta}{M_{\rm Pl}}\frac{d\phi}{dr}, \tag{4.10}$$

and we attempt to obtain similar constraints by inserting the nonzero values of $\epsilon = \pm 0.5$ in Eq. (4.10). The upper bound of ϕ_∞ changes from $10^{-4}M_{\rm Pl}$ for $\epsilon = 0$ to $0.6 \times 10^{-4}M_{\rm Pl}$ and $2.1 \times 10^{-4}M_{\rm Pl}$ for $\epsilon = 0.5$ and -0.5, respectively. Thus, the assumption of hydrostatic equilibrium is crucial to the constraint, but we may obtain a useful constraint if we can model the state of the gas correctly. Further study of this problem is necessary.

Finally, we assumed spherical symmetry for a cluster. The validity of the assumption should be checked when comparing with observational data. In the present paper, the results in Table 4.1 do not depend significantly on the direction (filament or void) which suggests the validity of this assumption.

4.2 The chameleon field applied to the Coma Cluster

4.2.1 Introduction

When the chameleon field is coupled with the gas component, the fifth force due to the chameleon field affects the gas density profile of the galaxy cluster. This causes an additional pressure gradient that balances the extra force, which leads to a more compact gas distribution in the cluster. This effect has been used in [42] (Section 4.1) to compare the X-ray temperature profile predicted by the chameleon model with measurements of the Hydra A cluster, yielding an upper bound of $\phi_\infty < 10^{-4} M_{\rm Pl}$ for the asymptotic scalar field value at large distances with a coupling constant between the chameleon field and matter of $\beta = 1$.

In the presence of a chameleon force, due to its effect on the gas distribution, the hydrostatic mass of a cluster, if interpreted assuming Newtonian gravity, will deviate from its underlying dark matter distribution, which can be measured via weak gravitational lensing, resulting in different mass estimates for the cluster (see [96] for a recent analysis of this mass bias in hydrodynamic simulations of $f(R)$ gravity). Therefore, the combination of gas and lensing measurements of a cluster may yield a powerful probe of gravity if they give statistically different mass estimates, which are not due to other astrophysical reasons.

In this section, we demonstrate the operability of this method with the Coma cluster. This is a massive cluster at a distance of approximately 100 Mpc, whose properties have been measured using several independent methods. The *Planck* team has, for instance, reported a precise observation of the Sunyaev-Zel'dovich (SZ) effect [97]. Moreover, the X-ray surface brightness and X-ray temperature have been measured [98–100], and weak-lensing observations have been conducted [101, 102]. We use the combination of these measurements to place tight constraints on β and ϕ_∞. Figure 1.2 illustrates the effectiveness of our approach. In that figure, we compare our result to current constraints from cosmological, astrophysical, and local tests in the well-studied case that the chameleon model reduces to $f(R)$ gravity. Our Coma constraint is currently the tightest constraint on cosmological scales.

An important element of our method is the reconstruction of the gas distribution in a galaxy cluster under the influence of the fifth force. In previous work [42], the hydrostatic equilibrium of the gas components was assumed when modeling the gas distribution of the Hydra A cluster in chameleon gravity. Hydrostatic equilibrium may, however, not always be realized because of turbulence and bulk motions of the gas caused by mergers with other clusters and groups of galaxies, as well as infalling material. The authors of Ref. [103] have demonstrated that the cluster masses in

numerical simulations, estimated under the assumption of hydrostatic equilibrium, can deviate from the true mass by up to 30%, and that the deviation is explained by the acceleration term in the Euler equation. We, therefore, carefully examine the systematic errors that deviations from hydrostatic equilibrium in the Coma Cluster may introduce to our results.

We first reconstruct the 3-dimensional profiles of the gas density, temperature, and pressure from the observational results using Newtonian gravity. We then compare the mass estimates from the gas observations with the mass estimate from lensing, finding good agreement between them and concluding that the assumption of hydrostatic equilibrium is a good approximation given the observational errors of the lensing mass. Moreover, these mass estimates are only marginally affected by the inclusion of an extremized non-thermal pressure component, which has been calibrated to hydrodynamical simulations.

While non-thermal pressure and other deviations from hydrostatic equilibrium enhance the hydrostatic mass estimate, we find a strong decrease of the reconstructed hydrostatic mass when the chameleon fifth force is introduced. The detection of an enhanced hydrostatic mass with respect to the lensing mass when interpreted in a Newtonian framework, may, therefore, be a smoking gun for modified gravity. On the other hand, the effects of non-thermal pressure and the chameleon force may become degenerate in the reconstruction, as the change in the hydrostatic mass by enhancing modifications of gravity can be compensated by increasing deviations from hydrostatic equilibrium. Given the small effect of the non-thermal pressure compared to the effect from modifying gravity, however, we decide that it is safe to assume hydrostatic equilibrium of the gas, and perform our analysis under this assumption.

Finally, note that Fusco-Femiano *et al.* [104] recently investigated the consistency between the X-ray observations of surface brightness and temperature and the SZ measurement in the Coma Cluster, adopting a "Supermodel". The Supermodel expresses the profiles of density and temperature in an entropy-modulated equilibrium of the intracluster plasma within the potential wells provided by the dominant dark matter [105]. This yields a direct link between the X-ray and SZ observations based on the entropy profile. They found a tension between the SZ and X-ray pressures of the plasma. In our analysis, we confirm these results, by finding a similar tension between the SZ and X-ray pressures. However, the tension is mainly represented by the asymptotic difference of the values of the pressure between the inner and the outer regions. On the other hand, the constraint on the chameleon gravity model comes from the shape of the density profile in the intermediate regime, so we can nevertheless put a useful constraint on the chameleon model.

This section is organized as follows. In Section 4.2.2, we review the hydrostatic equilibrium equations and hydrostatic mass, including a brief review of an analytic approximate solution of the scalar field profile in the cluster. In Section 4.2.3, we perform a Markov chain Monte Carlo (MCMC) analysis to place constraints on the Newtonian and chameleon model parameter space. We then discuss the systematic effects introduced by deviations from spherical symmetry, and study deviations from the hydrostatic equilibrium of the gas in Newtonian gravity by comparing the hydrostatic mass inferred from X-ray and SZ measurements with the lensing mass and analysing the effects of including non-thermal pressure in comparison to the effects from the chameleon force.

4.2.2 Hydrostatic and lensing mass in the presence of a chameleon force

We describe the hydrostatic mass of a spherically symmetric system of gas and introduce a non-thermal pressure model, which we use to analyze deviations from hydrostatic equilibrium. Then, we briefly review the derivation of an analytic approximate solution for the chameleon scalar field profile within a dark matter cluster, which we use to determine the effects on hydrostatic masses in the presence of the extra force. Next, we compare the reconstructed hydrostatic masses obtained from different gas observations with the observed lensing mass and discuss the effect on the mass reconstruction when incorporating the non-thermal pressure model and the chameleon modification.

We consider a spherically symmetric system of gas and dark matter. In this case, we can write the equation for the gas component in hydrostatic equilibrium as

$$\frac{1}{\rho_{\rm gas}(r)}\frac{dP_{\rm tot}(r)}{dr} = -\frac{GM(<r)}{r^2}, \tag{4.11}$$

where $\rho_{\rm gas}$ is the gas density, $P_{\rm tot}$ is the 'total' gas pressure, including both thermal and non-thermal pressure, and $M(<r)$ is the mass enclosed within the radius r. This equation describes the balance between the gas pressure gradient and the gravitational force. Note that we have not yet included the chameleon force. The total gas pressure can be written as the combination of the thermal pressure and the non-thermal pressure, $P_{\rm tot} = P_{\rm gas} + P_{\rm nth}$. Eq. (4.11) can then be rewritten as

$$M(<r) \;\; = \;\; M_{\rm th}(r) + M_{\rm nth}(r) \tag{4.12}$$

with the definitions

$$M_{\rm th}(r) \equiv -\frac{r^2}{G\rho_{\rm gas}(r)}\frac{dP_{\rm gas}(r)}{dr}, \tag{4.13}$$

$$M_{\rm nth}(r) \equiv -\frac{r^2}{G\rho_{\rm gas}(r)}\frac{dP_{\rm nth}(r)}{dr}. \tag{4.14}$$

$M_{\rm nth}$ is introduced to help mathematically describe the non-thermal pressure contribution to the total mass. Note that $M_{\rm th}$ is expressed in terms of $P_{\rm gas}$ and $\rho_{\rm gas}$ in Eq. (4.13). If we introduce the equation of state of the gas, $P_{\rm gas} = kn_{\rm gas}T_{\rm gas}$, we can express the thermal mass in terms of $T_{\rm gas}$ and $\rho_{\rm gas}$ instead:

$$M_{\rm th}(r) = -\frac{kT_{\rm gas}(r)r}{\mu m_{\rm p}G}\left(\frac{d\ln\rho_{\rm gas}(r)}{d\ln r} + \frac{d\ln T_{\rm gas}(r)}{d\ln r}\right), \tag{4.15}$$

where we have used $\rho_{\rm gas} = \mu m_{\rm p} n_{\rm gas}$.

We define the fraction of the total pressure attributed to the non-thermal contribution by

$$P_{\rm nth}(r) \equiv g(r)P_{\rm tot}(r). \tag{4.16}$$

Hence, using $P_{\rm tot} = g^{-1}P_{\rm nth} = (1 - f_{\rm nth})^{-1}P_{\rm gas}$, we may write

$$P_{\rm nth}(r) = \frac{f_{\rm nth}(r)}{1 - f_{\rm nth}(r)} n_{\rm gas}(r) kT_{\rm gas}(r). \tag{4.17}$$

According to hydrodynamical simulations [106, 107], the non-thermal contribution to the total pressure can be modeled with the expression

$$f_{\rm nth}(r) = \alpha_{\rm nt}(1+z)^{\beta_{\rm nt}}\left(\frac{r}{r_{500}}\right)^{n_{\rm nt}}\left(\frac{M_{200}}{3\times 10^{14}M_\odot}\right)^{n_{\rm M}}, \tag{4.18}$$

where $\alpha_{\rm nt}$, $\beta_{\rm nt}$, $n_{\rm nt}$, and $n_{\rm M}$ are constants. For illustration, and for an estimation of the effects of neglecting the non-thermal contribution, we adopt the parameter values $(\alpha_{\rm nt}, \beta_{\rm nt}, n_{\rm nt}, n_{\rm M}) = (0.3, 0.5, 0.8, 0.2)$, which are the best-fit values in [107] with the exception of $\alpha_{\rm nt}$. The best-fit value of $\alpha_{\rm nt}$ is 0.18, which is an averaged value over 16 simulated clusters. We set $\alpha_{\rm nt} = 0.3$, which is the maximum value obtained in the 16 clusters [107], in order to study the effect of the non-thermal pressure contribution in the extremized case.

We refer to next subsubsection for our approach to the reconstruction of the 3-

dimensional profiles of $\rho_{\rm gas}$, $T_{\rm gas}$, and $P_{\rm gas}$ from the gas observations via the X-ray temperature, X-ray surface brightness, and SZ effect, which enables us to estimate $M_{\rm th}$. Using Eqs. (4.16) and (4.18), we can then estimate the non-thermal contribution $M_{\rm nth}$ employing the results from hydrodynamical simulations.

In the presence of the chameleon field, the hydrostatic equilibrium in Eq. (4.11) is modified by the introduction of the extra force $F_\phi = -(\beta/M_{\rm Pl})d\phi/dr$ on the right-hand side of the equation. The chameleon force then modifies the mass inferred from hydrostatic equilibrium in Eq. (4.12) as

$$M(<r) \;=\; M_{\rm th}(r) + M_{\rm nth}(r) + M_\phi(r), \tag{4.19}$$

where we define an extra mass

$$M_\phi(r) \;\equiv\; -\frac{r^2}{G}\frac{\beta}{M_{\rm Pl}}\frac{d\phi(r)}{dr} \tag{4.20}$$

associated with the enhanced gravitational force due to the chameleon field.

Reconstruction of the 3-dimensional gas profiles

Here, we summarize the method for the reconstruction of the 3-dimensional profiles of the gas density, temperature, and pressure, using observations of X-ray temperature, surface brightness, and the SZ effect to derive hydrostatic masses.

Having summarized the quantities observed in the X-ray and SZ measurements in Section 3.2.5, we now use them to reconstruct the 3-dimensional gas density, temperature, and pressure profiles. For this purpose, we adopt the following fitting functions for the 3-dimensional profiles of $T_{\rm gas}(r)$, $n_{\rm e}(r)$, and $P_{\rm e}(r)$. For $T_{\rm gas}(r)$, we use the fitting formula calibrated to numerical simulations [108]

$$T_{\rm gas}(r) = T_0\left[1 + A\left(\frac{r}{r_0}\right)\right]^{b_0}, \tag{4.21}$$

where T_0, A, r_0, and b_0 are free parameters. For the electron number density, we assume a simple isothermal β model [86]:

$$n_{\rm e}(r) = n_0\left[1 + \left(\frac{r}{r_1}\right)^2\right]^{b_1}, \tag{4.22}$$

where the free parameters are n_0, r_1, and b_1. Finally, we adopt the generalized NFW

profile for the pressure proposed in Ref. [109],

$$P_{\rm e}(r) = \frac{P_0}{(r/r_2)^{b_2}(1+(r/r_2)^{b_3})^{b_4}}, \tag{4.23}$$

for the 3-dimensional electron pressure profile with the fitting parameters P_0, r_2, b_3, and b_4.

We compute the projected profiles in Eqs. (3.34), (3.36), and (3.37) with the fitting functions of Eqs. (4.21), (4.22), and (4.23), and determine the best fit parameters T_0, A, r_0, b_0, n_0, r_1, b_1, P_0, r_2, b_2, b_3 and b_4 by comparing the profiles with the observations from the X-ray temperature, X-ray surface brightness, and SZ effect of the Coma Cluster in Section 4.2.4. In this way, we obtain the reconstructed 3-dimensional gas density, temperature, and pressure profiles of the cluster.

Note that since we assume the hydrostatic equilibrium of Eq. (4.29) in the MCMC analysis in Section 4.2.3, we only need to define two of these profiles, from which the other profiles can be derived. One profile could also be the matter density profile;, however, in that case, the exact analytic expressions of the fitting functions are not necessarily reproduced. In Section 4.2.3, we choose to work with the electron number density Eq. (4.22) and the NFW profile Eq. (2.41). The choice of the NFW profile simplifies the computation of the chameleon force and allows the use of the analytic approximation derived in Section 3.4.1. Hence, the degrees of freedom reduce to T_0, n_0, r_1, b_1, including the NFW parameters $M_{\rm vir}$ and c as well as the chameleon model parameters β and ϕ_∞ (or β_2 and $\phi_{\infty,2}$), where T_0 is required to set the integration constant in Eq. (4.30). This approach yields reasonable reduced χ^2 values when fitted to the observational data in Section 4.2.3.

Inferring hydrostatic and lensing masses from observations

The thermal mass $M_{\rm th}$ of a cluster in Eq. (4.15) is determined by its gas density, temperature, and pressure, which can be deduced from X-ray and SZ observations. To obtain $M_{\rm th}$ from observations, we reconstruct the 3-dimensional gas profiles using parametric fits as described in detail in Appendix 4.2.2, which we substitute into Eq. (4.15). We assume that the gas is fully ionized and that the electron temperature is equal to both $T_{\rm gas}$ and the proton temperature. Note, however, that this assumption is nontrivial because the equipartition timescale between electrons and protons through Coulomb collisions is close to the dynamical timescale of the cluster (see, e.g., [110]).

With the 3-dimensional temperature, electron density, and pressure profiles re-

constructed as described above, we can now determine the thermal mass profile of the cluster. From X-ray observations, we infer

$$M_{\rm th} = -\frac{kT^{\rm (X)}_{\rm gas} r}{\mu m_{\rm p} G}\left(\frac{d\ln n^{\rm (X)}_{\rm e}}{d\ln r} + \frac{d\ln T^{\rm (X)}_{\rm gas}}{d\ln r}\right) \tag{4.24}$$

and similarly, from the SZ observations, we obtain

$$M_{\rm thermal} = -\frac{r^2}{G\rho^{\rm (X)}_{\rm gas}}\frac{dP^{\rm (SZ)}_{\rm gas}}{dr}, \tag{4.25}$$

where we use $n_{\rm e} = (2+\mu)n_{\rm gas}/5$ and $P_{\rm e} = n_{\rm e}kT_{\rm gas} = (2+\mu)P_{\rm gas}/5$. With this reconstruction, we can directly compare the two mass profiles with the lensing mass

$$M_{\rm WL} = 4\pi\rho_{\rm s} r_{\rm s}^3\left[\ln(1+r/r_{\rm s}) - \frac{r/r_{\rm s}}{1+r/r_{\rm s}}\right], \tag{4.26}$$

which is obtained by integration over the NFW density profile in Eq. (2.41), assuming that $\phi/M_{\rm Pl} \ll 1$ so that the lensing potential is related to the matter distribution by the standard Poisson equation. The subscript WL denotes weak lensing.

In the presence of a non-thermal pressure, Eqs. (4.24) and (4.25) are modified according to Eq. (4.18) with the mass

$$M_{\rm th} + M_{\rm nth} = -\frac{kT^{\rm (X)}_{\rm gas} r}{\mu m_{\rm p} G}\left(\frac{d\ln n^{\rm (X)}_{\rm e}}{d\ln r} + \frac{d\ln T^{\rm (X)}_{\rm gas}}{d\ln r}\right) - \frac{r^2}{G\rho^{\rm (X)}_{\rm gas}}\frac{d}{dr}\left(\frac{g}{1-f_{\rm nth}} n^{\rm (X)}_{\rm gas} kT^{\rm (X)}_{\rm gas}\right), \tag{4.27}$$

inferred from X-ray observations, whereas a combination of SZ and X-ray observations implies

$$M_{\rm th} + M_{\rm nth} = -\frac{r^2}{G\rho^{\rm (X)}_{\rm gas}}\frac{dP^{\rm (SZ)}_{\rm gas}}{dr} - \frac{r^2}{G\rho^{\rm (X)}_{\rm gas}}\frac{d}{dr}\left(\frac{g}{1-f_{\rm nth}} P^{\rm (SZ)}_{\rm gas}\right). \tag{4.28}$$

To derive our constraints in Section 4.2.3, we will assume hydrostatic equilibrium, Eq. (4.11), and thus require

$$M_{\rm th} + M_{\rm nth} + M_\phi \equiv M_{\rm WL}, \tag{4.29}$$

where M_ϕ is the chameleon contribution described in Eq. (4.20) and $M_{\rm nth} \ll M_{\rm th} + M_\phi$. We refer the reader to Section 4.2.4 for an analysis of the validity of the hydrostatic equilibrium assumption in the case of the Coma Cluster.

4.2.3 Constraints on the model parameters from an MCMC analysis

We chose to work with the Coma Cluster where the non-thermal pressure is expected to be subdominant (see, e.g., [111] and Section 4.2.4) and which has been well observed with a range of different methods [111–114]. The contribution of non-thermal pressure can also be assumed small in modified gravity [96]. Ref. [115] has recently pointed out that the cluster may not be very typical: its X-ray temperature and star formation rate is high but its kinematic features, like substructure and velocity dispersion, are not conspicuous. The authors urge caution in using the Coma Cluster as a $z \sim 0$ baseline cluster in galaxy evolution studies. On the other hand, according to references [116,117], the Coma cluster is in agreement with scaling relations obtained from typical cluster samples. We cannot exclude the possibility that extraordinary features of the cluster may affect our conclusions. However, our constraints rely only on the observed distribution of gas and dark matter and we allow a number of degrees of freedom in phenomenological models of these distributions, finding good agreement of our fits with the observational data. We also carefully examine a dynamical equilibrium model of the Coma Cluster. Note that our method applies to any cluster which is in hydrostatic equilibrium, and is not restricted to the Coma Cluster.

Method

The NFW density profile is specified by the virial mass $M_{\rm vir}$ and the concentration parameter c. For the gas distribution, we use Model A which is characterized by the NFW parameters and the parameters, T_0, n_0, r_1 and b_1. Then the solution for gas pressure is given by Eq. (3.66),

$$P_{\rm gas}(r) = P_{\rm gas,0} + \mu m_{\rm p} \int_0^r n_{\rm e}(r) \left(-\frac{GM(<r)}{r^2} - \frac{\beta}{M_{\rm Pl}} \frac{d\phi(r)}{dr} \right) dr, \tag{4.30}$$

with the electron number density, $n_{\rm e}$, represented by Eq. (3.30),

$$n_{\rm e} = n_0 \left[1 + \left(\frac{r}{r_1} \right)^2 \right]^{-b_1}. \tag{4.31}$$

The configuration of the scalar field is given by specifying the parameters β and ϕ_∞. Then, the complete list of parameters we analyze in our MCMC study becomes T_0, n_0, b_1, r_1, $M_{\rm vir}$, c, β, and ϕ_∞. Once these parameters are specified, we can compute the projected gas profiles in Eqs. (3.34), (3.36) and (3.37), which are then compared with the observational data from the X-ray surface brightness and temperature, and the SZ observations. Here, to estimate the cooling function for the surface brightness, we use the X-ray flux based on the APEC model corresponding to the observational band from 0.5 keV to 2.5 keV [98], and we adopt the metal abundance of $Z = 0.3Z_\odot$ throughout the cluster. The metal abundance in the innermost region of the cluster is larger than in the outer region, $Z = 0.4Z_\odot$ [104] and $Z = 0.3Z_\odot$ [118], respectively. However, as the difference is small and does not affect our conclusions, we use $Z = 0.3Z_\odot$.

We estimate the "goodness-of-fit" by computing the chi-squared statistic

$$\chi^2(M_{\rm vir}, c, T_0, n_0, b_1, r_1, \beta, \phi_\infty) = \chi^2_{\rm XT} + \chi^2_{\rm SB} + \chi^2_{\rm SZ} + \chi^2_{\rm WL}, \tag{4.32}$$

where

$$\chi^2_{\rm XT} = \sum_i \frac{(T_{\rm X}(r_{\perp,i}) - T^{\rm obs.}_{{\rm X},i})^2}{(\Delta T^{\rm obs.}_{{\rm X},i})^2}, \tag{4.33}$$

$$\chi^2_{\rm SB} = \sum_i \frac{(S_{\rm X}(r_{\perp,i}) - S^{\rm obs.}_{{\rm X},i})^2}{(\Delta S^{\rm obs.}_{{\rm X},i})^2}, \tag{4.34}$$

$$\chi^2_{\rm SZ} = \sum_i \frac{(y(r_{\perp,i}) - y^{\rm obs.}_i)^2}{(\Delta y^{\rm obs.}_i)^2}, \tag{4.35}$$

$$\chi^2_{\rm WL} = \frac{(M_{\rm vir} - M_{\rm WL})^2}{(\Delta M_{\rm WL})^2} + \frac{(c - c_{\rm WL})^2}{(\Delta c_{\rm WL})^2}. \tag{4.36}$$

Here, $T_{\rm X}(r_{\perp,i})$ and $T^{\rm obs.}_{{\rm X},i}$ are the theoretical and observed X-ray temperatures, and $\Delta T^{\rm obs}_{{\rm X},i}$ refers to the observational error. We adopt the analogous notation for the surface brightness $S_{\rm X}$ and the y-parameter, defined by the SZ temperature as $\Delta T_{\rm SZ}/T_{\rm CMB} \equiv -2y$. In addition, $M_{\rm WL}$ and $c_{\rm WL}$ are the observed virial mass and the concentration parameter from weak lensing, respectively.

For the X-ray temperature profile, we use the *XMM-Newton* data reported in Ref. [99] for the inner region and *Suzaku* data reported in Ref. [100] for the outer region. For the X-ray surface brightness profile, we use the *XMM-Newton* data reported in Ref. [98] and for the SZ pressure profile, we use the *Planck* measurements [97]. Finally, we use the weak-lensing measurement of the Coma Cluster reported by Ok-

abe *et al.* [102], who adopt a NFW fit in their analysis to obtain a virial mass for the cluster of $M_{\rm vir} = 8.92^{+20.05}_{-5.17} \times 10^{14} h^{-1} M_\odot$ and a concentration of $c = 3.5^{+2.57}_{-1.79}$ with virial overdensity $\Delta_{\rm c} = 100$.

In our likelihood analysis, we assume that the information contained in each data point is independent of the other data points, in other words, that there is no correlation between these four observations. This could be an over-simplification. These four observations are based on different measurement principles, and the X-ray, SZ effect, and weak-lensing observations are obtained at different wavelengths. On the other hand, the information contained in the data comes from the same astrophysical object, and thus the systematic errors might be correlated. For instance, the clumpiness of the cluster and other non-spherically symmetric features would introduce a correlated systematic error between the data sets. We do not take into account such correlations in our analysis and leave it for future work to address these observational issues in more detail. See, however, Section 4.2.4 for a discussion of these effects. We also note that the covariance of errors is not taken into account in our analysis because it is not available to us. For now, we assign a 5% systematic error to the measurement error of the X-ray surface brightness.

MCMC analysis

We perform an MCMC analysis with the 8 model parameters $T_0, n_0, b_1, r_1, M_{\rm vir}, c, \beta_2$, and $\phi_{\infty,2}$, which completely describe the X-ray temperature and surface brightness profiles, the SZ effect, and the weak-lensing mass profile as well as the chameleon modified gravity model. We use the re-normalized parameters

$$\beta_2 = \frac{\beta}{1+\beta}, \tag{4.37}$$

$$\phi_{\infty,2} = 1 - \exp\left[-\left(\frac{\phi_\infty}{10^{-4} M_{\rm Pl}}\right)\right], \tag{4.38}$$

instead of β and ϕ_∞, as β_2 and $\phi_{\infty,2}$ span the complete available parameter space of β and ϕ_∞ in the interval $[0, 1]$. Note, however, that some of the approximations made in Section 3.4.1 do not hold in the extreme limits of $\phi_{\infty,2} \to 1$ and $\beta_2 \to 1$. For our analysis, we use the MCMC module included in the COSMOMC [119] package, which employs a Metropolis-Hastings [120, 121] sampling algorithm. We require a Gelman-Rubin statistic [122] of $\mathcal{R} - 1 < 0.03$ to ensure convergence of our runs.

In Fig. 4.3 we compare the overall best-fit curves for the chameleon gravity model (solid) and Newtonian gravity (dashed) from the combination of all of the observa-

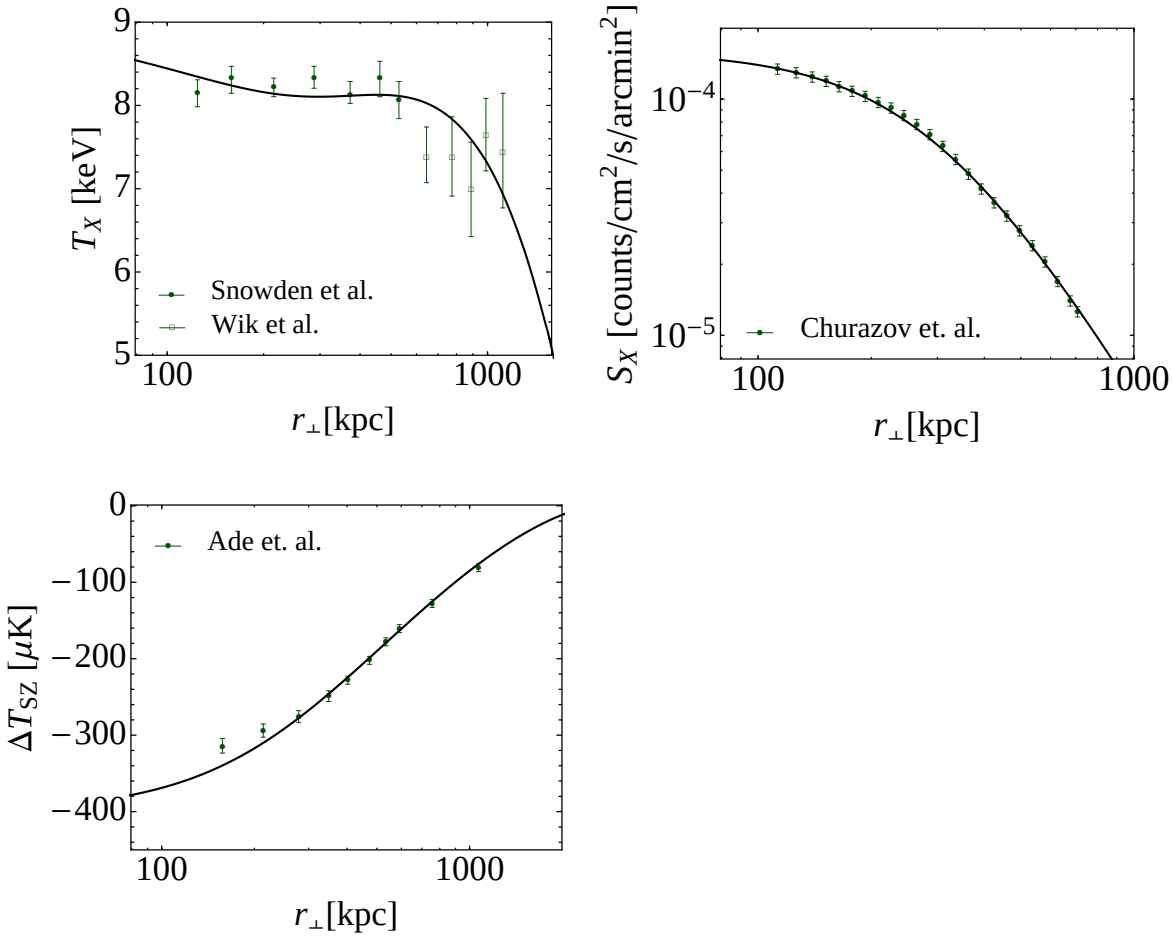

Figure 4.3: *Top left panel*: Radial gas temperature profile of the Coma Cluster. The circles and boxes represent the data points and errors from the *XMM-Newton* measurements by Snowden *et al.* [99] and the *Suzaku* measurements by Wik *et al.* [100], respectively. *Top right panel*: Radial surface brightness profile of the Coma Cluster. The data points represent the *XMM-Newton* measurements by Churazov *et al.* [98]. The error bars in the original data, which only account for the Poisson noise contribution, are small. We assign a systematic error of 5% to each data point to take into account clumpiness and other non-spherically symmetric features of the cluster. *Bottom panel*: Radial Sunyaev-Zel'dovich CMB temperature profile. The data points represent the *Planck* measurements by Ade *et al.* [97]. The best-fit values of the chameleon model parameters are (β, ϕ_∞)=(15, $4\times10^{-4}M_{\rm Pl}$), where the model parameters characterizing the profiles are given in Table 4.3. In the data analysis, we use the data points included within the radial range 100 kpc $< r_\perp <$ 1 Mpc and fit them using the model parameters T_0, n_0, b_1, r_1, $M_{\rm vir}, c$ in the Newtonian case (dashed lines) and in addition β_2 and $\phi_{\infty,2}$ in the chameleon scenario (solid lines). Note that the best-fits of the Newtonian and chameleon cases almost overlap.

Table 4.2: Best-fit values and 1-dimensional marginalized constraints (95% CL) for the model parameters $(T_0, n_0, b_1, r_1,\ M_{\rm vir}, c)$ characterizing the gas and dark matter profiles obtained from an MCMC analysis of the joint observational data sets.

parameter	Newtonian gravity	Modified gravity
$M_{\rm vir}$	$2.57^{+0.97}_{-0.54}\ 10^{15}\ M_\odot$	$2.46^{+1.33}_{-0.61}\ 10^{15}\ M_\odot$
c	$2.56^{+0.49}_{-0.52}$	$2.64^{+0.72}_{-0.7}$
n_0	$2.33^{+0.22}_{-0.17}\ 10^{-3}/\mathrm{cm}^3$	$2.34^{+0.21}_{-0.19}\ 10^{-3}/\mathrm{cm}^3$
b_1	$-0.921^{+0.089}_{-0.109}$	$-0.915^{+0.085}_{-0.107}$
r_1	$3.02^{+0.54}_{-0.47}\ 10^2$ kpc	$2.99^{+0.56}_{-0.45}\ 10^2$ kpc
T_0	$11.2^{+0.76}_{-0.84}$ keV	$11.3^{+0.79}_{-0.9}$ keV

tional data sets, that is, minimizing χ^2 in Eq. (4.32). The corresponding best-fit parameter values are listed in Table 4.3 along with the 1-dimensional marginalized 95% confidence levels (CL). We show the 2-dimensional marginalized contours for different combinations of the model parameters for the Newtonian case, that is, where we have fixed $\beta = 0$ and $\phi_\infty = 0$, in Fig. 4.8. The best fit in this case yields a reduced χ^2 of $\chi^2/\text{d.o.f.} = 32/41$. In Fig. 4.9, we show the analogous constraints for the model parameters of the chameleon modified gravity scenario. The best fit in this case yields a good reduced χ^2 of $\chi^2/\text{d.o.f.} = 32/39$. We refer to Section 4.2.4 for a discussion of possible sources of systematic error that have not been taken into account in this analysis.

Finally, in Fig. 4.4, we show the 2-dimensional marginalized contours of the parameters β_2 and $\phi_{\infty,2}$. Note that the lower shaded region is the allowed region. We recall that β describes the strength of the chameleon fifth force and ϕ_∞ determines the efficiency of the chameleon screening, and we introduced the parameters $\beta_2 = \beta/(1+\beta)$ and $\phi_{\infty,2} = 1 - \exp(-\phi_\infty/10^{-4}M_{\rm Pl})$ instead of β and ϕ_∞ to describe the entire parameter space of the chameleon modification. Newtonian gravity is recovered in the limits of $\beta_2 = 0$ or $\phi_{\infty,2} = 0$.

The boundaries in Fig. 4.4 can be understood by considering the phenomenology of the chameleon modification. At large β, if the chameleon field is not screened, the extra chameleon force reduces the hydrostatic mass compared to the Newtonian mass estimate and it becomes inconsistent with the lensing mass (see Section 4.2.4).

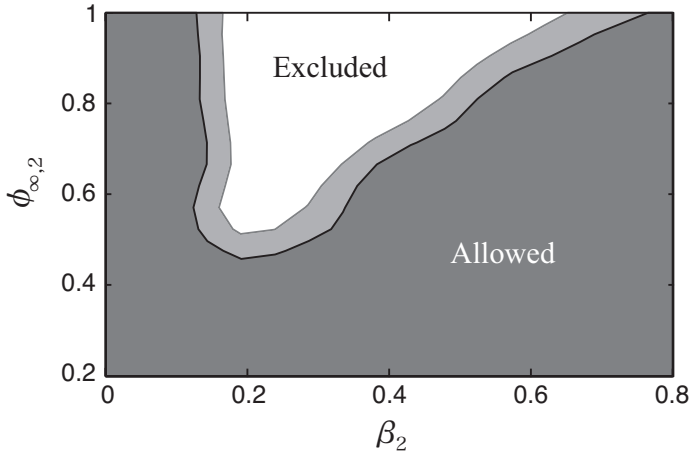

Figure 4.4: 95% (deep gray region) and 99% CL (pale gray region) contours for the chameleon model parameters $\beta_2 = \beta/(1+\beta)$ and $\phi_{\infty,2} = 1-\exp(-\phi_\infty/10^{-4}\mathrm{M_{Pl}})$, obtained from the MCMC analysis of the 8 model parameters, $T_0, n_0, b_1, r_1, M_{\rm vir}, c, \beta_2$, and $\phi_{\infty,2}$, using the joint set of X-ray, SZ, and weak-lensing data. The shaded region is the allowed region.

This causes a tension in the desired parameter values when fitting the joint set of observations and places constraints on the chameleon modification. On the other hand, the chameleon force contributes only outside of the critical radius $r_{\rm c}$, which is determined by Eq. (3.60) as

$$1 + \frac{r_{\rm c}}{r_{\rm s}} = \frac{\beta\rho_{\rm s}r_{\rm s}^2}{M_{\rm Pl}\phi_\infty}. \tag{4.39}$$

Due to the chameleon suppression mechanism, Newtonian gravity is recovered below $r_{\rm c}$. To put a useful constraint on the chameleon force, $r_{\rm c}$ must be smaller than the size of the cluster, which is about 1 Mpc. More precisely, with increasing $\beta M_{\rm Pl}/\phi_\infty$, the transition scale $r_{\rm c}$ becomes large and eventually surpasses the size of the cluster, in which case the chameleon mechanism completely screens the fifth force within the cluster. At this point, no further constraints on the chameleon model can be obtained. This implies that there is an upper bound on $\beta M_{\rm Pl}/\phi_\infty$, which can be constrained. In the opposite limit, when β is small, the fifth force is weak and the modifications become consistent with the observations within the given errors. Hence, at low β_2 in Fig. 4.4 the chameleon scalar field amplitude $\phi_{\infty,2}$ is unconstrained.

With the minimal scalar field in the background, $-\Lambda^{n+4} \simeq n^{-1}\beta\,\bar{R}_0\,\phi_\infty^{n+1}M_{\rm Pl}$, the Compton wavelength of the background scalar field today, assumed to be ϕ_∞ here,

becomes [65]

$$m_\infty^{-1} \simeq \left[\frac{\beta\,\bar{R}_0}{n+1}\frac{M_{\rm Pl}}{\phi_\infty}\right]^{-1/2} \sim \left[10^{-6}\frac{\beta}{n+1}\frac{M_{\rm Pl}}{\phi_\infty}\right]^{-1/2}\ {\rm Mpc}. \tag{4.40}$$

Whereas the chameleon mechanism suppresses the scalar field on scales below $r_{\rm c}$, on scales larger than the Compton wavelength m_∞^{-1}, modifications of gravity are Yukawa suppressed. With Solar System tests requiring that $\phi_\infty \lesssim 10^{-6}\beta$ [14, 65] and with $n \sim \mathcal{O}(1)$, one obtains $m_\infty^{-1} \sim$ Mpc. Hence, requiring Solar System tests to be satisfied, standard gravity is recovered on scales beyond $\mathcal{O}(1)$ Mpc (cf. [123]). Since we use observations on only scales smaller than 1 Mpc and constraints are weaker than the local bounds, we can safely ignore the Yukawa suppression.

Constraint on $f(R)$ gravity

Our constraints have important implications for $f(R)$ gravity [13–15], which corresponds to a subset of our models with the particular choice of the coupling constant $\beta = \sqrt{1/6}$. Here, we adopt the Hu-Sawiki model [14]. The $f(R)$ modification can be related to the chameleon field ϕ via

$$f_R = -\sqrt{\frac{2}{3}}\frac{\phi}{M_{\rm Pl}} \tag{4.41}$$

and hence, assuming that the Coma Cluster is isolated such that ϕ_∞ corresponds to the background scalar field value, we have $f_{R0} = -\sqrt{2/3}(\phi_\infty/M_{\rm Pl})$. From the 2-dimensional contours of $(\beta_2, \phi_{\infty,2})$ in Fig. 4.4 we, therefore, estimate an upper bound on $f(R)$ gravity of $\phi_\infty \lesssim 7\times10^{-5}M_{\rm Pl}$ or, equivalently, $|f_{\rm R0}| \lesssim 6\times10^{-5}$ at the 95% CL.

We emphasize that this result is comparable with the bounds on $f(R)$ gravity obtained from cosmology, such as from the abundance of clusters [34, 69, 124] (see Fig. 1.2) and the current constraints from redshift-space distortions in the large scale structure of galaxies [125]. Note that, in the case of $\tilde{n} = 1$, the value of $|f_{R0}|$ is related to the Compton wavenumber of the scalar field k_C by

$$k_C \simeq 0.04\left(\frac{10^{-4}}{|f_{R0}|}\right)^{1/2}\ h{\rm Mpc}^{-1}. \tag{4.42}$$

Then, $|f_{\rm R0}| \lesssim 6\times10^{-5}$ can be rephrased as $k_C \lesssim 0.05\ h{\rm Mpc}^{-1}$.

Note that the assumption that the Coma Cluster is an isolated system is non-

trivial. It is well known that, on large scales, the cluster is connected to a network of filaments [126, 127]. Hence, ϕ_∞ or f_{R0} should really be understood as the scalar field value in the mean density environment within a large radius around the Coma Cluster, which we expect to be close to the background value [128]. This interpretation does not differ from approaches taken to derive the constraints reported in Fig. 1.2. Another possible violation of our assumptions which may be introduced by the environment could be the presence of a large-scale non-spherically symmetric feature, as discussed in Section 4.2.4.

4.2.4 Systematic effects

So far we have assumed hydrostatic equilibrium of the gas and a spherically symmetric matter distribution. We therefore devote the remainder of this section to discuss the systematic errors that can be introduced in our analysis due to deviations from hydrostatic equilibrium and the presence of non-spherically symmetric features.

Invalidity of hydrostatic equilibrium

By employing the assumption of hydrostatic equilibrium in our analysis of the model parameter space, we have supposed that, for the Coma Cluster, the hydrostatic mass inferred from temperature and density, and that from pressure and density, are consistent with each other as well as with the lensing mass. Here, we test the validity of hydrostatic equilibrium within Newtonian gravity by comparing the different mass estimates, and study the effects of introducing non-thermal pressure.

In the top left and top right panels of Fig. 4.5, we compare the observed X-ray temperature and surface brightness, respectively, with the corresponding best fit curves, which are obtained by fitting the projected profiles of Eqs. (3.34) and (3.36) with Eqs. (4.21) and (4.22) to the combined X-ray data. Note that in the top right panel, for each data point, we have assigned a 5% systematic error on top of the measured errors. The measured errors for the X-ray surface brightness are extremely small because they include only the Poisson noise contribution. Systematic errors can be introduced by the clumpiness and non-spherical symmetry of the gas distribution and should be taken into account.

The bottom panel of Fig. 4.5 shows the SZ observations, which we compare with two different best-fit curves. The dashed curve is the best fit obtained by fitting the SZ profile Eq. (3.37) with Eq. (4.23) and the solid curve is the best fit to the joint X-ray temperature and surface brightness data, that is, with the same parameter values

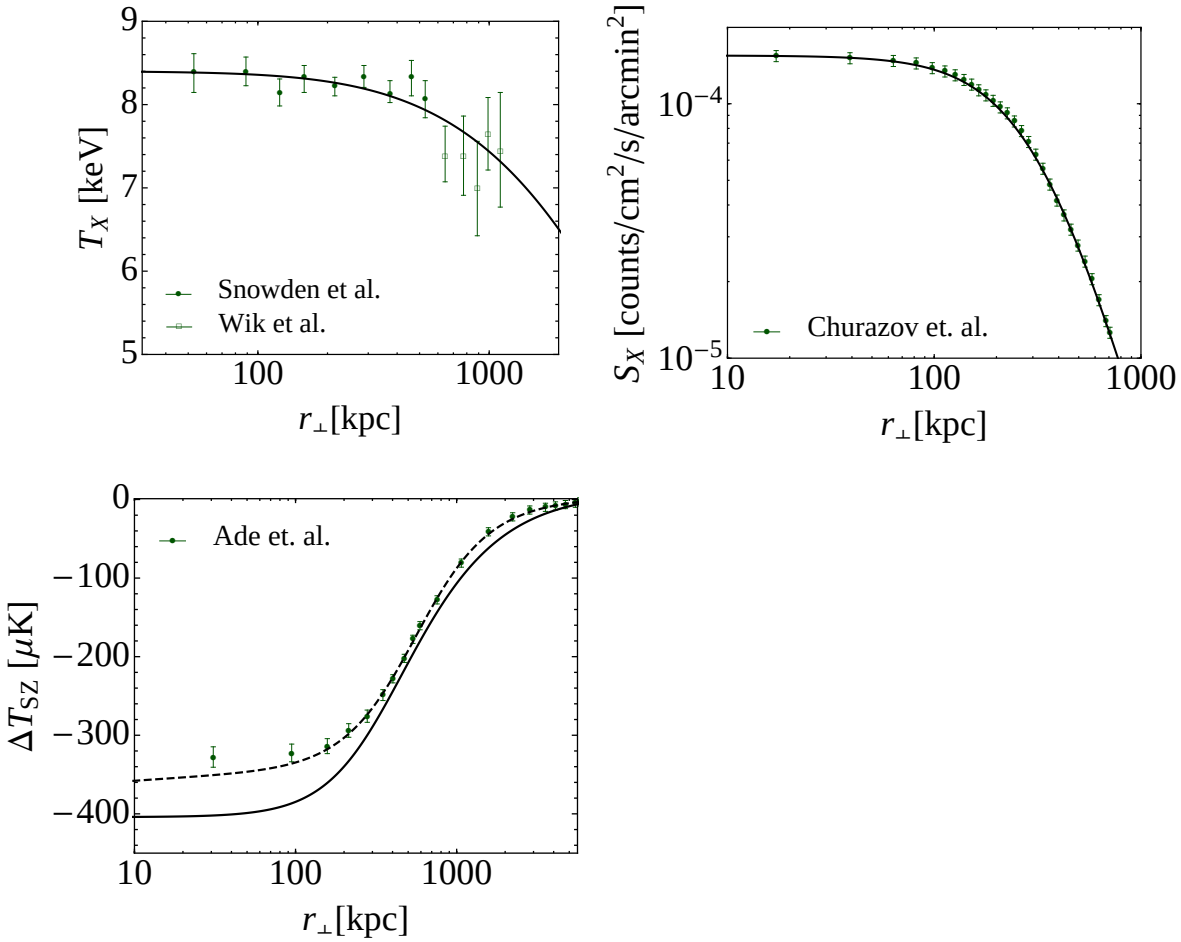

Figure 4.5: Same as Fig. 4.3, but curves are fitted by model-independent methods. *Top left panel*: The solid curve is the projected emission-weighted X-ray temperature profile in Eq. (3.36), using the fitting functions in Eqs. (4.21) and (4.22) for the 3-dimensional temperature and electron density profiles with best-fit parameter values $(T_0, A, r_0, b_0) = (8.6\text{ keV}, 0.082, 3.9\text{ Mpc}, -5.3)$ and $(n_0, r_1, b_1) = (2.3 \times 10^{-3}\text{cm}^{-3}, 0.34\text{ Mpc}, -1)$, respectively, for the joint X-ray data. *Top right panel*: The solid curve is the surface brightness profile Eq. (3.34), using the fitting functions Eqs. (4.22) and (4.21) for the 3-dimensional electron density profile temperature profile with best-fit parameter values $(T_0, A, r_0, b_0) = (8.6\text{ keV}, 0.082, 3.9\text{ Mpc}, -5.3)$ and $(n_0, r_1, b_1) = (2.3 \times 10^{-3}\text{cm}^{-3}, 0.34\text{ Mpc}, -1)$, respectively, for the joint X-ray data. *Bottom panel*: The dashed curve is the SZ effect of Eq. (3.37), using the fitting function Eq. (4.23) for the 3-dimensional pressure profile with best-fit parameter values $(P_0, b_3, b_4, b_5, r_4) = (1.1 \times 10^{-2}\text{ keV/cm}^3, 0.14, 2.2, 1.1, 0.53\text{ Mpc})$. The solid curve is the best fit model from the joint X-ray observations.

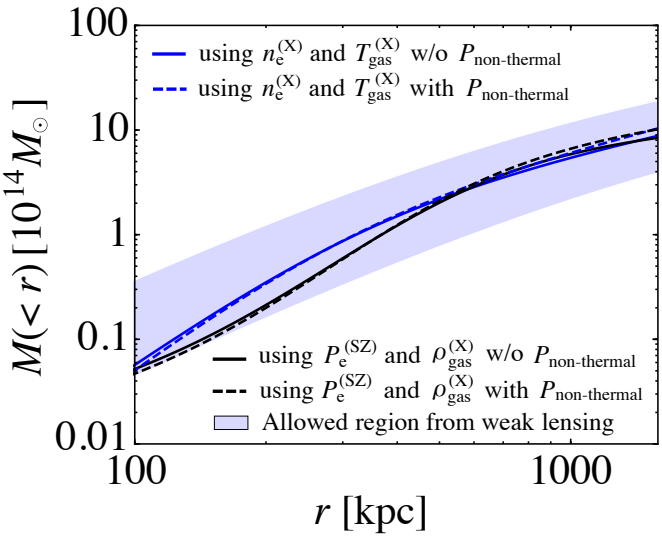

Figure 4.6: Radial mass profile of the Coma Cluster. The shaded region is the observationally allowed 1σ region from the weak-lensing observations of Ref. [102]. The blue solid curve is the thermal mass component $M_{\rm th}$ estimated from the X-ray observations only, and the black solid curve is $M_{\rm th}$ estimated from the combination of X-ray and SZ observations. The blue dashed and black dashed curves correspond to the same colour solid lines, however, now including a large non-thermal pressure contribution.

used in the top left and top right panels of Fig. 4.5. Note the difference between the two curves.

Recently, Fusco-Femiano *et al.* [104] analyzed the consistency between the observations of the X-ray surface brightness, X-ray temperature, and SZ observations, adopting a "Supermodel". The Supermodel yields a direct link between the X-ray and the SZ observations based on the entropy profile. They report a tension between the pressure from the X-ray observations and that from SZ observations in the Coma Cluster. The authors argue that an additional non-thermal pressure resolves the tension. In this paper, we adopt a similar observational data set and reconstruct the 3-dimensional gas profiles using the relations described in Appendix 4.2.2. We find a similar tension in our results and model a non-thermal pressure component as described in Section 4.2.2; this, however, is slightly different from the non-thermal pressure discussed in Ref. [104]. The non-thermal pressure in Ref. [104] is a constant, which is independent of the radius. The non-thermal pressure we introduce in

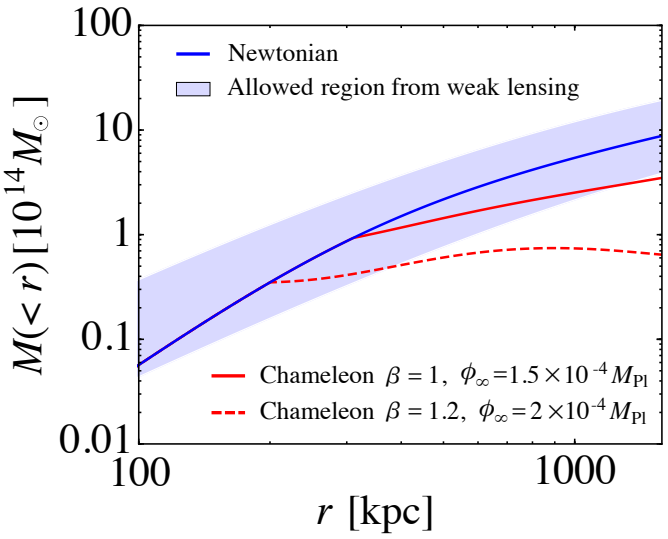

Figure 4.7: Same as Fig. 4.6 but in the presence of the chameleon field. The red solid and red dashed curves are the combination of the thermal mass and chameleon mass components, $M_{\rm th}+M_\phi$, when $(\beta, \phi_\infty/M_{\rm Pl}) = (1, 1.5\times10^{-4})$ and $(1.2, 2\times10^{-4})$, respectively.

Section 4.2.2 is a function of radius, and its fraction in the total pressure becomes large only in the outer region. Nevertheless, our models fit the data reasonably well and can be used to put a useful constraint on the chameleon modification. This is because we use limited data in only the range of radius 100 kpc $< r_\perp <$ 1 Mpc, where the shape of the mass profile drives the constraints.

Figure 4.6 shows the different radial mass profiles reconstructed from the different gas observations and the lensing mass in Newtonian gravity, including effects from the non-thermal pressure introduced in Section 4.2.2. The blue solid curve is the hydrostatic mass from Eq. (4.15) with $n_{\rm e}(=\rho_{\rm gas}(2+\mu)/5\mu m_{\rm p})$ and $T_{\rm gas}$ reconstructed from the X-ray observations. The black solid curve is the hydrostatic mass from Eq. (4.13) with $\rho_{\rm gas}$ and $P_{\rm gas}$ reconstructed from the X-ray and SZ observations. Finally, the shaded region in Fig. 4.6 shows the allowed 1σ-region of the weak-lensing mass profile fitted using an NFW density profile with $M_{\rm vir} = 8.92^{+20.05}_{-5.17}\times10^{14}h^{-1}M_\odot$ and $c = 3.5^{+2.57}_{-1.79}$. At the scales of 100 kpc $< r <$ 1 Mpc, the blue and black curves are consistent within the shaded region, while for $r <$ 100 kpc, the curves are out of the shaded region. Thus, for 100 kpc $< r <$ 1 Mpc, although the mass estimates differ up to the 50% level, within the observational error of the lensing

mass, the mass profiles estimated by the gas observations are consistent with each other and the lensing mass profile. This suggests that hydrostatic equilibrium is a good approximation for the outer region of the Coma Cluster, given the error of the lensing measurement. The discrepancies in the inner region $r < 100$ kpc are a known problem in the mass reconstruction and beyond the scope of this thesis. The validity of hydrostatic equilibrium in the inner region has been investigated by many authors (see, e.g., [129–131] and references therein) with no consensus found. Note, however, that the weak-lensing observations are not sensitive to the density profile in the inner region [102]. We therefore base our analysis on a simple extrapolation of the NFW profile. Recent lensing observations of the Coma Cluster [132] support the validity of this assumption for 100 kpc $< r <$ 1 Mpc as well as indicating its limitations for $r < 100$ kpc.

To estimate the influence of the non-thermal pressure on the mass profile, the blue and black dashed curves in Fig. 4.6 show the sum of the thermal mass profile $M_{\rm th}$ and the non-thermal mass component $M_{\rm nth}$ determined by Eq. (4.18). The blue dashed curve is obtained from X-ray observations using Eq. (4.27), whereas the black dashed curve is obtained from the combination of SZ and X-ray observations using Eq. (4.28). At $r = 1$ Mpc, the non-thermal pressure enhances the total hydrodynamical mass estimate by a few tens of percent. This reflects the limited effect of the non-thermal pressure predicted by hydrodynamical simulations.

Finally, we include the chameleon field in our mass comparison. In Fig. 4.7, we show the thermal radial mass profile in combination with the chameleon mass component: $M_{\rm th} + M_\phi$ (red curves). The red solid and red dashed curves are obtained for $(\beta, \phi_\infty/M_{\rm Pl}) = (1, 1.5 \times 10^{-4})$ and for $(1.2, 2 \times 10^{-4})$, respectively. These two sets of parameters for the chameleon model illustrate typical scenarios where the chameleon force causes a possible discrepancy between the gas and the lensing masses. Note that these curves are determined from $M_{\rm th}$ and M_ϕ in Eq. (4.19), where $M_{\rm th}$ is reconstructed from the observational data and M_ϕ is given by Eq. (4.20), and, therefore, the slightly oscillatory feature of the $\beta = 1.2$ curve does not reflect any physically meaningful effect. The blue curve represents the case without the chameleon force, which is close to the red solid curve and the red dashed curve in the inner region, where the chameleon field is suppressed. Further out, the chameleon force reduces the hydrostatic mass $M_{\rm th} + M_\phi$ with respect to the mass obtained in Newtonian gravity because the chameleon force introduces an extra attractive force. As is clear from this figure, we can put a constraint on the chameleon model that influences the gas distribution in only the range $r \lesssim 1$ Mpc. The critical radius at which the chameleon force begins to contribute is determined by β/ϕ_∞ [see Eq. (4.39)] and the

amplitude of the chameleon force is determined by β. Thus, these two parameters in the chameleon models are constrained by comparing the hydrostatic mass and lensing mass under the assumption of hydrostatic equilibrium.

Non-spherical symmetry

Next, let us consider systematic effects that can be introduced by deviations from spherical symmetry. Here, we assume that the 3-dimensional profiles of the electron number density, temperature, and pressure are

$$n_{\rm e}(r,\theta,\varphi) = \bar{n}_{\rm e}(r)[1+\delta_{n_{\rm e}}(r,\theta,\varphi)], \tag{4.43}$$

$$T_{\rm gas}(r,\theta,\varphi) = \bar{T}_{\rm gas}(r)[1+\delta_{T_{\rm gas}}(r,\theta,\varphi)], \tag{4.44}$$

$$P_{\rm e}(r,\theta,\varphi) = \bar{P}_{\rm e}(r)[1+\delta_{P_{\rm e}}(r,\theta,\varphi)], \tag{4.45}$$

where $\delta_{n_{\rm e}}, \delta_{T_{\rm gas}}$ and $\delta_{P_{\rm e}}$ describe deviation from the spherically symmetric profiles, $\bar{n}_{\rm e}(r)$, $\bar{T}_{\rm gas}(r)$, and $\bar{P}_{\rm e}(r)$, respectively.

The effect of clumpiness on the electron number density can then be estimated as follows. Introducing an average over the spherical symmetric profiles, we assume $\langle\delta_{n_{\rm e}}\rangle = 0$ and $\langle\delta^2_{n_{\rm e}}\rangle \neq 0$. Assuming that the temperature perturbation is negligible, that is, $\delta_{T_{\rm gas}} = 0$, the observed X-ray temperature profile is not changed. The SZ profile is not affected by clumping either because $\langle\delta_{P_{\rm e}}\rangle = \langle\delta_{n_{\rm e}}\rangle = 0$ from the equation of state. However, the surface brightness is increased by the clumpiness and can be rewritten as

$$S_{\rm X} \propto \int n_{\rm e}^2 dz = (1+\langle\delta^2_{n_{\rm e}}\rangle)\int \bar{n}_{\rm e}^2 dz, \tag{4.46}$$

where $1+\langle\delta^2_{n_{\rm e}}\rangle$ is referred to as the clumping factor. This affects the reconstruction of the electron number density. When the clumping factor is non-zero, $\bar{n}_{\rm e}$ is replaced by $\bar{n}_{\rm e}/\sqrt{1+\langle\delta^2_{n_{\rm e}}\rangle}$. Then, the thermal mass profile reconstructed from observations of the SZ effect and X-ray surface brightness, Eq. (4.25), is enhanced by a factor $\sqrt{1+\langle\delta^2_{n_{\rm e}}\rangle}$. However, the thermal mass profile reconstructed from X-ray observations, Eq. (4.24), is not affected by the clumpiness. In the case where $1+\langle\delta^2_{n_{\rm e}}\rangle = 1.5$, which corresponds to the estimated clumping factor for the A1835 cluster [133], we have an enhancement of the hydrostatic mass by a factor ~ 1.2. Thus, systematics from the clumpiness could be a few tens of percent.

Besides the clumpiness, large-scale spherical asymmetries of a cluster may cause an additional systematic bias. Three-dimensional ellipticity as well as substructures

of the Coma Cluster have been studied in Ref. [134]. They reported an ellipticity of the electron density in the cluster of only $\epsilon = \sqrt{1-e^2} = 0.84$, where e is the eccentricity, so we can ignore the effect in our analysis. Nonetheless, the assumption of spherical symmetry introduces systematic errors which should be investigated in more quantitative detail in a future work.

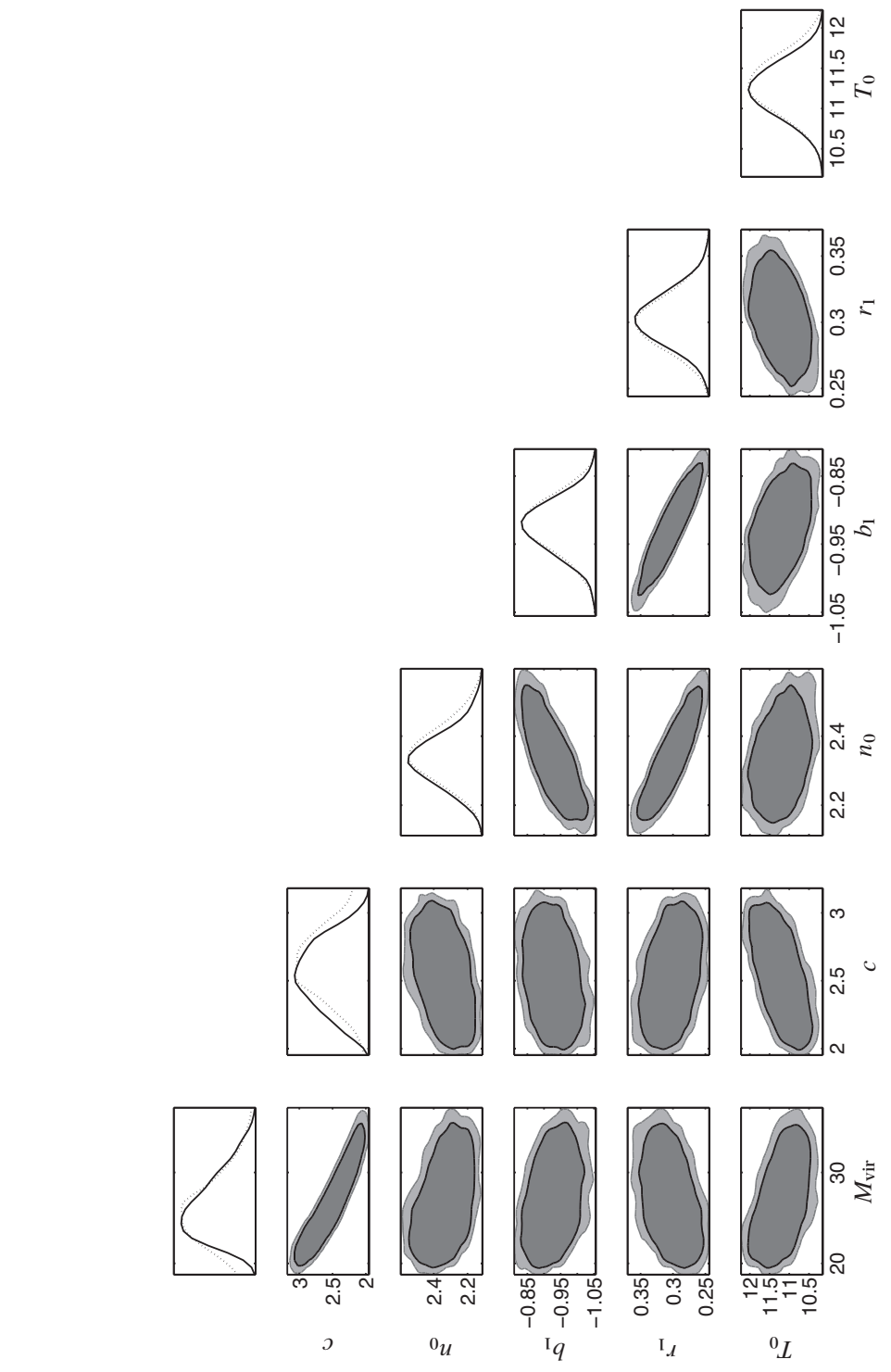

Figure 4.8: 95% (deep gray region) and 99% CL (pale gray region) 2-dimensional marginalized contours of the 6 model parameters T_0 [keV], n_0 $[10^{-2}\mathrm{cm}^{-3}]$, b_1, r_1 [Mpc], $M_{\rm vir}$ $[10^{14}M_\odot]$, and c in the Newtonian scenario, obtained from the MCMC analysis, using the joint set of X-ray, SZ, and weak-lensing data. The right-most panels of each row show the 1-dimensional marginalized constraints (solid) and likelihood distributions (dotted).

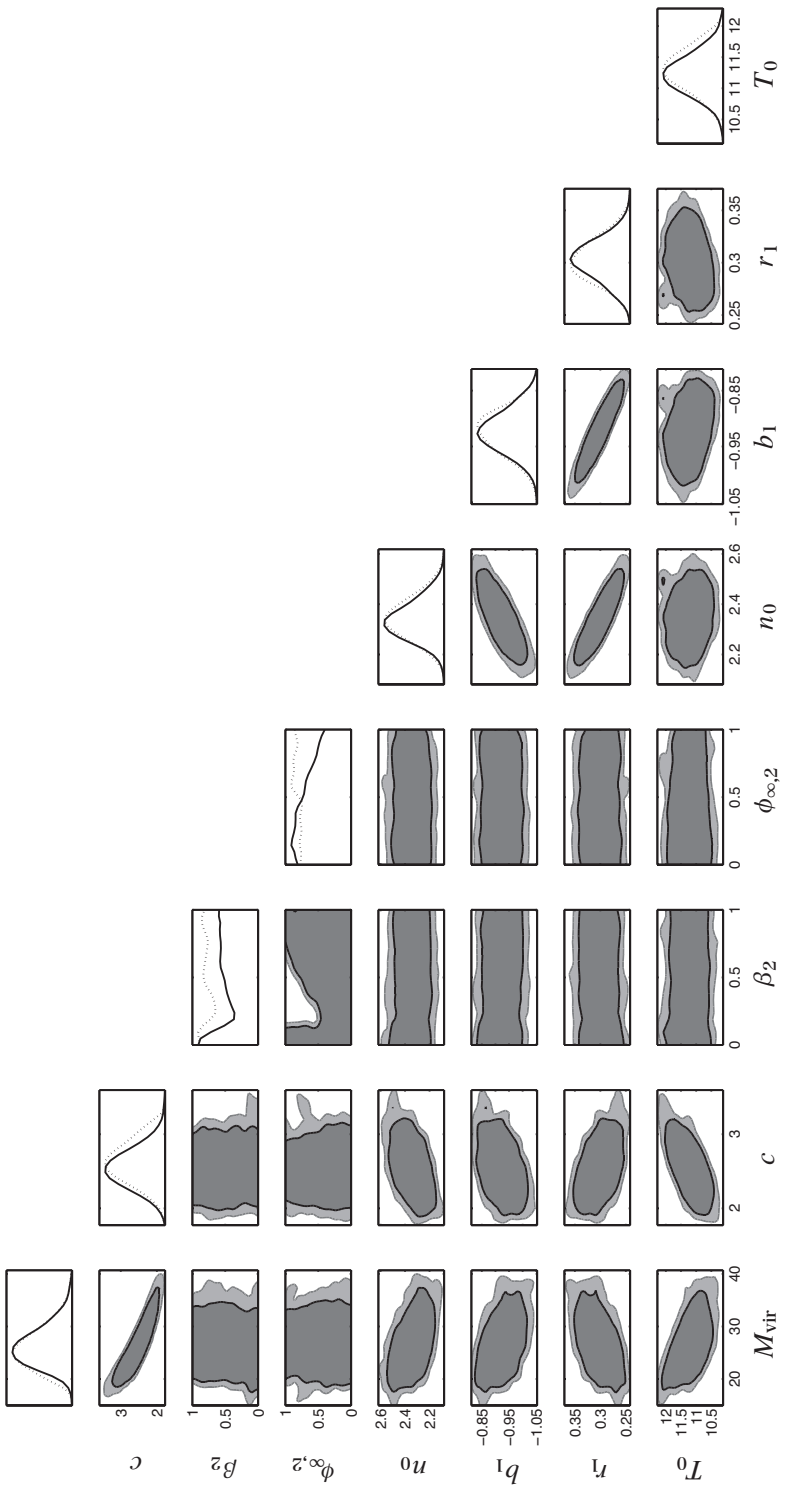

Figure 4.9: Same as Fig. 4.8 but including the chameleon parameters β_2 and $\phi_{\infty,2}$ in the MCMC analysis. The 2-dimensional marginalized contours of β_2 and $\phi_{\infty,2}$ are also shown in Fig. 4.4.

4.3 The Galileon field applied to the Coma Cluster

4.3.1 Introduction

The Vainshtein mechanism [17] is another relevant screening mechanism, which occurs in the Dvali–Gabadaze–Porrati (DGP) model [18,19], the simplest cubic Galileon model [20–23], and its generalized version [24, 25]. Our generalized cubic Galileon model is a generalized version of the simplest cubic Galileon model that retains important features and contains the DGP models. In these models, a scalar field giving rise to a fifth force is screened due to self-interaction on small scales where density perturbations become nonlinear.

Suto *et al.* [41, 60] have investigated a constraint on a generalized Galileon model exhibiting the Vainshtein mechanism, using the observed weak-lensing profile of clusters. They put a constraint on the transition scale and the amplitude of the modification of the lensing potential.

The purpose of the present analysis is twofold. First, it is a generalization of the methodology for testing a modified gravity model with a galaxy cluster. For this, we consider a generalized cubic Galileon model. Within the quasi-static approximation, the generalized cubic Galileon model is effectively characterized by 3 parameters: $\mu_{\rm G}$, $\mu_{\rm L}$ and ϵ. Detailed definitions are given later but, broadly, $\mu_{\rm G}$ and $\mu_{\rm L}$ are parameters that modify the effective amplitude of the gravitational potential and the lensing potential in the non-screened region, while ϵ determines the scale of the transition from the non-screened region to the screened region due to the Vainshtein mechanism. The parameters $\mu_{\rm G}$ are constrained by observations of the gas distribution, in particular the X-ray surface brightness profile and the SZ effect. However, the parameter $\mu_{\rm L}$ is constrained by observations of lensing measurements alone. Therefore, a combination of observations of the gas distribution and the lensing signal is essential to put a constraint on the 3 parameters characterizing the modified gravity model. We demonstrate how a combination of multi-wavelength observations of a cluster can be used to put a constraint on a generalized Galileon model.

The other purpose is to improve the analysis in Ref. [43] using new X-ray data [135, 136] and lensing [132] observations of the Coma Cluster. In our method of testing gravity modifications with a galaxy cluster, the modeling of the gas distribution is important. A basic assumption of the model for the gas distribution is hydrostatic equilibrium, that is, a balance between the gas pressure gradient force and the gravitational force. In the region where the fifth force is influential, the condition of the hydrostatic equilibrium is changed, and the gas density profile is modified. However, in general, galaxy clusters are dynamically evolving, and a deviation from

the equilibrium could be influential. Therefore, we first check the consistency of our model by comparing theoretical predictions with various observations of the Coma Cluster, including new X-ray data and lensing measurements.

This section is organized as follows. We first demonstrate how well our model fits observations of the Coma Cluster in Section 4.3.2. We also validate our model against the influence of non-thermal pressure. In Section 4.3.3, we put a constraint on the generalized cubic Galileon model. In Section 4.3.4, we discuss degeneracies of parameters and systematic errors focusing on the special circumstance of using the Coma Cluster.

4.3.2 Consistency test with Newtonian gravity

In this section, we use Coma Cluster observations. The Coma Cluster is one of the best observed nearby clusters, and has redshift of $z = 0.0236$. The X-ray distribution [98–100, 118, 135–140], the SZ effect [97] and weak-lensing [102, 132] have been reported. These observations revealed that the Coma Cluster has substructures and orientation dependence in the gas temperature profiles. The Coma Cluster is thus an unrelaxed system. However, we will show that our model based on hydrostatic equilibrium fits the data of the X-ray brightness profiles [135, 136], the SZ effect profile from the Planck measurement [97], and the weak-lensing profile from Subaru observations [132]. In general, the assumption of hydrostatic equilibrium holds only in the intermediate region of clusters, because of the cooling of the gas in the innermost region and environmental effects in the outermost region. So we use data points in the range 200 kpc to 1.5 Mpc to get rid of systematic effects from the innermost and outermost regions of the cluster.

In this work, we use the observational data of the XMM-Newton [135, 136], which are different from those used in a previous paper [43]. In that paper, the weak-lensing profile is not used; only the parameters $M_{\rm vir}$ and c are used as a prior profile from [102]. However, use of the weak-lensing profile is essential to our analysis of the generalized Galileon model.

Method

We first assume hydrostatic equilibrium between the gas pressure gradient and the gravitational force in the galaxy cluster:

$$\frac{1}{\rho_{\rm gas}}\frac{dP_{\rm tot}}{dr} = -\frac{d\Psi}{dr}, \tag{4.47}$$

where $P_{\rm tot} = P_{\rm gas} + P_{\rm nth}$ is the sum of the thermal gas pressure, $P_{\rm gas}$, and the non-thermal pressure, $P_{\rm nth}$. Here, we assume the NFW profile (2.41) and Model B for the solution of the gas distribution, which is given by Eq. (3.33),

$$P_{\rm e}(r) = n_0 T_0 \exp\left(\int_0^r dr \frac{\mu m_{\rm p}}{k T_{\rm e}(r)} \left[-\frac{d\Psi}{dr}\right]\right), \tag{4.48}$$

with electron temperature

$$T_{\rm e}(r) = T_0 \left[1 + \left(\frac{r}{r_1}\right)^{b_1}\right]^{-b_2/b_1}. \tag{4.49}$$

Thus our gas distribution model includes 7 parameters: $M_{\rm vir}$, c, n_0, T_0, b_1, b_2, and r_1. Using our model of the 3-dimensional profiles, we construct X-ray observables and the CMB temperature distribution. We use the X-ray brightness, $B_{\rm X}$, defined by Eq. (3.35) for the X-ray observable, and the CMB temperature distortion characterized by $\Delta_{\rm SZ}$ or the y-parameter defined by Eq. (3.37).

Next, considering a spatially flat cosmological background, and working in the cosmological Newtonian gauge, we use the reduced shear profile, g_+, defined by Eq. (3.43) for the lensing observable.

To compare the above theoretical predictions with observations of the Coma Cluster, we introduce the chi-squared statistic produced by summing the chi-squared statistic for each observation as

$$\chi^2_{\rm XB+SZ+WL} = \chi^2_{\rm XB} + \chi^2_{\rm SZ} + \chi^2_{\rm WL}, \tag{4.50}$$

where

$$\chi^2_{\rm XB} = \sum_i \frac{(B_{\rm X}(r_i) - B^{\rm obs.}_{{\rm X},i})^2}{(\Delta B^{\rm obs.}_{{\rm X},i})^2}, \tag{4.51}$$

$$\chi^2_{\rm SZ} = \sum_i \frac{(y(r_{\perp,i}) - y^{\rm obs.}_i)^2}{(\Delta y^{\rm obs.}_{,i})^2}, \tag{4.52}$$

$$\chi^2_{\rm WL} = \sum_i \frac{(g_+(r_{\perp,i}) - g^{\rm obs.}_{+,i})^2}{(\Delta g^{\rm obs.}_{+,i})^2}, \tag{4.53}$$

are the chi-square values for the X-ray brightness, the SZ effect and the weak-lensing, respectively. We note that covariance of errors is not taken into account in our analysis and leave it for future work to study how the observational systematics

Table 4.3: Best-fit parameters and 1-dimensional marginalized constraints (68% CL) to characterize the gas and lensing profiles. To avoid degeneracy of parameters, we fix b_1 and b_2. Our results do not depend on whether these parameters are fixed or not. This table shows the results for Newtonian gravity (second column) and the generalized Galileon model with all modification parameters (third column). The minimum chi-squared and the number of degrees of freedom, d.o.f. = (number of data points) − (number of model parameters), are listed at the bottom of each column.

Parameter	Newtonian gravity	Modified gravity (full parameters)
$M_{\rm vir}$	$1.08^{+0.06}_{-0.06} \times 10^{15}\ M_\odot$	$1.04^{+0.14}_{-0.06} \times 10^{15}\ M_\odot$
c	$3.59^{+0.23}_{-0.23}$	$3.64^{+0.21}_{-0.30}$
n_0	$6.14^{+0.28}_{-0.26} \times 10^{-3}/\mathrm{cm}^3$	$6.17^{+0.26}_{-0.31} \times 10^{-3}/\mathrm{cm}^3$
T_0	$6.36^{+0.11}_{-0.12}$ keV	$6.35^{+0.13}_{-0.11}$ keV
b_1	2.6 (fixed)	2.6 (fixed)
b_2	0.5 (fixed)	0.5 (fixed)
r_1	$0.74^{+0.06}_{-0.06}$ Mpc	$0.75^{+0.06}_{-0.07}$ Mpc
ϵ'	-	0.43
$\mu'_{\rm G}$	-	0.24
$\mu'_{\rm L}$	-	0.55
Minimum χ^2/d.o.f.	58/44	57/41

affect our analysis.

We perform an MCMC analysis using modified *Monte Python* code [141] that employs a Metropolis–Hastings [120, 121] sampling algorithm. This analysis includes 5 parameters in the chi-squared statistic, $\chi^2_{\rm BX+SZ+WL}$. We require Gelman–Rubin statistics [122] of $\mathcal{R} - 1 < 0.001$ for each parameter to ensure convergence of our runs. The black dashed curve in each panel of figure 4.10 shows the best-fit profiles for Newtonian gravity. The minimum value of the chi-squared statistic is $\chi^2_{\rm XB+SZ+WL}$/d.o.f. = 58/44, and the 2-dimensional marginalized contours of different combinations of model parameters are shown in figure 4.13.

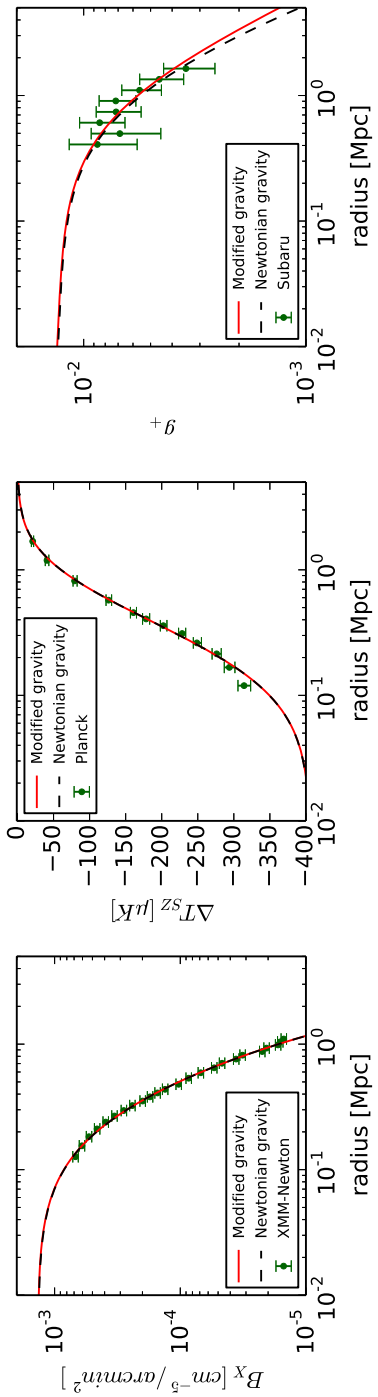

Figure 4.10: Best-fit profiles in the frameworks of Newtonian gravity (black dashed curve) and the generalized Galileon model (red solid curve), and the observational results. The best-fit parameters are listed in Table 4.3. *Left panel:* The X-ray surface brightness from the *XMM-Newton* observations [135, 136]. The errors bars are composed of the Poisson noise and systematic errors that we here assume to be 5%. *Center panel:* The SZ temperature profile from the *Planck* measurements [97]. *Right panel:* The weak-lensing profile from the Subaru observations [132].

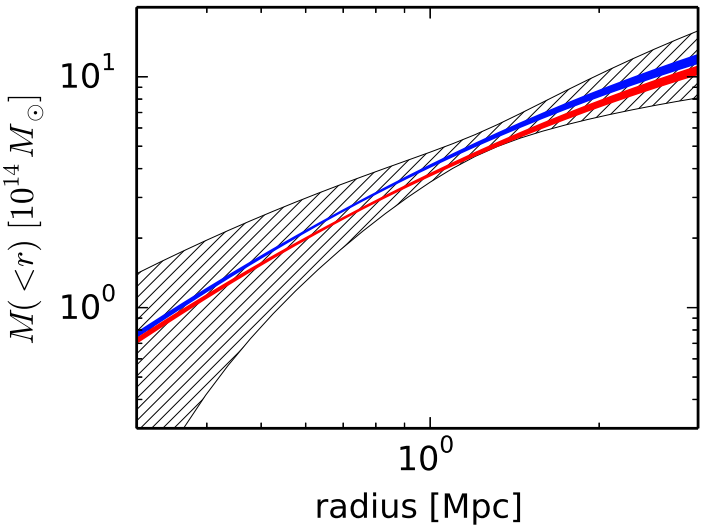

Figure 4.11: Spherical masses enclosed within different radii. The gray hatched region denotes the 1σ uncertainty interval for the lensing mass determined solely by weak-lensing analysis [102]. The blue and red regions denote the 1σ uncertainty intervals for hydrostatic masses without and with the non-thermal pressure component, respectively, determined by our joint-fit method. The hydrostatic and lensing masses agree with each other, irrespective of the presence or absence of a non-thermal pressure component.

Non-thermal pressure possibly caused by turbulent gas and bulk motion causes a systematic error when comparing observations of clusters with theoretical predictions. The estimated fraction of non-thermal pressure in the Coma Cluster can be larger than that of the thermal pressure by 10% [142]. Here, we estimate how non-thermal pressure affects our fitting based on a numerical simulation. To this end, we estimate the hydrostatic masses by comparison with the X-ray brightness and SZ effect profiles of the Coma Cluster. Here we define the non-thermal fraction $f_{\rm nth}$ by $f_{\rm nth} \equiv P_{\rm nth}/(P_{\rm nth} + P_{\rm gas})$, where $P_{\rm nth}$ and $P_{\rm th}$ are the non-thermal pressure and the thermal pressure, respectively. In the case which includes the non-thermal pressure, the thermal pressure is replaced by $P_{\rm gas} = (1 - f_{\rm nth})P_{\rm tot}$. We consider the following non-thermal pressure fraction as a function of the radius,

$$f_{\rm nth}(r) = \alpha_{\rm nt}(1+z)^{\beta_{\rm nt}} \left(\frac{r}{r_{500}}\right)^{n_{\rm nt}} \left(\frac{M_{200}}{3\times 10^{14} M_\odot}\right)^{n_{\rm M}}, \tag{4.54}$$

which is a theoretical prediction from numerical simulations in Ref. [106, 107]. The parameters r_{500} and M_{200} mean the radius and mass where the matter density in the galaxy cluster is 500 and 200 times of the critical density, respectively. In the present analysis we adopt $(\alpha_{\rm nt},\ \beta_{\rm nt},\ n_{\rm nt}, and n_{\rm M}) = (0.18, 0.5, 0.8.0.2)$, which are the best-fit values in Ref. [106] and are consistent with those in [142].

The best-fit profile in the presence of non-thermal pressure is not significantly different from the best-fit profile in the absence of non-thermal pressure. Figure 4.11 shows the enclosed mass profiles as a function of radius. The gray hatched region is the 1σ uncertainty interval for the lensing mass. The blue and red solid regions show the 1σ uncertainty intervals for hydrostatic masses fitted without and with non-thermal pressure, respectively. The hydrostatic mass estimates are in good agreement with the lensing mass, regardless of whether the non-thermal pressure components are included. This shows that our fitting method is not affected by non-thermal pressure, so we do not consider the non-thermal effect when putting a constraint on the modified gravity in the next section.

4.3.3 Constraints on the model parameters from an MCMC analysis

As described in Section 3.4.2, using the solution for the Galileon field, the gas pressure profile assuming Model B (3.33) and convergence (3.39) is given by

$$P_{\rm e}(r) = P_0 \exp\left(\int_0^r dr \frac{\mu m_{\rm p}}{kT_{\rm e}(r)}\left[-\frac{GM(<r)}{r^2} + \frac{\mu_{\rm G}}{4\epsilon^2}H_0^2 r\left(1-\sqrt{1+12\epsilon^2\frac{\rho_{\rm s}}{\rho_{\rm c0}}\frac{r_{\rm s}^3}{r^3}m(r)}\right)\right]\right), \tag{4.55}$$

$$\kappa(r_\perp) = \frac{2}{\Sigma_{\rm c}}\int_0^\infty dz\left[\rho(r) - \frac{\mu_{\rm L}\rho_{\rm c0}}{2\epsilon^2}\left(1-\sqrt{1+12\epsilon^2\frac{\rho_{\rm s}}{\rho_{\rm c0}}\frac{r_{\rm s}^3}{r^3}m(r)}\right) + \frac{\rho(r) - 3\rho_{\rm s}r_{\rm s}^3 m(r)/r^3}{\sqrt{1+12\epsilon^2\rho_{\rm s}r_{\rm s}^3 m(r)/\rho_{\rm c0}r^3}}\mu_{\rm L}\right]. \tag{4.56}$$

Since the gas pressure tracing the matter density deceases as the cluster-centric radius increases, the pressure gradient is restricted to $dP_{\rm e}/dr < 0$. This gives constraints on $\mu_{\rm G}$. Instead of $\mu_{\rm G}$, $\mu_{\rm L}$ and ϵ, we introduce

$$\mu'_{\rm G} = \frac{\mu_{\rm G}}{1+|\mu_{\rm G}|}, \tag{4.57}$$

$$\mu'_{\rm L} = \frac{\mu_{\rm L}}{1+|\mu_{\rm L}|}, \tag{4.58}$$

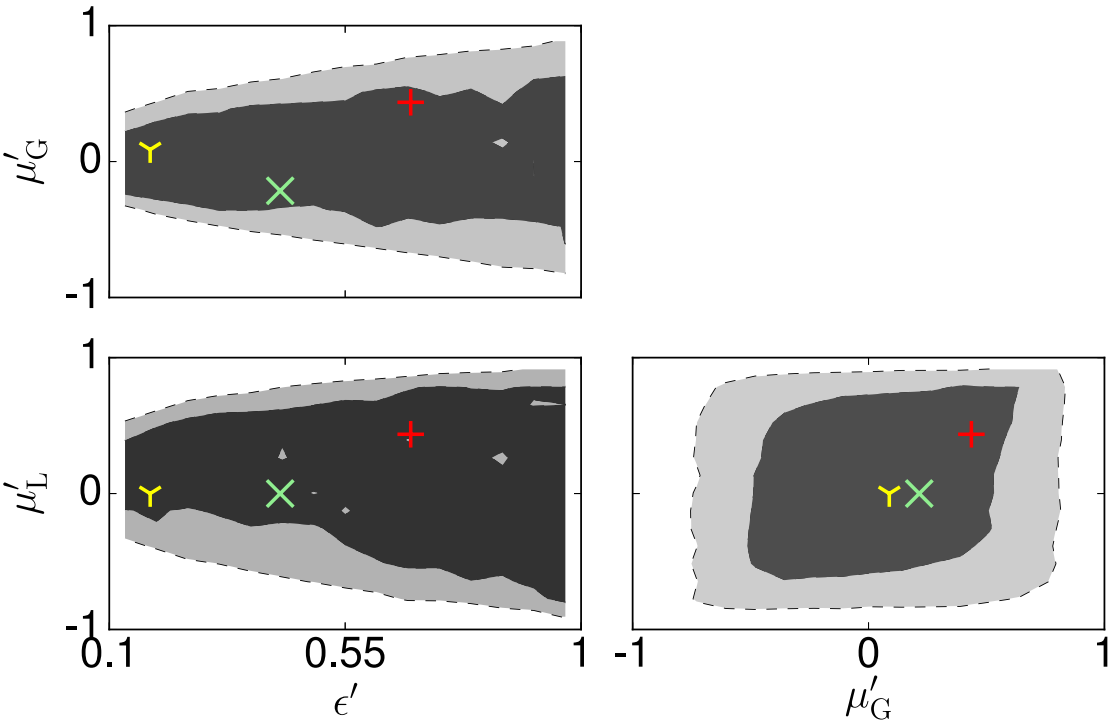

Figure 4.12: The 68% CL (dark gray regions) and 95% CL (light gray regions) 2-dimensional marginalized contours for the generalized Galileon model parameters. The red plus, green cross, and yellow Y symbols indicate models for the simplest cubic Galileon, sDGP, and nDGP models, respectively.

$$\epsilon' = 1 - \exp(-\epsilon), \tag{4.59}$$

which, respectively, span the complete available parameter space of $\mu_{\rm G}$ and $\mu_{\rm L}$ in the interval $[-1, 1]$ and that of ϵ in the interval $[0, 1]$. General relativity is recovered when $\mu'_{\rm G} = \mu'_{\rm L} = 0$ or $\epsilon' \to 1$. Using the same method adopted for the Newtonian case, we perform an MCMC analysis for the modified gravity model including 8 parameters with the chi-squared statistic, $\chi^2_{\rm BX+SZ+WL}$, defined by Eq. (4.50).

Figure 4.14 shows the 2-dimensional marginalized contours of different combinations of the model parameters. The best-fit parameters and their 1-dimensional marginalized 68% errors are listed in Table 4.3. The red curve in each panel of figure 4.10 shows the best-fit profile for the generalized Galileon model with the minimum value of the chi-squared/d.o.f., $\chi^2_{\rm XB+SZ+WL}/{\rm d.o.f.} = 57/41$. These profiles almost overlap with the profiles for Newtonian gravity (black dashed curves), which

shows that a large deviation from Newtonian gravity is rejected. We note that there is no significant difference between the red and black curves in the best-fit profiles. There is a slight difference in the shear profiles at large radii, $r > 1$Mpc, which seems to originate from the large error bars of the shear data.

Figure 4.12 shows 2-dimensional marginalized contours of the confidence levels for the parameters $\mu'_{\rm G}$, $\mu'_{\rm L}$ and ϵ'. The parameters $\mu'_{\rm G}$ and $\mu'_{\rm L}$ are from the modification of the gravitational potential and the lensing potential, and ϵ' is a parameter characterizing the Vainshtein radius. Large values of $\mu'_{\rm G}$ and $\mu'_{\rm L}$ are rejected at the 68% confidence level, which indicates that the possibility of a large deviation from Newtonian gravity may be ruled out, depending on the parameter ϵ'. When ϵ is smaller, the Vainshtein radius is smaller and we can put a tighter constraint on $\mu_{\rm G}$ and $\mu_{\rm L}$. However, when ϵ is large, the Vainshtein radius becomes large, which makes it difficult to distinguish between the Newtonian gravity model and the modified gravity model due to the Vainshtein mechanism. The red-plus, green cross, and yellow Y symbols in figure 4.12 indicate representative models (the simplest cubic Galileon model, the sDGP model and the nDGP model, respectively) at the redshift of $z = 0.0236$. The parameter values for each model are shown in Table 4.4.

In a previous work [41], only a constraint on the $\mu_{\rm L}$ and ϵ parameter space is obtained, based on the lensing observations. In another recent related study, Barreira *et al.* investigated cluster masses and the concentration parameters in modified gravity models using shear profiles [143]. They focused their investigation on the mass–concentration relation of 19 X-ray selected clusters from the CLASH survey in the simplest cubic Galileon and Nonlocal gravity models. They found that the mass–concentration relation obtained from the shear profiles for the cubic Galileon model is the same as those for the ΛCDM model, and no stringent constraint on the modified gravity models is obtained. Unfortunately the constraint obtained in the present paper is not very stringent either, but there is one advantage. Models with $\mu_{\rm L} = 0$, like the sDGP and nDGP models, are indistinguishable from Newtonian gravity in the method based on lensing observations. On the other hand, our method of combining the gas and weak-lensing profiles can solve the problem of this degeneracy. Future observations should improve our constraint.

4.3.4 Discussion

Degeneracies of parameters

In the MCMC analysis in the previous section, we do not take the range of $0 \leq \epsilon \leq 0.1$ into account because it is hard to converge the MCMC runs because of degeneracy in

Table 4.4: Values of modified gravity parameters for each model at the redshift of $z = 0.0236$.

Models	ϵ (ϵ')	$\mu_{\rm G}$ ($\mu'_{\rm G}$)	$\mu_{\rm L}$ ($\mu'_{\rm L}$)
simplest cubic Galileon	0.77 (0.44)	0.77 (0.44)	1.12 (0.67)
sDGP	-0.26 (-0.22)	0 (0)	0.53 (0.43)
nDGP	0.20 (0.18)	0 (0)	0.10 (0.09)

the parameter space. Here, we consider this parameter region to provide a complete discussion.

First, taking the limit $\epsilon \to 0$, which means the fifth force is unscreened everywhere, the solutions of the gas pressure (4.55) and the convergence (4.56) are reduced to

$$P_{\rm e}(r) = P_0 \exp\left(\int_0^r dr \frac{\mu m_{\rm p}}{kT_{\rm e}(r)}\left[-\frac{GM(<r)}{r^2}(1+\mu_{\rm G})\right]\right), \tag{4.60}$$

$$\kappa(r_\perp) = (1+\mu_{\rm L})\frac{2}{\Sigma_{\rm c}}\int_0^\infty dz \rho(r). \tag{4.61}$$

Then, the pressure profile and the convergence profile are simply modified by factors of $(1+\mu_{\rm G})$ and $(1+\mu_{\rm L})$, respectively. In this case, we have $P_{\rm e} \propto (1+\mu_{\rm G})M_{\rm vir}m(c)/c^3$ and $\kappa \propto \rho_{\rm s} \propto (1+\mu_{\rm L})M_{\rm vir}c^3/m(c)$, so there are degeneracies between the parameters, $M_{\rm vir}, c, \mu_{\rm G}$, and $\mu_{\rm L}$. Figure 4.15 compares the results of the MCMC analysis with ϵ fixed at zero (dark blue region (68% CL) and medium blue region (95% CL)) and the results of Newtonian gravity (dark gray region and medium gray region), which are the same as those of figure 4.13. The best-fit parameters are shown in the Table 4.5. The CL contours of the blue regions reflect the degeneracy between the parameters $M_{\rm vir}, c, \mu_{\rm G}$, and $\mu_{\rm L}$.

Next, we show how the presence of the fifth force affects the parameter estimation. For example, the blue confidence contours in figure 4.16 show the 68% and 95% confidence contours of the case with $\epsilon = 0.05$, $\mu_{\rm G} = 0.2$ and $\mu_{\rm L} = 0$. $M_{\rm vir}$ and c are different from those of Newtonian gravity (gray regions), but other parameters, n_0, T_0 and b_1, are not changed. The minimum value of chi-squared/d.o.f. in the presence of the fifth force is $\chi^2_{\rm XB+SZ+WL}/{\rm d.o.f.} = 60/44$, which is almost the same as the Newtonian case, despite the different cluster parameter, $M_{\rm vir} \sim 0.9 \times 10^{15} M_\odot$ (see Table 4.5). This result exemplifies the general result that the presence of the

Table 4.5: Same as Table 1 but for the results of the generalized Galileon model in the unscreened limit with only ϵ fixed ($\epsilon = 0$, second column), and the case of fixing all the modified gravity parameters ($\epsilon' = 0.05$, $\mu'_{\rm G} = 0.2$, and $\mu'_{\rm L} = 0$, third column).

Parameter	Modified gravity (unscreened)	Modified gravity (fifth force)
$M_{\rm vir}$	$1.26^{+0.15}_{-3.85} \times 10^{15}\ M_\odot$	$0.86^{+0.05}_{-0.05} \times 10^{15}\ M_\odot$
c	$3.78^{+0.13}_{-0.55}$	$3.84^{+0.24}_{-0.28}$
n_0	$6.15^{+0.27}_{-0.29} \times 10^{-3}/{\rm cm}^3$	$6.20^{+0.27}_{-0.32} \times 10^{-3}/{\rm cm}^3$
T_0	$6.35^{+0.13}_{-0.11}$ keV	$6.36^{+0.12}_{-0.12}$ keV
b_1	2.6 (fixed)	2.6 (fixed)
b_2	0.5 (fixed)	0.5 (fixed)
r_1	$0.75^{+0.06}_{-0.07}$ Mpc	$0.75^{+0.06}_{-0.06}$ Mpc
ϵ'	0 (fixed)	0.05 (fixed)
$\mu'_{\rm G}$	-0.10	0.2 (fixed)
$\mu'_{\rm L}$	-0.05	0 (fixed)
Minimum χ^2/d.o.f.	57/42	60/44

attractive fifth force affects the estimation of the NFW parameters, $M_{\rm vir}$ and c. This is understood to be a consequence of the degeneracy between the modification parameters $\mu_{\rm G}$ and $\mu_{\rm L}$ and $M_{\rm vir}$ and c.

Systematic errors

We now discuss possible systematic errors. In our analysis, we have assumed spherical symmetry for the matter distribution and an equilibrium state for the gas component, that is, balance between the pressure gradient and the gravitational force (including the fifth force in the case of its presence). We have demonstrated that non-thermal pressure at the level suggested by numerical simulations does not alter our results. A future X-ray satellite, ASTRO-H [144], will observe turbulent gas motion in the Coma Cluster in more detail, which will provide relevant information relating to our result. However, observations of the Coma Cluster suggest substructures [102, 132, 138, 145–147] and orientation dependence [118, 137, 140], so the cluster is not

thought to be a relaxed system. Dynamical states of the Coma Cluster would give a systematic difference between our results and temperature measurements. Our fitting results show that the temperature of the Coma Cluster is around 6.4 keV (see Table. 4.3), but this result seems lower than those of X-ray observations [99, 100, 118, 135–137, 140], which estimate that the temperature of the Coma Cluster is around 8–9 keV. Comparing the mass–temperature scaling relation for a sample of relaxed clusters [148] with an X-ray temperature observation of the Coma Cluster [135, 136], we find that the observed temperature is higher than the temperature expected from the mass. The enhancement is at the 3σ level of intrinsic scatter [148]. Similar results of high temperatures have also been reported by a comparison with other clusters [115]. Depending on the orientation and excluding the central region, the temperature of the Coma Cluster could be around 6–7 keV [135,137], but it is difficult to take this dependence into account. Therefore, a systematic error in temperature of the Coma Cluster would have a substantial impact on the proposed fitting method. To reduce the possible dependence of cluster-dynamical states and halo triaxiality, it is of vital importance to increase the number of sampled clusters. Ongoing and future multi-wavelength surveys, such as the Hyper Suprime-Cam (HSC) optical survey[1], the Dark Energy Survey (DES) [149], the *eROSITA* X-ray survey [150], and the ACT-Pol [151] and SPT surveys [152], will be powerful aids to providing better constraints on gravity models.

[1] http://subarutelescope.org/Projects/HSC/surveyplan.html

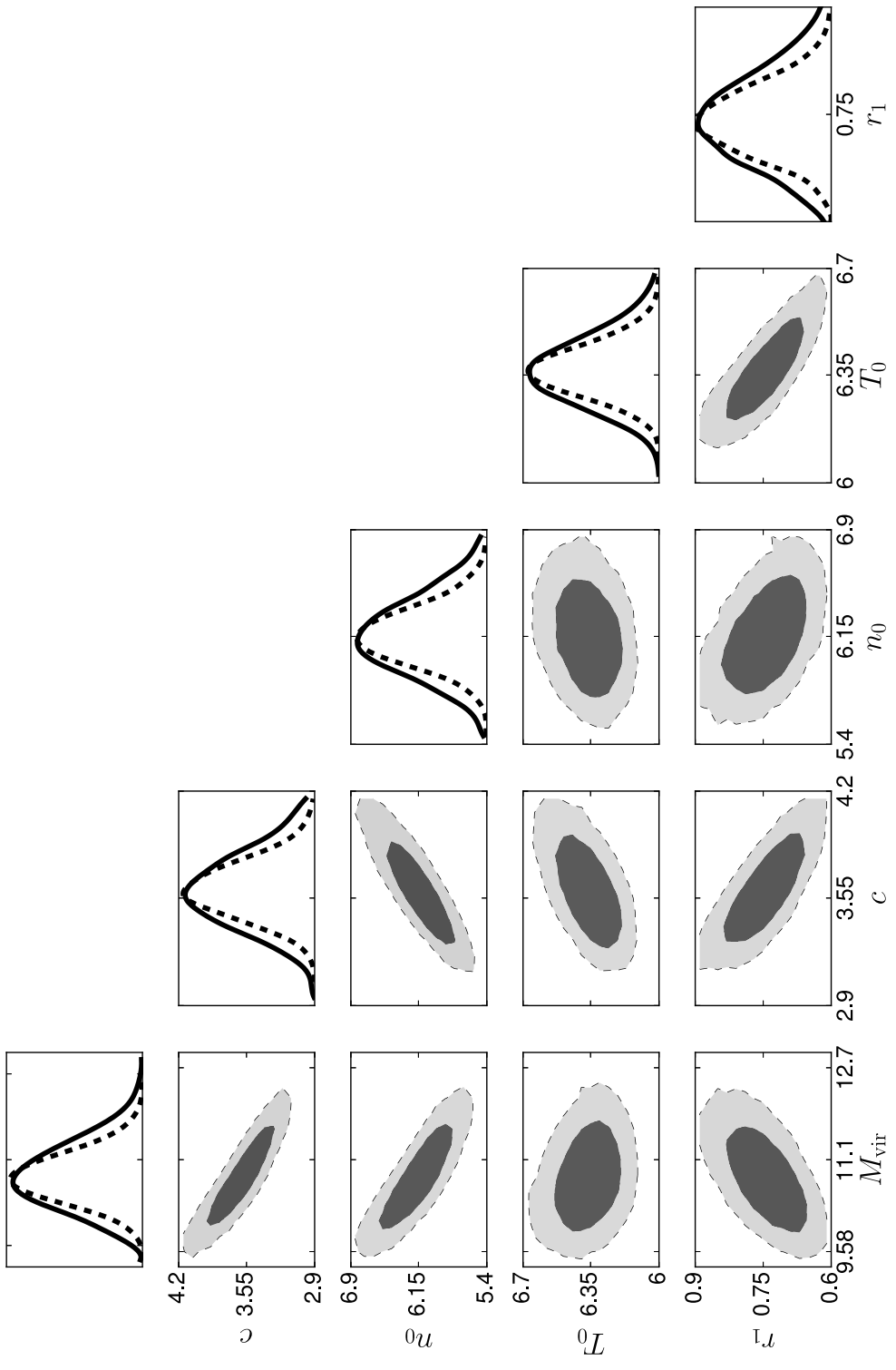

Figure 4.13: The 68% CL (dark gray region) and 95% CL (medium gray region) 2-dimensional marginalized contours for the 5 model parameters, $M_{\rm vir}$ [$10^{14} M_\odot$], c, n_0 [10^{-3}cm^{-3}], T_0 [keV] and r_1 [Mpc]. The right-most plots of each row show the 1-dimensional marginalized constraints (solid) and likelihood distributions (dotted).

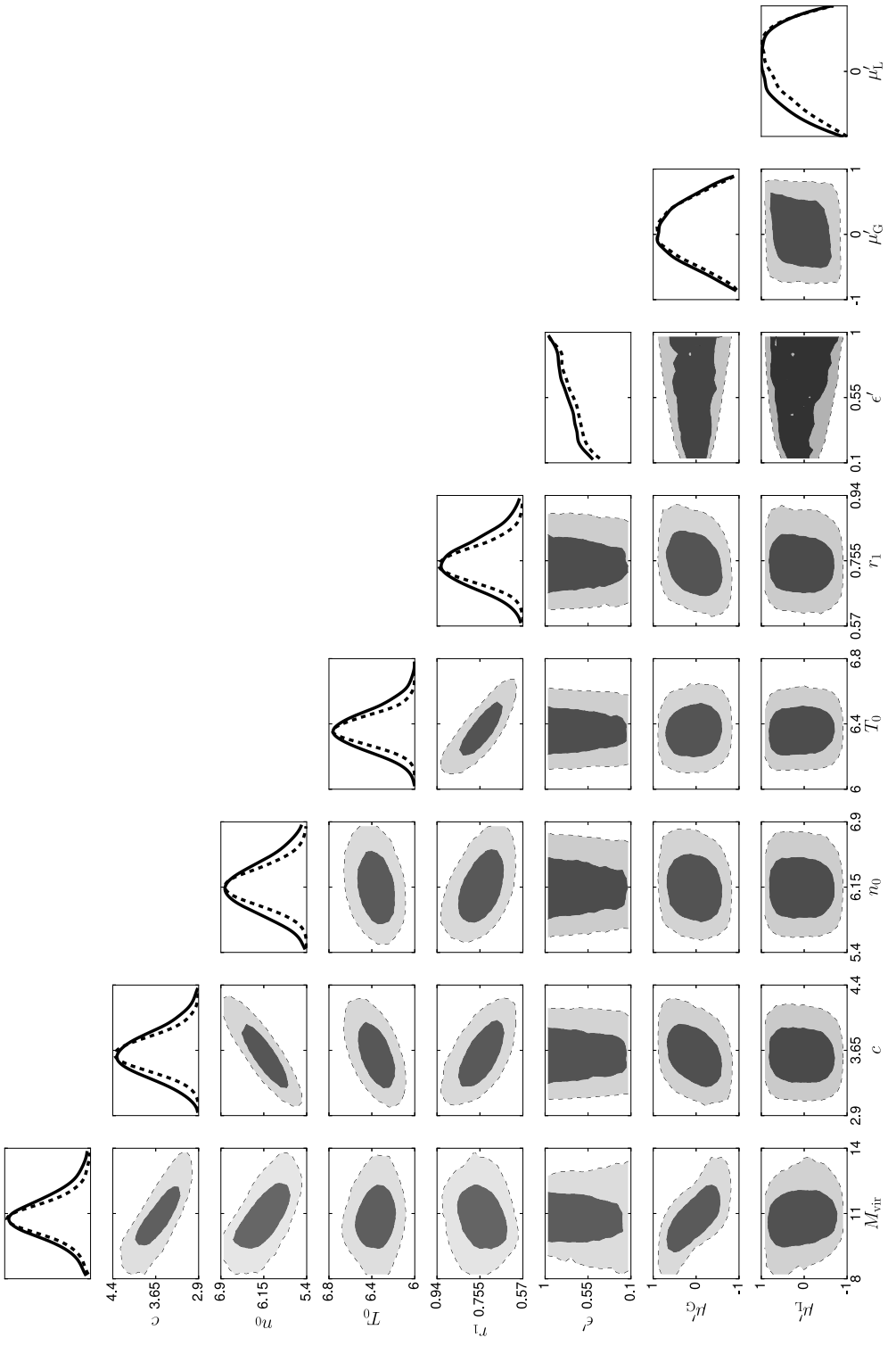

Figure 4.14: Same as figure 4.13 but including the modification parameters ϵ', $\mu'_{\rm G}$ and $\mu'_{\rm L}$ in the MCMC analysis.

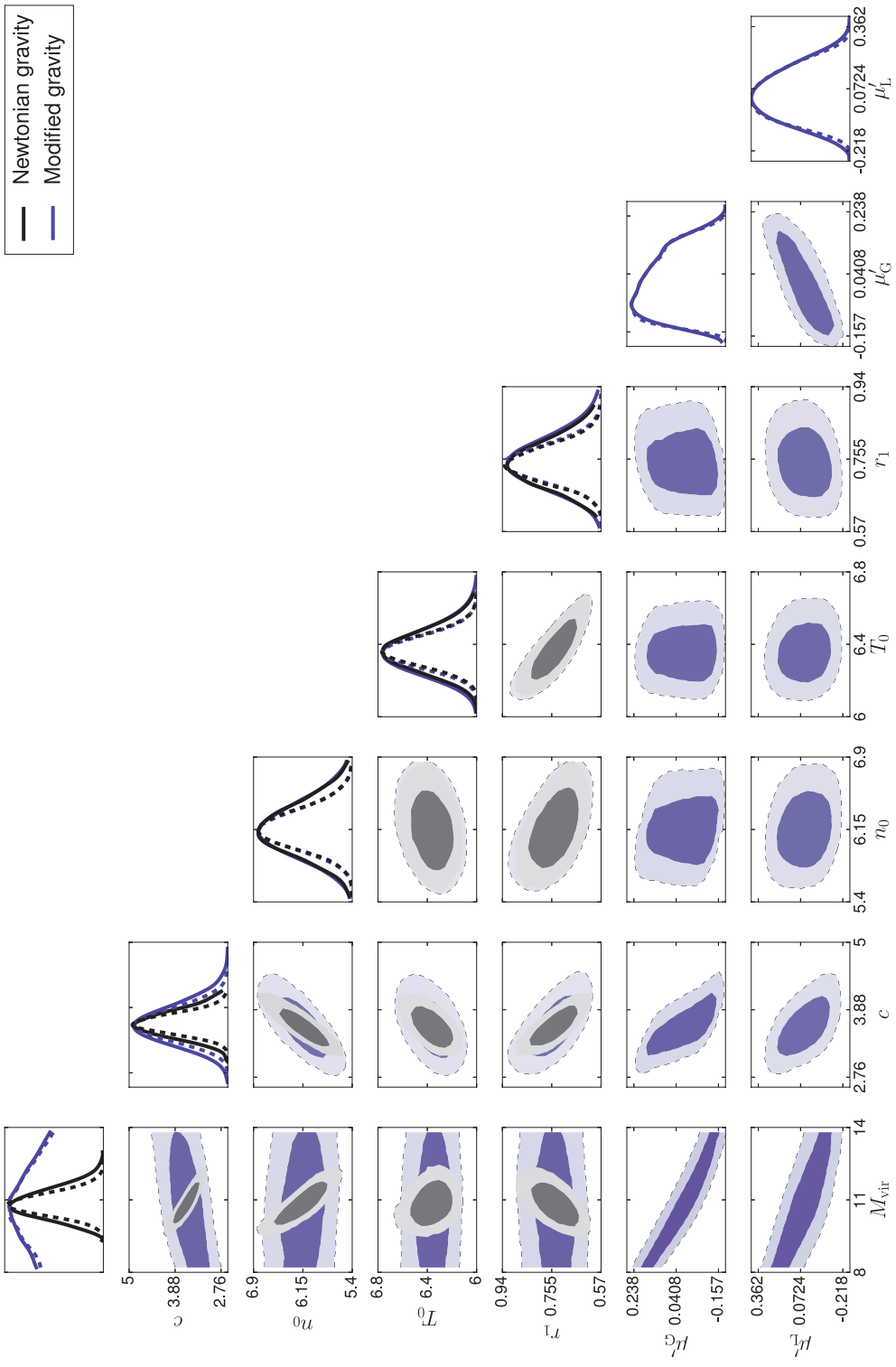

Figure 4.15: The dark blue region (68% CL) and the medium blue region (95% CL) are the results of the MCMC analysis for the modified gravity model with $\epsilon = 0$. The dark gray region (68% CL) and the medium gray region (95% CL) are the results for Newtonian gravity (same as Fig. 4.13).

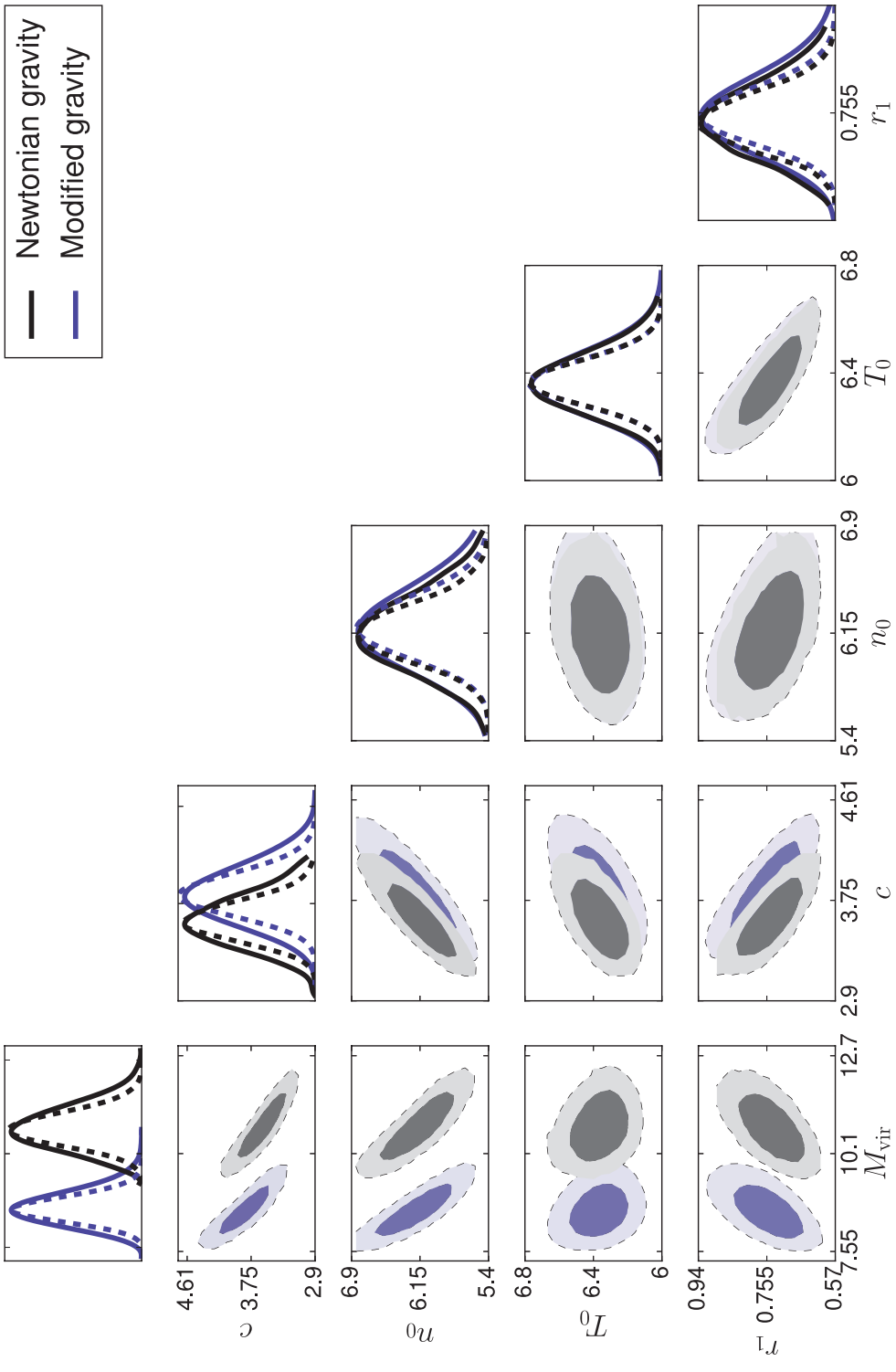

Figure 4.16: The dark blue region (68% CL) and the medium blue region (95% CL) are the results of the MCMC analysis for the modified gravity model with $\epsilon' = 0.05$, $\mu'_{\rm G} = 0.2$ and $\mu'_{\rm L} = 0$. The dark gray region (68% CL) and the medium gray region (95% CL) are the results for Newtonian gravity (same as Fig. 4.13).

Chapter 5

Summary and conclusion

In this thesis, we have studied the effects of modifications of gravity on gas distributions in galaxy clusters.

First, in Section 3, we derived the gas distribution profiles in an analytic manner under the assumption of hydrostatic equilibrium between the gas pressure gradient and the gravitational and fifth forces. In particular, using an analytic chameleon field solution, we also demonstrated that the attractive fifth force may give rise to a steep drop in the gas distribution in the outer region of a galaxy cluster. This feature is more significant when the mass of the cluster is small.

The gas density profile depends on the coupling strength between the chameleon field and gas components, β, and the background chameleon field, ϕ_∞, but it does not depend on the potential parameters, n and Λ. This provides us with an opportunity to constrain β and ϕ_∞ by comparison with observations. Using this feature, we showed that we can put a constraint on ϕ_∞ in the chameleon model, using the observation of the X-ray temperature profile of the Hydra A cluster [94] in Section 4.1. We obtained a useful upper bound of $\phi_\infty < 10^{-4} M_{\rm Pl}$ in the case $\beta = 1$ [1]; however, no useful constraint was obtained in the case $\beta = 1/\sqrt{6}$, which corresponds to an $f(R)$ model. To obtain a useful constraint, observations of the outer region of a smaller mass cluster are more advantageous. Furthermore, a combination with other observations, like weak-lensing measurements, might improve the constraint.

Next, in Section 4.3.2, we proposed a novel method to test gravity in the outskirts of galaxy clusters by comparing their hydrostatic and lensing mass estimates. The hydrostatic mass profile of a cluster can be inferred from the 3-dimensional gas temperature, electron number density, and electron pressure profiles obtained from the

[1] When we take environmental effects into account, this bound might be understood as a bound around the Hydra A cluster.

projected observations of the X-ray surface brightness, the X-ray temperature, and the Sunyaev–Zel'dovich (SZ) cosmic microwave background temperature profile, by implementing a parametric reconstruction method. The dark matter density profile can be further constrained by weak-lensing observations. Here, we adopt the NFW density profile to describe the dark matter distribution within the cluster. In the case of hydrostatic equilibrium of the gas and standard gravity, the different mass estimates should agree. In the presence of a chameleon field, coupling to the matter fields and introducing an attractive fifth force, the masses estimated from gas observations and from lensing changes differ and can therefore be used as a test of gravity models.

Combining measurements of the X-ray surface brightness, the X-ray temperature, the SZ effect, and lensing of the Coma Cluster, we performed a Markov chain Monte Carlo analysis of the model parameter space describing the cluster profiles and gravity theory. We have obtained competitive constraints on the chameleon gravity model parameters, β and ϕ_∞, the coupling strength of the chameleon field and the field value in the environment of the cluster, which we approximate here by the cosmological background. In contrast to the study in Ref. [42] (Section 4.1) that constrains the modified gas distribution in the Hydra A cluster measured using the X-ray temperature, our constraint does not rely on the assumption of a polytropic equation for the state of the gas, employs a Bayesian statistical approach for inferring parameter constraints on the full set of model parameters, and yields a tighter bound on the modified gravity parameters by using the combination of X-ray, SZ, and lensing observations available for the Coma Cluster. We emphasize that our results provide a powerful constraint on $f(R)$ gravity models, corresponding to a particular choice of the chameleon coupling constant $\beta = \sqrt{1/6}$, for which we obtain an upper bound of $|f_{\rm R0}| \lesssim 6 \times 10^{-5}$ at the 95% CL. This bound is comparable with the current strongest cosmological constraints on $f(R)$ gravity (see Fig. 1.2).

Finally, in Section 4.3, we obtained a constraint on a generalized cubic Galileon model using observations of Coma Cluster of X-ray brightness, the SZ effect, and weak lensing. We have constructed a simple analytic model of the gas distribution profiles and the weak-lensing profile (see [41, 43, 44]). The fifth force affects not only the gas distribution but also the weak-lensing profile. In general, the effects depend on the various parameters characterizing the generalized Galileon model. These features can be investigated by a combination of observations of a galaxy cluster reflecting the gas density profile and the lensing signals. These multi-wavelength observations are complementary to each other, and are useful for putting a constraint on the modified gravity model by breaking the degeneracy between the model parameters.

A systematic study compiling multi-wavelength datasets for a large number of clusters will enable us to reduce systematic errors and improve constraints on modified gravity models. However, the degeneracy between the parameters, $M_{\rm vir}$, c, $\mu_{\rm G}$ and $\mu_{\rm L}$, persists in the limit of the weak screening of the fifth force, which affects the estimation of the cluster parameters.

An important systematic that can affect our analysis is deviation from hydrostatic equilibrium of the cluster gas. We have therefore carefully examined the validity of the assumption of hydrostatic equilibrium in the Coma Cluster. Assuming Newtonian gravity, we compared the different mass estimates from the three different gas observations and the weak-lensing mass. We found that the mass profiles from the gas and weak-lensing observations can deviate from each other by up to 50% but that they are consistent within the observational errors of the lensing measurement. We also analyzed the effect of including a non-thermal pressure component with a radial profile calibrated to hydrodynamic simulations but with extremized amplitude. This contribution only marginally affects our reconstructed masses, and we conclude that hydrostatic equilibrium is a good approximation to describe the outer region of the Coma Cluster. Note, however, that the effect from the chameleon force on the hydrostatic mass is opposite to the effect of the non-thermal pressure. Hence, the chameleon force can compensate for a large contribution from non-thermal pressure and cause a degeneracy between the two effects. On the other hand, the magnitude of the non-thermal pressure that would be required to compensate for the effects of the chameleon force tested here is not expected from current hydrodynamical simulations. It is, however, not clear whether the presence of a chameleon field could significantly enhance the non-thermal pressure contribution in the Coma cluster, such that it could cancel the effects of the chameleon field and act to alleviate the constraints on the modification of gravity. In this regard, it will be useful to analyze the non-thermal pressure in chameleon gravity models using hydrodynamical simulations along with a more detailed study of the Newtonian case. As for $f(R)$ gravity, such hydrodynamical simulations have recently been conducted by Arnold *et al.* [96]. They estimate the non-thermal pressure from the bulk motion in the intracluster medium and find that it only leads to substantial contributions in merging clusters, which can be identified and excluded to obtain statistical quantities like X-ray and SZ scaling relations. Their results suggest that the effects of non-thermal pressure in a relaxed cluster are not significant, as in the case of the Coma Cluster, at least in the case of $f(R)$ gravity models.

Further effects which may cause deviations from the hydrostatic equilibrium have been discussed in Refs. [103, 104, 133]. Ref. [103] found that the mass in a simulated

halo estimated under the hydrostatic equilibrium assumption deviates from the true mass due to gas acceleration on average by $\sim (10-20)\%$. Given the large errors in the measurement of the lensing mass of the Coma cluster, we can ignore this deviation in our current analysis. Future measurements, such as those from Astro-H X-ray observations, will allow more precise modeling of the Coma Cluster.

Our results demonstrate that galaxy clusters are useful probes of gravity. The method described in this paper may be applied to other clusters. However, one should be cautious about the individual properties of each cluster: the assumptions adopted in the present paper might not be valid for other galaxy clusters and need to be considered in each case. The key is to understand the motion and distribution of the gas component in clusters. The combination of multi-wavelength observations, such as the recent results from the *Planck* satellite [153–156], will provide a clue on how to solve this difficult issue. In the near future, we will have stacked lensing, SZ, and X-ray profiles for hundreds of clusters. The combination of multi-wavelength observations for many clusters will significantly improve the tests of gravitational interactions on cluster scales.

Appendix A

Tips for modified gravity models

A.1 Equivalence between $f(R)$ model and chameleon model

In this appendix, we show the equivalence of the $f(R)$ model and the chameleon model (e.g., [157, 158]) in two steps, which are given in Sections A.1.1 and A.1.2. In Section A.1.3, we give the expression of the solution (3.50) and (3.54) in the Jordan frame.

A.1.1 Equivalence with the Brans–Dicke model

Introducing a scalar field χ, we consider the following action

$$S = \frac{M_{\rm Pl}^2}{2}\int d^4x\sqrt{-g}[\chi + f(\chi) + (1+f_\chi(\chi))(R-\chi)] + \int d^4x\mathcal{L}_{\rm m}(\Psi_{\rm m}, g_{\mu\nu}), \quad \text{(A.1)}$$

where $f_\chi \equiv df/d\chi$. First, the variation of the action (A.1) with respect to χ gives

$$f_{\chi\chi}(\chi)(R-\chi) = 0. \quad \text{(A.2)}$$

When $f_{\chi\chi} \neq 0$, the equation of motion for χ is $R = \chi$, then the action (A.1) is equivalent with the $f(R)$ model (1.36). Next, introducing a new scalar field defined by

$$\varphi \equiv \frac{M_{\rm Pl}^2}{2}(1+f_\chi), \quad \text{(A.3)}$$

the action (A.1) can be rewritten as

$$S = \int d^4x\sqrt{-g}\left[\frac{M_{\rm Pl}^2}{2}\varphi R - U(\varphi)\right] + \int d^4x\mathcal{L}_{\rm m}(\Psi_{\rm m}, g_{\mu\nu}), \tag{A.4}$$

where we define the potential $U(\varphi)$ by

$$U(\varphi) = \frac{M_{\rm Pl}^2}{2}[R(1+f_R) - (R+f(R))]. \tag{A.5}$$

On the other hand, the Brans–Dicke model with a potential is given by

$$S = \int d^4x\sqrt{-g}\left[\varphi R - \frac{\omega_{\rm BD}}{\varphi}g_{\mu\nu}\partial^\mu\varphi\partial^\nu\varphi - U(\varphi)\right] + \int d^4x\mathcal{L}_{\rm m}(\Psi_{\rm m}, g_{\mu\nu}). \tag{A.6}$$

Then, by setting the Brans–Dicke parameter $\omega_{\rm BD}$ to zero, we find that the Brans–Dicke model is equivalent with the action (A.4); that is, it is equivalent to the $f(R)$ model.

A.1.2 Conformal transformation

Next, we consider the conformal transformation

$$g_{\mu\nu} = \Omega^2\tilde{g}_{\mu\nu}, \tag{A.7}$$

where $g_{\mu\nu}$ and $\tilde{g}_{\mu\nu}$ are the metrics in the Einstein and Jordan frames, respectively. By this transformation, the first term of the action (A.6) reduces to

$$S_1 = \int d^4x\sqrt{-g}\Omega^{-2}\varphi\left[R + 6\Box\ln\Omega - 6g^{\mu\nu}\frac{\partial_\mu\Omega\partial_\nu\Omega}{\Omega^2}\right]. \tag{A.8}$$

When we choose

$$\Omega = \sqrt{\frac{2\varphi}{M_{\rm Pl}^2}}, \tag{A.9}$$

the action is minimally coupled with the scalar field. In this case, the first and the second terms of the action (A.6) reduce to

$$S_1 = \frac{M_{\rm Pl}^2}{2}\int d^4x\sqrt{-g}\left[R - \frac{3}{2\varphi^2}g^{\mu\nu}\partial_\mu\varphi\partial_\nu\varphi\right], \tag{A.10}$$

$$S_2 = \frac{M_{\rm Pl}^2}{2}\int d^4x\sqrt{-g}\left[-\frac{\omega}{\varphi^2}g^{\mu\nu}\partial_\mu\varphi\partial_\nu\varphi\right]. \tag{A.11}$$

Thus, we obtain

$$S_1+S_2 = \frac{M_{\rm Pl}^2}{2}\int d^4x\sqrt{-g}\left[R-\frac{1}{2\varphi^2}(3+2\omega_{\rm BD})g^{\mu\nu}\partial_\mu\varphi\partial_\nu\varphi\right]. \tag{A.12}$$

Introducing a new scalar field ϕ defined by

$$\varphi = \frac{M_{\rm Pl}^2}{2}e^{-A\phi}, \tag{A.13}$$

with

$$A = \sqrt{\frac{2}{M_{\rm Pl}^2(3+2\omega_{\rm BD})}}, \tag{A.14}$$

we obtain the relations

$$g_{\mu\nu} = e^{-2\beta\phi/M_{\rm Pl}}\tilde{g}_{\mu\nu}, \tag{A.15}$$

$$\beta = \sqrt{\frac{1}{2(3+2\omega_{\rm BD})}}. \tag{A.16}$$

When we define the potential V by

$$V(\phi) = e^{4\beta\phi/M_{\rm Pl}}U(\varphi(\phi)), \tag{A.17}$$

we obtain the expression of the action in the Einstein frame (1.16),

$$S = \int d^4x\sqrt{-g}\left[\frac{M_{\rm Pl}^2}{2}R-\frac{1}{2}g^{\mu\nu}\partial_\mu\phi\partial_\nu\phi-V(\phi)\right]+\int d^4x\mathcal{L}_{\rm m}(\Psi,e^{2\beta\phi/M_{\rm Pl}}g_{\mu\nu}). \tag{A.18}$$

The action for the $f(R)$ model is obtained by setting

$$\beta = \sqrt{\frac{1}{6}}, \tag{A.19}$$

$$e^{-\sqrt{2/3}(\phi/M_{\rm Pl})} = 1+f_R, \tag{A.20}$$

$$V(\phi) = \frac{M_{\rm Pl}^2}{2}\frac{R(1+f_R)-(R+f(R))}{(1+f_R)^2}. \tag{A.21}$$

A.1.3 Analytic solution in the Jordan frame

Using the conformal transformation (A.7), we can obtain an analytic solution of the equation of motion for f_R.

In the Jordan frame, the equation of motion for f_R is given by

$$\nabla^2 f_R = \frac{1}{3M_{\rm Pl}^2}\left[\rho_{\rm c}\left(1+4\frac{\Omega_\Lambda}{\Omega_{\rm m}}\right)\left(\frac{f_{R0}}{f_R}\right)^{1/(\tilde{n}+1)} - \rho_{\rm m}\right]. \tag{A.22}$$

Assuming the generalized Navarro–Frenk–White profile (3.2) for the matter density profile, we obtain a solution for f_R in the same manner as in Sec. 3.4.1:

$$f_{R,\rm int} = f_{R\rm s}[x(1+x)^b]^{\tilde{n}+1}, \qquad x \le x_{\rm c}, \tag{A.23}$$

$$f_{R,\rm ext} = -A\frac{1-(1+x)^{2-b}}{(b-2)x} - \frac{D}{x} + f_{R0}, \qquad x > x_{\rm c}, \tag{A.24}$$

for $b \neq 2$, and

$$f_{R,\rm int} = f_{R\rm s}[x(1+x)^2]^{\tilde{n}+1}, \qquad x \le x_{\rm c}, \tag{A.25}$$

$$f_{R,\rm ext} = -\frac{A\ln(1+x)}{x} - \frac{D}{x} + f_{R0}, \qquad x > x_{\rm c}, \tag{A.26}$$

for $b = 2$, where D is the integration constant and

$$f_{R\rm s} = f_{R0}\left[\frac{\rho_{\rm c}}{\rho_{\rm s}}\left(1+4\frac{\Omega_\Lambda}{\Omega_{\rm m}}\right)\right]^{\tilde{n}+1}, \qquad A = -\frac{\rho_{\rm s} r_{\rm s}^2}{3M_{\rm Pl}^2(b-1)}. \tag{A.27}$$

The values of $x_{\rm c}$ and D are related by connecting the inner solution and the outer solution at the radius $x_{\rm c}$, which gives

$$D = A\frac{(1+x_{\rm c})^{2-b}-1}{b-2} + f_{R0}x_{\rm c} - f_{R\rm s}[x_{\rm c}(1+x_{\rm c})^b]^{\tilde{n}+1}x_{\rm c}, \tag{A.28}$$

$$-A(1+x_{\rm c})^{2-b} + f_{R0}(1+x_{\rm c}) = f_{R\rm s}[x_c(1+x_{\rm c})^b]^{\tilde{n}+1}[(1+(b+1)x_{\rm c})\tilde{n}+2+(b+2)x_{\rm c}]. \tag{A.29}$$

Assuming $\beta\phi/M_{\rm Pl} \ll 1$, the conformal transformation (A.19) $\sim$ (A.21) gives a relation between f_R and the chameleon field ϕ:

$$f_R = -\sqrt{\frac{2}{3}}\frac{\phi}{M_{\rm Pl}} \tag{A.30}$$

and

$$f_{R\mathrm{s}} = -\sqrt{\frac{2}{3}}\frac{\phi_{\mathrm{s}}}{M_{\mathrm{Pl}}}, \quad A = -\sqrt{\frac{2}{3}}\frac{2\phi_0}{M_{\mathrm{Pl}}}, \quad D = -\sqrt{\frac{2}{3}}\frac{C}{M_{\mathrm{Pl}}}, \quad f_{R0} = -\sqrt{\frac{2}{3}}\frac{\phi_\infty}{M_{\mathrm{Pl}}}. \tag{A.31}$$

Furthermore, assuming the potential in the Einstein frame to be $V(\phi) = \Lambda^{4+n}/\phi^n$, we also obtain the relations

$$\tilde{n} + 1 = \frac{1}{n+1}, \qquad \frac{\Lambda^{4+n}}{M_{\mathrm{Pl}}^n} = \frac{1}{2n}\left(\frac{3}{2}\right)^{n/2}(\Omega_{\mathrm{m}} + 4\Omega_\Lambda)|f_{R0}|^{n+1}\rho_{\mathrm{c}}. \tag{A.32}$$

A.2 Definitions of the coefficients

In this appendix, we summarize the relations between the parameters in the Lagrangian and the coefficients in Eq. (3.75), and the relation between the generalized Galileon model and the specific models used in Sec. 4.3.3: the DGP model and the simplest cubic Galileon model (see also [40, 41]).

The coefficients in the perturbation equations (3.78)–(3.80) are defined by

$$\alpha = \alpha_1, \tag{A.33}$$

$$\xi = \alpha_2, \tag{A.34}$$

$$\zeta = \frac{4(\alpha_1 + \alpha_2)}{\beta}\frac{G_4 H}{\dot{\phi}\phi}, \tag{A.35}$$

$$\lambda^2 = \frac{2\beta_0 G_4 \phi H}{\beta X \dot{\phi}}, \tag{A.36}$$

$$\beta = -4(\alpha_0 + 2\alpha_1\alpha_2 + \alpha_2^2)\frac{G_4 H^2}{\dot{\phi}^2}, \tag{A.37}$$

where

$$\alpha_0 = \left(\frac{\dot{\Theta}}{H^2} + \frac{\Theta}{H} - 2G_4 - 4\frac{\dot{G}_4}{H} - \frac{\mathcal{E} + \mathcal{P}}{2H^2}\right)\frac{1}{2G_4}, \tag{A.38}$$

$$\alpha_1 = \left(2\frac{\dot{\phi}G_{4\phi}}{H}\right)\frac{1}{2G_4}, \tag{A.39}$$

$$\alpha_2 = \left(\frac{\dot{\phi}XG_{3X}}{H} - \frac{\dot{\phi}G_{4\phi}}{H}\right)\frac{1}{2G_4}, \tag{A.40}$$

$$\beta_0 = \left(\frac{\dot{\phi} X G_{3X}}{H} \right) \frac{1}{2G_4}, \tag{A.41}$$

$$\Theta = -\dot{\phi} X G_{3X} + 2HG_4 + \dot{\phi} G_{4\phi}. \tag{A.42}$$

These coefficients are determined by the background solutions in Eq. (1.79).

The coefficients in the perturbation equations of the simplest cubic Galileon model are

$$\alpha = 0, \tag{A.43}$$

$$\xi = 4\pi G_3 G_{3X} \dot{\phi}^2 \phi, \tag{A.44}$$

$$\zeta = \frac{G_{3X} \dot{\phi}^2}{\beta \phi}, \tag{A.45}$$

$$\lambda^2 = \frac{G_{3X} \phi}{\beta}, \tag{A.46}$$

$$\beta = -1 + 2G_{3X}(\ddot{\phi} + 2H\dot{\phi}) - 4\pi G_3 G_{3X}^2 \dot{\phi}^4. \tag{A.47}$$

When we adopt the late time de Sitter attractor solution [49], the combinations $\xi\zeta$ and $\lambda^2\zeta$ are given by

$$\xi\zeta = \frac{(1-\Omega_{\rm m})(2-\Omega_{\rm m})}{\Omega_{\rm m}(5-\Omega_{\rm m})}, \tag{A.48}$$

$$\lambda^2\zeta = \left(\frac{2-\Omega_{\rm m}}{H\Omega_{\rm m}(5-\Omega_{\rm m})} \right)^2, \tag{A.49}$$

where $\Omega_{\rm m}(a) = \rho_{\rm m}(a)/3M_{\rm Pl}^2 H^2(a)$ is the matter density parameter.

Within the sub-horizon approximation, the DGP model [26, 27, 30] can be effectively described by the coefficients

$$\alpha = -1, \tag{A.50}$$

$$\xi = \frac{1}{2}, \tag{A.51}$$

$$\zeta = -\frac{2}{3\beta}, \tag{A.52}$$

$$\lambda^2 = -\frac{r_{\rm c}^2}{3\beta}, \tag{A.53}$$

$$\beta = 1 \pm 2Hr_{\rm c}\left(1 + \frac{\dot{H}}{3H^2}\right), \tag{A.54}$$

where $r_{\rm c} = 1/(1-\Omega_{\rm m0})H_0$ and the sign "$\pm$" in β represents the cases of the sDGP model with the "$-$" sign and the nDGP model with the "$+$" sign.

Appendix B

Astrophysics of ionized gas in clusters of galaxies

B.1 Bremsstrahlung

The Bremsstrahlung is a quantum process [159], but we review this process as a quasi-quantum process in the following.

When an electron passes an ion with charge Z, an electromagnetic wave is radiated. The radiation has the energy

$$E = \int_{-\infty}^{\infty} \frac{2}{3} \frac{e^2 a(t)^2}{c^3} dt, \tag{B.1}$$

where c is the light speed, e is the elementary charge, v is the relative speed between the electron and the ion, b is the collision efficiency, and a is the rate of acceleration of the electron toward to the ion. Here, we consider the Fourier transformation F for a,

$$F(\omega) = \frac{1}{2\pi} \int_{-\infty}^{\infty} a(t) e^{-i\omega t} dt, \tag{B.2}$$

and its inverse,

$$a(t) = \int_{-\infty}^{\infty} F(\omega) e^{i\omega t} d\omega, \tag{B.3}$$

where ω is the angular frequency. First, by substituting Eq. (B.3) for Eq. (B.1), we

have

$$E = \int_0^\infty \frac{8\pi e^2}{3c^3} |F(\omega)|^2 d\omega. \tag{B.4}$$

Eq. (B.2) and a become large when $-b/v < t < b/v$. Then, we can approximate Eq. (B.3) as

$$F(\omega) = \frac{1}{2\pi} \int_{-\infty}^{\infty} a(t) e^{-i\omega t} dt \simeq 0 \tag{B.5}$$

for $\omega > v/b$, and

$$F(\omega) = \frac{1}{2\pi} \int_{-\infty}^{\infty} a(t) e^{-i\omega t} dt \sim \frac{\Delta v}{2\pi} = \frac{Ze^2}{\pi b m_\mathrm{e} v} \tag{B.6}$$

for $\omega < v/b$, where m_e is the electron mass and

$$\Delta v \equiv \frac{Ze^2}{m_\mathrm{e}} \int_{-\infty}^{\infty} \frac{b dt}{(b^2 + v^2 t^2)^{3/2}} = \frac{2Ze^2}{m_\mathrm{e} b v}. \tag{B.7}$$

Therefore, from Eqs. (B.4), (B.6), (B.5), the emissivity with angular frequency between ω and $\omega + d\omega$, $\eta\hbar\omega d\omega$, is given by

$$\eta\hbar\omega d\omega \equiv dE = \frac{8}{3\pi} \frac{Z^2 e^6}{v^2 m_\mathrm{e} c^3} \frac{1}{b^2} d\omega, \tag{B.8}$$

where $\hbar = h/2\pi$ is the reduced Planck constant. Multiplying Eq. (B.8) by the electron number density n_e, the ion number density n_i and $2\pi v b db$, and integrating with respect to b, we obtain the emissivity per unit time and per unit volume, dP, as

$$dP \equiv \int_{b_\mathrm{min}}^{b_\mathrm{max}} n_\mathrm{e} n_\mathrm{i} \eta\hbar\omega d\omega 2\pi v b db = \frac{16\pi}{3\sqrt{3}} \frac{e^6 Z^2 n_\mathrm{e} n_\mathrm{i}}{v m_\mathrm{e}^2 c^3} g_\mathrm{ff} d\omega, \tag{B.9}$$

where

$$g_\mathrm{ff} \equiv \frac{\sqrt{3}}{\pi} \ln\left(\frac{b_\mathrm{max}}{b_\mathrm{min}}\right) \tag{B.10}$$

is the Gaunt factor for free-free emission.

B.2 Inverse Compton scattering

The spectrum of scattered cosmic microwave background (CMB) photons from an arbitrary frequency to the frequency ν is given by [160, 161]

$$\frac{dW_{\rm out}(\nu,\beta)}{dtd\nu} = \int_{\xi_{\rm min}}^{\xi_{\rm max}} 4\pi\sigma_{\rm T} I_\nu \left(\frac{\nu}{\xi}\right) P_{\rm IC}(\xi,\beta)d\xi, \tag{B.11}$$

where I_ν is the intensity of incident CMB photons, which is

$$I_\nu(\nu) = \frac{2h_{\rm p}\nu^3}{c^2}\left[\exp\left(\frac{h_{\rm p}\nu}{kT_{\rm CMB}}\right) - 1\right]^{-1} \tag{B.12}$$

and $P_{\rm IC}$ is the probability that the energy of an incident CMB photon is by a factor ξ, which is

$$\begin{aligned} P_{\rm IC} = \frac{3}{16\gamma^6\beta^6}\Bigg[&-\frac{|1-\xi|}{2\xi}\{1+(4\gamma^4+6)\xi+\xi^2\} \\ &+(1+\xi)\{2\beta(\gamma^4+\gamma^2+1)-(2\gamma^2+1)(\ln\xi_{\rm max}-|\ln\xi|)\}\Bigg], \end{aligned} \tag{B.13}$$

and the range of integration is given by

$$\xi_{\rm max} = \frac{1}{\xi_{\rm min}} = \frac{1+\beta}{1-\beta}. \tag{B.14}$$

On the other hand, CMB photons which have frequency ν are scattered partially. This is represented by

$$\frac{dW_{\rm in}(\nu)}{dtd\nu} = 4\pi\sigma_{\rm T} I_\nu(\nu). \tag{B.15}$$

Then the net spectrum is given by

$$\begin{aligned} \frac{dW_{\rm IC}(\nu,\beta)}{dtd\nu} &= \frac{dW_{\rm out}}{dtd\nu} - \frac{dW_{\rm in}}{dtd\nu} \\ &= 4\pi\sigma_T \int_{\xi_{\rm min}}^{\xi_{\rm max}} \left[I_\nu\left(\frac{\nu}{\xi}\right) - I_\nu(\nu)\right] P_{\rm IC}(\xi,\beta)d\xi \\ &= 4\pi\sigma_{\rm T} I_\nu(\nu)\int_{-1}^{1} d\mu_2' \int_{-1}^{1} d\mu_1' \left[\frac{e^x-1}{e^{x(1+\beta\mu_1')/(1+\beta\mu_2')}-1} - 1\right] \end{aligned} \tag{B.16}$$

$$\times \frac{P_{\rm T}(\mu_1', \mu_2')}{2\gamma^4(1+\beta\mu_1')^3}, \tag{B.17}$$

where μ_1' and μ_2' are, respectively, the angles before and after scattering in the electron rest frame, and $P_{\rm T}$ is given by

$$P_{\rm T}(\mu_1', \mu_2') = \frac{3}{8}\left[1 + \mu_1'\mu_2' + \frac{1}{2}(1-{\mu_1'}^2)(1-{\mu_2'}^2)\right] \tag{B.18}$$

If we know the velocity distribution of electrons, $f(\beta)$, we obtain the SZ spectrum

$$\frac{dW_{\rm SZ}(\nu)}{dtd\nu} = \int \frac{dW_{\rm IC}(\nu,\beta)}{dtd\nu} f(\beta) d^3\beta. \tag{B.19}$$

Therefore, the radial profile of SZ effect is

$$\frac{\Delta I_\nu^{\rm (SZ)}(\nu, r_\perp)}{I_\nu(\nu)} = \frac{1}{4\pi I_\nu(\nu)} \int n_{\rm e} \frac{dW_{\rm SZ}(\nu)}{dtd\nu} dz. \tag{B.20}$$

Extended thermal SZ effect

We assume the following distribution function as the thermal electron distribution:

$$f_{\rm rel}(\beta)d\beta = \frac{\gamma^5 e^{-(\gamma-1)/\theta_{\rm e}}}{\theta_{\rm e} e^{1/\theta_{\rm e}} K_2(1/\theta_{\rm e})} \beta^2 d\beta, \tag{B.21}$$

where $\theta_{\rm e} = kT_{\rm e}/m_{\rm e}c^2$ and K_2 is the modified Bessel function. For the case of $\beta \ll 1$ and $\theta_{\rm e} \ll 1$, this distribution function can be approximated by

$$f_{\rm rel}(\beta) \simeq \exp\left(-\frac{\beta^2}{2\theta_{\rm e}}\right)\left(1 - \frac{3\beta^4}{8\theta_{\rm e}} - \frac{5\beta^6}{16\theta_{\rm e}}\right)\left(1 + \frac{5\beta^2}{2} + \frac{35\beta^4}{8} + \frac{105\beta^6}{16}\right) \times \left(\frac{\sqrt{2/\pi}}{\theta_{\rm e}^{3/2}} - \frac{15}{4\sqrt{2\pi\theta_{\rm e}}}\right)\beta^2, \tag{B.22}$$

In particular, the lowest order reproduces the well-known non-relativistic Maxwell distribution

$$f_{\rm M}(v)dv = 4\pi\left(\frac{m_{\rm e}}{2\pi kT_{\rm e}}\right)^{3/2} \exp\left(-\frac{m_{\rm e}v^2}{2kT_{\rm e}}\right) v^2 dv. \tag{B.23}$$

On the other hand, the inverse Compton intensity (B.17) in this limit can be approximated by

$$\frac{dW_{\rm IC}(\nu,\beta)}{dtd\nu} = 4\pi\sigma_{\rm T} I_\nu(\nu) \int_{-1}^{1} d\mu_2' \int_{-1}^{1} d\mu_1' \left[\frac{e^x-1}{e^{x(1+\beta\mu_1')/(1+\beta\mu_2')}-1} - 1\right] \frac{P_{\rm T}(\mu_1',\mu_2')}{2\gamma^4(1+\beta\mu_1')^3} \tag{B.24}$$

$$\simeq 2\pi\sigma_{\rm T} I_\nu(\nu) \frac{xe^x}{e^x-1} \int_{-1}^{1} d\mu_2 \tag{B.25}$$

$$\times \left[\mu_2\beta + \left\{-1-\mu_2^2 + x\coth\left(\frac{x}{2}\right)\left(\frac{3+11\mu_2^2}{20}\right)\right\}\beta^2 + \mathcal{O}(\beta^3) + \mathcal{O}(\beta^4)\right], \tag{B.26}$$

where $x = h_{\rm p}\nu/kT_{\rm CMB}$ and $\mu_2 = (\mu_2'+\beta)/(1+\beta\mu_2')$ is the angle after scattering in the observer rest frame. Then the SZ spectrum (B.19) is represented by

$$\frac{dW_{\rm SZ}(\nu)}{dtd\nu} = \int \frac{dW_{\rm IC}(\nu,\beta)}{dtd\nu} f_{\rm rel}(\beta) d\beta \tag{B.27}$$

$$\simeq 4\pi\sigma_{\rm T} I_\nu(\nu) \frac{xe^x}{e^x-1} \tag{B.28}$$

$$\times \left[\theta_{\rm e} F_0^{\rm T}(x) + \theta_{\rm e}^2 F_1^{\rm T}(x) + \beta_{\rm b} F_0^{\rm K}(x,\mu) + \beta_{\rm b}^2 F_1^{\rm K}(x,\mu) + \theta_{\rm e}\beta_{\rm b} F_1^{\rm TK}(x,\mu)\right], \tag{B.29}$$

where $\beta_{\rm b}$ is the bulk velocity of the electron cluster, μ is the angle of the bulk motion, and the functions $F_0^{\rm T}$, $F_1^{\rm T}$, $F_0^{\rm K}$, $F_1^{\rm K}$ and $F_1^{\rm TK}$ are defined by

$$F_0^{\rm T}(x) = -4 + F, \tag{B.30}$$

$$F_1^{\rm T}(x) = -10 + \frac{47}{2}F - \frac{42}{5}F^2 + \frac{7}{10}F^3 + \frac{7}{5}G^2(-3+F), \tag{B.31}$$

$$F_0^{\rm K}(\mu) = \mu, \tag{B.32}$$

$$F_1^{\rm K}(x,\mu) = -1-\mu^2 + \frac{(3+11\mu^2)F}{20}, \tag{B.33}$$

$$F_1^{\rm TK}(x,\mu) = \mu\left(9\mu - \frac{47F}{5} + \frac{7F^2}{5} + \frac{7}{10}G^2\right), \tag{B.34}$$

where $F = x\coth(x/2)$ and $G = x/\sinh(x/2)$.

Fig. B.1 shows the intensity of SZ effect as a function of x for thermal electron. The blue and green curves show the intensity up to orders $\theta_{\rm e}$ and $\theta_{\rm e}^2$ in Eq. B.19, respectively. The red curve shows the exact solution. This figure shows that the

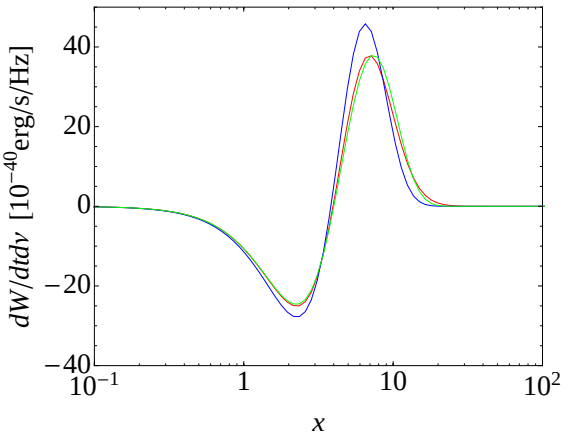

Figure B.1: The inverse Compton intensity as a function of x for a thermal electron. The blue and green curves show the intensity up to orders $\theta_{\rm e}$ and $\theta_{\rm e}^2$ in Eq. (B.19), respectively. The red curve shows the exact solution.

intensity of low frequency photons become lower than that before scattering, and the intensity of high frequency photons become higher than that before scattering. The borderline of the sign of the SZ intensity is $x = 3.83$ ($\nu = 218$ GHz, $\lambda = 1.38$ mm).

References

[1] A. G. Riess, A. V. Filippenko, P. Challis *et al.*, *Observational Evidence from Supernovae for an Accelerating Universe and a Cosmological Constant*, Astron. J. **116** (2008) 1009.

[2] S. Perlmutter, G. Aldering, G. Goldhaber *et al.*, *Measurements of Omega and Lambda from 42 High-Redshift Supernovae*, Astrophys. J. **517** (1999) 569.

[3] D. N. Spergel, R. Bean, O. Doré *et al.*, *Wilkinson Microwave Anisotropy Probe (WMAP) Three Year Results: Implications for Cosmology*, Astrophys. J. Suppl. **170** (2007) 377.

[4] E. Komatsu, K. M. Smith, J. Dunkley *et al.*, *Seven-year Wilkinson Microwave Anisotropy Probe (WMAP) Observations: Cosmological Interpretation*, Astrophys. J. Suppl. **192** (2011) 18.

[5] B. A. Reid, W. J. Percival, D. J. Eisenstein *et al.*, *Cosmological Constraints from the Clustering of the Sloan Digital Sky Survey DR7 Luminous Red Galaxies*, Mon. Not. Roy. Astron. Soc. **404** (2010) 60.

[6] M. Tegmark, D. J. Eisenstein, M. A. Strauss *et al.*, *Cosmological constraints from the SDSS luminous red galaxies*, Phys. Rev. D **74** (2006) 123507.

[7] K. Vanderlinde, T. M. Crawford, T. de Haan *et al.*, *Galaxy clusters selected with the Sunyaev-Zel'dovich effect from 2008 south pole telescope observations*, Astrophys. J. **722** (2010) 1180.

[8] C. Rapetti, S. Allen and J. Weller, *Constraining dark energy with X-ray galaxy clusters, supernovae and the cosmic microwave background*, Mon. Not. Roy. Astron. Soc. **360** (2005) 555.

[9] E. G. Adelberger, B. R. Heckel and A. E. Nelson, *Tests of the Gravitational Inverse-Square Law*, Annual Review of Nuclear and Particle Science **53** (2003) 77–121.

[10] C. M. Will, *The Confrontation between General Relativity and Experiment*, Living Reviews in Relativity **17** (2014) 4.

[11] J. Khoury and A. Weltman, *Chameleon cosmology*, Phys. Rev. D **69** (2004) 044026.

[12] D. F. Mota and J. D. Barrow, *Varying alpha in a more realistic universe*, Phys. Lett. B **581** (2004) 141–146.

[13] A. A. Starobinsky, *Disappearing cosmological constant in f(R) gravity*, JETP Lett. **86** (2007) 157–163.

[14] W. Hu and I. Sawicki, *Models of f(R) cosmic acceleration that evade solar system tests*, Phys. Rev. D **76** (2007) 064004.

[15] S. Tsujikawa, *Observational signatures of f(R) dark energy models that satisfy cosmological and local gravity constraints*, Phys. Rev. D **77** (2008) 023507.

[16] L. Lombriser, *Constraining chameleon models with cosmology*, Annalen der Physik **526** (2014) 259–282.

[17] A. I. Vainshtein, *To the problem of nonvanishing gravitation mass*, Phys. Lett. B **39** (1972) 393–394.

[18] G. Dvali, G. Gabadadze and M. Porrati, *4D gravity on a brane in 5D Minkowski space*, Phys. Lett. B **485** (2000) 208–214.

[19] C. Deffayet, *Cosmology on a brane in Minkowski bulk*, Phys. Lett. B **502** (2001) 199–208.

[20] A. Nicolis, R. Rattazzi and E. Trincherini, *Galileon as a local modification of gravity*, Phys. Rev. D **79** (2009) 064036.

[21] C. Deffayet, G. Esposito-Farèse and A. Vikman, *Covariant Galileon*, Phys. Rev. D **79** (2009) 084003.

[22] C. Deffayet, G. Dvali and G. Gabadadze, *Accelerated universe from gravity leaking to extra dimensions*, Phys. Rev. D **65** (2002) 044023.

[23] M. A. Luty, M. Porrati and R. Rattazzi, *Strong interactions and stability in the DGP model*, Journal of High Energy Physics **9** (2003) 29.

[24] T. Kobayashi, M. Yamaguchi and J. Yokoyama, *Inflation Driven by the Galileon Field*, Phys. Rev. Lett. **105** (2010) 231302.

[25] R. Kimura, T. Kobayashi and K. Yamamoto, *Vainshtein screening in a cosmological background in the most general second-order scalar-tensor theory*, Phys. Rev. D **85** (2012) 024023.

[26] K. Koyama and R. Maartens, *Structure formation in the Dvali Gabadadze Porrati cosmological model*, J. Cosmology Astropart. Phys. **1** (2006) 16.

[27] K. Koyama and F. P. Silva, *Nonlinear interactions in a cosmological background in the Dvali-Gabadadze-Porrati braneworld*, Phys. Rev. D **75** (2007) 084040.

[28] F. Schmidt, *Self-consistent cosmological simulations of DGP braneworld gravity*, Phys. Rev. D **80** (2009) 043001.

[29] C. Deffayet, G. Dvali and G. Gabadadze, *Accelerated universe from gravity leaking to extra dimensions*, Phys. Rev. D **65** (2002) 044023.

[30] B. Falck, K. Koyama and G.-B. Zhao, *Cosmic web and environmental dependence of screening: Vainshtein vs. chameleon*, J. Cosmology Astropart. Phys. **07** (2015) 049.

[31] F. Schmidt, *Cosmological simulations of normal-branch braneworld gravity*, Phys. Rev. D **80** (2009) 123003.

[32] A. Nicolis and R. Rattazzi, *Classical and Quantum Consistency of the DGP Model*, Journal of High Energy Physics **6** (2004) 59.

[33] D. Gorbunov, K. Koyama and S. Sibiryakov, *More on ghosts in the Dvali-Gabadaze-Porrati model*, Phys. Rev. D **73** (2006) 044016.

[34] F. Schmidt, A. Vikhlinin and W. Hu, *Cluster constraints on f(R) gravity*, Phys. Rev. D **80** (2009) 083505.

[35] F. Schmidt, *Dynamical masses in modified gravity*, Phys. Rev. D **81** (2010) 103002.

[36] G.-B. Zhao, B. Li and K. Koyama, *Testing Gravity Using the Environmental Dependence of Dark Matter Halos*, Phys. Rev. Lett. **107** (2011) 071303.

[37] L. Lombriser, F. Schmidt, T. Baldauf *et al.*, *Cluster density profiles as a test of modified gravity*, Phys. Rev. D **85** (2012) 102001.

[38] L. Lombriser, K. Koyama, G.-B. Zhao *et al.*, *Chameleon f(R) gravity in the virialized cluster*, Phys. Rev. D **85** (2012) 124054.

[39] T. Y. Lam, T. Nishimichi, F. Schmidt *et al.*, *Testing Gravity with the Stacked Phase Space around Galaxy Clusters*, Phys. Rev. Lett. **109** (2012) 051301.

[40] T. Narikawa, R. Kimura, T. Yano *et al.*, *Halo Models in Modified Gravity Theories with Self-Accelerated Expansion*, International Journal of Modern Physics D **20** (2011) 2383–2397.

[41] T. Narikawa and K. Yamamoto, *Testing gravity with halo density profile observed through gravitational lensing*, J. Cosmology Astropart. Phys. **05** (2012) 016.

[42] A. Terukina and K. Yamamoto, *Gas Density Profile in Dark Matter Halo in Chameleon Cosmology*, Phys. Rev. D **86** (2012) 103503.

[43] A. Terukina, L. Lombriser, K. Yamamoto *et al.*, *Thesting chameleon gravity with the Coma cluster*, J. Cosmology Astropart. Phys. **04** (2014) 013.

[44] H. Wilcox, D. Bacon, R. C. Nichol *et al.*, *The XMM Cluster Survey: testing chameleon gravity using the profiles of clusters*, Mon. Not. Roy. Astron. Soc. **452** (2015) 1171–1183.

[45] C. Llinares and D. F. Mota, *Shape of Clusters of Galaxies as a Probe of Screening Mechanisms in Modified Gravity*, Phys. Rev. Lett. **110** (2013) 151104.

[46] T. Narikawa, T. Kobayashi, D. Yamauchi *et al.*, *Testing general scalar-tensor gravity and massive gravity with cluster lensing*, Phys. Rev. D **87** (2013) 124006.

[47] A. De Felice and S. Tsujikawa, *f(R) theories*, Living Rev. Rel. **13** (2010) 3.

[48] R. Amendola, L. Gannouji and S. Polarski, D. Tsujikawa, *Conditions for the cosmological viablility of f(R) dark energy models*, Phys. Rev. D **75** (2007) 083504.

[49] S. Nesseris, A. de Felice and S. Tsujikawa, *Observational constraints on Galileon cosmology*, Phys. Rev. D **82** (2010) 124054.

[50] G. Horndeski, *Second-order scalar-tensor field equations in a four-dimensional space*, Int. J. Theor. Phys. **10** (1974) 363.

[51] C. Deffayet, X. Gao, D. Steer *et al.*, *From k-essence to generalized Galileons*, Phys. Rev. D **80** (2011) 064039.

[52] T. Kobayashi, M. Yamaguchi and J. Yokoyama, *Generalized G-Inflation — Inflation with the most general second-order field equations*, Prog. Theor. Phys. **126** (2011) 3.

[53] A. de Felice, R. Kase and S. Tsujikawa, *Vainshtein mechanism in second-order scalar-tensor theories*, Phys. Rev. D **85** (2012) 044059.

[54] R. Kimura and K. Yamamoto, *Large scale strructures in kinetic gravity brading model that can be unbraided*, J. Cosmology Astropart. Phys. **04** (2011) 025.

[55] A. Barreira, B. Li, C. Baugh *et al.*, *The observational status of Galileon gravity after Plank*, J. Cosmology Astropart. Phys. **08** (2014) 059.

[56] A. Fischbach and C. Talmadge, *Six years of the fifth force*, Nature **356** (1992) 207.

[57] D. J. Kapner, T. S. Cook, E. G. Adelberger *et al.*, *Tests of the Gravitational Inverse-Square Low below the Dark-Energy Lenght Scale*, Phys. Rev. Lett. **98** (2007) 021101.

[58] V. Bertotti, L. Iess and P. Tortora, *A test of general relativity using radio links with the Cassini spacecraft*, Nature **425** (2003) 374.

[59] B. Jain and J. Khoury, *Cosmological tests of gravity*, Annals of Physics **325** (2010) 1479.

[60] T. Narikawa, T. Kobayashi, D. Yamauchi *et al.*, *Testing general scalar-tensor gravity and massive gravity with cluster lensing*, Phys. Rev. D **87** (2013) 124006.

[61] A. Taruya, K. Koyama, T. Hiramatsu *et al.*, *Beyond consistency test of gravity with redshift-space distortions as quasi-linear scales*, Phys. Rev. D **89** (2014) 043509.

[62] T. Kanemaru, C. Hikage, G. Huetsi *et al.*, *What can we learn from higher multipole power spectra of galaxy distribution in redsift space?*, Phys. Rev. D **92** (2015) 023523.

[63] Y. Takushima, A. Terukin and K. Yamamoto, *Bispectrum of cosmological density perturbations in the most general second-order scalar-tensor theory*, Phys. Rev. D **89** (2014) 104007.

[64] Y. Takushima, A. Terukin and K. Yamamoto, *Third order solutions of the cosmological density perturbations in the Horndeski's most general scalar-tensor theory with the Vainshtein mechanism*, Phys. Rev. D **92** (2015) 104033.

[65] L. Lombriser, K. Koyama and B. Li, *Halo modelling in chameleon theories*, J. Cosmology Astropart. Phys. **3** (2014) 21.

[66] B. Jain, V. Vikram and J. Sakstein, *Astrophysical Tests of Modified Gravity: Constraints from Distance Indicators in the Nearby Universe*, Astrophys. J. **779** (2013) 39.

[67] B. Hu, M. Liguori, N. Bartolo *et al.*, *Parametrized modified gravity constraints after Planck*, Phys. Rev. D **88** (2013) 123514.

[68] A. Marchini and V. Salvatelli, *Updated constraints from the Planck experiment on modified gravity*, Phys. Rev. D **88** (2013) 027502.

[69] L. Lombriser, A. Slosar, U. Seljak *et al.*, *Constraints on f(R) gravity from probing the large-scale structure*, Phys. Rev. D **85** (2012) 124038.

[70] B. Jain, A. Joyce, R. Thompson *et al.*, *Novel Probes of Gravity and Dark Energy*, arXiv:1309.5389.

[71] B. Jain, A. Joyce, R. Thompson *et al.*, *Novel Probes of Gravity and Dark Energy*, FERMILAB-PUB-13-443-A.

[72] R. A. Sunyaev and Y. B. Zeldovich, *Small-Scale Fluctuations of Relic Radiation*, Ap&SS **7** (1970) 3–19.

[73] J. F. Navarro, C. S. Frenk and S. D. M. White, *A Universal Density Profile from Hierarchical Clustering*, Astrophys. J. **490** (1997) 493–508.

[74] G. Bulbul, N. Hasler, M. Nonamente *et al.*, *An Analytic Model of the Physical Properties of Galaxy Clusters*, Astrophys. J. **720** (2010) 1038.

[75] K. Umetsu, T. Broadhurst, A. Zitrin *et al.*, *A Precise Cluster Mass Profile Averaged from the Highest-quality Lensing Data*, Astrophys. J. **738** (2011) 41.

[76] M. Oguri, M. B. Bayliss, H. Dahle *et al.*, *Combined strong and weak lensing analysis of 28 clusters from the Sloan Giant Arcs Survey*, Mon. Not. Roy. Astron. Soc. **420** (2012) 3213–3239.

[77] P. Peebles, *Large-Scale Structure of the Universe*, Princeton University Press.

[78] C. Lacey and S. Cole, *Merger rates in hierarchical models of galaxy formation*, Mon. Not. Roy. Astron. Soc. **262** (1993) 627.

[79] V. Eke, S. Cole and C. Frenk, *Cluster evolution as a diagnostic for Omega*, Mon. Not. Roy. Astron. Soc. **282** (1996) 263.

[80] T. Nakamura and Y. Suto, *Strong Gravitational Lensing and Velocity Function as Tools to Probe Cosmological Parameters: Current Constraints and Future Predictions*, Prog. Theor. Phys. **97** (1997) 49.

[81] F. Schmidt, M. Lima, H. Oyaizu *et al.*, *Nonlinear evolution of f(R) cosmologies. III. Halo statistics*, Phys. Rev. D **79** (2009) 083518.

[82] T. H. Reiprich, K. Basu, S. Ettori *et al.*, *Outskirts of Galaxy Clusters*, Space Sci. Rev. **177** (2013) 195–245.

[83] Y. Suto, S. Sasaki and N. Makino, *Gas Density and X-Ray Surface Brightness Profiles of Clusters of Galaxies from Dark Matter Halo Potentials: Beyond the Isothermal β-Model*, Astrophys. J. **509** (1998) 544–550.

[84] E. Komatsu and U. Seljak, *Universal gas density and temperature profile*, Mon. Not. Roy. Astron. Soc. **327** (2001) 1353–1366.

[85] P. Capelo, P. Coppi and P. Natarajan, *The polytropic approximation and X-ray scaling relations: constraints on gas and dark matter profiles for galaxy groups and clusters*, Mon. Not. Roy. Astron. Soc. **422** (2012) 686–703.

[86] A. Cavaliere and R. Fusco-Femiano, *X-rays from hot plasma in clusters of galaxies*, Astron. Astrophys. **49** (1976) 137–144.

[87] M. Eke, J. Navarro and C. Frenk, *The Evolution of X-ray Clusters in Low Density Universes*, Astrophys. J. **503** (1998) 569.

[88] K. A. Arnaud. *XSPEC: The First Ten Years*. In G. H. Jacoby and J. Barnes, editors, *Astronomical Data Analysis Software and Systems V*, volume 101 of *Astronomical Society of the Pacific Conference Series*, page 17, (1996).

[89] R. K. Smith, N. S. Brickhouse, D. A. Liedahl *et al.*, *Collisional Plasma Models with APEC/APED: Emission-Line Diagnostics of Hydrogen-like and Helium-like Ions*, Astrophys. J. **556** (2001) L91–L95.

[90] P. Mazzotta, E. Rasia, L. Moscardini *et al.*, *Comparing the temperatures of galaxy clusters from hydrodynamical N-body simulations to Chandra and XMM-Newton observations*, Mon. Not. Roy. Astron. Soc. **354** (2004) 10–24.

[91] C. Oaxaca Wright and T. G. Brainerd, *Gravitational Lensing by NFW Halos*, arXiv:astro-ph/9908213.

[92] P. Burikham and S. Panpanich, *Effects of Chameleon Scalar Field on Rotation Curves of the Galaxies*, International Journal of Modern Physics D **21** (2012) 50041.

[93] R. Pourhasan, N. Afshordi, R. B. Mann *et al.*, *Chameleon gravity, electrostatics, and kinematics in the outer galaxy*, J. Cosmology Astropart. Phys. **12** (2011) 5.

[94] T. Sato, T. Sasaki, K. Matsushita *et al.*, *Suzaku Observations of the Hydra A Cluster out to the Virial Radius*, Publ. Astron. Soc. Jpn. **64** (2012) 95.

[95] E. Komatsu and U. Seljak, *The Sunyaev-Zel'dovich angular power spectrum as a probe of cosmological parameters*, Mon. Not. Roy. Astron. Soc. **336** (2002) 1256–1270.

[96] C. Arnold, E. Puchwein and V. Springel, *Scaling relations and mass bias in hydrodynamical f(R) gravity simulations of galaxy clusters*, Mon. Not. Roy. Astron. Soc. **440** (2014) 833–842.

[97] Planck Collaboration, P. A. R. Ade, N. Aghanim *et al.*, *Planck Intermediate Results. X. Physics of the hot gas in the Coma cluster*, Astron. Astrophys. **554** (2013) A140.

[98] E. Churazov, A. Vikhlinin, I. Zhuravleva *et al.*, *X-ray surface brightness and gas density fluctuations in the Coma cluster*, Mon. Not. Roy. Astron. Soc. **421** (2012) 1123–1135.

[99] S. L. Snowden, R. F. Mushotzky, K. D. Kuntz *et al.*, *A catalog of galaxy clusters observed by XMM-Newton*, Astron. Astrophys. **478** (2008) 615–658.

[100] D. R. Wik, C. L. Sarazin, A. Finoguenov *et al.*, *A Suzaku Search for Nonthermal Emission at Hard X-Ray Energies in the Coma Cluster*, Astrophys. J. **696** (2009) 1700–1711.

[101] R. Gavazzi, C. Adami, F. Durret *et al.*, *A weak lensing study of the Coma cluster*, Astron. Astrophys. **498** (2009) L33–L36.

[102] N. Okabe, Y. Okura and T. Futamase, *Weak-lensing Mass Measurements of Substructures in Coma Cluster with Subaru/Suprime-cam*, Astrophys. J. **713** (2010) 291–303.

[103] D. Suto, H. Kawahara, T. Kitayama *et al.*, *Validity of Hydrostatic Equilibrium in Galaxy Clusters from Cosmological Hydrodynamical Simulations*, Astrophys. J. **767** (2013) 79.

[104] R. Fusco-Femiano, A. Lapi and A. Cavaliere, *The Planck Sunyaev-Zel'dovich versus the X-Ray View of the Coma Cluster*, Astrophys. J. **763** (2013) L3.

[105] A. Cavaliere, A. Lapi and R. Fusco-Femiano, *Galaxy Clusters: A Novel Look at Diffuse Baryons Withstanding Dark Matter Gravity*, Astrophys. J. **698** (2009) 580–593.

[106] N. Battaglia, J. R. Bond, C. Pfrommer *et al.*, *On the Cluster Physics of Sunyaev-Zel'dovich and X-Ray Surveys. I. The Influence of Feedback, Nonthermal Pressure, and Cluster Shapes on Y-M Scaling Relations*, Astrophys. J. **758** (2012) 74.

[107] L. D. Shaw, D. Nagai, S. Bhattacharya *et al.*, *Impact of Cluster Physics on the Sunyaev-Zel'dovich Power Spectrum*, Astrophys. J. **725** (2010) 1452–1465.

[108] J. O. Burns, S. W. Skillman and B. W. O'Shea, *Galaxy Clusters at the Edge: Temperature, Entropy, and Gas Dynamics Near the Virial Radius*, Astrophys. J. **721** (2010) 1105–1112.

[109] D. Nagai, A. V. Kravtsov and A. Vikhlinin, *Effects of Galaxy Formation on Thermodynamics of the Intracluster Medium*, Astrophys. J. **668** (2007) 1–14.

[110] T. H. Reiprich, K. Basu, S. Ettori *et al.*, *Outskirts of Galaxy Clusters*, Space Sci. Rev. **177** (2013) 195–245.

[111] T. Arlen, T. Aune, M. Beilicke *et al.*, *Constraints on Cosmic Rays, Magnetic Fields, and Dark Matter from Gamma-Ray Observations of the Coma Cluster of Galaxies with VERITAS and Fermi*, Astrophys. J. **757** (2012) 123.

[112] P. Sreekumar, D. L. Bertsch, B. L. Dingus *et al.*, *EGRET Observations of the North Galactic Pole Region*, Astrophys. J. **464** (1996) 628.

[113] O. Reimer, M. Pohl, P. Sreekumar *et al.*, *EGRET Upper Limits on the High-Energy Gamma-Ray Emission of Galaxy Clusters*, Astrophys. J. **588** (2003) 155–164.

[114] M. Ackermann, M. Ajello, A. Allafort *et al.*, *GeV Gamma-ray Flux Upper Limits from Clusters of Galaxies*, Astrophys. J. **717** (2010) L71–L78.

[115] K. A. Pimbblet, S. J. Penny and R. L. Davies, *How typical is the Coma cluster?*, Mon. Not. Roy. Astron. Soc. **438** (2014) 3049–3057.

[116] Y.-Y. Zhang, H. Andernach, C. A. Caretta *et al.*, *HIFLUGCS: Galaxy cluster scaling relations between X-ray luminosity, gas mass, cluster radius, and velocity dispersion*, Astron. Astrophys. **526** (2011) A105.

[117] Planck Collaboration, P. A. R. Ade, N. Aghanim *et al.*, *Planck early results. VIII. The all-sky early Sunyaev-Zeldovich cluster sample*, Astron. Astrophys. **536** (2011) A8.

[118] T. Sato, K. Matsushita, N. Ota *et al.*, *Suzaku Observations of Iron K-Lines from the Intracluster Medium of the Coma Cluster*, Publ. Astron. Soc. Jpn. **63** (2011) 991.

[119] A. Lewis and S. Bridle, *Cosmological parameters from CMB and other data: A Monte Carlo approach*, Phys. Rev. D **66** (2002) 103511.

[120] N. Metropolis, A. W. Rosenbluth, M. N. Rosenbluth *et al.*, *Equation of State Calculations by Fast Computing Machines*, J. Chem. Phys. **21** (1953) 1087–1092.

[121] W. Hastings, *Monte Carlo sampling methods using Markov chains and their applications*, Biometrika **57** (1970) 97.

[122] A. Gelman and D. Rubin, *Inference from Iterative Simulation Using Multiple Sequences*, Statist. Sci **7** (1992) 457.

[123] J. Wang, L. Hui and J. Khoury, *No-Go Theorems for Generalized Chameleon Field Theories*, Phys. Rev. Lett. **109** (2012) 241301.

[124] L. Lombriser, B. Li, K. Koyama *et al.*, *Modeling halo mass functions in chameleon f(R) gravity*, Phys. Rev. D **87** (2013) 123511.

[125] K. Yamamoto, G. Nakamura, G. Hütsi *et al.*, *Constraint on the cosmological f(R) model from the multipole power spectrum of the SDSS luminous red galaxy sample and prospects for a future redshift survey*, Phys. Rev. D **81** (2010) 103517.

[126] S. A. Gregory and L. A. Thompson, *The Coma/A1367 supercluster and its environs*, Astrophys. J. **222** (1978) 784–799.

[127] M. J. West. *The Coma cluster in relation to its environs.* In A. Mazure, F. Casoli, F. Durret *et al.*, editors, *Untangling Coma Berenices: A New Vision of an Old Cluster*, page 36, (1998).

[128] K. Rines, M. J. Geller, M. J. Kurtz *et al.*, *Infrared Mass-to-Light Profile throughout the Infall Region of the Coma Cluster*, Astrophys. J. **561** (2001) L41–L44.

[129] A. C. Fabian, *Cooling Flows in Clusters of Galaxies*, Ann. Rev. Astron. Asrophys. **32** (1994) 277–318.

[130] J. R. Peterson and A. C. Fabian, *X-ray spectroscopy of cooling clusters*, Phys. Rep. **427** (2006) 1–39.

[131] Y. Fujita and Y. Ohira, *Stable Heating of Cluster Cooling Flows by Cosmic-Ray Streaming*, Astrophys. J. **738** (2011) 182.

[132] N. Okabe, T. Futamase, M. Kajisawa *et al.*, *Subaru Weak-lensing Survey of Dark Matter Subhalos in the Coma Cluster: Subhalo Mass Function and Statistical Properties*, Astrophys. J. **784** (2014) 90.

[133] A. Morandi, D. Nagai and W. Cui, *Non-parametric method for measuring gas inhomogeneities from X-ray observations of galaxy clusters*, Mon. Not. Roy. Astron. Soc. **436** (2013) 1123–1129.

[134] F. Andrade-Santos, P. E. J. Nulsen, R. P. Kraft *et al.*, *Dark Matter Subhalos and the X-Ray Morphology of the Coma Cluster*, Astrophys. J. **766** (2013) 107.

[135] K. Matsushita, *Radial profiles of Fe abundance in the intracluster medium of nearby clusters observed with XMM-Newton*, Astron. Astrophys. **527** (2011) A134.

[136] K. Matsushita, T. Sato, E. Sakuma *et al.*, *Distribution of Si, Fe, and Ni in the Intracluster Medium of the Coma Cluster*, Publ. Astron. Soc. Jpn. **65** (2013) 10.

[137] A. Simionescu, N. Werner, O. Urban *et al.*, *Thermodynamics of the Coma Cluster Outskirts*, Astrophys. J. **775** (2013) 4.

[138] D. M. Neumann, D. H. Lumb, G. W. Pratt *et al.*, *The dynamical state of the Coma cluster with XMM-Newton*, Astron. Astrophys. **400** (2003) 811–821.

[139] J. Sanders, A. Fabian, E. Churazov *et al.*, *Linear structures in the core of the Coma cluster of galaxies*, Science **341** (2013) 1365–1368.

[140] F. Gastaldello, D. R. Wik, S. Molendi *et al.*, *A NuSTAR Observation of the Center of the Coma Cluster*, Astrophys. J. **800** (2015) 139.

[141] B. Audren, J. Lesgourgues, K. Benabed *et al.*, *Conservative constraints on early cosmology: an illustration of the Monte Python cosmological parameter inference code*, JCAP **02** (2013) 001.

[142] P. Schuecker, A. Finoguenov, F. Miniati *et al.*, *Probing turbulence in the Coma galaxy cluster*, Astron. Astrophys. **426** (2004) 387–397.

[143] A. Barreira, B. Li, E. Jennings *et al.*, *Galaxy cluster lensing masses in modified lensing potentials*, Mon. Not. Roy. Astron. Soc. **454** (2015) 4085–4102.

[144] T. Kitayama, M. Bautz, M. Markevitch *et al.*, *ASTRO-H white paper — clusters of galaxies and related science*, arXiv:1412.1176.

[145] H. Honda, M. Hirayama, M. Watanabe *et al.*, *Detection of a Temperature Structure in the Coma Cluster of Galaxies with ASCA*, Astrophys. J. **473** (1996) L71.

[146] M. Watanabe, K. Yamashita, A. Furuzawa *et al.*, *Temperature Map of the Coma Cluster of Galaxies*, Astrophys. J. **527** (1999) 80–85.

[147] M. Arnaud, N. Aghanim, R. Gastaud *et al.*, *XMM-Newton observation of the Coma Galaxy cluster. The temperature structure in the central region*, Astron. Astrophys. **365** (2001) L67–L73.

[148] N. Okabe, K. Umetsu, T. Tamura *et al.*, *Universal profiles of the intracluster medium from Suzaku X-ray and Subaru weak-lensing observations**, Publ. Astron. Soc. Jpn. **66** (2014) 99.

[149] The Dark Energy Survey Collaboration, *The Dark Energy Survey*, arXiv:astro-ph/0510346.

[150] eROSITA collaboration, *eROSITA science book: mapping the structure of the energetic universe*, arXiv:1209.3114.

[151] M. D. Niemack, P. A. R. Ade, J. Aguirre *et al. ACTPol: a polarization-sensitive receiver for the Atacama Cosmology Telescope.* In *Society of Photo-Optical Instrumentation Engineers (SPIE) Conference Series*, volume 7741 of *Society of Photo-Optical Instrumentation Engineers (SPIE) Conference Series*, page 1, (2010).

[152] J. Ruhl, P. A. R. Ade, J. E. Carlstrom *et al. The South Pole Telescope.* In C. M. Bradford, P. A. R. Ade, J. E. Aguirre *et al.*, editors, *Z-Spec: a broadband millimeter-wave grating spectrometer: design, construction, and first cryogenic measurements*, volume 5498 of *Society of Photo-Optical Instrumentation Engineers (SPIE) Conference Series*, pages 11–29, (2004).

[153] Planck Collaboration, P. A. R. Ade, N. Aghanim *et al.*, *Planck 2013 results. I. Overview of products and scientific results*, Astron. Astrophys. **571** (2013) A1.

[154] Planck Collaboration, P. A. R. Ade, N. Aghanim *et al.*, *Planck intermediate results. III. The relation between galaxy cluster mass and Sunyaev-Zeldovich signal*, Astron. Astrophys. **550** (2013) A120–1.

[155] Planck Collaboration, P. A. R. Ade, N. Aghanim *et al.*, *Planck intermediate results. V. Pressure profiles of galaxy clusters from the Sunyaev-Zeldovich effect*, Astron. Astrophys. **554** (2013) A131–1.

[156] Planck Collaboration, P. A. R. Ade, N. Aghanim *et al.*, *Planck 2013 results. XX. Cosmology from Sunyaev-Zeldovich cluster counts*, Astron. Astrophys. **571** (2014) A20.

[157] G. Magnano and L. Sokolowski, *On Physical Equivalence between Nonlinear Gravity Theories*, Phys. Rev. D **50** (1994) 5039.

[158] V. Faraoni and V. Gunzig, *Einstein Frame or Jordan Frame?*, Int. J. Theo. Phys. **38** (1998) 1.

[159] J. Karzas and R. Latter, *Electron Radiative Transitions in a Coulomb Field*, Astrophys. J. Suppl. **6** (1961) 167.

[160] T. A. Enßlin and C. R. Kaiser, *Comptonization of the cosmic microwave background by relativistic plasma*, Astron. Astrophys. **360** (2000) 417–430.

[161] N. Itoh and S. Nozawa, *Relativistic Corrections to the Sunyaev-Zeldovich Effect for Clusters of Galaxies. V. Numerical Results for High Electron Temperatures*, arXiv:astro-ph/0307519.

公表論文

1. Gas Density Profile in Dark Matter Halo in Chameleon Cosmology
   A. Terukina and K. Yamamoto
   Physical Review D 86 (2012) 103503

2. Testing chameleon gravity with the Coma cluster
   A. Terukina, L. Lombriser, K. Yamamoto, D. Bacon, K. Koyama and R.C. Nichol
   Journal of Cosmology and Astroparticle Physics 04 (2014) 013

3. Testing a generalized cubic Galileon gravity model with the Coma Cluster
   A. Terukina, K. Yamamoto, N. Okabe, K. Matsushita and T. Sasaki
   Journal of Cosmology and Astroparticle Physics 10 (2015) 064

PHYSICAL REVIEW D **86,** 103503 (2012)

Gas Density Profile in Dark Matter Halo in Chameleon Cosmology

Ayumu Terukina* and Kazuhiro Yamamoto†

Department of Physical Science, Hiroshima University, Higashi-Hiroshima 739-8526, Japan

(Received 30 March 2012; revised manuscript received 30 July 2012; published 5 November 2012)

We investigate the gas density, temperature, and pressure profiles in a dark matter halo under the influence of the chameleon force. We solve the hydrostatic equilibrium equation for the gas coupled with the chameleon field in an analytic manner, using an approximate solution for the chameleon field equation with the source term, with a generalized Navarro-Frenk-White universal density profile. We find that the gas distribution becomes compact because a larger pressure gradient is necessary due to the additional chameleon force. By confronting the theoretical prediction with the data of the temperature profile of the Hydra A cluster according to Suzaku x-ray observations out to the virial radius, we demonstrate that a useful constraint on a model parameter can be obtained depending on the value of the coupling constant. For example, the upper bound of the background value of chameleon field, $\phi_\infty < 10^{-4} M_{\rm Pl}$, is obtained in the case $\beta = 1$, where β is the coupling constant between the chameleon field and the matter, and $M_{\rm Pl}$ is the Planck mass. However, the error of the present data is not so small that we obtain a useful constraint in the case $\beta = 1/\sqrt{6}$, which corresponds to an $f(R)$ model.

DOI: 10.1103/PhysRevD.86.103503 PACS numbers: 98.62.Gq, 95.35.+d, 98.80.−k

The accelerated expansion of the Universe is one of the most fundamental mysteries in basic science. Long-distance modification of the gravity theory is a challenging approach to this problem. However, any gravity theory must pass the stringent constraints from the Solar System. The chameleon mechanism is a noble mechanism for screening a scalar degree of freedom which appears in a class of modified gravity models, depending on the density of matter in the local environment [1,2]. Newtonian gravity is recovered in a high-density region, thereby evading the Solar System constraints. Recently, it has been pointed out that the modification of gravity might be detected using halos of galaxies and galaxy clusters, because the screening mechanism could not be complete in their outer regions [3–8].

In the present paper, we focus on the gas distribution in a dark matter halo under the influence of the chameleon force. In Ref. [9], the authors found an analytic solution of the chameleon field, assuming the matter distribution of the Navarro-Frenk-White (NFW) universal density profile [10] (cf. Ref. [11]). Utilizing their analytic method, we investigate the gas density, temperature, and pressure profiles under the influence of the chameleon force. We find that the chameleon force significantly influences the gas distribution. We also demonstrate a useful constraint on the chameleon gravity model from confronting the theoretical temperature profile with x-ray observations of a cluster of galaxies.

The chameleon field equation for a quasistatic system in the Einstein frame is

$$\nabla^2 \phi = V_{,\phi} + \frac{\beta}{M_{\rm Pl}} \rho e^{\beta\phi/M_{\rm Pl}}, \tag{1}$$

where V is the potential, ρ is the matter density, β is the coupling constant, and we have defined the reduced Planck mass by ${M_{\rm Pl}}^2 = 1/(8\pi G)$ with the gravitational constant G. Here, we assume $V(\phi) = \Lambda^{4+n}/\phi^n$, where Λ is the mass dimension parameter and n is the dimensionless parameter. We also assume $\beta\phi/M_{\rm Pl} \ll 1$. The coupling between the scalar field and the matter density is the key for the chameleon mechanism, as we see below.

We follow the analytic method in Ref. [9] to find a solution for Eq. (1). In the present paper, we assume the generalized NFW density profile $\rho(x) = \rho_s/x(1+x)^b$ with $x = r/r_s$, where ρ_s and r_s are the characteristic density and scale of a halo, respectively, and b is a parameter. The NFW density profile is the case $b = 2$. The mass within the radius x of the halo is given by $M(x) = 4\pi r_s^3 \int_0^x dx x^2 \rho(x)$. Instead of the parameters r_s and ρ_s, we introduce the virial mass $M_{\rm vir}$ and the concentration parameter c, which are defined by $M_{\rm vir} = (4\pi/3) {r_{\rm vir}}^3 \Delta_c \bar{\rho}_c$ and $c = r_{\rm vir}/r_s$, where Δ_c is the ratio of the spherical overdensity $\bar{\rho}(<c)$ within the virial radius $r_{\rm vir}$ to the critical density of the universe $\bar{\rho}_c$; i.e., $\Delta_c = \bar{\rho}(<c)/\bar{\rho}_c$, for which we adopt $\Delta_c = 100$ in a spherical collapse model.

The analytic solution for Eq. (1) is obtained by matching the interior solution $\phi_{\rm int}$ and the exterior solution $\phi_{\rm out}$, where $\phi_{\rm int}$ is given by solving Eq. (1) while neglecting the term on the left-hand side, while $\phi_{\rm out}$ is given by neglecting the first term on the right-hand side of Eq. (1). Then, we find

$$\phi(x) = \begin{cases} \phi_s [x(1+x)^b]^{1/(n+1)} \equiv \phi_{\rm int}, & x < x_c, \\ -B \frac{1-(1+x)^{2-b}}{(b-2)x} - \frac{C}{x} + \phi_\infty \equiv \phi_{\rm out}, & x > x_c, \end{cases} \tag{2}$$

where we have defined $\phi_s = (n\Lambda^{n+4} M_{\rm Pl}/\beta\rho_s)^{1/(n+1)}$, $B = \beta\rho_s r_s^2/M_{\rm Pl}$, and C and x_c are determined by solving the matching conditions at $x = x_c$:

*telkina@theo.phys.sci.hiroshima-u.ac.jp
†kazuhiro@hiroshima-u.ac.jp

 © 2012 American Physical Society

$$C = B\frac{(1+x_c)^{2-b}-1}{b-2} + \phi_\infty x_c - \phi_s[x_c(1+x_c)^b]^{1/(n+1)}x_c, \quad (3)$$

$$\phi_\infty - B(1+x_c)^{1-b} = \phi_s(x_c(1+x_c)^b)^{1/(n+1)}\left(1+\frac{(1+b)x_c+1}{(n+1)(1+x_c)}\right). \quad (4)$$

The validity of the analytic solution is demonstrated for the case $b = 2$ in Refs. [5,9].

Note that ϕ_s is the typical value of the chameleon field in the interior region, where the chameleon mechanism works. This means that $\phi_s \ll \phi_\infty$, because the chameleon mechanism screens the chameleon field. With this fact, Eqs. (3) and (4) are approximated as

$$C \simeq B((1+x_c)^{2-b}-1)/(b-2) + \phi_\infty x_c, \quad (5)$$

$$\phi_\infty - B(1+x_c)^{1-b} \simeq 0, \quad (6)$$

since we are considering the case $x_c = \mathcal{O}(1)$. Hence, the scalar field in the exterior region is independent of n and Λ. This is important because the constraint we obtain becomes independent of n and Λ.

In our modeling of the gas distribution in a dark matter halo, we make a few assumptions for simplicity. First, we assume that the dark matter dominates the dark halo described by the generalized NFW density profile. The halo density profile could be affected by the modification of the gravity theory; however, we assume the same profile, since its validity is partially supported by N-body simulations for the Dvali-Gabadadze-Porrati model and $f(R)$ model [3–5,12]. Recently, Ref. [5] confirmed this validity for an $f(R)$ model, and argued a qualitative explanation for the validity. Second, we assume that the baryon density is negligible in the dark matter halo, which allows us to neglect its effect on the scalar field equation. The effect of the baryon component is discussed in Ref. [13]. The validity of this assumption is also supported by the recent measurements of the density profile of a cluster halo through gravitational lensing, which show that the NFW profile fits the data well [14,15]. Third, we assume that the scalar field is coupled with the baryon component as well as the dark matter component. For example, in an $f(R)$ model, the chameleon force is coupled with both the dark matter and the baryon components.

Within Newtonian gravity, a useful model of the gas density profile is considered in Refs. [13,16]. By assuming hydrostatic equilibrium between the gas pressure and the gravitational force from the dark matter with the NFW density profile, the universal gas density, temperature, and pressure profiles are derived. We follow the method of Refs. [13,16], but taking into account the chameleon force as well as the gravitational force, we derive the gas distribution in a halo. Now the hydrostatic equilibrium gives

$$\frac{(1+\epsilon)}{\rho_g}\frac{dP_g}{dr} = -\frac{1}{M_{\rm Pl}}\left[\frac{d\phi_G}{dr}+\beta\frac{d\phi}{dr}\right], \quad (7)$$

where ρ_g and P_g are the gas density and the pressure, respectively, and $\epsilon = 0$ unless explicitly stated otherwise. Here ϕ_G denotes the gravitational potential, given by solving the gravitational Poisson equation, $\triangle\phi_G = \rho/(2M_{\rm Pl})$. For the generalized NFW density profile, we find the solution $\phi_G(x) = \phi_0[1-(1+x)^{2-b}/(b-2)x]$, where we define $\phi_0 = -\rho_s r_s^2/2M_{\rm Pl}(b-1)$. We assume that the gas obeys the polytropic equation of state $P_g \propto \rho_g T_g \propto \rho_g^\gamma$ with the polytropic index γ and the gas temperature T_g. Introducing the function $y_g(x)$ by $\rho_g(x) = \rho_g(0)y_g(x)$, $P_g(x) = P_g(0)y_g^\gamma(x)$, and $T_g(x) = T_g(0)y_g^{\gamma-1}(x)$, we obtain the solution

$$y_g(x) = \left[1-\frac{\mu m_p}{kT_g(0)M_{\rm Pl}(1+\epsilon)}\frac{\gamma-1}{\gamma}(\phi_G(x)-\phi_G(0)+\beta\phi(x)-\beta\phi(0))\right]^{1/(\gamma-1)} \quad (8)$$

$$= \begin{cases} \left[1-A\left(1+\frac{(1+x)^{2-b}-1}{(b-2)x}-\frac{\beta\phi_s}{\phi_0}[x(1+x)^b]^{1/(n+1)}\right)\right]^{1/(\gamma-1)}, & \text{for } x<x_c, \\ \left[1-A\left(1+(1+2\beta^2)\frac{(1+x)^{2-b}-1}{(b-2)x}-\frac{\beta}{\phi_0}\left(\phi_\infty-\frac{C}{x}\right)\right)\right]^{1/(\gamma-1)}, & \text{for } x>x_c, \end{cases} \quad (9)$$

where we have defined $A = -\mu m_p\phi_0(\gamma-1)/kT_g(0)M_{\rm Pl}(1+\epsilon)\gamma$, k is the Boltzmann constant, and μm_p represents the mean molecular mass. We determine the parameter γ by following Expression (17) in Ref. [17]. Our conclusions are not altered qualitatively for the assumption on γ within $1.1 \le \gamma \le 1.3$.

Figure 1 shows the gas density profiles, comparing the case with the chameleon force (solid curves) and the case of Newtonian gravity (dashed curves), adopting virial masses of $M_{\rm vir} = 10^{13}M_\odot$, $10^{14}M_\odot$, and $4\times10^{14}M_\odot$, from top to bottom, respectively. The gas density decreases rapidly in the outer region (see the solid curves), where the chameleon force is influential. For the large mass cluster, the chameleon mechanism works out to large radii, because the density of dark matter is high enough even outside the halo. On the other hand, for the small mass cluster,

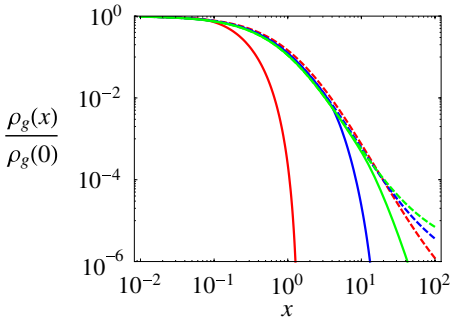

FIG. 1 (color online). Gas density profile as a function of the radius r/r_s. The solid (dashed) curves are with (without) the chameleon force, with virial masses $M_{\rm vir} = 4 \times 10^{14} M_\odot$ (green light curve), $10^{14} M_\odot$ (blue dark curve), and $M_{\rm vir} = 10^{13} M_\odot$ (red curve), from top to bottom, respectively. Here we have adopted $\beta = 1$, $n = 1.8 \times 10^{-5}$, $\Lambda = 2.4 \times 10^{-3}$ eV, and $\phi_\infty = 1.1 \times 10^{-5} M_{\rm Pl}$.

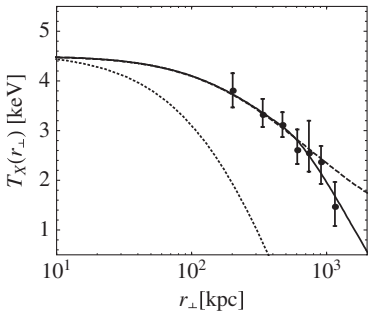

FIG. 2. Temperature profiles as a function of the radius $r_\perp$. The points with error bars show the observation data of the filament direction [18]. The curves show our theoretical model. The solid curve adopts the best-fit parameters $(\phi_\infty, M_{\rm vir}, c, T_g(0)) = (5.4 \times 10^{-5} M_{\rm Pl}, 5.1 \times 10^{14} M_\odot, 5.8, 4.9 {\rm keV})$. The dashed curve adopts $\phi_\infty = 2 \times 10^{-5} M_{\rm Pl}$, while the dotted curve adopts $\phi_\infty = 1.3 \times 10^{-4} M_{\rm Pl}$, where the other parameters are the same as those of the solid curve. Here we have fixed $\beta = 1$ and $b = 2$.

the chameleon mechanism works only at small radii, because the dark matter density is high only in the central region. Because the chameleon force is an attractive force, a larger pressure gradient is necessary for balancing between them. This makes the gas distribution compact. This feature is more significant for the smaller-mass halo.

Using this characteristic feature, let us consider a constraint on the chameleon gravity model. To this end, we consider x-ray observations of a cluster of galaxies. Because of the steep drop of the gas density in the presence of the chameleon force, a similar drop in the x-ray surface brightness may appear in the outer region. In the present paper, we compare the x-ray temperature profile with the data reported from Suzaku observations of the Hydra A cluster out to the virial radius [18]. The Hydra A cluster is a medium-sized cluster located at a distance of 230 Mpc. Two different fields are observed in Ref. [18]. One is the northwest offset from the x-ray peak of the cluster, and the other is the northeast offset. The former and latter fields are called the filament and void, respectively, because each field continues into the filament and void structures. In Fig. 2, the points with error bars show the data of the filament direction in Ref. [18].

The curves in Fig. 2 show our theoretical model of the x-ray surface brightness temperature, computed with the formula

$$T_X(r_\perp) = \frac{\int \lambda_c(T_g) \rho_g^2\left(\sqrt{r_\perp^2 + z^2}\right) T_g\left(\sqrt{r_\perp^2 + z^2}\right) dz}{\int \lambda_c(T_g) \rho_g^2\left(\sqrt{r_\perp^2 + z^2}\right) dz}, \quad (10)$$

where $\lambda_c(T_g)$ is the cooling function, for which we have assumed $\lambda_c(T_g) \propto T_g^{1/2}$ (e.g., Ref. [19]), and $r_\perp$ is the radial coordinate perpendicular to the line-of-sight direction. The solid curve is the best-fit curve, whose parameters are noted in the caption. The dashed curve and the dotted curve adopt $\phi_\infty = 2 \times 10^{-5} M_{\rm Pl}$ and $1.3 \times 10^{-4} M_{\rm Pl}$, respectively, where the other parameters are the same as those for the solid curve.

The dotted curve, the solid curve, and the dashed curve in Fig. 2 represent the characteristic curves which appear when we vary ϕ_∞ from a sufficiently large value to a smaller one. First, the dotted curve represents the limit of the modified gravity. Namely, for the large value of $\phi_\infty \geq B$, x_c becomes negative from Eq. (6). This means that there appears no interior region in a halo where the chameleon mechanism works to recover Newtonian gravity. Thus, for the case $\phi_\infty \geq B$, we have $\phi(x) = \phi_{\rm out}(x)$ for the entire region, and therefore the solution Eq. (8) should be replaced with

$$y_g(x) = \left[1 - A(1 + 2\beta^2)\left(1 + \frac{(1+x)^{2-b} - 1}{(b-2)x}\right)\right]^{1/(\gamma-1)}. \quad (11)$$

On the other hand, the dashed curve is the same as the limit of Newtonian gravity. For a small value of ϕ_∞, we have a large value of x_c from Eq. (6). This means that the chameleon force is influential only at very large radii. Note that the interior solution $y_g(x)$, Eq. (9) for $x < x_c$, can be approximated by taking the limit of $\beta \to 0$ in Eq. (11), because ϕ_s takes a very small value to screen the scalar field where the chameleon mechanism works. In summary, the dotted curve and the dashed curve are the two opposite limits, and our theoretical curve is restricted by these two limits. Note that the limit of the modified gravity Eq. (11) depends on the coupling constant β.

Figure 3 shows the contours of $\Delta\chi^2$ on the parameter plane for ϕ_∞ and $M_{\rm vir}$, where χ^2 is simply defined by $\chi^2 = \sum_{i=1}^{7} (T_X(r_{\perp,i}) - T_i^{\rm obs})^2 / (\Delta T_i^{\rm obs})^2$, where $T_i^{\rm obs}$ and $\Delta T_i^{\rm obs}$ are the observed data and the error of the filament direction, respectively, and $T_X(r_{\perp,i})$ is our theoretical model. Here, we have fixed $\beta = 1$ and $b = 2$, but the parameters c and $T_g(0)$ are varied so as to minimize χ^2

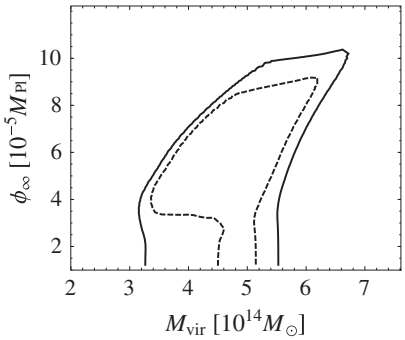

FIG. 3. The contours of $\Delta\chi^2$ on the parameter plane ϕ_∞-$M_{\rm vir}$. Here we have fixed $\beta = 1$ and $b = 2$, but c and $T_g(0)$ are varied as fitting parameters. The contour levels of the inner dashed curve and the outer solid curve are $\Delta\chi^2 = 2.7$ and 6.6, respectively.

within the range $3 \leq c \leq 10$ and $T_0^*/\alpha \leq T_g(0) \leq T_0^*\alpha$ with $\alpha = 1.1$, where T_0^* is given by Eq. (19) in Ref. [17]. When taking $T_g(0)$ as a completely free parameter, it is difficult to obtain a useful constraint from the present data due to the degeneracy between $T_g(0)$ and $M_{\rm vir}$. The minimum value of χ^2 is 1.0, where the number of degrees of freedom is 3. The behavior of the contour is explained by the fact that the theoretical curve approaches that of Newtonian gravity as ϕ_∞ becomes small and that the steep drop becomes significant as ϕ_∞ increases. Figure 3 gives an upper bound of $\phi_\infty < 10^{-4} M_{\rm Pl}$ at the 2-sigma level for the case $b = 2$ and $\beta = 1$. We obtain a similar upper bound of ϕ_∞ for different values of b, which are summarized in Table I. The upper bound of ϕ_∞ becomes larger for smaller b, but we may conclude that the results do not significantly depend on b. Table I includes the results with the void direction. The upper bound of ϕ_∞ depends on the data, i.e., the filament direction and the void direction; however, our conclusion does not alter significantly.

So far, we have considered the case $\beta = 1$; let us now discuss the case $\beta = 1/\sqrt{6}$, which corresponds to an $f(R)$ model [20]. In this case, we could not obtain a useful constraint on ϕ_∞, which is explained as follows. The theoretical density profile is limited by two characteristic curves, Eq. (11) and (11) with $\beta = 0$. When β is small, the difference between these two characteristic curves is small, because the drop of the gas density is not steep. This is the reason why no useful constraint on the $f(R)$ model was obtained from the present x-ray data.

In summary, under the assumption of hydrostatic equilibrium between the gas pressure gradient and the gravitational and chameleon forces, we derived the gas density profile in an analytic manner. Here we assumed the polytropic equation of state for the gas and the generalized NFW density profile for the dark matter distribution. The chameleon force may give rise to a steep drop in the gas distribution in the outer region of a halo. This feature is more significant when the mass of a halo is small and β and ϕ_∞ are large. The gas density profile depends on β and ϕ_∞, but it does not depend on n and Λ. This provides us with an opportunity to constrain β and ϕ_∞ by comparison with observations. We demonstrated a constraint on ϕ_∞ in the chameleon gravity model, using the data of the temperature profile from the x-ray observation [18]. We obtained a useful upper bound of $\phi_\infty < 10^{-4} M_{\rm Pl}$ in the case $\beta = 1$ [21]; however, no useful constraint was obtained in the case $\beta = 1/\sqrt{6}$, which corresponds to an $f(R)$ model. In order to obtain a useful constraint, observations of the outer region of a smaller mass cluster are more advantageous. Furthermore, a combination with other observations like the weak lensing measurements might improve the constraint. In our investigation, the assumption of the hydrostatic equilibrium of hot gas might be crucial. To estimate the effect of deviation from it, we obtained similar constraints by adopting the nonzero values of $\epsilon = \pm 0.5$ in Eq. (7). The upper bound of ϕ_∞ changes from $10^{-4} M_{\rm Pl}$ for $\epsilon = 0$ to $0.6 \times 10^{-4} M_{\rm Pl}$ and $2.1 \times 10^{-4} M_{\rm Pl}$ for $\epsilon = 0.5$ and -0.5, respectively. Thus, the assumption of hydrostatic equilibrium is crucial to the constraint, but we may obtain a useful constraint if we can model the state of the gas correctly. Further study is necessary for this problem. Finally, we assumed spherical symmetry for a halo, an assumption whose validity must be checked when comparing with observational data. In the present paper, the results in Table I do not depend on the filament direction and the void direction significantly, which suggests the validity of our assumption.

TABLE I. Upper bounds of ϕ_∞ at the 2-sigma level for different values of b and the data for the filament and void directions. Here we have fixed $\beta = 1$.

	Upper limit for ϕ_∞ in units of [$M_{\rm Pl}$]	
	Filament	Void
$b = 1.7$	1.4×10^{-4}	0.9×10^{-4}
$b = 2.0$	1.0×10^{-4}	0.8×10^{-4}
$b = 2.5$	0.8×10^{-4}	0.6×10^{-4}

We thank R. Kimura and T. Narikawa for fruitful discussions. We also thank S. Nishino, Y. Fukazawa, T. Kobayashi, K. Koyama, R. C. Nichol, A. Taruya, and Y. Suto for useful conversation related to the topic in the present paper. This work was supported by a Grant-in-Aid for Scientific Research from the Japanese Ministry of Education, Culture, Sports, Science, and Technology (Grants No. 21540270, No. 21244033).

[1] J. Khoury and A. Weltman, Phys. Rev. D **69**, 044026 (2004).
[2] D. F. Mota and J. D. Barrow, Phys. Lett. B **581**, 141 (2004).
[3] F. Schmidt, Phys. Rev. D **81**, 103002 (2010).
[4] T. Y. Lam, T. Nishimichi, F. Schmidt, and M. Takada, *et al.*, Phys. Rev. Lett. **109**, 051301 (2012).
[5] L. Lombriser, K. Koyama, G.-B. Zhao, and B. Li, Phys. Rev. D **85**, 124054 (2012).
[6] L. Lombriser, F. Schmidt, T. Baldauf, R. Mandelbaum, U. Seljak, and R. E. Smith, Phys. Rev. D **85**, 102001 (2012).
[7] T. Narikawa, R. Kimura, T. Yano, and K. Yamamoto, Int. J. Mod. Phys. D **20**, 2383 (2011).
[8] T. Narikawa and K. Yamamoto, J. Cosmol. Astropart. Phys. 05 (2012) 016.
[9] R. Pourhasan, N. Afshordi, R. B. Mann, and A. C. Davis, J. Cosmol. Astropart. Phys. 12 (2011) 005.
[10] J. F. Navarro, C. S. Frenk, and S. D. M. White, Astrophys. J. **490**, 493 (1997).
[11] P. Burikham and S. Panpanichi, Int. J. Mod. Phys. D **21**, 1250041 (2012).
[12] G.-B. Zhao, B. Li, and K. Koyama, Phys. Rev. Lett. **107**, 071303 (2011).
[13] Y. Suto, S. Sasaki, and N. Makino, Astrophys. J. **509**, 544 (1998).
[14] K. Umetsu, T. Broadhurst, A. Zitrin, E. Medezinski, D. Coe, and M. Postman, Astrophys. J. **738**, 41 (2011).
[15] M. Oguri, M. B. Bayliss, H. Dahle, K. Sharon, M. D. Gladders, P. Natarajan, J. F. Hennawi, and B. P. Koester, Mon. Not. R. Astron. Soc. **420**, 3213 (2012).
[16] E. Komatsu and U. Seljak, Mon. Not. R. Astron. Soc. **327**, 1353 (2001).
[17] E. Komatsu and U. Seljak, Mon. Not. R. Astron. Soc. **336**, 1256 (2002).
[18] T. Sato *et al.*, arXiv:1203.1700 [Publ. Astron. Soc. Jpn. (to be published)].
[19] V. R. Eke, J. F. Navarro, and C. S. Frenk, Astrophys. J. **503**, 569 (1998).
[20] A. A. Starobinsky, JETP Lett. **86**, 157 (2007); W. Hu and I. Sawicki, Phys. Rev. D **76**, 064004 (2007); S. Tsujikawa, Phys. Rev. D **77**, 023507 (2008).
[21] When we take the environment effect into account, this bound might be understood as the bound around the Hydra A cluster.

Journal of Cosmology and Astroparticle Physics
An IOP and SISSA journal

Testing chameleon gravity with the Coma cluster

Ayumu Terukina,[a] **Lucas Lombriser,**[b,c] **Kazuhiro Yamamoto,**[a,d] **David Bacon,**[b] **Kazuya Koyama**[b] **and Robert C. Nichol**[b]

[a]Department of Physical Science, Hiroshima University, Higashi-Hiroshima, Kagamiyama 1-3-1, 739-8526, Japan
[b]Institute of Cosmology and Gravitation, University of Portsmouth, Dennis Sciama Building, Portsmouth, PO1 3FX, U.K.
[c]Institute for Astronomy, University of Edinburgh, Royal Observatory, Edinburgh, EH9 3HJ, U.K.
[d]Hiroshima Astrophysical Science Center, Hiroshima University, Higashi-Hiroshima, Kagamiyama 1-3-1, 739-8526, Japan
E-mail: telkina@theo.phys.sci.hiroshima-u.ac.jp, lucas.lombriser@port.ac.uk, kazuhiro@hiroshima-u.ac.jp, david.bacon@port.ac.uk, kazuya.koyama@port.ac.uk, bob.nichol@port.ac.uk

Received December 27, 2013
Revised March 4, 2014
Accepted March 17, 2014
Published April 14, 2014

Abstract. We propose a novel method to test the gravitational interactions in the outskirts of galaxy clusters. When gravity is modified, this is typically accompanied by the introduction of an additional scalar degree of freedom, which mediates an attractive fifth force. The presence of an extra gravitational coupling, however, is tightly constrained by local measurements. In chameleon modifications of gravity, local tests can be evaded by employing a screening mechanism that suppresses the fifth force in dense environments. While the chameleon field may be screened in the interior of the cluster, its outer region can still be affected by the extra force, introducing a deviation between the hydrostatic and lensing mass of the cluster. Thus, the chameleon modification can be tested by combining the gas and lensing measurements of the cluster. We demonstrate the operability of our method with the Coma cluster, for which both a lensing measurement and gas observations from the X-ray surface brightness, the X-ray temperature, and the Sunyaev-Zel'dovich effect are available. Using the joint observational data set, we perform a Markov chain Monte Carlo analysis of the parameter space describing the different profiles in both the Newtonian and chameleon scenarios. We report competitive constraints on the chameleon field amplitude and its coupling strength to matter. In the case of $f(R)$ gravity, corresponding to a specific choice of the coupling, we find an upper bound on the background field amplitude of $|f_{R0}| < 6 \times 10^{-5}$, which is currently the tightest constraint on cosmological scales.

Keywords: modified gravity, galaxy clusters
ArXiv ePrint: 1312.5083

© 2014 IOP Publishing Ltd and Sissa Medialab srl
doi:10.1088/1475-7516/2014/04/013

JCAP04(2014)013

Contents

1 Introduction

Modifications of the theory of gravity can serve as an alternative approach to using dark energy models to explain the cosmic acceleration of our Universe [1, 2]. Any covariant modification of General Relativity introduces an additional degree of freedom. The chameleon model modifies gravity by introducing a scalar field in addition to the tensor field, which is non-minimally coupled with the matter components and gives rise to a fifth force that can be of the same order as the standard gravitational force. The scope for extra gravitational forces is, however, severely constrained by experiments in the Solar System. The chameleon model employs a screening mechanism of the scalar field which depends on the local matter density [3, 4] and allows it to evade these constraints; however in this model cosmic acceleration must be driven by the contribution of a cosmological constant or dark energy rather than being a genuine modified gravity effect [5].When the curvature of space-time is small, gravity remains modified, which renders galaxy clusters a useful regime for testing modified gravity models: while the interior of a cluster may be screened, the chameleon mechanism may not completely screen the modifications of gravity in the outer region of the cluster [6–16]. When the chameleon field is coupled with the gas component, the fifth force due to the chameleon field affects the gas density profile of the galaxy cluster. This causes an additional pressure gradient that balances the extra force, which leads to a more compact gas distribution in the cluster. This effect has been used in [14] to compare the X-ray temperature profile predicted by the chameleon model with measurements of the Hydra A cluster, yielding an upper bound on the asymptotic scalar field value at large distances of $\phi_\infty < 10^{-4}\ M_{\rm Pl}$ for a coupling constant between the chameleon field and matter of $\beta = 1$.

JCAP04(2014)013

The chameleon model parameter β determines the strength of the fifth force when it is not screened (see section 2.2). The second chameleon parameter, ϕ_∞, controls the effectiveness of the screening mechanism, describing the transition from the inner region of a cluster where gravity may be Newtonian to the outer region where the fifth force contributes [17, 18]. The critical radius, where the transition occurs, is determined by both ϕ_∞ and β [see eq. (3.8)]. In the absence of environmental effects, we may regard ϕ_∞ as the cosmological background value of the chameleon field. When $\beta = \sqrt{1/6}$ the chameleon model reduces to a $f(R)$ gravity model [19–21] with the scalar field potential determined by the choice of $f(R)$ [22], a nonlinear function of the Ricci scalar R that is added to the Einstein-Hilbert action. In this case, the parameter ϕ_∞ is proportional to the parameter $|f_{R0}|$ of the $f(R)$ model, where f_{R0} is the present background value of the scalar field $df(R)/dR$ (see section 3.1.3 for details).

In the presence of a chameleon force, due to its effect on the gas distribution, the hydrostatic mass of a cluster if interpreted assuming Newtonian gravity will deviate from its underlying dark matter distribution, which can be measured via weak gravitational lensing, resulting in different mass estimates for the cluster (see [23] for a recent analysis of this mass bias in hydrodynamic simulations of $f(R)$ gravity). Therefore, the combination of the gas and lensing measurements of a cluster may yield a powerful probe of gravity if they give statistically different mass estimates, which are not due to other astrophysical reasons.

In this paper, we demonstrate the operability of this method with the Coma cluster; a massive cluster at a distance of approximately 100 Mpc, whose properties are measured with several independent methods. The *Planck* team has, for instance, reported a precise observation of the Sunyaev-Zel'dovich (SZ) [24] effect [25]. Moreover, the X-ray surface brightness and X-ray temperature have been measured in [26–28], and weak lensing (WL) observations have been conducted by [29, 30]. We use the combination of these measurements to place tight constraints on β and ϕ_∞. To illustrate the effectiveness of our approach, in figure 1, we compare our result to current constraints from cosmological, astrophysical, and local tests in the well studied case that the chameleon model reduces to $f(R)$ gravity. Our Coma constraint is currently the tightest constraint on cosmological scales.

An important element of our method is the reconstruction of the gas distribution in a cluster of galaxies under the influence of the fifth force. In previous work [14], the hydrostatic equilibrium of the gas components was assumed when modelling the gas distribution of the Hydra A cluster in chameleon gravity. Hydrostatic equilibrium may, however, not always be realised because of turbulence and bulk motions of the gas caused by mergers with other clusters and groups of galaxies, as well as infalling material. The authors of [31] have demonstrated that the cluster masses in numerical simulations, estimated under the assumption of hydrostatic equilibrium, can deviate from the true mass by up to 30%, and that the deviation is explained by the acceleration term in the Euler equation. We therefore carefully examine the systematics that deviations from the hydrostatic equilibrium in the Coma cluster may introduce on our results.

We first reconstruct the 3-dimensional profiles of the gas density, temperature, and pressure from the observational results using Newtonian gravity. We then compare the mass estimates from the gas observations with the mass estimate from lensing, finding good agreement between them and that the assumption of hydrostatic equilibrium is a good approximation given the observational errors of the lensing mass. Moreover, these mass estimates are only marginally affected by the inclusion of an extremised non-thermal pressure component, which has been calibrated to hydrodynamical simulations.

JCAP04(2014)013

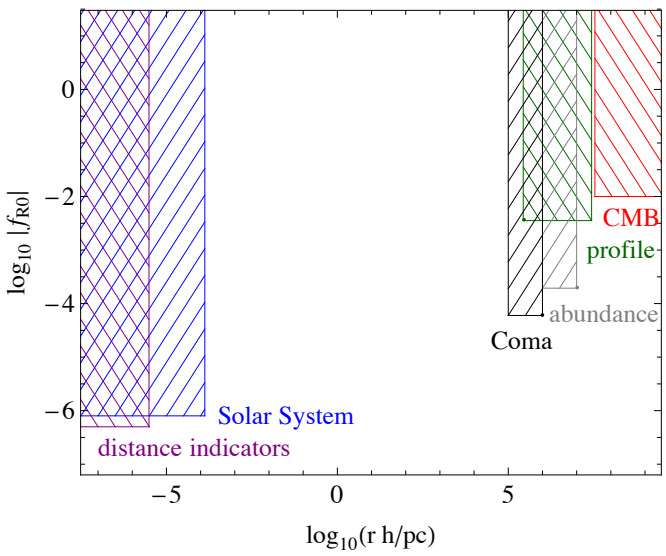

Figure 1. Comparison of our Coma cluster constraint to current constraints on $f(R)$ gravity from the Solar System [20, 32], distance indicators in unscreened dwarf galaxies [33], the cosmic microwave background (CMB) [34, 35], cluster density profiles [9] and abundance [6, 36]. The figure is adapted from [9]. Also compare to figure 2 (resp. 3) of [2, 37] for prospective constraints on $f(R)$ gravity.

While non-thermal pressure and other deviations from the hydrostatic equilibrium enhance the hydrostatic mass estimate, we find a strong decrease of the reconstructed hydrostatic mass when the chameleon fifth force is introduced. The detection of an enhanced hydrostatic mass with respect to the lensing mass when interpreted in a Newtonian framework, may, therefore, be a smoking gun for modified gravity. On the other hand, the effects of non-thermal pressure and chameleon force may become degenerate in the reconstruction, as the change in the hydrostatic mass by enhancing modifications of gravity can be compensated by increasing deviations from hydrostatic equilibrium. Given the small effect of the non-thermal pressure compared to the effect from modifying gravity, however, we decide that it is safe to assume hydrostatic equilibrium of the gas, and perform our analysis under this assumption.

Finally, note that Fusco-Femiano, Lapi, and Cavaliere [38] recently investigated the consistency between the X-ray observations, from surface brightness and temperature, and the SZ measurement in the Coma cluster, adopting a "Supermodel". The Supermodel expresses the profiles of density and temperature in the entropy-modulated equilibrium of the intracluster plasma within the potential wells provided by the dominant dark matter [39]. This yields a direct link between the X-ray and the SZ observations based on the entropy profile. They found a tension between the SZ and the X-ray pressure emitted by the plasma. In our analysis, we confirm these results, by finding a similar tension between the SZ and the X-ray pressures. However, the tension is mainly represented by the asymptotic difference of the values of the pressure between the inner and the outer regions. On the other hand, the constraint on the chameleon gravity model comes from the shape of the density profile in the intermediate regime, so we can nevertheless put a useful constraint on the chameleon model.

The paper is organised as follows: in section 2, we review the hydrostatic equilibrium equations and hydrostatic mass, including a brief review of an analytic approximate solution

JCAP04(2014)013

of the scalar field profile in the cluster. In section 3, we perform a Markov chain Monte Carlo (MCMC) analysis to place constraints on the Newtonian and chameleon model parameter space. We then discuss the systematic effects introduced by deviations from spherical symmetry, and study deviations from the hydrostatic equilibrium of the gas in Newtonian gravity by comparing the hydrostatic mass inferred from X-ray and SZ measurements with the lensing mass and analysing the effects of including non-thermal pressure in comparison to the effects from the chameleon force. In section 4, we present our conclusions. Finally, in appendix A, we discuss our reconstruction method for the gas profiles.

2 Hydrostatic and lensing mass in the presence of a chameleon force

We describe the hydrostatic mass of a spherically symmetric system of gas and introduce the non-thermal pressure model, which we use to analyse deviations from hydrostatic equilibrium. Then, we briefly review a derivation of an analytic approximate solution for the chameleon scalar field profile within a dark matter cluster, which we use to determine the effects on hydrostatic masses in the presence of the extra force. Next, we compare the reconstructed hydrostatic masses, from different gas observations, with the observed lensing mass and discuss the effect on the mass reconstruction when incorporating the non-thermal pressure model and the chameleon modification.

2.1 Hydrostatic mass

We consider a spherically symmetric system of gas and dark matter. In this case, we can write the equation for the gas component in hydrostatic equilibrium as

$$\frac{1}{\rho_{\rm gas}(r)}\frac{dP_{\rm total}(r)}{dr} = -\frac{GM(<r)}{r^2}, \tag{2.1}$$

where $\rho_{\rm gas}$ is the gas density, $P_{\rm total}$ is the 'total' gas pressure, including both thermal and non-thermal pressure, and $M(<r)$ is the mass enclosed within the radius r. This equation describes the balance between the gas pressure gradient and the gravitational force. Note that we have not yet included the chameleon force (see section 2.2). The total gas pressure can be written as the combination of the thermal pressure and the non-thermal pressure, $P_{\rm total} = P_{\rm thermal} + P_{\rm non-thermal}$. Eq. (2.1) can then be rephrased as

$$M(<r) = M_{\rm thermal}(r) + M_{\rm non-thermal}(r) \tag{2.2}$$

with the definitions:

$$M_{\rm thermal}(r) \equiv -\frac{r^2}{G\rho_{\rm gas}(r)}\frac{dP_{\rm thermal}(r)}{dr}, \tag{2.3}$$

$$M_{\rm non-thermal}(r) \equiv -\frac{r^2}{G\rho_{\rm gas}(r)}\frac{dP_{\rm non-thermal}(r)}{dr}. \tag{2.4}$$

$M_{\rm non-thermal}$ is introduced to help mathematically describe the non-thermal pressure contribution to the total mass. Note that $M_{\rm thermal}$ is expressed in terms of $P_{\rm thermal}$ and $\rho_{\rm gas}$ in eq. (2.3). If we introduce the equation of state of gas, $P_{\rm thermal} = kn_{\rm gas}T_{\rm gas}$, we can express the thermal mass in terms of $T_{\rm gas}$ and $\rho_{\rm gas}$ instead,

$$M_{\rm thermal}(r) = -\frac{kT_{\rm gas}(r)r}{\mu m_{\rm p}G}\left(\frac{d\ln\rho_{\rm gas}(r)}{d\ln r} + \frac{d\ln T_{\rm gas}(r)}{d\ln r}\right), \tag{2.5}$$

JCAP04(2014)013

where we have used $\rho_{\rm gas} = \mu m_{\rm p} n_{\rm gas}$ with the mean molecular weight μ and the proton mass $m_{\rm p}$. The mean molecular weight of the fully ionised gas is defined by $\mu(n_{\rm e} + n_{\rm H} + n_{\rm He})m_{\rm p} = m_{\rm p} n_{\rm H} + 4m_{\rm p} n_{\rm He}$ with $n_{\rm e} = n_{\rm H} + 2n_{\rm He}$, where $n_{\rm e}$, $n_{\rm H}$ and $n_{\rm He}$ is the number density of electron, hydrogen, and helium, respectively. Adopting the mass fraction of hydrogen $n_{\rm H}/(n_{\rm H} + 4n_{\rm He}) = 0.75$, we have $\mu = 0.59$.

We define the fraction of the total pressure attributed to the non-thermal contribution by

$$P_{\rm non-thermal}(r) \equiv g(r) P_{\rm total}(r). \tag{2.6}$$

Hence, using $P_{\rm total} = g^{-1} P_{\rm non-thermal} = (1-g)^{-1} P_{\rm thermal}$, we may write

$$P_{\rm non-thermal}(r) = \frac{g(r)}{1-g(r)} n_{\rm gas}(r) k T_{\rm gas}(r). \tag{2.7}$$

According to hydrodynamical simulations [40, 41], the non-thermal contribution to the total pressure can be modelled with the expression

$$g(r) = \alpha_{\rm nt}(1+z)^{\beta_{\rm nt}} \left(\frac{r}{r_{500}}\right)^{n_{\rm nt}} \left(\frac{M_{200}}{3\times 10^{14} M_\odot}\right)^{n_{\rm M}}, \tag{2.8}$$

where $\alpha_{\rm nt}$, $\beta_{\rm nt}$, $n_{\rm nt}$, and $n_{\rm M}$ are constants. For illustration, and for an estimation of the effects from neglecting the non-thermal contribution, we adopt the parameter values $(\alpha_{\rm nt}, \beta_{\rm nt}, n_{\rm nt}, n_{\rm M}) = (0.3, 0.5, 0.8, 0.2)$, which are the best-fit values in [41] with the exception of $\alpha_{\rm nt}$. The best-fit value of $\alpha_{\rm nt}$ is 0.18, which is an averaged value over 16 simulated clusters. We set $\alpha_{\rm nt} = 0.3$, which is the maximum value obtained in the 16 clusters [41], in order to study the effect of the non-thermal pressure contribution in the extremised case.

We refer to appendix A for our approach to reconstruction of the 3-dimensional profiles of $\rho_{\rm gas}$, $T_{\rm gas}$, and $P_{\rm thermal}$ from the gas observations via the X-ray temperature, X-ray surface brightness, and SZ effect, which enables us to estimate $M_{\rm thermal}$. Using eqs. (2.6) and (2.8), we can then estimate the non-thermal contribution $M_{\rm non-thermal}$ employing the results from hydrodynamical simulations.

2.2 Chameleon fifth force

We now consider the effect on the hydrostatically inferred cluster mass profile when introducing the chameleon force. The field equation of the chameleon field ϕ in a quasi-static system is given by [3]

$$\nabla^2 \phi = V_{,\phi} + \frac{\beta}{M_{\rm Pl}} \rho, \tag{2.9}$$

where ρ is the matter density, V is the scalar field potential, β is the coupling between the scalar field and matter, taken to be constant here, and $M_{\rm Pl}$ is the Planck mass. We shall assume that the potential is a monotonic function of the scalar field, $V = \Lambda^{4+n}/\phi^n$ with constant exponent n (see, e.g., [14, 18]). Note that the choice of the potential is not essential to our analysis because the scalar field in the cluster is not sensitive to the parameters of the potential, Λ and n, as will be described below. Our results will also be applicable to the Hu-Sawicki $f(R)$ model in section 3.1.3, where the potential can be written approximately as $V = V_0 - \Lambda^{4+n}/\phi^n$ with $-1 < n < 0$ and a constant V_0 that yields cosmic acceleration. We

JCAP04(2014)013

also assume $\beta\phi \ll M_{\rm Pl}$, so that the coupling is not too strong and we can use the weak-field approximation. The chameleon fifth force is written as

$$F_\phi = -\frac{\beta}{M_{\rm Pl}}\nabla\phi. \tag{2.10}$$

Note that we are considering a model where both matter components, i.e., baryonic and dark matter, are coupled to the chameleon field. In this scenario, both matter components are subject to the gravitational force and the chameleon force F_ϕ. This is, for instance, the case in $f(R)$ gravity models and any other chameleon theory that can be formulated in the Jordan frame with a single metric. It is possible to consider a model where the baryonic component does not couple to the chameleon field [42, 43]. Such a model would not be constrained by our method as it would not introduce a difference between the hydrostatic and lensing masses. Hence, we do not consider this possibility in this paper, nor the possibility of introducing different coupling strengths for the different components.

We further assume that the dark matter component dominates over the baryonic contribution in the cluster and that the matter density of the cluster ρ is well described by a Navarro-Frenk-White (NFW) [44] profile

$$\rho(r) = \frac{\rho_{\rm s}}{r/r_{\rm s}\left(1+r/r_{\rm s}\right)^2}, \tag{2.11}$$

where the characteristic density $\rho_{\rm s}$, and characteristic scale $r_{\rm s}$, are fitted parameters. The mass of the dark matter within the radius r is then given by

$$M(<r) = 4\pi\int_0^r dr r^2\rho(r) = 4\pi\rho_{\rm s}r_{\rm s}^3\left[\ln(1+r/r_{\rm s}) - \frac{r/r_{\rm s}}{1+r/r_{\rm s}}\right]. \tag{2.12}$$

Note that the NFW fitting function eq. (2.11) is based on N-body dark matter simulations of the concordance model. It is nontrivial to extend this assumption to modified gravity models. However, it was shown in [10] that the NFW profile provides equally good fits for $f(R)$ clusters as it does for the Newtonian scenario. This was shown using N-body simulations of the Hu-Sawicki $f(R)$ gravity model corresponding to $\beta = \sqrt{1/6}$, which characterises only a subgroup of models of the more general chameleon model studied here. The effects of the modifications on observables are, however, qualitatively similar between different values of the coupling strength β and can even partially be mapped into each other, suggesting the applicability of the NFW profile. Its validity for the full range of parameters considered in this paper may still be worthwhile checking using N-body simulations. From an observational perspective, recent work by [45, 46] supports the consistency of the NFW profile with measurements. Hence, even independent of the simulation results, the NFW profile could be used for the reconstruction of the lensing mass with the same motivation as introducing the gas profiles in the reconstruction of the hydrostatic mass in appendix A.

We consider the virial mass of a halo within the virial radius $r_{\rm vir}$, which is related to the concentration parameter c by

$$c \equiv \frac{r_{\rm vir}}{r_{\rm s}}. \tag{2.13}$$

The virial radius is defined such that the averaged density within this radius is $\Delta_{\rm c}$ times the critical density. Then the virial mass $M_{\rm vir}$ is written as

$$M_{\rm vir} \equiv M(<r_{\rm vir}) = \frac{4\pi}{3}r_{\rm vir}^3\Delta_{\rm c}\bar{\rho}_{\rm c}, \tag{2.14}$$

JCAP04(2014)013

where $\bar{\rho}_{\rm c}$ is the critical density. We use $\Delta_{\rm c} = 100$ obtained in the spherical collapse model in the cold dark matter scenario with cosmological constant Λ [47]. Note that the critical overdensity contrast $\Delta_{\rm c}$ generally depends on the modified gravity parameters. For example, the authors in ref. [48] found $\Delta_{\rm c} \sim 80$ in an $f(R)$ model, which is equivalent to $\Delta_{\rm vir} \sim 300$ at redshift $z \sim 0$. Nonetheless, our final conclusion is independent of this modification of $\Delta_{\rm c}$ because our MCMC analysis includes the parameters $M_{\rm vir}$ and c, which are degenerate with $\Delta_{\rm c}$. Therefore, the change of $\Delta_{\rm c}$ only introduces shifts in the values of c and $M_{\rm vir}$.

Instead of $\rho_{\rm s}$ and $r_{\rm s}$, we can alternatively use the virial mass $M_{\rm vir}$ and concentration c as the underlying fitting parameters of eq. (2.11), from which one can determine $\rho_{\rm s}$ and $r_{\rm s}$ using the relations

$$r_{\rm s} = \frac{1}{c}\left[\frac{M_{\rm vir}}{(4\pi/3)\Delta_{\rm c}\bar{\rho}_{\rm c}}\right]^{1/3}, \tag{2.15}$$

$$\rho_{\rm s} = \frac{M_{\rm vir}}{4\pi r_{\rm s}^3}\left(\ln(1+c) - \frac{c}{1+c}\right)^{-1}. \tag{2.16}$$

These relations directly follow from eqs. (2.13) and (2.14).

With the assumption of a NFW dark matter density profile of the cluster, we can derive an approximate, but analytic, solution for the radial profile of the chameleon field from eq. (2.9) [14, 17, 18]. The analytic solution for eq. (2.9) is obtained by connecting the interior solution $\phi_{\rm int}$ and the outer solution $\phi_{\rm out}$. The interior solution is obtained when the scalar field is in the minimum of the effective potential, which corresponds to the right-hand side of eq. (2.9). Thus, the solution of the chameleon field can be inferred by setting $\nabla^2\phi$ to zero. This represents the regime of the chameleon suppression of the scalar field and the chameleon field does not mediate a fifth force. On the other hand, the outer solution is obtained when the contribution of the scalar field potential, the first term on the right-hand side of eq. (2.9), is subdominant to the matter density and $\nabla^2\phi$. This describes the case where the chameleon field mediates a long-range fifth force, the matter density is still large compared to the background, and the scalar field has not settled in the minimum of the effective potential. For these two limits of the chameleon field, we find

$$\phi(r) = \begin{cases} \phi_{\rm s}[r/r_{\rm s}(1+r/r_{\rm s})^2] \equiv \phi_{\rm int}(\simeq 0) & (r < r_{\rm c}) \\ -\dfrac{\beta\rho_{\rm s}r_{\rm s}^2}{M_{\rm Pl}}\dfrac{\ln(1+r/r_{\rm s})}{r/r_{\rm s}} - \dfrac{C}{r/r_{\rm s}} + \phi_\infty \equiv \phi_{\rm out} & (r > r_{\rm c}) \end{cases}, \tag{2.17}$$

where C is an integration constant and $r_{\rm c}$ is the transition scale, connecting $\phi_{\rm int}$ and $\phi_{\rm out}$. We have furthermore defined $\phi_{\rm s}^{n+1} = (n\Lambda^{n+4}M_{\rm Pl}/\beta\rho_{\rm s})$, which represents the value of the chameleon field in the interior region, and ϕ_∞, the value of the scalar field at large distance from the cluster. The chameleon field at the background is in the minimum of the effective potential, hence, we have $\phi_\infty^{n+1} = (n\Lambda^{n+4}M_{\rm Pl}/\beta\rho_0)$, where ρ_0 is the matter density at large distance from the cluster, e.g., the cosmological background density. Due to the high density inside the cluster, $\rho_{\rm s} \gg \rho_0$, the chameleon field is strongly suppressed with $\phi_{\rm s} \ll \phi_\infty$. Thus the interior solution for the scalar field eq. (2.17) may be approximated as $\phi_{\rm int} \simeq 0$. The integration constant C and the transition scale $r_{\rm c}$ are then determined from requiring $\phi_{\rm int}(r_{\rm c}) = \phi_{\rm out}(r_{\rm c})$ and $\phi'_{\rm int}(r_{\rm c}) = \phi'_{\rm out}(r_{\rm c})$. Finally we have the approximate solution

$$C \simeq -\frac{\beta\rho_{\rm s}r_{\rm s}^2}{M_{\rm Pl}}\ln(1+r_{\rm c}/r_{\rm s}) + \phi_\infty r_{\rm c}/r_{\rm s} \tag{2.18}$$

$$\phi_\infty - \frac{\beta\rho_{\rm s}r_{\rm s}^2}{M_{\rm Pl}}(1+r_{\rm c}/r_{\rm s})^{-1} \simeq 0. \tag{2.19}$$

JCAP04(2014)013

Note that in our approximation, the chameleon field eq. (2.17) and the transition relations eqs. (2.19) and (2.18) do not depend on the parameters of the scalar field potential, Λ and n, as we consider ϕ_∞ as the degree of freedom of the model, which, depending on the environment of a cluster, may be different from the cosmological background value of the scalar field.

From eq. (2.19), we can see that the critical radius r_c, below which the chameleon field is screened, is determined by $\beta M_{\rm Pl}/\phi_\infty$. Hence, the smaller ϕ_∞ at fixed β, the larger the critical radius becomes. As a consequence, the entire cluster can be screened. The smaller β, the smaller the strength of the fifth force becomes. Thus, Newtonian gravity is recovered in each of the limits $\beta = 0$ and $\phi_\infty = 0$.

In the presence of the chameleon field, the hydrostatic equilibrium eq. (2.1) is modified by the introduction of the extra force $F_\phi = -(\beta/M_{\rm Pl})d\phi/dr$ on the right-hand side of the equation. The chameleon force then modifies the mass inferred from hydrostatic equilibrium in eq. (2.2) as

$$M(<r) = M_{\rm thermal}(r) + M_{\rm non-thermal}(r) + M_\phi(r), \tag{2.20}$$

where we define an extra mass

$$M_\phi(r) \equiv -\frac{r^2}{G}\frac{\beta}{M_{\rm Pl}}\frac{d\phi(r)}{dr} \tag{2.21}$$

associated with the enhanced gravitational force due to the chameleon field.

2.3 Inferring hydrostatic and lensing masses from observations

The thermal mass $M_{\rm thermal}$ of a cluster in eq. (2.5) is determined by its gas density, temperature, and pressure, which can be measured in X-ray and SZ observations. In order to obtain $M_{\rm thermal}$ from observations, we reconstruct the three dimensional gas profiles using parametric fits as described in detail in appendix A, which we substitute into eq. (2.5). We assume that the gas is fully ionised and that the electron temperature is equal to $T_{\rm gas}$. For a relaxed cluster such as Coma, used in section 3 to derive constraints on the chameleon model, we assume that the electrons and protons have the same temperature. Note, however, that this assumption is nontrivial because the equipartition timescale between electrons and protons through Coulomb collisions is close to the dynamical timescale of the cluster (see, e.g., [49]). Here, we use the notation $n_{\rm e}$ for the three dimensional electron number density, which is related to the gas number density $n_{\rm gas}$ by

$$n_{\rm e} = \frac{2+\mu}{5} n_{\rm gas}. \tag{2.22}$$

Similarly, we introduce the electron pressure $P_{\rm e}$, which is related to the gas thermal pressure $P_{\rm thermal}$ by

$$P_{\rm e} = n_{\rm e} k T_{\rm gas} = \frac{2+\mu}{5} P_{\rm thermal}. \tag{2.23}$$

With the definitions in eqs. (2.22) and (2.23) and the reconstructed 3-dimensional temperature, electron density, and pressure profiles from appendix A, we can now determine the thermal mass profile of the cluster. From X-ray observations, we infer

$$M_{\rm thermal} = -\frac{k T_{\rm gas}^{\rm (X)} r}{\mu m_{\rm p} G}\left(\frac{d\ln n_{\rm e}^{\rm (X)}}{d\ln r} + \frac{d\ln T_{\rm gas}^{\rm (X)}}{d\ln r}\right) \tag{2.24}$$

JCAP04(2014)013

and similarly, from the SZ observations, we obtain

$$M_{\rm thermal} = -\frac{r^2}{G\rho_{\rm gas}^{\rm (X)}}\frac{dP_{\rm thermal}^{\rm (SZ)}}{dr}. \tag{2.25}$$

With this reconstruction, we can directly compare the two mass profiles with the lensing mass

$$M_{\rm WL} = 4\pi\rho_{\rm s}r_{\rm s}^3\left[\ln(1+r/r_{\rm s}) - \frac{r/r_{\rm s}}{1+r/r_{\rm s}}\right], \tag{2.26}$$

which is obtained by integration over the NFW density profile in eq. (2.11), assuming that $\phi/M_{\rm Pl} \ll 1$ such that the lensing potential is related to the matter distribution by the standard Poisson equation.

In the presence of a non-thermal pressure, eqs. (2.24) and (2.25) are modified according to eq. (2.8) with the mass inferred from X-ray by

$$\begin{aligned} M_{\rm thermal} + M_{\rm non-thermal} \\ = -\frac{kT_{\rm gas}^{\rm (X)}r}{\mu m_{\rm p}G}\left(\frac{d\ln n_{\rm e}^{\rm (X)}}{d\ln r} + \frac{d\ln T_{\rm gas}^{\rm (X)}}{d\ln r}\right) - \frac{r^2}{G\rho_{\rm gas}^{\rm (X)}}\frac{d}{dr}\left(\frac{g}{1-g}n_{\rm gas}^{\rm (X)}kT_{gas}^{\rm (X)}\right), \end{aligned} \tag{2.27}$$

whereas a combination of SZ and X-ray infers

$$M_{\rm thermal} + M_{\rm non-thermal} = -\frac{r^2}{G\rho_{\rm gas}^{\rm (X)}}\frac{dP_{\rm thermal}^{\rm (SZ)}}{dr} - \frac{r^2}{G\rho_{\rm gas}^{\rm (X)}}\frac{d}{dr}\left(\frac{g}{1-g}P_{\rm thermal}^{\rm (SZ)}\right). \tag{2.28}$$

To derive our constraints in section 3, we will assume hydrostatic equilibrium, eq. (2.1), and thus require

$$M_{\rm thermal} + M_{\rm non-thermal} + M_\phi \equiv M_{\rm WL}, \tag{2.29}$$

where M_ϕ is the chameleon contribution described in eq. (2.21) and $M_{\rm non-thermal} \ll M_{\rm thermal} + M_\phi$. We refer the reader to section 3.2.1 for an analysis on the validity of the hydrostatic equilibrium assumption in the case of the Coma cluster.

3 Application to the Coma cluster

Having established the notion of hydrostatic and lensing mass, and having described the effects from the presence of a chameleon field on the relation between the two in section 2, we now analyse constraints on the chameleon gravity model by confronting our predictions with observations of the Coma cluster. We chose to work with the Coma cluster as it is a relaxed system, where the non-thermal pressure is expected to be subdominant (e.g. [50] and also see section 3.2.1) and which has been well measured through a range of different observations [50–53]. The contribution of non-thermal pressure can also be assumed small in modified gravity [23]. Ref. [54] has recently pointed out that the cluster may not be very typical: its X-ray temperature and star formation rate is high but the kinematic features like substructure and velocity dispersion are not conspicuous. The authors urge caution in using Coma cluster as a $z \sim 0$ baseline cluster in galaxy evolution studies. On the other hand, according to references [55, 56], the Coma cluster is in agreement with scaling relations obtained from typical cluster samples. We cannot exclude that extraordinary features of the cluster may

JCAP04(2014)013

affect our conclusions. However, our constraints rely only on the observed distribution of gas and dark matter and we allow a number of degrees of freedom to phenomenologically model these distributions, finding good agreement of our fits with the observational data. We also carefully examine a dynamical equilibrium model of the Coma cluster. Note that our method applies to any cluster which is in hydrostatic equilibrium, and is not restricted to the Coma cluster. This section is organized as follows: in section 3.1, we first assume hydrostatic equilibrium and model the effect from chameleon gravity using the analytic scalar field solution described in section 2.2 to derive and compare the theoretical gas distribution profiles with the corresponding observations of the Coma cluster. Then we simultaneously fit for the observed X-ray surface brightness, the X-ray temperature, the SZ effect, and the WL profile based on a parametric fit for the electron number density and the NFW profile. We obtain competitive constraints on the chameleon model. In particular, our method provides the currently strongest cosmological constraint on $f(R)$ gravity (see figure 1). In section 3.2, we then analyse the validity of the hydrostatic equilibrium assumption of gas in the Coma cluster and study the potential systematic effects on the reconstructed mass profiles as well as possible errors induced by non-spherically symmetric features of the cluster.

3.1 Constraints on the model parameters from an MCMC analysis

We estimate the 3-dimensional profiles of the temperature, electron density, and pressure from observations of the X-ray temperature, surface brightness, and SZ effect employing the parametric fits described in appendix A, as well as the lensing mass, for which we use a NFW profile. In hydrostatic equilibrium, the hydrostatic mass can then be inferred from any combination of two of these profiles. Here, we choose to work with the electron number density eq. (A.5) and the NFW profile eq. (2.12), and perform an MCMC analysis of the model parameter space, including the chameleon model parameters β and ϕ_∞ discussed in section 2.2.

3.1.1 Method

We write the hydrostatic equilibrium equation as

$$\frac{1}{\rho_{\rm gas}(r)}\frac{P_{\rm thermal}(r)}{dr} = -\frac{GM(<r)}{r^2} - \frac{\beta}{M_{\rm Pl}}\frac{d\phi(r)}{dr} \tag{3.1}$$

and assume that the equation of state for the gas is given by $P_{\rm thermal} = n_{\rm gas}kT_{\rm gas}$, which is equivalent to $P_{\rm e} = n_{\rm e}kT_{\rm gas}$, where the electron temperature equals to $T_{\rm gas}$. Integration of eq. (3.1) yields

$$P_{\rm thermal}(r) = P_{\rm thermal,0} + \mu m_{\rm p}\int_0^r n_{\rm e}(r)\left(-\frac{GM(<r)}{r^2} - \frac{\beta}{M_{\rm Pl}}\frac{d\phi(r)}{dr}\right)dr. \tag{3.2}$$

Hereby, $P_{\rm thermal,0}$ is an integration constant equal to the thermal gas pressure at $r = 0$, which can be written as $P_{\rm thermal,0} = n_{\rm gas,0}kT_0$, where $n_{\rm gas,0}$ and T_0 are the thermal gas number density and the gas (electron) temperature at $r = 0$, respectively. We adopt eq. (A.5) to describe the electron number density $n_{\rm e}(r)$ and the NFW profile eq. (2.11) for the matter density which determines the cluster mass profile $M(<r)$ in eq. (2.12). Note from eq. (2.22) that $n_{\rm gas,0}$ is expressed by n_0 as $n_{\rm gas,0} = 5n_0/(2+\mu)$.

The NFW density profile is specified by the virial mass $M_{\rm vir}$ and the concentration parameter c. The configuration of the scalar field is given by specifying the parameters

JCAP04(2014)013

β and ϕ_∞. Including the parameters for the electron number density, the complete list of parameters we analyse in our MCMC study becomes $T_0, n_0, b_1, r_1, M_{\rm vir}, c, \beta, \phi_\infty$, where r_1 and b_1 determine a characteristic scale and slope, respectively, for $n_{\rm e}(r)$ in eq. (A.5). Once these parameters are specified, we can compute the projected gas profiles in eqs. (A.1), (A.2), and (A.3), which are then compared with the observational data from the X-ray surface brightness and temperature, and the SZ observations.

We estimate the "goodness-of-fit" by computing the chi-squared distribution

$$\chi^2(M_{\rm vir}, c, T_0, n_0, b_1, r_1, \beta, \phi_\infty) = \chi^2_{\rm XT} + \chi^2_{\rm SB} + \chi^2_{\rm SZ} + \chi^2_{\rm WL}, \tag{3.3}$$

where

$$\chi^2_{\rm XT} = \sum_i \frac{(T_{\rm X}(r_{\perp,i}) - T^{\rm obs.}_{{\rm X},i})^2}{(\Delta T^{\rm obs.}_{{\rm X},i})^2}, \tag{3.4}$$

$$\chi^2_{\rm SB} = \sum_i \frac{(S_{\rm X}(r_{\perp,i}) - S^{\rm obs.}_{{\rm X},i})^2}{(\Delta S^{\rm obs.}_{{\rm X},i})^2}, \tag{3.5}$$

$$\chi^2_{\rm SZ} = \sum_i \frac{(y(r_{\perp,i}) - y^{\rm obs.}_{i})^2}{(\Delta y^{\rm obs.}_{i})^2}, \tag{3.6}$$

$$\chi^2_{\rm WL} = \frac{(M_{\rm vir} - M_{\rm WL})^2}{(\Delta M_{\rm WL})^2} + \frac{(c - c_{\rm WL})^2}{(\Delta c_{\rm WL})^2}. \tag{3.7}$$

Here, $T_{\rm X}(r_{\perp,i})$ and $T^{\rm obs.}_{{\rm X},i}$ are the theoretical and observed X-ray temperatures, and $\Delta T^{\rm obs}_{{\rm X},i}$ refers to the observational error. We adopt the analogous notation for the surface brightness $S_{\rm X}$ and the y-parameter, defined by the SZ temperature as $\Delta T_{\rm SZ}/T_{\rm CMB} \equiv -2y$. In addition, $M_{\rm WL}$ and $c_{\rm WL}$ are the observed virial mass and the concentration parameter from weak lensing, respectively.

For the X-ray temperature profile, we use the *XMM-Newton* data reported in [27] for the inner region and *Suzaku* data reported in [28] for the outer region. For the X-ray surface brightness profile, we use the *XMM-Newton* data reported in [26] and for the SZ pressure profile, we use the *Planck* measurements [25]. Finally, we use the WL measurement of the Coma cluster reported by Okabe et al. [30], who adopt a NFW fit in their analysis to obtain a virial mass of the Coma cluster of $M_{\rm vir} = 8.92^{+20.05}_{-5.17} \times 10^{14} h^{-1} M_\odot$ and a concentration of $c = 3.5^{+2.57}_{-1.79}$ with virial overdensity $\Delta_{\rm c} = 100$.

In our likelihood analysis, we assume that the information contained in each data point is independent of the other data points, i.e., that there is no correlation between these four observations. This could be an over-simplification. These four observations are based on different measurement principles, and the X-ray, SZ effect, and WL observations are obtained at different wavelengths. On the other hand, the information contained in the data comes from the same astrophysical object, and thus the systematic errors might be correlated. For instance, the clumpiness of the cluster and other non-spherically symmetric features would introduce a correlated systematic error between the data sets. We do not take into account such correlations in our analysis and leave it for future work to address these observational issues in more detail. See, however, section 3.2 for a discussion of these effects. We also note that the covariance of errors is not taken into account in our analysis because it is not available to us. For now, we assign a 5% systematic error to the measurement error of the X-ray surface brightness.

JCAP04(2014)013

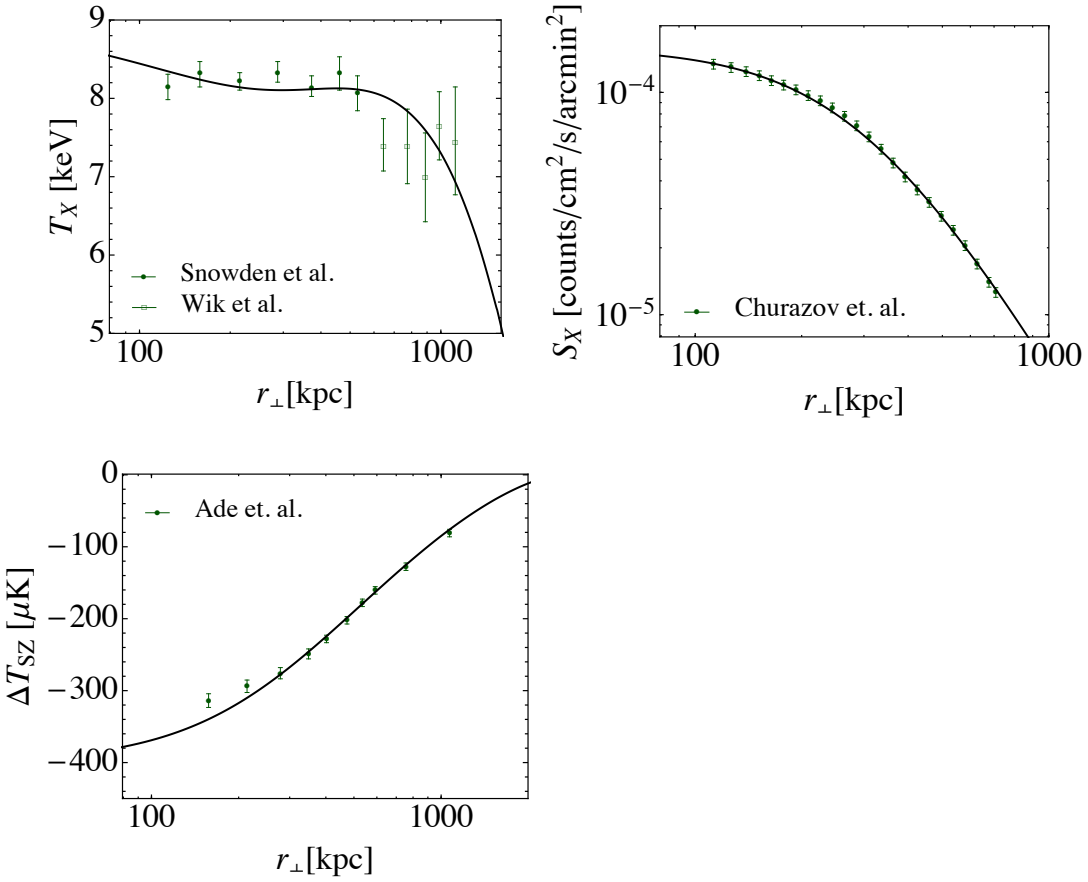

Figure 2. X-ray temperature (top-left), surface brightness (top-right), and SZ effect (bottom). The best-fit values of the chameleon model parameters are $(\beta,\, \phi_\infty)$=$(15,\, 4\times10^{-4}M_{\rm Pl})$, where the model parameters characterising the profiles are given in table 1. In the data analysis, we use the data points included within the radial range 100 kpc $< r_\perp <$ 1 Mpc and fit them using the model parameters $T_0, n_0, b_1, r_1,\ M_{\rm vir}, c$ in the Newtonian case and in addition β_2 and $\phi_{\infty,2}$ in the chameleon scenario. Note that the best-fits of the Newtonian and chameleon cases almost overlap.

3.1.2 MCMC analysis

We perform an MCMC analysis with the 8 model parameters $T_0, n_0, b_1, r_1,\ M_{\rm vir}, c, \beta_2$, and $\phi_{\infty,2}$, which completely describe the X-ray temperature and surface brightness profiles, the SZ effect, and the WL mass profile as well as the chameleon modified gravity model. We re-normalise the parameters $\beta_2 = \beta/(1+\beta)$ and $\phi_{\infty,2} = 1-\exp(-\phi_\infty/10^{-4}M_{\rm Pl})$ (instead of β and ϕ_∞) as β_2 and $\phi_{\infty,2}$ span the complete available parameter space of β and ϕ_∞ in the interval $[0,1]$. Note, however, that some of the approximations made in section 2 do not hold in the extreme limits of $\phi_{\infty,2}\to1$ and $\beta_2\to1$. For our analysis, we use the MCMC module included in the COSMOMC [57] package, which employs a Metropolis-Hastings [58, 59] sampling algorithm. We require a Gelman-Rubin statistic [60] of $\mathcal{R}-1<0.03$ to ensure convergence of our runs.

In figure 2, we compare the overall best-fit curves for the chameleon gravity model (dashed) and Newtonian gravity (solid) from the combination of all of the observational data

JCAP04(2014)013

parameter	Newtonian gravity	Modified gravity
$M_{\rm vir}$	$2.57^{+0.97}_{-0.54}\ 10^{15}\ M_\odot$	$2.46^{+1.33}_{-0.61}\ 10^{15}\ M_\odot$
c	$2.56^{+0.49}_{-0.52}$	$2.64^{+0.72}_{-0.7}$
n_0	$2.33^{+0.22}_{-0.17}\ 10^{-3}/\mathrm{cm}^3$	$2.34^{+0.21}_{-0.19}\ 10^{-3}/\mathrm{cm}^3$
b_1	$-0.921^{+0.089}_{-0.109}$	$-0.915^{+0.085}_{-0.107}$
r_1	$3.02^{+0.54}_{-0.47}\ 10^2$ kpc	$2.99^{+0.56}_{-0.45}\ 10^2$ kpc
T_0	$11.2^{+0.76}_{-0.84}$ keV	$11.3^{+0.79}_{-0.9}$ keV

Table 1. Best-fit values and 1-dimensional marginalised constraints (95% CL) for the model parameters $(T_0, n_0, b_1, r_1, M_{\rm vir}, c)$ characterising the gas and dark matter profiles obtained from an MCMC analysis of the joint observational data sets.

sets, i.e., minimising χ^2 in eq. (3.3). The corresponding best-fit parameter values are listed in table 1 along with the 1-dimensional marginalised 95% confidence levels (CL). We show the 2-dimensional marginalised contours of the different combinations between the model parameters for the Newtonian case, i.e., where we have fixed $\beta = 0$ and $\phi_\infty = 0$, in figure 3. The best fit in this case yields a reduced χ^2 of $\chi^2/\mathrm{d.o.f.} = 32/41$. In figure 4, we show the analogous constraints for the model parameters of the chameleon modified gravity scenario. The best fit in this case yields a good reduced χ^2 of $\chi^2/\mathrm{d.o.f.} = 32/39$. We refer to section 3.2 for a discussion of possible sources of systematic error that have not been taken into account in this analysis.

Finally, in figure 5, we show the 2-dimensional marginalised contours of the parameters β_2 and $\phi_{\infty,2}$. Note that the lower shaded region is the allowed region. We recall that β describes the strength of the chameleon fifth force and ϕ_∞ determines the efficiency of the chameleon screening, and we introduced the parameters $\beta_2 = \beta/(1+\beta)$, which we mapped into $\phi_{\infty,2} = 1 - \exp(-\phi_\infty/10^{-4} M_{\rm Pl})$ instead of β and ϕ_∞ to describe the entire parameter space of the chameleon modification. Newtonian gravity is recovered in both limits of $\beta_2 = 0$ and $\phi_{\infty,2} = 0$.

The boundaries in figure 5 can be understood by considering the phenomenology of the chameleon modification. At large β, if the chameleon field is not screened, the extra chameleon force reduces the hydrostatic mass compared to the Newtonian mass estimate and it becomes inconsistent with the lensing mass (see section 3.2). This causes a tension in the desired parameter values when fitting the joint set of observations and places constraints on the chameleon modification. On the other hand, the chameleon force contributes only outside of the critical radius $r_{\rm c}$, which is determined by eq. (2.19) as

$$1 + \frac{r_{\rm c}}{r_{\rm s}} = \frac{\beta \rho_{\rm s} r_{\rm s}^2}{M_{\rm Pl} \phi_\infty}. \tag{3.8}$$

Due to the chameleon suppression mechanism, Newtonian gravity is recovered below $r_{\rm c}$. To put a useful constraint on the chameleon force, $r_{\rm c}$ must be smaller than the size of the cluster, which is about 1 Mpc. More precisely, with increasing $\beta M_{\rm Pl}/\phi_\infty$, the transition scale $r_{\rm c}$ becomes large and eventually surpasses the size of the cluster, in which case the chameleon mechanism completely screens the fifth force within the cluster. At this point, no further constraints on the chameleon model can be obtained. This implies that there is an

JCAP04(2014)013

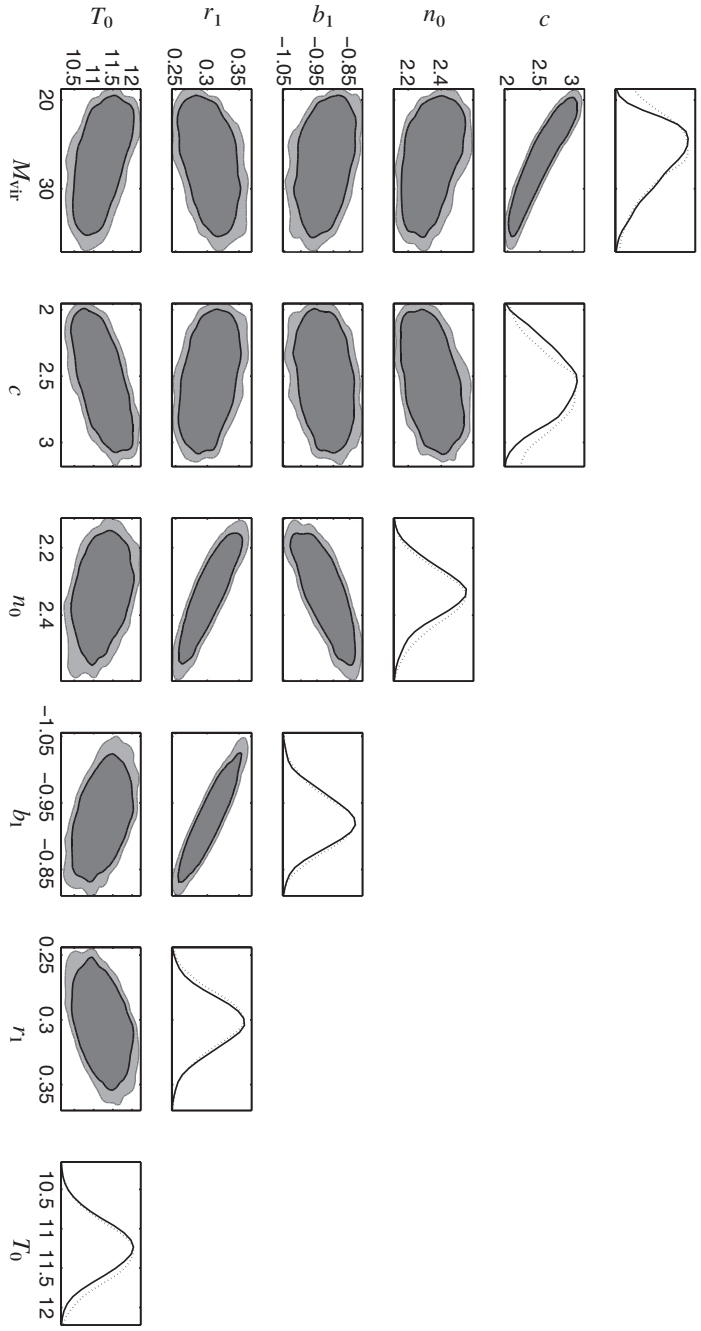

Figure 3. 95% (deep gray region) and 99% CL (pale gray region) 2-dimensional marginalised contours of the 6 model parameters T_0 [keV], n_0 [10^{-2}cm^{-3}], b_1, r_1 [Mpc], $M_{\rm vir}$ [$10^{14}M_\odot$], and c in the Newtonian scenario, obtained from the MCMC analysis, using the joint set of X-ray, SZ, and WL data. The most-right panels of each row show the 1-dimensional marginalised constraints (solid) and likelihood distributions (dotted).

JCAP04(2014)013

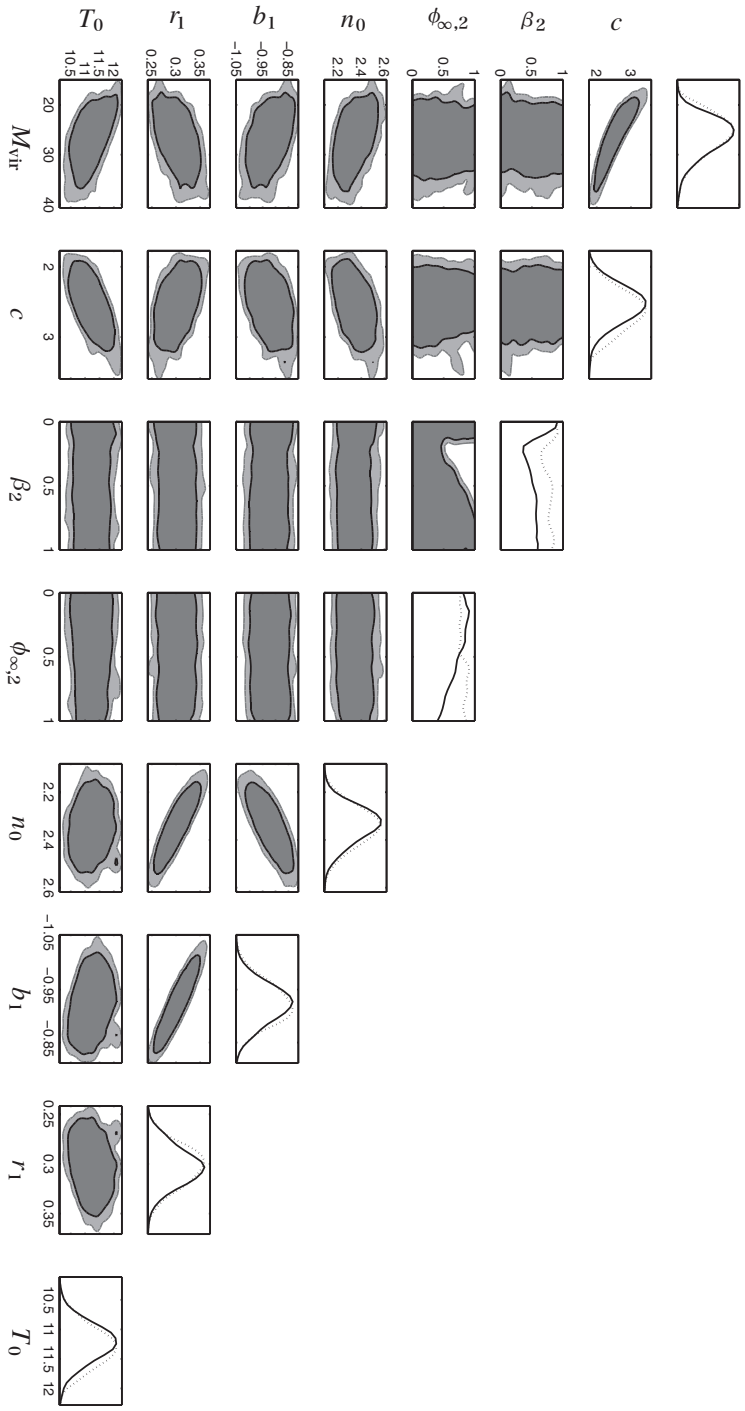

Figure 4. Same as figure 3 but when including the chameleon parameters β_2 and $\phi_{\infty,2}$ in the MCMC analysis. The 2-dimensional marginalised contours of β_2 and $\phi_{\infty,2}$ are also shown in figure 5.

JCAP04(2014)013

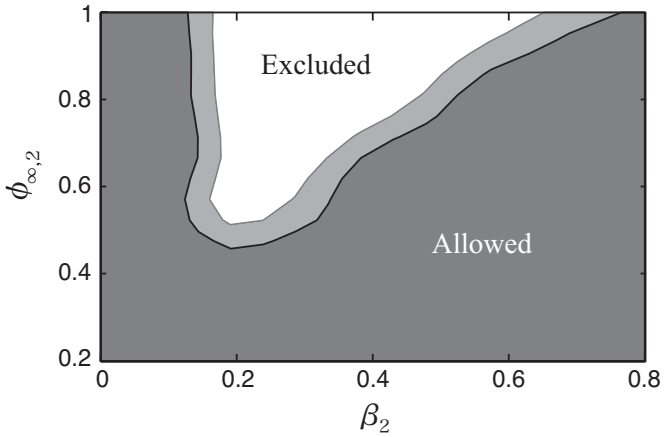

Figure 5. 95% (deep gray region) and 99% CL (pale gray region) contours for the chameleon model parameters $\beta_2 = \beta/(1+\beta)$ and $\phi_{\infty,2} = 1 - \exp(-\phi_\infty/10^{-4}\mathrm{M_{Pl}})$, obtained from the MCMC analysis of the 8 model parameters, $T_0, n_0, b_1, r_1, M_{\rm vir}, c, \beta_2$, and $\phi_{\infty,2}$, using the joint set of X-ray, SZ, and WL data. The shaded region is the allowed region.

upper bound on $\beta M_{\rm Pl}/\phi_\infty$, which can be constrained. In the opposite limit, when β is small, the fifth force is weak and the modifications become consistent with the observations within the given errors. Hence, at low β_2 in figure 5 the chameleon scalar field amplitude $\phi_{\infty,2}$ is unconstrained.

With the minimal scalar field in the background, $-\Lambda^{n+4} \simeq n^{-1}\beta\,\bar{R}_0\,\phi_\infty^{n+1} M_{\rm Pl}$, the Compton wavelength of the background scalar field today, assumed to be ϕ_∞ here, becomes [32]

$$m_\infty^{-1} \simeq \left[\frac{\beta\,\bar{R}_0}{n+1}\frac{M_{\rm Pl}}{\phi_\infty}\right]^{-1/2} \sim \left[10^{-6}\frac{\beta}{n+1}\frac{M_{\rm Pl}}{\phi_\infty}\right]^{-1/2}\ \text{Mpc}. \tag{3.9}$$

Whereas the chameleon mechanism suppresses the scalar field on scales below $r_{\rm c}$, on scales larger than the Compton wavelength m_∞^{-1}, modifications of gravity are Yukawa suppressed. With Solar System tests requiring that $\phi_\infty \lesssim 10^{-6}\beta$ [20, 32] and with $n \sim \mathcal{O}(1)$, one obtains $m_\infty^{-1} \sim$ Mpc. Hence, requiring Solar System tests to be satisfied, standard gravity is recovered on scales beyond $\mathcal{O}(1)$ Mpc (cf. [5]). Since we only use observations on scales smaller than 1 Mpc and constraints are weaker than the local bounds, we can safely ignore the Yukawa suppression.

3.1.3 Constraint on $f(R)$ gravity

Our constraints have important implications for $f(R)$ gravity [19–21], which corresponds to a subset of our models with a particular choice of the coupling constant $\beta = \sqrt{1/6}$. In $f(R)$ gravity, the Einstein-Hilbert action is supplemented by a free nonlinear function $f(R)$ of the Ricci scalar R,

$$S = \frac{1}{16\pi G}\int d^4x\sqrt{-g}(R + f(R)) + \int d^4x\sqrt{-g}L_{\rm m}, \tag{3.10}$$

where $L_{\rm m}$ is the matter Lagrangian. Here, we adopt the particular expression $f(R) = -m^2c_1/c_2 + (m^2c_1/c_2^2)(R/m^2)^{-\tilde{n}}$ of the Hu-Sawicki model [20], where $\tilde{n}$, m, c_1 and c_2 are constant model parameters. Note that $m^2c_1/c_2/2$ can be chosen such that the modification

JCAP04(2014)013

exhibits an effective cosmological constant and mimics the expansion history of the concordance model. Hence, we specify $m^2 = \Omega_{\rm m} H_0^2$ and $c_1/c_2 = 6\Omega_\Lambda/\Omega_{\rm m}$, where $\Omega_{\rm m}$ and H_0 are the matter density parameter and the Hubble parameter at the present epoch, respectively, and $\Omega_\Lambda \equiv 1 - \Omega_{\rm m}$. Furthermore, we have $\tilde{n} c_1/c_2^2 = -f_{R0}[3(1 + 4\Omega_\Lambda/\Omega_{\rm m})]^{\tilde{n}+1}$, where we introduced the model parameter f_{R0}, which is the value of $df(R)/dR$ at present time and at the background. The $f(R)$ modification can be related to the chameleon field ϕ via

$$f_R = -\sqrt{\frac{2}{3}} \frac{\phi}{M_{\rm Pl}} \tag{3.11}$$

and hence, assuming that the Coma cluster is isolated such that ϕ_∞ corresponds to the background scalar field value, we have $f_{R0} = -\sqrt{2/3}(\phi_\infty/M_{\rm Pl})$. From the 2-dimensional contours of $(\beta_2, \phi_{\infty,2})$ in figure 5, we therefore estimate an upper bound on $f(R)$ gravity of $\phi_\infty \lesssim 7 \times 10^{-5} M_{\rm Pl}$ or equivalently, $|f_{\rm R0}| \lesssim 6 \times 10^{-5}$ at 95% CL.

We emphasise that this is a competitive result with the bounds on $f(R)$ gravity obtained from cosmology such as from the abundance of clusters [6, 36, 64] (see figure 1) and the current constraints from redshift-space distortions in the large scale structure of galaxies [65]. Note that in the case of $\tilde{n} = 1$, the value of $|f_{R0}|$ is related to the Compton wavenumber of the scalar field k_C by

$$k_C \simeq 0.04 \left(\frac{10^{-4}}{|f_{R0}|}\right)^{1/2} \ h{\rm Mpc}^{-1}. \tag{3.12}$$

Then, $|f_{\rm R0}| \lesssim 6 \times 10^{-5}$ can be rephrased as $k_C \lesssim 0.05\ h{\rm Mpc}^{-1}$.

Note that the assumption that the Coma cluster is an isolated system is nontrivial. It is well known that on large scales, the cluster is connected to a network of filaments [61, 62]. Hence, ϕ_∞ or f_{R0} should really be understood as the scalar field value in the mean density environment within a large radius around the Coma cluster, which we expect to be close to the background value [63]. This interpretation does not differ from approaches taken to derive the constraints reported in figure 1. Another possible effect which may be introduced by the environment could be a large-scale non-spherically symmetric feature as discussed in section 3.2.2.

3.2 Systematic effects

So far we have assumed hydrostatic equilibrium of the gas and a spherically symmetric matter distribution. We therefore devote the remainder of this section to discuss the systematic errors that can be introduced in our analysis due to deviations of the hydrostatic equilibrium (section 3.2.1) and to adumbrate the systematics caused by the presence of non-spherically symmetric features (section 3.2.2).

3.2.1 Invalidity of hydrostatic equilibrium

By employing the assumption of hydrostatic equilibrium in our analysis of the model parameter space, we have supposed that for the Coma cluster, the hydrostatic masses inferred from temperature and density, and that from pressure and density, are consistent, as well as that the two hydrostatic masses are also consistent with the lensing mass. Here, we test the validity of hydrostatic equilibrium within Newtonian gravity by comparing the different mass estimates, and study the effects of introducing non-thermal pressure.

JCAP04(2014)013

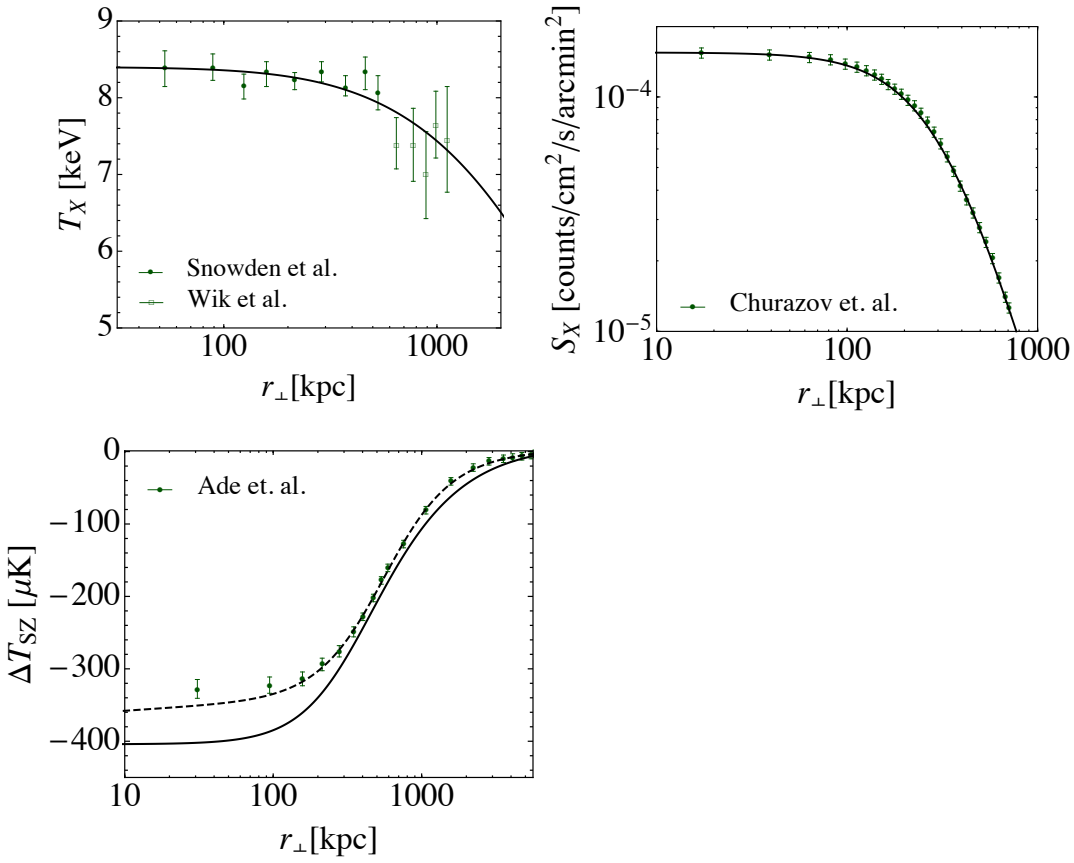

Figure 6. *Top left panel*: Radial gas temperature profile of the Coma cluster. The circles and boxes represent the the data points and errors from the *XMM-Newton* measurements by Snowden et al. [27] and the *Suzaku* measurements by Wik et al. [28], respectively. The solid curve is the projected emission weighted temperature eq. (A.1), using the fitting functions eqs. (A.4) and (A.5) for the 3-dimensional temperature and electron density profiles with best-fit parameter values $(T_0, A, r_0, b_0) = (8.6\ \mathrm{keV}, 0.082, 3.9\ \mathrm{Mpc}, -5.3)$ and $(n_0, r_1, b_1) = (2.3 \times 10^{-3}\mathrm{cm}^{-3}, 0.34\ \mathrm{Mpc}, -1)$, respectively, to the joint X-ray data. *Top right panel*: radial surface brightness profile of the Coma cluster. The data points represent the *XMM-Newton* measurements by Churazov et al. [26]. The error bars in the original data, which only account for the Poisson noise contribution, are small. We assign a systematic error of 5% to each data point to take into account clumpiness and other non-spherically symmetrical features of the cluster. The solid curve is the surface brightness profile eq. (A.2), using the fitting functions eqs. (A.5) and (A.4) for the 3-dimensional electron density profile temperature profile with best-fit parameter values $(T_0, A, r_0, b_0) = (8.6\ \mathrm{keV}, 0.082, 3.9\ \mathrm{Mpc}, -5.3)$ and $(n_0, r_1, b_1) = (2.3 \times 10^{-3}\mathrm{cm}^{-3}, 0.34\ \mathrm{Mpc}, -1)$, respectively, to the joint X-ray data. *Bottom panel*: radial Sunyaev-Zel'dovich CMB temperature profile. The data points represent the *Planck* measurements by Ade et al. [25]. The dashed curve is the SZ effect eq. (A.3), using the fitting function eq. (A.6) for the 3-dimensional pressure profile with best-fit parameter values $(P_0, b_3, b_4, b_5, r_4) = (1.1 \times 10^{-2}\ \mathrm{keV/cm}^3, 0.14, 2.2, 1.1, 0.53\ \mathrm{Mpc})$. The solid curve is the best fit model from the joint X-ray observations.

In the top left and top right panel of figure 6, we compare the observed X-ray temperature and surface brightness, respectively, against the corresponding best fit curves, which are

JCAP04(2014)013

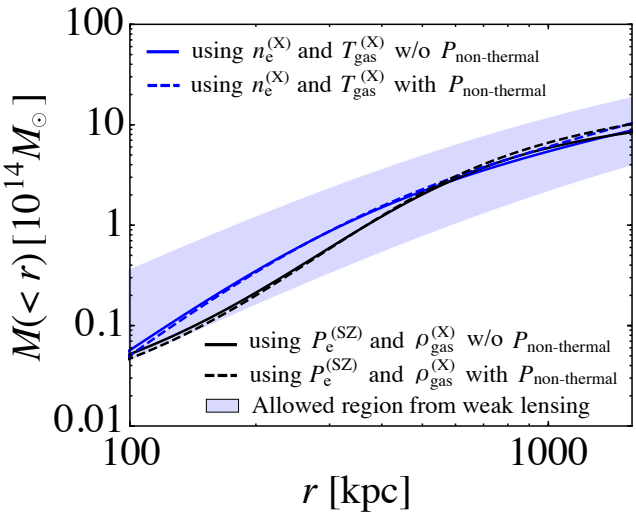

Figure 7. Radial mass profile of the Coma cluster. The shaded region is the observationally allowed 1-σ region from the WL observations of [30]. The blue solid curve is the thermal mass component $M_{\rm thermal}$ estimated from the X-ray observations only, and the black solid curve is $M_{\rm thermal}$ estimated from the combination of X-ray and SZ observations. The blue dashed and black dashed curves correspond to the same colour solid lines, however, now including a large non-thermal pressure contribution.

obtained by fitting the projected profiles of eqs. (A.1) and (A.2) with eqs. (A.4) and (A.5) to the combined X-ray data. Note that in the top right panel, for each data point, we have assigned a 5% systematic error on top of the measured errors. The measured errors for the X-ray surface brightness are extremely small because they only include the Poisson noise contribution. Systematic errors can be introduced from the clumpiness and the non-spherical symmetry of the gas distribution and should be taken into account (see section 3.2.2).

The bottom panel of figure 6 shows the SZ observations by the *Planck* satellite reported in [25], which we compare with the two different best-fit curves. The dashed curve is the best fit obtained by fitting the SZ profile eq. (A.3) with eq. (A.6) and the solid curve is the best fit to the joint X-ray temperature and surface brightness data, i.e., with the same parameter values used in the top left and top right panels of figure 6. Note the deviation between the two curves.

Recently, Fusco-Femiano, Lapi, and Cavaliere [38] analysed the consistency between the observations of the X-ray surface brightness, X-ray temperature, and SZ observations, adopting a "Supermodel". The Supermodel yields a direct link between the X-ray and the SZ observations based on the entropy profile. They report a tension between the pressure from the X-ray observations and that from SZ observation in the Coma cluster. The authors argue that an additional non-thermal pressure resolves the tension. In this paper, we adopt a similar observational data set and reconstruct the 3-dimensional gas profiles using the relations described in appendix A. We find a similar tension in our results and model a non-thermal pressure component as described in section 2.1, which however, is slightly different from the non-thermal pressure discussed in [38]. The non-thermal pressure in [38] is a constant, which is independent of the radius. The non-thermal pressure we introduce in section 2.1 is

JCAP04(2014)013

a function of radius, and its fraction in the total pressure becomes large only in the outer region. Nevertheless, our models fit the data reasonably well and can be used to put a useful constraint on the chameleon modification. This is because we only use the limited data in the range of radii of 100 kpc $< r_\perp <$ 1 Mpc, where the shape of the mass profile drives the constraints.

Figure 7 shows the different radial mass profiles reconstructed from the different gas observations and the lensing mass in Newtonian gravity, including effects from the non-thermal pressure introduced in section 2.1. The blue solid curve is the hydrostatic mass from eq. (2.5) with the reconstructed $n_{\rm e}(=\rho_{\rm gas}(2+\mu)/5\mu m_{\rm p})$ and $T_{\rm gas}$ from the X-ray observations. The black solid curve is the hydrostatic mass from eq. (2.3) with the reconstructed $\rho_{\rm gas}$ and $P_{\rm gas}$ from the X-ray observations and the SZ observations. Finally, the shaded region in figure 7 shows the allowed 1σ-region of the WL mass profile fitted using a NFW density profile with $M_{\rm vir} = 8.92^{+20.05}_{-5.17}\times 10^{14}h^{-1}M_\odot$ and $c = 3.5^{+2.57}_{-1.79}$. At the scales of 100 kpc $< r <$ 1 Mpc, the blue and black curves are consistent within the shaded region, while for $r <$ 100 kpc, the curves are out of the shaded region. Thus, for 100 kpc $< r <$ 1 Mpc, although the mass estimates differ up to the 50% level, within the observational error of the lensing mass, the mass profiles estimated by the gas observations are consistent with each other and the lensing mass profile. This suggests that hydrostatic equilibrium is a good approximation for the outer region of the Coma cluster, given the error of the lensing measurement. The discrepancies in the inner region $r <$ 100 kpc are a known problem in the mass reconstruction and beyond the scope of the present paper: the validity of hydrostatic equilibrium in the inner region has been investigated by many authors (see, e.g., [66–68] and references therein) with no consensus found. Note, however, that the WL observations are not sensitive to the density profile in the inner region [30]. We, therefore, base our analysis on a simple extrapolation of the NFW profile. Recent lensing observations of the Coma cluster [69] support the validity of this assumption for 100 kpc $< r <$ 1 Mpc as well as indicate its limitation for $r <$ 100 kpc.

In order to estimate the influence of the non-thermal pressure on the mass profile, the blue and black dashed curves in figure 7 show the sum of the thermal mass profile $M_{\rm thermal}$ and the non-thermal mass component $M_{\rm non-thermal}$ determined by eq. (2.8). The blue dashed curve is obtained from the X-ray observations via eq. (2.27), whereas the black dashed curve is obtained from the combination of the SZ and X-ray observations from eq. (2.28). At $r = 1$ Mpc, the non-thermal pressure enhances the total hydrodynamical mass estimation by a few $\times 10\%$. This reflects the limited effect of the non-thermal pressure predicted by hydrodynamical simulations.

Finally, we include the chameleon field in our mass comparison. In figure 8, we show the thermal radial mass profile and the combination with the chameleon mass component $M_{\rm thermal}+M_\phi$ (red curves). The red solid and red dashed curve is obtained for $(\beta, \phi_\infty/M_{\rm Pl}) = (1, 1.5\times 10^{-4})$ and for $(1.2, 2\times 10^{-4})$, respectively. These two sets of parameters of the chameleon model illustrate typical scenarios where the chameleon force causes a possible discrepancy between the gas and the lensing masses. Note that these curves are determined from $M_{\rm thermal}$ and M_ϕ in eq. (2.20), where $M_{\rm thermal}$ is reconstructed from the observational data and M_ϕ is given by eq. (2.21), and, therefore, the slightly oscillatory feature of the $\beta = 1.2$ curve does not reflect any physically meaningful effect. The blue curve represents the case without the chameleon force, which is close to the red solid curve and the red dashed curve in the inner region, where the chameleon field is suppressed. Further out, the chameleon force reduces the hydrostatic mass $M_{\rm thermal} + M_\phi$ with respect to the mass obtained in Newtonian gravity because the chameleon force introduces an extra attractive

JCAP04(2014)013

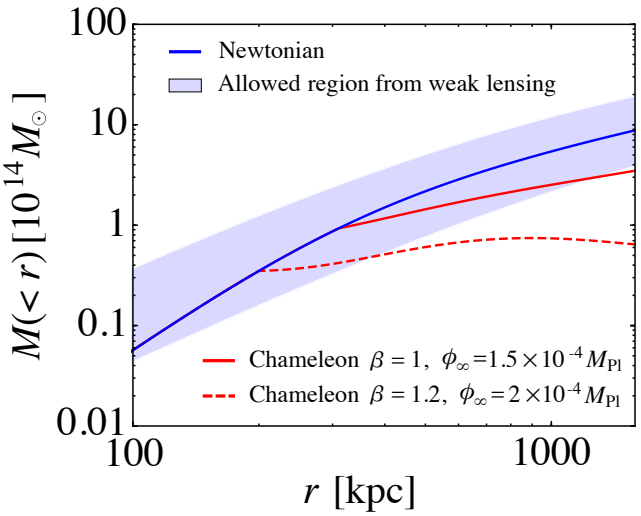

Figure 8. Same as figure 7 but in the presence of the chameleon field. The red solid and red dashed curves are the combination of the thermal mass and chameleon mass components, $M_{\rm thermal}+M_\phi$, when $(\beta, \phi_\infty/M_{\rm Pl}) = (1, 1.5\times10^{-4})$ and $(1.2, 2\times10^{-4})$, respectively.

force. As is clear from this figure, we can only put a constraint on the chameleon model that influences the gas distribution in the range $r \lesssim 1$ Mpc. The critical radius at which the chameleon force begins to contribute is determined by β/ϕ_∞ [see eq. (3.8)] and the amplitude of the chameleon force is determined by β (see section 2.2). Thus, these two parameters in the chameleon models are constrained by comparing the hydrostatic mass and lensing mass under the assumption of hydrostatic equilibrium.

3.2.2 Non-spherical symmetry

Next, let us consider systematic effects that can be introduced by deviations from spherical symmetry. Here, we assume that the three dimensional profile of the electron number density, temperature, and pressure are written as,

$$n_{\rm e}(r,\theta,\varphi) = \bar{n}_{\rm e}(r)[1+\delta_{n_{\rm e}}(r,\theta,\varphi)], \tag{3.13}$$
$$T_{\rm gas}(r,\theta,\varphi) = \bar{T}_{\rm gas}(r)[1+\delta_{T_{\rm gas}}(r,\theta,\varphi)], \tag{3.14}$$
$$P_{\rm e}(r,\theta,\varphi) = \bar{P}_{\rm e}(r)[1+\delta_{P_{\rm e}}(r,\theta,\varphi)], \tag{3.15}$$

where $\delta_{n_{\rm e}}, \delta_{T_{\rm gas}}$ and $\delta_{P_{\rm e}}$ describe deviation from the spherical symmetric profiles, $\bar{n}_{\rm e}(r)$, $\bar{T}_{\rm gas}(r)$, and $\bar{P}_{\rm e}(r)$, respectively.

The effect of the clumpiness on the electron number density can then be estimated as follows. Introducing an average over the spherical symmetric profiles, we assume $\langle\delta_{n_{\rm e}}\rangle = 0$ and $\langle\delta^2_{n_{\rm e}}\rangle \neq 0$. Assuming that the temperature perturbation is negligible, i.e., $\delta_{T_{\rm gas}} = 0$, the observed X-ray temperature profile is not changed. The SZ profile is not affected by clumping either because $\langle\delta_{P_{\rm e}}\rangle = \langle\delta_{n_{\rm e}}\rangle = 0$ from the equation of state. However, the surface brightness is increased by the clumpiness and can be rewritten as

$$S_{\rm X} \propto \int n_{\rm e}^2 dz = (1+\langle\delta^2_{n_{\rm e}}\rangle)\int \bar{n}_{\rm e}^2 dz, \tag{3.16}$$

JCAP04(2014)013

where $1+\langle\delta^2_{n_e}\rangle$ is referred to as the clumping factor. This affects the reconstruction of the electron number density. When the clumping factor is non-zero, $\bar{n}_e$ is replaced by $\bar{n}_e/\sqrt{1+\langle\delta^2_{n_e}\rangle}$. Then, the thermal mass profile reconstructed from observations of the SZ effect and X-ray surface brightness, eq. (2.25), is enhanced by a factor $\sqrt{1+\langle\delta^2_{n_e}\rangle}$. However, the thermal mass profile reconstructed from X-ray observations, eq. (2.24), is not affected by the clumpiness. In the case where $1+\langle\delta^2_{n_e}\rangle = 1.5$, which corresponds to the estimated clumping factor for the A1835 cluster [70], we have an enhancement of the hydrostatic mass by a factor ~ 1.2. Thus, systematics from the clumpiness could be of order a few $\times 10\%$.

Besides the clumpiness, large-scale spherical asymmetries of a cluster may cause an additional systematic bias. Three dimensional ellipticity as well as substructures of the Coma cluster have been studied in ref. [71]. They have reported an ellipticity of the electron density in the Coma cluster of $\epsilon = \sqrt{1-e^2} = 0.84$ with eccentricity e such that we can ignore the effect in our analysis. Nonetheless the assumption of spherical symmetry introduces systematics errors, which should be investigated in more quantitative detail in a future work.

4 Summary and conclusions

We have proposed a novel method to test gravity in the outskirts of galaxy clusters by comparing their hydrostatic and lensing mass estimates. The hydrostatic mass profile of a cluster can be inferred from the 3-dimensional gas temperature, electron number density, and electron pressure profiles from the projected observations of the X-ray surface brightness, the X-ray temperature, and the SZ CMB temperature profile, by implementing a parametric reconstruction method. The dark matter density profile can furthermore be constrained by WL observations. Here, we adopt the NFW density profile to describe the dark matter distribution within the cluster. In the case of hydrostatic equilibrium of the gas and standard gravity, the different mass estimates should agree. In the presence of a chameleon field, coupling to the matter fields and introducing an attractive fifth force, the relation between the mass estimated from the gas observations and from lensing changes, and can therefore be used as a test of gravity.

Combining measurements of the X-ray surface brightness, the X-ray temperature, the SZ effect, and lensing of the Coma cluster, we performed an MCMC analysis of the model parameter space, describing the cluster profiles and gravity theory, and have obtained competitive constraints on the chameleon gravity model parameters β and ϕ_∞, the coupling strength of the chameleon field and the field value in the environment of the cluster, which we approximate here by the cosmological background. Contrary to a previous study in [14] that constrains the modified gas distribution in the Hydra A cluster measured through the X-ray temperature, our new constraint does not rely on the assumption of a polytropic equation of state of the gas, employs a Bayesian statistical approach for inferring parameter constraints on the full set of model parameters, and yields a tighter bound on the modified gravity parameters than these previous results through the combination of the X-ray, SZ, and lensing observations available for the Coma cluster. We emphasise that our results provide a powerful constraint on $f(R)$ gravity models, corresponding to a particular choice of the chameleon coupling constant $\beta = \sqrt{1/6}$, for which we obtain an upper bound of $|f_{R0}| \lesssim 6\times 10^{-5}$ at the 95% CL. This bound is competitive with the current strongest cosmological constraints inferred on $f(R)$ gravity (see figure 1).

An important systematic that can affect our analysis can be introduced by deviations from hydrostatic equilibrium of the cluster gas. We have therefore carefully examined the

JCAP04(2014)013

validity of hydrostatic equilibrium in the Coma cluster. Assuming Newtonian gravity, we compare the different mass estimates from the three different gas observations and the WL mass. We find that the mass profiles from the gas and WL observations can deviate from each other by up to 50% but that they are consistent within the observational errors of the lensing measurement. We analyse the effect of including a non-thermal pressure component, with a radial profile calibrated to hydrodynamic simulations but with extremised amplitude. This contribution only marginally affects our reconstructed masses, and we conclude that hydrostatic equilibrium is a good approximation to describe the outer region of the Coma cluster. Note, however, that the effect from the chameleon force on the hydrostatic mass is opposite to the effect of the non-thermal pressure. Hence, the chameleon force can compensate for a large contribution from non-thermal pressure and cause a degeneracy between the two effects. On the other hand, the magnitude of the non-thermal pressure that would be required to compensate for the effects of the chameleon force tested here is not to be expected from current hydrodynamical simulations. It is, however, not clear whether the presence of a chameleon field could significantly enhance the non-thermal pressure contribution in the Coma cluster such that it could cancel the effects of the chameleon field, and act to alleviate the constraints on the modification of gravity. In this regard, it will be useful to analyse the non-thermal pressure of chameleon gravity models using hydrodynamical simulations along with a more detailed study of the Newtonian case. As for $f(R)$ gravity, such hydrodynamical simulations have recently been conducted by Arnold et al. [23]. They estimate the non-thermal pressure from the bulk motion in the intracluster medium and find that it only leads to substantial contributions in merging clusters, which can be identified and excluded to obtain statistical quantities like X-ray and SZ scaling relations. Their results suggest that the effects of non-thermal pressure in a relaxed cluster like Coma are not significant, at least in the case of the $f(R)$ gravity models.

Further effects which may cause deviations from the hydrostatic equilibrium have been discussed in [31, 38, 70]. Ref. [31] found that the mass estimated under the hydrostatic equilibrium assumption deviates from the true mass on average by $\sim (10-20)\%$ fractionally in a simulated halo due to gas acceleration. Given the large errors on the measurement of the lensing mass of the Coma cluster, we can ignore this deviation in our current analysis. Future measurements such as from the Astro-H X-ray observations will allow more precise modelling of the Coma cluster.

Our results demonstrate that galaxy clusters are useful probes of gravity. The method described in this paper may be applied to other clusters. However, one should be cautious about the individual properties of each cluster; the assumptions adopted in the present paper might not be guaranteed for other galaxy clusters and need to be considered for each case. The key is to understand the motion and distribution of the gas component in clusters; the combination of multi-wavelength observations, as demonstrated by the recent results by the *Planck* satellite [72–75], will provide a clue on how to solve this difficult issue. In the near future, we will have stacked lensing, SZ, and X-ray profiles for hundreds of clusters. The combination of multi-wavelength observations for many clusters will significantly improve the tests of gravitational interactions on cluster scales.

We thank Y. Fukazawa, Y. Suto, D. Suto, T. Kitayama, T. Kobayashi for support and useful discussions. We thank A. Vikhlinin and E. Churazov for providing the X-ray data used in this paper. LL and KK were supported by the European Research Council starting grant. LL acknowledges support from the STFC Consolidated Grant for Astronomy and Astrophysics at the University of Edinburgh. The research by KY is supported in part by

JCAP04(2014)013

Grant-in-Aid for Scientific researcher of Japanese Ministry of Education, Culture, Sports, Science and Technology (No. 21540270 and No. 21244033). DB, KK and BN are supported by STFC grants ST/K00090/1 and KK is also supported by STFC grant ST/L005573/1. KK thanks the Leverhulme trust for its support. KY thanks Prof. L. Amendola and the people at ITP of Heidelberg University for their hospitality during his stay. This work is supported by exchange visits between JSPS and DFG.

A Reconstruction of the 3-dimensional gas profiles

We summarise the reconstruction method for the 3-dimensional profiles of the gas density, temperature, and pressure, using observations of the X-ray temperature, surface brightness, and SZ effect used in section 3.1 to derive constraints on chameleon gravity from the Coma cluster. We begin with a short discussion on the quantities that are observed in the X-ray measurements and through the SZ effect.

From X-ray observations, one obtains the projected X-ray temperature profile

$$T_{\rm X}(r_\perp) = \frac{\int W\left(\sqrt{r_\perp^2+z^2}\right) T_{\rm gas}\left(\sqrt{r_\perp^2+z^2}\right) dz}{\int W\left(\sqrt{r_\perp^2+z^2}\right) dz}, \tag{A.1}$$

where $r_\perp$ is the radius perpendicular to the line of sight direction, and $W(r)$ is the weight factor, which may be written as $W(r) = n_{\rm e}^2(r)T_{\rm gas}^{1/2}(r)$ for the emission weighted temperature and as $W(r) = n_{\rm e}^2(r)T_{\rm gas}^{-3/4}(r)$ for the spectroscopic-like temperature [76]. Here, $n_{\rm e}(r)$ denotes the electron density profile. In this paper, we use the emission weighted temperature, but we checked that the 3-dimensional temperature and electron number density profiles do not depend on the choice between the two weightings.

The X-ray surface brightness is given by

$$S_{\rm X}(r_\perp) = \int n_{\rm e}^2\left(\sqrt{r_\perp^2+z^2}\right) \lambda_{\rm c}\left(T_{\rm gas}\right) dz, \tag{A.2}$$

where $\lambda_{\rm c}(T_{\rm gas})$ is the cooling function. To estimate the cooling function, we used XSPEC [77] adopting the thermal plasma emission spectra model with the APEC code [78]. The XSPEC software gives the X-ray flux based on the APEC model corresponding to the observational band from 0.5keV to 2.5keV [26]. The X-ray flux can be converted to the cooling function by the flux-luminosity relation. The metal abundance in the innermost region of the cluster is larger than in the outer region, $Z = 0.4Z_\odot$ [38] and $Z = 0.3Z_\odot$ [79], respectively. However, as the difference is small and does not affect our constraints, we adopt a metal abundance of $Z = 0.3Z_\odot$ throughout the cluster.

Photons from the CMB passing through clusters are scattered by the hot gas, and this distorts the CMB spectrum as a function of frequency. This SZ effect yields a contribution to the CMB temperature of

$$\Delta T_{\rm SZ}(r_\perp) = -2T_{\rm CMB}\frac{\sigma_{\rm T}}{m_{\rm e}}\int P_{\rm e}\left(\sqrt{r_\perp^2+z^2}\right) dz, \tag{A.3}$$

where $T_{\rm CMB} = 2.725K$ is the CMB temperature, $\sigma_{\rm T}$ is the Thomson cross section, $m_{\rm e}$ is the electron mass, and $P_{\rm e}(r)$ is the electron pressure.

JCAP04(2014)013

Having summarised the quantities observed in the X-ray and SZ measurements, we now use them to reconstruct the 3-dimensional gas density, temperature, and pressure profiles. For this purpose, we adopt the following fitting functions for the 3-dimensional profiles of $T_{\rm gas}(r)$, $n_{\rm e}(r)$, and $P_{\rm e}(r)$. For $T_{\rm gas}(r)$, we use the fitting formula calibrated to numerical simulations [80]

$$T_{\rm gas}(r) = T_0 \left[1 + A\left(\frac{r}{r_0}\right)\right]^{b_0}, \tag{A.4}$$

where T_0, A, r_0, and b_0 are free parameters. For the electron number density, we assume a simple isothermal β model [81]

$$n_{\rm e}(r) = n_0 \left[1 + \left(\frac{r}{r_1}\right)^2\right]^{b_1}, \tag{A.5}$$

where the free parameters are n_0, r_1, and b_1. Finally, we adopt the generalised NFW profile for the pressure proposed by [82],

$$P_{\rm e}(r) = \frac{P_0}{(r/r_2)^{b_2}(1 + (r/r_2)^{b_3})^{b_4}}, \tag{A.6}$$

for the 3-dimensional electron pressure profile with the fitting parameters P_0, r_2, b_3, and b_4.

We compute the projected profiles in eqs. (A.1), (A.2), and (A.3) with the fitting functions of eqs. (A.4), (A.5), and (A.6), and determine the best fit parameters T_0, A, r_0, b_0, n_0, r_1, b_1, P_0, r_2, b_2, b_3 and b_4 by comparing the profiles with the observations from the X-ray temperature, X-ray surface brightness, and SZ effect of the Coma cluster in section 3.2.1. In this way, we obtain the reconstructed 3-dimensional gas density, temperature, and pressure profiles of the cluster.

Note that since we assume the hydrostatic equilibrium eq. (2.29) in the MCMC analysis in section 3.1, we only need to define two of these profiles, of which one can also be the matter density profile and from which the other profiles can be derived, however, not necessarily reproducing the exact analytic expressions of the fitting functions. In section 3.1, we choose to work with the electron number density eq. (A.5) and the NFW profile eq. (2.11). The choice of the NFW profile simplifes the computation of the chameleon force and allows the use of the analytic approximation derived in section 2.2. Hence, the degrees of freedom reduce to T_0, n_0, r_1, b_1, including the NFW parameters $M_{\rm vir}$ and c as well as the chameleon model parameters β and ϕ_∞ (or β_2 and $\phi_{\infty,2}$), where T_0 is required to set the integration constant in eq. (3.2). This approach yields reasonable reduced χ^2 values when fitted to the observational data in section 3.1.2.

References

[1] T. Clifton, P.G. Ferreira, A. Padilla and C. Skordis, *Modified Gravity and Cosmology*, *Phys. Rept.* **513** (2012) 1 [arXiv:1106.2476] [INSPIRE].

[2] B. Jain, A. Joyce, R. Thompson, A. Upadhye, J. Battat et al., *Novel Probes of Gravity and Dark Energy*, [arXiv:1309.5389] [INSPIRE].

[3] J. Khoury and A. Weltman, *Chameleon cosmology*, *Phys. Rev.* **D 69** (2004) 044026 [astro-ph/0309411] [INSPIRE].

JCAP04(2014)013

[4] D.F. Mota and J.D. Barrow, *Varying alpha in a more realistic Universe*, *Phys. Lett.* **B 581** (2004) 141 [astro-ph/0306047] [INSPIRE].

[5] J. Wang, L. Hui and J. Khoury, *No-Go Theorems for Generalized Chameleon Field Theories*, *Phys. Rev. Lett.* **109** (2012) 241301 [arXiv:1208.4612] [INSPIRE].

[6] F. Schmidt, A. Vikhlinin and W. Hu, *Cluster Constraints on f(R) Gravity*, *Phys. Rev.* **D 80** (2009) 083505 [arXiv:0908.2457] [INSPIRE].

[7] F. Schmidt, *Dynamical Masses in Modified Gravity*, *Phys. Rev.* **D 81** (2010) 103002 [arXiv:1003.0409] [INSPIRE].

[8] G.B. Zhao, B. Li and K. Koyama, *Testing gravity using the environmental dependence of dark matter halos*, *Phys. Rev. Lett.* **107** (2011) 071303 [arXiv:1105.0922].

[9] L. Lombriser, F. Schmidt, T. Baldauf, R. Mandelbaum, U. Seljak et al., *Cluster Density Profiles as a Test of Modified Gravity*, *Phys. Rev.* **D 85** (2012) 102001 [arXiv:1111.2020] [INSPIRE].

[10] L. Lombriser, K. Koyama, G.-B. Zhao and B. Li, *Chameleon f(R) gravity in the virialized cluster*, *Phys. Rev.* **D 85** (2012) 124054 [arXiv:1203.5125] [INSPIRE].

[11] T.Y. Lam, T. Nishimichi, F. Schmidt and M. Takada, *Testing Gravity with the Stacked Phase Space around Galaxy Clusters*, *Phys. Rev. Lett.* **109** (2012) 051301 [arXiv:1202.4501] [INSPIRE].

[12] T. Narikawa, R. Kimura, T. Yano and K. Yamamoto, *Halo models in modified gravity theories with self-accelerated expansion*, *Int. J. Mod. Phys.* **D 20** (2011) 2383 [arXiv:1108.2346] [INSPIRE].

[13] T. Narikawa and K. Yamamoto, *Testing gravity with halo density profiles observed through gravitational lensing*, *JCAP* **05** (2012) 016 [arXiv:1201.4037] [INSPIRE].

[14] A. Terukina and K. Yamamoto, *Gas density profile in dark matter halo in chameleon cosmology*, *Phys. Rev.* **D 86** (2012) 103503 [arXiv:1203.6163] [INSPIRE].

[15] C. Llinares and D.F. Mota, *Shape of Clusters of Galaxies as a Probe of Screening Mechanisms in Modified Gravity*, *Phys. Rev. Lett.* **110** (2013) 151104 [arXiv:1205.5775] [INSPIRE].

[16] T. Narikawa, T. Kobayashi, D. Yamauchi and R. Saito, *Testing general scalar-tensor gravity and massive gravity with cluster lensing*, *Phys. Rev.* **D 87** (2013) 124006 [arXiv:1302.2311] [INSPIRE].

[17] P. Burikham and S. Panpanich, *Effects of Chameleon Scalar Field on Rotation Curves of the Galaxies*, *Int. J. Mod. Phys. D* **21** (2012) 50041 [arXiv:1103.1198].

[18] R. Pourhasan, N. Afshordi, R.B. Mann and A.C. Davis, *Chameleon gravity, electrostatics, and kinematics in the outer galaxy*, *JCAP* **12** (2011) 005 [arXiv:1109.0538].

[19] A.A. Starobinsky, *Disappearing cosmological constant in f(R) gravity*, *JETP Lett.* **86** (2007) 157 [arXiv:0706.2041] [INSPIRE].

[20] W. Hu and I. Sawicki, *Models of f(R) cosmic acceleration that evade solar system tests*, *Phys. Rev.* **D 76** (2007) 064004.

[21] S. Tsujikawa, *Observational signatures of f(R) dark energy models that satisfy cosmological and local gravity constraints*, *Phys. Rev.* **D 77** (2008) 023507.

[22] P. Brax, C. van de Bruck, A.C. Davis and D.J. Shaw, *f(R) gravity and chameleon theories*, *Phys. Rev.* **D 78** (2008) 104021.

[23] Heidelberg Institute for Theoretical Studies collaboration, C. Arnold, E. Puchwein and V. Springel, *Scaling relations and mass bias in hydrodynamical f(R) gravity simulations of galaxy clusters*, [arXiv:1311.5560] [INSPIRE].

JCAP04(2014)013

[24] R.A. Sunyaev and Y. Zeldovich, *Small scale fluctuations of relic radiation*, *Astrophys. Space Sci.* **7** (1970) 3 [INSPIRE].

[25] PLANCK collaboration, P.A.R. Ade et al., *Planck Intermediate Results. X. Physics of the hot gas in the Coma cluster*, [arXiv:1208.3611] [INSPIRE].

[26] E. Churazov, A. Vikhlinin, I. Zhuravleva, A. Schekochihin, I. Parrish et al., *X-Ray surface brightness and gas density fluctuations in the Coma cluster*, *Mon. Not. Roy. Astron. Soc.* **421** (2012) 1123 [arXiv:1110.5875] [INSPIRE].

[27] S.L. Snowden, R.F. Mushotzky, K.D. Kuntz and D.S. Davis, *A catalog of galaxy clusters observed by XMM-Newton*, *Astron. Astrophys.* **478** (2008) 615.

[28] D.R. Wik, C.L. Sarazin, A. Finoguenov, K. Matsushita, K. Nakazawa et al., *A Suzaku Search for Non-thermal Emission at Hard X-ray Energies in the Coma Cluster*, *Astrophys. J.* **696** (2009) 1700 [arXiv:0902.3658] [INSPIRE].

[29] R. Gavazzi et al., *A weak lensing study of the Coma cluster*, *Astron. Astrophys.* **498** (2009) L33.

[30] N. Okabe, Y. Okura and T. Futamase, *Weak Lensing Mass Measurements of Substructures in COMA Cluster with Subaru/Suprime-Cam*, *Astrophys. J.* **713** (2010) 291 [arXiv:1001.2402] [INSPIRE].

[31] D. Suto, H. Kawahara, T. Kitayama, S. Sasaki, Y. Suto et al., *Validity of Hydrostatic Equilibrium in Galaxy Clusters from Cosmological Hydrodynamical Simulations*, *Astrophys. J.* **767** (2013) 79 [arXiv:1302.5172] [INSPIRE].

[32] L. Lombriser, K. Koyama and B. Li, *Halo modelling in chameleon theories*, *JCAP* **03** (2014) 021 [arXiv:1312.1292] [INSPIRE].

[33] B. Jain, V. Vikram and J. Sakstein, *Astrophysical Tests of Modified Gravity: Constraints from Distance Indicators in the Nearby Universe*, *Astrophys. J.* **779** (2013) 39 [arXiv:1204.6044] [INSPIRE].

[34] B. Hu, M. Liguori, N. Bartolo and S. Matarrese, *Parametrized modified gravity constraints after Planck*, *Phys. Rev.* **D 88** (2013) 123514 [arXiv:1307.5276] [INSPIRE].

[35] A. Marchini and V. Salvatelli, *Updated constraints from the PLANCK experiment on modified gravity*, *Phys. Rev.* **D 88** (2013) 027502 [arXiv:1307.2002] [INSPIRE].

[36] L. Lombriser, A. Slosar, U. Seljak and W. Hu, *Constraints on f(R) gravity from probing the large-scale structure*, *Phys. Rev.* **D 85** (2012) 124038 [arXiv:1003.3009] [INSPIRE].

[37] B. Jain et al., *Novel Probes of Gravity and Dark Energy*, FERMILAB-PUB-13-443-A (2013) [arXiv:1309.5389].

[38] R. Fusco-Femiano, A. Lapi and A. Cavaliere, *The Planck Sunyaev-Zel'dovich vs. the X-ray View of the Coma Cluster*, *Astrophys. J.* **763** (2013) L3 [arXiv:1212.3082] [INSPIRE].

[39] A. Cavaliere, A. Lapi and R. Fusco-Femiano, *Galaxy Clusters, a Novel Look at Diffuse Baryons Withstanding Dark Matter Gravity*, *Astrophys. J.* **698** (2009) 580 [arXiv:0903.5224] [INSPIRE].

[40] N. Battaglia, J.R. Bond, C. Pfrommer and J.L. Sievers, *On the Cluster Physics of Sunyaev-Zel'dovich Surveys I: The Influence of Feedback, Non-thermal Pressure and Cluster Shapes on Y-M Scaling Relations*, *Astrophys. J.* **758** (2012) 74 [arXiv:1109.3709] [INSPIRE].

[41] L.D. Shaw, D. Nagai, S. Bhattacharya and E.T. Lau, *Impact of Cluster Physics on the Sunyaev-Zel'dovich Power Spectrum*, *Astrophys. J.* **725** (2010) 1452 [arXiv:1006.1945] [INSPIRE].

[42] B. Li and J.D. Barrow, *N-Body Simulations for Coupled Scalar Field Cosmology*, *Phys. Rev.* **D 83** (2011) 024007 [arXiv:1005.4231] [INSPIRE].

JCAP04(2014)013

[43] B. Li and J.D. Barrow, *On the Effects of Coupled Scalar Fields on Structure Formation*, *Mon. Not. Roy. Astron. Soc.* **413** (2011) 262 [arXiv:1010.3748] [INSPIRE].

[44] J.F. Navarro, C.S. Frenk and S.D.M. White, *A Universal Density Profile from Hierarchical Clustering*, *Astrophys. J.* **490** (1997) 493.

[45] K. Umetsu, T. Broadhurst, A. Zitrin, E. Medezinski, D. Coe et al., *A Precise Cluster Mass Profile Averaged from the Highest-Quality Lensing Data*, *Astrophys. J.* **738** (2011) 41 [arXiv:1105.0444] [INSPIRE].

[46] M. Oguri, M.B. Bayliss, H. Dahle, K. Sharon, M.D. Gladders et al., *Combined strong and weak lensing analysis of 28 clusters from the Sloan Giant Arcs Survey*, *Mon. Not. Roy. Astron. Soc.* **420** (2012) 3213 [arXiv:1109.2594] [INSPIRE].

[47] T.T. Nakamura and Y. Suto, *Strong gravitational lensing and velocity function as tools to probe cosmological parameters: Current constraints and future predictions*, *Prog. Theor. Phys.* **97** (1997) 49 [astro-ph/9612074] [INSPIRE].

[48] F. Schmidt, M.V. Lima, H. Oyaizu and W. Hu, *Non-linear Evolution of f(R) Cosmologies III: Halo Statistics*, *Phys. Rev.* **D 79** (2009) 083518 [arXiv:0812.0545] [INSPIRE].

[49] T.H. Reiprich, K. Basu, S. Ettori, H. Israel, L. Lovisari et al., *Outskirts of Galaxy Clusters*, *Space Sci. Rev.* **177** (2013) 195 [arXiv:1303.3286] [INSPIRE].

[50] VERITAS collaboration, T. Arlen et al., *Constraints on Cosmic Rays, Magnetic Fields and Dark Matter from Gamma-Ray Observations of the Coma Cluster of Galaxies with VERITAS and Fermi*, *Astrophys. J.* **757** (2012) 123 [arXiv:1208.0676] [INSPIRE].

[51] P. Sreekumar et al., *EGRET Observations of the North Galactic Pole Region*, *Astrophys. J.* **464** (1996) 628.

[52] O. Reimer, M. Pohl, P. Sreekumar and J.R. Mattox, *Egret upper limits on the high-energy gamma-ray emission of galaxy clusters*, *Astrophys. J.* **588** (2003) 155 [astro-ph/0301362] [INSPIRE].

[53] FERMI-LAT collaboration, M. Ackermann et al., *GeV Gamma-ray Flux Upper Limits from Clusters of Galaxies*, *Astrophys. J. Lett.* **717** (2010) L71.

[54] K.A. Pimbblet, S.J. Penny and R.L. Davies, *How typical is the Coma cluster?*, *Mon. Not. Roy. Astron. Soc.* **438** (2014) 3049 [arXiv:1312.3698] [INSPIRE].

[55] Y.-Y. Zhang et al., *HIFLUGCS: Galaxy cluster scaling relations between X-ray luminosity, gas mass, cluster radius, and velocity dispersion*, *Astron. Astrophys.* **526** (2011) A105.

[56] PLANCK collaboration, P.A.R. Ade et al., *Planck early results. VIII. The all-sky early Sunyaev-Zeldovich cluster sample*, *Astron. Astrophys.* **536** (2011) A8.

[57] A. Lewis and S. Bridle, *Cosmological parameters from CMB and other data: A Monte Carlo approach*, *Phys. Rev.* **D 66** (2002) 103511.

[58] N. Metropolis, A.W. Rosenbluth, M.N. Rosenbluth, A.H. Teller and E. Teller, *Equation of state calculations by fast computing machines*, *J. Chem. Phys.* **21** (1953) 1087 [INSPIRE].

[59] W.K. Hastings, *Monte Carlo sampling methods using Markov chains and their applications*, *Biometrika* **57** (1970) 97.

[60] A. Gelman and D.B. Rubin, *Inference from Iterative Simulation Using Multiple Sequences*, *Statist. Sci.* **7** (1992) 457.

[61] S.A. Gregory and L.A. Thompson, *The Coma/A1367 supercluster and its environs*, *Astrophys. J.* **222** (1978) 784.

[62] M.J. West, *The coma cluster in relation to its environs*, Proceedings of the Rencontres Astrophysiques meeting *A New Vision of an Old Cluster: Untangling Coma Berenices* held in Marseille (France), eds. F. Durret et al. (1997) 36, [astro-ph/9709289] [INSPIRE].

JCAP04(2014)013

[63] K. Rines, M.J. Geller, M.J. Kurtz, A. Diaferio, T.H. Jarrett et al., *Infrared mass-to-light profile throughout the infall region of the coma cluster*, *Astrophys. J.* **561** (2001) L41 [astro-ph/0109425] [INSPIRE].

[64] L. Lombriser, B. Li, K. Koyama and G.-B. Zhao, *Modeling halo mass functions in chameleon f(R) gravity*, *Phys. Rev.* **D 87** (2013) 123511 [arXiv:1304.6395] [INSPIRE].

[65] K. Yamamoto et al. , *Constraint on the cosmological f(R) model from the multipole power spectrum of the SDSS luminous red galaxy sample and prospects for a future redshift survey*, *Phys. Rev.* **D 81** (2010) 103517.

[66] A.C. Fabian, *Cooling flows in clusters of galaxies*, *Ann. Rev. Astron. Astrophys.* **32** (1994) 277 [INSPIRE].

[67] J.R. Peterson and A.C. Fabian, *X-ray spectroscopy of cooling clusters*, *Phys. Rept.* **427** (2006) 1 [astro-ph/0512549] [INSPIRE].

[68] Y. Fujita and Y. Ohira, *Stable Heating of Cluster Cooling Flows by Cosmic-Ray Streaming*, *Astrophys. J.* **738** (2011) 182 [arXiv:1106.5790] [INSPIRE].

[69] N. Okabe, T. Futamase, M. Kajisawa and R. Kuroshima, *Subaru Weak-lensing Survey of Dark Matter Subhalos in the Coma Cluster: Subhalo Mass Function and Statistical Properties*, *Astrophys. J.* **784** (2014) 90 [arXiv:1304.2399] [INSPIRE].

[70] A. Morandi, D. Nagai and W. Cui, *Non-parametric method for measuring gas inhomogeneities from X-ray observations of galaxy clusters*, *Mon. Not. Roy. Astron. Soc.* **436** (2013) 1123 [arXiv:1305.5256] [INSPIRE].

[71] F. Andrade-Santos, P.E.J. Nulsen, R.P. Kraft, W.R. Forman, C. Jones et al., *Dark Matter Subhalos and the X-ray Morphology of the Coma Cluster*, *Astrophys. J.* **766** (2013) 107 [arXiv:1302.1917] [INSPIRE].

[72] PLANCK collaboration, P.A.R. Ade et al., *Planck 2013 results. I. Overview of products and scientific results*, [arXiv:1303.5062] [INSPIRE].

[73] PLANCK collaboration, P.A.R. Ade et al., *Planck intermediate results. III. The relation between galaxy cluster mass and Sunyaev-Zeldovich signal*, *Astron. Astrophys.* **550** A129-1 (2013) [arXiv:1204.2743].

[74] PLANCK collaboration, P.A.R. Ade et al., *Planck intermediate results. V. Pressure profiles of galaxy clusters from the Sunyaev-Zeldovich effect*, *Astron. Astrophys.* **554** A131-1 (2013) [arXiv:1207.4061].

[75] PLANCK collaboration, P.A.R. Ade et al., *Planck 2013 results. XX. Cosmology from Sunyaev-Zeldovich cluster counts*, [arXiv:1303.5080] [INSPIRE].

[76] P. Mazzotta, E. Rasia, L. Moscardini and G. Tormen, *Comparing the temperatures of galaxy clusters from hydrodynamical N-body simulations to Chandra and XMM-Newton observations*, *Mon. Not. Roy. Astron. Soc.* **354** (2004) 10.

[77] K.A. Arnaud, *XSPEC: The First Ten Years* Astronomical Data Analysis Software and Systems V, eds. G. Jacoby and J. Barnes, ASP Conf. Series volume **101** (1996) 17 [http://heasarc.gsfc.nasa.gov/docs/xanadu/xspec/index.html].

[78] R.K. Smith, N.S. Brickhouse, D.A. Liedahl and J.C. Raymond, *Collisional plasma models with APEC/APED: Emission line diagnostics of hydrogen-like and helium-like ions*, *Astrophys. J.* **556** (2001) L91 [astro-ph/0106478] [INSPIRE].

[79] T. Sato, K. Matsushita, N. Ota, K. Sato, K. Nakazawa et al., *Suzaku Observations of Iron K-lines from the Intracluster Medium of the Coma Cluster*, *Publ. Astron. Soc. Jpn.* **63** (2011) 991 [arXiv:1109.0154] [INSPIRE].

JCAP04(2014)013

[80] J.O. Burns, S.W. Skillman and B.W. O'Shea, *Galaxy Clusters at the Edge: Temperature, Entropy and Gas Dynamics at the Virial Radius*, *Astrophys. J.* **721** (2010) 1105 [arXiv:1004.3553] [INSPIRE].

[81] A. Cavaliere and R. Fusco-Femiano, *X-rays from hot plasma in clusters of galaxies*, *Astron. Astrophys.* **49** (1976) 137 [INSPIRE].

[82] D. Nagai, A.V. Kravtsov and A. Vikhlinin, *Effects of Galaxy Formation on Thermodynamics of the Intracluster Medium*, *Astrophys. J.* **668** (2007) 1 [astro-ph/0703661] [INSPIRE].

JCAP04(2014)013

Journal of Cosmology and Astroparticle Physics
An IOP and SISSA journal

Testing a generalized cubic Galileon gravity model with the Coma Cluster

Ayumu Terukina,[a] **Kazuhiro Yamamoto,**[a,b] **Nobuhiro Okabe,**[a,b] **Kyoko Matsushita**[c] **and Toru Sasaki**[c]

[a]Department of Physical Sciences, Hiroshima University,
1-3-1 Kagamiyama, Higashi-Hiroshima, Hiroshima 739-8526, Japan
[b]Hiroshima Astrophysical Science Center, Hiroshima University,
1-3-1 Kagamiyama, Higashi-Hiroshima, Hiroshima 739-8526, Japan
[c]Department of Physics, Tokyo University of Science,
1-3 Kagurazaka, Shinjuku-ku, Tokyo 162-8601, Japan

E-mail: telkina@theo.phys.sci.hiroshima-u.ac.jp, kazuhiro@hiroshima-u.ac.jp, okabe@hiroshima-u.ac.jp, matusita@rs.kagu.tus.ac.jp, j1213703@ed.tus.ac.jp

Received May 15, 2015
Revised August 10, 2015
Accepted September 29, 2015
Published October 29, 2015

Abstract. We obtain a constraint on the parameters of a generalized cubic Galileon gravity model exhibiting the Vainshtein mechanism by using multi-wavelength observations of the Coma Cluster. The generalized cubic Galileon model is characterized by three parameters of the turning scale associated with the Vainshtein mechanism, and the amplitude of modifying a gravitational potential and a lensing potential. X-ray and Sunyaev-Zel'dovich (SZ) observations of the intra-cluster medium are sensitive to the gravitational potential, while the weak-lensing (WL) measurement is specified by the lensing potential. A joint fit of a complementary multi-wavelength dataset of X-ray, SZ and WL measurements enables us to simultaneously constrain these three parameters of the generalized cubic Galileon model for the first time. We also find a degeneracy between the cluster mass parameters and the gravitational modification parameters, which is influential in the limit of the weak screening of the fifth force.

Keywords: modified gravity, galaxy clusters

ArXiv ePrint: 1505.03692

© 2015 IOP Publishing Ltd and Sissa Medialab srl
doi:10.1088/1475-7516/2015/10/064

JCAP10(2015)064

Contents

JCAP10(2015)064

1 Introduction

Modifications of gravity theory is an interesting approach to explaining the accelerated expansion of the universe. However, any covariant modification of general relativity introduces additional degrees of freedom, giving rise to a fifth force. This is strictly constrained by gravity tests in the solar system. Solar system experiments [1, 2] are in excellent agreement with general relativity, requiring that this additional degree of freedom be hidden on the scale of the solar system. Such a process is referred to as a "screening mechanism," which is key for a viable modified gravity model. In general, this screening mechanism works in high-density regions where the matter density contrast is nonlinear. However, this does not work on large cosmological scales. A screening mechanism that characterizes viable modified gravity models is an important feature to be tested with observations.

The chameleon mechanism [3, 4] is a screening mechanism that works in an $f(R)$ gravity model and the chameleon gravity model [5–7]. In these models, a scalar degree of freedom that gives rise to the fifth force is screened in a high-density region due to coupling with matter. The chameleon gravity model and an $f(R)$ model can be viable owing to the chameleon mechanism [8]. The Vainshtein mechanism [9] is another relevant screening mechanism, which is exhibited in the Dvali-Gabadaze-Porrati (DGP) model [10, 11], the simplest cubic Galileon model ([12–15], see also the appendix), and its generalized version [16, 17]. The DGP model is an archetypal modified gravity model developed in the context of the brane-world scenario. There are two branches of solutions in the DGP model. The self-acceleration branch DGP (sDGP) model [18–20] includes a mechanism to explain self-acceleration in the late universe, while the normal branch DGP (nDGP) model [21–23] with a cosmological constant is a healthy modified gravity model avoiding the ghost problem [24, 25]. The simplest cubic Galileon model is also a typical modified gravity model that explains self-acceleration of the universe while avoiding the ghost problem. Our generalized cubic Galileon model is a generalized version of the simplest cubic Galileon model that retains important features and

contains the DGP models. In these models, a scalar field giving rise to a fifth force is screened due to self-interaction on small scales where density perturbations become nonlinear.

Galaxy clusters provide a unique laboratory for testing modified gravity models exhibiting screening mechanisms, because they are objects on the borderline between linear and nonlinear scales, that is, between non-screened and screened scales. The authors of [26–28] have investigated a cosmological constraint on the chameleon gravity model using galaxy clusters. They put a constraint on the turning scale and the amplitude of the fifth force at large scales. The authors of [29, 30] have investigated a constraint on a generalized Galileon model exhibiting the Vainshtein mechanism, using an observed weak-lensing profile of clusters. They put a constraint on the turning scale and the amplitude of modification of the lensing potential.

The purpose of the present paper is twofold. One purpose is a generalization of the methodology for testing a modified gravity model with a galaxy cluster. In the present paper, we consider a generalized cubic Galileon model. Within the quasi-static approximation, the generalized cubic Galileon model is effectively characterized by three parameters, $\mu_{\rm G}$, $\mu_{\rm L}$ and ϵ. Detailed definitions are given later, but, broadly, $\mu_{\rm G}$ and $\mu_{\rm L}$ are parameters that modify the effective amplitude of the gravitational potential and the lensing potential in the non-screened region, while ϵ determines the turning scale from the non-screened region to the screened region due to the Vainshtein mechanism. The parameters $\mu_{\rm G}$ are constrained by observations of the gas distribution, in particular an X-ray surface brightness profile and the SZ effect [31]. However, the parameter $\mu_{\rm L}$ is only constrained by observations of lensing measurements. Therefore, a combination of observations of gas distribution and the lensing signal is essential to put a constraint on the three parameters characterizing the modified gravity model. We demonstrate how a combination of multi-wavelength observations of a cluster is useful to put a constraint on a generalized Galileon model.

The other purpose is improvement of the analysis in [27] using new X-ray data [32, 33] and lensing [34] observations of the Coma Cluster. In our method of testing gravity with a galaxy cluster, the modeling of the gas distribution is important. A basic assumption of the model for the gas distribution is hydrostatic equilibrium, that is, a balance between the gas pressure gradient force and the gravitational force. In the region where the fifth force is influential, the condition of the hydrostatic equilibrium is changed, and the gas density profile is modified. However, in general, galaxy clusters are dynamically evolving, and a deviation from the equilibrium could be influential. Therefore, we first check the consistency of our model by comparing theoretical predictions with various observations of the Coma Cluster, including the new X-ray data and lensing measurements.

This paper is organized as follows: in section 2, we first review our model for the dark matter and gas distribution of a galaxy cluster within Newtonian gravity. We demonstrate how well our model fits observations of the Coma Cluster in section 3. We also validate our model against the influence of non-thermal pressure. In section 4, we introduce a generalized cubic Galileon model, and explain the modification of our model by the fifth force of the scalar field. In section 5, we discuss degeneracies on parameters and systematic errors focusing on special circumstance of using the Coma Cluster. Section 6 is devoted to a summary and conclusions. Throughout this paper, we adopt $\Omega_{\rm m0} = 0.3$, $\Omega_\Lambda = 0.7$ and $H_0 = 70$km/s/Mpc, and we follow the convention $(-,+,+,+)$.

2 Modeling of cluster profiles

We review our model for the dark matter and gas density distribution connecting with observational quantities, X-ray brightness, the SZ effect temperature profile, and the weak-lensing profile (see also [27, 29]). Our model is based on an assumption of hydrostatic equilibrium,

JCAP10(2015)064

but we also take the possible influence of non-thermal pressure into account. In this section, we first consider the case of Newtonian gravity.

2.1 Mass profile

We employ a universal mass density profile, namely the Navarro-Frenk-White (NFW) profile [35], motivated by predictions of numerical simulations,

$$\rho(r) = \frac{\rho_{\rm s}}{r/r_{\rm s}(1+r/r_{\rm s})^2}, \tag{2.1}$$

where $\rho_{\rm s}$ and $r_{\rm s}$ are the normalization and the scale radius, respectively. The mass within the radius r is given by $M(<r) = 4\pi\int_0^r dr r^2\rho(r) = 4\pi\rho_{\rm s}r_{\rm s}^3 m(r)$, with $m(r) = \ln(1+r/r_{\rm s}) - r/r_{\rm s}/(1+r/r_{\rm s})$. We introduce the concentration parameter c and the virial mass $M_{\rm vir}$ instead of $\rho_{\rm s}$ and $r_{\rm s}$,

$$c = \frac{r_{\rm vir}}{r_{\rm s}}, \tag{2.2}$$

$$M_{\rm vir} \equiv M(<r_{\rm vir}) = \frac{4\pi}{3}r_{\rm vir}^3\Delta_{\rm c}\rho_{\rm c}(z) \tag{2.3}$$

with the virial radius $r_{\rm vir}$. Here, $\rho_{\rm c}$ is the critical density at the redshift z, and $\Delta_{\rm c} = 100$ is the overdensity contrast determined by the spherical collapse model [36].

2.2 Gas profile with hydrostatic equilibrium

We first assume hydrostatic equilibrium between the gas pressure gradient and the gravitational force in galaxy clusters as

$$\frac{1}{\rho_{\rm gas}}\frac{dP_{\rm tot}}{dr} = -\frac{d\Psi}{dr}, \tag{2.4}$$

where $\rho_{\rm gas}$ is the gas density, $P_{\rm tot} = P_{\rm th} + P_{\rm nth}$ is the sum of the thermal pressure, $P_{\rm th}$ and the non-thermal pressure, $P_{\rm nth}$ (see below for details), and Ψ is the gravitational potential. We employ three assumptions to describe the gas physics. First, the equation of state for the gas components, $P_{\rm th} = n_{\rm gas}kT_{\rm gas}$, where $n_{\rm gas}$ and $T_{\rm gas}$ are the number density and the temperature of the total gas component, respectively. Second, the temperature of electrons is the same as that of the gas, $T_{\rm e} = T_{\rm gas}$. Third, the electron pressure satisfies $P_{\rm e} = n_{\rm e}kT_{\rm gas}$ with the electron number density $n_{\rm e} = (2+\mu)n_{\rm gas}/5$, where $\mu = 0.59$ is the mean molecular weight. In the present paper, for the electron temperature we assume the functional form

$$T_{\rm e}(r) = T_0\left[1+\left(\frac{r}{r_1}\right)^{b_1}\right]^{-b_2/b_1}, \tag{2.5}$$

where T_0, b_1, b_2 and r_1 are parameters. Integrating (2.4) with (2.5), we obtain the electron pressure profile

$$P_{\rm e}(r) = n_0T_0\exp\left(\int_0^r dr\frac{\mu m_{\rm p}}{kT_{\rm e}(r)}\left[-\frac{GM(<r)}{r^2}\right]\right), \tag{2.6}$$

and the electron number density $n_{\rm e}(r) = P_{\rm e}(r)/kT_{\rm e}(r)$, where n_0 is the normalization parameter of the electron number density, $n_{\rm e}$. In deriving equation (2.6), we use the relation, $\rho_{\rm gas} = \mu m_{\rm p}n_{\rm gas}$, where $m_{\rm p}$ is the proton mass. Equation (2.6) is the case of the absence of non-thermal pressure; the case including non-thermal pressure is described below.

JCAP10(2015)064

Thus our gas distribution model includes 7 parameters ($M_{\rm vir}$,c,n_0,T_0,b_1,b_2,r_1). Using our model of the three-dimensional profiles, we construct the observables for the observations of X-ray and the cosmic microwave background (CMB) temperature distortion. The X-ray emission from clusters are dominated by the bremsstrahlung and line emission caused by the ionized gas. For the X-ray observable, we define the X-ray brightness as $B_{\rm X} \equiv norm/area$, where *norm* is the spectrum normalization obtained from XSPEC software [37, 38] adopting the APEC emission spectrum [39], and *area* is the area of the spectrum. The spectrum normalization is given by $norm \propto \int n_{\rm e} n_{\rm H} dV$, where $n_{\rm H} = 0.86 n_{\rm e}$ is the hydrogen number density and V is the volume of the spectrum. Then, we write the X-ray brightness as

$$B_{\rm X}(r_\perp) = \frac{10^{-14}}{4\pi(1+z)^2} \int n_{\rm e}(r) n_{\rm H}(r) dz \ [{\rm cm}^{-5}/{\rm arcmin}^2], \tag{2.7}$$

where $r_\perp$ is the radius perpendicular to the line-of-sight direction, which is related with r and z as $r = \sqrt{r_\perp^2 + z^2}$. The CMB temperature distortion is caused by CMB photons passsing through clusters and being scttered by electrons in clusters, can be expressed as the difference between the averaged CMB temperature and the observed CMB temperature, $\Delta T_{\rm SZ}$, or y-parameter,

$$y(r_\perp) = -\frac{\Delta T_{\rm SZ}}{2T_{\rm CMB}} = \frac{\sigma_{\rm T}}{m_{\rm e}} \int P_{\rm e}(r) dz, \tag{2.8}$$

where $T_{\rm CMB} = 2.725$ K is the CMB temperature, $\sigma_{\rm T}$ is the Thomson cross section, $m_{\rm e}$ is the electron mass.

2.3 Shear profile by gravitational weak-lensing

We consider a spatially flat cosmological background, and work with the cosmological Newtonian gauge, whose line element is written as

$$ds^2 = -(1+2\Psi)dt^2 + a(t)^2(1+2\Phi)d\mathbf{x}^2, \tag{2.9}$$

where $a(t)$ is the scale factor, and Ψ and Φ are the gravitational and curvature potentials, respectively. The propagation of light is determined by the lensing potential $(\Phi - \Psi)/2$, which means that the weak-lensing signal is determined by $(\Phi - \Psi)/2$. For example, the convergence is given by

$$\kappa = -\frac{1}{2} \int_0^\chi d\chi' \frac{(\chi - \chi')\chi'}{\chi} \triangle^{(2{\rm D})} (\Phi - \Psi), \tag{2.10}$$

where χ is the comoving distance and $\triangle^{(2{\rm D})}$ is the comoving two-dimensional Laplacian. For the case of general relativity, we may set $\triangle\Psi = -\triangle\Phi = 4\pi G a^2 \rho$. Then, using the thin lens approximation, (2.10) reduces to

$$\kappa = \frac{(\chi_{\rm S} - \chi_{\rm L})\chi_{\rm L}}{\chi_{\rm S}} \int_0^{\chi_{\rm S}} d\chi' \left[4\pi G \rho(r')\right] a_{\rm L}^2, \tag{2.11}$$

where $\chi_{\rm L}$ and $\chi_{\rm S}$ denote the comoving distance between the observer and lens and that between the observer and the source, respectively, and $a_{\rm L} = 1/(1+z_{\rm L})$ is the scale factor specified by the redshift of the lens object $z_{\rm L}$. For a spherically symmetric cluster, (2.11) is represented as

$$\kappa(r_\perp) = \frac{2}{\Sigma_{\rm c}} \int_0^\infty dz \rho(r) \tag{2.12}$$

JCAP10(2015)064

with the physical coordinate $r = \sqrt{r_\perp^2 + z^2}$. We define $\Sigma_{\rm c} = \chi_{\rm S}/[4\pi G(\chi_{\rm S} - \chi_{\rm L})\chi_{\rm L} a_{\rm L}]$. We then define the reduced shear

$$g_+(r_\perp) \equiv \frac{\gamma_+(r_\perp)}{1 - \kappa(r_\perp)}, \tag{2.13}$$

where $\gamma_+(r_\perp)$ is the tangential shear, which is related with the convergence as

$$\gamma_+(r_\perp) = \bar{\kappa}(< r_\perp) - \kappa(r_\perp), \tag{2.14}$$

with

$$\bar{\kappa}(< r_\perp) \equiv \frac{2}{r_\perp^2} \int_0^{r_\perp} dr'_\perp r'_\perp \kappa(r'_\perp). \tag{2.15}$$

For the NFW profile, the convergence is given by [40] as

$$\kappa_{\rm nfw}(x) = \begin{cases} \dfrac{2r_{\rm s}\rho_{\rm s}}{\Sigma_{\rm c}(x^2-1)}\left[1 - \dfrac{2}{\sqrt{1-x^2}}\mathrm{arctanh}\sqrt{\dfrac{1-x}{1+x}}\right], & (x<1) \\ \dfrac{2r_{\rm s}\rho_{\rm s}}{3\Sigma_{\rm c}}, & (x=1) \\ \dfrac{2r_{\rm s}\rho_{\rm s}}{\Sigma_{\rm c}(x^2-1)}\left[1 - \dfrac{2}{\sqrt{x^2-1}}\arctan\sqrt{\dfrac{x-1}{1+x}}\right], & (x>1) \end{cases} \tag{2.16}$$

$$\bar{\kappa}_{\rm nfw}(< x) = \begin{cases} \dfrac{4r_{\rm s}\rho_{\rm s}}{\Sigma_{\rm c}x^2}\left[\dfrac{2}{\sqrt{1-x^2}}\mathrm{arctanh}\sqrt{\dfrac{1-x}{1+x}} + \ln\left(\dfrac{x}{2}\right)\right], & (x<1) \\ \dfrac{4r_{\rm s}\rho_{\rm s}}{\Sigma_{\rm c}}\left[1 + \ln\left(\dfrac{1}{2}\right)\right], & (x=1) \\ \dfrac{4r_{\rm s}\rho_{\rm s}}{\Sigma_{\rm c}x^2}\left[\dfrac{2}{\sqrt{x^2-1}}\arctan\sqrt{\dfrac{x-1}{1+x}} + \ln\left(\dfrac{x}{2}\right)\right], & (x>1) \end{cases} \tag{2.17}$$

with $x = r/r_{\rm s}$.

Here, we assume that the source galaxies have random orientation of ellipticity $\epsilon_{\rm S}$, the average of which is $\langle \epsilon_{\rm S} \rangle = 0$. When we observe the tangential ellipticity of the source galaxies $\epsilon_{\rm obs.}$, the average is given by $\langle \epsilon_{\rm obs.} \rangle = g_+$. Hereafter, we assume that the redshift of the source galaxies is $\langle z_{\rm S} \rangle = 0.6$, but the results are not influenced by the redshift of the source galaxies for nearby clusters.

3 Consistency test with Newtonian gravity

In the present paper, we use Coma Cluster observations. The Coma Cluster is one of the best observed nearby clusters, and has redshift $z = 0.0236$. The X-ray distribution [32, 33, 41–48], the SZ effect [49] and the weak-lensing measurement [34, 50] have been reported. These observations revealed that the Coma Cluster has substructures and orientation dependence on the gas temperature profiles. The Coma Cluster is thus an unrelaxed system. However, we will show that our model based on the hydrostatic equilibrium fits the data of the X-ray brightness profiles [32, 33], the SZ effect profile from the Planck measurement [49], and the weak-lensing profile by Subaru observations [34]. In general, the assumption of hydrostatic equilibrium holds only at the intermediate region of clusters, because of the cooling of the gas at the innermost region and the environmental effects at the outermost region. Then we use data points in the range 200 kpc to 1.5 Mpc to get rid of systematic effects from the innermost and outermost regions of the cluster.

JCAP10(2015)064

Parameter	Newtonian gravity	Modified gravity (full parameters)
$M_{\rm vir}$	$1.08^{+0.06}_{-0.06} \times 10^{15}\ M_\odot$	$1.04^{+0.14}_{-0.06} \times 10^{15}\ M_\odot$
c	$3.59^{+0.23}_{-0.23}$	$3.64^{+0.21}_{-0.30}$
n_0	$6.14^{+0.28}_{-0.26} \times 10^{-3}/{\rm cm}^3$	$6.17^{+0.26}_{-0.31} \times 10^{-3}/{\rm cm}^3$
T_0	$6.36^{+0.11}_{-0.12}$ keV	$6.35^{+0.13}_{-0.11}$ keV
b_1	2.6 (fixed)	2.6 (fixed)
b_2	0.5 (fixed)	0.5 (fixed)
r_1	$0.74^{+0.06}_{-0.06}$ Mpc	$0.75^{+0.06}_{-0.07}$ Mpc
ϵ'	-	0.43
$\mu'_{\rm G}$	-	0.24
$\mu'_{\rm L}$	-	0.55
Minimum χ^2/d.o.f.	58/44	57/41

Table 1. Best-fitting parameters and 1-dimensional marginalized constraints (68% CL) to characterize the gas and lensing profiles. To avoid degeneracy between parameters, we fix b_1 and b_2 simply. Our results do not depend on whether these parameters are fixed or not. This table shows the results for the Newtonian gravity (second column) and the generalized Galileon model with all modification parameters (third column). The minimum chi-squared and the number of degrees of freedom, d.o.f. = (number of data points) − (number of model parameters), are listed at the bottom of each column.

In this work, we use the observational data of the XMM-Newton [32, 33], which are different from those used in a previous paper [27]. In that paper, the weak-lensing profile is not used; only the parameters $M_{\rm vir}$ and c are used as a prior profile from [50]. However, use of the weak-lensing profile is essential to our analysis of the generalized Galileon model.

To address the theoretical predictions in the previous section with observations of the Coma Cluster, we introduce the chi-squared by summing the chi-squared for each observation as

$$\chi^2_{\rm XB+SZ+WL} = \chi^2_{\rm XB} + \chi^2_{\rm SZ} + \chi^2_{\rm WL}, \tag{3.1}$$

where

$$\chi^2_{\rm XB} = \sum_i \frac{(B_{\rm X}(r_i) - B^{\rm obs.}_{{\rm X},i})^2}{(\Delta B^{\rm obs.}_{{\rm X},i})^2}, \tag{3.2}$$

$$\chi^2_{\rm SZ} = \sum_i \frac{(y(r_{\perp,i}) - y^{\rm obs.}_i)^2}{(\Delta y^{\rm obs.}_{,i})^2}, \tag{3.3}$$

$$\chi^2_{\rm WL} = \sum_i \frac{(g_+(r_{\perp,i}) - g^{\rm obs.}_{+,i})^2}{(\Delta g^{\rm obs.}_{+,i})^2}, \tag{3.4}$$

are the chi-square values for the X-ray brightness, the SZ effect and the weak-lensing, respectively. We note that the covariance of errors is not taken into account in our analysis and leave it for future work to study how the observational systematics affect our analysis.

We perform an MCMC analysis using modified *Monte Python* code [51] that employs a Metropolis-Hastings [52, 53] sampling algorithm. This analysis includes 5 parameters with the chi-squared (3.1), $\chi^2_{\rm BX+SZ+WL}$. We require Gelman-Rubin statistics [54] of $\mathcal{R}-1 < 0.001$ for each parameter to ensure convergence of our runs. The black dashed curve in each panel of figure 1 shows the best-fit profiles for the Newtonian gravity. The minimum value of the chi-squared is $\chi^2_{\rm XB+SZ+WL}$/d.o.f. = 58/44, and the 2-dimensional marginalized contours of the different combinations between the model parameters are shown in figure 4.

JCAP10(2015)064

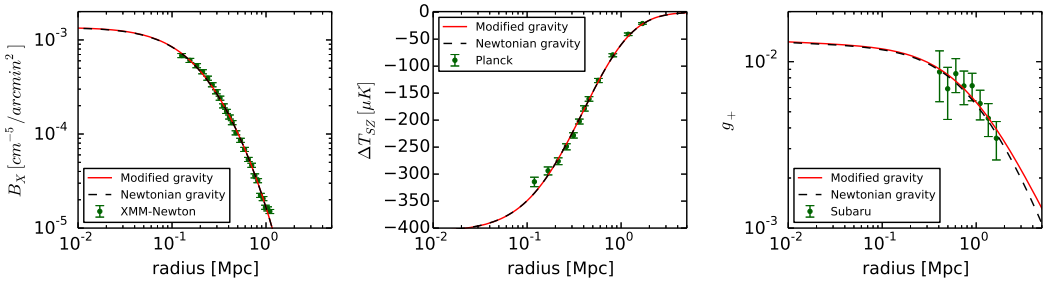

Figure 1. Best-fit profiles in the frameworks of Newtonian gravity (black dashed curve) and the generalized Galileon model (red solid curve), and the observational results. The best-fit parameters are listed in table 1. *Left panel*: the X-ray surface brightness from the *XMM-Newton* observations [32, 33]. The errors bars are composed of the Poisson noise and systematic errors that we here assume as 5%. *Center panel*: the SZ temperature profile from the *Planck* measurements [49]. *Right panel*: the weak-lensing profile from the Subaru observations [50].

Non-thermal pressure possibly caused by turbulent gas and bulk motion causes a systematic error when comparing observations of clusters. The authors estimated the fraction of non-thermal pressure in the Coma Cluster [55], which can be larger than that of the thermal pressure by 10 percent. Here, we estimate how non-thermal pressure affects our fitting based on an estimation with a numerical simulation. To this end, we estimate the hydrostatic masses by comparison with the X-ray brightness and SZ effect profiles of the Coma Cluster. Here we define the non-thermal fraction $f_{\rm nth}$ by $f_{\rm nth} \equiv P_{\rm nth}/(P_{\rm nth} + P_{\rm th})$, where $P_{\rm nth}$ and $P_{\rm th}$ are the non-thermal pressure and the thermal pressure, respectively. In the case including non-thermal pressure, the thermal pressure is replaced by $P_{\rm th} = (1 - f_{\rm nth})P_{\rm tot}$. We consider the following non-thermal pressure fraction as a function of the radius,

$$f_{\rm nth}(r) = \alpha_{\rm nt}(1+z)^{\beta_{\rm nt}} \left(\frac{r}{r_{500}}\right)^{n_{\rm nt}} \left(\frac{M_{200}}{3\times 10^{14} M_\odot}\right)^{n_{\rm M}}, \tag{3.5}$$

which is a theoretical prediction with numerical simulations in ref. [56, 57]. r_{500} and M_{200} mean the radius and mass at the radius where the matter density in the galaxy cluster is 500 and 200 times of the critical density, respectively. In the present paper we adopt $(\alpha_{\rm nt},\ \beta_{\rm nt},\ n_{\rm nt}, n_{\rm M}) = (0.18, 0.5, 0.8.0.2)$, which are the best-fit values in [57] consistent with those in [55].

The best-fit profile in the presence of non-thermal pressure is not significantly altered, compared with the best-fit profile in the absence of non-thermal pressure. Figure 2 shows the enclosed mass profiles as a function of radius. The gray-hatched region is the 1σ uncertainty interval for the lensing mass. The blue-solid and red-solid regions show the 1σ uncertainty intervals for hydrostatic masses fitted without and with non-thermal pressure, respectively. The hydrostatic mass estimates are in good agreement with the lensing mass, regardless of the inclusion of the non-thermal pressure components. This shows that our fitting method is not affected by non-thermal pressure, so we do not consider the non-thermal effect when putting a constraint on the modified gravity in the next section.

4 Testing the generalized Galileon gravity model

We here consider the generalized cubic Galileon model, with action given by [58],

$$S = \int d^4x\sqrt{-g}\Big[G_4(\phi)R + K(\phi, X) - G_3(\phi, X)\Box\phi + \mathcal{L}_{\rm m}\Big], \tag{4.1}$$

where $K(\phi, X)$, $G_3(\phi, X)$ and $G_4(\phi)$ are arbitrary functions depending on the scalar field ϕ and its kinetic term $X \equiv -(\partial\phi)^2/2$ and $\mathcal{L}_{\rm m}$ is the matter Lagrangian. This model is a non-minimal coupling version of the kinetic gravity braiding mode [59], and a subclass of the most general second-order scalar-tensor theory [60–62] with $G_{4X} = G_5 = 0$, where $G_{4X} \equiv \partial G_4/\partial X$. The simplest cubic Galileon model is the case with $K = -X$, $G_3 \propto X$, and $G_4 = M_{\rm Pl}^2/2$, where $M_{\rm Pl}^2 = 1/(8\pi G)$ is the Planck mass. The DGP model is originally a 5-dimensional brane-world model, however, it can be effectively described as a Galileon model. Note that the DGP model has two branches of cosmological solutions, the self-accelerating branch (sDGP) model [18, 19] and the normal branch DGP (nDGP) model [21]. The relation between the generalized Galileon model and the specific models are summarized in the appendix.

We consider perturbations of space-time metric and scalar field. We choose the Newtonian gauge for the space-time metric (2.9). Assuming spherical symmetry of the system,

JCAP10(2015)064

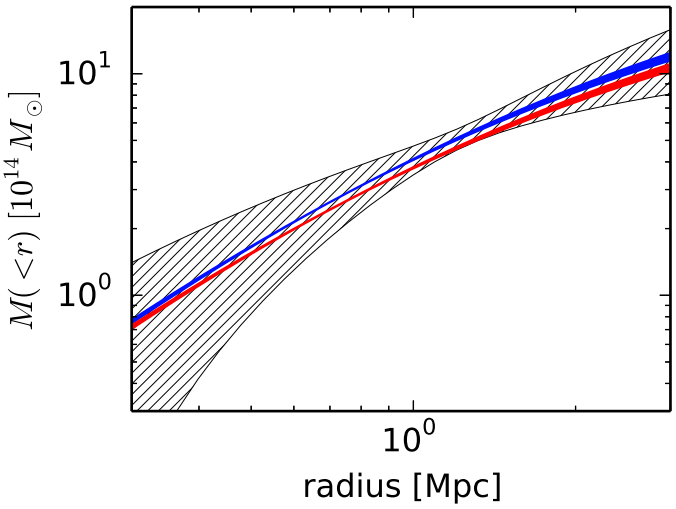

Figure 2. Spherical masses enclosed within the radii. The gray-hatched region denotes the 1σ uncertainty interval for the lensing mass determined solely by weak-lensing analysis [50]. The blue-solid and red-solid regions denote the 1σ uncertainty intervals for hydrostatic masses without and with the non-thermal pressure component, respectively, determined by our joint-fit method. The hydrostatic and lensing masses agree with each other, irrespective of the presence of a non-thermal pressure component.

within the sub-horizon scale with the quasi-static approximation keeping with the Vainshtein feature, the equations for the gravity and the scalar field lead to [17]

$$\frac{d\Psi}{dr} = \frac{GM(<r)}{r^2} - (\alpha+\xi)\frac{dQ}{dr}, \tag{4.2}$$

$$\frac{d\Phi}{dr} = -\frac{GM(<r)}{r^2} + \xi\frac{dQ}{dr}, \tag{4.3}$$

$$\frac{dQ}{dr} = \frac{r}{4\lambda^2}\left(1-\sqrt{1+\frac{8G\lambda^2\zeta M(<r)}{r^3}}\right), \tag{4.4}$$

where $Q(\mathbf{x})$ is perturbation of the scalar field defined by $\phi(t,\mathbf{x}) = \phi(t)(1+Q(\mathbf{x}))$, and $M(<r) \equiv 4\pi\int_0^r dr' r'^2 \rho(r')$ is the enclosed mass of the halo within the physical radius r. Note that the perturbed values Ψ, Φ and Q in (4.2)$\sim$(4.4) are written in the physical coordinate. In (4.2)$\sim$(4.4), we introduce free model parameters α, ξ, ζ and λ^2, which are determined by the arbitrary functions K, G_3 and G_4. The expressions for α, ξ, ζ and λ^2 are given in the appendix A. The explicit expressions for the simplest cubic Galileon, the sDGP and the nDGP models are also presented there.

Here, we define the Vainshtein radius $r_{\rm V}$ as

$$r_{\rm V} \equiv [8G\lambda^2\zeta M_{\rm vir}]^{1/3} = \left[\frac{8G\epsilon^2 M_{\rm vir}}{H_0^2}\right]^{1/3}, \tag{4.5}$$

where we define $\epsilon = \sqrt{H_0^2\lambda^2\zeta}$ using the Hubble constant H_0. For $r \ll r_{\rm V}$, the scalar field can be negligible compared with the Newton potential, so Newtonian gravity is recovered.

JCAP10(2015)064

For $r \gg r_{\rm V}$ the scalar field cannot be negligible, and we have

$$\frac{d\Psi}{dr} \simeq \frac{(1+\zeta(\alpha+\xi))GM(<r)}{r^2}, \tag{4.6}$$

$$\frac{d\Phi}{dr} \simeq -\frac{(1+\zeta\xi)GM(<r)}{r^2}. \tag{4.7}$$

Thus the gravitational and curvature potentials are modified at $r \gg r_{\rm V}$. These modifications affect both the gas and weak-lensing profiles.

We next construct observational quantities of the gas and weak-lensing profiles considering the scalar field. Since gas components feel gravitational force through the gravitational potential Ψ, the X-ray brightness and the SZ profiles are modified through modification of Ψ. On the other hand, the gravitational lensing is characterized by the lensing potential $(\Phi-\Psi)/2$, so the modified lensing potential alters the observed lensing profile. We therefore introduce the parameters

$$\mu_{\rm G} \equiv (\alpha+\xi)\zeta, \tag{4.8}$$

$$\mu_{\rm L} \equiv \frac{1}{2}(\alpha+2\xi)\zeta, \tag{4.9}$$

with which we can write $d\Psi/dr \simeq (1+\mu_{\rm G})GM(<r)/r^2$ and $d(\Psi-\Phi)/dr/2 \simeq (1+\mu_{\rm L})GM(<r)/r^2$ at $r \gg r_{\rm V}$.

In the generalized Galileon model, with the use of parameters $\mu_{\rm G}$, $\mu_{\rm L}$ and ϵ our modeling for the electron pressure profile (2.6) and the weak-lensing profile (2.12) are modified as follows:

$$P_{\rm e}(r) = P_0 \exp\left(\int_0^r dr \frac{\mu m_{\rm p}}{kT_{\rm e}(r)}\left[-\frac{GM(<r)}{r^2} + \frac{\mu_{\rm G}}{4\epsilon^2}H_0^2 r\left(1-\sqrt{1+12\epsilon^2\frac{\rho_{\rm s}}{\rho_{\rm c0}}\frac{r_{\rm s}^3}{r^3}m(r)}\right)\right]\right), \tag{4.10}$$

$$\kappa(r_\perp) = \frac{2}{\Sigma_{\rm c}}\int_0^\infty dz\left[\rho(r) - \frac{\mu_{\rm L}\rho_{\rm c0}}{2\epsilon^2}\left(1-\sqrt{1+12\epsilon^2\frac{\rho_{\rm s}}{\rho_{\rm c0}}\frac{r_{\rm s}^3}{r^3}m(r)}\right) + \frac{\rho(r)-3\rho_{\rm s}r_{\rm s}^3 m(r)/r^3}{\sqrt{1+12\epsilon^2\rho_{\rm s}r_{\rm s}^3 m(r)/\rho_{\rm c0}r^3}}\mu_{\rm L}\right]. \tag{4.11}$$

Since the gas pressure tracing the matter density deceases with the cluster-centric radius increasing, the pressure gradient is restricted to $dP_{\rm e}/dr < 0$. This gives the constraints on $\mu_{\rm G}$.

Instead of $\mu_{\rm G}$, $\mu_{\rm L}$ and ϵ, we introduce $\mu'_{\rm G} = \mu_{\rm G}/(1+|\mu_{\rm G}|)$, $\mu'_{\rm L} = \mu_{\rm L}/(1+|\mu_{\rm L}|)$, and $\epsilon' = 1-\exp(-\epsilon)$, which span the complete available parameter space of $\mu'_{\rm G}$ and $\mu'_{\rm L}$ in the interval $[-1,1]$ and ϵ' in the interval $[0,1]$, respectively. General relativity is recovered when $\mu'_{\rm G} = \mu'_{\rm L} = 0$ or $\epsilon' \to 1$. Using the same method adopted for Newtonian case, we perform an MCMC analysis for the modified gravity model including 8 parameters with the chi-squared $\chi^2_{\rm BX+SZ+WL}$, defined by (3.1).

Figure 5 shows the 2-dimensional marginalized contours of the different combinations between the model parameters. The best-fit parameters and their 1-dimensional marginalized 68% errors are listed in the table. 1. The red curve in each panel of figure 1 shows the best-fit profile for the generalized Galileon model with the minimum value of the chi-squared/d.o.f., $\chi^2_{\rm XB+SZ+WL}/{\rm d.o.f.} = 57/41$. These profiles almost overlap with the profiles for Newtonian gravity (black dashed curves), which shows that the large deviation from Newtonian gravity

JCAP10(2015)064

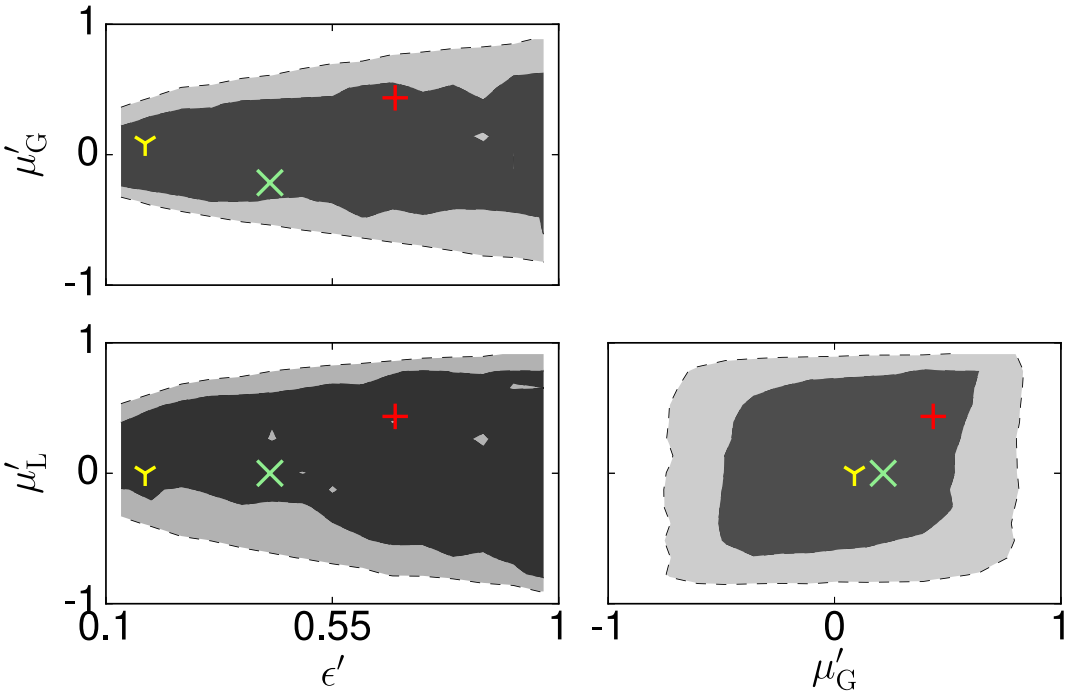

Figure 3. The 68% (dark gray regions) and the 95% CL (light gray regions) 2-dimensional marginalized contours for the generalized Galileon model parameters. The red-plus, green-cross and yellow-triangle points present models for the simplest cubic Galileon, the sDGP and the nDGP models, respectively.

is rejected. We note that there is no significant difference between the red and black curves in the best-fit profiles. There is a slight difference in the shear profiles at the large radius $r > 1$Mpc, which seems to be originated from the large errorbars of the shear data.

Figure 3 shows 2-dimensional marginalized contours of the confidence levels for the parameters $\mu'_{\rm G}$, $\mu'_{\rm L}$ and ϵ'. $\mu'_{\rm G}$ and $\mu'_{\rm L}$ are parameters from the modification of the gravitational potential and the lensing potential, and ϵ' is a parameter characterizing the Vainshtein radius. Large values of $\mu_{\rm G}$ and $\mu_{\rm L}$ are rejected at the 68% confidence level, which indicates that the possibility of a large deviation from the Newtonian gravity is ruled out, depending on the parameter ϵ. When ϵ is smaller, the Vainshtein radius becomes smaller, we can put a tighter constraint on $\mu_{\rm G}$ and $\mu_{\rm L}$. However, ϵ is large, the Vainshtein radius becomes large, which makes difficult to distinguish between the Newtonian gravity model and the modified gravity model due to the Vainshtein mechanism. The red-plus, green-cross and yellow-triangle points in figure 3 show the representative models, the simplest cubic Galileon model, the sDGP model and nDGP model, respectively, at the redshift $z = 0.0236$. The parameter values for each models are shown in table 2.

In a previous work [29], a constraint only on the parameter space $\mu_{\rm L}$ and ϵ is obtained, based on the lensing observations. As a other recent related work, Barreira et al. investigated cluster masses and the concentration parameters in modified gravity models from shear profiles [63]. They focused their investigation on the mass-concentration relation of 19 X-ray

JCAP10(2015)064

Models	ϵ (ϵ')	$\mu_{\rm G}$ ($\mu'_{\rm G}$)	$\mu_{\rm L}$ ($\mu'_{\rm L}$)
simplest cubic Galileon	0.77 (0.44)	0.77 (0.44)	1.12 (0.67)
sDGP	−0.26 (−0.22)	0 (0)	0.53 (0.43)
nDGP	0.20 (0.18)	0 (0)	0.10 (0.09)

Table 2. Values of modified gravity parameters for each model at the redshift $z = 0.0236$.

Parameter	Modified gravity (unscreened)	Modified gravity (fifth force)
$M_{\rm vir}$	$1.26^{+0.15}_{-3.85} \times 10^{15}\ M_\odot$	$0.86^{+0.05}_{-0.05} \times 10^{15}\ M_\odot$
c	$3.78^{+0.13}_{-0.55}$	$3.84^{+0.24}_{-0.28}$
n_0	$6.15^{+0.27}_{-0.29} \times 10^{-3}/{\rm cm}^3$	$6.20^{+0.27}_{-0.32} \times 10^{-3}/{\rm cm}^3$
T_0	$6.35^{+0.13}_{-0.11}$ keV	$6.36^{+0.12}_{-0.12}$ keV
b_1	2.6 (fixed)	2.6 (fixed)
b_2	0.5 (fixed)	0.5 (fixed)
r_1	$0.75^{+0.06}_{-0.07}$ Mpc	$0.75^{+0.06}_{-0.06}$ Mpc
ϵ'	0 (fixed)	0.05 (fixed)
$\mu'_{\rm G}$	−0.10	0.2 (fixed)
$\mu'_{\rm L}$	−0.05	0 (fixed)
Minimum χ^2/d.o.f.	57/42	60/44

Table 3. Same as table 1 but for the results of the generalized Galileon model in the unscreened limit with only fixing $\epsilon = 0$ (second column), and the case with fixing all the modified gravity parameters $\epsilon' = 0.05$, $\mu'_{\rm G} = 0.2$, and $\mu'_{\rm L} = 0$ (third column).

JCAP10(2015)064

selected clusters from the CLASH survey in the simplest cubic Galileon and Nonlocal gravity models. They found that the mass-concentration relation obtaining from the shear profiles for the cubic Galileon model is the same as those for the ΛCDM model, but no stringent constraint on the modified gravity models is obtained. Unfortunately the constraint obtained in the present paper is not very stringent too, but one can find the following possibility. We emphasize that models with $\mu_{\rm L} = 0$ like the sDGP and the nDGP models are indistinguishable with Newtonian gravity in the method based on the lensing observations. On the other hand, our method of combining the gas and weak-lensing profiles can solve the problem from this degeneracy. Future observations would improve the constraint.

5 Discussion

5.1 Degeneracies on parameters

On the MCMC analysis in the previous section, we do not take the range of ϵ, $[0, 0.1]$, into account because it is hard to converge the MCMC runs because of degeneracy in the parameter space. Here, we treat this parameter region for complemental discussion.

First, taking the limit $\epsilon \to 0$, which means the fifth force is unscreened everywhere, the solutions of the gas pressure (4.10) and the convergence (4.11) are reduced to

$$P_{\rm e}(r) = P_0 \exp\left(\int_0^r dr \frac{\mu m_{\rm p}}{kT_{\rm e}(r)}\left[-\frac{GM(<r)}{r^2}(1+\mu_{\rm G})\right]\right), \tag{5.1}$$

$$\kappa(r_\perp) = (1+\mu_{\rm L})\frac{2}{\Sigma_{\rm c}}\int_0^\infty dz \rho(r). \tag{5.2}$$

Then, the pressure profile and the convergence profile are simply modified by a factor of $(1+\mu_{\rm G})$ and $(1+\mu_{\rm L})$, respectively. In this case, we have $P_{\rm e} \propto (1+\mu_{\rm G})M_{\rm vir}m(c)/c^3$ and $\kappa \propto \rho_{\rm s} \propto (1+\mu_{\rm L})M_{\rm vir}c^3/m(c)$, then, there are degeneracies between the parameters, $M_{\rm vir}, c, \mu_{\rm G}$, and $\mu_{\rm L}$. Figure 6 compares the results of the MCMC analysis with fixing $\epsilon = 0$ (dark blue region (68% CL) and mid blue region (95% CL)) and the results of the Newtonian gravity (dark gray region and mid gray region), which is the same as those of figure 4. The best-fit parameters are shown in the table. 3. The CL contours of the blue regions reflect the degeneracy between the parameters, $M_{\rm vir}, c, \mu_{\rm G}$, and $\mu_{\rm L}$.

Next, we show how the presence of the fifth force affects the parameter estimation. For example, the blue confidence contours in figure 7 shows the 68% and 95% confidence contours of the case with fixing $\epsilon = 0.05$, $\mu_{\rm G} = 0.2$ and $\mu_{\rm L} = 0$. $M_{\rm vir}$ and c are different from those of the Newtonian gravity (gray regions), but other parameters, n_0, T_0 and b_1, are not changed. The minimum value of the chi-squared/d.o.f. in the presence of the fifth force is $\chi^2_{\rm XB+SZ+WL}/{\rm d.o.f.} = 60/44$, which is almost the same as the Newtonian case, despite the different cluster parameter, $M_{\rm vir} \sim 0.9 \times 10^{15} M_\odot$ (see table. 3). This result exemplifies that the presence of the attractive fifth force affects the estimation of the NFW parameters, $M_{\rm vir}$ and c. This is understood as the consequence of the degeneracy between the modification parameters $\mu_{\rm G}$ and $\mu_{\rm L}$ and $M_{\rm vir}$ and c.

5.2 Systematic errors

We shall discuss possible systematic errors. In our analysis, we have assumed spherical symmetry for the matter distribution and an equilibrium state for the gas component of the balance between the pressure gradient and the gravitational force and the fifth force in the case of its presence. We have demonstrated that non-thermal pressure at the level suggested by numerical simulations does not alter our results. A future X-ray satellite, ASTRO-H [64], will observe turbulent gas motion in the Coma Cluster in more detail, which will be informative regarding our result. However, observations of the Coma Cluster suggest substructures [34, 50, 65–68] and orientation dependence [41, 42, 48], so the Coma Cluster is not thought to be a relaxed system. Dynamical states of the Coma Cluster would give a systematic difference between our results and temperature measurement. Our fitting results show that the temperature of the Coma Cluster is around 6.4 keV (see table. 1), but this result seems lower than those of X-ray observations [32, 33, 41, 42, 46–48], which estimate that the temperature of the Coma Cluster is around 8–9 keV. Comparing the mass-temperature scaling relation for a sample of relaxed clusters [69] with an X-ray temperature observation of the Coma Cluster [32, 33], the observed temperature is higher that the temperature expected by the mass. The enhancement is at 3σ level of intrinsic scatter [69]. Similar results of high temperatures have also been reported by a comparison with other clusters [70]. Depending on the orientation and excluding the central region, the temperature of the Coma Cluster could be around 6–7 keV [32, 41], but it is difficult to take this dependence into account. Therefore, systematic

JCAP10(2015)064

error of temperature in the Coma Cluster would cause a substantial influence to the proposed fitting method. In order to reduce a possible dependence of cluster-dynamical states and halo triaxiality, it is of vital importance to increase the number of sampling clusters. Ongoing and future multi-wavelength surveys such as the Hyper Suprime-Cam (HSC) optical survey,[1] the Dark Energy Survey (DES) [71], the *eROSITA* X-ray survey [72, 73], and the ACT-Pol [74] and SPT surveys [75, 76] will be powerful aids to better constraining the gravity model.

6 Summary and conclusion

In this paper, we obtained a constraint on the generalized Galileon model through the Coma Cluster observations of X-ray brightness, the SZ effect and weak lensing. We have constructed a simple analytic model of the gas distribution profiles and the weak-lensing profile (cf. [27–29]). The fifth force affects not only the gas distribution but also the weak-lensing profile. In general, the effects depend on different parameters characterizing the generalized Galileon model. These features can be investigated by combination of the observations of a galaxy cluster reflecting the gas density profile and the lensing signals. Their multi-wavelength observations are complementary to each other, and are useful to put a constraint on the modified gravity model by breaking the degeneracy between the model parameters. Systematic study compiling multi-wavelength datasets for a large number of clusters enables us to well reduce the systematic errors and constraints on the modified gravity models. However, the degeneracy between the parameters, $M_{\rm vir}$, c, $\mu_{\rm G}$ and $\mu_{\rm L}$, persists in the limit of the weak screening of the fifth force, which affects the estimation of the cluster parameters. Future and ongoing surveys and their joint analysis would be a powerful aid to obtaining a more stringent constraint on modified gravity models.

Acknowledgments

This work is supported by a research support program of Hiroshima University, the Funds for the Development of Human Resources in Science and Technology under MEXT, Japan, and Core Research for Energetic Universe at Hiroshima University (the MEXT Program for Promoting the Enhancement of Research Universities, Japan). We thank Kuniaki Masai, Lucas Lombriser, Yuying Zhang and Tatsuya Narikawa for their useful comments and discussions. N. Okabe is supported by a Grant-in-Aid from the Ministry of Education, Culture, Sports, Science, and Technology of Japan (26800097).

A Definitions of the coefficients

In this appendix, we summarize the coefficients between the generalized Galileon model and the specific models used in section 4 (see also [29, 77]). The coefficients in the perturbation equations (4.2)–(4.4) are defined as

$$\alpha = \alpha_1, \tag{A.1}$$

$$\xi = \alpha_2, \tag{A.2}$$

[1] http://subarutelescope.org/Projects/HSC/surveyplan.html.

JCAP10(2015)064

$$\zeta = \frac{4(\alpha_1+\alpha_2)}{\beta}\frac{G_4 H}{\dot\phi\phi}, \tag{A.3}$$

$$\lambda^2 = \frac{2\beta_0 G_4 \phi H}{\beta X \dot\phi}, \tag{A.4}$$

$$\beta = -4(\alpha_0 + 2\alpha_1\alpha_2 + \alpha_2^2)\frac{G_4 H^2}{\dot\phi^2}, \tag{A.5}$$

where

$$\alpha_0 = \left(\frac{\dot\Theta}{H^2} + \frac{\Theta}{H} - 2G_4 - 4\frac{\dot G_4}{H} - \frac{\mathcal{E}+\mathcal{P}}{2H^2}\right)\frac{1}{2G_4}, \tag{A.6}$$

$$\alpha_1 = \left(2\frac{\dot\phi G_{4\phi}}{H}\right)\frac{1}{2G_4}, \tag{A.7}$$

$$\alpha_2 = \left(\frac{\dot\phi X G_{3X}}{H} - \frac{\dot\phi G_{4\phi}}{H}\right)\frac{1}{2G_4}, \tag{A.8}$$

$$\beta_0 = \left(\frac{\dot\phi X G_{3X}}{H}\right)\frac{1}{2G_4}, \tag{A.9}$$

$$\Theta = -\dot\phi X G_{3X} + 2HG_4 + \dot\phi G_{4\phi}. \tag{A.10}$$

These coefficients are determined by the background solution, which follows:

$$2XK_X - K + 6X\dot\phi H G_{3X} - 2XG_{3\phi} - 6H^2 G_4 - 6H\dot\phi G_\phi = \rho_{\rm m}, \tag{A.11}$$

$$K - 2X\left(G_{3\phi} + \ddot\phi G_{3X}\right) + 2\left(3H^2 + 2\dot H\right)G_4 + 2\left(\ddot\phi + 2H\dot\phi\right)G_{4\phi} + 4XG_{4\phi\phi} = 0, \tag{A.12}$$

where $\rho_{\rm m}$ is the non-relativistic matter energy density and $H = \dot a/a$ is the Hubble parameter. The background equation for the scalar field is written as

$$\dot J + 3HJ - P = 0, \tag{A.13}$$

with

$$J \equiv \dot\phi K_X + 6HXG_{3X} - 2\dot\phi G_{3\phi}, \tag{A.14}$$

$$P \equiv K_\phi - 2X\left(G_{3\phi\phi} + \ddot\phi G_{3\phi X}\right) + 6\left(2H^2 + \dot H\right)G_{4\phi}. \tag{A.15}$$

The simplest cubic Galileon model is defined by $G_4 = M_{\rm Pl}^2/2$, $K = -X$ and $G_3 = (r_{\rm c}^2/M_{\rm Pl})X$, which corresponds to taking $c_1 = -1$ in ref. [78], and thus the coefficients in the perturbation equations are

$$\alpha = 0, \tag{A.16}$$

$$\xi = 4\pi G_3 G_{3X}\dot\phi^2\phi, \tag{A.17}$$

$$\zeta = \frac{G_{3X}\dot\phi^2}{\beta\phi}, \tag{A.18}$$

JCAP10(2015)064

$$\lambda^2 = \frac{G_{3X}\phi}{\beta}, \tag{A.19}$$

$$\beta = -1 + 2G_{3X}(\ddot{\phi} + 2H\dot{\phi}) - 4\pi G_3 G_{3X}^2 \dot{\phi}^4. \tag{A.20}$$

When we adopt the late time de Sitter attractor solution [79],

$$\left(\frac{H(a)}{H_0}\right)^2 = \frac{1}{2}\left[\frac{\Omega_{\rm m0}}{a^3} + \sqrt{\left(\frac{\Omega_{\rm m0}}{a^3}\right)^2 + 4(1-\Omega_{\rm m0})}\right]. \tag{A.21}$$

The combinations $\xi\zeta$ and $\lambda^2\zeta$ are given by

$$\xi\zeta = \frac{(1-\Omega_{\rm m})(2-\Omega_{\rm m})}{\Omega_{\rm m}(5-\Omega_{\rm m})}, \tag{A.22}$$

$$\lambda^2\zeta = \left(\frac{2-\Omega_{\rm m}}{H\Omega_{\rm m}(5-\Omega_{\rm m})}\right)^2, \tag{A.23}$$

where $\Omega_{\rm m}(a) = \rho_{\rm m}(a)/3M_{\rm Pl}^2H^2(a)$ is the matter density parameter.

Within the sub-horizon approximation, the DGP model [18, 19, 22] can be effectively described by the coefficients

$$\alpha = -1, \tag{A.24}$$

$$\xi = \frac{1}{2}, \tag{A.25}$$

$$\zeta = -\frac{2}{3\beta}, \tag{A.26}$$

$$\lambda^2 = -\frac{r_{\rm c}^2}{3\beta}, \tag{A.27}$$

$$\beta = 1 \pm 2Hr_{\rm c}\left(1 + \frac{\dot{H}}{3H^2}\right), \tag{A.28}$$

where the sign "$\pm$" in β represents the case of the sDGP model with "$-$" sign and the nDGP model with "$+$" sign. For the sDGP model, we adopt the self-accelerating background solution, which is specified by the modified Friedmann equation in the sDGP model [21],

$$\frac{H(a)}{H_0} = \frac{1-\Omega_{\rm m0}}{2} + \sqrt{\frac{\Omega_{\rm m0}}{a^3} + \frac{(1-\Omega_{\rm m0})^2}{4}}, \tag{A.29}$$

and $r_{\rm c} = 1/(1-\Omega_{\rm m0})H_0$. On the other hand, the nDGP model has no self-accelerating solution without introducing the cosmological constant [11, 13]. Here we consider the nDGP model with introducing a dynamical dark energy component on the brane, which is tuned such that the background evolves as in the lambda cold dark matter model [80].

JCAP10(2015)064

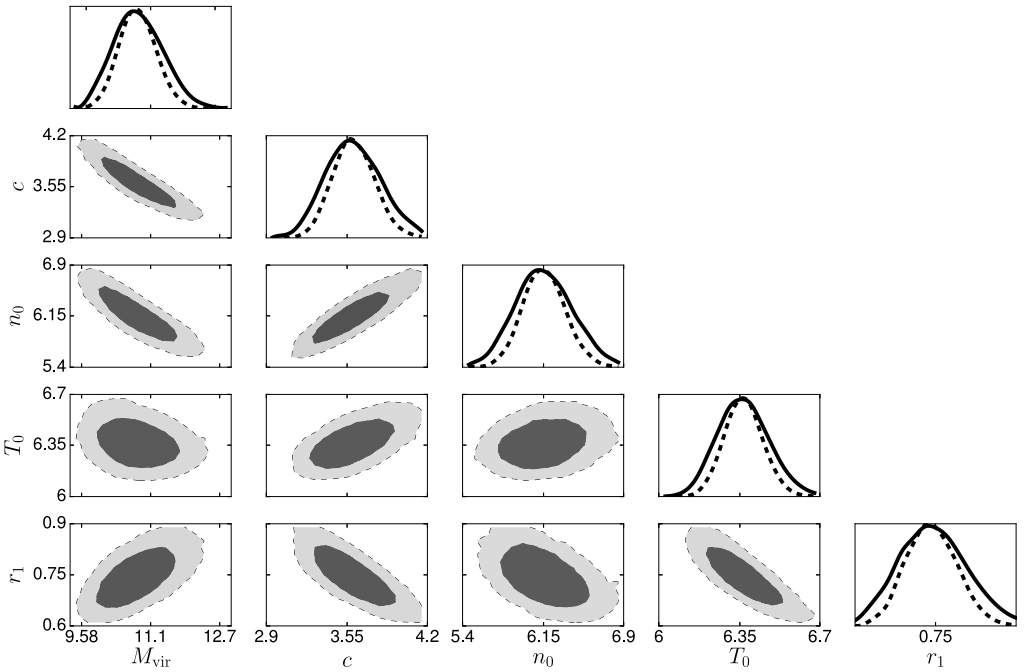

Figure 4. The 68% (dark gray region) and the 95% CL (mid gray region) 2-dimensional marginalized contours for the 5 model parameters, $M_{\rm vir}$ [$10^{14}M_{\odot}$], c, n_0 [$10^{-3}{\rm cm}^{-3}$], T_0 [keV] and r_1 [Mpc]. The rightmost plots of each row show the 1-dimensional marginalized constraints (solid) and likelihood distributions (dotted).

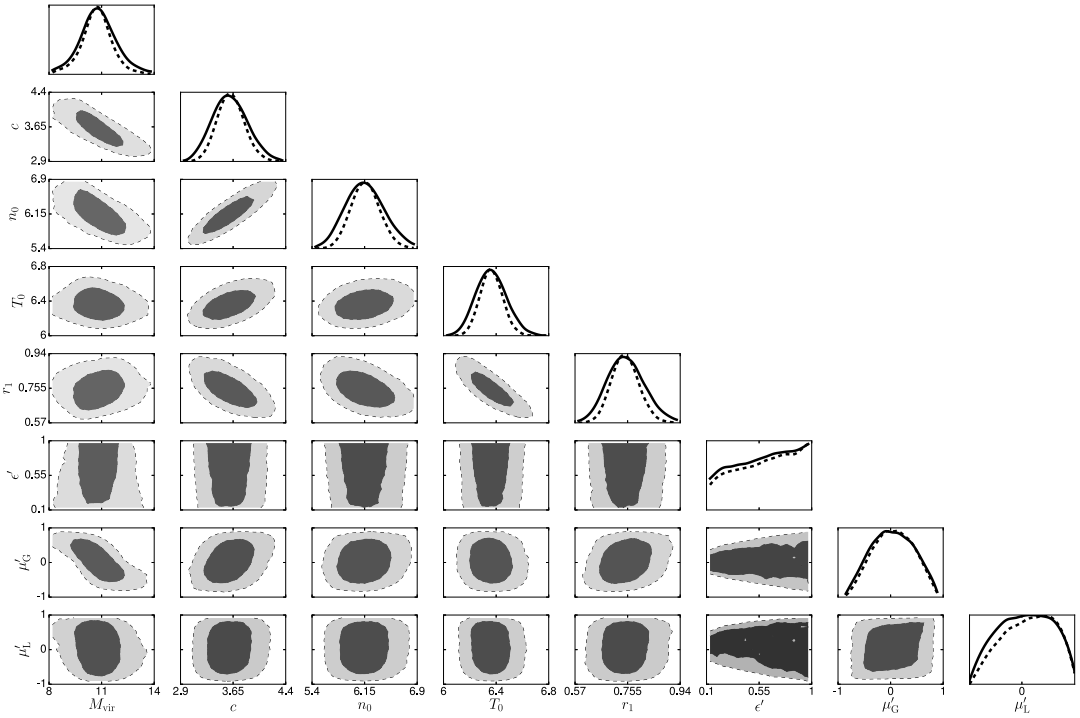

Figure 5. Same as figure 4 but when including the modification parameters ϵ', $\mu'_{\rm G}$ and $\mu'_{\rm L}$ in the MCMC analysis.

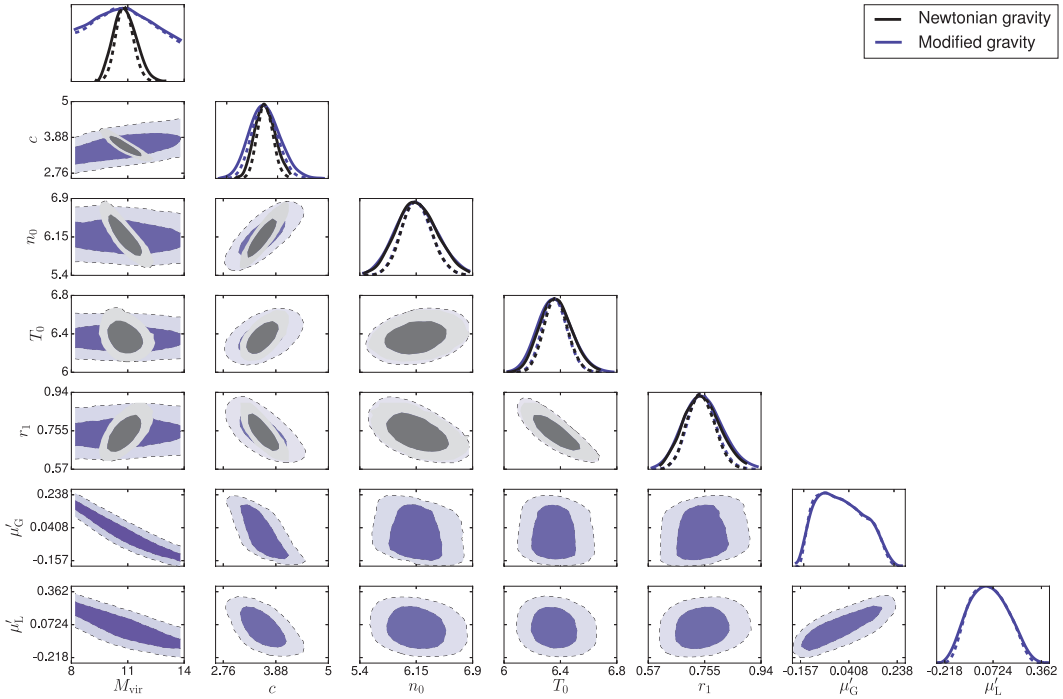

Figure 6. The dark blue region (68% CL) and the mid blue region (95% CL) are the results of the MCMC analysis for the modified gravity model with fixing $\epsilon = 0$. The dark gray region (68% CL) and the mid gray region (95% CL) are the results for the Newtonian gravity (same as the figure 4).

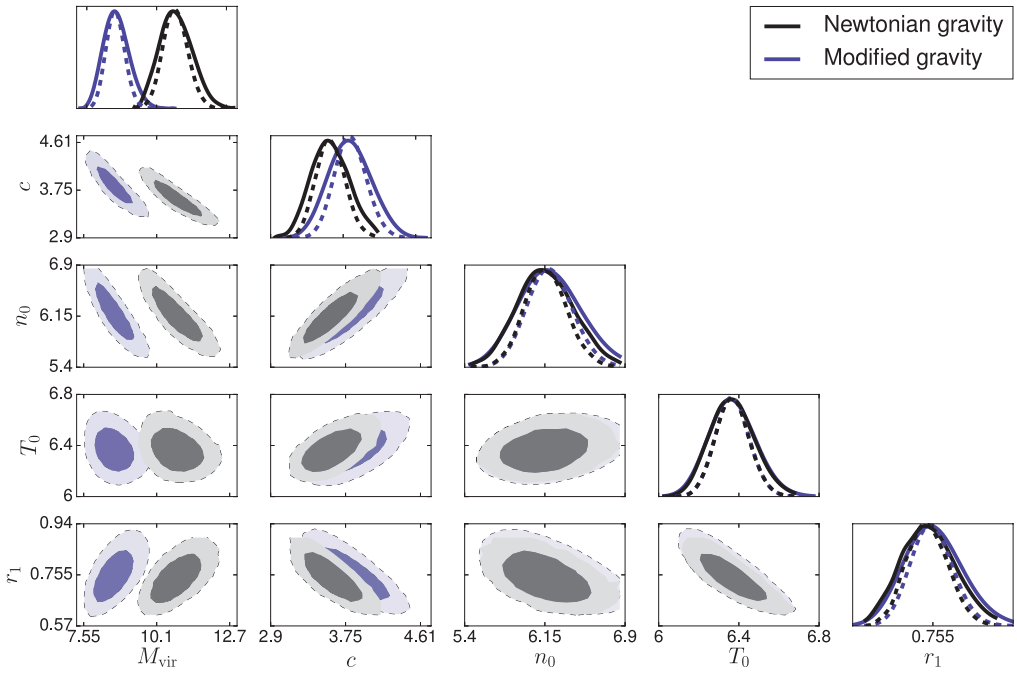

Figure 7. The dark blue region (68% CL) and the mid blue region (95% CL) are the results of the MCMC analysis for the modified gravity model with fixing $\epsilon' = 0.05$, $\mu'_{\rm G} = 0.2$ and $\mu'_{\rm L} = 0$. The dark gray region (68% CL) and the mid gray region (95% CL) are the results for the Newtonian gravity (same as the figure 4).

References

[1] E.G. Adelberger, B.R. Heckel and A.E. Nelson, *Tests of the gravitational inverse square law*, *Ann. Rev. Nucl. Part. Sci.* **53** (2003) 77 [hep-ph/0307284] [INSPIRE].

[2] C.M. Will, *The confrontation between general relativity and experiment*, *Living Rev. Rel.* **17** (2014) 4 [arXiv:1403.7377] [INSPIRE].

[3] J. Khoury and A. Weltman, *Chameleon cosmology*, *Phys. Rev.* **D 69** (2004) 044026 [astro-ph/0309411] [INSPIRE].

[4] D.F. Mota and J.D. Barrow, *Varying alpha in a more realistic universe*, *Phys. Lett.* **B 581** (2004) 141 [astro-ph/0306047] [INSPIRE].

[5] A.A. Starobinsky, *Disappearing cosmological constant in $f(R)$ gravity*, *JETP Lett.* **86** (2007) 157 [arXiv:0706.2041] [INSPIRE].

[6] W. Hu and I. Sawicki, *Models of $f(R)$ cosmic acceleration that evade solar-system tests*, *Phys. Rev.* **D 76** (2007) 064004 [arXiv:0705.1158] [INSPIRE].

[7] S. Tsujikawa, *Observational signatures of $f(R)$ dark energy models that satisfy cosmological and local gravity constraints*, *Phys. Rev.* **D 77** (2008) 023507 [arXiv:0709.1391] [INSPIRE].

[8] L. Lombriser, *Constraining chameleon models with cosmology*, *Annalen Phys.* **526** (2014) 259 [arXiv:1403.4268] [INSPIRE].

[9] A.I. Vainshtein, *To the problem of nonvanishing gravitation mass*, *Phys. Lett.* **B 39** (1972) 393 [INSPIRE].

[10] G.R. Dvali, G. Gabadadze and M. Porrati, *4D gravity on a brane in 5D Minkowski space*, *Phys. Lett.* **B 485** (2000) 208 [hep-th/0005016] [INSPIRE].

[11] C. Deffayet, *Cosmology on a brane in Minkowski bulk*, *Phys. Lett.* **B 502** (2001) 199 [hep-th/0010186] [INSPIRE].

[12] A. Nicolis, R. Rattazzi and E. Trincherini, *The Galileon as a local modification of gravity*, *Phys. Rev.* **D 79** (2009) 064036 [arXiv:0811.2197] [INSPIRE].

[13] C. Deffayet, G. Esposito-Farese and A. Vikman, *Covariant Galileon*, *Phys. Rev.* **D 79** (2009) 084003 [arXiv:0901.1314] [INSPIRE].

[14] C. Deffayet, G.R. Dvali and G. Gabadadze, *Accelerated universe from gravity leaking to extra dimensions*, *Phys. Rev.* **D 65** (2002) 044023 [astro-ph/0105068] [INSPIRE].

[15] M.A. Luty, M. Porrati and R. Rattazzi, *Strong interactions and stability in the DGP model*, *JHEP* **09** (2003) 029 [hep-th/0303116] [INSPIRE].

[16] T. Kobayashi, M. Yamaguchi and J. Yokoyama, *G-inflation: inflation driven by the Galileon field*, *Phys. Rev. Lett.* **105** (2010) 231302 [arXiv:1008.0603] [INSPIRE].

[17] R. Kimura, T. Kobayashi and K. Yamamoto, *Vainshtein screening in a cosmological background in the most general second-order scalar-tensor theory*, *Phys. Rev.* **D 85** (2012) 024023 [arXiv:1111.6749] [INSPIRE].

[18] K. Koyama and R. Maartens, *Structure formation in the DGP cosmological model*, *JCAP* **01** (2006) 016 [astro-ph/0511634] [INSPIRE].

[19] K. Koyama and F.P. Silva, *Non-linear interactions in a cosmological background in the DGP braneworld*, *Phys. Rev.* **D 75** (2007) 084040 [hep-th/0702169] [INSPIRE].

[20] F. Schmidt, *Self-consistent cosmological simulations of DGP braneworld gravity*, *Phys. Rev.* **D 80** (2009) 043001 [arXiv:0905.0858] [INSPIRE].

[21] C. Deffayet, G.R. Dvali and G. Gabadadze, *Accelerated universe from gravity leaking to extra dimensions*, *Phys. Rev.* **D 65** (2002) 044023 [astro-ph/0105068] [INSPIRE].

JCAP10(2015)064

[22] B. Falck, K. Koyama and G.-B. Zhao, *Cosmic web and environmental dependence of screening: Vainshtein vs. chameleon*, *JCAP* **07** (2015) 049 [arXiv:1503.06673] [INSPIRE].

[23] F. Schmidt, *Cosmological simulations of normal-branch braneworld gravity*, *Phys. Rev.* **D 80** (2009) 123003 [arXiv:0910.0235] [INSPIRE].

[24] A. Nicolis and R. Rattazzi, *Classical and quantum consistency of the DGP model*, *JHEP* **06** (2004) 059 [hep-th/0404159] [INSPIRE].

[25] D. Gorbunov, K. Koyama and S. Sibiryakov, *More on ghosts in DGP model*, *Phys. Rev.* **D 73** (2006) 044016 [hep-th/0512097] [INSPIRE].

[26] A. Terukina and K. Yamamoto, *Gas density profile in dark matter halo in chameleon cosmology*, *Phys. Rev.* **D 86** (2012) 103503 [arXiv:1203.6163] [INSPIRE].

[27] A. Terukina, L. Lombriser, K. Yamamoto, D. Bacon, K. Koyama and R.C. Nichol, *Testing chameleon gravity with the Coma cluster*, *JCAP* **04** (2014) 013 [arXiv:1312.5083] [INSPIRE].

[28] H. Wilcox et al., *The XMM cluster survey: testing chameleon gravity using the profiles of clusters*, *Mon. Not. Roy. Astron. Soc.* **452** (2015) 1171 [arXiv:1504.03937] [INSPIRE].

[29] A. Ibarra, H.M. Lee, S. López Gehler, W.-I. Park and M. Pato, *Gamma-ray boxes from axion-mediated dark matter*, *JCAP* **05** (2013) 016 [arXiv:1303.6632] [INSPIRE].

[30] T. Narikawa, T. Kobayashi, D. Yamauchi and R. Saito, *Testing general scalar-tensor gravity and massive gravity with cluster lensing*, *Phys. Rev.* **D 87** (2013) 124006 [arXiv:1302.2311] [INSPIRE].

[31] R.A. Sunyaev and Ya. B. Zeldovich, *Small scale fluctuations of relic radiation*, *Astrophys. Space Sci.* **7** (1970) 3 [INSPIRE].

[32] K. Matsushita, *Radial profiles of Fe abundance in the intracluster medium of nearby clusters observed with XMM-Newton*, *Astron. Astrophys.* **527** (2011) A134 [arXiv:1101.1849] [INSPIRE].

[33] K. Matsushita, T. Sato, E. Sakuma and K. Sato, *Distribution of Si, Fe and Ni in the intracluster medium of the Coma cluster*, *Publ. Astron. Soc. Jap.* **65** (2013) 10 [arXiv:1208.6098] [INSPIRE].

[34] N. Okabe, T. Futamase, M. Kajisawa and R. Kuroshima, *Subaru weak-lensing survey of dark matter subhalos in the Coma cluster: subhalo mass function and statistical properties*, *Astrophys. J.* **784** (2014) 90 [arXiv:1304.2399] [INSPIRE].

[35] J.F. Navarro, C.S. Frenk and S.D.M. White, *A universal density profile from hierarchical clustering*, *Astrophys. J.* **490** (1997) 493 [astro-ph/9611107] [INSPIRE].

[36] T.T. Nakamura and Y. Suto, *Strong gravitational lensing and velocity function as tools to probe cosmological parameters: current constraints and future predictions*, *Prog. Theor. Phys.* **97** (1997) 49 [astro-ph/9612074] [INSPIRE].

[37] K.A. Arnaud, *The first ten years astronomical data analysis software and systems V*, G. Jacoby and J. Barnes eds., *ASP Conf. Ser.* **101** (1996) 17.

[38] *Xspec: an X-ray spectral fitting package webpage*, http://heasarc.gsfc.nasa.gov/docs/xanadu/xspec/index.html.

[39] R.K. Smith, N.S. Brickhouse, D.A. Liedahl and J.C. Raymond, *Collisional plasma models with APEC/APED: emission line diagnostics of hydrogen-like and helium-like ions*, *Astrophys. J.* **556** (2001) L91 [astro-ph/0106478] [INSPIRE].

[40] C.O. Wright and T.G. Brainerd, *Gravitational lensing by NFW halos*, astro-ph/9908213 [INSPIRE].

[41] A. Simionescu et al., *Thermodynamics of the Coma cluster outskirts*, *Astrophys. J.* **775** (2013) 4 [arXiv:1302.4140] [INSPIRE].

JCAP10(2015)064

[42] T. Sato, K. Matsushita, N. Ota, K. Sato, K. Nakazawa and C.L. Sarazin, *Suzaku observations of iron K-lines from the intracluster medium of the Coma cluster*, *Publ. Astron. Soc. Jap.* **63** (2011) 991 [arXiv:1109.0154] [INSPIRE].

[43] D.M. Neumann, D.H. Lumb, G.W. Pratt and U.G. Briel, *The dynamical state of the Coma cluster with XMM-Newton*, *Astron. Astrophys.* **400** (2003) 811 [astro-ph/0212432] [INSPIRE].

[44] J.S. Sanders, A.C. Fabian, E. Churazov, A.A. Schekochihin, A. Simionescu, S.A. Walker et al., *Linear structures in the core of the Coma cluster of galaxies*, arXiv:1309.4866 [INSPIRE].

[45] E. Churazov, A. Vikhlinin, I. Zhuravleva, A. Schekochihin, I. Parrish, R. Sunyaev et al., *X-ray surface brightness and gas density fluctuations in the Coma cluster*, *Mon. Not. Roy. Astron. Soc.* **421** (2012) 1123 [arXiv:1110.5875] [INSPIRE].

[46] S.L. Snowden, R.M. Mushotzky, K.D. Kuntz and D.S. Davis, *A catalog of galaxy clusters observed by XMM-Newton*, *Astron. Astrophys.* **478** (2008) 615 [arXiv:0710.2241] [INSPIRE].

[47] D.R. Wik, C.L. Sarazin, A. Finoguenov, K. Matsushita, K. Nakazawa and T.E. Clarke, *A Suzaku search for non-thermal emission at hard X-ray energies in the Coma cluster*, *Astrophys. J.* **696** (2009) 1700 [arXiv:0902.3658] [INSPIRE].

[48] F. Gastaldello et al., *A NuSTAR observation of the center of the Coma cluster*, *Astrophys. J.* **800** (2015) 139 [arXiv:1411.1573] [INSPIRE].

[49] PLANCK collaboration, P.A.R. Ade et al., *Planck intermediate results. X. Physics of the hot gas in the Coma cluster*, *Astron. Astrophys.* **554** (2013) A140 [arXiv:1208.3611] [INSPIRE].

[50] N. Okabe, Y. Okura and T. Futamase, *Weak lensing mass measurements of substructures in Coma cluster with Subaru/Suprime-Cam*, *Astrophys. J.* **713** (2010) 291 [arXiv:1001.2402] [INSPIRE].

[51] B. Audren, J. Lesgourgues, K. Benabed and S. Prunet, *Conservative constraints on early cosmology: an illustration of the Monte Python cosmological parameter inference code*, *JCAP* **02** (2013) 001 [arXiv:1210.7183] [INSPIRE].

[52] N. Metropolis, A.W. Rosenbluth, M.N. Rosenbluth, A.H. Teller and E. Teller, *Equation of state calculations by fast computing machines*, *J. Chem. Phys.* **21** (1953) 1087 [INSPIRE].

[53] W.K. Hastings, *Monte Carlo sampling methods using Markov chains and their applications*, *Biometrika* **57** (1970) 97.

[54] A. Gelman and D.B. Rubin, *Inference from iterative simulation using multiple sequences*, *Statist. Sci.* **7** (1992) 457.

[55] P. Schuecker, A. Finoguenov, F. Miniati, H. Bohringer and U.G. Briel, *Probing turbulence in the Coma galaxy cluster*, *Astron. Astrophys.* **426** (2004) 387 [astro-ph/0404132] [INSPIRE].

[56] L.D. Shaw, D. Nagai, S. Bhattacharya and E.T. Lau, *Impact of cluster physics on the Sunyaev-Zel'dovich power spectrum*, *Astrophys. J.* **725** (2010) 1452 [arXiv:1006.1945] [INSPIRE].

[57] N. Battaglia, J.R. Bond, C. Pfrommer and J.L. Sievers, *On the cluster physics of Sunyaev-Zel'dovich surveys I: the influence of feedback, non-thermal pressure and cluster shapes on Y-M scaling relations*, *Astrophys. J.* **758** (2012) 74 [arXiv:1109.3709] [INSPIRE].

[58] A. De Felice, R. Kase and S. Tsujikawa, *Vainshtein mechanism in second-order scalar-tensor theories*, *Phys. Rev.* **D 85** (2012) 044059 [arXiv:1111.5090] [INSPIRE].

[59] R. Kimura and K. Yamamoto, *Large scale structures in kinetic gravity braiding model that can be unbraided*, *JCAP* **04** (2011) 025 [arXiv:1011.2006] [INSPIRE].

[60] G.W. Horndeski, *Second-order scalar-tensor field equations in a four-dimensional space*, *Int. J. Theor. Phys.* **10** (1974) 363 [INSPIRE].

JCAP10(2015)064

[61] C. Deffayet, X. Gao, D.A. Steer and G. Zahariade, *From k-essence to generalised Galileons*, *Phys. Rev.* **D 84** (2011) 064039 [arXiv:1103.3260] [INSPIRE].

[62] T. Kobayashi, M. Yamaguchi and J. Yokoyama, *Generalized G-inflation: inflation with the most general second-order field equations*, *Prog. Theor. Phys.* **126** (2011) 511 [arXiv:1105.5723] [INSPIRE].

[63] A. Barreira, B. Li, E. Jennings, J. Merten, L. King, C. Baugh et al., *Galaxy cluster lensing masses in modified lensing potentials*, arXiv:1505.03468 [INSPIRE].

[64] T. Kitayama et al., *ASTRO-H white paper — clusters of galaxies and related science*, arXiv:1412.1176 [INSPIRE].

[65] H. Honda et al., *Detection of a temperature structure in the Coma cluster of galaxies with ASCA*, *Astrophys. J.* **473** (1996) L71.

[66] M. Watanabe et al., *Temperature map of the Coma cluster of galaxies*, *Astrophys. J.* **527** (1999) 80.

[67] M. Arnaud et al., *XMM-Newton observation of the Coma galaxy cluster: the temperature structure in the central region*, *Astron. Astrophys.* **365** (2001) L67 [astro-ph/0011086] [INSPIRE].

[68] D.M. Neumann, D.H. Lumb, G.W. Pratt and U.G. Briel, *The dynamical state of the Coma cluster with XMM-Newton*, *Astron. Astrophys.* **400** (2003) 811 [astro-ph/0212432] [INSPIRE].

[69] N. Okabe et al., *Universal profiles of the intracluster medium from Suzaku X-ray and Subaru weak-lensing observations*, *Publ. Astron. Soc. Jap.* **66** (2014) 99 [arXiv:1406.3451] [INSPIRE].

[70] K.A. Pimbblet, S.J. Penny and R.L. Davies, *How typical is the Coma cluster?*, *Mon. Not. Roy. Astron. Soc.* **438** (2014) 3049 [arXiv:1312.3698] [INSPIRE].

[71] DARK ENERGY SURVEY collaboration, T. Abbott et al., *The dark energy survey*, astro-ph/0510346 [INSPIRE].

[72] EROSITA collaboration, A. Merloni et al., *eROSITA science book: mapping the structure of the energetic universe*, arXiv:1209.3114 [INSPIRE].

[73] *The dark energy survey webpage*, http://www.darkenergysurvey.org.

[74] M.D. Niemack et al., *ACTPol: a polarization-sensitive receiver for the Atacama Cosmology Telescope*, *Proc. SPIE Int. Soc. Opt. Eng.* **7741** (2010) 77411S [arXiv:1006.5049] [INSPIRE].

[75] SPT collaboration, J.E. Ruhl et al., *The South Pole Telescope*, *Proc. SPIE Int. Soc. Opt. Eng.* **5498** (2004) 11 [astro-ph/0411122] [INSPIRE].

[76] *The South Pole Telescope webpage*, http://pole.uchicago.edu/index.php.

[77] T. Narikawa, R. Kimura, T. Yano and K. Yamamoto, *Halo models in modified gravity theories with self-accelerated expansion*, *Int. J. Mod. Phys.* **D 20** (2011) 2383 [arXiv:1108.2346] [INSPIRE].

[78] A. Barreira, B. Li, C. Baugh and S. Pascoli, *The observational status of Galileon gravity after Planck*, *JCAP* **08** (2014) 059 [arXiv:1406.0485] [INSPIRE].

[79] S. Nesseris, A. De Felice and S. Tsujikawa, *Observational constraints on Galileon cosmology*, *Phys. Rev.* **D 82** (2010) 124054 [arXiv:1010.0407] [INSPIRE].

[80] F. Schmidt, *Cosmological simulations of normal-branch braneworld gravity*, *Phys. Rev.* **D 80** (2009) 123003 [arXiv:0910.0235] [INSPIRE].

JCAP10(2015)064

参考論文

1. Bispectrum of cosmological density perturbations in the most general second-order scalar-tensor theory
   Y. Takushima, A. Terukina and K. Yamamoto
   Physical Review D 89 (2014) 104007

2. What can we learn from higher multipole power spectra of galaxy distribution in redshift space?
   T. Kanemaru, C. Hikage, G. Huetsi, A. Terukina and K. Yamamoto
   Physical Review D 02 (2015) 92

3. Third order solutions of the cosmological density perturbations in the Horndeski's most general scalar-tensor theory with the Vainshtein mechanism
   Y. Takushima, A. Terukina and K. Yamamoto

4. The XMM Cluster Survey: Testing chameleon gravity using the profiles of clusters
   H. Wilcox, D. Bacon, R.C Nichol, P.J.Rooney, A. Terukina, A.K Romer, K. Koyama, G-B, Zhao, R. Hood, R.G. Mann, M. Hilton, M. Manolopoulou, M. Sahlen, C.A. Collins, A.R. Liddle, J.A. Mayers, N. Mehrtens, C.J. Miller, J.P. Stott and P.T.P. Viana
   Monthly Notices of the Royal Astronomical Society 452 (2015) 1171

PHYSICAL REVIEW D **89,** 104007 (2014)

Bispectrum of cosmological density perturbations in the most general second-order scalar-tensor theory

Yuichiro Takushima,[1] Ayumu Terukina,[1] and Kazuhiro Yamamoto[1,2]

[1]*Department of Physical Sciences, Hiroshima University, 1-3-1 Kagamiyama, Higashi-hiroshima, Hiroshima 739-8526, Japan*

[2]*Hiroshima Astrophysical Science Center, Hiroshima University, 1-3-1 Kagamiyama, Higashi-hiroshima, Hiroshima 739-8526, Japan*

(Received 10 November 2013; published 5 May 2014)

We study the bispectrum of matter density perturbations induced by the large-scale structure formation in the most general second-order scalar-tensor theory that may possess the Vainshtein mechanism as a screening mechanism. On the basis of the standard perturbation theory, we derive the bispectrum being expressed by a kernel of the second-order density perturbations. We find that the leading-order kernel is characterized by one parameter, which is determined by the solutions of the linear density perturbations, the Hubble parameter, and the other function specifying nonlinear interactions. This is because our model, which may be equipped with the Vainshtein mechanism, includes only one simple function that describes mode couplings of the nonlinear interactions. This feature does not allow for varied behavior in the bispectrum of the matter density perturbations in the most general second-order scalar-tensor theory equipped with the Vainshtein mechanism. We exemplify the typical behavior of the bispectrum in a kinetic gravity braiding model.

DOI: 10.1103/PhysRevD.89.104007 PACS numbers: 04.50.Kd, 95.36.+x

I. INTRODUCTION

Researchers are interested in modified gravity models as alternatives for explaining the accelerated expansion of the universe without introducing the cosmological constant [1–13]. The most general second-order scalar-tensor theory was first constructed by Horndeski [14] and was rediscovered in [15] as a generalization of the Galileon theories [16–36]. In addition to the possibility of constructing cosmological models with accelerated expansion, this theory has the following interesting features. The equation of motion is a second-order differential equation. Thus, an additional degree of freedom is not introduced, which is advantageous to avoid the appearance of ghosts. Furthermore, the Galileon theory is endowed with the Vainshtein mechanism [33], which is a screening mechanism useful for evading local gravity constraints. In the most general second-order scalar-tensor theory, the Vainshtein mechanism may work depending on the model parameters (e.g., [37–39]).

The results from the Planck satellite have shown that the primordial perturbations almost obey Gaussian statistics [40]. Even if the initial perturbations were completely Gaussian, the non-Gaussian nature of the density perturbations is induced in the large-scale structure formation through nonlinear fluid equations under the influence of the gravitational force. The bispectrum is often used to characterize the nonlinear and non-Gaussian nature of the density perturbations (e.g., [41–45]). Recently, the bispectrum and nonlinear features in the structure formation in the Galileon models have been investigated [46–52]. In the present paper, we focus on the bispectrum in the most general second-order scalar-tensor theory, which we regard as an effective theory, in order to elucidate the characteristic features of a wide class of modified gravity models. An advantage of such a general theory is that we can discuss general features of a wide class of modified gravity models, which is useful for forecasting their detectability in future large surveys.

In the present paper, we consider the bispectrum of the matter density perturbations induced in the large-scale structure formation after the matter-dominated era. We present an expression of the bispectrum in the most general second-order scalar-tensor theory based on the standard density perturbation theory, which is written in terms of a kernel of second-order perturbations. We find that the kernel is characterized by only *one* parameter, which is determined by the solutions of the linear density perturbations, the Hubble parameter, and the other function that describes the nonlinear interactions of the background universe. This paper is organized as follows. In Sec. II, we apply the standard perturbation theory to the most general second-order scalar-tensor theory that may possess the Vainshtein mechanism, and we find the solution of the second-order of density perturbations. In Sec. III, we present the expression of the bispectrum of the density perturbations, and we investigate the influence of the modification of gravity. The results are applied to a simple kinetic gravity braiding model in Sec. IV. Section V presents a summary and conclusions.

II. FORMULATION

We consider the most general second-order scalar-tensor theory on the expanding universe background. The action is given by

 © 2014 American Physical Society

$$S = \int d^4x\sqrt{-g}(\mathcal{L}_{\rm GG} + \mathcal{L}_{\rm m}), \tag{1}$$

where we define

$$\begin{aligned}\mathcal{L}_{\rm GG} &= K(\phi, X) - G_3(\phi, X)\Box\phi + G_4(\phi, X)R \\ &\quad + G_{4X}[(\Box\phi)^2 - (\nabla_\mu\nabla_\nu\phi)^2] + G_5(\phi, X)G_{\mu\nu}\nabla^\mu\nabla^\nu\phi \\ &\quad - \frac{1}{6}G_{5X}[(\Box\phi)^3 - 3\Box\phi(\nabla_\mu\nabla_\nu\phi)^2 + 2(\nabla_\mu\nabla_\nu\phi)^3],\end{aligned} \tag{2}$$

with four arbitrary functions of ϕ and $X := -(\partial\phi)^2/2$, K, G_3, G_4, and G_5. Furthermore, G_{iX} stands for $\partial G_i/\partial X$, R is the Ricci scalar, $G_{\mu\nu}$ is the Einstein tensor, and $\mathcal{L}_{\rm m}$ is the matter Lagrangian, which is assumed to be minimally coupled to gravity. This theory is found in [15] as a generalization of the Galileon theory, but is shown to be equivalent to Horndeski's theory in [16]. We consider a spatially flat expanding universe and the metric perturbations in the Newtonian gauge, whose line element is written as

$$ds^2 = -(1 + 2\Phi)dt^2 + a^2(1 - 2\Psi)d\mathbf{x}^2. \tag{3}$$

We define the scalar field with perturbations by

$$\phi \to \phi(t) + \delta\phi(t, \mathbf{x}), \tag{4}$$

with which we introduce $Q := H\delta\phi/\dot{\phi}$.

We consider the case where the Vainshtein mechanism may work as a screening mechanism. The basic equations for the cosmological density perturbations are derived in Ref. [37]. Here we briefly review the method and the results. The basic equations of the gravitational and scalar fields are derived on the basis of the quasistatic approximation of the subhorizon scales. The models for which the Vainshtein mechanism works can be found as follows. The equations are derived by keeping the leading terms schematically written as $(\partial\partial Y)^n$, with $n \geq 1$, where ∂ denotes a spatial derivative and Y denotes any of Φ, Ψ, or Q. Such terms make a leading contribution of the order $(L_{\rm H}^2\partial\partial Y)^n$, where $L_{\rm H}$ is a typical horizon length scale. According to Ref. [37], from the gravitational field equation, we have

$$\begin{aligned}&\nabla^2(\mathcal{F}_T\Psi - \mathcal{G}_T\Phi - A_1Q) \\ &\quad = \frac{B_1}{2a^2H^2}\mathcal{Q}^{(2)} + \frac{B_3}{a^2H^2}(\nabla^2\Phi\nabla^2Q - \partial_i\partial_j\Phi\partial^i\partial^jQ),\end{aligned} \tag{5}$$

$$\begin{aligned}\mathcal{G}_T\nabla^2\Psi &= \frac{a^2}{2}\rho_{\rm m}\delta - A_2\nabla^2Q - \frac{B_2}{2a^2H^2}\mathcal{Q}^{(2)} \\ &\quad - \frac{B_3}{a^2H^2}(\nabla^2\Psi\nabla^2Q - \partial_i\partial_j\Psi\partial^i\partial^jQ) \\ &\quad - \frac{C_1}{3a^4H^4}\mathcal{Q}^{(3)},\end{aligned} \tag{6}$$

where $\rho_{\rm m}$ is the matter density, δ is the matter density contrast, and we define

$$\mathcal{Q}^{(2)} := (\nabla^2Q)^2 - (\partial_i\partial_jQ)^2, \tag{7}$$

$$\mathcal{Q}^{(3)} := (\nabla^2Q)^3 - 3\nabla^2Q(\partial_i\partial_jQ)^2 + 2(\partial_i\partial_jQ)^3. \tag{8}$$

From the equation of motion of the scalar field, we have

$$\begin{aligned}&A_0\nabla^2Q - A_1\nabla^2\Psi - A_2\nabla^2\Phi + \frac{B_0}{a^2H^2}\mathcal{Q}^{(2)} \\ &\quad - \frac{B_1}{a^2H^2}(\nabla^2\Psi\nabla^2Q - \partial_i\partial_j\Psi\partial^i\partial^jQ) \\ &\quad - \frac{B_2}{a^2H^2}(\nabla^2\Phi\nabla^2Q - \partial_i\partial_j\Phi\partial^i\partial^jQ) \\ &\quad - \frac{B_3}{a^2H^2}(\nabla^2\Phi\nabla^2\Psi - \partial_i\partial_j\Phi\partial^i\partial^j\Psi) \\ &\quad - \frac{C_0}{a^4H^4}\mathcal{Q}^{(3)} - \frac{C_1}{a^4H^4}\mathcal{U}^{(3)} = 0,\end{aligned} \tag{9}$$

where we define

$$\begin{aligned}\mathcal{U}^{(3)} &:= \mathcal{Q}^{(2)}\nabla^2\Phi - 2\nabla^2Q\partial_i\partial_jQ\partial^i\partial^j\Phi \\ &\quad + 2\partial_i\partial_jQ\partial^j\partial^kQ\partial_k\partial^i\Phi.\end{aligned} \tag{10}$$

The coefficients ($\mathcal{F}_T$, A_1, B_1, etc.) in the field equations here and below are defined in Appendix A. A_i, B_i, and C_i are the coefficients of the linear, quadratic, and cubic terms of Ψ, Φ, and Q, respectively.

Equations for the matter density contrast δ and the velocity field u^i are given by

$$\frac{\partial\delta(t, \mathbf{x})}{\partial t} + \frac{1}{a}\partial_i[(1 + \delta(t, \mathbf{x}))u^i(t, \mathbf{x})] = 0, \tag{11}$$

$$\frac{\partial u^i(t, \mathbf{x})}{\partial t} + \frac{\dot{a}}{a}u^i(t, \mathbf{x}) + \frac{1}{a}u^j(t, \mathbf{x})\partial_ju^i(t, \mathbf{x}) = -\frac{1}{a}\partial^i\Phi(t, \mathbf{x}), \tag{12}$$

where the dot denotes differentiation with respect to t. Gravity exerts an effect via the gravitational potential Φ, which is determined by (5), (6), and (9). Here, we consider the scalar mode of the density perturbations, and then we introduce a scalar function by $\theta \equiv \nabla\mathbf{u}/(aH)$. Let us define the Fourier expansion of the quantities δ and θ:

$$\delta(t, \mathbf{x}) = \frac{1}{(2\pi)^3}\int d^3p\,\delta(t, \mathbf{p})e^{i\mathbf{p}\cdot\mathbf{x}}, \tag{13}$$

$$u^j(t, \mathbf{x}) = \frac{1}{(2\pi)^3}\int d^3p\,\frac{-ip^j}{p^2}aH\theta(t, \mathbf{p})e^{i\mathbf{p}\cdot\mathbf{x}}. \tag{14}$$

The Fourier expansion of Φ, Ψ, and Q is defined as in (13). Then, (5) and (6) yield

$$-p^2(\mathcal{F}_T\Psi(t,\mathbf{p})-\mathcal{G}_T\Phi(t,\mathbf{p})-A_1Q(t,\mathbf{p}))=\frac{B_1}{2a^2H^2}\Gamma[t,\mathbf{p};Q,Q]+\frac{B_3}{a^2H^2}\Gamma[t,\mathbf{p};Q,\Phi], \tag{15}$$

$$\begin{aligned}-p^2(\mathcal{G}_T\Psi(t,\mathbf{p})+A_2Q(t,\mathbf{p}))-\frac{a^2}{2}\rho_{\rm m}\delta(t,\mathbf{p})=&-\frac{B_2}{2a^2H^2}\Gamma[t,\mathbf{p};Q,Q]-\frac{B_3}{a^2H^2}\Gamma[t,\mathbf{p};Q,\Psi]\\&-\frac{C_1}{3a^4H^4}\frac{1}{(2\pi)^6}\int d\mathbf{k}_1d\mathbf{k}_2d\mathbf{k}_3\delta^{(3)}(\mathbf{k}_1+\mathbf{k}_2+\mathbf{k}_3-\mathbf{p})\\&\times[-k_1^2k_2^2k_3^2+3k_1^2(\mathbf{k}_2\cdot\mathbf{k}_3)^2-2(\mathbf{k}_1\cdot\mathbf{k}_2)(\mathbf{k}_2\cdot\mathbf{k}_3)(\mathbf{k}_3\cdot\mathbf{k}_1)]\\&\times Q(t,\mathbf{k}_1)Q(t,\mathbf{k}_2)Q(t,\mathbf{k}_3),\end{aligned} \tag{16}$$

where we define

$$\Gamma[t,\mathbf{p};Y,Z]=\frac{1}{(2\pi)^3}\int d\mathbf{k}_1d\mathbf{k}_2\delta^{(3)}(\mathbf{k}_1+\mathbf{k}_2-\mathbf{p})(k_1^2k_2^2-(\mathbf{k}_1\cdot\mathbf{k}_2)^2)Y(t,\mathbf{k}_1)Z(t,\mathbf{k}_2). \tag{17}$$

Here, Y and Z denote any of Q, Φ, or Ψ. Equation (9) leads to

$$\begin{aligned}&-p^2(A_0Q(t,\mathbf{p})-A_1\Psi(t,\mathbf{p})-A_2\Phi(t,\mathbf{p}))\\&=-\frac{B_0}{a^2H^2}\Gamma[t,\mathbf{p};Q,Q]+\frac{B_1}{a^2H^2}\Gamma[t,\mathbf{p};Q,\Psi]+\frac{B_2}{a^2H^2}\Gamma[t,\mathbf{p};Q,\Phi]+\frac{B_3}{a^2H^2}\Gamma[t,\mathbf{p};\Psi,\Phi]\\&\quad+\frac{C_0}{a^4H^4}\frac{1}{(2\pi)^6}\int d\mathbf{k}_1d\mathbf{k}_2d\mathbf{k}_3\delta^{(3)}(\mathbf{k}_1+\mathbf{k}_2+\mathbf{k}_3-\mathbf{p})[-k_1^2k_2^2k_3^2+3k_1^2(\mathbf{k}_2\cdot\mathbf{k}_3)^2-2(\mathbf{k}_1\cdot\mathbf{k}_2)(\mathbf{k}_2\cdot\mathbf{k}_3)(\mathbf{k}_3\cdot\mathbf{k}_1)]\\&\quad\times Q(t,\mathbf{k}_1)Q(t,\mathbf{k}_2)Q(t,\mathbf{k}_3)+\frac{C_1}{a^4H^4}\frac{1}{(2\pi)^6}\int d\mathbf{k}_1d\mathbf{k}_2d\mathbf{k}_3\delta^{(3)}(\mathbf{k}_1+\mathbf{k}_2+\mathbf{k}_3-\mathbf{p})[-k_1^2k_2^2k_3^2+(\mathbf{k}_1\cdot\mathbf{k}_2)^2k_3^2\\&\quad+2k_1^2(\mathbf{k}_2\cdot\mathbf{k}_3)^2-2(\mathbf{k}_1\cdot\mathbf{k}_2)(\mathbf{k}_2\cdot\mathbf{k}_3)(\mathbf{k}_3\cdot\mathbf{k}_1)]Q(t,\mathbf{k}_1)Q(t,\mathbf{k}_2)\Phi(t,\mathbf{k}_3).\end{aligned} \tag{18}$$

Equations (11) and (12) are rewritten as

$$\frac{1}{H}\frac{\partial\delta(t,\mathbf{p})}{\partial t}+\theta(t,\mathbf{p})=-\frac{1}{(2\pi)^3}\int d\mathbf{k}_1d\mathbf{k}_2\delta^{(3)}(\mathbf{k}_1+\mathbf{k}_2-\mathbf{p})\left(1+\frac{\mathbf{k}_1\cdot\mathbf{k}_2}{k_1^2}\right)\theta(t,\mathbf{k}_1)\delta(t,\mathbf{k}_2), \tag{19}$$

$$\begin{aligned}\frac{1}{H}\frac{\partial\theta(t,\mathbf{p})}{\partial t}+\left(2+\frac{\dot H}{H^2}\right)\theta(t,\mathbf{p})-\frac{p^2}{a^2H^2}\Phi(t,\mathbf{p})=&-\frac{1}{2}\frac{1}{(2\pi)^3}\int d\mathbf{k}_1d\mathbf{k}_2\delta^{(3)}(\mathbf{k}_1+\mathbf{k}_2-\mathbf{p})\left(\frac{(\mathbf{k}_1\cdot\mathbf{k}_2)|\mathbf{k}_1+\mathbf{k}_2|^2}{k_1^2k_2^2}\right)\\&\times\theta(t,\mathbf{k}_1)\theta(t,\mathbf{k}_2).\end{aligned} \tag{20}$$

We find the solution in terms of a perturbative expansion, which can be written in the form

$$Y(t,\mathbf{p})=\sum_{n=1}Y_n(t,\mathbf{p}), \tag{21}$$

where Y denotes δ,θ,Ψ,Φ, or Q, and Y_n denotes the nth order solution of the expansion. In the present paper, we aim to solve the second-order solution. At the first order of the perturbative expansion, Φ_1, Ψ_1, and Q_1 are expressed by δ_1 as (25), (26), and (27), respectively. The modified gravity affects the matter density perturbation via Φ in the Euler equation at any order of perturbation. Using the continuity equation (33), we find that δ_1 obeys (34). At the second order of the perturbative expansion, Φ_2, Ψ_2, and Q_2 are expressed by the terms in proportion to δ_2 and $\mathcal{W}_\gamma$, (46), (47), and (48), and we find that δ_2 obeys (56). Note that the homogeneous equation of (56) is the same as the equation for δ_1. The source term of (56) is given by (64). From (56) with (64), we find that the modification due to the nonlinear interaction enters through only the function of $N_\gamma(t)$, while the other parts have the same structure as those in general relativity. These facts are important for our conclusion that the second-order kernel is characterized by only one parameter.

Now we start from the first-order equations, which can easily be solved as follows [53]. From (15), (16), and (18), we have

$$\mathcal{F}_T p^2 \Psi_1(t,\mathbf{p}) - \mathcal{G}_T p^2 \Phi_1(t,\mathbf{p}) - A_1 p^2 Q_1(t,\mathbf{p}) = 0, \quad (22)$$

$$\mathcal{G}_T p^2 \Psi_1(t,\mathbf{p}) + A_2 p^2 Q_1(t,\mathbf{p}) = -\frac{a^2}{2}\rho_{\rm m}\delta_1(t,\mathbf{p}), \quad (23)$$

$$A_0 p^2 Q_1(t,\mathbf{p}) - A_1 p^2 \Psi_1(t,\mathbf{p}) - A_2 p^2 \Phi_1(t,\mathbf{p}) = 0, \quad (24)$$

which give the solutions

$$\Phi_1(t,\mathbf{p}) = -\frac{a^2H^2}{p^2}\kappa_\Phi(t)\delta_1(t,\mathbf{p}), \quad (25)$$

$$\Psi_1(t,\mathbf{p}) = -\frac{a^2H^2}{p^2}\kappa_\Psi(t)\delta_1(t,\mathbf{p}), \quad (26)$$

$$Q_1(t,\mathbf{p}) = -\frac{a^2H^2}{p^2}\kappa_Q(t)\delta_1(t,\mathbf{p}). \quad (27)$$

Here, we define

$$\kappa_\Phi(t) = \frac{\rho_{\rm m}\mathcal{R}(t)}{H^2\mathcal{Z}(t)}, \quad \kappa_\Psi(t) = \frac{\rho_{\rm m}\mathcal{S}(t)}{H^2\mathcal{Z}(t)}, \quad \kappa_Q(t) = \frac{\rho_{\rm m}\mathcal{T}(t)}{H^2\mathcal{Z}(t)}, \quad (28)$$

and

$$\mathcal{R}(t) = A_0\mathcal{F}_T - A_1^2, \quad (29)$$

$$\mathcal{S}(t) = A_0\mathcal{G}_T + A_1A_2, \quad (30)$$

$$\mathcal{T}(t) = A_1\mathcal{G}_T + A_2\mathcal{F}_T, \quad (31)$$

$$\mathcal{Z}(t) = 2(A_0\mathcal{G}_T^2 + 2A_1A_2\mathcal{G}_T + A_2^2\mathcal{F}_T). \quad (32)$$

The first-order equation of (19) is

$$\theta_1(t,\mathbf{p}) = -\frac{1}{H}\frac{\partial\delta_1(t,\mathbf{p})}{\partial t}. \quad (33)$$

Substituting (33) and (25) into the first-order equation of (20), we have

$$\frac{\partial^2\delta_1(t,\mathbf{p})}{\partial t^2} + 2H\frac{\partial\delta_1(t,\mathbf{p})}{\partial t} + L(t)\delta_1(t,\mathbf{p}) = 0, \quad (34)$$

where we defined

$$L(t) = -\kappa_\Phi H^2 \quad (35)$$

$$= -\frac{(A_0\mathcal{F}_T - A_1^2)\rho_{\rm m}}{2(A_0\mathcal{G}_T^2 + 2A_1A_2\mathcal{G}_T + A_2^2\mathcal{F}_T)}. \quad (36)$$

This second-rank differential equation has the growing mode solution $D_+(t)$ and the decaying mode solution $D_-(t)$. Neglecting the decaying mode solution, we write the first-order solution,

$$\delta_1(t,\mathbf{p}) = D_+(t)\delta_{\rm L}(\mathbf{p}), \quad (37)$$

where $\delta_{\rm L}(\mathbf{p})$ is a constant, which is determined by the initial density fluctuations. We assume that $\delta_{\rm L}(\mathbf{p})$ obeys the Gaussian random statistics. Here we adopt the normalization $D_+(a) = a$ at $a \ll 1$. The first-order solutions for the other quantities can be expressed in terms of $\delta_1(t,\mathbf{p})$.

Then, we consider the second-order equations of the perturbative expansion. From (15), (16), and (18), the second-order equations are

$$-p^2(\mathcal{F}_T\Psi_2(t,\mathbf{p}) - \mathcal{G}_T\Phi_2(t,\mathbf{p}) - A_1Q_2(t,\mathbf{p})) = \frac{B_1}{2a^2H^2}\Gamma[t,\mathbf{p};Q_1,Q_1] + \frac{B_3}{a^2H^2}\Gamma[t,\mathbf{p};Q_1,\Phi_1], \quad (38)$$

$$-p^2(\mathcal{G}_T\Psi_2(t,\mathbf{p}) + A_2Q_2(t,\mathbf{p}) = \frac{a^2}{2}\rho_{\rm m}\delta_2(t,\mathbf{p}) - \frac{B_2}{2a^2H^2}\Gamma[t,\mathbf{p};Q_1,Q_1] - \frac{B_3}{a^2H^2}\Gamma[t,\mathbf{p};Q_1,\Psi_1], \quad (39)$$

$$-p^2(A_0Q_2(t,\mathbf{p}) - A_1\Psi_2(t,\mathbf{p}) - A_2\Phi_2(t,\mathbf{p})) = -\frac{B_0}{a^2H^2}\Gamma[t,\mathbf{p};Q_1,Q_1] + \frac{B_1}{a^2H^2}\Gamma[t,\mathbf{p};Q_1,\Psi_1] + \frac{B_2}{a^2H^2}\Gamma[t,\mathbf{p};Q_1,\Phi_1] + \frac{B_3}{a^2H^2}\Gamma[t,\mathbf{p};\Psi_1,\Phi_1]. \quad (40)$$

Using the first-order solutions (25), (26), (27), and (37), the above equations are rewritten as

$$-p^2(\mathcal{F}_T\Psi_2(t,\mathbf{p}) - \mathcal{G}_T\Phi_2(t,\mathbf{p}) - A_1Q_2(t,\mathbf{p})) = D_+^2(t)a^2H^2\left(\frac{1}{2}B_1\kappa_Q^2 + B_3\kappa_\Phi\kappa_Q\right)\mathcal{W}_\gamma(\mathbf{p}), \quad (41)$$

$$-p^2(\mathcal{G}_T\Psi_2(t,\mathbf{p}) + A_2Q_2(t,\mathbf{p})) = \frac{a^2}{2}\rho_{\rm m}\delta_2(t,\mathbf{p}) + D_+^2(t)a^2H^2\left(-\frac{1}{2}B_2\kappa_Q^2 - B_3\kappa_\Psi\kappa_Q\right)\mathcal{W}_\gamma(\mathbf{p}), \quad (42)$$

$$-p^2(A_0Q_2(t,\mathbf{p}) - A_1\Psi_2(t,\mathbf{p}) - A_2\Phi_2(t,\mathbf{p})) = D_+^2(t)a^2H^2(-B_0\kappa_Q^2 + B_1\kappa_\Psi\kappa_Q + B_2\kappa_\Phi\kappa_Q + B_3\kappa_\Phi\kappa_\Psi)\mathcal{W}_\gamma(\mathbf{p}), \quad (43)$$

where we defined

$$\mathcal{W}_\gamma(\mathbf{p}) = \frac{1}{(2\pi)^3}\int d\mathbf{k}_1 d\mathbf{k}_2 \delta^{(3)}(\mathbf{k}_1+\mathbf{k}_2-\mathbf{p})\gamma(\mathbf{k}_1,\mathbf{k}_2) \times \delta_{\rm L}(\mathbf{k}_1)\delta_{\rm L}(\mathbf{k}_2), \tag{44}$$

$$\gamma(\mathbf{k}_1,\mathbf{k}_2) = 1-\frac{(\mathbf{k}_1\cdot\mathbf{k}_2)^2}{k_1^2k_2^2}. \tag{45}$$

These equations yield

$$\Phi_2(t,\mathbf{p}) = -\frac{a^2H^2}{p^2}(\kappa_\Phi(t)\delta_2(t,\mathbf{p}) + D_+^2(t)\tau_\Phi(t)\mathcal{W}_\gamma(\mathbf{p})), \tag{46}$$

$$\Psi_2(t,\mathbf{p}) = -\frac{a^2H^2}{p^2}(\kappa_\Psi(t)\delta_2(t,\mathbf{p}) + D_+^2(t)\tau_\Psi(t)\mathcal{W}_\gamma(\mathbf{p})), \tag{47}$$

$$Q_2(t,\mathbf{p}) = -\frac{a^2H^2}{p^2}(\kappa_Q(t)\delta_2(t,\mathbf{p}) + D_+^2(t)\tau_Q(t)\mathcal{W}_\gamma(\mathbf{p})), \tag{48}$$

where we defined

$$\tau_\Phi(t) = \frac{1}{\mathcal{Z}}(2B_0\mathcal{T}\kappa_Q^2 - 3B_1\mathcal{S}\kappa_Q^2 - 3B_2\mathcal{R}\kappa_Q^2 - 6B_3\mathcal{R}\kappa_\Psi\kappa_Q), \tag{49}$$

$$\tau_\Psi(t) = \frac{1}{\mathcal{Z}}(2B_0A_2\mathcal{G}_T\kappa_Q^2 + B_1(A_2^2\kappa_Q^2 - 2A_2\mathcal{G}_T\kappa_\Psi\kappa_Q) - B_2(\mathcal{S}\kappa_Q^2 + 2A_2\mathcal{G}_T\kappa_\Phi\kappa_Q) - 2B_3(\mathcal{S}\kappa_\Psi\kappa_Q - A_2^2\kappa_\Phi\kappa_Q + A_2\mathcal{G}_T\kappa_\Phi\kappa_\Psi)), \tag{50}$$

$$\tau_Q(t) = -\frac{1}{\mathcal{Z}}(2B_0\mathcal{G}_T^2\kappa_Q^2 + B_1(A_2\mathcal{G}_T\kappa_Q^2 - 2\mathcal{G}_T^2\kappa_\Psi\kappa_Q) + B_2(\mathcal{T}\kappa_Q^2 - 2\mathcal{G}_T^2\kappa_\Phi\kappa_Q) + 2B_3(\mathcal{T}\kappa_\Psi\kappa_Q + A_2\mathcal{G}_T\kappa_\Phi\kappa_Q - \mathcal{G}_T^2\kappa_\Phi\kappa_\Psi)). \tag{51}$$

The second-order equations of (19) and (20) are

$$\frac{1}{H}\frac{\partial\delta_2(t,\mathbf{p})}{\partial t} + \theta_2(t,\mathbf{p}) = -\frac{1}{(2\pi)^3}\int d\mathbf{k}_1 d\mathbf{k}_2\delta^{(3)}(\mathbf{k}_1+\mathbf{k}_2-\mathbf{p})\alpha(\mathbf{k}_1,\mathbf{k}_2) \times \theta_1(t,\mathbf{k}_1)\delta_1(t,\mathbf{k}_2), \tag{52}$$

$$\frac{1}{H}\frac{\partial\theta_2(t,\mathbf{p})}{\partial t} + \left(2+\frac{\dot H}{H^2}\right)\theta_2(t,\mathbf{p}) - \frac{p^2}{a^2H^2}\Phi_2(t,\mathbf{p}) = -\frac{1}{(2\pi)^3}\int d\mathbf{k}_1 d\mathbf{k}_2\delta^{(3)}(\mathbf{k}_1+\mathbf{k}_2-\mathbf{p})\beta(\mathbf{k}_1,\mathbf{k}_2) \times \theta_1(t,\mathbf{k}_1)\theta_1(t,\mathbf{k}_2), \tag{53}$$

where we define

$$\alpha(\mathbf{k}_1,\mathbf{k}_2) = 1+\frac{\mathbf{k}_1\cdot\mathbf{k}_2}{k_1^2}, \tag{54}$$

$$\beta(\mathbf{k}_1,\mathbf{k}_2) = \frac{(\mathbf{k}_1\cdot\mathbf{k}_2)|\mathbf{k}_1+\mathbf{k}_2|^2}{2k_1^2k_2^2}. \tag{55}$$

Combining (52) and (53), and using the first-order solution and (46), we have

$$\frac{\partial^2\delta_2(t,\mathbf{p})}{\partial t^2} + 2H\frac{\partial\delta_2(t,\mathbf{p})}{\partial t} + L(t)\delta_2(t,\mathbf{p}) = S_\delta(t,\mathbf{p}), \tag{56}$$

where we define

$$S_\delta(t,\mathbf{p}) = (\dot D_+^2(t) - L(t)D_+^2(t))\mathcal{W}_\alpha(\mathbf{p}) + \dot D_+^2(t)\mathcal{W}_\beta(\mathbf{p}) + N_\gamma(t)D_+^2(t)\mathcal{W}_\gamma(\mathbf{p}), \tag{57}$$

$$\mathcal{W}_\alpha(\mathbf{p}) = \frac{1}{(2\pi)^3}\int d\mathbf{k}_1 d\mathbf{k}_2\delta^{(3)}(\mathbf{k}_1+\mathbf{k}_2-\mathbf{p}) \times \alpha(\mathbf{k}_1,\mathbf{k}_2)\delta_{\rm L}(\mathbf{k}_1)\delta_{\rm L}(\mathbf{k}_2), \tag{58}$$

$$\mathcal{W}_\beta(\mathbf{p}) = \frac{1}{(2\pi)^3}\int d\mathbf{k}_1 d\mathbf{k}_2\delta^{(3)}(\mathbf{k}_1+\mathbf{k}_2-\mathbf{p}) \times \beta(\mathbf{k}_1,\mathbf{k}_2)\delta_{\rm L}(\mathbf{k}_1)\delta_{\rm L}(\mathbf{k}_2), \tag{59}$$

and

$$N_\gamma(t) = \tau_\Phi H^2 = \frac{H^4}{\rho_{\rm m}}(2B_0\kappa_Q^3 - 3B_1\kappa_\Psi\kappa_Q^2 - 3B_2\kappa_\Phi\kappa_Q^2 - 6B_3\kappa_\Phi\kappa_\Psi\kappa_Q). \tag{60}$$

In deriving (57), we use (34). Because of the symmetry with respect to the interchange of $\mathbf{k}_1$ and $\mathbf{k}_2$, we define $\alpha^{(s)}(\mathbf{k}_1,\mathbf{k}_2)$ as follows:

$$\alpha^{(s)}(\mathbf{k}_1,\mathbf{k}_2) = 1+\frac{\mathbf{k}_1\cdot\mathbf{k}_2(k_1^2+k_2^2)}{2k_1^2k_2^2}. \tag{61}$$

Using the symmetry, we redefine $\mathcal{W}_\alpha(\mathbf{p})$ as

$$\mathcal{W}_\alpha(\mathbf{p}) = \frac{1}{(2\pi)^3}\int d\mathbf{k}_1 d\mathbf{k}_2\delta^{(3)}(\mathbf{k}_1+\mathbf{k}_2-\mathbf{p})\alpha^{(s)}(\mathbf{k}_1,\mathbf{k}_2) \times \delta_{\rm L}(\mathbf{k}_1)\delta_{\rm L}(\mathbf{k}_2). \tag{62}$$

By the relation

$$\beta(\mathbf{k}_1,\mathbf{k}_2) = \alpha^{(s)}(\mathbf{k}_1,\mathbf{k}_2) - \gamma(\mathbf{k}_1,\mathbf{k}_2) \quad \text{or} \quad \mathcal{W}_\beta(\mathbf{p}) = \mathcal{W}_\alpha(\mathbf{p}) - \mathcal{W}_\gamma(\mathbf{p}), \tag{63}$$

Eq. (57) reduces to

$$S_\delta(t,\mathbf{p}) = D_+^2(t)\{(2f^2H^2 - L(t))\mathcal{W}_\alpha(\mathbf{p}) + (N_\gamma(t) - f^2H^2)\mathcal{W}_\gamma(\mathbf{p})\}, \tag{64}$$

where we define the growth rate as $f = d\ln D_+(t)/d\ln a$.

Note that the homogeneous equation of (56) is the same as that of the first-order equation. Therefore, we have the second-order solution:

$$\delta_2(t,\mathbf{p}) = c_+(\mathbf{p})D_+(t) + c_-(\mathbf{p})D_-(t) + \int_0^t dt' \frac{D_+(t')D_-(t) - D_+(t)D_-(t')}{W(t')} S_\delta(t',\mathbf{p}), \tag{65}$$

where $c_+(\mathbf{p})$ and $c_-(\mathbf{p})$ are constants, and $W(t)$ is the Wronskian $W(t) = D_+(t)\dot{D}_-(t) - \dot{D}_+(t)D_-(t)$. From equations for $D_+(t)$ and $D_-(t)$, Eq. (34), the Wronskian obeys $\dot{W}(t) + 2HW(t) = 0$, which yields

$$W(t) = \frac{C}{a^2}, \tag{66}$$

where C is a constant. In the present paper, we assume the initial density perturbations obey the Gaussian statistics, and we set $c_\pm(\mathbf{p}) = 0$. Then, the second-order solution is written in the form

$$\delta_2(t,\mathbf{p}) = D_+^2(t)\left(\kappa(t)\mathcal{W}_\alpha(\mathbf{p}) - \frac{2}{7}\lambda(t)\mathcal{W}_\gamma(\mathbf{p})\right), \tag{67}$$

with

$$\kappa(t) = \frac{1}{D_+^2(t)}\int_0^t \frac{D_-(t)D_+(t') - D_+(t)D_-(t')}{W(t')} \times D_+^2(t')(2f^2H^2 - L(t'))dt', \tag{68}$$

$$\lambda(t) = \frac{7}{2D_+^2(t)}\int_0^t \frac{D_-(t)D_+(t') - D_+(t)D_-(t')}{W(t')} \times D_+^2(t')(f^2H^2 - N_\gamma(t'))dt'. \tag{69}$$

These expressions are a generalization of the results in Ref. [51]. In Sec. IV, we numerically evaluate the function $\lambda(t)$ without neglecting the decaying model in a specific model.

In the case of the matter-dominated universe within general relativity, $a(t) \propto t^{2/3}$, $D_+(t) = a$, $D_-(t) = a^{-3/2}$, $L(t) = -3/(2H^2)$, and $N_\gamma(t) = 0$, then the second-order solution reduces to

$$\delta_2(t,\mathbf{p}) = D_+^2(t)\left(\mathcal{W}_\alpha(\mathbf{p}) - \frac{2}{7}\mathcal{W}_\gamma(\mathbf{p})\right). \tag{70}$$

That is, one finds $\kappa(t) = \lambda(t) = 1$ in the Einstein–de Sitter universe. Even in the general second-order scalar-tensor theory, we may consider models where the matter-dominated era is realized in the early stage of the universe. In this stage, the effect of the scalar field perturbations would be negligible, and we may naturally expect that the matter density perturbations grow in the same way as those in general relativity. In this case, $\kappa(t) = 1$ and $\lambda(t) = 1$ at $a \ll 1$.

Interestingly, we can show that (68) generally reduces to $\kappa(t) = 1$ for all times. Using the expression for the Wronskian (66), Eq. (68) is rewritten as

$$\kappa(t) = \frac{1}{CD_+^2(t)}\int_0^t a^2(t')(D_-(t)D_+(t') - D_+(t)D_-(t')) \times \{2\dot{D}_+^2(t') + D_+(t')(\ddot{D}_+(t') + 2H\dot{D}_+(t'))\}dt', \tag{71}$$

where we used the fact that $D_+(t')$ satisfies (34) to eliminate the term $L(t')$. Partially integrating the term $\ddot{D}_+(t')$ in (71), we have

$$\kappa(t) = \frac{1}{CD_+(t)}\int_0^t a^2(t')\{\dot{D}_-(t')D_+(t') - D_-(t')\dot{D}_+(t')\}\dot{D}_+(t')dt'. \tag{72}$$

Using the Wronskian, we finally obtain

$$\kappa(t) = 1, \tag{73}$$

for all times. Therefore, the kernel (81) depends on only the parameter $\lambda(t)$, which is determined by the solution of the linear density perturbation, $H(t)$ and the function $N_\gamma(t)$. This conclusion is a generalization of the results in Ref. [46]. The authors of Ref. [46] investigated the standard density perturbation theory in the Dvali, Gabadadze and Porrati model, and a similar result is obtained at the second order of perturbation (Appendix B.1 in their paper). The result is explained by $\alpha^{(s)}(\mathbf{k}_1,\mathbf{k}_2)$ and $\gamma(\mathbf{k}_1,\mathbf{k}_2)$ being independent of each other and the modification of gravity coming through only the terms in proportion to $\gamma(\mathbf{k}_1,\mathbf{k}_2)$ at the second order of perturbation. Therefore, the term in proportion to $\alpha^{(s)}(\mathbf{k}_1,\mathbf{k}_2)$ is not modified.

Finally, in this section, we present the expression of the velocity divergence at the second order of perturbation. We obtain the expression by inserting $\delta_1(t,\mathbf{p})$, $\theta_1(t,\mathbf{p})$, and $\delta_2(t,\mathbf{p})$ into (52),

$$\theta_2(t,\mathbf{p}) = -D_+^2(t)f\left(\mathcal{W}_\alpha(\mathbf{p}) - \frac{4}{7}\lambda_\theta(t)\mathcal{W}_\gamma(\mathbf{p})\right), \tag{74}$$

where we defined

$$\lambda_\theta(t) = \lambda(t) + \frac{\dot{\lambda}(t)}{2fH}. \tag{75}$$

In the Einstein–de Sitter universe, we have $\lambda_\theta(t) = 1$.

III. BISPECTRUM

In this section, we consider the bispectrum of the density perturbations in the most general second-order scalar-tensor theory on the cosmological background. The power spectrum and the bispectrum are defined by

$$\langle \delta(t,\mathbf{k}_1)\delta(t,\mathbf{k}_2)\rangle \equiv (2\pi)^3\delta^{(3)}(\mathbf{k}_1+\mathbf{k}_2)P(t,k_1), \tag{76}$$

$$\langle \delta(t,\mathbf{k}_1)\delta(t,\mathbf{k}_2)\delta(t,\mathbf{k}_3)\rangle \equiv (2\pi)^3\delta^{(3)}(\mathbf{k}_1+\mathbf{k}_2+\mathbf{k}_3)B(t,k_1,k_2,k_3), \tag{77}$$

respectively. The three-point function at the lowest order of the standard perturbation theory is evaluated as

$$\langle \delta(t,\mathbf{k}_1)\delta(t,\mathbf{k}_2)\delta(t,\mathbf{k}_3)\rangle = D_+^4(t)(\langle \delta_{\rm L}(\mathbf{k}_1)\delta_{\rm L}(\mathbf{k}_2)\delta_{\rm 2K}(t,\mathbf{k}_3)\rangle + 2 \text{ cyclic terms}), \tag{78}$$

where we define

$$\delta_{\rm 2K}(t,\mathbf{k}) = \mathcal{W}_\alpha(\mathbf{k}) - \frac{2}{7}\lambda(t)\mathcal{W}_\gamma(\mathbf{k}). \tag{79}$$

The first term in parentheses in the right-hand side of (78) is

$$\langle \delta_{\rm L}(\mathbf{k}_1)\delta_{\rm L}(\mathbf{k}_2)\delta_{\rm 2K}(t,\mathbf{k}_3)\rangle = \int \frac{d^3q_1}{(2\pi)^3} F_2(t,\mathbf{q}_1,\mathbf{k}_3-\mathbf{q}_1) \times \langle \delta_{\rm L}(\mathbf{k}_1)\delta_{\rm L}(\mathbf{k}_2)\delta_{\rm L}(\mathbf{q}_1)\delta_{\rm L}(\mathbf{k}_3-\mathbf{q}_1)\rangle, \tag{80}$$

where we define the kernel

$$F_2(t,\mathbf{k}_1,\mathbf{k}_2) \equiv \alpha^{(s)}(\mathbf{k}_1,\mathbf{k}_2) - \frac{2}{7}\lambda(t)\gamma(\mathbf{k}_1,\mathbf{k}_2). \tag{81}$$

Using the definition of the linear matter power spectrum,

$$\langle \delta_{\rm L}(\mathbf{k}_1)\delta_{\rm L}(\mathbf{k}_2)\rangle = (2\pi)^3\delta^{(3)}(\mathbf{k}_1+\mathbf{k}_2)P_{11}(k_1), \tag{82}$$

and Wick's theorem, we have

$$\langle \delta_{\rm L}(\mathbf{k}_1)\delta_{\rm L}(\mathbf{k}_2)\delta_{\rm 2K}(t,\mathbf{k}_3)\rangle = 2(2\pi)^3\delta^{(3)}(\mathbf{k}_1+\mathbf{k}_2+\mathbf{k}_3)F_2(t,\mathbf{k}_1,\mathbf{k}_2)P_{11}(k_1)P_{11}(k_2), \tag{83}$$

where we use $F_2(t,-\mathbf{k}_1,-\mathbf{k}_2) = F_2(t,\mathbf{k}_1,\mathbf{k}_2)$. Finally, we have the expression for the bispectrum at the lowest order of the perturbation theory,

$$B(t,k_1,k_2,k_3) = D_+^4(t)B_4(t,k_1,k_2,k_3) \tag{84}$$

with

$$B_4(t,k_1,k_2,k_3) = 2F_2(t,\mathbf{k}_1,\mathbf{k}_2)P_{11}(k_1)P_{11}(k_2) + 2 \text{ cyclic terms}. \tag{85}$$

The reduced bispectrum is given by

$$Q_{123}(t,k_1,k_2,\theta_{12}) = \frac{B_4(t,k_1,k_2,k_3)}{P_{11}(k_1)P_{11}(k_2)+P_{11}(k_2)P_{11}(k_3)+P_{11}(k_3)P_{11}(k_1)}, \tag{86}$$

at the lowest order of perturbations. Note that the (reduced) bispectrum is described by the kernel (81), which depends on only the parameter $\lambda(t)$, which is given by (69).

Because $\mathbf{k}_1+\mathbf{k}_2+\mathbf{k}_3 = 0$ is satisfied, the reduced bispectrum is a function of only three parameters, which we take as $k_1 = |\mathbf{k}_1|$, $k_2 = |\mathbf{k}_2|$, and the angle θ_{12} between $\mathbf{k}_1$ and $\mathbf{k}_2$. Explicit expressions for $\alpha^{(s)}(\mathbf{k}_i,\mathbf{k}_j)$, and $\gamma(\mathbf{k}_i,\mathbf{k}_j)$, where (i,j) denotes any of (1,2), (2,3), or (3,1), are summarized in Appendix B. Each panel of Fig. 1 shows a typical behavior of Q_{123} as a function of θ_{12} with fixed k_1 and k_2, whose values are described in the caption. In each panel, we adopt a different value of $\lambda(t) = 1$ (blue solid curve), $\lambda(t) = 1.2$ (red dotted curve), and $\lambda(t) = 0.8$ (yellow dashed curve), assuming a spatially flat universe with the CDM model and the cosmological constant Λ, whose density parameters are $\Omega_0 = 0.3$ and $\Omega_\Lambda = 0.7$, for the linear matter power spectrum $P_{11}(k)$. Note that the reduced bispectrum depends on time t through only $\lambda(t)$. One can see the following features. First, the overall amplitude of Q_{123} depends on the value of k_1 and k_2. However, when the values of k_1 and k_2 are fixed, the reduced bispectrum is enhanced for $\lambda < 1$ but reduced for $\lambda > 1$. This feature is explained by kernel (81) and the fact $\gamma(\mathbf{k}_i,\mathbf{k}_j) \geq 0$.

With the limit $\theta_{12} = 0$, we have $\gamma(\mathbf{k}_1,\mathbf{k}_2) = \gamma(\mathbf{k}_2,\mathbf{k}_3) = \gamma(\mathbf{k}_3,\mathbf{k}_1) = 0$ (see also Appendix B). Then, Q_{123} is independent of λ at $\theta_{12} = 0$. With the limit $\theta_{12} = \pi$, Q_{123} behave differently depending on the conditions $k_1 = k_2$ and $k_1 \neq k_2$. If $k_1 \neq k_2$, then we have $\gamma(\mathbf{k}_1,\mathbf{k}_2) = \gamma(\mathbf{k}_2,\mathbf{k}_3) = \gamma(\mathbf{k}_3,\mathbf{k}_1) = 0$, which is the same as with the limit $\theta_{12} = 0$. In the case $k_1 = k_2$, however, we have $\gamma(\mathbf{k}_1,\mathbf{k}_2) = 0$, $\gamma(\mathbf{k}_2,\mathbf{k}_3) = \gamma(\mathbf{k}_3,\mathbf{k}_1) = 1$, and $k_3 = 0$; that is, $P_{11}(k_3) = 0$. Then the bispectrum approaches zero with this limit, though the rate of convergence depends on $\lambda(t)$, as is discussed in the next section.

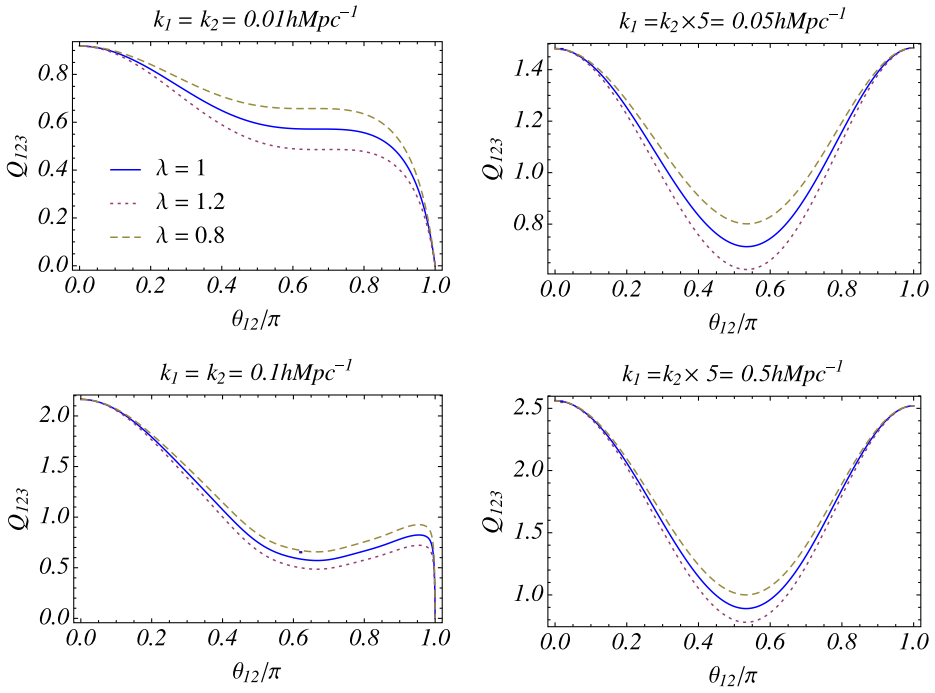

FIG. 1 (color online). Q_{123} as a function of θ_{12} with $k_1 = k_2 = 0.01h$ Mpc^{-1} (upper left panel), $k_1 = k_2 = 0.1h$ Mpc^{-1} (lower left panel), $k_1 = 5 \times k_2 = 0.05h$ Mpc^{-1} (upper right panel), and $k_1 = 5 \times k_2 = 0.5h$ Mpc^{-1} (lower right panel). For the linear matter power spectrum $P_{11}(k)$, we adopt the spatially flat universe with the cold dark matter (CDM) model and the cosmological constant Λ, whose density parameters are $\Omega_0 = 0.3$ and $\Omega_\Lambda = 0.7$, respectively. Note that the reduced bispectrum depends on time t through only $\lambda(t)$, for which we adopt different values of $\lambda(t) = 1$ (blue solid curve), $\lambda(t) = 1.2$ (red dotted curve), and $\lambda(t) = 0.8$ (yellow dashed curve), irrespective of the ΛCDM model.

All the influence of the nonlinear interaction of the modified gravity arises through only the parameter $\lambda(t)$, which appears as the term in proportion to $\gamma(\mathbf{k}_1, \mathbf{k}_2)$ in the kernel (81). The bispectrum of the matter density perturbations behaves in a restricted way only, which is a feature of the general second-order scalar-tensor theory equipped with the Vainshtein mechanism.

IV. KINETIC GRAVITY BRAIDING MODEL

In this section, we consider a simple example to demonstrate how the modification of gravity influences the behavior of the bispectrum at a quantitative level. We consider the kinetic gravity braiding model investigated in Refs. [31,52], whose action is written as

$$S = \int d^4x\sqrt{-g}\left[\frac{M_{\rm pl}^2}{2}R + K - G_3\Box\phi + \mathcal{L}_{\rm m}\right], \quad (87)$$

with the Planck mass $M_{\rm pl}$, which is related with the gravitational constant G_N by $8\pi G_N = 1/M_{\rm pl}^2$. Comparing this action (87) with that of the most general second-order scalar-tensor theory, the action of the kinetic gravity braiding model is produced by setting

$$G_4 = \frac{M_{\rm pl}^2}{2}, \qquad G_5 = 0. \quad (88)$$

In Ref. [52], K and G_3 are chosen as

$$K = -X, \qquad G_3 = M_{\rm pl}\left(\frac{r_c^2}{M_{\rm pl}^2}X\right)^n, \quad (89)$$

where n and r_c are parameters. In this model, we have

$$L(t) = -\frac{A_0\mathcal{F}_T\rho_{\rm m}}{2(A_0\mathcal{G}_T + A_2^2\mathcal{F}_T)}, \quad (90)$$

$$N_\gamma(t) = \frac{B_0A_2^3\mathcal{F}_T^3\rho_{\rm m}^2}{4(A_0\mathcal{G}_T^2 + A_2^2\mathcal{F}_T)^3H^2}. \quad (91)$$

Useful expressions of the kinetic gravity braiding model are summarized in Appendix A.

When we consider the attractor solution, which satisfies

$$3\dot{\phi}HG_{3X} = 1, \quad (92)$$

the Friedmann equation is written in the form

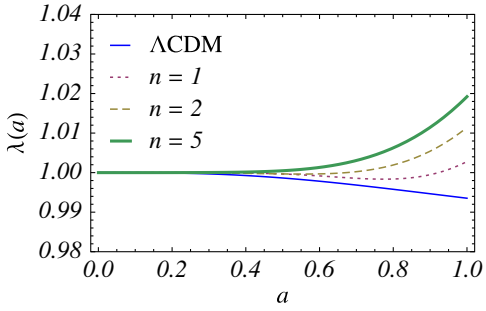

FIG. 2 (color online). $\lambda(t)$ as a function of a in the ΛCDM model (blue solid curve) and the kinetic gravity braiding model with $n = 1$ (red dotted curve), $n = 2$ (yellow dashed curve), and 5 (green thick curve).

$$\left(\frac{H}{H_0}\right)^2 = \frac{\Omega_0}{a^3} + (1-\Omega_0)\left(\frac{H}{H_0}\right)^{-2/(2n-1)}, \quad (93)$$

where H_0 is the Hubble constant and Ω_0 is the density parameter at the present time, and the model parameters must satisfy

$$H_0 r_c = \left(\frac{2^{n-1}}{3n}\right)^{1/2n}\left[\frac{1}{6(1-\Omega_0)}\right]^{(2n-1)/4n}. \quad (94)$$

On the attractor solution, $L(t)$ and $N_\gamma(t)$ reduce to

$$L(t) = -\frac{3}{2}\frac{2n+(3n-1)\Omega_m(t)}{5n-\Omega_m(t)}H^2, \quad (95)$$

$$N_\gamma(t) = -\frac{9}{4}\frac{(1-\Omega_m(t))(2n-\Omega_m(t))^3}{\Omega_m(t)(5n-\Omega_m(t))^3}H^2, \quad (96)$$

where $\Omega_m(a)$ is defined by $\Omega_m(a) = \Omega_0 H_0^2/H(a)^2 a^3$. Note that the quasistatic approximation on the scales of the large-scale structure holds for $n \lesssim 10$ (see [52]).

Figure 2 shows the evolution of $\lambda(t)$ as a function of a for the kinetic gravity braiding model with $n = 1, 2, 5$ and the ΛCDM model. For $a \ll 1$, we have $\lambda(t) = 1$, which is the prediction of the Einstein–de Sitter universe. However, the accelerated expansion arises due to domination of the Galileon field as a approaches 1, and so the value of $\lambda(t)$ starts to deviate from 1.

The deviation of $\lambda(t)$ from 1 is small. The value of $\lambda(t)$ at the present epoch is 0.994 under the ΛCDM model with the density parameter $\Omega_0 = 0.3$. The value of $\lambda(t)$ at the present epoch is 1.003, 1.011, and 1.019 under the kinetic gravity braiding (KGB) model with $n = 1, 2, 5$, respectively. Our results demonstrate the validity of the approximation setting $\lambda(t) = 1$, which is usually adopted in the standard density perturbations theory.

Figure 3 shows the relative deviation of the bispectrum at the present epoch under the KGB model from that under the ΛCDM model, $Q_{123}(t, k_1, k_2, \theta_{12})/Q_{123\Lambda}(t, k_1, k_2, \theta_{12}) - 1$, as a function of θ_{12}, where $Q_{123\Lambda}(t, k_1, k_2, \theta_{12})$ is the reduced bispectrum of the ΛCDM model. The relative deviation from the ΛCDM model is less than 2%. For the case $k_1 \neq k_2$, the deviation between the models does not appear at $\theta_{12} = 0, \pi$, which is simply understood by the fact that $\gamma(\mathbf{k}_i, \mathbf{k}_j) = 0$ there.

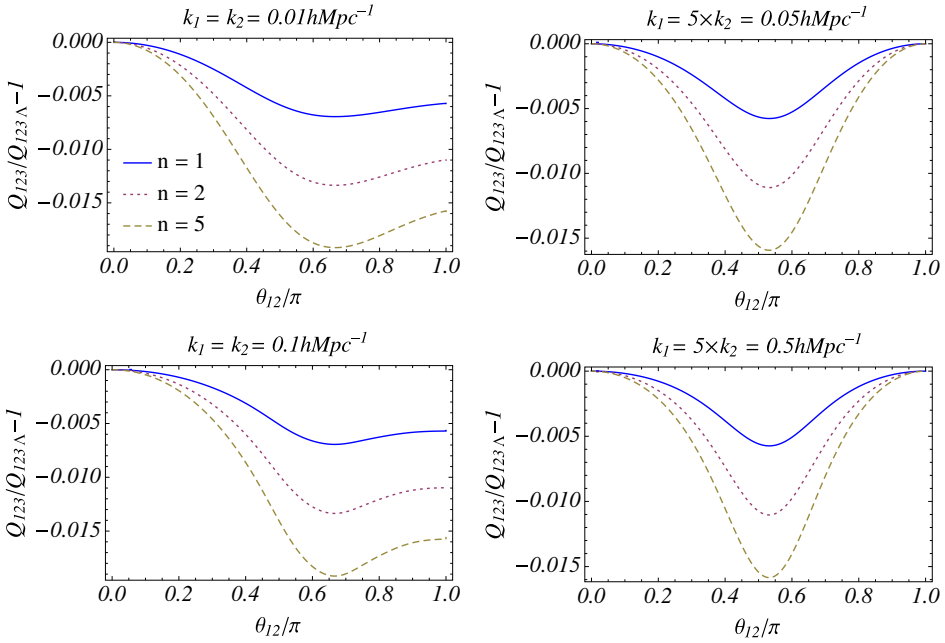

FIG. 3 (color online). Relative deviation of the reduced bispectrum at the present epoch under the kinetic gravity braiding model with $n = 1$ (blue solid curve), $n = 2$ (red dotted curve), $n = 5$ (yellow dashed curve) from that under the ΛCDM model $Q_{123\Lambda}$, as a function of θ_{12}, where k_1 and k_2 are fixed, whose values are noted on each panel. Here the density parameter is fixed as $\Omega_0 = 0.3$.

In the case $k_1 = k_2$ with the limit $\theta_{12} = \pi$, we have $\alpha^{(s)}(\mathbf{k}_1, \mathbf{k}_2) \sim (\pi - \theta_{12})^2$, $\alpha^{(s)}(\mathbf{k}_2, \mathbf{k}_3) = \alpha^{(s)}(\mathbf{k}_3, \mathbf{k}_1) = 3/4$, $\gamma(\mathbf{k}_1, \mathbf{k}_2) \sim (\pi - \theta_{12})^2$, $\gamma(\mathbf{k}_2, \mathbf{k}_3) = \gamma(\mathbf{k}_3, \mathbf{k}_1) = 1$, and $P(k_3) \propto k_3^{n_s} \propto (\pi - \theta_{12})^{n_s}$, where n_s is the spectral index. (See Appendix B for details.)

Then, the bispectrum has the asymptotic form

$$B_4(t, k_1, k_1, \theta_{12}) \sim 4\left(\frac{3}{4} - \frac{2}{7}\lambda(t)\right) P_{11}(k_3) P_{11}(k_1) \quad (97)$$

around the limit $\theta_{12} = \pi$. This leads to the ratio of the reduced bispectrum in this limit,

$$\frac{Q_{123}(t, k_1, k_1, \theta_{12})}{Q_{123\Lambda}(t, k_1, k_1, \theta_{12})} = \frac{21 - 8\lambda(t)}{21 - 8\lambda_\Lambda(t)}, \quad (98)$$

where $\lambda_\Lambda(t)$ is the parameter $\lambda(t)$ of the ΛCDM model, which explains the behavior shown in the left panels of Fig. 3.

The behavior of the reduced bispectrum is almost the same when the ratio k_1/k_2 is the same. This is because the functions $\alpha^{(s)}(\mathbf{k}_i, \mathbf{k}_j)$ and $\gamma(\mathbf{k}_i, \mathbf{k}_j)$ depend only on the ratio k_1/k_2 and θ_{12} (see also Appendix B). Recently, the bispectrum in the covariant cubic galileon cosmology is investigated in Ref. [51]. Our kinetic gravity braiding model with $n = 1$ is a cubic Galileon model; however, there is the difference between our model and the covariant cubic Galileon cosmology in Ref. [51]. The cosmic accelerated expansion in the covariant cubic Galileon model is derived by a potential of the scalar field. This causes the differences in the evolution of the background universe and the linear density perturbations.

V. SUMMARY AND CONCLUSIONS

In the present paper, we investigated the bispectrum of the matter density perturbations induced by gravitational instability in the most general second-order scalar-tensor theory that may possess the Vainshtein mechanism. We discussed a general feature of this wide class of modified gravity models in the most general second-order scalar-tensor theory. We analytically obtained the expression of the bispectrum of the second-order perturbations on the basis of the standard density perturbation theory. The bispectrum is expressed by the kernel (81), depending on only the parameter $\lambda(t)$, which is determined by the growing and decaying solutions of the linear density perturbations $D_\pm(t)$, the Hubble parameter $H(t)$, and the other function $N_\gamma(t)$ for the nonlinear interactions. These simple results come from the fact that the basic equations for the gravitational and scalar fields have the same form as the nonlinear mode couplings, which are derived as the leading terms under the quasistatic approximation within the subhorizon scales. Thus, all the effects of the modified gravity in the bispectrum come via the parameter $\lambda(t)$ in the kernel (81), which has a simple structure. This makes the behavior of the bispectrum less complex. As an application of our results, we exemplified the behavior of the bispectrum in the kinetic gravity braiding model proposed in Ref. [52]. We investigated the evolution of $\lambda(t)$ in this model and demonstrated the deviation of the reduced bispectrum from that of the ΛCDM model is less than 2%. Higher order solutions of the density perturbations can be obtained in a similar way, which is left as a future problem.

ACKNOWLEDGMENTS

We thank R. Kimura, T. Kobayashi, and T. Futamase for useful discussions at the early stage of this work. We also thank A. Taruya for critical comments at the beginning of this work and for useful discussion about our results. K. Y. thanks Prof. L. Amendola for the hospitality during K. Y.'s stay at Heidelberg University. He also thanks E. Bellini and M. Takada for useful comments related to the topic of the present paper. This work was supported by exchange visits between JSPS and DFG. K. Y. was supported in part by a Grant-in-Aid for Scientific Research of Japanese Ministry of Education, Culture, Sports, Science, and Technology (No. 21540270 and No. 21244033).

APPENDIX A: DEFINITION OF THE COEFFICIENTS

We first summarize the definitions of the coefficients in the field equations presented in Sec. II.

$$A_0 = \frac{\dot{\Theta}}{H^2} + \frac{\Theta}{H} + \mathcal{F}_T - 2\mathcal{G}_T - 2\frac{\dot{\mathcal{G}}_T}{H} - \frac{\mathcal{E} + \mathcal{P}}{2H^2}, \quad (A1)$$

$$A_1 = \frac{\dot{\mathcal{G}}_T}{H} + \mathcal{G}_T - \mathcal{F}_T, \quad (A2)$$

$$A_2 = \mathcal{G}_T - \frac{\Theta}{H}, \quad (A3)$$

$$B_0 = \frac{X}{H}\{\dot{\phi}G_{3X} + 3(\dot{X}+2HX)G_{4XX} + 2X\dot{X}G_{4XXX} - 3\dot{\phi}G_{4\phi X} + 2\dot{\phi}XG_{4\phi XX} + (\dot{H}+H^2)\dot{\phi}G_{5X} + \dot{\phi}[2H\dot{X} + (\dot{H}+H^2)X]G_{5XX} + H\dot{\phi}X\dot{X}G_{5XXX} - 2(\dot{X}+2HX)G_{5\phi X} - \dot{\phi}XG_{5\phi\phi X} - X(\dot{X}-2HX)G_{5\phi XX}\}, \quad \text{(A4)}$$

$$B_1 = 2X[G_{4X} + \ddot{\phi}(G_{5X} + XG_{5XX}) - G_{5\phi} + XG_{5\phi X}], \quad \text{(A5)}$$

$$B_2 = -2X(G_{4X} + 2XG_{4XX} + H\dot{\phi}G_{5X} + H\dot{\phi}XG_{5XX} - G_{5\phi} - XG_{5\phi X}), \quad \text{(A6)}$$

$$B_3 = H\dot{\phi}XG_{5X}, \quad \text{(A7)}$$

$$C_0 = 2X^2G_{4XX} + \frac{2X^2}{3}(2\ddot{\phi}G_{5XX} + \ddot{\phi}XG_{5XXX} - 2G_{5\phi X} + XG_{5\phi XX}), \quad \text{(A8)}$$

$$C_1 = H\dot{\phi}X(G_{5X} + XG_{5XX}), \quad \text{(A9)}$$

where we also defined

$$\mathcal{F}_T = 2[G_4 - X(\ddot{\phi}G_{5X} + G_{5\phi})], \quad \text{(A10)}$$

$$\mathcal{G}_T = 2[G_4 - 2XG_{4X} - X(H\dot{\phi}G_{5X} - G_{5\phi})], \quad \text{(A11)}$$

$$\Theta = -\dot{\phi}XG_{3X} + 2HG_4 - 8HXG_{4X} - 8HX^2G_{4XX} + \dot{\phi}G_{4\phi} + 2X\dot{\phi}G_{4\phi X} - H^2\dot{\phi}(5XG_{5X} + 2X^2G_{5XX}) + 2HX(3G_{5\phi} + 2XG_{5\phi X}), \quad \text{(A12)}$$

$$\mathcal{E} = 2XK_X - K + 6X\dot{\phi}HG_{3X} - 2XG_{3\phi} - 6H^2G_4 + 24H^2X(G_{4X} + XG_{4XX}) - 12HX\dot{\phi}G_{4\phi X} - 6H\dot{\phi}G_{4\phi} + 2H^3X\dot{\phi}(5G_{5X} + 2XG_{5XX}) - 6H^2X(3G_{5\phi} + 2XG_{5\phi X}), \quad \text{(A13)}$$

$$\mathcal{P} = K - 2X(G_{3\phi} + \ddot{\phi}G_{3X}) + 2(3H^2 + 2\dot{H})G_4 - 12H^2XG_{4X} - 4H\dot{X}G_{4X} - 8\dot{H}XG_{4X} - 8HX\dot{X}G_{4XX} + 2(\ddot{\phi} + 2H\dot{\phi})G_{4\phi} + 4XG_{4\phi\phi} + 4X(\ddot{\phi} - 2H\dot{\phi})G_{4\phi X} - 2X(2H^3\dot{\phi} + 2H\dot{H}\dot{\phi} + 3H^2\ddot{\phi})G_{5X} - 4H^2X^2\ddot{\phi}G_{5XX} + 4HX(\dot{X} - HX)G_{5\phi X} + 2[2(HX)^{\cdot} + 3H^2X]G_{5\phi} + 4HX\dot{\phi}G_{5\phi\phi}. \quad \text{(A14)}$$

In the kinetic gravity braiding model considered in Sec. IV, the coefficients are written as follows:

$$\mathcal{F}_T = M_{\rm pl}^2, \qquad \mathcal{G}_T = M_{\rm pl}^2, \quad \text{(A15)}$$

$$\Theta = -nM_{\rm pl}\left(\frac{r_c^2}{M_{\rm pl}^2}\right)^n \dot{\phi}X^n + HM_{\rm pl}^2, \quad \text{(A16)}$$

$$\dot{\Theta} = -n(2n+1)M_{\rm pl}\left(\frac{r_c^2}{M_{\rm pl}^2}\right)^n \ddot{\phi}X^n + \dot{H}M_{\rm pl}^2, \quad \text{(A17)}$$

$$\mathcal{E} = -X + 6nM_{\rm pl}\left(\frac{r_c^2}{M_{\rm pl}^2}\right)^n \dot{\phi}HX^n - 3H^2M_{\rm pl}^2, \quad \text{(A18)}$$

$$\mathcal{P} = -X - 2nM_{\rm pl}\left(\frac{r_c^2}{M_{\rm pl}^2}\right)^n \ddot{\phi}X^n + (3H^2 + 2\dot{H})M_{pl}^2, \quad \text{(A19)}$$

$$A_0 = \frac{X}{H^2} - 2nM_{\rm pl}\left(\frac{r_c^2}{M_{\rm pl}^2}\right)^n \left(\frac{2\dot{\phi}}{H} + n\frac{\ddot{\phi}}{H^2}\right)X^n, \quad \text{(A20)}$$

$$A_2 = B_0 = nM_{\rm pl}\left(\frac{r_c^2}{M_{\rm pl}^2}\right)^n \frac{\dot{\phi}}{H}X^n, \quad \text{(A21)}$$

$$A_1 = B_1 = B_2 = B_3 = C_0 = C_1 = 0. \quad \text{(A22)}$$

In the present paper, we consider the attractor solution satisfying (92), thus obtaining

$$\ddot{\phi} = -\frac{1}{2n-1}\frac{\dot{\phi}\dot{H}}{H}, \quad \text{(A23)}$$

$$\frac{\dot{H}}{H^2} = -\frac{(2n-1)3\Omega_m(a)}{2(2n-\Omega_m(a))}, \quad \text{(A24)}$$

$$A_0 = -\frac{M_{\rm pl}^2(1-\Omega_m(a))(2n+(3n-1)\Omega_m(a))}{2n-\Omega_m(a)}, \tag{A25}$$

$$A_2 = M_{\rm pl}^2(1-\Omega_m(a)), \tag{A26}$$

$$B_0 = M_{\rm pl}^2(1-\Omega_m(a)), \tag{A27}$$

where we define $\Omega_m(a) = \rho_m(a)/3M_{\rm pl}^2H^2$.

APPENDIX B: EXPLICIT EXPRESSIONS OF α AND γ

For the bispectrum, we may write the wave number vector that satisfies $\mathbf{k}_1+\mathbf{k}_2+\mathbf{k}_3=0$ as follows:

$$\mathbf{k}_1 = (0,0,k_1), \tag{B1}$$

$$\mathbf{k}_2 = (0, k_2\sin\theta_{12}, k_2\cos\theta_{12}), \tag{B2}$$

$$\mathbf{k}_3 = (0, -k_2\sin\theta_{12}, -k_1-k_2\cos\theta_{12}), \tag{B3}$$

where θ_{12} is the angle between the vectors $\mathbf{k}_1$ and $\mathbf{k}_2$. Then, we have

$$\frac{\mathbf{k}_1\cdot\mathbf{k}_2}{k_1k_2} = \cos\theta_{12}, \tag{B4}$$

$$\frac{\mathbf{k}_2\cdot\mathbf{k}_3}{k_2k_3} = \frac{-k_2-k_1\cos\theta_{12}}{\sqrt{k_1^2+k_2^2+2k_1k_2\cos\theta_{12}}}, \tag{B5}$$

$$\frac{\mathbf{k}_3\cdot\mathbf{k}_1}{k_3k_1} = \frac{-k_1-k_2\cos\theta_{12}}{\sqrt{k_1^2+k_2^2+2k_1k_2\cos\theta_{12}}}, \tag{B6}$$

where we use $k_3 = \sqrt{k_1^2+k_2^2+2k_1k_2\cos\theta_{12}}$. Introducing the constant c by $k_1 = ck_2$, we have

$$k_3 = k_1\sqrt{c^2+2c\cos\theta_{12}+1}, \tag{B7}$$

$$\frac{\mathbf{k}_2\cdot\mathbf{k}_3}{k_2k_3} = -\frac{c+\cos\theta_{12}}{\sqrt{c^2+2c\cos\theta_{12}+1}}, \tag{B8}$$

$$\frac{\mathbf{k}_3\cdot\mathbf{k}_1}{k_3k_1} = -\frac{c\cos\theta_{12}+1}{\sqrt{c^2+2c\cos\theta_{12}+1}}. \tag{B9}$$

For convenience, we summarize the explicit expressions of $\alpha^{(s)}(\mathbf{k}_i,\mathbf{k}_j)$ and $\gamma(\mathbf{k}_i,\mathbf{k}_j)$. The above relations yield

$$\alpha^{(s)}(\mathbf{k}_1,\mathbf{k}_2) = 1+\frac{(c^2+1)\cos\theta_{12}}{2c}, \tag{B10}$$

$$\alpha^{(s)}(\mathbf{k}_2,\mathbf{k}_3) = 1-\frac{(2c^2+2c\cos\theta_{12}+1)(c+\cos\theta_{12})}{2c(c^2+2c\cos\theta_{12}+1)}, \tag{B11}$$

$$\alpha^{(s)}(\mathbf{k}_3,\mathbf{k}_1) = 1-\frac{(c^2+2c\cos\theta_{12}+2)(c\cos\theta_{12}+1)}{2(c^2+2c\cos\theta_{12}+1)}, \tag{B12}$$

$$\gamma(\mathbf{k}_1,\mathbf{k}_2) = 1-\cos^2\theta_{12}, \tag{B13}$$

$$\gamma(\mathbf{k}_2,\mathbf{k}_3) = \frac{\sin^2\theta_{12}}{c^2+2c\cos\theta_{12}+1}, \tag{B14}$$

$$\gamma(\mathbf{k}_3,\mathbf{k}_1) = \frac{c^2\sin^2\theta_{12}}{c^2+2c\cos\theta_{12}+1}. \tag{B15}$$

Thus, $\alpha^{(s)}$ and γ depend on only c and θ_{12}, which means that $F_2(t,\mathbf{k}_i,\mathbf{k}_j)$ depends on only c and θ_{12}, irrespective of t. It is trivial that $\alpha^{(s)}(\mathbf{k}_1,\mathbf{k}_2)$ and $\gamma(\mathbf{k}_1,\mathbf{k}_2)$ are invariant under the interchange between $\mathbf{k}_1$ and $\mathbf{k}_2$, or the replacement of c with $1/c$. Note also that $\alpha^{(s)}(\mathbf{k}_2,\mathbf{k}_3)$ and $\gamma(\mathbf{k}_2,\mathbf{k}_3)$ are transformed into $\alpha^{(s)}(\mathbf{k}_3,\mathbf{k}_1)$ and $\gamma(\mathbf{k}_3,\mathbf{k}_1)$, respectively, by the replacement of c with $1/c$.

[1] W. Hu and I. Sawicki, Phys. Rev. D **76**, 064004 (2007).
[2] A. A. Starobinsky, JETP Lett. **86**, 157 (2007).
[3] S. Tsujikawa, Phys. Rev. D **77**, 023507 (2008).
[4] S. Nojiri and S. Odintsov, Phys. Lett. B **657**, 238 (2007).
[5] G. R. Dvali, G. Gabadadze, and M. Porrati, Phys. Lett. B **485**, 208 (2000).
[6] Y.-S. Song, I. Sawicki, and W. Hu, Phys. Rev. D **75**, 064003 (2007).
[7] R. Maartens and E. Majerotto, Phys. Rev. D **74**, 023004 (2006).
[8] R. Maartens and K. Koyama, Living Rev. Relativity **13**, 5 (2010).
[9] C. de Rham and G. Gabadadze, Phys. Rev. D **82**, 044020 (2010).
[10] C. de Rham, G. Gabadadze, and A. J. Tolley, Phys. Rev. Lett. **106**, 231101 (2011).
[11] C. de Rham and L. Heisenberg, Phys. Rev. D **84**, 043503 (2011).
[12] S. F. Hassan and R. A. Rosen, Phys. Rev. Lett. **108**, 041101 (2012).
[13] A. R. Gomes and L. Amendola, J. Cosmol. Astropart. Phys. 03 (2014) 041.
[14] G. W. Horndeski, Int. J. Theor. Phys. **10**, 363 (1974).

[15] C. Deffayet, X. Gao, D. A. Steer, and G. Zahariade, Phys. Rev. D **84**, 064039 (2011).
[16] T. Kobayashi, M. Yamaguchi, and J. Yokoyama, Prog. Theor. Phys. **126**, 511 (2011).
[17] N. Chow and J. Khoury, Phys. Rev. D **80**, 024037 (2009).
[18] F. P. Silva and K. Koyama, Phys. Rev. D **80**, 121301 (2009).
[19] T. Kobayashi, H. Tashiro, and D. Suzuki, Phys. Rev. D **81**, 063513 (2010).
[20] T. Kobayashi, Phys. Rev. D **81**, 103533 (2010).
[21] A. De Felice and S. Tsujikawa, Phys. Rev. D **84**, 124029 (2011).
[22] A. De Felice and S. Tsujikawa, J. Cosmol. Astropart. Phys. 07 (2010) 024.
[23] A. De Felice, S. Mukohyama, and S. Tsujikawa, Phys. Rev. D **82**, 023524 (2010).
[24] C. Deffayet, G. Esposito-Farese, and A. Vikman, Phys. Rev. D **79**, 084003 (2009).
[25] R. Gannouji and M. Sami, Phys. Rev. D **82**, 024011 (2010).
[26] A. Ali, R. Gannouji, and M. Sami, Phys. Rev. D **82**, 103015 (2010).
[27] A. De Felice and S. Tsujikawa, Phys. Rev. Lett. **105**, 111301 (2010).
[28] S. Nesseris, A. De Felice, and S. Tsujikawa, Phys. Rev. D **82**, 124054 (2010).
[29] D. F. Mota, M. Sandstad, and T. Zlosnik, J. High Energy Phys. 12 (2010) 051.
[30] A. De Felice, R. Kase, and S. Tsujikawa, Phys. Rev. D **83**, 043515 (2011).
[31] C. Deffayet, O. Pujolas, I. Sawicki, and A. Vikman, J. Cosmol. Astropart. Phys. 10 (2010) 026.
[32] C. Deffayet, S. Deser, and G. Esposito-Farese, Phys. Rev. D **80**, 064015 (2009).
[33] A. Nicolis, R. Rattazzi, and E. Trincherini, Phys. Rev. D **79**, 064036 (2009).
[34] C. Burrage and D. Seery, J. Cosmol. Astropart. Phys. 08 (2010) 011.
[35] G. L. Goon, K. Hinterbichler, and M. Trodden, Phys. Rev. D **83**, 085015 (2011).
[36] C. de Rham and A. J. Tolley, J. Cosmol. Astropart. Phys. 05 (2010) 015.
[37] R. Kimura, T. Kobayashi, and K. Yamamoto, Phys. Rev. D **85**, 024023 (2012).
[38] R. Kase and S. Tsujikawa, J. Cosmol. Astropart. Phys. 08 (2013) 054.
[39] T. Narikawa, T. Kobayashi, D. Yamauchi, and R. Saito, Phys. Rev. D **87**, 124006 (2013).
[40] P. A. R. Ade *et al.* (Planck Collaboration), arXiv:1303.5084.
[41] R. Scoccimarro, H. M. Couchman, and J. A. Frieman, Astrophys. J. **517**, 531 (1999).
[42] T. Nishimichi, I. Kayo, C. Hikage, K. Yahata, A. Taruya, Y. P. Jing, R. K. Sheth, and Y. Suto, Publ. Astron. Soc. Jpn. **59**, 93 (2007).
[43] F. Bernardeau, S Colombi, E. Gaztanaga, and R. Scoccimarro, Phys. Rep. **367**, 1 (2002).
[44] N. Bartolo, S. Matarrese, and A. Riotto, J. Cosmol. Astropart. Phys. 10 (2005) 010.
[45] N. Bartolo, S. Matarrese, and A. Riotto, J. Cosmol. Astropart. Phys. 01 (2007) 019.
[46] K. Koyama, A. Taruya, and T. Hiramatsu, Phys. Rev. D **79**, 123512 (2009).
[47] A. Barreira, B. Li, W. Hellwing, C. M. Baugh, and S. Pascoli, J. Cosmol. Astropart. Phys. 10 (2013) 027.
[48] B. Li, A. Barreira, C. M. Baugh, W. A. Hellwing, and K. Koyama, J. Cosmol. Astropart. Phys. 11 (2013) 012.
[49] M. Wyman, E. Jennings, and M. Lima, Phys. Rev. D **88**, 084029 (2013).
[50] E. Bellini, N. Bartolo, and S. Matarrese, J. Cosmol. Astropart. Phys. 06 (2012) 019.
[51] N. Bartolo, E. Bellini, D. Bertacca, and S. Matarrese, J. Cosmol. Astropart. Phys. 03 (2013) 034.
[52] R. Kimura and K. Yamamoto, J. Cosmol. Astropart. Phys. 04 (2011) 025.
[53] A. De Felice, T. Kobayashi, and S. Tsujikawa, Phys. Lett. B **706**, 123 (2011).

PHYSICAL REVIEW D **92,** 023523 (2015)

What can we learn from higher multipole power spectra of galaxy distribution in redshift space?

Tatsuro Kanemaru,[1] Chiaki Hikage,[2,3] Gert Hütsi,[4] Ayumu Terukina,[1] and Kazuhiro Yamamoto[1]

[1]*Department of Physical Sciences, Hiroshima University, Kagamiyama 1-3-1, Higashi-hiroshima 739-8526, Japan*

[2]*Kobayashi-Maskawa Institute, Nagoya University, Nagoya 464-8602, Japan*

[3]*Kavli Institute for the Physics and Mathematics of the Universe (WPI), University of Tokyo, Kashiwa 277-8583, Japan*

[4]*Tartu Observatory, Tõravere 61602, Estonia*

(Received 22 January 2015; published 16 July 2015)

We investigate the potential of the higher multipole power spectra of the galaxy distribution in redshift space as a cosmological probe on halo scales. Based on the fact that a halo model explains well the multipole power spectra of the luminous red galaxy sample in the Sloan Digital Sky Survey, we focus our investigation on the random motions of the satellite luminous red galaxies that determine the higher multipole spectra at large wave numbers. We show that our theoretical model fits the higher multipole spectra at large wave numbers from N-body numerical simulations, and we apply these results for testing the gravity theory and the velocity structure of galaxies on the halo scales. In this analysis, we use the multipole spectra $P_4(k)$ and $P_6(k)$ on the small scales of the range of wave number $0.3 \leq k/[h\mathrm{Mpc}^{-1}] \leq 0.6$, which is in contrast to the usual method of testing gravity by targeting the linear growth rate on very large scales. We demonstrate that our method could be useful for testing gravity on the halo scales.

DOI: 10.1103/PhysRevD.92.023523 PACS numbers: 98.80.Es, 04.50.Kd, 04.80.Cc, 98.62.Py

I. INTRODUCTION

Redshift surveys of galaxies are a promising way to explore the nature of dark energy and test gravity on the cosmological scales. Recent results of the baryon oscillation spectroscopic survey (BOSS) date release (DR) 11 of the Sloan Digital Sky Survey (SDSS) III have demonstrated the usefulness of redshift surveys [1,2]. A possible tension in the cosmological parameters between the results by the Planck satellite and the BOSS is reported [3–6], which attracts the interest of researchers. An interesting question that arises is whether this tension could be resolved in models where the gravity gets modified from its usual general relativistic form.

The redshift-space distortion plays an important role in testing gravity [7,8], which reflects the information on the velocity of galaxies. One of the targets of the redshift surveys is a measurement of the redshift-space distortions in the linear regime of the density perturbations [9], which provides us with a chance to test gravity through the linear growth rate. On the other hand, the finger-of-god (FoG) effect is the redshift-space distortion in the nonlinear regime of density perturbations reflecting the random motion of galaxies. The primary purpose of the present paper is to investigate an effective method to evaluate the random velocity of galaxies in halos, which might provide us with a unique chance of testing gravity on halo scales. This can be achieved by precisely modeling the FoG effect on the basis of the halo model.

In order to quantify the redshift-space distortions, the multipole power spectrum, defined as a multipole coefficient of the multipole expansion of the anisotropic power spectrum (e.g., [6,8,10]), is useful. Recently, the authors of Ref. [11] found that a halo model describes well the small-scale behavior of the higher multipole power spectra of the luminous red galaxy (LRG) sample of SDSS DR7. Based on this new finding, we consider the potential of measuring the velocity of satellite galaxies in halos and testing the gravity theory on the halo scales with the multipole power spectrum. The key to this method is the random motion of the satellite galaxies and their one-dimensional velocity dispersion in a halo with mass M, for which we adopt a simple formula,

$$\sigma_{\mathrm{v}}^2(M) = \beta \frac{GM}{2r_{\mathrm{vir}}}, \tag{1}$$

where β is a constant parameter, G is the Newton's universal gravitational constant, and r_{vir} is the virial radius defined by $r_{\mathrm{vir}} = (3M/4\pi\bar{\rho}_{\mathrm{m}}(z)\Delta_{\mathrm{vir}}(z))^{1/3}$, where $\bar{\rho}_{\mathrm{m}}(z)$ is the mean matter density and $\Delta_{\mathrm{vir}}(z)$ is the density contrast of a halo, respectively, at the redshift z. We adopt $\Delta_{\mathrm{vir}} = 265$ at $z = 0.3$ for the sample corresponding to our LRG mock samples. We carefully check this velocity dispersion relation using the numerical simulations, as well as the validity of the theoretical model for the higher multipole power spectra. This theoretical model is compared with the SDSS LRG sample, and we put a useful constraint on the

 © 2015 American Physical Society

velocity dispersion and the gravitational constant on the halo scales.

II. FORMULATION

Here we briefly review the multipole spectrum in a halo model according to Ref. [9,11]. Following the general prescription of the halo approach [12–14], we write the anisotropic power spectrum in the redshift space consisting of the one-halo and two-halo terms, $P_{\rm LRG}(k,\mu) = P^{\rm 1h}(k,\mu) + P^{\rm 2h}(k,\mu)$. We consider the model which consists of the central galaxies and the satellite galaxies. We adopt the following expression (2) for the one-halo term,

$$P^{\rm 1h}(k,\mu) = \frac{1}{\bar{n}^2}\int dM \frac{dn}{dM} \times [2\langle N_{\rm sat}\rangle \tilde{u}_{\rm NFW}(k,M) e^{-(\sigma_c^2+\sigma_s^2)k^2\mu^2/2a^2H^2} + \langle N_{\rm sat}\rangle^2 \tilde{u}^2_{\rm NFW}(k,M) e^{-\sigma_s^2 k^2\mu^2/a^2H^2}], \quad (2)$$

where we adopt the halo mass function dn/dM given by [15], $\bar{n}$ is the mean number density of LRGs given by $\bar{n} = \int dM (dn/dM) N_{\rm HOD}(M)$, $N_{\rm HOD}(M) = \langle N_{\rm cen}\rangle + \langle N_{\rm sat}\rangle$ is the halo occupation distribution (HOD), for which we adopt the following form [16],

$$\langle N_{\rm cen}\rangle = \frac{1}{2}\left[1 + {\rm erf}\left(\frac{\log_{10}(M) - \log_{10}(M_{\rm min})}{\sigma_{\log M}}\right)\right], \quad (3)$$

$$\langle N_{\rm sat}\rangle = \langle N_{\rm cen}\rangle \left(\frac{M - M_{\rm cut}}{M_1}\right)^{\alpha}, \quad (4)$$

with the error function ${\rm erf}(x)$, and $\sigma_c^2(M)$ and $\sigma_s^2(M)$ are the velocity dispersion of the central LRGs and the satellite LRGs, respectively. We adopt the mass function proposed in [15]; however, our results are not significantly altered by the other choices of the mass functions proposed in [17] or [18]. Table I lists the HOD parameters matching the SDSS DR7 LRG catalog in Ref. [19]. We assume that the distribution of the satellite galaxies follows the Navarro-Frenk-White (NFW) profile [20] and $\tilde{u}_{\rm NFW}(k)$ denotes the Fourier transform of truncated NFW profile [21]. Results of Ref. [22] support this assumption. We may assume that central LRGs reside near the halo center, thus their velocity difference relative to the host halo should be small (cf. [23]). On the other hand, satellite LRGs are off-centered, and their random velocity should be the main source of the FoG effect. Here we assume

$$\sigma_c^2(M) = \alpha_c^2 \sigma_{\rm v}^2(M), \quad (5)$$

$$\sigma_s^2(M) = \alpha_s^2 \sigma_{\rm v}^2(M), \quad (6)$$

where α_c and α_s are the constant parameters.

In the previous paper [11], the two-halo term was modeled with an analytic fitting formula from N-body simulations. However, in the present paper, we adopt a very simple treatment for the two-halo term of the higher multipole power spectrum, because it is not trivial to construct a precise analytic model in redshift space which is applicable even at large wave numbers. Using the mock catalogs corresponding to the LRG sample is an alternative way to incorporate precise theoretical predictions for the two-halo term. For this modeling, we adopt the results in the previous paper [9], which has constructed mock catalogs, corresponding to the SDSS LRG sample, and has investigated the behavior of the multipole spectra. In the present paper, we use the following modeling for $P_4^{2h}(k)$ and $P_6^{2h}(k)$. The results in [9] demonstrate that the contribution from the two-halo term to $P_6(k)$ is negligible, i.e., $P_6^{2h}(k) \simeq 0$, and $P_4^{2h}(k)$ is simply expressed as $kP_4^{2h}(k) \simeq 15[h{\rm Mpc}^{-1}]^2$, which we also adopt here. Because the contribution of the two-halo term to $P_2(k)$ is rather large compared to that of $P_4(k)$ and $P_6(k)$ [11], it is not included in our analysis.

Even though the relative contribution of the two-halo term to $P_4(k)$ and $P_6(k)$ is small, it could still be influential to our results. Therefore a more detailed modeling of the two-halo term might be important. The above treatment for the two-halo term is based on the simulations within the framework of the general relativity. However, in general the two-halo term might depend on modified gravity models. Therefore our modeling might not be universally correct for the modified gravity models, including the possibility that a modification of gravity changes the mass function, the density profile of a halo and the mass-concentration relation, e.g., [24,25]. Nevertheless, the current treatment should be enough for the purposes of just demonstrating the validity of our method as a new test of the general relativity.

TABLE I. HOD parameters of the LRG sample [19].

	Simulation/LRG
$M_{\rm min}$	$5.7 \times 10^{13} M_\odot/h$
$\sigma_{\log M}$	0.7
$M_{\rm cut}$	$3.5 \times 10^{13} M_\odot/h$
M_1	$3.5 \times 10^{14} M_\odot/h$
α	1

III. RESULTS

A. Simulation sample

We first demonstrate the validity of our theoretical model by comparing with the results of N-body simulations. The simulations assume the spatially flat cold dark matter model with a cosmological constant, adopting $\Omega_0 = 0.273$ and $\sigma_8 = 0.82$. We run ten realizations of N-body simulations using GADGET-2 code [26] with Gaussian initial condition. Each simulation has a side length of $600h^{-1}$ Mpc and the particle number of 800^3 (each particle

mass is $2.8 \times 10^{10} h^{-1} M_{\odot}$). We use $z = 0.3$ snapshots and identify halos by a friends-of-friends algorithm with a linking length of 0.2. Mock catalogs are constructed so that the bias and the HOD match the SDSS DR7 LRG catalog in Ref. [19]. The position of a central LRG is given by the potential minimum of the host halo and the velocity is given as the averaged velocity of all particles within the halos. We substitute randomly picked up dark matter particles for satellite LRGs. In this analysis, we constructed mock samples both with and without including the fiber collision effect [27]. The mock samples including the effect of fiber collisions are constructed as follows. We first make uncollided samples by removing one of the adjacent subhalos within 55 arcsec at $z = 0.3$. In this process, we follow the method of Ref. [27], intending to maximize the number of galaxies of the uncollided sample. For example, if one of the galaxies in a triplet system is collided with both of the other two which are uncollided with each other, we remove the former galaxy only and leave the uncollided two galaxies. In the observed survey area where the spectroscopic tiling is overlapped, both spectra of collided pairs can be measured. To incorporate this effect, we randomly reintroduce a fraction of removed subhalos in the sample at 10% probability regardless of their positions in the sky. In our simulation, the central LRGs locate near the halo center, and their velocity is negligible. We assume no velocity bias for satellites. Thus, our mock catalogs should be understood as $\alpha_c = 0$ and $\alpha_s = 1$.

Using the mock catalogs, we show the validity of our expression (1) for the velocity dispersion of satellite galaxies. The velocity dispersion of satellite galaxies in a halo has not been well understood, though there are a few works that investigate the velocity dispersion of LRGs [28,29]. Recently, Guo *et al.* have studied the velocity bias of galaxies in the SDSS III CMASS sample in the context of a halo model [30]. Their results have implications for our results, as will be discussed below.

Figure 1 compares the velocity dispersion $\sigma_{\rm v}^2(M)$ of satellites as a function of the host halo's mass M. Here the cross symbols show the results of the N-body numerical simulation, while the curve shows $(GM/2r_{\rm vir})^{1/2}$, i.e., Eq. (1) with $\beta = 1$. This suggests that Eq. (1) with $\beta = 1$ reproduces well the relation between the velocity dispersion of satellite and the halo mass of our N-body simulations.

The effect of the fiber collision, which misses galaxies located closely to each other, could be crucial in the analysis of the redshift-space clustering on small scales [31]. The fiber collision dominantly occurs for pairs in the same halo. In the previous work [11], the effect of the fiber collision is included by a multiplying factor reducing the satellite fraction. In the present paper, we adopt a similar prescription, for simplicity. Instead of introducing the satellite fraction, we float the HOD parameter M_1, which changes the satellite fraction, as a fitting parameter in our Markov chain Monte Carlo (MCMC) analysis.

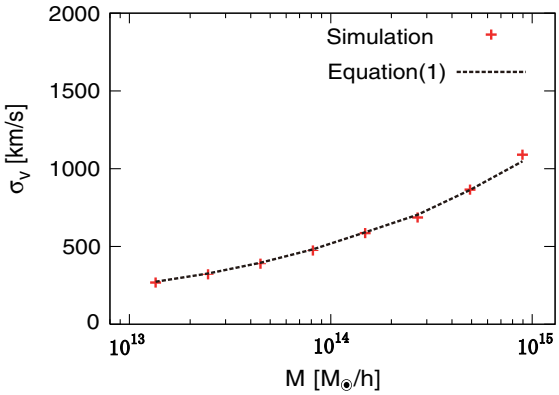

FIG. 1 (color online). One-dimensional velocity dispersion $\sigma_{\rm v}(M)$ as a function of halo mass. The crosses are from N-body simulation, while the curve is Eq. (1) with $\beta = 1$.

We compare the results of the averaged power spectra over 10 mock simulations with the theoretical multipole power spectra, with floating the two parameters β and M_1. We demonstrate that β and M_1 can be measured from $P_4(k)$ and $P_6(k)$. The errors of the simulated power spectra are obtained from the dispersions of ten mock results multiplied by $1/\sqrt{10}$, which roughly corresponds to the errors for their mean. In particular, we fixed $\alpha_c = 0$ and $\alpha_s = 1$, taking into account the consistency with our numerical simulations. Note that the HOD parameters other than M_1 are fixed. When additional HOD parameter is floated, we cannot obtain useful constraints due to a problem of degeneracy between the HOD parameters. This occurs because we use only $P_4(k)$ and $P_6(k)$ on small scales. If we had used the projected angular correlation function simultaneously in our analysis, we would have been able to avoid this problem. We leave this as a future work.

In the MCMC analysis we only use $P_4(k)$ and $P_6(k)$ in the range of wave numbers $0.3 \le k/[h\mathrm{Mpc}^{-1}] \le 0.6$ in order to reduce the influences from the uncertain contribution of the two-halo term. Table II summarizes our results, where the best-fitting values with one sigma statistical errors are presented for (A) simulation with the fiber collision (F.C.), (B) simulation without the fiber collision, and (C) LRG sample, (D) LRG sample with the two-halo term modeled with the brightest LRG (BLRG) sample [11], from the left to the right column, respectively. The chi-squared and the degrees of freedom are also shown. In this table, the values within parentheses are the results for the data in the range of $0.2 \le k/[h\mathrm{Mpc}^{-1}] \le 0.6$. The chi-squared values in the parentheses of (A) and (B) become very large. This comes from the failure of our analytic model in fitting the N-body simulations at the wave numbers $k \lesssim 0.3 h\mathrm{Mpc}^{-1}$, where the two-halo term becomes relatively important. The left-hand two columns of Fig. 2 show the best-fit curves of the HOD and the multipole power spectra for the simulations (A) and (B).

TABLE II. Results of our MCMC analysis with floating the two parameters β and M_1, where we fixed $\alpha_c = 0$ and $\alpha_s = 1$ and the other cosmological parameters. The best-fitting values with one sigma statistical errors, the satellite fraction $\int dM(dn/dM)\langle N_{\rm sat}\rangle/\bar{n}$, and the chi-squared along with the number of d.o.f. are presented when fitted with (A) the simulation with the fiber collision (F.C.), (B) the simulation without the fiber collision, (C) LRG sample and (D) LRG sample with the two-halo term modeled using the BLRG sample, from the left to the right column, respectively. The results are obtained using the data in the range of the wave numbers $0.3 \le k/[h\mathrm{Mpc}^{-1}] \le 0.6$, and the values in the parentheses are the same but use the data in the range of the wave numbers $0.2 \le k/[h\mathrm{Mpc}^{-1}] \le 0.6$.

	(A) Mock with F.C.	(B) Mock without F.C.	(C) LRG	(D) LRG with BLRG
β	$1.17^{+0.56}_{-0.40}(0.96^{+0.43}_{-0.30})$	$0.97^{+0.30}_{-0.24}(0.83^{+0.23}_{-0.20})$	$1.70^{+0.83}_{-0.55}(1.79^{+0.83}_{-0.59})$	$1.35^{+0.68}_{-0.45}(1.38^{+0.65}_{-0.47})$
$M_1[10^{14}M_\odot/h]$	$6.5^{+0.9}_{-1.0}(6.1^{+1.0}_{-1.1})$	$4.1^{+0.4}_{-0.4}(4.0^{+0.6}_{-0.6})$	$4.0^{+0.4}_{-0.4}(4.0^{+0.4}_{-0.4})$	$4.0^{+0.4}_{-0.5}(4.0^{+0.4}_{-0.5})$
Satellite fraction(%)	$3.8^{+0.7}_{-0.5}(4.1^{+0.8}_{-0.5})$	$5.9^{+0.6}_{-0.5}(6.2^{+0.7}_{-0.6})$	$6.3^{+0.5}_{-0.4}(6.3^{+0.5}_{-0.4})$	$6.4^{+0.5}_{-0.4}(6.4^{+0.5}_{-0.4})$
χ^2	16(58)	18(59)	47(56)	6.4(7.3)
d.o.f.	10(12)	10(12)	60(80)	60(80)

These results demonstrate that our theoretical model reproduces those of the numerical simulations.

B. LRG sample

We next apply our method to the multipole power spectra measured with the SDSS DR7 [32]. Our DR7 LRG sample is selected to cover a redshift range, $0.16 < z < 0.36$, only in the northern cap in order to reduce systematic uncertainties and to match the analysis in Ref. [19]. Thus, the sky coverage is limited to 7189 deg^2 and the total number of LRGs is 61899. We adopt the same method for the measurement as that in Refs. [11,33,34], but with the fiducial cosmological background for the distant-redshift relation of the spatially flat ΛCDM cosmology with

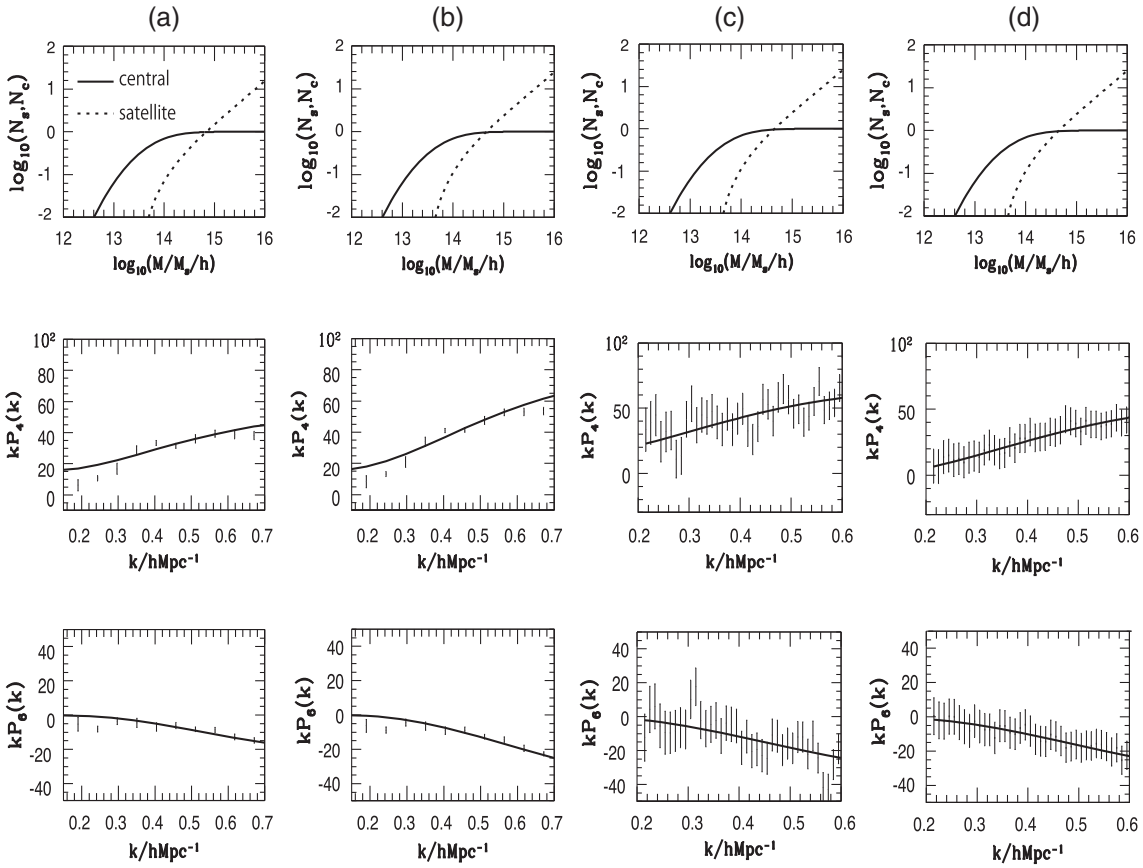

FIG. 2. Top panels show the HOD $N_s(M)$ (dotted lines) and $N_c(M)$ (solid lines), middle panels $kP_4(k)$, and bottom panels $kP_6(k)$. In each panel, the curves correspond to the best-fitting models, excepting the dash-dotted curve. Each column shows the results of (A) mock with fiber collision, (B) mock without fiber collision, (C) LRG sample, and (D) LRG sample subtracted the two-halo term modeled using the BLRG sample, from left to right, respectively.

$\Omega_m = 0.3$. The statistical errors of the multipole spectra may be estimated by the formula in Ref. [10], which is derived on the basis of the so-called FKP method [35]. The cosmological distortion (Alcock-Paczynski) effect is very small because we are considering the higher multipole spectra on small scales, though it has a marginal effect of changing the overall normalization (e.g., [6]). The right-hand two columns in Table II list the results of the MCMC analysis with the LRG multipole spectra, whose difference comes from the modeling for the two-halo term. The right two columns of Fig. 2 show the best-fitting curve and the data.

The results of MCMC analysis with the SDSS LRG sample can be used for testing the gravitational constant on the halo scales. This is because the velocity dispersion in a modified gravity models could be written as $\sigma_v^2(M) = G_{\rm eff}M/2r_{\rm vir}$, where $G_{\rm eff}$ is an effective gravitational constant. Regarding $G_{\rm eff} = \beta G$, we may put a constraint on the effective gravitational constant from the SDSS LRG sample on the halo scales, $\beta = 1.70^{+0.83}_{-0.55}$ from the column (C) in Table II, in which we adopted the same modeling for the two-halo term as that of the mock catalogs. This value is rather larger than the prediction of the numerical simulations, although the error is not small.

Though the contribution of the two-halo term to P_4 and P_6 is rather small compared with the one-halo term, but it might be influential to our results. As a check of our results, we model the contribution of the two-halo term using the BLRG sample [11]. Because the BLRG catalog roughly corresponds to the central galaxies catalog, then we may

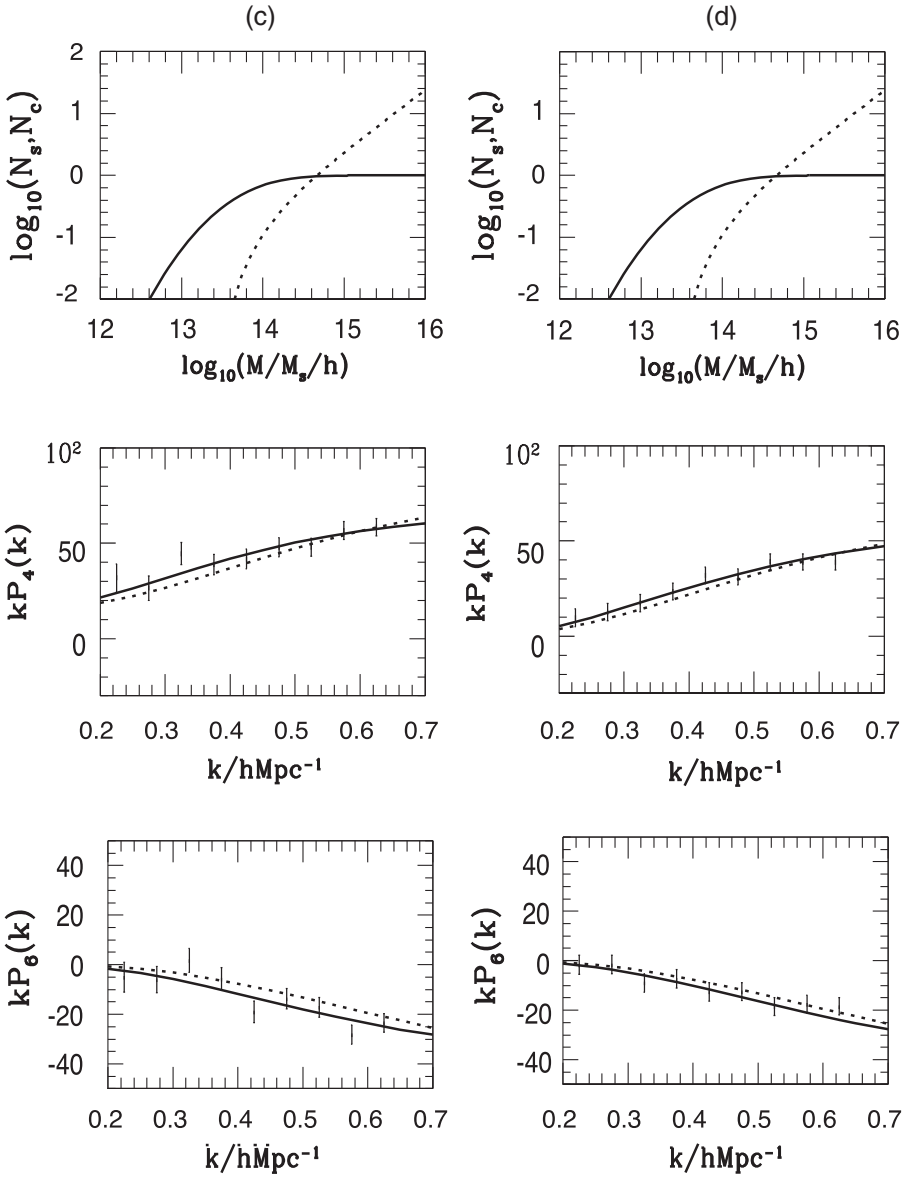

FIG. 3. Same as (C) and (D) of Fig. 2, except with different binning of k. The dashed curves in the middle panels, $kP_4(k)$, and bottom panels, $kP_6(k)$, assume $\beta = 1$ while keep the other parameters the same.

model the two-halo term by computing the multipole spectrum of the BLRG catalog. The column (D) of Table II represents the results $\beta = 1.35^{+0.68}_{-0.45}$. Compared with the case of the modeling for the two-halo term from the numerical simulation, the value of β becomes small and $\beta = 1$ is in the one-sigma error of the results.

The reason why the chi-squared of the case (D) is small is understood as follows. Since BLRG sample is a subset of LRGs, most of the LRG pairs hosted by different halos are overlapped. The error for the difference $\Delta P = P_{\rm LRG} - P_{\rm BLRG}$ is, therefore, significantly reduced and thus the chi-squared values for the error of $P_{\rm LRG}$ become small.

Our results are not altered significantly by the binning of k. For example, when we adopt the similar binning to that of (A) and (B), $\Delta k = 0.05h{\rm Mpc}^{-1}$, for the observational data, we obtain the best-fitting value of β, $1.79^{+0.96}_{-0.64}(1.89^{+0.94}_{-0.64})$ and $1.44^{+0.74}_{-0.50}(1.44^{+0.64}_{-0.46})$ for (C) and (D), respectively. Correspondingly, Fig. 3 shows the same as (C) and (D) of Fig. 2, but the case with the wider binning $\Delta k = 0.05h{\rm Mpc}^{-1}$. Thus, the effect of the binning does not alter our conclusions qualitatively.

Our estimation of the chi-squared is not strict but rather optimistic because we neglected the covariances between different k bins as well as those between different ℓth multipole spectra. Inclusion of the covariance matrix would weaken the constraint. Some aspects and these covariances of the multipole power spectra were investigated in [6,36], but they focused on the lower multipole spectra at smaller wave numbers. According to the statistical errors of the multipole spectra on the basis of the FKP method [10,35], the shot-noise contribution dominates the error at the larger wave numbers $k \gtrsim 0.3h{\rm Mpc}^{-1}$. Naively, the constraint will be improved by increasing the mean number density of a galaxy sample. The covariances for the higher multipole spectra need further investigations, which is out of the scope of the present paper.

Let us discuss the reason why the higher value of β is obtained from the analysis of the LRG sample. It could be a smoking gun of a modified gravity. For example, an $f(R)$ gravity model has an effective gravitation constant $G_{\rm eff} = 4G/3$, as long as the chameleon mechanism does not work. However, we should discuss the possible systematics that may lead to a larger value of β. Because the satellite fraction is small, being around 6% of the total LRGs, the first term dominates the right-hand side of Eq. (2). Then, taking the degeneracy in the central and the satellite galaxy velocities, we should understand that the constraint is

$$\frac{\sigma_c^2 + \sigma_s^2}{\sigma_{\rm v}^2} = \beta(\alpha_c^2 + \alpha_s^2) = 1.35^{+0.68}_{-0.45}, \tag{7}$$

in the case (D) when we use the BLRG sample for modeling the two-halo term. The results might be explained by a larger velocity dispersion of the central galaxy in the multiple system. Recently, Guo *et al.* have reported the velocity bias of galaxies in the SDSS CMASS samples [30]. The sample is different from ours, but they report that $\alpha_c \sim 0.3$. However, this value $\alpha_c \sim 0.3$ is rather small to explain our results, and $\alpha_c \sim 0.6$ is required within the general relativity $\beta = 1$. Other possible systematics is the modeling of the two-halo term in $P_\ell(k)$, as we obtained somewhat different values between (C) and (D) in Table II. This suggests that there exists a systematic error of the same order in our modeling of the two-halo term. More sophisticated simulations based on subhalo catalogs from N-body simulations could be necessary and useful.

The fiber collision effect influences pairs closer than a critical separation. We checked that our treatment for the fiber collisions works within the error. Namely, we have shown that the effect of the fiber collision can be modeled as an effective reduction of the satellite fraction, the validity of which is limited to the range of wave numbers $k < 0.6h{\rm Mpc}^{-1}$. However, this effect could be more complicated and a more careful modeling of the fiber collision might be necessary. The fiber collision effect will induce an additional anisotropic signature on very small scales in redshift space. This could be a systematic for our method, which needs more careful analysis.

IV. CONCLUSION

In summary, we have investigated the potential of the higher multipole power spectra of the galaxy distribution in redshift space. This method is based on the recent finding that a halo model accounts well for the behavior of the multipole power spectrum of LRGs on small scales. Our method uses the data of the spectrum on small scales $0.3 \le k/[h{\rm Mpc}^{-1}] \le 0.6$. This is quite in contrast to the usual method of testing gravity by measuring the linear growth rate on very large scales. Our method is based on the fact that the one-halo term makes a dominant contribution to the higher multipole power spectra at large wave numbers, which reflects the random motions of the satellite galaxies. We carefully investigated the relation between the velocity dispersion of the random motions of satellite galaxies and the host halo mass on the basis of the mock catalogs from N-body simulations. The validity of our theoretical model for the higher multipole power spectrum is tested using the results of the mock catalogs. By confronting our theoretical model and the observed multipole spectra of the SDSS LRG samples, we obtained a value for an effective gravitational constant somewhat larger than that predicted by the numerical simulations. This could be a smoking gun of the modified gravity. However, we might need to check our theoretical model for the two-halo term and the fiber collision effect more carefully. Our constraints on the velocity bias are not very tight. This is mainly due to the degeneracy with the HOD parameters because P_4 and P_6 are sensitive to the fraction of satellite galaxies [9,11]. The degeneracy can be largely

broken by jointly analyzing the projected correlation functions [30]. Including the information on the quadrupole power spectrum will also improve our constraint. We leave this for future work.

ACKNOWLEDGMENTS

K. Y. thanks the workshop, APC-YITP Collaboration: Mini-Workshop on Gravitation and Cosmology, which was held at YITP Kyoto University for a useful chance for discussions on the topic of the present paper. We thank L. Lombriser for useful discussions. This work is supported by a research support program of Hiroshima University. The research by C. H. is supported in part by a Grant-in-Aid for Scientific Research of Japanese Ministry of Education, Culture, Sports, Science, and Technology (No. 24740160).

[1] L. Anderson *et al.*, Mon. Not. R. Astron. Soc. **441**, 24 (2014).
[2] W. J. Percival *et al.*, Mon. Not. R. Astron. Soc. **439**, 2531 (2014).
[3] L. Samushia *et al.*, Mon. Not. R. Astron. Soc. **439**, 3504 (2014).
[4] C-H. Chuang *et al.*, arXiv:1312.4889.
[5] A. G. Sanchez *et al.*, Mon. Not. R. Astron. Soc. **440**, 2692 (2014).
[6] F. Beutler *et al.*, Mon. Not. R. Astron. Soc. **443**, 1065 (2014).
[7] L. Guzzo *et al.*, Nature (London) **451**, 541 (2008).
[8] K. Yamamoto, T. Sato, and G. Huetsi, Prog. Theor. Phys. **120**, 609 (2008).
[9] C. Hikage, Mon. Not. R. Astron. Soc. **441**, L21 (2014).
[10] K. Yamamoto, M. Nakamichi, A. Kamino, B. A. Bassett, and H. Nishioka, Publ. Astron. Soc. Jpn. **58**, 93 (2006).
[11] C. Hikage and K. Yamamoto, J. Cosmol. Astropart. Phys. 08 (2013) 019.
[12] U. Seljak, Mon. Not. R. Astron. Soc. **318**, 203 (2000).
[13] M. White, Mon. Not. R. Astron. Soc. **321**, 1 (2001).
[14] A. Cooray and R. Sheth, Phys. Rep. **372**, 1 (2002).
[15] R. K. Sheth and G. Tormen, Mon. Not. R. Astron. Soc. **308**, 119 (1999).
[16] Z. Zheng, A. A. Berlind, D. H. Weinberg, A. J. Benson, C. M. Baugh, S. Cole, R. Dave, C. S. Frenk, N. Katz, and C. G. Lacey, Astrophys. J. **633**, 791 (2005).
[17] J. Tinker, A. V. Kravtsov, A. Klypin, K. Abazajian, M. Warren, G. Yepes, S. Gottlöber, and D. E. Holz, Astrophys. J. **688**, 709 (2008).
[18] A. Jenkins, C. S. Frenk, S. D. M. White, J. M. Colberg, S. Cole, A. E. Evrard, H. M. P. Couchman, and N. Yoshida, Mon. Not. R. Astron. Soc. **321**, 372 (2001).
[19] B. A. Reid and D. N. Spergel, Astrophys. J. **698**, 143 (2009).
[20] J. F. Navarro, C. S. Frenk, and S. D. M. White, Astrophys. J. **490**, 493 (1997).
[21] R. Scoccimarro, R. K. Sheth, L. Hui, and B. Jain, Astrophys. J. **546**, 20 (2001).
[22] H. Guo *et al.*, Mon. Not. R. Astron. Soc. **441**, 2398 (2014).
[23] C. Hikage, R. Mandelbaum, M. Takada, and D. N. Spergel, Mon. Not. R. Astron. Soc. **435**, 2345 (2013).
[24] L. Lombriser, K. Koyama, G-B Zhao, and B. Li, Phys. Rev. D **85**, 124054 (2012).
[25] L. Lombriser, B. Li, K. Koyama, and G-B Zhao, Phys. Rev. D **87**, 123511 (2013).
[26] V. Springel, Mon. Not. R. Astron. Soc. **364**, 1105 (2005).
[27] M. R. Blanton, H. Lin, R. H. Lupton, F. M. Maley, N. Young, I. Zehavi, and J. Loveday, Astron. J. **125**, 2276 (2003).
[28] C. Hikage, M. Takada, and D. N. Spergel, Mon. Not. R. Astron. Soc. **419**, 3457 (2012).
[29] S. Masaki, C. Hikage, M. Takada, D. N. Spergel, and N. Sugiyama, Mon. Not. R. Astron. Soc. **433**, 3506 (2013).
[30] H. Guo, Z. Zheng, I. Zehavi, K. Dawson, R. A. Skibba, J. L. Tinker, D. H. Weinberg, M. White, and D. P. Schneider, Mon. Not. R. Astron. Soc. **446**, 578 (2015).
[31] H. Guo, I. Zehav, and Z. Zheng, Astrophys. J. **756**, 127 (2012).
[32] K. N. Abazajian *et al.*, Astrophys. J. Suppl. Ser. **182**, 543 (2009).
[33] A. Oka, S. Saito, T. Nishimichi, A. Taruya, and K. Yamamoto, Mon. Not. R. Astron. Soc. **439**, 2515 (2014).
[34] K. Yamamoto, G. Nakamura, G. Hütsi, T. Narikawa, and T. Sato, Phys. Rev. D **81**, 103517 (2010).
[35] H. A. Feldman, N. Kaiser, and J. A. Peacock, Astrophys. J. **426**, 23 (1994).
[36] T. Sato, G. Huetsi, and K. Yamamoto, Prog. Theor. Phys. **125**, 187 (2011).

Third order solutions of cosmological density perturbations in Horndeski's most general scalar-tensor theory with the Vainshtein mechanism

Yuichiro Takushima,[1] Ayumu Terukina,[1] and Kazuhiro Yamamoto[1,2]

[1]*Department of Physical Science, Graduate School of Science, Hiroshima University, Kagamiyama 1-3-1, Higashi-hiroshima, 739-8526, Japan*

[2]*Hiroshima Astrophysical Science Center, Hiroshima University, Kagamiyama 1-3-1, Higashi-hiroshima, 739-8526, Japan*

(Received 13 February 2015; published 17 November 2015)

We study the third order solutions of the cosmological density perturbations in Horndeski's most general scalar-tensor theory under the condition that the Vainshtein mechanism is at work. In this work, we thoroughly investigate the independence property of the functions describing the nonlinear mode couplings, which is also useful for models within general relativity. Then, we find that the solutions of the density contrast and the velocity divergence up to third order are characterized by six parameters. Furthermore, the one-loop order power spectra obtained with third order solutions are described by four parameters. We exemplify the behavior of the one-loop order power spectra assuming the kinetic gravity braiding model, which demonstrates that the effect of modified gravity appears more significantly in the power spectrum of the velocity divergence than the density contrast.

DOI: 10.1103/PhysRevD.92.104033 PACS numbers: 04.50.Kd, 95.36.+x, 98.80.-k

I. INTRODUCTION

The accelerated expansion of the Universe is one of the most fundamental problems in modern cosmology. The standard cosmological model introducing the cosmological constant is consistent with various observations [1,2]. However, the small value of the cosmological constant raises the problem of fine-tuning [3–5]. As an alternative to the cosmological constant, the cosmic accelerated expansion might be explained by modifying gravity theory (see, e.g., Refs. [6–18]). In the present paper, we focus on the most general scalar-tensor theory with second order differential field equations [19,20], which was first discovered by Horndeski [21]. Horndeski's most general scalar-tensor theory, including four arbitrary functions of the scalar field and kinetic term, reduces to various modified gravity models by choosing four specific functions. Because Horndeski's theory includes a wide class of modified gravity models, we adopt it as an effective theory of the generalized theories of gravity.

In the present paper, we investigate the aspects of the quasinonlinear evolution of the cosmological density perturbations in Horndeski's most general scalar-tensor theory, assuming that the Vainshtein mechanism is at work [22–25]. The Vainshtein mechanism is the screening mechanism, which is useful to evade the constraints from the gravity tests in the solar system. We investigate the effects of the nonlinear terms in the matter's fluid equations as well as the nonlinear derivative interaction terms in the scalar field equation. In a previous work [26], the second order solution of the cosmological density perturbations was obtained. In the present paper, we extend the analysis to the third order solution, which enables us to compute the one-loop order matter power spectrum.

There are many works on the higher order cosmological density perturbations and the quasinonlinear matter power spectrum which have been developed from the standard perturbative approach (see, e.g., Refs. [27–37]). Improvements to include the nonperturbative effects have been investigated (see, e.g., Refs. [38–43]), but here we adopt the standard perturbative approach of the cosmological density perturbations as a starting place for the analysis of Horndeski's most general scalar-tensor theory. Related to the present paper, we refer to the recent work by Lee, Park, and Biern [44], in which a similar solution was obtained for the dark energy model within general relativity.

This paper is organized as follows. In Sec. II, we review the basic equations and the second order solution [26]. In Sec. III, we construct the third order solutions of the cosmological density perturbations. Here, we carefully investigate independent functions of mode couplings describing nonlinear interactions. In Sec. IV, we derive the expression of the one-loop order power spectra of the matter density contrast and the velocity divergence. In Sec. V, we demonstrate the behavior of the one-loop order power spectra in the kinetic gravity braiding (KGB) model. Section VI is devoted to a summary and conclusions. In Appendix A, definitions of the coefficients to characterize Horndeski's theory are summarized. In Appendix B, definitions of the functions to describe the nonlinear mode coupling for the third order solutions are summarized. In Appendix C, a derivation of the one-loop power spectra is summarized. Expressions in Appendix D are useful for the deviation of the one-loop power spectra. Appendix E lists the coefficients to characterize the kinetic gravity braiding model.

 © 2015 American Physical Society

II. REVIEW OF THE SECOND ORDER SOLUTION

Let us start by reviewing the basic formulas [23,26]. We consider Horndeski's most general scalar-tensor theory, whose action is given by

$$S = \int d^4x\sqrt{-g}(\mathcal{L}_{\rm GG} + \mathcal{L}_{\rm m}), \tag{1}$$

where we define

$$\begin{aligned}\mathcal{L}_{\rm GG} &= K(\phi, X) - G_3(\phi, X)\Box\phi + G_4(\phi, X)R \\ &\quad + G_{4X}[(\Box\phi)^2 - (\nabla_\mu\nabla_\nu\phi)^2] \\ &\quad + G_5(\phi, X)G_{\mu\nu}\nabla^\mu\nabla^\nu\phi \\ &\quad - \frac{1}{6}G_{5X}[(\Box\phi)^3 - 3\Box\phi(\nabla_\mu\nabla_\nu\phi)^2 + 2(\nabla_\mu\nabla_\nu\phi)^3],\end{aligned} \tag{2}$$

where K, G_3, G_4, and G_5 are arbitrary functions of the scalar field ϕ and the kinetic term $X \coloneqq -(\partial\phi)^2/2$, G_{iX} denotes $\partial G_i/\partial X$, R is the Ricci scalar, $G_{\mu\nu}$ is the Einstein tensor, and $\mathcal{L}_{\rm m}$ is the Lagrangian of the matter field, which is minimally coupled to gravity.

The basic equations for the cosmological density perturbations are derived in Ref. [23]. Here, we briefly review the method and the results (see Ref. [23] for details). This theory was discovered in Ref. [19] as a generalization of Galileon theory (see Ref. [45] and also Refs. [20,46–64]), but the equivalence to Horndeski's theory [21] is shown in Ref. [20]. We consider a spatially flat expanding universe and metric perturbations in Newtonian gauge, whose line element is written as

$$ds^2 = -(1 + 2\Phi(t, \mathbf{x}))dt^2 + a^2(t)(1 - 2\Psi(t, \mathbf{x}))d\mathbf{x}^2. \tag{3}$$

We define the scalar field with perturbations by

$$\phi \to \phi(t) + \delta\phi(t, \mathbf{x}), \tag{4}$$

and we introduce $Q = H\delta\phi/\dot{\phi}$.

The basic equations of the gravitational and scalar fields are derived on the basis of the quasistatic approximation of the subhorizon scales [23]. In the models where the Vainshtein mechanism may work, the basic equations can be found by keeping the leading terms schematically written as $(\partial\partial Y)^n$, with $n \geq 1$, where ∂ denotes a spatial derivative and Y denotes Φ, Ψ, or Q. Such terms make a leading contribution of order $(L_{\rm H}^2\partial\partial Y)^n$, where $L_{\rm H}$ is a typical horizon length scale, and we have

$$\begin{aligned}\nabla^2(\mathcal{F}_T\Psi - \mathcal{G}_T\Phi - A_1Q) &= \frac{B_1}{2a^2H^2}\mathcal{Q}^{(2)} \\ &\quad + \frac{B_3}{a^2H^2}(\nabla^2\Phi\nabla^2Q - \partial_i\partial_j\Phi\partial^i\partial^jQ)\end{aligned} \tag{5}$$

and

$$\begin{aligned}\mathcal{G}_T\nabla^2\Psi &= \frac{a^2}{2}\rho_{\rm m}\delta - A_2\nabla^2Q - \frac{B_2}{2a^2H^2}\mathcal{Q}^{(2)} \\ &\quad - \frac{B_3}{a^2H^2}(\nabla^2\Psi\nabla^2Q - \partial_i\partial_j\Psi\partial^i\partial^jQ) - \frac{C_1}{3a^4H^4}\mathcal{Q}^{(3)},\end{aligned} \tag{6}$$

where $\rho_{\rm m}$ is the background matter density and δ is the matter density contrast. We define

$$\mathcal{Q}^{(2)} \coloneqq (\nabla^2Q)^2 - (\partial_i\partial_jQ)^2, \tag{7}$$

$$\mathcal{Q}^{(3)} \coloneqq (\nabla^2Q)^3 - 3\nabla^2Q(\partial_i\partial_jQ)^2 + 2(\partial_i\partial_jQ)^3. \tag{8}$$

The equation of the scalar field perturbation is

$$\begin{aligned}&A_0\nabla^2Q - A_1\nabla^2\Psi - A_2\nabla^2\Phi + \frac{B_0}{a^2H^2}\mathcal{Q}^{(2)} \\ &\quad - \frac{B_1}{a^2H^2}(\nabla^2\Psi\nabla^2Q - \partial_i\partial_j\Psi\partial^i\partial^jQ) \\ &\quad - \frac{B_2}{a^2H^2}(\nabla^2\Phi\nabla^2Q - \partial_i\partial_j\Phi\partial^i\partial^jQ) \\ &\quad - \frac{B_3}{a^2H^2}(\nabla^2\Phi\nabla^2\Psi - \partial_i\partial_j\Phi\partial^i\partial^j\Psi) \\ &\quad - \frac{C_0}{a^4H^4}\mathcal{Q}^{(3)} - \frac{C_1}{a^4H^4}\mathcal{U}^{(3)} = 0,\end{aligned} \tag{9}$$

where we define

$$\begin{aligned}\mathcal{U}^{(3)} &\coloneqq \mathcal{Q}^{(2)}\nabla^2\Phi - 2\nabla^2Q\partial_i\partial_jQ\partial^i\partial^j\Phi \\ &\quad + 2\partial_i\partial_jQ\partial^j\partial^kQ\partial_k\partial^i\Phi.\end{aligned} \tag{10}$$

Here the coefficients $\mathcal{F}_T$, A_1, B_1, C_1, etc., are defined in Appendix A. A_i, B_i, and C_i are the coefficients of the linear, quadratic, and cubic terms of Ψ, Φ, and Q, respectively.

From the continuity equation and the Euler equation for the matter fluid, we have the following equations for the density contrast δ and the velocity field u^i,

$$\frac{\partial\delta(t, \mathbf{x})}{\partial t} + \frac{1}{a}\partial_i[(1 + \delta(t, \mathbf{x}))u^i(t, \mathbf{x})] = 0, \tag{11}$$

$$\frac{\partial u^i(t, \mathbf{x})}{\partial t} + \frac{\dot{a}}{a}u^i(t, \mathbf{x}) + \frac{1}{a}u^j(t, \mathbf{x})\partial_ju^i(t, \mathbf{x}) = -\frac{1}{a}\partial_i\Phi(t, \mathbf{x}), \tag{12}$$

respectively. The properties of the gravity sector are influenced through Φ in Eq. (12), where Φ is determined by Eqs. (5), (6), and (9).

Now, introducing the scalar function $\theta \equiv \nabla\mathbf{u}/(aH)$, which we call velocity divergence, we perform the Fourier expansions for δ and θ,

$$\delta(t,\mathbf{x}) = \frac{1}{(2\pi)^3}\int d^3p\,\delta(t,\mathbf{p})e^{i\mathbf{p}\cdot\mathbf{x}}, \tag{13}$$

$$u^j(t,\mathbf{x}) = \frac{1}{(2\pi)^3}\int d^3p\,\frac{-ip^j}{p^2}aH\theta(t,\mathbf{p})e^{i\mathbf{p}\cdot\mathbf{x}}. \tag{14}$$

In a similar way, we perform the Fourier expansions for Φ, Ψ, and Q. Then, the gravity equations (5) and (6) lead to

$$-p^2(\mathcal{F}_T\Psi(t,\mathbf{p}) - \mathcal{G}_T\Phi(t,\mathbf{p}) - A_1Q(t,\mathbf{p})) = \frac{B_1}{2a^2H^2}\Gamma[t,\mathbf{p};Q,Q] + \frac{B_3}{a^2H^2}\Gamma[t,\mathbf{p};Q,\Phi], \tag{15}$$

$$\begin{aligned}-p^2(\mathcal{G}_T\Psi(t,\mathbf{p}) + A_2Q(t,\mathbf{p})) - \frac{a^2}{2}\rho_{\mathrm{m}}\delta(t,\mathbf{p}) = &-\frac{B_2}{2a^2H^2}\Gamma[t,\mathbf{p};Q,Q] - \frac{B_3}{a^2H^2}\Gamma[t,\mathbf{p};Q,\Psi]\\ &-\frac{C_1}{3a^4H^4}\Xi_1[t,\mathbf{p};Q,Q,Q],\end{aligned} \tag{16}$$

respectively, where we define

$$\Gamma[t,\mathbf{p};Z_1,Z_2] = \frac{1}{(2\pi)^3}\int d\mathbf{k}_1d\mathbf{k}_2\delta^{(3)}(\mathbf{k}_1+\mathbf{k}_2-\mathbf{p})(k_1^2k_2^2-(\mathbf{k}_1\cdot\mathbf{k}_2)^2)Z_1(t,\mathbf{k}_1)Z_2(t,\mathbf{k}_2), \tag{17}$$

$$\begin{aligned}\Xi_1[t,\mathbf{p};Z_1,Z_2,Z_3] = &\frac{1}{(2\pi)^6}\int d\mathbf{k}_1d\mathbf{k}_2d\mathbf{k}_3\delta^{(3)}(\mathbf{k}_1+\mathbf{k}_2+\mathbf{k}_3-\mathbf{p})\\ &\times[-k_1^2k_2^2k_3^2+3k_1^2(\mathbf{k}_2\cdot\mathbf{k}_3)^2-2(\mathbf{k}_1\cdot\mathbf{k}_2)(\mathbf{k}_2\cdot\mathbf{k}_3)(\mathbf{k}_3\cdot\mathbf{k}_1)]Z_1(t,\mathbf{k}_1)Z_2(t,\mathbf{k}_2)Z_3(t,\mathbf{k}_3),\end{aligned} \tag{18}$$

where Z_1, Z_2, and Z_3 denote Q, Φ, or Ψ. The equation for scalar field perturbation (9) leads to

$$\begin{aligned}-p^2(A_0Q(t,\mathbf{p}) - A_1\Psi(t,\mathbf{p}) - A_2\Phi(t,\mathbf{p})) = &-\frac{B_0}{a^2H^2}\Gamma[t,\mathbf{p};Q,Q] + \frac{B_1}{a^2H^2}\Gamma[t,\mathbf{p};Q,\Psi]\\ &+\frac{B_2}{a^2H^2}\Gamma[t,\mathbf{p};Q,\Phi] + \frac{B_3}{a^2H^2}\Gamma[t,\mathbf{p};\Psi,\Phi] + \frac{C_0}{a^4H^4}\Xi_1[t,\mathbf{p};Q,Q,Q]\\ &+\frac{C_1}{a^4H^4}\Xi_2[t,\mathbf{p};Q,Q,\Phi],\end{aligned} \tag{19}$$

where we define

$$\begin{aligned}\Xi_2[t,\mathbf{p};Z_1,Z_2,Z_3] = &\frac{1}{(2\pi)^6}\int d\mathbf{k}_1d\mathbf{k}_2d\mathbf{k}_3\delta^{(3)}(\mathbf{k}_1+\mathbf{k}_2+\mathbf{k}_3-\mathbf{p})[-k_1^2k_2^2k_3^2+(\mathbf{k}_1\cdot\mathbf{k}_2)^2k_3^2\\ &+2k_1^2(\mathbf{k}_2\cdot\mathbf{k}_3)^2-2(\mathbf{k}_1\cdot\mathbf{k}_2)(\mathbf{k}_2\cdot\mathbf{k}_3)(\mathbf{k}_3\cdot\mathbf{k}_1)]Z_1(t,\mathbf{k}_1)Z_2(t,\mathbf{k}_2)Z_3(t,\mathbf{k}_3).\end{aligned} \tag{20}$$

The fluid equations (11) and (12) lead to

$$\frac{1}{H}\frac{\partial\delta(t,\mathbf{p})}{\partial t} + \theta(t,\mathbf{p}) = -\frac{1}{(2\pi)^3}\int d\mathbf{k}_1d\mathbf{k}_2\delta^{(3)}(\mathbf{k}_1+\mathbf{k}_2-\mathbf{p})\alpha(\mathbf{k}_1,\mathbf{k}_2)\theta(t,\mathbf{k}_1)\delta(t,\mathbf{k}_2), \tag{21}$$

$$\frac{1}{H}\frac{\partial\theta(t,\mathbf{p})}{\partial t} + \left(2+\frac{\dot{H}}{H^2}\right)\theta(t,\mathbf{p}) - \frac{p^2}{a^2H^2}\Phi(t,\mathbf{p}) = -\frac{1}{(2\pi)^3}\int d\mathbf{k}_1d\mathbf{k}_2\delta^{(3)}(\mathbf{k}_1+\mathbf{k}_2-\mathbf{p})\beta(\mathbf{k}_1,\mathbf{k}_2)\theta(t,\mathbf{k}_1)\theta(t,\mathbf{k}_2), \tag{22}$$

where we define

$$\alpha(\mathbf{k}_1,\mathbf{k}_2) = 1 + \frac{\mathbf{k}_1\cdot\mathbf{k}_2}{k_1^2}, \tag{23}$$

$$\beta(\mathbf{k}_1,\mathbf{k}_2)=\frac{(\mathbf{k}_1\cdot\mathbf{k}_2)|\mathbf{k}_1+\mathbf{k}_2|^2}{2k_1^2k_2^2}. \tag{24}$$

Note that $\alpha(\mathbf{k}_1,\mathbf{k}_2)$ does not have symmetry with respect to the exchange between $\mathbf{k}_1$ and $\mathbf{k}_2$. We find the solution in terms of a perturbative expansion, which can be written in the form

$$Y(t,\mathbf{p})=\sum_{n=1}Y_n(t,\mathbf{p}), \tag{25}$$

where Y denotes δ, θ, Ψ, Φ, or Q, and Y_n denotes the nth order solution of the perturbative expansion. Neglecting the decaying mode solution, the linear order solution is written as [23,65]

$$\delta_1(t,\mathbf{p})=D_+(t)\delta_{\rm L}(\mathbf{p}), \tag{26}$$

$$\theta_1(t,\mathbf{p})=-D_+(t)f(t)\delta_{\rm L}(\mathbf{p}), \tag{27}$$

$$\Phi_1(t,\mathbf{p})=-\frac{a^2H^2}{p^2}D_+(t)\kappa_\Phi(t)\delta_{\rm L}(\mathbf{p}), \tag{28}$$

$$\Psi_1(t,\mathbf{p})=-\frac{a^2H^2}{p^2}D_+(t)\kappa_\Psi(t)\delta_{\rm L}(\mathbf{p}), \tag{29}$$

$$Q_1(t,\mathbf{p})=-\frac{a^2H^2}{p^2}D_+(t)\kappa_Q(t)\delta_{\rm L}(\mathbf{p}), \tag{30}$$

where $D_+(t)$ is the growth factor obeying

$$\frac{d^2D_+(t)}{dt^2}+2H\frac{dD_+(t)}{dt}+L(t)D_+(t)=0, \tag{31}$$

with

$$L(t)=-\frac{(A_0\mathcal{F}_T-A_1^2)\rho_{\rm m}}{2(A_0\mathcal{G}_T^2+2A_1A_2\mathcal{G}_T+A_2\mathcal{F}_T)}, \tag{32}$$

and $\delta_{\rm L}(\mathbf{p})$ describes the linear density perturbations, which are assumed to obey the Gaussian random distribution. Here we adopt the normalization for the growth factor $D_+(a)=a$ at $a\ll1$, and introduce the linear growth rate defined by $f(t)=d\ln D_+(t)/\ln a$.

The second order solution is written as (see Ref. [26] for details)

$$\delta_2(t,\mathbf{p})=D_+^2(t)\left(\mathcal{W}_\alpha(\mathbf{p})-\frac{2}{7}\lambda(t)\mathcal{W}_\gamma(\mathbf{p})\right), \tag{33}$$

$$\theta_2(t,\mathbf{p})=-D_+^2(t)f\left(\mathcal{W}_\alpha(\mathbf{p})-\frac{4}{7}\lambda_\theta(t)\mathcal{W}_\gamma(\mathbf{p})\right), \tag{34}$$

$$\Phi_2(t,\mathbf{p})=-\frac{a^2H^2}{p^2}D_+^2(t)(\kappa_\Phi(t)\mathcal{W}_\alpha(\mathbf{p})+\lambda_\Phi(t)\mathcal{W}_\gamma(\mathbf{p})), \tag{35}$$

$$\Psi_2(t,\mathbf{p})=-\frac{a^2H^2}{p^2}D_+^2(t)(\kappa_\Psi(t)\mathcal{W}_\alpha(\mathbf{p})+\lambda_\Psi(t)\mathcal{W}_\gamma(\mathbf{p})), \tag{36}$$

$$Q_2(t,\mathbf{p})=-\frac{a^2H^2}{p^2}D_+^2(t)(\kappa_Q(t)\mathcal{W}_\alpha(\mathbf{p})+\lambda_Q(t)\mathcal{W}_\gamma(\mathbf{p})), \tag{37}$$

where the coefficients κ_Φ, κ_Ψ, κ_Q, λ, λ_θ, λ_Φ, λ_Ψ, and λ_Q are determined by the functions in the Lagrangian and the Hubble parameter, whose definitions are summarized in Appendix A. Here $\mathcal{W}_\alpha(\mathbf{p})$ and $\mathcal{W}_\gamma(\mathbf{p})$ are defined as

$$\mathcal{W}_\alpha(\mathbf{p})=\frac{1}{(2\pi)^3}\int d\mathbf{k}_1d\mathbf{k}_2\delta^{(3)}(\mathbf{k}_1+\mathbf{k}_2-\mathbf{p})\alpha^{(s)}(\mathbf{k}_1,\mathbf{k}_2)\times\delta_{\rm L}(\mathbf{k}_1)\delta_{\rm L}(\mathbf{k}_2), \tag{38}$$

$$\mathcal{W}_\gamma(\mathbf{p})=\frac{1}{(2\pi)^3}\int d\mathbf{k}_1d\mathbf{k}_2\delta^{(3)}(\mathbf{k}_1+\mathbf{k}_2-\mathbf{p})\gamma(\mathbf{k}_1,\mathbf{k}_2)\times\delta_{\rm L}(\mathbf{k}_1)\delta_{\rm L}(\mathbf{k}_2), \tag{39}$$

with

$$\alpha^{(s)}(\mathbf{k}_1,\mathbf{k}_2)=1+\frac{\mathbf{k}_1\cdot\mathbf{k}_2(k_1^2+k_2^2)}{2k_1^2k_2^2}, \tag{40}$$

$$\gamma(\mathbf{k}_1,\mathbf{k}_2)=1-\frac{(\mathbf{k}_1\cdot\mathbf{k}_2)^2}{k_1^2k_2^2}, \tag{41}$$

where $\alpha^{(s)}(\mathbf{k}_1,\mathbf{k}_2)$ is obtained by symmetrizing $\alpha(\mathbf{k}_1,\mathbf{k}_2)$ with respect to $\mathbf{k}_1$ and $\mathbf{k}_2$, and $\gamma(\mathbf{k}_1,\mathbf{k}_2)$ is the function that describes the mode couplings for the nonlinear interaction in the gravitational field equations and the scalar field equation. Here, $\alpha^{(s)}(\mathbf{k}_1,\mathbf{k}_2)$, $\beta(\mathbf{k}_1,\mathbf{k}_2)$, and $\gamma(\mathbf{k}_1,\mathbf{k}_2)$ have symmetry with respect to the exchange between $\mathbf{k}_1$ and $\mathbf{k}_2$. One can easily check that the functions that describe the nonlinear mode couplings, $\alpha^{(s)}(\mathbf{k}_1,\mathbf{k}_2)$, $\beta(\mathbf{k}_1,\mathbf{k}_2)$, and $\gamma(\mathbf{k}_1,\mathbf{k}_2)$, satisfy

$$\beta(\mathbf{k}_1,\mathbf{k}_2)=\alpha^{(s)}(\mathbf{k}_1,\mathbf{k}_2)-\gamma(\mathbf{k}_1,\mathbf{k}_2). \tag{42}$$

We briefly compare our work with Ref. [44], which is essentially the same as ours, though the authors of Ref. [44] restrict their investigations to the dark energy model within general relativity. The difference is that our approach includes the relations between the functions of mode couplings, e.g., Eqs. (42), (B19), (B20), and (B21). For example, the second order solution of the density contrast (33) agrees with Eq. (12) in Ref. [44] by finding the relations

$$c_{21}=1-\frac{2}{7}\lambda(t),\qquad c_{22}=-\frac{1}{7}\lambda(t). \tag{43}$$

This predicts the relation $c_{21}-2c_{22}=1$. Thus, the difference is the inclusion of the independence property of

mode-coupling functions, which reduces the number of parameters to characterize the model, as is also described in the next sections. However, the consistency is demonstrated by computing the power spectrum $P_{\delta\delta}(k)$ for a ΛCDM model (see Fig. 1).

III. THIRD ORDER EQUATIONS

In this section we consider the third order solutions. The third order solution of the cosmological density perturbations has been investigated in various models [27–33,35–37,44]. We present the third order solution for Horndeski's theory in the cosmological background. Our results are general and applicable to various modified gravity models. Plus, our results are useful for the case of general relativity because we clarify the independence property of the mode-coupling functions and the relevant parameters to characterize the third order solution. We start by solving the third order equations for gravity and the scalar field,

$$-p^2(\mathcal{F}_T\Psi_3(t,\mathbf{p})-\mathcal{G}_T\Phi_3(t,\mathbf{p})-A_1Q_3(t,\mathbf{p}))=\frac{B_1}{a^2H^2}\Gamma[t,\mathbf{p};Q_1,Q_2]+\frac{B_3}{a^2H^2}(\Gamma[t,\mathbf{p};Q_1,\Phi_2]+\Gamma[t,\mathbf{p};Q_2,\Phi_1]), \tag{44}$$

$$-p^2(\mathcal{G}_T\Psi_3(t,\mathbf{p})+A_2Q_3(t,\mathbf{p}))-\frac{a^2}{2}\rho_{\rm m}\delta_3(t,\mathbf{p})=-\frac{B_2}{a^2H^2}\Gamma[t,\mathbf{p};Q_1,Q_2]-\frac{B_3}{a^2H^2}(\Gamma[t,\mathbf{p};Q_1,\Psi_2]+\Gamma[t,\mathbf{p};Q_2,\Psi_1])$$
$$-\frac{C_1}{3a^4H^4}\Xi_1[t,\mathbf{p};Q_1,Q_1,Q_1], \tag{45}$$

$$-p^2(A_0Q_3(t,\mathbf{p})-A_1\Psi_3(t,\mathbf{p})-A_2\Phi_3(t,\mathbf{p}))=-\frac{2B_0}{a^2H^2}\Gamma[t,\mathbf{p};Q_1,Q_2]+\frac{B_1}{a^2H^2}(\Gamma[t,\mathbf{p};Q_1,\Psi_2]+\Gamma[t,\mathbf{p};Q_2,\Psi_1])$$
$$+\frac{B_2}{a^2H^2}(\Gamma[t,\mathbf{p};Q_1,\Phi_2]+\Gamma[t,\mathbf{p};Q_2,\Phi_1])+\frac{B_3}{a^2H^2}(\Gamma[t,\mathbf{p};\Psi_1,\Phi_2]$$
$$+\Gamma[t,\mathbf{p};\Psi_2,\Phi_1])+\frac{C_0}{a^4H^4}\Xi_1[t,\mathbf{p};Q_1,Q_1,Q_1]+\frac{C_1}{a^4H^4}\Xi_2[t,\mathbf{p};Q_1,Q_1,\Phi_1]. \tag{46}$$

Inserting the first and second order solutions into the above equations, we finally have

$$\mathcal{F}_T\Psi_3(t,\mathbf{p})-\mathcal{G}_T\Phi_3(t,\mathbf{p})-A_1Q_3(t,\mathbf{p})=-\frac{a^2H^2}{p^2}D_+^3(t)((B_1\kappa_Q^2+2B_3\kappa_\Phi\kappa_Q)\mathcal{W}_{\gamma\alpha}(\mathbf{p})$$
$$+(B_1\kappa_Q\lambda_Q+B_3(\kappa_\Phi\lambda_Q+\kappa_Q\lambda_\Phi))\mathcal{W}_{\gamma\gamma}(\mathbf{p})), \tag{47}$$

$$\mathcal{G}_T\Psi_3(t,\mathbf{p})+A_2Q_3(t,\mathbf{p})+\frac{a^2}{2p^2}\rho_{\rm m}\delta_3(t,\mathbf{p})=\frac{a^2H^2}{p^2}D_+^3(t)((B_2\kappa_Q^2+2B_3\kappa_\Psi\kappa_Q)\mathcal{W}_{\gamma\alpha}(\mathbf{p})$$
$$+(B_2\kappa_Q\lambda_Q+B_3(\kappa_\Psi\lambda_Q+\kappa_Q\lambda_\Psi))\mathcal{W}_{\gamma\gamma}(\mathbf{p})+\frac{C_1}{3}\kappa_Q^3\mathcal{W}_\xi(\mathbf{p})), \tag{48}$$

$$A_0Q_3(t,\mathbf{p})-A_1\Psi_3(t,\mathbf{p})-A_2\Phi_3(t,\mathbf{p})=-\frac{a^2H^2}{p^2}D_+^3(t)((-2B_0\kappa_Q^2+2B_1\kappa_\Psi\kappa_Q+2B_2\kappa_\Phi\kappa_Q+2B_3\kappa_\Phi\kappa_\Psi)\mathcal{W}_{\gamma\alpha}(\mathbf{p})$$
$$+((-2B_0\kappa_Q\lambda_Q+B_1(\kappa_\Psi\lambda_Q+\kappa_Q\lambda_\Psi)+B_2(\kappa_\Phi\lambda_Q+\kappa_Q\lambda_\Phi)+B_3(\kappa_\Phi\lambda_\Psi+\kappa_\Psi\lambda_\Phi))\mathcal{W}_{\gamma\gamma}(\mathbf{p})$$
$$+(C_0\kappa_Q^3+C_1\kappa_\Phi\kappa_Q^2)\mathcal{W}_\xi(\mathbf{p})), \tag{49}$$

where we define $\mathcal{W}_{\gamma\alpha}(\mathbf{p})$, $\mathcal{W}_{\gamma\gamma}(\mathbf{p})$, and $\mathcal{W}_\xi(\mathbf{p})$ using Eqs. (B1), (B2), and (B3), respectively, in Appendix B. Then, the gravitational and curvature potentials and the scalar field perturbations are written as

$$\Phi_3(t,\mathbf{p})=-\frac{a^2H^2}{p^2}(\kappa_\Phi(t)\delta_3(t,\mathbf{p})+D_+^3(t)(\sigma_\Phi(t)\mathcal{W}_{\gamma\alpha}(\mathbf{p})+\mu_\Phi(t)\mathcal{W}_{\gamma\gamma}(\mathbf{p})+\nu_\Phi(t)\mathcal{W}_\xi(\mathbf{p}))), \tag{50}$$

$$\Psi_3(t,\mathbf{p})=-\frac{a^2H^2}{p^2}(\kappa_\Psi(t)\delta_3(t,\mathbf{p})+D_+^3(t)(\sigma_\Psi(t)\mathcal{W}_{\gamma\alpha}(\mathbf{p})+\mu_\Psi(t)\mathcal{W}_{\gamma\gamma}(\mathbf{p})+\nu_\Psi(t)\mathcal{W}_\xi(\mathbf{p}))), \tag{51}$$

$$Q_3(t,\mathbf{p})=-\frac{a^2H^2}{p^2}(\kappa_Q(t)\delta_3(t,\mathbf{p})+D_+^3(t)(\sigma_Q(t)\mathcal{W}_{\gamma\alpha}(\mathbf{p})+\mu_Q(t)\mathcal{W}_{\gamma\gamma}(\mathbf{p})+\nu_Q(t)\mathcal{W}_\xi(\mathbf{p}))), \tag{52}$$

where the coefficients $\sigma_\Phi(t)$, $\mu_\Phi(t)$, $\nu_\Phi(t)$, etc., are defined in Appendix A. The third order equations for $\delta_3(t,\mathbf{p})$ and $\theta_3(t,\mathbf{p})$ are

$$\frac{1}{H}\frac{\partial\delta_3(t,\mathbf{p})}{\partial t}+\theta_3(t,\mathbf{p}) = -\frac{1}{(2\pi)^3}\int d\mathbf{k}_1 d\mathbf{k}_2\delta^{(3)}(\mathbf{k}_1+\mathbf{k}_2-\mathbf{p})\alpha(\mathbf{k}_1,\mathbf{k}_2) \times(\theta_1(t,\mathbf{k}_1)\delta_2(t,\mathbf{k}_2)+\theta_2(t,\mathbf{k}_1)\delta_1(t,\mathbf{k}_2)), \tag{53}$$

$$\frac{1}{H}\frac{\partial\theta_3(t,\mathbf{p})}{\partial t}+\left(2+\frac{\dot H}{H^2}\right)\theta_3(t,\mathbf{p})-\frac{p^2}{a^2H^2}\Phi_3(t,\mathbf{p}) = -\frac{2}{(2\pi)^3}\int d\mathbf{k}_1 d\mathbf{k}_2\delta^{(3)}(\mathbf{k}_1+\mathbf{k}_2-\mathbf{p})\beta(\mathbf{k}_1,\mathbf{k}_2) \times\theta_1(t,\mathbf{k}_1)\theta_2(t,\mathbf{k}_2). \tag{54}$$

Using the first and second order solutions, these equations are rewritten as

$$\frac{1}{H}\frac{\partial\delta_3(t,\mathbf{p})}{\partial t}+\theta_3(t,\mathbf{p}) = D_+^3(t)f\Big(\mathcal{W}_{\alpha\alpha R}(\mathbf{p})-\frac{2}{7}\lambda\mathcal{W}_{\alpha\gamma R}(\mathbf{p}) +\mathcal{W}_{\alpha\alpha L}(\mathbf{p})-\frac{4}{7}\lambda_\theta\mathcal{W}_{\alpha\gamma L}(\mathbf{p})\Big), \tag{55}$$

$$\frac{1}{H}\frac{\partial\theta_3(t,\mathbf{p})}{\partial t}+\left(2+\frac{\dot H}{H^2}\right)\theta_3(t,\mathbf{p})-\frac{p^2}{a^2H^2}\Phi_3(t,\mathbf{p}) = 2D_+^3(t)f^2\Big(-\mathcal{W}_{\alpha\alpha}(\mathbf{p})+\frac{4}{7}\lambda_\theta\mathcal{W}_{\alpha\gamma}(\mathbf{p}) +\mathcal{W}_{\gamma\alpha}(\mathbf{p})-\frac{4}{7}\lambda_\theta\mathcal{W}_{\gamma\gamma}(\mathbf{p})\Big), \tag{56}$$

where we introduce the functions defined by Eqs. (B7)–(B12), for which we find that the following relations hold,

$$2\mathcal{W}_{\gamma\alpha}(\mathbf{p}) = \mathcal{W}_{\alpha\gamma R}(\mathbf{p})+2\mathcal{W}_{\gamma\gamma}(\mathbf{p})-\mathcal{W}_{\xi}(\mathbf{p}), \tag{57}$$

$$2\mathcal{W}_{\alpha\alpha}(\mathbf{p}) = \mathcal{W}_{\alpha\alpha R}(\mathbf{p})+\mathcal{W}_{\alpha\alpha L}(\mathbf{p}), \tag{58}$$

$$2\mathcal{W}_{\alpha\gamma}(\mathbf{p}) = \mathcal{W}_{\alpha\gamma R}(\mathbf{p})+\mathcal{W}_{\alpha\gamma L}(\mathbf{p}). \tag{59}$$

Then, Eqs. (55) and (56) reduce to

$$\frac{1}{H}\frac{\partial\delta_3(t,\mathbf{p})}{\partial t}+\theta_3(t,\mathbf{p}) = D_+^3(t)f\Big(2\mathcal{W}_{\alpha\alpha}(\mathbf{p})-\frac{2}{7}\lambda\mathcal{W}_{\alpha\gamma R}(\mathbf{p})-\frac{4}{7}\lambda_\theta\mathcal{W}_{\alpha\gamma L}(\mathbf{p})\Big), \tag{60}$$

$$\frac{1}{H}\frac{\partial\theta_3(t,\mathbf{p})}{\partial t}+\left(2+\frac{\dot H}{H^2}\right)\theta_3(t,\mathbf{p})-\frac{p^2}{a^2H^2}\Phi_3(t,\mathbf{p}) = 2D_+^3(t)f^2\Big(-\mathcal{W}_{\alpha\alpha}(\mathbf{p})+\left(\frac{2}{7}\lambda_\theta+\frac{1}{2}\right)\mathcal{W}_{\alpha\gamma R}(\mathbf{p}) +\frac{2}{7}\lambda_\theta\mathcal{W}_{\alpha\gamma L}(\mathbf{p})+\left(1-\frac{4}{7}\lambda_\theta\right)\mathcal{W}_{\gamma\gamma}(\mathbf{p})-\frac{1}{2}\mathcal{W}_{\xi}(\mathbf{p})\Big). \tag{61}$$

Combining these two equations, we have the third order equation for $\delta_3(t,\mathbf{p})$ as

$$\frac{\partial^2\delta_3(t,\mathbf{p})}{\partial t^2}+2H\frac{\partial\delta_3(t,\mathbf{p})}{\partial t}+L(t)\delta_3(t,\mathbf{p}) = S_{\delta 3}(t,\mathbf{p}), \tag{62}$$

where we define

$$S_{\delta 3}(t) = D_+^3(t)(N_{\alpha\alpha}(t)\mathcal{W}_{\alpha\alpha}(\mathbf{p})+N_{\alpha\gamma R}(t)\mathcal{W}_{\alpha\gamma R}(\mathbf{p}) +N_{\alpha\gamma L}(t)\mathcal{W}_{\alpha\gamma L}(\mathbf{p})+N_{\gamma\gamma}(t)\mathcal{W}_{\gamma\gamma}(\mathbf{p})+N_{\xi}(t)\mathcal{W}_{\xi}(\mathbf{p})), \tag{63}$$

and

$$N_{\alpha\alpha}(t) = 6f^2H^2-2L, \tag{64}$$

$$N_{\alpha\gamma R}(t) = -f^2H^2-\frac{8}{7}f^2H^2\lambda+\frac{2}{7}L\lambda-\frac{4}{7}fH\dot\lambda+\frac{1}{2}H^2\sigma_\Phi, \tag{65}$$

$$N_{\alpha\gamma L}(t) = -f^2H^2-\frac{8}{7}f^2H^2\lambda+\frac{2}{7}L\lambda-\frac{4}{7}fH\dot\lambda+N_\gamma, \tag{66}$$

$$N_{\gamma\gamma}(t) = -2f^2H^2+\frac{8}{7}f^2H^2\lambda+\frac{4}{7}fH\dot\lambda+H^2(\sigma_\Phi+\mu_\Phi), \tag{67}$$

$$N_{\xi}(t) = f^2H^2+H^2\left(-\frac{1}{2}\sigma_\Phi+\nu_\Phi\right), \tag{68}$$

where we used Eqs. (A24) and (A28), and

$$\dot f(t) = \frac{1}{H}(-2fH^2-L-f^2H^2-f\dot H), \tag{69}$$

which follows from the definition of the growth rate $f(t)=d\ln D_+/d\ln a$ and Eq. (31). We can prove that $N_{\alpha\gamma L}(t)$ is equivalent to $N_{\alpha\gamma R}(t)$, using Eqs. (66) and (65), and $N_\gamma(t)=\frac{1}{2}H^2\sigma_\Phi$, which is demonstrated by Eqs. (A22) and (A29). Then, we write

$$N_{\alpha\gamma}(t)\equiv N_{\alpha\gamma R}(t)=N_{\alpha\gamma L}(t). \tag{70}$$

The general solution of Eq. (62) with (63) is

$$\delta_3(t,\mathbf{p}) = c_+(\mathbf{p})D_+(t) + c_-(\mathbf{p})D_-(t) + \int_0^t \frac{D_-(t)D_+(t') - D_+(t)D_-(t')}{W(t')} S_{\delta 3}(t',\mathbf{p})dt', \tag{71}$$

where $D_+(t)$ and $D_-(t)$ are the growing mode solution and the decaying mode solution, satisfying Eq. (31), $c_+(\mathbf{p})$ and $c_-(\mathbf{p})$ are integral constants, and $W(t)$ is the Wronskian defined by $W(t) = D_+(t)\dot{D}_-(t) - \dot{D}_+(t)D_-(t)$. Since we assume that the initial density perturbations obey the Gaussian distribution, we set $c_\pm(\mathbf{p}) = 0$, as is done in deriving the second order solution. Then, the solution of the third order density perturbations is given by

$$\delta_3(t,\mathbf{p}) = D_+^3(t)\left(\kappa_{\delta 3}(t)\mathcal{W}_{\alpha\alpha}(\mathbf{p}) - \frac{2}{7}\lambda_{\delta 3}(t)\mathcal{W}_{\alpha\gamma R}(\mathbf{p}) - \frac{2}{7}\lambda_{\delta 3}(t)\mathcal{W}_{\alpha\gamma L}(\mathbf{p}) - \frac{2}{21}\mu(t)\mathcal{W}_{\gamma\gamma}(\mathbf{p}) + \frac{1}{9}\nu(t)\mathcal{W}_{\xi}(\mathbf{p})\right), \tag{72}$$

where we define

$$\kappa_{\delta 3}(t) = \frac{1}{D_+^3(t)}\int_0^t \frac{D_-(t)D_+(t') - D_+(t)D_-(t')}{W(t')} \times D_+^3(t')N_{\alpha\alpha}(t')dt', \tag{73}$$

$$\lambda_{\delta 3}(t) = -\frac{7}{2D_+^3(t)}\int_0^t \frac{D_-(t)D_+(t') - D_+(t)D_-(t')}{W(t')} \times D_+^3(t')N_{\alpha\gamma}(t')dt', \tag{74}$$

$$\mu(t) = -\frac{21}{2D_+^3(t)}\int_0^t \frac{D_-(t)D_+(t') - D_+(t)D_-(t')}{W(t')} \times D_+^3(t')N_{\gamma\gamma}(t')dt', \tag{75}$$

$$\nu(t) = \frac{9}{D_+^3(t)}\int_0^t \frac{D_-(t)D_+(t') - D_+(t)D_-(t')}{W(t')} \times D_+^3(t')N_{\xi}(t')dt'. \tag{76}$$

Here note that the parameters in front of $\mathcal{W}_{\alpha\gamma R}(\mathbf{p})$ and $\mathcal{W}_{\alpha\gamma L}(\mathbf{p})$ in expression (72) are the same, originating from the relation (70). In the limit of the Einstein–de Sitter universe in general relativity, the coefficients $\kappa_{\delta 3}(t)$, $\lambda_{\delta 3}(t)$, $\mu(t)$, and $\nu(t)$ reduce to 1.

We can redefine these coefficients using the differential equations. Inserting the general form of the solution (72) into (62), we obtain the following differential equations for the coefficients:

$$\ddot{\kappa}_{\delta 3}(t) + (6f+2)\dot{\kappa}_{\delta 3}(t) + (6f^2H^2 - 2L)\kappa_{\delta 3}(t) = N_{\alpha\alpha}(t), \tag{77}$$

$$\ddot{\lambda}_{\delta 3}(t) + (6f+2)\dot{\lambda}_{\delta 3}(t) + (6f^2H^2 - 2L)\lambda_{\delta 3}(t) = -\frac{7}{2}N_{\alpha\gamma}(t), \tag{78}$$

$$\ddot{\mu}(t) + (6f+2)\dot{\mu}(t) + (6f^2H^2 - 2L)\mu(t) = -\frac{21}{2}N_{\gamma\alpha}(t), \tag{79}$$

$$\ddot{\nu}(t) + (6f+2)\dot{\nu}(t) + (6f^2H^2 - 2L)\nu(t) = 9N_{\xi}(t). \tag{80}$$

The homogeneous solution of all these equations is $1/D_+^2(t)$ and $D_-(t)/D_+^3(t)$. Therefore, the differential equations (77)–(80) consistently yield the inhomogeneous solutions (73)–(76), respectively.

We next show that $\kappa_{\delta 3}(t) = 1$ identically. Using the expression (64), we easily find that $\kappa_{\delta 3} = 1$ is the solution of (77). This means that the inhomogeneous solution (73) reduces to $\kappa_{\delta 3} = 1$. We can prove $\kappa_{\delta 3} = 1$ directly from (73), using a partial integral.

Furthermore, we can show that $\lambda_{\delta 3}(t) = \lambda(t)$ identically. We can rewrite Eq. (78) as follows,

$$\ddot{\lambda}_{\delta 3}(t) + (4f+2)H\dot{\lambda}_{\delta 3}(t) + (2f^2H^2 - L)\lambda_{\delta 3}(t) + 2fH(\dot{\lambda}_{\delta 3} - \dot{\lambda}) + (4f^2H^2 - L)(\lambda_{\delta 3} - \lambda) = \frac{7}{2}(f^2H^2 - N_\gamma), \tag{81}$$

where we used (70) and (66). We can easily check that $\lambda_{\delta 3}(t)$ and $\lambda(t)$ satisfy the same differential equation [see Eq. (A28)], which leads to $\lambda_{\delta 3}(t) = \lambda(t)$.

In summary, we have an expression equivalent to (72),

$$\delta_3(t,\mathbf{p}) = D_+^3(t)\left(\mathcal{W}_{\alpha\alpha}(\mathbf{p}) - \frac{2}{7}\lambda(t)\mathcal{W}_{\alpha\gamma R}(\mathbf{p}) - \frac{2}{7}\lambda(t)\mathcal{W}_{\alpha\gamma L}(\mathbf{p}) - \frac{2}{21}\mu(t)\mathcal{W}_{\gamma\gamma}(\mathbf{p}) + \frac{1}{9}\nu(t)\mathcal{W}_{\xi}(\mathbf{p})\right). \tag{82}$$

Thus, the third order solution of density contrast is characterized by $\lambda(t)$, $\mu(t)$, and $\nu(t)$. Note that $\lambda(t)$ is defined in order to describe the second order solution; then $\mu(t)$ and $\nu(t)$ are the new coefficients which appear at the third order. Table I summarizes the parameters and the mode-coupling functions necessary to describe the second order solution and the third order solution.

Recently, the authors of Ref. [44] investigated the third order solution of the density perturbations, in a similar way, but within a model of general relativity. In their paper, six parameters are introduced to describe the third order density perturbations. Our results suggest that less parameters are independent.

TABLE I. Functions for the mode couplings and parameters necessary to describe the second and third order solutions.

	Parameters	Mode-coupling functions
$\delta_2(t,\mathbf{p})$	$\lambda(t)$	$\mathcal{W}_\alpha(\mathbf{p})$
$\theta_2(t,\mathbf{p})$	$\lambda_\theta(t)$	$\mathcal{W}_\gamma(\mathbf{p})$
$\delta_3(t,\mathbf{p})$	$\lambda(t)$, $\mu(t)$, $\nu(t)$	$\mathcal{W}_{\alpha\alpha}(\mathbf{p})$, $\mathcal{W}_{\alpha\gamma R}(\mathbf{p})$, $\mathcal{W}_{\alpha\gamma L}(\mathbf{p})$
$\theta_3(t,\mathbf{p})$	$\lambda(t)$, $\lambda_\theta(t)$, $\mu_\theta(t)$, $\nu_\theta(t)$	$\mathcal{W}_{\gamma\gamma}(\mathbf{p})$, $\mathcal{W}_\xi(\mathbf{p})$

Inserting the solution (82) into Eq. (60), we find the solution for the velocity divergence,

$$\theta_3(t,\mathbf{p}) = -D_+^3(t) f \left(\mathcal{W}_{\alpha\alpha}(\mathbf{p}) - \frac{4}{7}\lambda_\theta(t)\mathcal{W}_{\alpha\gamma R} - \frac{2}{7}\lambda(t)\mathcal{W}_{\alpha\gamma L}(\mathbf{p}) - \frac{2}{7}\mu_\theta(t)\mathcal{W}_{\gamma\gamma}(\mathbf{p}) + \frac{1}{3}\nu_\theta(t)\mathcal{W}_\xi(\mathbf{p}) \right), \tag{83}$$

where we define

$$\mu_\theta(t) = \mu(t) + \frac{\dot{\mu}(t)}{3fH}, \tag{84}$$

$$\nu_\theta(t) = \nu(t) + \frac{\dot{\nu}(t)}{3fH}. \tag{85}$$

Here note that $\lambda_\theta(t)$ is the parameter that describes the second order solution, and $\mu_\theta(t)$ and $\nu_\theta(t)$ are the new parameters that appear at the third order.

In summary, we first introduced nine mode-coupling functions in the third order equations, Eqs. (55) and (56) with Eq. (50). We find the three identities (57), (58), and (59). Then, only six mode-coupling functions are independent out of nine. This conclusion, that the number of linearly independent mode-coupling functions is six, can be proved by using the generalized Wronskian. The coefficients in front of $\mathcal{W}_{\alpha\alpha R}$ and $\mathcal{W}_{\alpha\alpha L}$ in Eq. (55) are the same, which leads to the final third order solution, Eqs. (82) and (83) expressed in terms of the five mode-coupling functions.

IV. POWER SPECTRUM

The third order solution of the density perturbations enables one to compute the one-loop (second order) power spectrum. The second order matter power spectrum has been computed by many authors [27–33,35–37,44], in general relativity and modified gravity models. We find the expression for the one-loop order power spectra of density contrast and velocity divergence by

$$\langle \delta(t,\mathbf{k}_1)\delta(t,\mathbf{k}_2)\rangle = (2\pi)^3\delta^{(3)}(\mathbf{k}_1+\mathbf{k}_2)P_{\delta\delta}(t,k), \tag{86}$$

$$\langle \delta(t,\mathbf{k}_1)\theta(t,\mathbf{k}_2)\rangle = (2\pi)^3\delta^{(3)}(\mathbf{k}_1+\mathbf{k}_2)(-f)P_{\delta\theta}(t,k), \tag{87}$$

$$\langle \theta(t,\mathbf{k}_1)\theta(t,\mathbf{k}_2)\rangle = (2\pi)^3\delta^{(3)}(\mathbf{k}_1+\mathbf{k}_2)f^2P_{\theta\theta}(t,k), \tag{88}$$

where we use the notation $k = |\mathbf{k}_1|$. Some details of their derivations are described in Appendix C; here we show the results,

$$P_{\delta\delta}(t,k) = D_+^2(t)P_{\rm L}(k) + D_+^4(t)(P_{\delta\delta}^{(22)}(t,k) + 2P_{\delta\delta}^{(13)}(t,k)), \tag{89}$$

$$P_{\delta\theta}(t,k) = D_+^2(t)P_{\rm L}(k) + D_+^4(t)(P_{\delta\theta}^{(22)}(t,k) + 2P_{\delta\theta}^{(13)}(t,k)), \tag{90}$$

$$P_{\theta\theta}(t,k) = D_+^2(t)P_{\rm L}(k) + D_+^4(t)(P_{\theta\theta}^{(22)}(t,k) + 2P_{\theta\theta}^{(13)}(t,k)), \tag{91}$$

where $D_+^2(t)P_{\rm L}(k)$ is the linear matter power spectrum, and we define

$$P_{\delta\delta}^{(22)}(t,k) = \frac{k^3}{98(2\pi)^2}\int drP_{\rm L}(rk)\int_{-1}^{1}dxP_{\rm L}(k(1+r^2-2rx)^{1/2})\frac{((7-4\lambda)r+7x+2(2\lambda-7)rx^2)^2}{(1+r^2-2rx)^2}, \tag{92}$$

$$P_{\delta\theta}^{(22)}(t,k) = \frac{k^3}{98(2\pi)^2}\int drP_{\rm L}(rk)\int_{-1}^{1}dxP_{\rm L}(k(1+r^2-2rx)^{1/2}) \times \frac{((7-4\lambda)r+7x+2(2\lambda-7)rx^2)((7-8\lambda_\theta)r+7x+2(4\lambda_\theta-7)rx^2)}{(1+r^2-2rx)^2}, \tag{93}$$

$$P_{\theta\theta}^{(22)}(t,k) = \frac{k^3}{98(2\pi)^2}\int drP_{\rm L}(rk)\int_{-1}^{1}dxP_{\rm L}(k(1+r^2-2rx)^{1/2})\frac{((7-8\lambda_\theta)r+7x+2(4\lambda_\theta-7)rx^2)^2}{(1+r^2-2rx)^2}, \tag{94}$$

and

$$2P^{(13)}_{\delta\delta}(t,k) = \frac{k^3}{252(2\pi)^2}P_{\rm L}(k)\int drP_{\rm L}(rk)\Big[12\mu\frac{1}{r^2} - 2(21+36\lambda+22\mu) + 4(84-48\lambda-11\mu)r^2 - 6(21-12\lambda-2\mu)r^4 + \frac{3}{r^3}(r^2-1)^3((21-12\lambda-2\mu)r^2+2\mu)\ln\left(\frac{r+1}{|r-1|}\right)\Big], \tag{95}$$

$$2P^{(13)}_{\delta\theta}(t,k) = \frac{k^3}{252(2\pi)^2}P_{\rm L}(k)\int drP_{\rm L}(rk)\Big[6(\mu+3\mu_\theta)\frac{1}{r^2} - 2(21+36\lambda+11\mu+33\mu_\theta) + 2(168-96\lambda-11\mu-33\mu_\theta)r^2 - 6(21-12\lambda-\mu-3\mu_\theta)r^4 + \frac{3}{r^3}(r^2-1)^3((21-12\lambda-\mu-3\mu_\theta)r^2+(\mu+3\mu_\theta))\ln\left(\frac{r+1}{|r-1|}\right)\Big], \tag{96}$$

$$2P^{(13)}_{\theta\theta}(t,k) = \frac{k^3}{84(2\pi)^2}P_{\rm L}(k)\int drP_{\rm L}(rk)\Big[12\mu_\theta\frac{1}{r^2} - 2(7+12\lambda+22\mu_\theta) + 4(28-16\lambda-11\mu_\theta)r^2 - 6(7-4\lambda-2\mu_\theta)r^4 + \frac{3}{r^3}(r^2-1)^3((7-4\lambda-2\mu_\theta)r^2+2\mu_\theta)\ln\left(\frac{r+1}{|r-1|}\right)\Big]. \tag{97}$$

The third order solutions of the density contrast and the velocity divergence are described by six parameters in Table I. The one-loop power spectra are described by four parameters, and they do not depend on $\nu(t)$ and $\nu_\theta(t)$ (see Table II). In deriving the one-loop power spectrum, we find that the relation

$$\xi(\mathbf{k},\mathbf{q}_1,-\mathbf{q}_1) = 0 \tag{98}$$

holds, which prevents the one-loop power spectrum from depending on $\nu(t)$ and $\nu_\theta(t)$. Details are described in Appendixes C and D.

Figure 1 shows $P_{\delta\delta}(t,k)$ (thick curve) and the corresponding linear power spectrum $D_+^2(t)P_L(k)$ (thin curve), at the redshift $z=0$ (solid curve), $z=1$ (dashed curve), and $z=1.5$ (dotted curve), respectively, for the ΛCDM model, with the cosmological parameters describe in the caption. A comparison between this figure and Fig. 1 in Ref. [44] shows the consistency between both results.

V. APPLICATION OF KGB MODEL

In this section, we exemplify the effect of modified gravity on the one-loop power spectrum. Here we consider the KGB model [60,66], which is considered in Ref. [26] to demonstrate the effect of modified gravity on the bispectrum. We briefly review the model. The action of the KGB model is written as

$$S = \int d^4x\sqrt{-g}\left[\frac{M_{\rm pl}^2}{2}R + K(\phi,X) - G_3(\phi,X)\Box\phi + \mathcal{L}_{\rm m}\right], \tag{99}$$

where $M_{\rm pl}$ is the Planck mass, which is related to the gravitational constant G_N by $8\pi G_N = 1/M_{\rm pl}^2$. Comparing action (99) with that of the most general second order

TABLE II. Summary of the parameters that characterize the one-loop order power spectra $P_{\delta\delta}$, $P_{\delta\theta}$, and $P_{\theta\theta}$, respectively.

	Parameters
$P_{\delta\delta}$	$\lambda(t)$, $\mu(t)$
$P_{\delta\theta}$	$\lambda(t)$, $\mu(t)$, $\lambda_\theta(t)$, $\mu_\theta(t)$
$P_{\theta\theta}$	$\lambda(t)$, $\lambda_\theta(t)$, $\mu_\theta(t)$

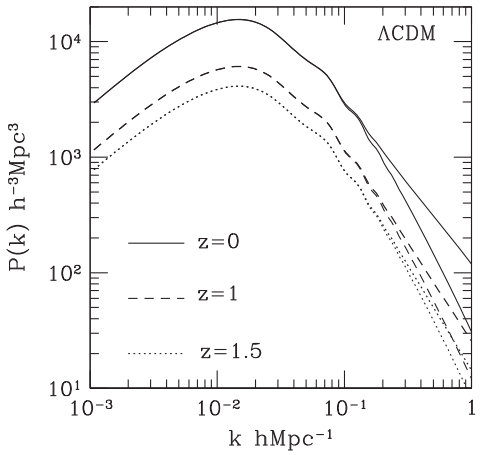

FIG. 1. $P_{\delta\delta}(t,k)$ (thick curve) and the corresponding linear power spectrum $D_+^2(t)P_L(k)$ (thin curve) at the redshift $z=0$ (solid curve), $z=1$ (dashed curve), and $z=1.5$ (dotted curve), respectively, for the ΛCDM model with the cosmological parameters $\Omega_0=0.26$, $\Omega_b=0.044$, $h=0.72$, $n_s=0.96$, $\sigma_8=0.58$. This figure shows the consistency with Fig. 1 in Ref. [44].

scalar-tensor theory (1), the action of the kinetic gravity braiding model is produced by setting

$$G_4 = \frac{M_{\rm pl}^2}{2}, \qquad G_5 = 0, \tag{100}$$

and we choose K and G_3 as

$$K = -X, \qquad G_3 = M_{\rm pl}\left(\frac{r_c^2}{M_{\rm pl}^2}X\right)^n, \tag{101}$$

where n and r_c are the model parameters. Useful expressions of the kinetic gravity braiding model are summarized in Appendix E.

When we consider the attractor solution, which satisfies $3\dot{\phi}HG_{3X} = 1$, the Friedmann equation is written in the form

$$\left(\frac{H}{H_0}\right)^2 = \frac{\Omega_0}{a^3} + (1-\Omega_0)\left(\frac{H}{H_0}\right)^{-2/(2n-1)}, \tag{102}$$

where H_0 is the Hubble constant and Ω_0 is the density parameter at the present time, and the model parameters must satisfy

$$H_0 r_c = \left(\frac{2^{n-1}}{3n}\right)^{1/2n}\left[\frac{1}{6(1-\Omega_0)}\right]^{(2n-1)/4n}. \tag{103}$$

On the attractor solution, $L(t)$, defined by Eq. (32), reduces to

$$L(t) = -\frac{3}{2}\frac{2n+(3n-1)\Omega_{\rm m}}{5n-\Omega_{\rm m}}H^2, \tag{104}$$

where $\Omega_{\rm m}$ is defined by $\Omega_{\rm m}(a) = \Omega_0 H_0^2/H(a)^2a^3$. The linear growth factor D_+ is obtained from Eq. (31) with Eqs. (104) and (102). However, note that the quasistatic approximation on the scales of the large scale structures holds for $n \lesssim 10$ (see Ref. [66]).

The second and third order solutions are obtained with

$$N_\gamma(t) = \frac{1}{2}H^2\sigma_\Phi(t) = -\frac{9}{4}\frac{(1-\Omega_{\rm m})(2n-\Omega_{\rm m})^3}{\Omega_{\rm m}(5n-\Omega_{\rm m})^3}H^2, \tag{105}$$

$$H^2\mu_\Phi(t) = \frac{9(1-\Omega_{\rm m})(2n-\Omega_{\rm m})^3(4n^2(21+25\lambda\Omega_{\rm m}) - 4n\Omega_{\rm m}(21+10\lambda\Omega_{\rm m}) + \Omega_{\rm m}^2(21+4\lambda\Omega_{\rm m}))}{28\Omega_{\rm m}^2(5n-\Omega_{\rm m})^5}H^2, \tag{106}$$

$$\nu_\Phi(t) = 0. \tag{107}$$

We have $\lambda(t)$ from Eq. (A23) with (105). Using these results and Eqs. (67) and (68), we have the expressions for $\mu(t)$ and $\nu(t)$ from Eqs. (75) and (76). Equations (A24), (84), and (85) give expressions for $\lambda_\theta(t)$, $\mu_\theta(t)$, and $\nu_\theta(t)$, respectively.

Table III lists the numerical values of these variables at redshifts $z = 1$, 0.5, and 0, for the KGB model with $n = 1$, 2, 5, as well as the ΛCDM model with $\Omega_0 = 0.3$.

Figure 2 shows λ, μ, ν, λ_θ, μ_θ, ν_θ as functions of the scale factor a. In each panel, the blue dash-dotted curve is the ΛCDM model, and the red dotted curve, the yellow dashed curve, and the green thick solid curve show the KGB model with $n = 1$, 2, and 5, respectively. All the curves take the limiting value of unity at $a = 0$ but deviate from unity as a evolves. Note that the deviation of λ, μ, ν from unity is small, of the order of a few percent, but the

TABLE III. Numerical values of the growth factor D_+, the linear growth rate f, and the coefficients λ, μ, ν, λ_θ, μ_θ, ν_θ at redshifts $z = 1.0$, 0.5, and 0, for the ΛCDM model and the KGB model with $n = 1$, 2, 5. In each cell, set of three numbers means values at redshifts $z = 1.0$, 0.5, and 0 from left to right, respectively. Here we adopted $\Omega_0 = 0.3$.

	ΛCDM	KGB($n=1$)	KGB($n=2$)	KGB($n=5$)
$D_+(z=1/0.5/0)$	0.477/0.602/0.779	0.496/0.642/0.858	0.489/0.628/0.838	0.484/0.620/0.827
$f(z=1/0.5/0)$	0.869/0.749/0.513	0.951/0.835/0.593	0.919/0.813/0.605	0.904/0.805/0.612
$\lambda(z=1/0.5/0)$	0.999/0.997/0.994	1.000/0.999/1.003	1.000/1.000/1.011	1.000/1.002/1.019
$\mu(z=1/0.5/0)$	0.999/0.998/0.996	1.000/1.001/1.015	1.001/1.005/1.015	1.003/1.007/1.011
$\nu(z=1/0.5/0)$	0.998/0.996/0.991	1.000/0.999/1.014	1.000/1.003/1.034	1.002/1.008/1.049
$\lambda_\theta(z=1/0.5/0)$	0.994/0.991/0.983	0.998/0.995/1.043	0.999/1.004/1.073	1.003/1.014/1.095
$\mu_\theta(z=1/0.5/0)$	0.997/0.995/0.991	1.000/1.006/1.041	1.006/1.018/1.008	1.010/1.021/0.974
$\nu_\theta(z=1/0.5/0)$	0.994/0.990/0.980	0.998/0.998/1.089	1.002/1.014/1.136	1.009/1.030/1.169

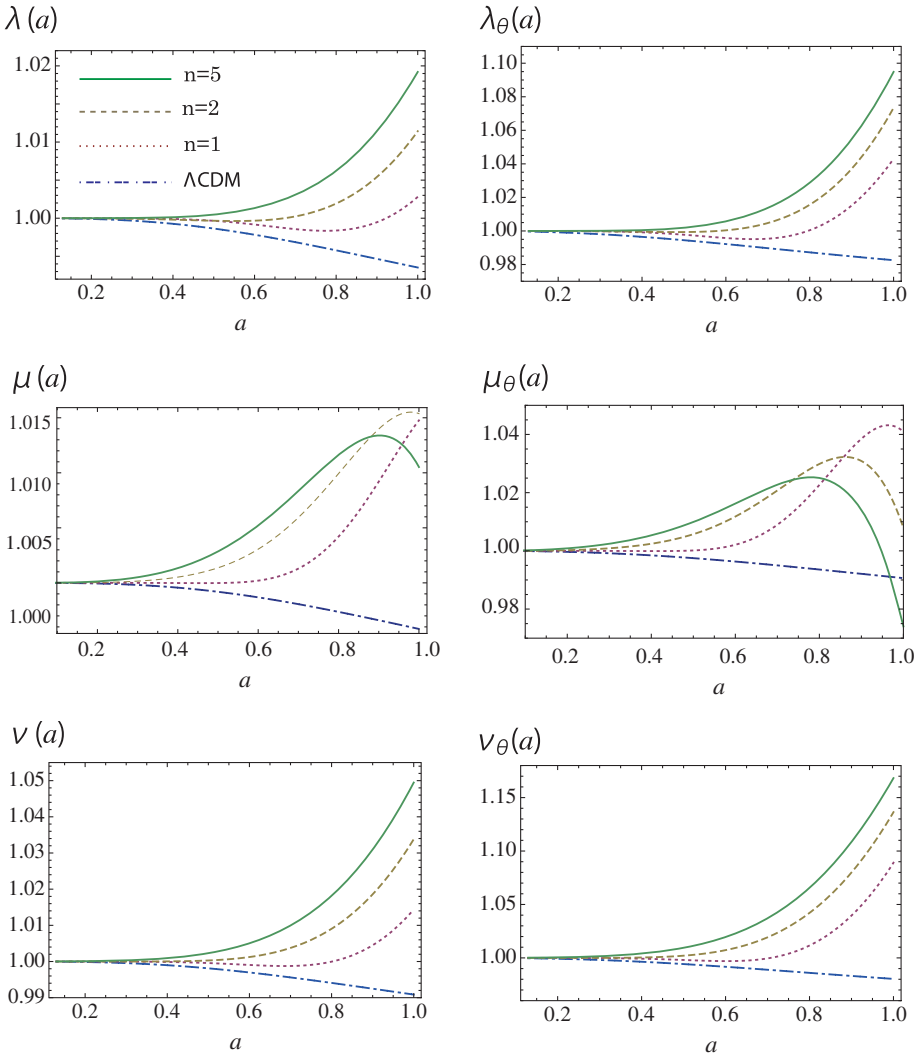

FIG. 2 (color online). $\lambda, \mu, \nu, \lambda_\theta, \mu_\theta, \nu_\theta$ as functions of the scale factor a. In each panel, the blue dash-dotted curve is the ΛCDM model, and the red dotted curve, the yellow dashed curve, and the green thick solid curve show the KGB model with $n = 1$, 2, and 5, respectively.

deviation of λ_θ, ν_θ is rather large, up to 10%. This is because the parameters associated with the velocity, λ_θ and ν_θ defined by Eqs. (A24) and (85), respectively, contain the time derivative term, which makes a large contribution. Plus, some of the difference between the ΛCDM and KGB models comes from the difference of the growth rate f. Deviation of μ_θ in the KGB model from that in the ΛCDM model is rather small compared with the deviations of λ_θ and ν_θ, which come from the fact that μ is not a monotonic increasing function but there exists a maximum value at $a \lesssim 1$.

Figure 3 shows the one-loop power spectra $P_{\delta\delta}$ (thick solid curve), $P_{\delta\theta}$ (dashed curve), and $P_{\theta\theta}$ (dotted curve), as well as the linear power spectrum (thin solid curve) at redshift $z = 0$ for the ΛCDM model (upper left panel) and the KGB model with $n = 1$, 2, 5, respectively, as is noted in each panel. This figure demonstrates how the nonlinear effect at one-loop order changes the linear power spectrum. In this figure, we adopted the same linear matter power spectrum. Therefore, all the models resemble each other, but there are small differences in the one-loop power spectra, depending on the cosmological models, which are compared in detail in Fig. 4. This smallness of the deviation from the ΛCDM model could be understood by the Vainshtein effect. The deviation in the bispectrum from the ΛCDM model is demonstrated to be small compared with that in the quantities of the linear theory, e.g., the linear growth rate [26,67].

Figure 4 shows the one-loop power spectra $P_{\delta\delta}$, $P_{\delta\theta}$, $P_{\theta\theta}$, from top to bottom, respectively, which are normalized by those of the ΛCDM model in Fig. 3. These are the snapshots at $z = 0$, and all the models have the same normalization $\sigma_8 = 0.8$; it follows that all four models

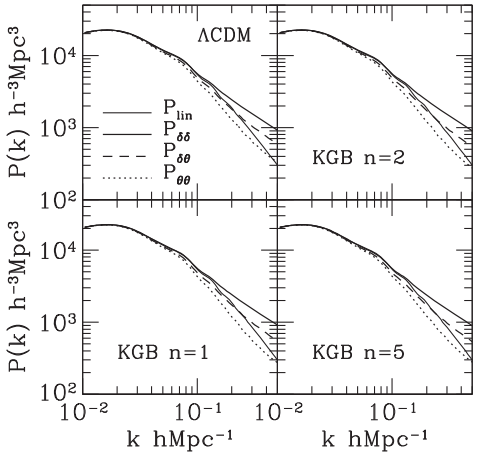

FIG. 3. Comparison of $P_{\delta\delta}(k)$ (thick solid curve), $P_{\delta\theta}(k)$ (dashed curve), $P_{\theta\theta}(k)$ (dotted curve), and the linear power spectrum $P_{\rm lin} = D_+^2(t)P_L(k)$ (thin solid curve), at the redshift $z = 0$. The upper left panel is the ΛCDM model, and the other panels show the KGB model with $n = 1$, 2, and 3, as described in each panel. Here we adopted $\Omega_0 = 0.3$, $\Omega_b = 0.044$, $h = 0.7$, $n_s = 0.96$, and $\sigma_8 = 0.8$. In this figure, the same linear power spectrum is adopted for all the models.

have the same linear matter power spectrum. In each panel, the red dotted curve, the yellow dashed curve, and the green thick curve show the KGB model with $n = 1$, 2, and 5, respectively. In the linear regime $k \lesssim 0.1$ [hMpc^{-1}], all the models converge because they have the same linear matter power spectrum. The differences between the KGB model and the ΛCDM model appear for the quasinonlinear regime $k \gtrsim 0.1$ [hMpc^{-1}] due to the nonlinear effect. Because all the models have the same linear matter power spectrum, this figure shows that the enhancement of the power spectrum due to the nonlinear effect is small in the KGB models compared with that in the ΛCDM model. Furthermore, the deviation from the ΛCDM model is more significant in the velocity power spectrum than that in the density power spectrum. In general, the amplitudes of the one-loop power spectra $P_{\delta\delta}$, $P_{\delta\theta}$, and $P_{\theta\theta}$ are decreased when $\lambda(t)$, $\mu(t)$, $\lambda_\theta(t)$, or $\mu_\theta(t)$ is increased. The behavior of $P_{\delta\theta}$ and $P_{\theta\theta}$ in the quasinonlinear regime is dominantly influenced by $\lambda_\theta(t)$ and $\mu_\theta(t)$.

The nonlinear effect in $P_{\delta\delta}$ is substantially influenced by $\lambda(t)$, while $P_{\delta\delta}$ also depends partially on $\mu(t)$. On the other hand, $\mu_\theta(t)$ substantially influences the nonlinear effect in $P_{\theta\theta}$, while the influence of $\lambda_\theta(t)$ is more subdominant than $\mu_\theta(t)$. The deviation of the KGB models in $P_{\delta\delta}$ and $P_{\theta\theta}$ from the ΛCDM model reflects the behavior $\lambda(t)$ and $\mu_\theta(t)$, respectively. Namely, the deviation of the values of $\lambda(t)$ and $\mu_\theta(t)$ from the ΛCDM model at $z = 0$ determines the behaviors of $P_{\delta\delta\rm KGB}/P_{\delta\delta\Lambda\rm CDM}$ and $P_{\theta\theta\rm KGB}/P_{\theta\theta\Lambda\rm CDM}$ in Fig. 4.

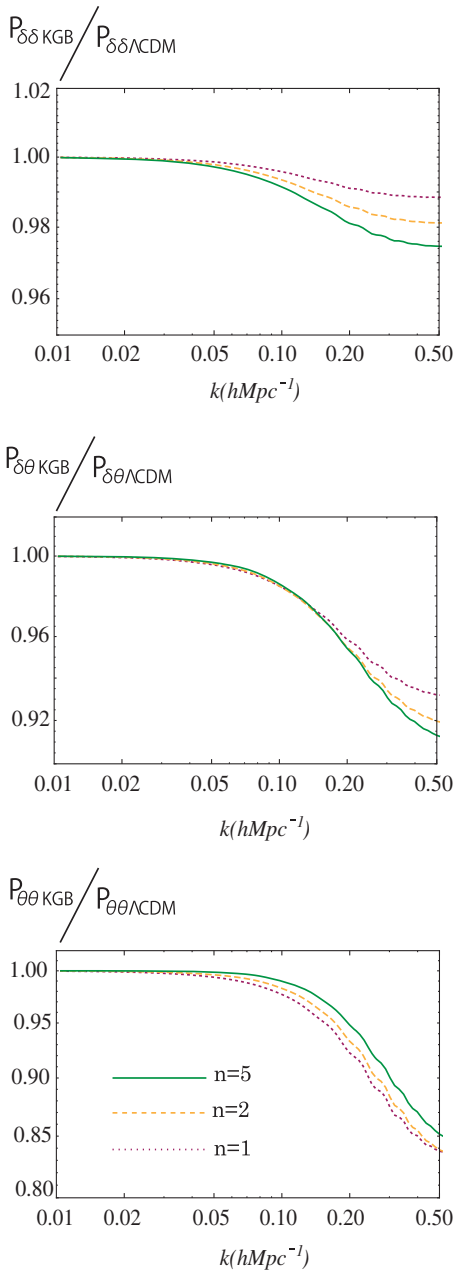

FIG. 4 (color online). Relative deviation of the power spectra $P_{\delta\delta}(k)$ (top panel), $P_{\delta\theta}(k)$ (middle panel), and $P_{\theta\theta}(k)$ (bottom panel), under the kinetic gravity braiding model with $n = 1$ (red dotted curve), $n = 2$ (yellow dashed curve), and $n = 5$ (green thick curve), which are divided by those under the ΛCDM model. The panels show the snapshot at the redshift $z = 0$.

VI. SUMMARY AND CONCLUSIONS

We found the third order solutions of the cosmological density perturbations in Horndeski's most general scalar-tensor theory assuming that the Vainshtein mechanism is at work. We solved the equations under the quasistatic approximation, and the solutions describe the quasinonlinear aspects of the cosmological density contrast and the

velocity divergence under the Vainshtein mechanism. In this work, we thoroughly investigated the independence property of the mode-coupling functions describing the nonlinear interactions. We found that the third order solution of the density contrast is characterized by three parameters for the nonlinear interactions, one of which is the same as that for the second order solutions. The third order solution of the velocity divergence is characterized by four parameters for the nonlinear interactions, two of which are the same parameters as those of the second order solutions. The nonlinear features of the perturbative solutions up to third order are characterized by six parameters. Furthermore, the one-loop order power spectra obtained with the third order solutions are described by four parameters. Assuming the KGB model, we demonstrated the effect of the modified gravity in the one-loop order power spectra at the quantitative level. We found that the deviation from the ΛCDM model in the power spectra of the density contrast and the velocity divergence is small, which can be understood as the result of the Vainshtein mechanism in nonlinear quantities [67]. However, the deviation from the ΛCDM model is more significant in the velocity divergence than the density contrast, which is explained by a dominant contribution of the parameters $\lambda_\theta(t)$ and $\mu_\theta(t)$. It is interesting to investigate whether this is a general feature of modified gravity with the Vainshtein mechanism or not.

ACKNOWLEDGMENTS

This work was supported by a research support program of Hiroshima University and MEXT/JSPS KAKENHI Grant No. 15H05895.

APPENDIX A: COEFFICIENTS IN EQUATIONS AND SOLUTIONS

We summarize the definitions of the coefficients in the gravitational and scalar field equations (5), (6), and (9).

$$A_0 = \frac{\dot{\Theta}}{H^2} + \frac{\Theta}{H} + \mathcal{F}_T - 2\mathcal{G}_T - 2\frac{\dot{\mathcal{G}}_T}{H} - \frac{\mathcal{E}+\mathcal{P}}{2H^2}, \tag{A1}$$

$$A_1 = \frac{\dot{\mathcal{G}}_T}{H} + \mathcal{G}_T - \mathcal{F}_T, \tag{A2}$$

$$A_2 = \mathcal{G}_T - \frac{\Theta}{H}, \tag{A3}$$

$$\begin{aligned} B_0 = \frac{X}{H}\{&\dot{\phi}G_{3X} + 3(\dot{X}+2HX)G_{4XX} + 2X\dot{X}G_{4XXX} - 3\dot{\phi}G_{4\phi X} + 2\dot{\phi}XG_{4\phi XX} \\ &+ (\dot{H}+H^2)\dot{\phi}G_{5X} + \dot{\phi}[2H\dot{X} + (\dot{H}+H^2)X]G_{5XX} + H\dot{\phi}X\dot{X}G_{5XXX} \\ &- 2(\dot{X}+2HX)G_{5\phi X} - \dot{\phi}XG_{5\phi\phi X} - X(\dot{X}-2HX)G_{5\phi XX}\}, \end{aligned} \tag{A4}$$

$$B_1 = 2X[G_{4X} + \ddot{\phi}(G_{5X} + XG_{5XX}) - G_{5\phi} + XG_{5\phi X}], \tag{A5}$$

$$B_2 = -2X(G_{4X} + 2XG_{4XX} + H\dot{\phi}G_{5X} + H\dot{\phi}XG_{5XX} - G_{5\phi} - XG_{5\phi X}) \quad , \tag{A6}$$

$$B_3 = H\dot{\phi}XG_{5X}, \tag{A7}$$

$$C_0 = 2X^2G_{4XX} + \frac{2X^2}{3}(2\ddot{\phi}G_{5XX} + \ddot{\phi}XG_{5XXX} - 2G_{5\phi X} + XG_{5\phi XX}), \tag{A8}$$

$$C_1 = H\dot{\phi}X(G_{5X} + XG_{5XX}), \tag{A9}$$

where we define

$$\mathcal{F}_T = 2[G_4 - X(\ddot{\phi}G_{5X} + G_{5\phi})], \tag{A10}$$

$$\mathcal{G}_T = 2[G_4 - 2XG_{4X} - X(H\dot{\phi}G_{5X} - G_{5\phi})], \tag{A11}$$

$$\Theta = -\dot{\phi}XG_{3X} + 2HG_4 - 8HXG_{4X} - 8HX^2G_{4XX} + \dot{\phi}G_{4\phi} + 2X\dot{\phi}G_{4\phi X} - H^2\dot{\phi}(5XG_{5X} + 2X^2G_{5XX}) + 2HX(3G_{5\phi} + 2XG_{5\phi X}), \tag{A12}$$

$$\mathcal{E} = 2XK_X - K + 6X\dot{\phi}HG_{3X} - 2XG_{3\phi} - 6H^2G_4 + 24H^2X(G_{4X} + XG_{4XX}) - 12HX\dot{\phi}G_{4\phi X} - 6H\dot{\phi}G_{4\phi} + 2H^3X\dot{\phi}(5G_{5X} + 2XG_{5XX}) - 6H^2X(3G_{5\phi} + 2XG_{5\phi X}), \tag{A13}$$

$$\mathcal{P} = K - 2X(G_{3\phi} + \ddot{\phi}G_{3X}) + 2(3H^2 + 2\dot{H})G_4 - 12H^2XG_{4X} - 4H\dot{X}G_{4X} - 8\dot{H}XG_{4X} - 8HX\dot{X}G_{4XX} + 2(\ddot{\phi} + 2H\dot{\phi})G_{4\phi} + 4XG_{4\phi\phi} + 4X(\ddot{\phi} - 2H\dot{\phi})G_{4\phi X} - 2X(2H^3\dot{\phi} + 2H\dot{H}\,\dot{\phi} + 3H^2\ddot{\phi})G_{5X} - 4H^2X^2\ddot{\phi}G_{5XX} + 4HX(\dot{X} - HX)G_{5\phi X} + 2[2(HX)^{\cdot} + 3H^2X]G_{5\phi} + 4HX\dot{\phi}G_{5\phi\phi}. \tag{A14}$$

The coefficients in the first and second order solutions are defined as follows,

$$\mathcal{R}(t) = A_0\mathcal{F}_T - A_1^2, \tag{A15}$$

$$\mathcal{S}(t) = A_0\mathcal{G}_T + A_1A_2, \tag{A16}$$

$$\mathcal{T}(t) = A_1\mathcal{G}_T + A_2\mathcal{F}_T, \tag{A17}$$

$$\mathcal{Z}(t) = 2(A_0\mathcal{G}_T^2 + 2A_1A_2\mathcal{G}_T + A_2^2\mathcal{F}_T), \tag{A18}$$

$$\kappa_\Phi(t) = \frac{\rho_{\rm m}\mathcal{R}}{H^2\mathcal{Z}}, \tag{A19}$$

$$\kappa_\Psi(t) = \frac{\rho_{\rm m}\mathcal{S}}{H^2\mathcal{Z}}, \tag{A20}$$

$$\kappa_Q(t) = \frac{\rho_{\rm m}\mathcal{T}}{H^2\mathcal{Z}}, \tag{A21}$$

$$N_\gamma(t) = \frac{H^4}{\rho_{\rm m}}(2B_0\kappa_Q^3 - 3B_1\kappa_\Psi\kappa_Q^2 - 3B_2\kappa_\Phi\kappa_Q^2 - 6B_3\kappa_\Phi\kappa_\Psi\kappa_Q), \tag{A22}$$

$$\lambda(t) = \frac{7}{2D_+^2(t)}\int_0^t \frac{D_-(t)D_+(t') - D_+(t)D_-(t')}{W(t')}D_+^2(t')(f^2H^2 - N_\gamma(t'))dt', \tag{A23}$$

$$\lambda_\theta(t) = \lambda(t) + \frac{\dot{\lambda}(t)}{2fH}, \tag{A24}$$

$$\lambda_\Phi(t) = -\frac{2}{7}\kappa_\Phi\lambda(t) + \frac{1}{\mathcal{Z}}(2B_0\mathcal{T}\kappa_Q^2 - 3B_1\mathcal{S}\kappa_Q^2 - 3B_2\mathcal{R}\kappa_Q^2 - 6B_3\mathcal{R}\kappa_\Psi\kappa_Q), \tag{A25}$$

$$\lambda_\Psi(t) = -\frac{2}{7}\kappa_\Psi\lambda(t) + \frac{1}{\mathcal{Z}}(2B_0A_2\mathcal{G}_T\kappa_Q^2 + B_1(A_2^2\kappa_Q^2 - 2A_2\mathcal{G}_T\kappa_\Psi\kappa_Q) - B_2(\mathcal{S}\kappa_Q^2 + 2A_2\mathcal{G}_T\kappa_\Phi\kappa_Q) - 2B_3(\mathcal{S}\kappa_\Psi\kappa_Q - A_2^2\kappa_\Phi\kappa_Q + A_2\mathcal{G}_T\kappa_\Phi\kappa_\Psi)), \tag{A26}$$

$$\lambda_Q(t) = -\frac{2}{7}\kappa_Q\lambda(t) - \frac{1}{\mathcal{Z}}(2B_0\mathcal{G}_T^2\kappa_Q^2 + B_1(A_2\mathcal{G}_T\kappa_Q^2 - 2\mathcal{G}_T^2\kappa_\Psi\kappa_Q) + B_2(\mathcal{T}\kappa_Q^2 - 2\mathcal{G}_T^2\kappa_\Phi\kappa_Q) + 2B_3(\mathcal{T}\kappa_\Psi\kappa_Q + A_2\mathcal{G}_T\kappa_\Phi\kappa_Q - \mathcal{G}_T^2\kappa_\Phi\kappa_\Psi)). \tag{A27}$$

Some details are described in the previous paper [26], but one can show that $\lambda(t)$ obeys the differential equation,

$$\ddot{\lambda}(t) + (4f+2)H\dot{\lambda}(t) + (2f^2H^2 - L)\lambda(t) = \frac{7}{2}(f^2H^2 - N_\gamma). \tag{A28}$$

The coefficients for the third order solutions are defined as

$$\sigma_\Phi(t) = \frac{2}{\mathcal{Z}}(2B_0\mathcal{T}\kappa_Q^2 - 3B_1\mathcal{S}\kappa_Q^2 - 3B_2\mathcal{R}\kappa_Q^2 - 6B_3\mathcal{R}\kappa_\Psi\kappa_Q), \tag{A29}$$

$$\mu_\Phi(t) = \frac{2}{\mathcal{Z}}(2B_0\mathcal{T}\kappa_Q\lambda_Q - B_1(2\mathcal{S}\kappa_Q\lambda_Q + \mathcal{T}\kappa_Q\lambda_\Psi) - B_2(2\mathcal{R}\kappa_Q\lambda_Q + \mathcal{T}\kappa_Q\lambda_\Phi) - 2B_3(\mathcal{R}\kappa_\Psi\lambda_Q + \mathcal{R}\kappa_Q\lambda_\Psi + \mathcal{S}\kappa_Q\lambda_\Phi)), \tag{A30}$$

$$\nu_\Phi(t) = \frac{2}{3\mathcal{Z}}(-3C_0\mathcal{T}\kappa_Q^3 - 4C_1\mathcal{R}\kappa_Q^3), \tag{A31}$$

$$\begin{aligned}\sigma_\Psi(t) = \frac{2}{\mathcal{Z}}&(2B_0A_2\mathcal{G}_T\kappa_Q^2 - B_1(2A_2\mathcal{G}_T\kappa_\Psi\kappa_Q - A_2^2\kappa_Q^2) - B_2(\mathcal{S}\kappa_Q^2 + 2A_2\mathcal{G}_T\kappa_\Phi\kappa_Q)\\ &-2B_3(\mathcal{S}\kappa_\Psi\kappa_Q + A_2\mathcal{G}_T\kappa_\Phi\kappa_\Psi - A_2^2\kappa_\Phi\kappa_Q)),\end{aligned} \tag{A32}$$

$$\begin{aligned}\mu_\Psi(t) = \frac{2}{\mathcal{Z}}&(2B_0A_2\mathcal{G}_T\kappa_Q\lambda_Q - B_1(A_2\mathcal{G}_T(\kappa_\Psi\lambda_Q + \kappa_Q\lambda_\Psi) - A_2^2\kappa_Q\lambda_Q) - B_2(\mathcal{S}\kappa_Q\lambda_Q + A_2\mathcal{G}_T(\kappa_\Phi\lambda_Q + \kappa_Q\lambda_\Phi))\\ &-B_3(\mathcal{S}(\kappa_\Psi\lambda_Q + \kappa_Q\lambda_\Psi) + A_2\mathcal{G}_T(\kappa_\Phi\lambda_\Psi + \kappa_\Psi\lambda_\Phi) - A_2^2(\kappa_\Phi\lambda_Q + \kappa_Q\lambda_\Phi))),\end{aligned} \tag{A33}$$

$$\nu_\Psi(t) = \frac{2}{3\mathcal{Z}}(-3C_0A_2\mathcal{G}_T\kappa_Q^3 - C_1(\mathcal{S}\kappa_Q^3 + 3A_2\mathcal{G}_T\kappa_\Phi\kappa_Q^2)), \tag{A34}$$

$$\sigma_Q(t) = \frac{2}{\mathcal{Z}}(-2B_0\mathcal{G}_T^2\kappa_Q^2 + B_1(2\mathcal{G}_T^2\kappa_\Psi\kappa_Q - A_2\mathcal{G}_T\kappa_Q^2) - B_2(\mathcal{T}\kappa_Q^2 - 2\mathcal{G}_T^2\kappa_\Phi\kappa_Q) - 2B_3(\mathcal{S}\kappa_Q^2 - \mathcal{G}_T^2\kappa_\Phi\kappa_\Psi + A_2\mathcal{G}_T\kappa_\Phi\kappa_Q)), \tag{A35}$$

$$\begin{aligned}\mu_Q(t) = \frac{2}{\mathcal{Z}}&(-2B_0\mathcal{G}_T^2\kappa_Q\lambda_Q + B_1(\mathcal{G}_T^2(\kappa_\Psi\lambda_Q + \kappa_Q\lambda_\Psi) - A_2\mathcal{G}_T\kappa_Q\lambda_Q)\\ &- B_2(\mathcal{T}\kappa_Q\lambda_Q - \mathcal{G}_T^2(\kappa_\Phi\lambda_Q + \kappa_Q\lambda_\Phi))\\ &-B_3((\mathcal{S}\kappa_Q\lambda_Q + \mathcal{T}\kappa_Q\lambda_\Psi) - \mathcal{G}_T^2(\kappa_\Phi\lambda_\Psi + \kappa_\Psi\lambda_\Phi) + A_2\mathcal{G}_T(\kappa_\Phi\lambda_Q + \kappa_Q\lambda_\Phi))),\end{aligned} \tag{A36}$$

$$\nu_Q(t) = \frac{2}{3\mathcal{Z}}(3C_0\mathcal{G}_T^2\kappa_Q^3 + C_1(-\mathcal{T}\kappa_Q^3 + 3\mathcal{G}_T^2\kappa_\Phi\kappa_Q^2)). \tag{A37}$$

APPENDIX B: THIRD ORDER MODE-COUPLING FUNCTIONS

In this appendix, we summarize the functions that describe the nonlinear mode couplings of the third order solutions. In order to derive Eqs. (47), (48), and (49), we define

$$\mathcal{W}_{\gamma\alpha}(\mathbf{p}) \equiv \frac{1}{(2\pi)^6}\int d\mathbf{k}_1 d\mathbf{k}_2 d\mathbf{k}_3 \delta^{(3)}(\mathbf{k}_1+\mathbf{k}_2+\mathbf{k}_3-\mathbf{p})\gamma\alpha(\mathbf{k}_1,\mathbf{k}_2,\mathbf{k}_3)\delta_L(\mathbf{k}_1)\delta_L(\mathbf{k}_2)\delta_L(\mathbf{k}_3), \tag{B1}$$

$$\mathcal{W}_{\gamma\gamma}(\mathbf{p}) \equiv \frac{1}{(2\pi)^6}\int d\mathbf{k}_1 d\mathbf{k}_2 d\mathbf{k}_3 \delta^{(3)}(\mathbf{k}_1+\mathbf{k}_2+\mathbf{k}_3-\mathbf{p})\gamma\gamma(\mathbf{k}_1,\mathbf{k}_2,\mathbf{k}_3)\delta_L(\mathbf{k}_1)\delta_L(\mathbf{k}_2)\delta_L(\mathbf{k}_3), \tag{B2}$$

$$\mathcal{W}_{\xi}(\mathbf{p}) \equiv \frac{1}{(2\pi)^6}\int d\mathbf{k}_1 d\mathbf{k}_2 d\mathbf{k}_3 \delta^{(3)}(\mathbf{k}_1+\mathbf{k}_2+\mathbf{k}_3-\mathbf{p})\xi(\mathbf{k}_1,\mathbf{k}_2,\mathbf{k}_3)\delta_L(\mathbf{k}_1)\delta_L(\mathbf{k}_2)\delta_L(\mathbf{k}_3), \tag{B3}$$

with

$$\gamma\alpha(\mathbf{k}_1,\mathbf{k}_2,\mathbf{k}_3) = \frac{1}{3}(\gamma(\mathbf{k}_1,\mathbf{k}_2+\mathbf{k}_3)\alpha^{(s)}(\mathbf{k}_2,\mathbf{k}_3) + 2 \text{ cyclic terms}), \tag{B4}$$

$$\gamma\gamma(\mathbf{k}_1,\mathbf{k}_2,\mathbf{k}_3) = \frac{1}{3}(\gamma(\mathbf{k}_1,\mathbf{k}_2+\mathbf{k}_3)\gamma(\mathbf{k}_2,\mathbf{k}_3) + 2\,\text{cyclic terms}), \tag{B5}$$

$$\xi(\mathbf{k}_1,\mathbf{k}_2,\mathbf{k}_3)=1-\frac{k_1^2(\mathbf{k}_2\cdot\mathbf{k}_3)^2+k_2^2(\mathbf{k}_3\cdot\mathbf{k}_1)^2+k_3^2(\mathbf{k}_1\cdot\mathbf{k}_2)^2-2(\mathbf{k}_1\cdot\mathbf{k}_2)(\mathbf{k}_2\cdot\mathbf{k}_3)(\mathbf{k}_3\cdot\mathbf{k}_1)}{k_1^2k_2^2k_3^2}. \tag{B6}$$

In deriving Eqs. (55) and (56), we define

$$\mathcal{W}_{\alpha\alpha R}(\mathbf{p})=\frac{1}{(2\pi)^6}\int d\mathbf{k}_1d\mathbf{k}_2d\mathbf{k}_3\delta^{(3)}(\mathbf{k}_1+\mathbf{k}_2+\mathbf{k}_3-\mathbf{p})\alpha\alpha_R(\mathbf{k}_1,\mathbf{k}_2,\mathbf{k}_3)\delta_L(\mathbf{k}_1)\delta_L(\mathbf{k}_2)\delta_L(\mathbf{k}_3), \tag{B7}$$

$$\mathcal{W}_{\alpha\gamma R}(\mathbf{p})=\frac{1}{(2\pi)^6}\int d\mathbf{k}_1d\mathbf{k}_2d\mathbf{k}_3\delta^{(3)}(\mathbf{k}_1+\mathbf{k}_2+\mathbf{k}_3-\mathbf{p})\alpha\gamma_R(\mathbf{k}_1,\mathbf{k}_2,\mathbf{k}_3)\delta_L(\mathbf{k}_1)\delta_L(\mathbf{k}_2)\delta_L(\mathbf{k}_3), \tag{B8}$$

$$\mathcal{W}_{\alpha\alpha L}(\mathbf{p})=\frac{1}{(2\pi)^6}\int d\mathbf{k}_1d\mathbf{k}_2d\mathbf{k}_3\delta^{(3)}(\mathbf{k}_1+\mathbf{k}_2+\mathbf{k}_3-\mathbf{p})\alpha\alpha_L(\mathbf{k}_1,\mathbf{k}_2,\mathbf{k}_3)\delta_L(\mathbf{k}_1)\delta_L(\mathbf{k}_2)\delta_L(\mathbf{k}_3), \tag{B9}$$

$$\mathcal{W}_{\alpha\gamma L}(\mathbf{p})=\frac{1}{(2\pi)^6}\int d\mathbf{k}_1d\mathbf{k}_2d\mathbf{k}_3\delta^{(3)}(\mathbf{k}_1+\mathbf{k}_2+\mathbf{k}_3-\mathbf{p})\alpha\gamma_L(\mathbf{k}_1,\mathbf{k}_2,\mathbf{k}_3)\delta_L(\mathbf{k}_1)\delta_L(\mathbf{k}_2)\delta_L(\mathbf{k}_3), \tag{B10}$$

$$\mathcal{W}_{\alpha\alpha}(\mathbf{p})=\frac{1}{(2\pi)^6}\int d\mathbf{k}_1d\mathbf{k}_2d\mathbf{k}_3\delta^{(3)}(\mathbf{k}_1+\mathbf{k}_2+\mathbf{k}_3-\mathbf{p})\alpha\alpha(\mathbf{k}_1,\mathbf{k}_2,\mathbf{k}_3)\delta_L(\mathbf{k}_1)\delta_L(\mathbf{k}_2)\delta_L(\mathbf{k}_3), \tag{B11}$$

$$\mathcal{W}_{\alpha\gamma}(\mathbf{p})=\frac{1}{(2\pi)^6}\int d\mathbf{k}_1d\mathbf{k}_2d\mathbf{k}_3\delta^{(3)}(\mathbf{k}_1+\mathbf{k}_2+\mathbf{k}_3-\mathbf{p})\alpha\gamma(\mathbf{k}_1,\mathbf{k}_2,\mathbf{k}_3)\delta_L(\mathbf{k}_1)\delta_L(\mathbf{k}_2)\delta_L(\mathbf{k}_3), \tag{B12}$$

with

$$\alpha\alpha_R(\mathbf{k}_1,\mathbf{k}_2,\mathbf{k}_3)=\frac{1}{3}(\alpha(\mathbf{k}_1,\mathbf{k}_2+\mathbf{k}_3)\alpha^{(s)}(\mathbf{k}_2,\mathbf{k}_3)+2\,\text{cyclic terms}), \tag{B13}$$

$$\alpha\gamma_R(\mathbf{k}_1,\mathbf{k}_2,\mathbf{k}_3)=\frac{1}{3}(\alpha(\mathbf{k}_1,\mathbf{k}_2+\mathbf{k}_3)\gamma(\mathbf{k}_2,\mathbf{k}_3)+2\,\text{cyclic terms}), \tag{B14}$$

$$\alpha\alpha_L(\mathbf{k}_1,\mathbf{k}_2,\mathbf{k}_3)=\frac{1}{3}(\alpha(\mathbf{k}_1+\mathbf{k}_2,\mathbf{k}_3)\alpha^{(s)}(\mathbf{k}_2,\mathbf{k}_3)+2\,\text{cyclic terms}), \tag{B15}$$

$$\alpha\gamma_L(\mathbf{k}_1,\mathbf{k}_2,\mathbf{k}_3)=\frac{1}{3}(\alpha(\mathbf{k}_1+\mathbf{k}_2,\mathbf{k}_3)\gamma(\mathbf{k}_2,\mathbf{k}_3)+2\,\text{cyclic terms}), \tag{B16}$$

$$\alpha\alpha(\mathbf{k}_1,\mathbf{k}_2,\mathbf{k}_3)=\frac{1}{3}(\alpha^{(s)}(\mathbf{k}_1,\mathbf{k}_2+\mathbf{k}_3)\alpha^{(s)}(\mathbf{k}_2,\mathbf{k}_3)+2\,\text{cyclic terms}), \tag{B17}$$

$$\alpha\gamma(\mathbf{k}_1,\mathbf{k}_2,\mathbf{k}_3)=\frac{1}{3}(\alpha^{(s)}(\mathbf{k}_1,\mathbf{k}_2+\mathbf{k}_3)\gamma(\mathbf{k}_2,\mathbf{k}_3)+2\,\text{cyclic terms}). \tag{B18}$$

For the functions describing the mode couplings defined above, we find the following relations,

$$2\gamma\alpha(\mathbf{k}_1,\mathbf{k}_2,\mathbf{k}_3)=\alpha\gamma_R(\mathbf{k}_1,\mathbf{k}_2,\mathbf{k}_3)+2\gamma\gamma(\mathbf{k}_1,\mathbf{k}_2,\mathbf{k}_3)-\xi(\mathbf{k}_1,\mathbf{k}_2,\mathbf{k}_3), \tag{B19}$$

$$2\alpha\alpha(\mathbf{k}_1,\mathbf{k}_2,\mathbf{k}_3)=\alpha\alpha_R(\mathbf{k}_1,\mathbf{k}_2,\mathbf{k}_3)+\alpha\alpha_L(\mathbf{k}_1,\mathbf{k}_2,\mathbf{k}_3), \tag{B20}$$

$$2\alpha\gamma(\mathbf{k}_1,\mathbf{k}_2,\mathbf{k}_3)=\alpha\gamma_R(\mathbf{k}_1,\mathbf{k}_2,\mathbf{k}_3)+\alpha\gamma_L(\mathbf{k}_1,\mathbf{k}_2,\mathbf{k}_3). \tag{B21}$$

There is no additional relation between the functions of the third order perturbations, which can be proved by using the generalized Wronskian. These relations yield Eqs. (57)–(59).

APPENDIX C: DERIVATION OF THE ONE-LOOP POWER SPECTRA

The cosmological density contrast $\delta(t,\mathbf{k})$ and the velocity divergence $\theta(t,\mathbf{k})$ up to third order of the perturbative expansion are expressed as

$$\delta(t,\mathbf{k}) = D_+(t)\delta_{\rm L}(\mathbf{k}) + D_+^2(t)\delta_{2K}(t,\mathbf{k}) + D_+^3(t)\delta_{3K}(t,\mathbf{k}), \tag{C1}$$

$$\theta(t,\mathbf{k}) = -f(D_+(t)\delta_{\rm L}(\mathbf{k}) + D_+^2(t)\theta_{2K}(t,\mathbf{k}) + D_+^3(t)\theta_{3K}(t,\mathbf{k})), \tag{C2}$$

where we define

$$\delta_{2K}(t,\mathbf{k}) = \mathcal{W}_\alpha(\mathbf{k}) - \frac{2}{7}\lambda(t)\mathcal{W}_\gamma(\mathbf{k}), \tag{C3}$$

$$\delta_{3K}(t,\mathbf{k}) = \mathcal{W}_{\alpha\alpha}(\mathbf{k}) - \frac{2}{7}\lambda(t)\mathcal{W}_{\alpha\gamma R}(\mathbf{k}) - \frac{2}{7}\lambda(t)\mathcal{W}_{\alpha\gamma L}(\mathbf{k}) - \frac{2}{21}\mu(t)\mathcal{W}_{\gamma\gamma}(\mathbf{k}) + \frac{1}{9}\nu(t)\mathcal{W}_\xi(\mathbf{k}), \tag{C4}$$

$$\theta_{2K}(t,\mathbf{k}) = \mathcal{W}_\alpha(\mathbf{k}) - \frac{4}{7}\lambda_\theta(t)\mathcal{W}_\gamma(\mathbf{k}), \tag{C5}$$

$$\theta_{3K}(t,\mathbf{k}) = \mathcal{W}_{\alpha\alpha}(\mathbf{k}) - \frac{4}{7}\lambda_\theta(t)\mathcal{W}_{\alpha\gamma R}(\mathbf{k}) - \frac{2}{7}\lambda(t)\mathcal{W}_{\alpha\gamma L}(\mathbf{k}) - \frac{2}{7}\mu_\theta(t)\mathcal{W}_{\gamma\gamma}(\mathbf{k}) + \frac{1}{3}\nu_\theta(t)\mathcal{W}_\xi(\mathbf{k}), \tag{C6}$$

and the kernels for the density contrast F_2 and F_3, and those for the velocity divergence G_2 and G_3 are as follows,

$$F_2(t,\mathbf{k}_1,\mathbf{k}_2) = \alpha(\mathbf{k}_1,\mathbf{k}_2) - \frac{2}{7}\lambda(t)\gamma(\mathbf{k}_1,\mathbf{k}_2), \tag{C7}$$

$$G_2(t,\mathbf{k}_1,\mathbf{k}_2) = \alpha(\mathbf{k}_1,\mathbf{k}_2) - \frac{4}{7}\lambda_\theta(t)\gamma(\mathbf{k}_1,\mathbf{k}_2), \tag{C8}$$

$$\begin{aligned} F_3(t,\mathbf{k}_1,\mathbf{k}_2,\mathbf{k}_3) = {}& \alpha\alpha(\mathbf{k}_1,\mathbf{k}_2,\mathbf{k}_3) - \frac{2}{7}\lambda(t)\alpha\gamma_R(\mathbf{k}_1,\mathbf{k}_2,\mathbf{k}_3) - \frac{2}{7}\lambda(t)\alpha\gamma_L(\mathbf{k}_1,\mathbf{k}_2,\mathbf{k}_3) \\ & - \frac{2}{21}\mu(t)\gamma\gamma(\mathbf{k}_1,\mathbf{k}_2,\mathbf{k}_3) + \frac{1}{9}\nu(t)\xi(\mathbf{k}_1,\mathbf{k}_2,\mathbf{k}_3), \end{aligned} \tag{C9}$$

$$\begin{aligned} G_3(t,\mathbf{k}_1,\mathbf{k}_2,\mathbf{k}_3) = {}& \alpha\alpha(\mathbf{k}_1,\mathbf{k}_2,\mathbf{k}_3) - \frac{4}{7}\lambda_\theta(t)\alpha\gamma_R(\mathbf{k}_1,\mathbf{k}_2,\mathbf{k}_3) - \frac{2}{7}\lambda(t)\alpha\gamma_L(\mathbf{k}_1,\mathbf{k}_2,\mathbf{k}_3) \\ & - \frac{2}{7}\mu_\theta(t)\gamma\gamma(\mathbf{k}_1,\mathbf{k}_2,\mathbf{k}_3) + \frac{1}{3}\nu_\theta(t)\xi(\mathbf{k}_1,\mathbf{k}_2,\mathbf{k}_3). \end{aligned} \tag{C10}$$

These kernels have two types of symmetries. One type is the symmetry in the replacement of the wave numbers,

$$F_2(t,\mathbf{k}_1,\mathbf{k}_2) = F_2(t,\mathbf{k}_2,\mathbf{k}_1), \tag{C11}$$

$$\begin{aligned} F_3(t,\mathbf{k}_1,\mathbf{k}_2,\mathbf{k}_3) &= F_3(t,\mathbf{k}_2,\mathbf{k}_3,\mathbf{k}_1) = F_3(t,\mathbf{k}_3,\mathbf{k}_1,\mathbf{k}_2) \\ &= F_3(t,\mathbf{k}_1,\mathbf{k}_3,\mathbf{k}_2) = F_3(t,\mathbf{k}_2,\mathbf{k}_1,\mathbf{k}_3) = F_3(t,\mathbf{k}_3,\mathbf{k}_2,\mathbf{k}_1). \end{aligned} \tag{C12}$$

The second is the symmetry in the conversion of the sign of the wave numbers,

$$F_2(t,\mathbf{k}_1,\mathbf{k}_2) = F_2(t,-\mathbf{k}_1,-\mathbf{k}_2), \tag{C13}$$

$$F_3(t,\mathbf{k}_1,\mathbf{k}_2,\mathbf{k}_3) = F_3(t,-\mathbf{k}_1,-\mathbf{k}_2,-\mathbf{k}_3). \tag{C14}$$

The same relations hold for $G_2(t,\mathbf{k}_1,\mathbf{k}_2)$ and $G_3(t,\mathbf{k}_1,\mathbf{k}_2,\mathbf{k}_3)$.

The above properties are useful in deriving the expressions of the power spectra, $P_{\delta\delta}(t,k)$, $P_{\delta\theta}(t,k)$, $P_{\theta\theta}(t,k)$, defined by Eqs. (86), (87), and (88). Using the expressions (C1) and (C2), we find

$$P_{\delta\delta}(t,k) = D_+^2(t)P_{\rm L}(k) + D_+^4(t)(P_{\delta\delta}^{(22)}(t,k) + 2P_{\delta\delta}^{(13)}(t,k)), \tag{C15}$$

$$P_{\delta\theta}(t,k) = D_+^2(t)P_{\rm L}(k) + D_+^4(t)(P_{\delta\theta}^{(22)}(t,k) + 2P_{\delta\theta}^{(13)}(t,k)), \tag{C16}$$

$$P_{\theta\theta}(t,k) = D_+^2(t)P_{\rm L}(k) + D_+^4(t)(P_{\theta\theta}^{(22)}(t,k) + 2P_{\theta\theta}^{(13)}(t,k)), \tag{C17}$$

where $D_+^2(t)P_{\rm L}(k)$ is the linear matter power spectrum,

$$\langle \delta_{\rm L}(\mathbf{k}_1)\delta_{\rm L}(\mathbf{k}_2)\rangle = (2\pi)^3\delta^{(3)}(\mathbf{k}_1+\mathbf{k}_2)P_{\rm L}(k), \tag{C18}$$

and we define

$$\langle \delta_{2K}(t,\mathbf{k}_1)\delta_{2K}(t,\mathbf{k}_2)\rangle = (2\pi)^3\delta^{(3)}(\mathbf{k}_1+\mathbf{k}_2)P_{\delta\delta}^{(22)}(t,k), \tag{C19}$$

$$\langle \delta_{\rm L}(\mathbf{k}_1)\delta_{3K}(t,\mathbf{k}_2)\rangle = (2\pi)^3\delta^{(3)}(\mathbf{k}_1+\mathbf{k}_2)P_{\delta\delta}^{(13)}(t,k), \tag{C20}$$

$$\langle \delta_{2K}(t,\mathbf{k}_1)\theta_{2K}(t,\mathbf{k}_2)\rangle = (2\pi)^3\delta^{(3)}(\mathbf{k}_1+\mathbf{k}_2)P_{\delta\theta}^{(22)}(t,k), \tag{C21}$$

$$\langle \theta_{2K}(t,\mathbf{k}_1)\theta_{2K}(t,\mathbf{k}_2)\rangle = (2\pi)^3\delta^{(3)}(\mathbf{k}_1+\mathbf{k}_2)P_{\theta\theta}^{(22)}(t,k), \tag{C22}$$

$$\langle \delta_{\rm L}(\mathbf{k}_1)\theta_{3K}(t,\mathbf{k}_2)\rangle = (2\pi)^3\delta^{(3)}(\mathbf{k}_1+\mathbf{k}_2)P_{\theta\theta}^{(13)}(t,k), \tag{C23}$$

and

$$\frac{1}{2}(\langle \delta_{\rm L}(\mathbf{k}_1)\theta_{3K}(t,\mathbf{k}_2)\rangle + \langle \delta_{3K}(t,\mathbf{k}_1)\delta_{\rm L}(\mathbf{k}_2)\rangle) = (2\pi)^3\delta^{(3)}(\mathbf{k}_1+\mathbf{k}_2)P_{\delta\theta}^{(13)}(t,k). \tag{C24}$$

As an example, let us explain the derivation of $P_{\delta\delta}^{(22)}(t,k)$. Inserting Eq. (C3) into (C19), we have

$$\begin{aligned}\langle \delta_{2K}(t,\mathbf{k}_1)\delta_{2K}(t,\mathbf{k}_2)\rangle &= \left\langle \frac{1}{(2\pi)^3}\int d^3q_1 d^3q_2 \delta^{(3)}(\mathbf{k}_1-\mathbf{q}_1-\mathbf{q}_2)F_2(t,\mathbf{q}_1,\mathbf{q}_2)\delta_{\rm L}(\mathbf{q}_1)\delta_{\rm L}(\mathbf{q}_2)\right.\\ &\quad\left.\times\frac{1}{(2\pi)^3}\int d^3q_3 d^3q_4 \delta^{(3)}(\mathbf{k}_2-\mathbf{q}_3-\mathbf{q}_4)F_2(t,\mathbf{q}_3,\mathbf{q}_4)\delta_{\rm L}(\mathbf{q}_3)\delta_{\rm L}(\mathbf{q}_4)\right\rangle\\ &= \frac{1}{(2\pi)^6}\int d^3q_1 d^3q_3 F_2(t,\mathbf{q}_1,\mathbf{k}_1-\mathbf{q}_1)F_2(t,\mathbf{q}_3,\mathbf{k}_2-\mathbf{q}_3)\\ &\quad\times\langle \delta_L(\mathbf{q}_1)\delta_L(\mathbf{k}_1-\mathbf{q}_1)\delta_L(\mathbf{q}_3)\delta_L(\mathbf{k}_2-\mathbf{q}_3)\rangle.\end{aligned} \tag{C25}$$

Using the relation that holds for the Gaussian variables, we have

$$\begin{aligned}\langle \delta_L(\mathbf{q}_1)\delta_L(\mathbf{k}_1-\mathbf{q}_1)\delta_L(\mathbf{q}_3)\delta_L(\mathbf{k}_2-\mathbf{q}_3)\rangle &= \langle \delta_L(\mathbf{q}_1)\delta_L(\mathbf{k}_1-\mathbf{q}_1)\rangle\langle \delta_L(\mathbf{q}_3)\delta_L(\mathbf{k}_2-\mathbf{q}_3)\rangle\\ &\quad+\langle \delta_L(\mathbf{q}_1)\delta_L(\mathbf{q}_3)\rangle\langle \delta_L(\mathbf{k}_2-\mathbf{q}_3)\delta_L(\mathbf{k}_1-\mathbf{q}_1)\rangle\\ &\quad+\langle \delta_L(\mathbf{q}_1)\delta_L(\mathbf{k}_2-\mathbf{q}_3)\rangle\langle \delta_L(\mathbf{k}_1-\mathbf{q}_1)\delta_L(\mathbf{q}_3)\rangle,\end{aligned} \tag{C26}$$

which yields

$$\begin{aligned}\langle \delta_L(\mathbf{k}_{11})\delta_L(\mathbf{k}_1-\mathbf{k}_{11})\delta_L(\mathbf{k}_{21})\delta_L(\mathbf{k}_2-\mathbf{k}_{21})\rangle &= (2\pi)^6\delta^{(3)}(\mathbf{q}_1+\mathbf{q}_3)\delta^{(3)}(\mathbf{k}_1+\mathbf{k}_2-\mathbf{q}_1-\mathbf{q}_3)P_{\rm L}(q_1)P_{\rm L}(|\mathbf{k}_1-\mathbf{q}_1|)\\ &\quad+(2\pi)^6\delta^{(3)}(\mathbf{q}_1+\mathbf{k}_2-\mathbf{q}_3)\delta^{(3)}(\mathbf{k}_1-\mathbf{q}_1+\mathbf{q}_3)P_{\rm L}(q_1)P_{\rm L}(q_3),\end{aligned} \tag{C27}$$

with Eq. (C18). Then, Eq. (C25) yields

$$\begin{aligned}\langle \delta_{2K}(t,\mathbf{k}_1)\delta_{2K}(t,\mathbf{k}_2)\rangle &= \delta^{(3)}(\mathbf{k}_1+\mathbf{k}_2)\int d^3q_1 (F_2(t,\mathbf{q}_1,\mathbf{k}_1-\mathbf{q}_1)F_2(t,-\mathbf{q}_1,\mathbf{k}_2+\mathbf{q}_1)\\ &\quad+F_2(t,\mathbf{q}_1,\mathbf{k}_1-\mathbf{q}_1)F_2(t,\mathbf{k}_2+\mathbf{q}_1,-\mathbf{q}_1))P_{\rm L}(q_1)P_{\rm L}(|\mathbf{k}_1-\mathbf{q}_1|).\end{aligned} \tag{C28}$$

Using the relation (C13), we have

$$P^{(22)}_{\delta\delta}(t,k) = \frac{2}{(2\pi)^3}\int d^3q_1 F_2^2(t,\mathbf{q}_1,\mathbf{k}-\mathbf{q}_1)P_{\rm L}(q_1)P_{\rm L}(|\mathbf{k}-\mathbf{q}_1|), \tag{C29}$$

which reduces to Eq. (92). In the derivation, we define $x=\cos\theta$, where θ is the angle between $\mathbf{k}_1$ and $\mathbf{q}_1$. Similarly, the expressions (93) and (94) are obtained for $P^{(22)}_{\delta\theta}(t,k)$ and $P^{(22)}_{\theta\theta}(t,k)$. In the limit of the Einstein–de Sitter universe within general relativity, $\lambda(t)=\lambda_\theta(t)=\mu(t)=\mu_\theta(t)=1$, which gives the well-known expressions

$$P^{(22)}_{\delta\delta}(k) = \frac{k^3}{98(2\pi)^2}\int drP_{\rm L}(rk)\int_{-1}^{1}dxP_{\rm L}((1+r^2-2rx)^{1/2})\frac{(3r+7x-10rx^2)^2}{(1+r^2-2rx)^2}, \tag{C30}$$

$$P^{(22)}_{\delta\theta}(k) = \frac{k^3}{98(2\pi)^2}\int drP_{\rm L}(rk)\int_{-1}^{1}dxP_{\rm L}((1+r^2-2rx)^{1/2})\frac{(3r+7x-10rx^2)(-r+7x-6rx^2)}{(1+r^2-2rx)^2}, \tag{C31}$$

$$P^{(22)}_{\theta\theta}(k) = \frac{k^3}{98(2\pi)^2}\int drP_{\rm L}(rk)\int_{-1}^{1}dxP_{\rm L}((1+r^2-2rx)^{1/2})\frac{(-r+7x-6rx^2)^2}{(1+r^2-2rx)^2}, \tag{C32}$$

which are constants as a function of time.

Next, let us explain the derivation of $P^{(13)}_{\delta\delta}(t,k)$. Inserting Eq. (C4) into (C20), we have

$$2\langle\delta_L(\mathbf{k}_1)\delta_{3K}(t,\mathbf{k}_2)\rangle = \frac{2}{(2\pi)^6}\int d^3q_1d^3q_2F_3(t,\mathbf{q}_1,\mathbf{q}_2,\mathbf{k}_2-\mathbf{q}_1-\mathbf{q}_2)\langle\delta_L(\mathbf{k}_1)\delta_L(\mathbf{q}_1)\delta_L(\mathbf{q}_2)\delta_L(\mathbf{k}_2-\mathbf{q}_1-\mathbf{q}_2)\rangle. \tag{C33}$$

Using the relations

$$\begin{aligned}&\langle\delta_L(\mathbf{k}_1)\delta_L(\mathbf{q}_1)\delta_L(\mathbf{q}_2)\delta_L(\mathbf{k}_2-\mathbf{q}_1-\mathbf{q}_2)\rangle\\ &=(2\pi)^6\delta^{(3)}(\mathbf{k}_1+\mathbf{q}_1)P_{\rm L}(k_1)\delta^{(3)}(\mathbf{k}_2-\mathbf{q}_1)P_{\rm L}(q_2)\\ &+(2\pi)^6\delta^{(3)}(\mathbf{k}_1+\mathbf{q}_2)P_{\rm L}(k_1)\delta^{(3)}(\mathbf{k}_2-\mathbf{q}_2)P_{\rm L}(q_1)\\ &+(2\pi)^6\delta^{(3)}(\mathbf{k}_1+\mathbf{k}_2-\mathbf{q}_1-\mathbf{q}_2)P_{\rm L}(\mathbf{k}_1)\delta^{(3)}(\mathbf{q}_1+\mathbf{q}_2)P_{\rm L}(q_1),\end{aligned} \tag{C34}$$

and the symmetries, Eq. (C12), we have

$$2P^{(13)}_{\delta\delta}(t,k) = \frac{6}{(2\pi)^3}\int d^3q_1F_3(t,\mathbf{k},\mathbf{q}_1,-\mathbf{q}_1)P_{\rm L}(k)P_{\rm L}(q_1). \tag{C35}$$

After performing the angular integration with respect to the spherical coordinate of $\mathbf{q_1}$, we finally have Eq. (95). Note that Eq. (95) does not depend on $\nu(t)$, which occurs because of the identity $\xi(\mathbf{k},\mathbf{q}_1,-\mathbf{q}_1)=0$. $P^{(13)}_{\delta\delta}(t,k)$ is characterized by $\lambda(t)$ and $\mu(t)$. Similarly, we have the expressions (96) and (97) for $P^{(13)}_{\delta\theta}(t,k)$ and $P^{(13)}_{\theta\theta}(t,k)$, respectively. For the same reason as $P^{(13)}_{\delta\delta}(t,k)$, $P^{(13)}_{\delta\theta}(t,k)$ and $P^{(13)}_{\theta\theta}(t,k)$ do not depend on $\nu(t)$ and $\nu_\theta(t)$. Furthermore, $P^{(13)}_{\delta\theta}(t,k)$ and $P^{(13)}_{\theta\theta}(t,k)$ do not depend on $\lambda_\theta(t)$. This is because of the nature of the integration

$$\int dx\alpha\gamma_R(\mathbf{k},\mathbf{q}_1,-\mathbf{q}_1)=0. \tag{C36}$$

Finally, $P^{(13)}_{\delta\theta}(t,k)$ depends on $\lambda(t)$, $\mu(t)$, and $\mu_\theta(t)$, and $P^{(13)}_{\theta\theta}(t,k)$ depends on $\lambda(t)$ and $\mu_\theta(t)$. We find the following relation holds, in general: $P^{(13)}_{\delta\theta}(t,k)=[P^{(13)}_{\delta\delta}(t,k)+P^{(13)}_{\theta\theta}(t,k)]/2$, from Eq. (C24).

In the limit of the Einstein–de Sitter universe within general relativity, all the coefficients $\lambda(t)$, $\mu(t)$, $\mu_\theta(t)$ reduce to 1, which reproduces the well-known expressions

$$\begin{aligned}2P^{(13)}_{\delta\delta}(k) &= \frac{k^3}{252(2\pi)^2}P_{\rm L}(k)\int drP_{\rm L}(rk)\\ &\times\left[12\frac{1}{r^2}-158+100r^2-42r^4\right.\\ &\left.+\frac{3}{r^3}(r^2-1)^3(7r^2+2)\ln\left(\frac{r+1}{|r-1|}\right)\right],\end{aligned} \tag{C37}$$

$$\begin{aligned}2P^{(13)}_{\delta\theta}(k) &= \frac{k^3}{252(2\pi)^2}P_{\rm L}(k)\int drP_{\rm L}(rk)\\ &\times\left[24\frac{1}{r^2}-202+56r^2-30r^4\right.\\ &\left.+\frac{3}{r^3}(r^2-1)^3(5r^2+4)\ln\left(\frac{r+1}{|r-1|}\right)\right],\end{aligned} \tag{C38}$$

$$\begin{aligned}2P^{(13)}_{\theta\theta}(k) &= \frac{k^3}{84(2\pi)^2}P_{\rm L}(k)\int drP_{\rm L}(rk)\\ &\times\left[12\frac{1}{r^2}-82+4r^2-6r^4\right.\\ &\left.+\frac{3}{r^3}(r^2-1)^3(r^2+2)\ln\left(\frac{r+1}{|r-1|}\right)\right].\end{aligned} \tag{C39}$$

APPENDIX D: INTEGRATIONS OF MODE-COUPLING FUNCTIONS

Here we summarize the expressions that are useful in deriving the one-loop order power spectra,

$$\alpha^2(\mathbf{q}_1,\mathbf{k}_1-\mathbf{q}_1)=\frac{(r+x-2rx^2)^2}{4r^2(1+r^2-2rx)^2}, \tag{D1}$$

$$\alpha(\mathbf{q}_1,\mathbf{k}_1-\mathbf{q}_1)\gamma(\mathbf{q}_1,\mathbf{k}_1-\mathbf{q}_1)=\frac{(r+x-2rx^2)(-1+x^2)}{2r(1+r^2-2rx)^2}, \tag{D2}$$

$$\gamma^2(\mathbf{q}_1,\mathbf{k}_1-\mathbf{q}_1)=\frac{(-1+x^2)^2}{(1+r^2-2rx)^2}, \tag{D3}$$

and

$$\int d^3q_1 P_{\rm L}(rk)\alpha\alpha(\mathbf{k},\mathbf{q}_1,-\mathbf{q}_1)=\frac{2\pi k^3}{72}\int dr P_{\rm L}(rk)\left[-2+16r^2-6r^4+\frac{3}{r^3}(r^2-1)^3\ln\left(\frac{r+1}{|r-1|}\right)\right], \tag{D4}$$

$$\int d^3q_1 P_{\rm L}(rk)\alpha\gamma_R(\mathbf{k},\mathbf{q}_1,-\mathbf{q}_1)=0, \tag{D5}$$

$$\int d^3q_1 P_{\rm L}(rk)\alpha\gamma_L(\mathbf{k},\mathbf{q}_1,-\mathbf{q}_1)=\frac{2\pi k_1^3}{36}\int dr P_{\rm L}(rk)[6+16r^2-6r^4+\frac{3}{r^3}(r^2-1)^3\ln\left(\frac{r+1}{|r-1|}\right)\Big], \tag{D6}$$

$$\int d^3q_1 P_{\rm L}(rk)\gamma\gamma(\mathbf{k}_1,\mathbf{q}_1,-\mathbf{q}_1)=\frac{2\pi k_1^3}{72}\int dr P_{\rm L}(rk)\left[-6\frac{1}{r^2}+22+22r^2-6r^4+\frac{3}{r^3}(r^2-1)^4\ln\left(\frac{r+1}{|r-1|}\right)\right], \tag{D7}$$

$$\int d^3q_1 P_{\rm L}(rk)\xi(\mathbf{k}_1,\mathbf{q}_1,-\mathbf{q}_1)=0. \tag{D8}$$

APPENDIX E: COEFFICIENTS IN THE KGB MODEL

In the KGB model, we find the coefficients in basic equations,

$$\mathcal{F}_T=M_{\rm pl}^2, \qquad \mathcal{G}_T=M_{\rm pl}^2, \tag{E1}$$

$$\Theta=-nM_{\rm pl}\left(\frac{r_c^2}{M_{\rm pl}^2}\right)^n\dot\phi X^n+HM_{\rm pl}^2, \tag{E2}$$

$$\dot\Theta=-n(2n+1)M_{\rm pl}\left(\frac{r_c^2}{M_{\rm pl}^2}\right)^n\ddot\phi X^n+\dot HM_{\rm pl}^2, \tag{E3}$$

$$\mathcal{E}=-X+6nM_{\rm pl}\left(\frac{r_c^2}{M_{\rm pl}^2}\right)^n\dot\phi HX^n-3H^2M_{\rm pl}^2, \tag{E4}$$

$$\mathcal{P}=-X-2nM_{\rm pl}\left(\frac{r_c^2}{M_{\rm pl}^2}\right)^n\ddot\phi X^n+(3H^2+2\dot H)M_{\rm pl}^2, \tag{E5}$$

$$A_0=\frac{X}{H^2}-2nM_{\rm pl}\left(\frac{r_c^2}{M_{\rm pl}^2}\right)^n\left(\frac{2\dot\phi}{H}+n\frac{\ddot\phi}{H^2}\right)X^n, \tag{E6}$$

$$A_2=B_0=n\frac{\dot\phi}{H}M_{\rm pl}\left(\frac{r_c^2}{M_{\rm pl}^2}\right)^nX^n, \tag{E7}$$

$$A_1=B_1=B_2=B_3=C_0=C_1=0, \tag{E8}$$

and the nontrivial expressions

$$L(t)=-\frac{A_0\mathcal{F}_T\rho_{\rm m}}{2(A_0\mathcal{G}_T+A_2^2\mathcal{F}_T)}, \tag{E9}$$

$$N_\gamma(t)=\frac{B_0A_2^3\mathcal{F}_T^3\rho_{\rm m}^2}{4(A_0\mathcal{G}_T^2+A_2^2\mathcal{F}_T)^3H^2}, \tag{E10}$$

$$H^2\mu_\Phi=-\frac{8B_0\mathcal{T}^3\rho_{\rm m}^2}{7H^2\mathcal{Z}^3}\lambda-\frac{8B_0^2\mathcal{G}_T^2\mathcal{T}^4\rho_{\rm m}^3}{H^4\mathcal{Z}^5}. \tag{E11}$$

We use the attractor solution, which satisfies $3\dot\phi HG_{3X}=1$. Then we have

$$\ddot\phi=-\frac{1}{2n-1}\frac{\dot\phi\,\dot H}{H}, \tag{E12}$$

$$\frac{\dot H}{H^2}=-\frac{(2n-1)3\Omega_{\rm m}}{2(2n-\Omega_{\rm m})}, \tag{E13}$$

$$A_0 = -\frac{M_{\rm pl}^2(1-\Omega_{\rm m})(2n+(3n-1)\Omega_{\rm m})}{2n-\Omega_{\rm m}}, \tag{E14}$$

$$A_2 = M_{\rm pl}^2(1-\Omega_{\rm m}), \tag{E15}$$

$$B_0 = M_{\rm pl}^2(1-\Omega_{\rm m}), \tag{E16}$$

where we define $\Omega_{\rm m} = \rho_m(a)/3M_{\rm pl}^2H^2$. We also have

$$\mathcal{R} = -\frac{M_{\rm pl}^4(1-\Omega_{\rm m})(2n+(3n-1)\Omega_{\rm m})}{2n-\Omega_{\rm m}}, \tag{E17}$$

$$\mathcal{S} = -\frac{M_{\rm pl}^4(1-\Omega_{\rm m})(2n+(3n-1)\Omega_{\rm m})}{2n-\Omega_{\rm m}}, \tag{E18}$$

$$\mathcal{T} = M_{\rm pl}^4(1-\Omega_{\rm m}), \tag{E19}$$

$$\mathcal{Z} = 2\frac{M_{\rm pl}^6\Omega_{\rm m}(5n-\Omega_{\rm m})(1-\Omega_{\rm m})}{2n-\Omega_{\rm m}}. \tag{E20}$$

[1] P. J. E. Peebles and B. Ratra, Rev. Mod. Phys. **75**, 559 (2003).
[2] P. A. R. Ade *et al.* (Planck Collaboration), arXiv: 1502.01589.
[3] S. Weinberg, Rev. Mod. Phys. **61**, 1 (1989).
[4] S. Weinberg, arXiv:astro-ph/0005265.
[5] J. Martin, C.R. Phys. **13**, 566 (2012).
[6] W. Hu and I. Sawicki, Phys. Rev. D **76**, 064004 (2007).
[7] A. A. Starobinsky, JETP Lett. **86**, 157 (2007).
[8] S. Tsujikawa, Phys. Rev. D **77**, 023507 (2008).
[9] S. Nojiri and S. Odintsov, Phys. Lett. B **657**, 238 (2007).
[10] G. R. Dvali, G. Gabadadze, and M. Porrati, Phys. Lett. B **485**, 208 (2000).
[11] Y-S. Song, I. Sawicki, and W. Hu, Phys. Rev. D **75**, 064003 (2007).
[12] R. Maartens and E. Majerotto, Phys. Rev. D **74**, 023004 (2006).
[13] R. Maartens and K. Koyama, Living Rev. Relativity **13**, 5 (2010).
[14] C. de Rham and G. Gabadadze, Phys. Rev. D **82**, 044020 (2010).
[15] C. de Rham, G. Gabadadze, and A. J. Tolley, Phys. Rev. Lett. **106**, 231101 (2011).
[16] C. de Rham and L. Heisenberg, Phys. Rev. D **84**, 043503 (2011).
[17] S. F. Hassan and R. A. Rosen, Phys. Rev. Lett. **108**, 041101 (2012).
[18] A. R. Gomes and L. Amendola, J. Cosmol. Astropart. Phys. 03 (2014) 041.
[19] C. Deffayet, X. Gao, D. A. Steer, and G. Zahariade, Phys. Rev. D **84**, 064039 (2011).
[20] T. Kobayashi, M. Yamaguchi, and J. Yokoyama, Prog. Theor. Phys. **126**, 511 (2011).
[21] G. W. Horndeski, Int. J. Theor. Phys. **10**, 363 (1974).
[22] A. I. Vainshtein, Phys. Lett. **39B**, 393 (1972).
[23] R. Kimura, T. Kobayashi, and K. Yamamoto, Phys. Rev. D **85**, 024023 (2012).
[24] R. Kase and S. Tsujikawa, J. Cosmol. Astropart. Phys. 08 (2013) 054.
[25] T. Narikawa, T. Kobayashi, D. Yamauchi, and R. Saito, Phys. Rev. D **87**, 124006 (2013).
[26] Y. Takushima, A. Terukina, and K. Yamamoto, Phys. Rev. D **89**, 104007 (2014).
[27] R. Juszkiewicz, Mon. Not. R. Astron. Soc. **197**, 931 (1981).
[28] E. T. Vishniac, Mon. Not. R. Astron. Soc. **203**, 345 (1983).
[29] M. H. Goroff, B. Grinstein, S. J. Rey, and M. B. Wise, Astrophys. J. **311**, 6 (1986).
[30] Y. Suto and M. Sasaki, Phys. Rev. Lett. **66**, 264 (1991).
[31] N. Makino, M. Sasaki, and Y. Suto, Phys. Rev. D **46**, 585 (1992).
[32] B. Jain and E. Bertschinger, Astrophys. J. **431**, 495 (1994).
[33] R. Scoccimarro, S. Colombi, J. N. Fry, J. A. Frieman, E. Hivon, and A. Melott, Astrophys. J. **496**, 586 (1998).
[34] F. Bernardeau, S. Colombi, E. Gaztanaga, and R. Scoccimarro, Phys. Rep. **367**, 1 (2002).
[35] R. Takahashi, Prog. Theor. Phys. **120**, 549 (2008).
[36] M. Shoji and E. Komatsu, Astrophys. J. **700**, 705 (2009).
[37] K. Koyama, A. Taruya, and T. Hiramatsu, Phys. Rev. D **79**, 123512 (2009).
[38] M. Crocce and R. Scoccimarro, Phys. Rev. D **73**, 063519 (2006).
[39] M. Crocce and R. Scoccimarro, Phys. Rev. D **73**, 063520 (2006).
[40] M. Crocce and R. Scoccimarro, Phys. Rev. D **77**, 023533 (2008).
[41] T. Matsubara, Phys. Rev. D **77**, 063530 (2008).
[42] A. Taruya and T. Hiramatsu, Astrophys. J. **674**, 617 (2008).
[43] A. Taruya, T. Nishimichi, F. Bernardeau, T. Hiramatsu, and K. Koyama, Phys. Rev. D **90**, 123515 (2014).
[44] S. Lee, C. Park, and S. G. Biern, Phys. Lett. B **736**, 403 (2014).
[45] A. Nicolis, R. Rattazzi, and E. Trincherini, Phys. Rev. D **79**, 064036 (2009).
[46] N. Chow and J. Khoury, Phys. Rev. D **80**, 024037 (2009).
[47] F. P. Silva and K. Koyama, Phys. Rev. D **80**, 121301 (2009).
[48] T. Kobayashi, H. Tashiro, and D. Suzuki, Phys. Rev. D **81**, 063513 (2010).
[49] T. Kobayashi, Phys. Rev. D **81**, 103533 (2010).

[50] A. De Felice and S. Tsujikawa, Phys. Rev. D **84**, 124029 (2011).
[51] A. De Felice and S. Tsujikawa, J. Cosmol. Astropart. Phys. 07 (2010) 024.
[52] A. De Felice, S. Mukohyama, and S. Tsujikawa, Phys. Rev. D **82**, 023524 (2010).
[53] C. Deffayet, G. Esposito-Farese, and A. Vikman, Phys. Rev. D **79**, 084003 (2009).
[54] R. Gannouji and M. Sami, Phys. Rev. D **82**, 024011 (2010).
[55] A. Ali, R. Gannouji, and M. Sami, Phys. Rev. D **82**, 103015 (2010).
[56] A. De Felice and S. Tsujikawa, Phys. Rev. Lett. **105**, 111301 (2010).
[57] S. Nesseris, A. De Felice, and S. Tsujikawa, Phys. Rev. D **82**, 124054 (2010).
[58] D. F. Mota, M. Sandstad, and T. Zlosnik, J. High Energy Phys. 12 (2010) 051.
[59] A. De Felice, R. Kase, and S. Tsujikawa, Phys. Rev. D **83**, 043515 (2011).
[60] C. Deffayet, O. Pujolas, I. Sawicki, and A. Vikman, J. Cosmol. Astropart. Phys. 10 (2010) 026.
[61] C. Deffayet, S. Deser, and G. Esposito-Farese, Phys. Rev. D **80**, 064015 (2009).
[62] C. Burrage and D. Seery, J. Cosmol. Astropart. Phys. 08 (2010) 011.
[63] G. L. Goon, K. Hinterbichler, and M. Trodden, Phys. Rev. D **83**, 085015 (2011).
[64] C. de Rham and A. J. Tolley, J. Cosmol. Astropart. Phys. 05 (2010) 015.
[65] A. De Felice, T. Kobayashi, and S. Tsujikawa, Phys. Lett. B **706**, 123 (2011).
[66] R. Kimura and K. Yamamoto, J. Cosmol. Astropart. Phys. 04 (2011) 025.
[67] N. Bartolo, E. Bellini, D. Bertacca, and S. Matarrese, J. Cosmol. Astropart. Phys. 03 (2013) 034.

Monthly Notices of the ROYAL ASTRONOMICAL SOCIETY
MNRAS **452,** 1171–1183 (2015) doi:10.1093/mnras/stv1366

The *XMM* Cluster Survey: testing chameleon gravity using the profiles of clusters

Harry Wilcox,[1⋆] David Bacon,[1] Robert C. Nichol,[1] Philip J. Rooney,[2] Ayumu Terukina,[3] A. Kathy Romer,[2] Kazuya Koyama,[1] Gong-Bo Zhao,[1,4] Ross Hood,[5] Robert G. Mann,[5] Matt Hilton,[6] Maria Manolopoulou,[5] Martin Sahlén,[7] Chris A. Collins,[8] Andrew R. Liddle,[5] Julian A. Mayers,[2] Nicola Mehrtens,[9,10] Christopher J. Miller,[11] John P. Stott[12] and Pedro T. P. Viana[13,14]

[1]*Institute of Cosmology and Gravitation, University of Portsmouth, Dennis Sciama Building, Portsmouth PO1 3FX, UK*
[2]*Astronomy Centre, University of Sussex, Falmer, Brighton BN1 9QH, UK*
[3]*Department of Physical Science, Hiroshima University, Higashi-Hiroshima 739-8526, Japan*
[4]*National Astronomy Observatories, Chinese Academy of Science, Beijing 100012, People's Republic of China*
[5]*Institute for Astronomy, University of Edinburgh, Royal Observatory, Blackford Hill, Edinburgh EH9 3HJ, UK*
[6]*Astrophysics & Cosmology Research Unit, School of Mathematics, Statistics & Computer Science, University of KwaZulu-Natal, Westville Campus, Durban 4041, South Africa*
[7]*BIPAC, Department of Physics, University of Oxford, Denys Wilkinson Building, 1 Keble Road, Oxford OX1 3RH, UK*
[8]*Astrophysics Research Institute, Liverpool John Moores University, IC2, Liverpool Science Park, Brownlow Hill, Liverpool L5 3AF, UK*
[9]*George P. and Cynthia Woods Mitchell Institute for Fundamental Physics and Astronomy, Texas A&M University, College Station, TX 77843-4242, USA*
[10]*Department of Physics and Astronomy, Texas A&M University, College Station, TX 77843-4242, USA*
[11]*Astronomy Department, University of Michigan, Ann Arbor, MI 48109, USA*
[12]*Sub-department of Astrophysics, Department of Physics, University of Oxford, Denys Wilkinson Building, Keble Road, Oxford OX1 3RH, UK*
[13]*Instituto de Astrofísica e Ciências do Espaço, Universidade do Porto, CAUP, Rua das Estrelas, P-4150-762 Porto, Portugal*
[14]*Departamento de Física e Astronomia, Faculdade de Ciências, Universidade do Porto, Rua do Campo Alegre, 687, P-4169-007 Porto, Portugal*

Accepted 2015 June 17. Received 2015 June 15; in original form 2015 April 15

ABSTRACT

The chameleon gravity model postulates the existence of a scalar field that couples with matter to mediate a fifth force. If it exists, this fifth force would influence the hot X-ray emitting gas filling the potential wells of galaxy clusters. However, it would not influence the clusters weak lensing signal. Therefore, by comparing X-ray and weak lensing profiles, one can place upper limits on the strength of a fifth force. This technique has been attempted before using a single, nearby cluster (Coma, $z = 0.02$). Here we apply the technique to the stacked profiles of 58 clusters at higher redshifts ($0.1 < z < 1.2$), including 12 new to the literature, using X-ray data from the *XMM* Cluster Survey and weak lensing data from the Canada–France–Hawaii–Telescope Lensing Survey. Using a multiparameter Markov chain Monte Carlo analysis, we constrain the two chameleon gravity parameters (β and ϕ_∞). Our fits are consistent with general relativity, not requiring a fifth force. In the special case of $f(R)$ gravity (where $\beta = \sqrt{1/6}$), we set an upper limit on the background field amplitude today of $|f_{R0}| < 6 \times 10^{-5}$ (95 per cent CL). This is one of the strongest constraints to date on $|f_{R0}|$ on cosmological scales. We hope to improve this constraint in future by extending the study to hundreds of clusters using data from the Dark Energy Survey.

Key words: gravitation – gravitational lensing: weak – X-rays: galaxies: clusters.

1 INTRODUCTION

An accepted explanation for the accelerated expansion of the late-time Universe (Riess et al. 1998; Perlmutter et al. 1999) is to modify the Einstein equation, either by adding a component to the energy–momentum tensor via dark energy or to the Einstein tensor via a

⋆ E-mail: harry.wilcox@port.ac.uk

© 2015 The Authors
Published by Oxford University Press on behalf of the Royal Astronomical Society

Downloaded from http://mnras.oxfordjournals.org/ at Hiroshima University on December 17, 2015

modification to gravity (Milgrom 1983; Clifton et al. 2012). The latter often involves the introduction of a scalar field coupled to the matter components of the Universe, giving rise to a fifth force of the same order of magnitude as gravity (Jain, Vikram & Sakstein 2013). Through a variety of experiments and astronomical observations, this fifth force has been demonstrated to be negligible at terrestrial and Solar system densities (Wagner et al. 2012). Therefore, if a fifth force does exist it must be it must be suppressed, or 'screened', in high-density regions and only take effect in low-density regions.

One model with such a screening is the chameleon mechanism (Khoury & Weltman 2004). In this approach, the scalar field coupling strength is sensitive to the depth of the local gravitational potential. In regions with a large potential well, this screening suppresses the fifth force and gravity behaves as predicted by general relativity (GR). However when the potential becomes small, the fifth force is unsuppressed and gravity becomes 'modified' compared to GR (Lombriser 2014).

By definition, the chameleon field satisfies

$$\nabla^2\phi = V_{,\phi} + \frac{\beta}{M_{\rm Pl}}\rho \tag{1}$$

(Khoury & Weltman 2004), where V is the potential of the scalar field, β is the coupling between matter and the scalar field, ϕ gives the position-dependent screening efficiency, $M_{\rm Pl}$ is the *Planck* mass and ρ is the matter density. This leads to the chameleon fifth force of

$$F_\phi = -\frac{\beta}{M_{\rm Pl}}\nabla\phi. \tag{2}$$

There is a particular set of gravity models, known as $f(R)$ models (Buchdahl 1970) which exhibit a chameleon, where the strength of the fifth force (parametrized by β in equation 1) has a fixed value $\beta = \sqrt{1/6}$. This force arises from adding a scalar function $f(R)$ to the Ricci scalar in the Einstein–Hilbert action (Capozziello 2002; Nojiri & Odintsov 2003). These models can reproduce observed late time acceleration of the Universe whilst still suppressing the fifth force in high-density environments, such as the Solar system (Chiba, Smith & Erickcek 2007). These $f(R)$ models possess an extra scalar degree of freedom, $f_{\rm R} = {\rm d}f/{\rm d}R$, where the value at the current epoch is $|f_{\rm R0}|$ (Sotiriou & Faraoni 2010). Then $f(R)$ gravity can be related to ϕ_∞, (ϕ in equation 2 at infinity) via the relation (Joyce et al. 2015)

$$f_{\rm R}(z) = -\sqrt{\frac{2}{3}}\frac{\phi_\infty}{M_{\rm Pl}}. \tag{3}$$

Hu & Sawicki (2007) provide theoretical arguments showing that for GR to be preserved at parsec scales within the Solar system, then $|f_{\rm R0}| < 10^{-6}$. At kiloparsec scales, Jain et al. (2013) constrained $|f_{\rm R0}| < 5 \times 10^{-7}$ in dwarf galaxies. On megaparsec and larger scales, Raveri et al. (2014) used the cosmic microwave background (CMB) to measure $|f_{\rm R0}| < 10^{-3}$. Also on large scales, Rapetti et al. (2011), Ferraro, Schmidt & Hu (2011) and Cataneo et al. (2014) used the abundance of galaxy clusters to constrain $|f_{\rm R0}|$, e.g. Cataneo et al. (2014) measured (under the assumption of $n = 1$), $|f_{\rm R0}| < 2.6 \times 10^{-5}$.

In this paper, we also use clusters of galaxies to constrain $|f_{\rm R0}|$ on megaparsec scales. However, unlike Rapetti et al. (2011), Ferraro et al. (2011) and Cataneo et al. (2014), we use cluster profiles, rather than abundances to do so. The hypothesis is that a fifth force would be screened in the dense cluster cores, but not in the rarefied cluster outskirts (Burikham & Panpanich 2012; Lombriser et al. 2012). The majority of baryonic matter in a cluster is ionized gas that has been pressure-heated to temperatures in excess of 10^7 K (Gursky et al. 1971; Loewenstein 2004), leading to the emission of X-rays via thermal bremsstrahlung radiation (Jones & Forman 1978; Sarazin 2009). The gas can also be observed indirectly through its influence on the cosmic background radiation, via the so-called Sunyaev–Zel'dovich (SZ) effect (Sunyaev & Zeldovich 1980).

By measuring the properties of this X-ray gas, we are able to infer, under the assumption of hydrostatic equilibrium, the cluster mass and density from its X-ray surface brightness or SZ effect profiles (Reiprich & Böhringer 2002; Kettula et al. 2014). In a chameleon gravity model, the intracluster gas would feel the fifth force in addition to gravity in the cluster outskirts, i.e. the gas will be slightly more compact and the temperature boosted (Arnold, Puchwein & Springel 2014), compared to the influence of GR alone.

By contrast, weak gravitational lensing is dependent only upon the gravitational deflection of light by matter along the line of sight, therefore providing a technique to measure the underlying mass distribution without assuming hydrostatic equilibrium. Crucially for this study, the fifth force would not modify the deflection of light through the cluster (compared to GR) because the scalar chameleon field is coupled to the trace of the energy–momentum tensor (Hui, Nicolis & Stubbs 2009). Therefore, we can search for evidence of a fifth force by comparing the X-ray surface brightness, and/or SZ effect, profiles of clusters with their gravitational lensing shear profiles (Ostriker & Vishniac 1986; Terukina & Yamamoto 2012).

Terukina et al. (2014) used this approach to constrain $f(R)$ gravity models using a combination of lensing shear, X-ray surface brightness, X-ray temperature, and SZ profiles for the Coma cluster (a massive cluster at $z = 0.02$). Combining these measurements, they performed a Markov chain Monte Carlo (MCMC) analysis of the parameter space describing the cluster profiles in the modified gravity regime. Under the assumption of hydrostatic equilibrium, they obtained constraints of $|f_{\rm R0}| < 6 \times 10^{-5}$. They also examined the assumption of hydrostatic equilibrium, and concluded that any contribution of non-thermal pressure was small compared to the reconstructed mass.

The Coma cluster is at low redshift meaning its weak lensing shear signal is low. Moreover, it is known to have non-spherical geometry (Fitchett & Webster 1987; Briel, Henry & Boehringer 1992; Colless & Dunn 1996). These factors motivate us to apply the Terukina et al. (2014) method to many more clusters at higher redshifts, allowing for a higher signal-to-noise weak lensing shear profile and an averaging out of non-spherical cluster shapes. We do this by comparing stacked X-ray surface brightness and shear profiles of 58 X-ray-selected clusters. We utilize high-quality weak lensing data from the Canada–France–Hawaii Telescope Lensing Survey (CFHTLenS; Heymans et al. 2012; Erben et al. 2013), and X-ray observations from the *XMM* Cluster Survey (XCS; Romer et al. 2001; Lloyd-Davies et al. 2011; Mehrtens et al. 2012). We also investigate the Terukina et al. (2014) conclusion that deviations from hydrostatic equilibrium do not invalidate the chameleon gravity test.

In Section 2, we review the underlying theoretical background. In Section 3, we describe the development of the cluster sample used in the analysis, and the MCMC methods used to simultaneously fit the X-ray surface brightness and weak lensing profiles. In Section 4, we discuss our results and the implications of our results in the framework of $f(R)$ gravity models. In Section 5, we discuss the influence of cluster environment and of our assumption of hydrostatic equilibrium. In Section 6, we present our conclusions. Throughout this paper, we use a 95 per cent confidence level

Downloaded from http://mnras.oxfordjournals.org/ at Hiroshima University on December 17, 2015

when quoting upper limits, adopt a cosmology with $\Omega_{\rm m} = 0.27$, $\Omega_\Lambda = 0.73$, and $H_0 = 70$ km s^{-1} Mpc^{-1}.

2 THEORETICAL BACKGROUND

In this study, we adopt the Navarro–Frenk–White (NFW; Navarro, Frenk & White 1996) model for the dark matter halo mass distribution:

$$\rho(r) = \frac{\rho_{\rm c}\delta_{\rm c}}{\frac{r}{r_{\rm s}}(1+\frac{r}{r_{\rm s}})^2}, \tag{4}$$

where r here and throughout is the radial distance from the halo centre, $\rho_{\rm c} = 3H^2(z)/8\pi G$ is the critical density at a given redshift, $H(z)$ is the Hubble parameter at a given redshift, G is Newton's gravitational constant, $\delta_{\rm c}$ is the characteristic overdensity, given by

$$\delta_{\rm c} = \frac{200}{3}\frac{c^3}{\ln(1+c) - c/(1+c)}, \tag{5}$$

where c is a dimensionless concentration parameter and $r_{\rm s}$ is the scale radius given by

$$r_{\rm s} = \frac{1}{c}\left(\frac{3M_{200}}{4\pi\rho_{\rm c}\delta_{\rm c}}\right)^{1/3}, \tag{6}$$

where M_{200} is the mass enclosed by r_{200}, the radius at which the dark matter haloes average density is 200 times the critical density,

$$M(<r_{200}) = 4\pi\delta_{\rm c}\rho_{\rm c}r_{\rm s}^3\left(\ln(1+c) - \frac{c}{1+c}\right). \tag{7}$$

The NFW profile described in equation (7) is well supported by N-body simulations of Λ cold dark matter, but it is not immediately obvious that this profile would pertain to cluster profiles in the $f(R)$ regime. However, it has been shown (Lombriser et al. 2012; Moran, Teyssier & Li 2015) that the NFW profile is able to provide fits to both modified gravity and concordance cosmology that are equally good, sharing the same χ^2. It should be noted that the simulations in Lombriser et al. (2012) were generated using a fixed $\beta = \sqrt{1/6}$, as opposed to the general chameleon gravity model investigated here. However, as we are probing a β range around this value, we expect any modifications to the profiles to be similar, suggesting the suitability of the NFW profile. Further checks using hydrodynamical simulations of modified gravity models would allow this assumption to be verified.

We adopt the Terukina et al. (2014) approach describing the chameleon mechanism using three parameters. The first of these, β, is the coupling between matter and the scalar field (see equation 1). The second, ϕ_∞, describes the position-dependent screening efficiency. The third, $r_{\rm crit}$, is a critical radius, i.e. the distance from the dark matter halo centre at which the screening mechanism takes effect (Terukina & Yamamoto 2012),

$$r_{\rm crit} = \frac{\beta\rho_{\rm s}r_{\rm s}^3}{M_{\rm Pl}\phi_\infty} - r_{\rm s}, \tag{8}$$

where $\rho_{\rm s}$ is the density at this radius.

Terukina & Yamamoto (2012) showed the hydrostatic equilibrium equation in the presence of a fifth force (equation 2) is

$$\frac{1}{\rho_{\rm gas}(r)}\frac{{\rm d}P_{\rm gas}(r)}{{\rm d}r} = -\frac{GM(<r)}{r^2} - \frac{\beta}{M_{\rm Pl}}\nabla\phi, \tag{9}$$

where $\rho_{\rm gas}$ is the gas density, M the total mass within a radius r and $P_{\rm gas}$ is the electron pressure.

In an ideal cluster, i.e. one that is isolated, isothermal, and spherical, this total pressure is felt by the electrons and ions in the ionized intracluster plasma, so that $P_{\rm gas} = n_{\rm e}kT$, where $n_{\rm e}$ is the electron number density and T is the electron temperature. By adopting the standard *beta-model*[1] electron density profile (e.g. Cavaliere & Fusco-Femiano 1978), we can integrate equation (9) to give

$$P_{\rm e}(r) = P_{\rm e,0} + \mu m_{\rm p}\int_0^r n_{\rm e}(r)\left(-\frac{GM(<r)}{r^2} - \frac{\beta}{M_{\rm Pl}}\frac{{\rm d}\phi(r)}{{\rm d}r}\right){\rm d}r, \tag{10}$$

where $P_{\rm e,0}$ is the electron gas pressure at $r = 0$, given by $P_{\rm e,0} = n_{\rm e,0}kT$ and $n_{\rm e,0} = 5n_0/(2+\mu)$ and $M(<r)$, the halo mass. The integral of equation (10) can be re-expressed in terms of a projected X-ray surface brightness $S_{\rm B}(r)$ using the temperature- and electron-density-dependent cooling function (see Section 3.2),

$$S_{\rm B}(r_\perp) = \frac{1}{4\pi(1+z)^4}\int n_{\rm e}^2\left(\sqrt{r_\perp^2+z^2}\right)\lambda_{\rm c}(T_{\rm gas})\,{\rm d}z, \tag{11}$$

where $r_\perp$ is the projected distance from the cluster centre and z the cluster redshift. This is the expression we fit to when comparing stacked X-ray cluster profiles to the chameleon model (Section 3.5).

The expression used to fit the weak lensing shear profiles (under the assumption of an underlying NFW profile) for comparison is given in Wright & Brainerd (2000).

To recap, our method makes the following assumptions: that modifications to GR include a chameleon screening mechanism and can be described by equation (1); that dark matter haloes follow an NFW profile (equation 4); that a fifth force can be included in the hydrostatic equilibrium expression according to equation (9); that clusters of galaxies are isolated, isothermal and spherical (which in turn implies that the clusters are in hydrostatic equilibrium, have an electron number density that follows a *beta-model* and their X-ray emission can be predicted from a thermal cooling function); and that the weak lensing shear profiles of clusters are given in Wright & Brainerd (2000). We discuss the impact of some of these assumptions in Section 5.

3 METHODS

3.1 Compiling the X-ray cluster sample

In this paper, we used public weak lensing data (galaxy ellipticities and photometric redshifts) provided by the CFHTLenS (Heymans et al. 2012). The CFHTLenS covers 154 deg^2 with high-quality shape measurements. The galaxy ellipticities were generated by the CFHTLenS team using the THELI (Erben et al. 2013) and LENSFIT (Miller et al. 2013) routines. Photometric redshifts were produced using PSF-matched photometry to an accuracy of $0.04(1+z)$ with a 4 per cent catastrophic outlier rate (Hildebrandt et al. 2012).

We also used public X-ray data taken from the *XMM–Newton* archive and have collated a sample of X-ray clusters in the CFHTLenS region using pipelines developed for the XCS (Lloyd-Davies et al. 2011). First, we determined which of the *XMM* observations overlapped with the CFHTLenS fields. We then used the XCS pipelines to carry out the following tasks in an automated manner: cleaning the event lists of background flares; creating detector and exposure images; producing duplicate free source lists; and identifying extended X-ray sources. A total of 348 extended *XMM* sources, with more than 100 background-subtracted photon

[1] The *beta* in this model is not the same as the β in equation (1).

Downloaded from http://mnras.oxfordjournals.org/ at Hiroshima University on December 17, 2015

counts, were located in the CFHTLenS fields, although 44 were close to the edge of the *XMM* field of view and were not considered further (please see Lloyd-Davies et al. 2011 for the relevant, XCS specific, definition of source counts).

The majority of these sources were not included in the XCS first data release (XCS-DR1; Mehrtens et al. 2012). This meant that candidate identification needed to be carried out before the sources could be used in our study. This process is non-trivial: as shown in Mehrtens et al. (2012), a large fraction of XCS extended sources (especially those with fewer than 300 counts) are either hard to confirm as clusters – because the available imaging is not deep enough – or are associated with other types of X-ray source. Therefore, for this paper, we have taken a conservative approach and only included *XMM* extended sources in our study if they correspond to an overdensity of galaxies in false colour images produced using the CFHTLenS cutout service.[2] 186 sources were excluded from the study as a result. These were excluded for several different reasons: there were no optical data as the cluster sat in a masked region of the CFHTLenS footprint; there was a bright star or galaxy lying close to the cluster centre that was obscuring it; or the optical image resembled an AGN rather than a cluster. The coordinates of the remaining 119 can be found in Table B1.

As our analysis required information about the distance to the cluster, a further 37 sources were excluded from the study because redshifts were not available at the time of writing. These are flagged with a 2 in Table B1. The majority (63 of 82) of the redshifts we used came from the new Gaussian mixture model redshift estimator described in detail in Hood & Mann (2015). We also used 18 redshifts taken from NED[3] and 3 from Ford et al. (2014).

We judged these remaining 82 *XMM* extended sources in the CFHTLenS region to be confirmed clusters and ran them through the XSPEC-based XCS spectral pipeline. We determined X-ray temperatures when the signal to noise was sufficient. This produced X-ray temperatures of 58 of these clusters which form our final sample, including 12 clusters new to the literature, the other 23 clusters were excluded from the analysis and are flagged with a 3 in Table B1. The details of this pipeline can be found in Lloyd-Davies et al. (2011). These 58 clusters with measured temperatures span the redshift range $0.1 < z < 1.2$ (median $z = 0.33$) and temperature range $0.2 < T_{\rm x} < 8$ keV (median $T_{\rm x} = 2.3$ keV). A selection of these new to the literature clusters, along with several clusters that were optically confirmed but excluded due to a lack of redshift, are shown in Fig. C1.

3.2 Making stacked X-ray surface brightness profiles

Our analysis involves stacking multiple different *XMM* observations of our 58 clusters, in order to build up signal to noise in the outer parts of the ensemble cluster profile. This process needs to account for the following complexities: most of the 58 clusters were covered by more than one *XMM* observation. Each of these observations has different background properties and flare corrected exposure times. The X-ray telescope comprises of three cameras that operate simultaneously (mos1, mos2, pn), so most *XMM* observations comprise of three separate images with different, energy-dependent sensitivities. The clusters all have different energy spectra, because, even if one ignores non thermal processes, they have different X-ray temperatures, redshifts and line of sight absorbing column densities. Therefore, for each cluster, we have to calculate, using XSPEC, camera-specific count rate to luminosity conversion factors for each *XMM* observation that it falls in. We then, for a given cluster, take the photon count images generated by the XCS pipeline, divide these by the respective exposure map and multiply by the cluster-dependent conversion factor. This allows us to combine all the images for that cluster in a self-consistent manner.

To produce a single stack, we first re-scaled the 58 combined images of individual clusters to a standard projected size. For this we estimated M_{500}, the mass enclosed within a sphere at which the average density is 500 times the critical density, using the prescription described in Sahlén et al. (2009). A conversion between M_{500} and M_{200} was made following the formulae derived in Hu & Kravtsov (2003), where we assume $c = 5$. This is an accurate description of the typical density profiles in clusters (Arnaud 2005) and is consistent with the findings of Kettula et al. (2014) in the CFHTLenS region. Using the M_{200} values we calculated the radius at which the average density is 200 times the critical density, r_{200}, following the method in Croston et al. (2008). The 58 stacked images could then be re-scaled using linear interpolation to a common 500 by 500 pixel format, so that they each had an r_{200} radius of 125 pixels. Each of these 500 by 500 images was centred on the source centroid as determined by XCS.

We re-scaled the individual cluster images by the overall amplitude of their X-ray surface brightness, as adding clusters over a range of different masses and luminosities would result in significant off-diagonal elements in the covariance matrix of the final stacked profile. Therefore, we calculate the mean value of the X-ray surface brightness profile for each cluster, and re-scale individual cluster surface brightness maps by this value (we found that using the median value instead of the mean gave similar results). A final stacked surface brightness map of the 58 individual clusters is then produced by taking the mean value for each pixel across all these maps. This re-scaling of the amplitudes is permitted as our constraints on modified gravity parameters focus on the shape of the cluster profiles; we marginalize over the amplitudes of the stacked X-ray surface brightness profiles in Section 4. The error covariance matrix of the stacked profile was then measured directly.

3.3 Making stacked weak lensing profiles

We outline here the procedure used to obtain the stacked cluster shear profile, $\gamma_{\rm t}$, using source galaxies from CFHTLenS. The CFHTLenS catalogue provides measurements of both ellipticity components (e_1 and e_2), as well as photometric redshifts for each source galaxy. Before shears can be derived from these quantities, small multiplicative and additive corrections (m and c_2) must be applied, derived from the data set. We calculate c_2 and m for each galaxy as a function of size and signal to noise (using equations 17 and 19 in Heymans et al. 2012). Each galaxy was weighted with the CFHTLenS catalogue WEIGHT parameter and calibrated by

$$e_{\rm int,i} = \frac{e_{\rm i} - c_{2,\rm i}}{1 + \bar{m}}, \tag{12}$$

where c_2 was applied on a galaxy by galaxy basis and $\bar{m}$ is a summation of $1 + m$ for each galaxy, applied as an ensemble average to each radial bin (discussed below).

We have an effective galaxy density, $n_{\rm eff}$, (Heymans et al. 2012) of 12 galaxies per arcmin^2. In order to minimize the contamination

[2] http://www.cadc-ccda.hia-iha.nrc-cnrc.gc.ca/community/CFHTLens/cutout.html

[3] The NASA/IPAC Extragalactic Database (NED) is operated by the Jet Propulsion Laboratory, California Institute of Technology, under contract with the National Aeronautics and Space Administration.

Downloaded from http://mnras.oxfordjournals.org/ at Hiroshima University on December 17, 2015

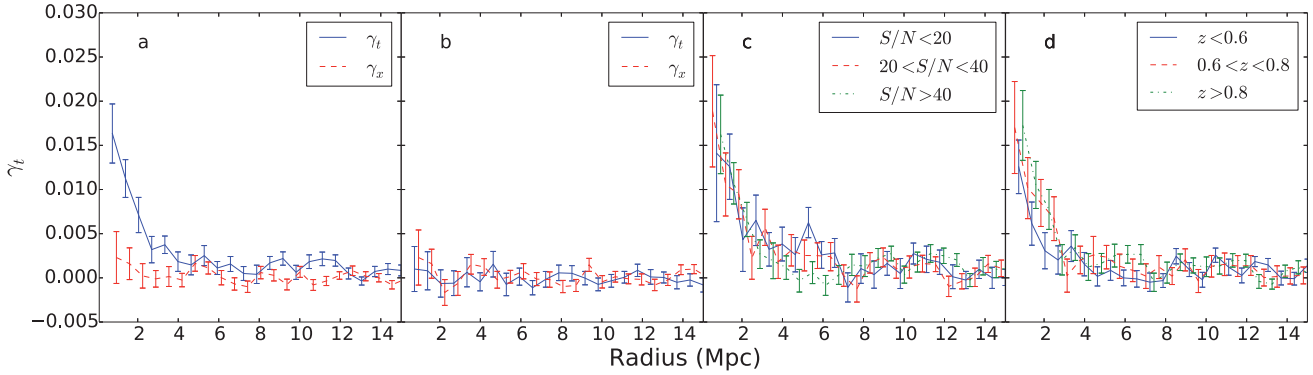

Figure 1. Tests around the 58 CFHTLenS stacked cluster; details are provided in the text. 1(a) Tangential and cross shear. 1(b) Tangential and cross shear around 58 stacked random points. 1(c) Tangential shear for three different signal-to-noise bins. 1(d) Tangential shear for three different redshift cuts.

between the lensed galaxies and the cluster members, we only use source galaxies with a photometric redshift greater than $z_{\rm cluster} + 0.2$. Our redshift cut is made so that there is negligible contamination between cluster and source galaxies. The photo-z cut does not require a redshift dependence as the photo-z errors of the source galaxies in CFHTLenS are approximately flat close to the redshift of our clusters (Hildebrandt et al. 2012).

For each galaxy, we calculate the tangential and cross shears ($\gamma_{\rm t}$, $\gamma_{\rm x}$) as a function of their position relative to the cluster position, via the angle ϕ between the cluster and galaxy from a baseline of zero declination. The tangential shear measured around each XCS-determined cluster centroid was binned into 24 equal spaced logarithmic annuli out to a distance of $10 \times r_{200}$ (calculated in Section 3.2). We then scaled the values in each of these bins in the same way that we previously scaled the X-ray profiles in Section 3.2 for consistency.

Finally, in order to improve the signal to noise of the tangential profiles, the 58 individual cluster profiles were stacked. This was achieved by summing the profiles of each cluster and calculating an average shear in each bin across all clusters (McKay et al. 2001; Sheldon et al. 2009). The error covariance matrix was then directly measured for our stacked profile. Due to the large uncertainty in the central bin, driven by the low number density of galaxies, we exclude the central $0.1 \times r_{200}$.

We perform consistency and null tests upon the CFHTLenS shape data to ensure our recovered profiles are unbiased and not artefacts of the data. Fig. 1(a) shows the tangential signal (solid blue) and the cross shear (dashed red) around the stacked clusters. The tangential shear signal has a detection significance of $>30\sigma$ while the cross shear signal is consistent with zero at all radii.

Fig. 1(b) shows the tangential shear (solid blue) and cross shear (dashed red) around 58 random stacked positions within the overlap of the CFHTLenS region and the XCS footprint. The measurements in both these cases were found to be consistent with zero on all scales.

For Fig. 1(c), we show the tangential shear around the stacked clusters after we have split the source galaxies into three bins based upon their signal-to-noise ratio, S/N $<$ 20, 20 $<$ S/N $<$ 40, and S/N $>$ 40, with similar redshift distributions (median redshifts of 0.85, 0.82, 0.79, respectively). We find that the three measurements are consistent with each other as expected.

Finally, Fig. 1(d) shows the tangential shear around the stacked clusters with the source galaxies cut into three bins based upon their photometric redshift, $z < 0.6$, $0.6 < z < 0.8$ and $z > 0.8$. At higher redshifts there are a smaller fraction of cluster galaxies and galaxies in front of the clusters, and the weak lensing signal grows with redshift. We see these effects as our measured signal is strongest in the high-redshift bin. We therefore conclude that we are detecting a genuine weak lensing signal.

3.4 Binning in X-ray temperature

To generate tighter constraints upon the modified gravity parameters, we split our data set into two separate mass bins to reduce errors caused by mixing clusters of varying sizes and masses. We find doing so improves our constraints on the modified gravity parameters compared to using a single bin. We cut at an X-ray temperature of $T = 2.5$ keV, to give two bins of mass with equal errors on their stacked profiles. We note that this temperature cut approximately cuts our sample into galaxy clusters and galaxy groups (Stott et al. 2012). Our low-temperature bin ($T < 2.5$ keV) has a median redshift of $z = 0.32$ and is flagged with a 0 in Table B1, while the other (with $T > 2.5$ keV) has a median redshift of $z = 0.34$ and a flag of 1. We repeated the analyses with three and four temperature bins and found no improvement in the constraints on the modified gravity parameters. Therefore, to aid with computation, we complete our analysis with the simplest two bin case.

3.5 MCMC analysis

We use MCMC (Gilks, Richardson & Spiegelhalter 1996) to fit models to our stacked profiles. We allow all parameters that depend upon the cluster properties to vary for each temperature bin. This leads to a total of 14 free parameters for the four stacked profiles (our measured weak lensing and X-ray profiles in two temperature bins) used to constrain modified gravity. Four of these were used to model the weak lensing mass (defined in equations 4, 5 and 6). We introduce the notation I, II to indicate the temperature bins $T < 2.5$, $T > 2.5$, respectively, so $c^{\rm I}$, $c^{\rm II}$, $M^{\rm I}_{200}$ and $M^{\rm II}_{200}$ are the concentration and mass parameters for each temperature bin, respectively.

We modelled the X-ray surface brightness, using the method prescribed in Section 2 by defining, for both temperature bins, the electron number density (itself dependent upon $n^{\rm I}_0$, $n^{\rm II}_0$, $b^{\rm I}_1$, $b^{\rm II}_1$, $r^{\rm I}_1$ and $r^{\rm II}_1$), and the normalization of the gas temperature $T^{\rm I}_0$ and $T^{\rm II}_0$. We reconfigure the parameters as $\beta_2 = \beta/(1 + \beta)$ and $\phi_{\infty,2} = 1 - \exp(-\phi_\infty/10^{-4} M_{\rm Pl})$ to span the parameter range of β and ϕ_∞ in the interval [0,1]. To obtain the cooling function (used in equation 11), we used the XSPEC software (Arnaud 1996) and utilize the APEC model (Smith et al. 2001) over a range of 0.5–2 keV, i.e. the

Downloaded from http://mnras.oxfordjournals.org/ at Hiroshima University on December 17, 2015

same energy range as our observations from *XMM*. This model has as inputs the gas temperature, the cluster redshift, the cluster metallicity and a normalization, and provides the X-ray cluster flux. We adopt a metallicity $Z = 0.3\,Z_{\odot}$ (Sato et al. 2011) throughout. Using this model we generate fluxes for a range of temperatures which are interpolated for use in our chameleon gravity model.

The chameleon parameters β_2 and $\phi_{\infty,2}$ are the same across the two bins, as the modifications to gravity should be independent of the cluster's mass.

We performed an MCMC analysis using the EMCEE code (Foreman-Mackey et al. 2013), which implements a Metropolis–Hastings algorithm (MacKay 2003). We minimized the goodness of fit using a χ^2 statistic derived from joint fitting of both models (see Appendix A).

Our MCMC run was a parallelized implementation using 128 walkers with 10 000 time steps. We removed the first 2000 iterations as a 'burn in' phase.

4 RESULTS

In Fig. 2, we show our measured X-ray and weak lensing profiles for both X-ray temperature bins. Our X-ray surface brightness profiles have been measured out to $1.2 \times r_{200}$ with high signal to noise. Likewise for our two weak lensing profiles, we have recovered a shear signal out to $10 \times r_{200}$ with high signal to noise. Also shown in Fig. 2 are our best-fitting models for the each profile using the parameters outlined in Section 3.5 and minimizing χ^2 as described in equation (A1). We show the 2D contours for constraints on model parameters in Fig. D1.

In Fig. 3, we show the 2D constraints for β_2 and $\phi_{\infty,2}$. To generate our constraints, we have marginalized over the measured likelihoods of the nuisance parameters (those that are not β_2 and $\phi_{\infty,2}$). We are able to do so as we are insensitive to the overall amplitude of our profiles, only the profiles shape matters for our constraints. In Fig. 3, we also show the dashed (dash–dotted) line the 95 per cent (99 per cent) confidence limit excluded region from Terukina et al.

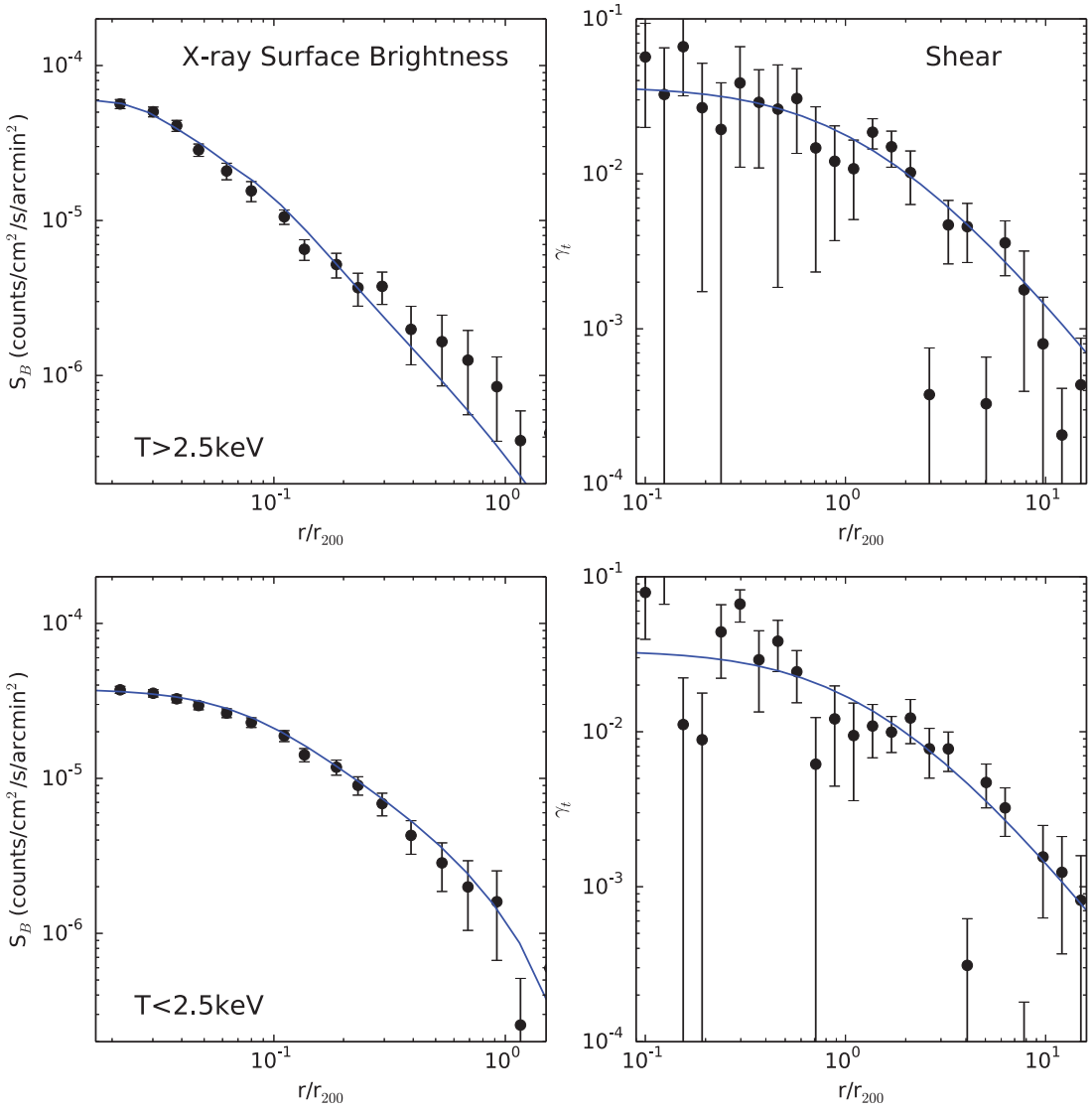

Figure 2. X-ray surface brightness profiles (left) and weak lensing (right) for the two bins of X-ray temperature: $T < 2.5$ keV (top) and $T > 2.5$ keV (bottom), against radial distance normalized by r_{200}, the radius at which the density is 200 times the critical density. We choose to show the modified gravity profiles with the highest likelihood parameters, $T_0^{\rm I} = 12.6$ keV, $n_0^{\rm I} = 2.0 \times 10^{-2}\,{\rm cm}^{-3}$, $b_1^{\rm I} = -0.42$, $r_1^{\rm I} = 0.06$ Mpc, $M_{200}^{\rm I} = 12.2 \times 10^{14}\,{\rm M}_{\odot}$, $c^{\rm I} = 3.5$, $T_0^{\rm II} = 7.8$ keV, $n_0^{\rm II} = 4.9 \times 10^{-2}\,{\rm cm}^{-3}$, $b_1^{\rm II} = -0.89$, $r_1^{\rm II} = 0.05$ Mpc, $M_{200}^{\rm II} = 13.7 \times 10^{14}\,{\rm M}_{\odot}$, $c^{\rm II} = 3.8$, $\beta = 2$, $\phi_{\infty} = 2.1 \times 10^{-4} M_{\rm Pl}$.

Downloaded from http://mnras.oxfordjournals.org/ at Hiroshima University on December 17, 2015

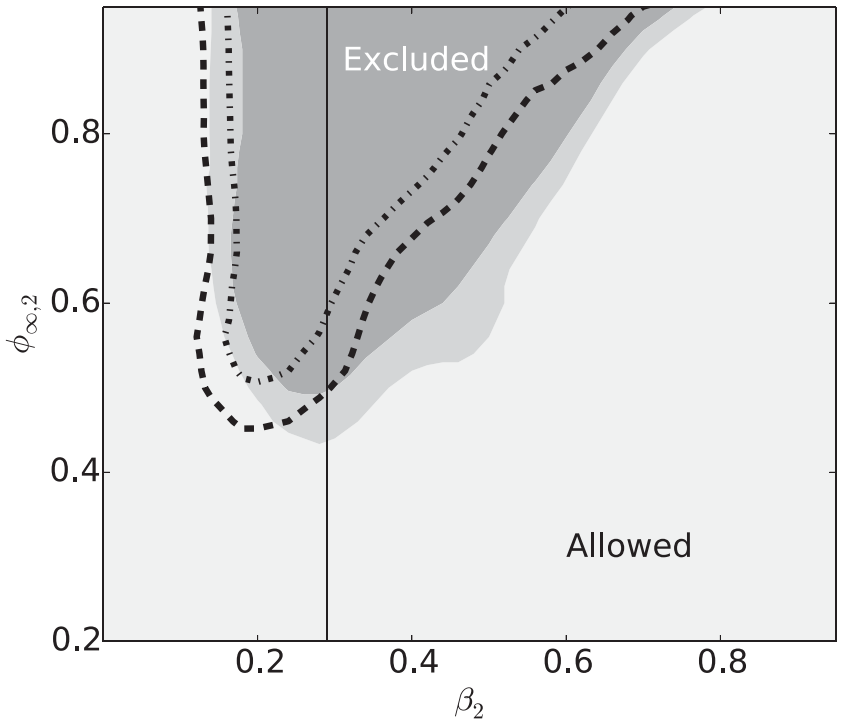

Figure 3. The 95 per cent (light grey region) and the 99 per cent confidence limit (mid grey region) constraints for the chameleon model parameters renormalized between [0,1], $\beta_2 = \beta/(1+\beta)$ and $\phi_{\infty,2} = 1 - \exp(-\phi_\infty/10^{-4}M_{\rm Pl})$ obtained from the MCMC analysis of our combination of weak lensing and X-ray surface brightness for our two cluster stacks. Above the dashed (dash–dotted) line is the 95 per cent (99 per cent) confidence limit excluded region from Terukina et al. (2014). The vertical line is at $\beta = \sqrt{1/6}$, showing our constraints for $f(R)$ gravity models.

(2014). The constraints are tighter from this work on larger values of β than in Terukina et al. (2014), whilst the constraints on smaller values of β are looser. As the profiles presented in this work extend further from the cluster than the Coma profile, we probe further outside the critical radius, $r_{\rm c}$ and are able to better constrain large values of β. However, as the errors on the X-ray profiles (and the lack of available SZ data) used in this work are larger than those measured in Terukina et al. (2014), we are less able to differentiate a chameleon profile from a GR one at lower values of β, leading to less constraining power.

The shape of the contours in Fig. 3 can be understood by considering the meaning of the parameters used in defining chameleon gravity. Recall that β dictates the strength of the fifth force and ϕ_∞ is the effectiveness of the screening mechanism. Therefore, at low values of β, the fifth force causes a deviation to the profile which is too small to be distinguished from GR given the observational errors. Likewise as GR gravity is recovered outside the critical radius $r_{\rm crit}$, this sets an upper limit on β/ϕ_∞. As β increases, a lower value for ϕ_∞ is required to keep $r_{\rm crit}$ within the cluster, giving rise to the triangular shape of the excluded region.

4.1 Implications for $f(R)$ gravity

Our constraints have implications for $f(R)$ gravity models, which contain a chameleon mechanism for which $\beta = \sqrt{1/6}$ (Starobinsky 2007) (shown as the vertical line in Fig. 3).

From Fig. 3, we estimate an upper bound on $f(R)$ gravity of $\phi_\infty < 5.8 \times 10^{-5} M_{\rm Pl}$ at 95 per cent confidence limit, and therefore using equation (3), $f_{\rm R}(z = 0.33) < 4.7 \times 10^{-5}$ at 95 per cent confidence limit (where $z = 0.33$ is our cluster samples median redshift). The time-evolution of the background $f_{\rm R}(z)$ for a Hu–Sawicki follows (Li et al. 2013),

$$f_{\rm R}(z) = |f_{\rm R0}| \frac{1}{n} [(1 + 3\Omega_\Lambda)/(\Omega_{\rm M}(1+z)^3 + 4\Omega_\Lambda)]^{n+1}, \quad (13)$$

where n is a free parameter of the model. At high redshifts, the background energy density is higher, therefore $f_{\rm R}(z)$ is smaller and the screening is more efficient. So $f_{\rm R}(z)$ decreases by 22 per cent from our median redshift ($z = 0.33$) to $z = 0$, when $n = 1$, and our constraint at $z = 0$ is $|f_{\rm R0}| < 6 \times 10^{-5}$ at 95 per cent confidence limit. Considering a Hu–Sawicki model with $n = 3$, our constraint becomes $|f_{\rm R0}| < 2 \times 10^{-4}$ at 95 per cent confidence limit. Our results are comparable to the results for the Coma cluster reported in Terukina et al. (2014) of $|f_{\rm R0}| < 6 \times 10^{-5}$.

5 DISCUSSION

In this section, we discuss the influence of local overdensities upon our cluster sample. We also question the validity of the assumptions we have made while constraining chameleon gravity, primarily the assumption that our cluster stack is in hydrostatic equilibrium.

5.1 Influence of cluster environment

In addition to self-screening, a cluster may be screened by nearby clusters and therefore still show no evidence of modified gravity, even in its outskirts. To check whether this was expected for any of our clusters, we estimated the D parameter detailed in Zhao, Li & Koyama (2011), a parametrization of the separation between a given cluster and the nearest larger cluster, scaled by the given cluster's r_{200}. We describe clusters with $\log_{10} D > 1$ as 'isolated' and clusters with $\log_{10} D < 1$ as living in dense environments, and therefore

Downloaded from http://mnras.oxfordjournals.org/ at Hiroshima University on December 17, 2015

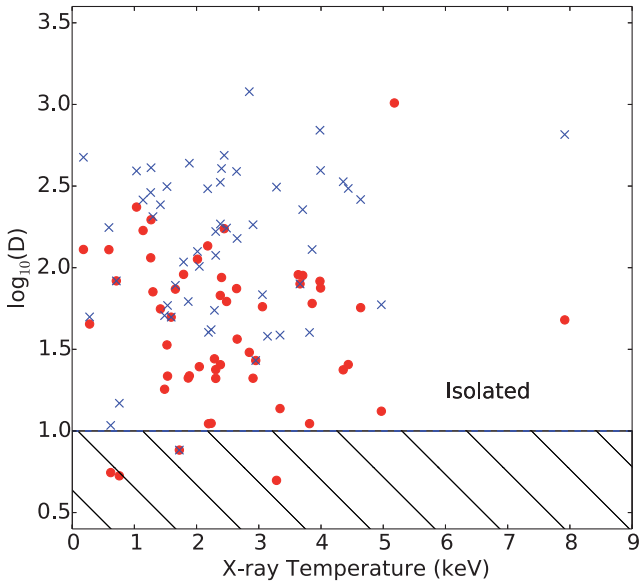

Figure 4. The minimum D parameter for each cluster against X-ray temperature, where $\log_{10}D$ is a measure of the distance between a cluster and the nearest overdensity in the top 30 per cent (10 per cent) of overdensity values, shown as a red circle (blue cross). The shaded region contains clusters with potential screening from neighbouring overdensities. The majority of the clusters are in an isolated region.

screened. As our X-ray clusters are an incomplete set of all clusters in our area, we looked at overdensities in the galaxy density field as a proxy for nearby clusters. We binned the galaxies in the CFHTLenS catalogue into 3D pixels of volume 1 Mpc^2 in area, and 0.01 in redshift. Fig. 4 shows X-ray temperature against $\log_{10}D$, where we have calculated $\log_{10}D$ values between each cluster and overdensity and selected the smallest $\log_{10}D$ as a measure of environment. It is seen that only 7 per cent (2 per cent) of our clusters are found to be near ($\log_{10}D < 1$) the most overdense 30 per cent (10 per cent) of the 3D pixels. We therefore conclude that our sample appears to be largely environmentally unscreened by nearby clusters, and therefore will apply our analysis to the full cluster sample. We note that it is possible that clusters outside the edge of the CFHTLenS observations could screen at most 6 per cent of our sample, which lie within $\log_{10}D = 1$ of the edge.

5.2 Assumption of hydrostatic equilibrium

Even in the absence of a fifth force, the interpretation of apparent differences in cluster mass profiles derived from X-ray or SZ observations and lensing measurements is complicated by both astrophysical processes in clusters, such as gas clumping in the cluster outskirts, and systematic errors in the measurements themselves. This has led to uncertainty in mass calibration being the dominant source of error on cosmological constraints derived from SZ cluster catalogues (e.g. Hasselfield et al. 2013; Reichardt et al. 2013; Planck Collaboration XX 2014). The absolute cluster mass scale is affected by uncertainty in the effects of feedback from active galactic nuclei, and non-thermal processes such as bulk motions, on the cluster gas (e.g. Nagai, Kravtsov & Vikhlinin 2007). Instrumental calibration uncertainties may also play a role (e.g. Israel et al. 2015; Schellenberger et al. 2015). Lensing measurements, which are affected by different systematics, are being used to quantify any bias in the absolute mass scale, but at present, samples are small, and there is some disagreement (e.g. von der Linden et al. 2014; Hoekstra et al. 2015).

In this work, we have investigated one of these issues: the impact of non-thermal pressure on our conclusions about chameleon gravity (whilst maintaining the simplifying assumptions of spherical symmetry). We plan to investigate the other issues, using hydrodynamic simulations, in future publications. The thermal mass of a cluster is defined by the gas pressure, density and temperature, which we infer from the X-ray surface brightness. We follow the parametric fits described in Terukina et al. (2014) to reconstruct the stacked cluster temperature profile and electron number densities from the profile parameters fit for by our MCMC. We infer from X-ray observations,

$$M_{\rm thermal} = \frac{-kT_{\rm gas}r}{\mu m_{\rm p}G}\left(\frac{{\rm d}\ln n_{\rm e}}{{\rm d}\ln r} + \frac{{\rm d}\ln T_{\rm gas}}{{\rm d}\ln r}\right), \quad (14)$$

where k is the Boltzmann constant, $m_{\rm p}$ is the proton mass. According to the hydrodynamical simulations in Shaw et al. (2010), the non-thermal pressure can be modelled as a function of the total pressure, such that $P_{\rm non-thermal}(r) = g(r)P_{\rm total}(r)$, where

$$g(r) = \alpha_{\rm nt}(1+z)^{\beta_{\rm nt}}\left(\frac{r}{r_{500}}\right)^{n_{\rm nt}}\left(\frac{M_{200}}{3\times10^{14}\,{\rm M}_\odot}\right)^{n_{\rm M}}, \quad (15)$$

with $\alpha_{\rm nt}$, $\beta_{\rm nt}$, $n_{\rm nt}$ and $n_{\rm M}$ are constants determined from 16 simulated clusters, with a mass range between 0.35 and 9.02 $\times$ 10^{14} M$_\odot$ at $z = 0$ (Lau, Kravtsov & Nagai 2009). We adopt their best-fitting values of $\beta_{\rm nt}$, $n_{\rm nt}$, $n_{\rm M} = 0.5$, 0.8, 0.2, respectively. In order to test the robustness of our assumptions, we select $\alpha = 0.3$, which was the most extreme value found in the 16 clusters in their analysis. The extra mass component which would be inferred from X-rays due to such non-thermal pressure would be

$$M_{\rm non-thermal} = \frac{-r^2}{G\rho_{\rm gas}}\frac{\rm d}{{\rm d}r}\left(\frac{g(r)}{1-g(r)}n_{\rm gas}kT_{\rm gas}\right), \quad (16)$$

where r is the radial distance, $g(r)$ is defined in equation (15) and $\rho_{\rm gas}$, $n_{\rm gas}$ and $T_{\rm gas}$ are the gas density, number density and temperature, respectively.

In Fig. 5, we show our mass profiles for 0.3 Mpc $< r_\perp <$ 2 Mpc for the lensing mass and X-ray mass reconstruction, including the effects of non-thermal pressure. The solid lines are the hydrostatic mass recovered from the X-ray measurements using equation (14), while the dashed lines are the hydrostatic mass plus a non-thermal component from equation (16). The shaded area is the 68 per cent confidence limit allowed region from the weak lensing measurements, fitted with an NFW profile. The vertical dotted line is the upper bound of our X-ray data; to the right of this line we have extrapolated to illustrate the possible divergence of the mass estimates with and without significant non-thermal pressure.

At all scales in Fig. 5 the thermal pressure profile (solid line) is consistent with the shaded region, showing that the mass profiles estimated by the X-rays and lensing mass are consistent. This suggests that hydrostatic equilibrium is an acceptable approximation for our stacked profiles, given the error in our lensing measurements.

We also see in Fig. 5 that the thermal pressure profile with a non-thermal component (dashed line) enhances the hydrodynamical mass by 20 per cent (10 per cent) in the $T < 2.5$ keV ($T > 2.5$ keV) cluster bin, but is still seen to be consistent with our lensing measurements. This shows that the non-thermal pressure expected from simulations falls within our present observed errors', if present it acts in the opposite sense to chameleon gravity, reducing the detectable signal.

Downloaded from http://mnras.oxfordjournals.org/ at Hiroshima University on December 17, 2015

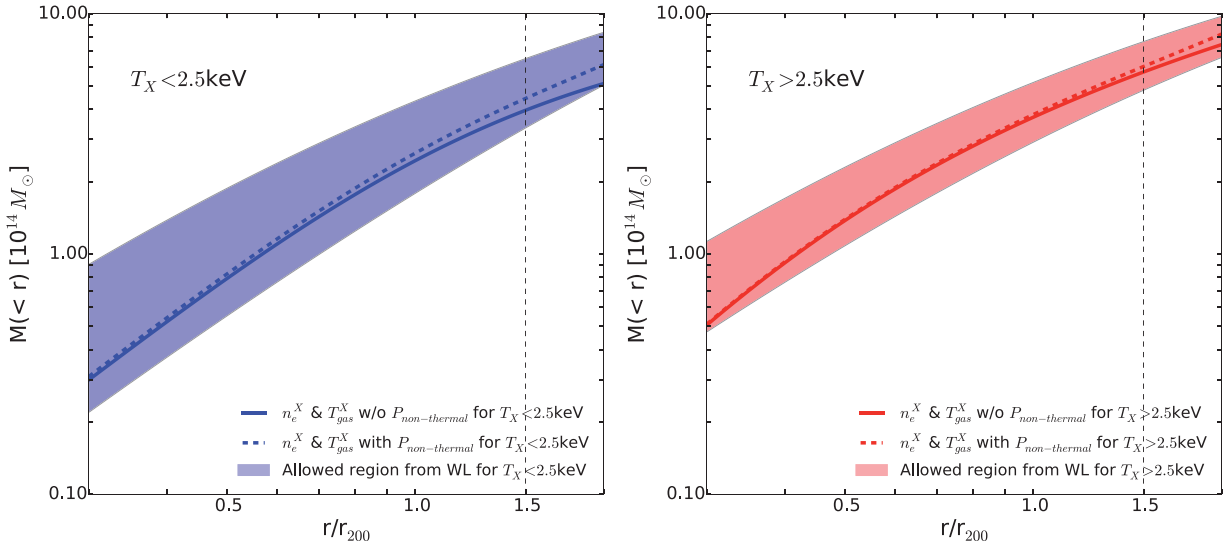

Figure 5. Mass profile from the $T < 2.5$ keV ($T > 2.5$ keV) cluster bin in blue (red). The shaded area is the 1σ allowed region from the weak lensing measurement and the solid line is the thermal mass reconstructed from the X-rays. The dashed line shows the thermal mass with an additional non-thermal component as discussed in the text. The vertical line is the upper extent of our X-ray data; to its right we have extrapolated the X-ray data.

With future X-ray measurements we will be able to fit out to a larger distance, allowing us to better constrain the effect of non-thermal pressure, which would be most prominent at large radii. We also note that our weak lensing profiles have lower signal to noise than the X-ray profiles; however, with future lensing surveys we will be able to more accurately constrain these profiles also allowing us to better characterize not only chameleon gravity but non-thermal pressure too.

6 CONCLUSIONS

We have investigated the constraining power of stacked galaxy cluster profiles for testing chameleon gravity. We have examined 58 X-ray-selected galaxy clusters, which have both good quality weak lensing data from CFHTlenS and X-ray data from XCS. After binning our clusters by X-ray temperature, we have generated weak lensing profiles and X-ray surface brightness profiles. Chameleon gravity predicts an additional pressure existing within clusters, which causes their gas component to become more compressed than GR gravity predicts. We have therefore investigated this phenomena by comparing the X-ray profile with the weak lensing profile, which is unaffected by the fifth force. Using a multiparameter MCMC analysis we have obtained constraints on the common chameleon parameters β and ϕ_∞, which in turn lead to constraints for $|f_{R0}|$, a parameter charactering $f(R)$ theories.

We find our results are competitive with other cosmological constraints on chameleon models. In particular, our constraints are an order of magnitude stronger than those from the CMB (Raveri et al. 2014). They are comparable to Cataneo et al. (2014) which provides $|f_{R0}| < 2.6 \times 10^{-5}$ for $n = 1$, compared with our measurement of $|f_{R0}| < 6 \times 10^{-5}$, and $|f_{R0}| < 3.1 \times 10^{-4}$ for $n = 3$ compared with our measurement of $|f_{R0}| < 2 \times 10^{-4}$, all at the 95 per cent CL. A comparison of these constraints is shown in Table 1.

We examined the assumption of hydrostatic equilibrium by comparing the masses inferred from the X-ray observations with weak lensing and found them to be consistent. Deviations from hydrostatic equilibrium would cause a disparity between the weak lensing and X-rays with the opposite sign to that from the chameleon effect.

Table 1. Comparison of the constraints on $\log_{10}|f_{R0}|$.

Scale	Scale	$\log_{10}\lvert f_{R0}\rvert$
Solar system (Hu & Sawicki 2007)	pc	−6
Dwarf galaxies (Jain et al. 2013)	kpc	−6.3
Coma cluster (Terukina et al. 2014)	Mpc	−4.2
Cluster abundance (Cataneo et al. 2014)	Mpc	−4.6 ($n = 1$) −3.5 ($n = 3$)
Cluster stack (This work)	Mpc	−4.2 ($n = 1$) −3.7 ($n = 3$)
CMB (Raveri et al. 2014)	Gpc	−3.0

We modelled a non-thermal pressure X-ray component, and given current observational errors found this to be a subdominant effect on our constraints.

As we are interested in the shape of the respective profiles, the absolute mass of the stacked cluster, measured through both weak lensing and X-rays, is a nuisance parameter which we have marginalized over. We therefore are not sensitive to the relative biases between these two techniques, such as reported in von der Linden et al. (2014) and Hoekstra et al. (2015).

For the next generation of constraints via this method, we will need detailed modified-gravity hydrodynamic simulations. These will allow us to check a range of assumptions used in this analysis such as hydrostaticity, non-thermal pressure, gas clumping in the cluster outskirts, spherical symmetry and the reliability of the NFW profile.

We find our constraint on $|f_{R0}|$ to be consistent with the literature, and competitive at these cosmic scales and redshifts. We have therefore demonstrated that it is possible to constrain chameleon gravity using stacked galaxy clusters; with the advent of wide-area lensing surveys promising a much larger area, such as the Dark Energy Survey (DES; The Dark Energy Survey Collaboration 2005), the KIlo

Downloaded from http://mnras.oxfordjournals.org/ at Hiroshima University on December 17, 2015

Degree Survey (KIDS; de Jong et al. 2013), *Euclid* (Laureijs et al. 2011) and the Large Synoptic Survey Telescope (LSST; LSST Dark Energy Science Collaboration 2012), it will become possible to use stacks containing many more clusters to beat down systematics and obtain stronger constraints.

ACKNOWLEDGEMENTS

This work is based on observations obtained with MegaPrime/MegaCam, a joint project of CFHT and CEA/DAPNIA, at the CFHT, which is operated by the National Research Council (NRC) of Canada, the Institut National des Sciences de l'Univers of the Centre National de la Recherche Scientifique (CNRS) of France and the University of Hawaii. This research used the facilities of the Canadian Astronomy Data Centre operated by the National Research Council of Canada with the support of the Canadian Space Agency. CFHTLenS data processing was made possible thanks to significant computing support from the NSERC Research Tools and Instruments grant programme. HW acknowledges support from SEPNet, the ICG and the UK Science and Technology Facilities Council (STFC). DB, RN, AKR, KK and ARL are supported by the UK STFC grants ST/K00090/1, ST/K00090/1, STL000652/1, ST/L005573/1 and ST/L000644/1. GBZ is supported by the 1000 Young Talents programme in China, and by the Strategic Priority Research Program 'The Emergence of Cosmological Structures' of the Chinese Academy of Sciences, Grant no. XDB09000000. JPS acknowledges support from a Hintze Fellowship. PTPV acknowledges financial support by Fundação para a Ciência e a Tecnologia through project UID/FIS/04434/2013. We thank the referee for their thoughtful comments on the paper.

Numerical computations were performed on the Sciama High Performance Computing (HPC) cluster which is supported by the ICG, SEPNet and the University of Portsmouth.

REFERENCES

Arnaud K. A., 1996, in Jacoby G. H., Barnes J., eds, ASP Conf. Ser. Vol. 101, Astronomical Data Analysis Software and Systems V. Astron. Soc. Pac., San Francisco, p. 17
Arnaud M., 2005, in Melchiorri F., Rephaeli Y., eds, Background Microwave Radiation and Intracluster Cosmology. IOS Press, the Netherlands, p. 77
Arnold C., Puchwein E., Springel V., 2014, MNRAS, 440, 833
Briel U. G., Henry J. P., Boehringer H., 1992, A&A, 259, L31
Buchdahl H. A., 1970, MNRAS, 150, 1
Burikham P., Panpanich S., 2012, Int. J. Mod. Phys., D21, 1250041
Capozziello S., 2002, Int. J. Mod. Phys., D11, 483
Cataneo M. et al., 2014, preprint (arXiv:1412.0133)
Cavaliere A., Fusco-Femiano R., 1978, A&A, 70, 677
Chiba T., Smith T. L., Erickcek A. L., 2007, Phys. Rev. D, 75, 124014
Clifton T., Ferreira P. G., Padilla A., Skordis C., 2012, Phys. Rep., 513, 1
Colless M., Dunn A. M., 1996, ApJ, 458, 435
Croston J. H. et al., 2008, A&A, 487, 431
de Jong J. T. A., Verdoes Kleijn G. A., Kuijken K. H., Valentijn E. A., 2013, Exp. Astron., 35, 25
Erben T., Hildebrandt H., Miller L., van Waerbeke L., Heymans C., Hoekstra H., 2013, MNRAS, 433, 2545
Ferraro S., Schmidt F., Hu W., 2011, Phys. Rev. D, 83, 063503
Fitchett M., Webster R., 1987, ApJ, 317, 653
Ford J., Hildebrandt H., Van Waerbeke L., Erben T., Laigle C., Milkeraitis M., Morrison C. B., 2014, MNRAS, 439, 3755
Foreman-Mackey D., Hogg D. W., Lang D., Goodman J., 2013, PASP, 125, 306
Gilks W., Richardson S., Spiegelhalter D., 1996, Markov Chain Monte Carlo in Practice. Chapman and Hall, London
Gursky H., Kellogg E., Murray S., Leong C., Tananbaum H., Giacconi R., 1971, ApJ, 167, L81
Hasselfield M. et al., 2013, J. Cosmol. Astropart. Phys., 7, 8
Heymans C., Van Waerbeke L., Miller L., Erben T., Hildebrandt H., 2012, MNRAS, 427, 146
Hildebrandt H., Erben T., Kuijken K., van Waerbeke L., Heymans C., Coupon J., Benjamin J., 2012, MNRAS, 421, 2355
Hoekstra H., Herbonnet R., Muzzin A., Babul A., Mahdavi A., Viola M., Cacciato M., 2015, MNRAS, 449, 685
Hood R., Mann R., 2015, MNRAS, submitted
Hu W., Kravtsov A. V., 2003, ApJ, 584, 702
Hu W., Sawicki I., 2007, Phys. Rev. D, 76, 064004
Hui L., Nicolis A., Stubbs C. W., 2009, Phys. Rev. D, 80, 104002
Israel H., Schellenberger G., Nevalainen J., Massey R., Reiprich T. H., 2015, MNRAS, 448, 814
Jain B., Vikram V., Sakstein J., 2013, ApJ, 779, 39
Jones C., Forman W., 1978, ApJ, 224, 1
Joyce A., Jain B., Khoury J., Trodden M., 2015, Phys. Rep., 568, 1
Kettula K. et al., 2014, preprint (arXiv:1410.8769)
Khoury J., Weltman A., 2004, Phys. Rev. Lett., 93, 171104
Lau E. T., Kravtsov A. V., Nagai D., 2009, ApJ, 705, 1129
Laureijs R. et al., 2011, preprint (arXiv:1110.3193)
Li B., Hellwing W. A., Koyama K., Zhao G.-B., Jennings E., Baugh C. M., 2013, MNRAS, 428, 743
Lloyd-Davies E. J. et al., 2011, MNRAS, 418, 14
Loewenstein M., 2004, Origin and Evolution of the Elements. Cambridge Univ. Press, Cambridge, p. 422
Lombriser L., 2014, Ann. Phys., Lpz., 526, 259
Lombriser L., Koyama K., Zhao G.-B., Li B., 2012, Phys. Rev. D, 85, 124054
LSST Dark Energy Science Collaboration 2012, preprint (arXiv:1211.0310)
MacKay D. J. C., 2003, Information Theory, Inference and Learning Algorithms. Cambridge Univ. Press, Cambridge
McKay T. A. et al., 2001, preprint (astro-ph/0108013)
Mehrtens N. et al., 2012, MNRAS, 423, 1024
Milgrom M., 1983, ApJ, 270, 365
Miller L., Heymans C., Kitching T. D., van Waerbeke L., Erben T., Hildebrandt H., Hoekstra H., 2013, MNRAS, 429, 2858
Moran C. C., Teyssier R., Li B., 2015, MNRAS, 448, 307
Nagai D., Kravtsov A. V., Vikhlinin A., 2007, ApJ, 668, 1
Navarro J. F., Frenk C. S., White S. D. M., 1996, ApJ, 462, 563
Nojiri S., Odintsov S. D., 2003, Phys. Rev. D, 68, 123512
Ostriker J. P., Vishniac E. T., 1986, Nature, 322, 804
Perlmutter S. et al., 1999, ApJ, 517, 565
Planck Collaboration XX, 2014, A&A, 571, A20
Rapetti D., Allen S. W., Mantz A., Ebeling H., 2011, Prog. Theor. Phys. Suppl., 190, 179
Raveri M., Hu B., Frusciante N., Silvestri A., 2014, Phys. Rev. D, 90, 043513
Reichardt C. L. et al., 2013, ApJ, 763, 127
Reiprich T. H., Böhringer H., 2002, ApJ, 567, 716
Riess A. G. et al., 1998, AJ, 116, 1009
Romer A. K., Viana P. T. P., Liddle A. R., Mann R. G., 2001, ApJ, 547, 594
Sahlén M. et al., 2009, MNRAS, 397, 577
Sarazin C. L., 2009, X-Ray Emission from Clusters of Galaxies. Cambridge University Press, Cambridge, UK
Sato T., Matsushita K., Ota N., Sato K., Nakazawa K., Sarazin C. L., 2011, PASJ, 63, 991
Schellenberger G., Reiprich T. H., Lovisari L., Nevalainen J., David L., 2015, A&A, 575, A30
Shaw L. D., Nagai D., Bhattacharya S., Lau E. T., 2010, ApJ, 725, 1452
Sheldon E. S. et al., 2009, ApJ, 703, 2217
Smith R. K., Brickhouse N. S., Liedahl D. A., Raymond J. C., 2001, ApJ, 556, L91
Sotiriou T. P., Faraoni V., 2010, Rev. Mod. Phys., 82, 451
Starobinsky A. A., 2007, Sov. J. Exp. Theor. Phys. Lett., 86, 157
Stott J. P. et al., 2012, MNRAS, 422, 2213
Sunyaev R. A., Zeldovich I. B., 1980, ARA&A, 18, 537

Downloaded from http://mnras.oxfordjournals.org/ at Hiroshima University on December 17, 2015

Terukina A., Yamamoto K., 2012, Phys. Rev. D, 86, 103503
Terukina A., Lombriser L., Yamamoto K., Bacon D., Koyama K., Nichol R. C., 2014, J. Cosmol. Astropart. Phys., 4, 13
The Dark Energy Survey Collaboration 2005, preprint (astro-ph/0510346)
von der Linden A. et al., 2014, MNRAS, 439, 2
Wagner T. A., Schlamminger S., Gundlach J. H., Adelberger E. G., 2012, Class. Quantum Gravity, 29, 184002
Wright C. O., Brainerd T. G., 2000, ApJ, 534, 34
Zhao G.-B., Li B., Koyama K., 2011, Phys. Rev. Lett., 107, 071303

SUPPORTING INFORMATION

Additional Supporting Information may be found in the online version of this paper:

Table B1. The extended X-ray sources in CFHTLenS footprint. (http://mnras.oxfordjournals.org/lookup/suppl/doi:10.1093/mnras/stv1366/-/DC1).

Please note: Oxford University Press are not responsible for the content or functionality of any supporting materials supplied by the authors. Any queries (other than missing material) should be directed to the corresponding author for the paper.

APPENDIX A: GOODNESS OF FIT

To characterize the goodness of fit of our profiles, we adopt the following χ^2 statistic

$$\chi^2(T_0^{\rm I}, n_0^{\rm I}, b_1^{\rm I}, r_1^{\rm I}, M_{200}^{\rm I}, c^{\rm I}, T_0^{\rm II}, n_0^{\rm II}, b_1^{\rm II}, r_1^{\rm II}, M_{200}^{\rm II}, c^{\rm II}, \beta_2, \phi_{\infty,2}) = {\chi_{\rm WL}^{\rm I}}^2 + {\chi_{\rm WL}^{\rm II}}^2 + {\chi_{\rm SB}^{\rm I}}^2 + {\chi_{\rm SB}^{\rm II}}^2, \quad \text{(A1)}$$

where we adopt the notation I, II to indicate the temperature bins $T < 2.5$, $T > 2.5$, respectively, and

$${\chi_{\rm WL}^{\rm I}}^2 = \sum_i \frac{(\gamma(r_{\perp,\rm i}^{\rm I}) - \gamma_{\rm i}^{\rm obs,I})^2}{(\sigma\gamma_{\rm i}^{\rm obs,I})^2}, \quad \text{(A2)}$$

$${\chi_{\rm WL}^{\rm II}}^2 = \sum_i \frac{(\gamma(r_{\perp,\rm i}^{\rm II}) - \gamma_{\rm i}^{\rm obs,II})^2}{(\sigma\gamma_{\rm i}^{\rm obs,II})^2}, \quad \text{(A3)}$$

$${\chi_{\rm SB}^{\rm I}}^2 = \sum_{i,j} (S_{\rm B}(r_{\perp,\rm i}^{\rm I}) - S_{\rm B,i}^{\rm obs,I}) C_{i,j}^{-1} (S_{\rm B}(r_{\perp,\rm j}^{\rm I}) - S_{\rm B,j}^{\rm obs,I}), \quad \text{(A4)}$$

$${\chi_{\rm SB}^{\rm II}}^2 = \sum_{i,j} (S_{\rm B}(r_{\perp,\rm i}^{\rm II}) - S_{\rm B,i}^{\rm obs,II}) C_{i,j}^{-1} (S_{\rm B}(r_{\perp,\rm j}^{\rm II}) - S_{\rm B,j}^{\rm obs,II}). \quad \text{(A5)}$$

In the weak lensing case, we approximate the covariance matrix as diagonal; we find strong leading diagonals for the measured correlation matrices. For the surface brightness fits, we minimize over the full covariance matrix due to the covariances that exist between bins; here C is the error covariance matrix. Then $\gamma(r_{\perp,\rm i})$ is the value of the lensing model at a distance $r_\perp$ from the clusters' centre; likewise $S_{\rm B}(r_{\perp,\rm i})$ is the value of the surface brightness model at a distance $r_\perp$ from the clusters centre. $\gamma_{\rm i}^{\rm obs}$, $S_{\rm B,i}^{\rm obs}$ are the observed shear profile and surface brightness profile, respectively, while $\sigma\gamma_{\rm i}^{\rm obs}$ is the observed error on the shear profile.

APPENDIX B: SOURCE LIST

Table B1. Sample of the extended X-ray sources in CFHTLenS footprint. The XCS name and position are listed for all clusters. Redshifts are provided where available. The clusters forming the sample used throughout this work have a flag of 0 in the $T < 2.5$ keV bin and a flag of 1 in the $T > 2.5$ keV bin. A flag of 2 denotes the source was discounted for having no measured redshift. A flag of 3 denotes the source was discounted for having no measured X-ray temperature. The full version of this table is provided via the online edition of the article. An excerpt is provided to illustrate form and content.

XCS name	z	Flag
XMMXCS J020045.8−064229.2	0.36	0
XMMXCS J020119.0−064954.6	0.33	0
XMMXCS J020232.1−073343.8	0.55	1
XMMXCS J020334.3−055049.5		2
XMMXCS J020359.1−055031.6		3
XMMXCS J020405.2−050142.5		2
XMMXCS J020428.5−070221.6		2
XMMXCS J020432.7−064449.4		2
XMMXCS J020514.7−045640.0	0.29	0
XMMXCS J020611.4−061129.2	0.88	1

Downloaded from http://mnras.oxfordjournals.org/ at Hiroshima University on December 17, 2015

APPENDIX C: CLUSTER IMAGES

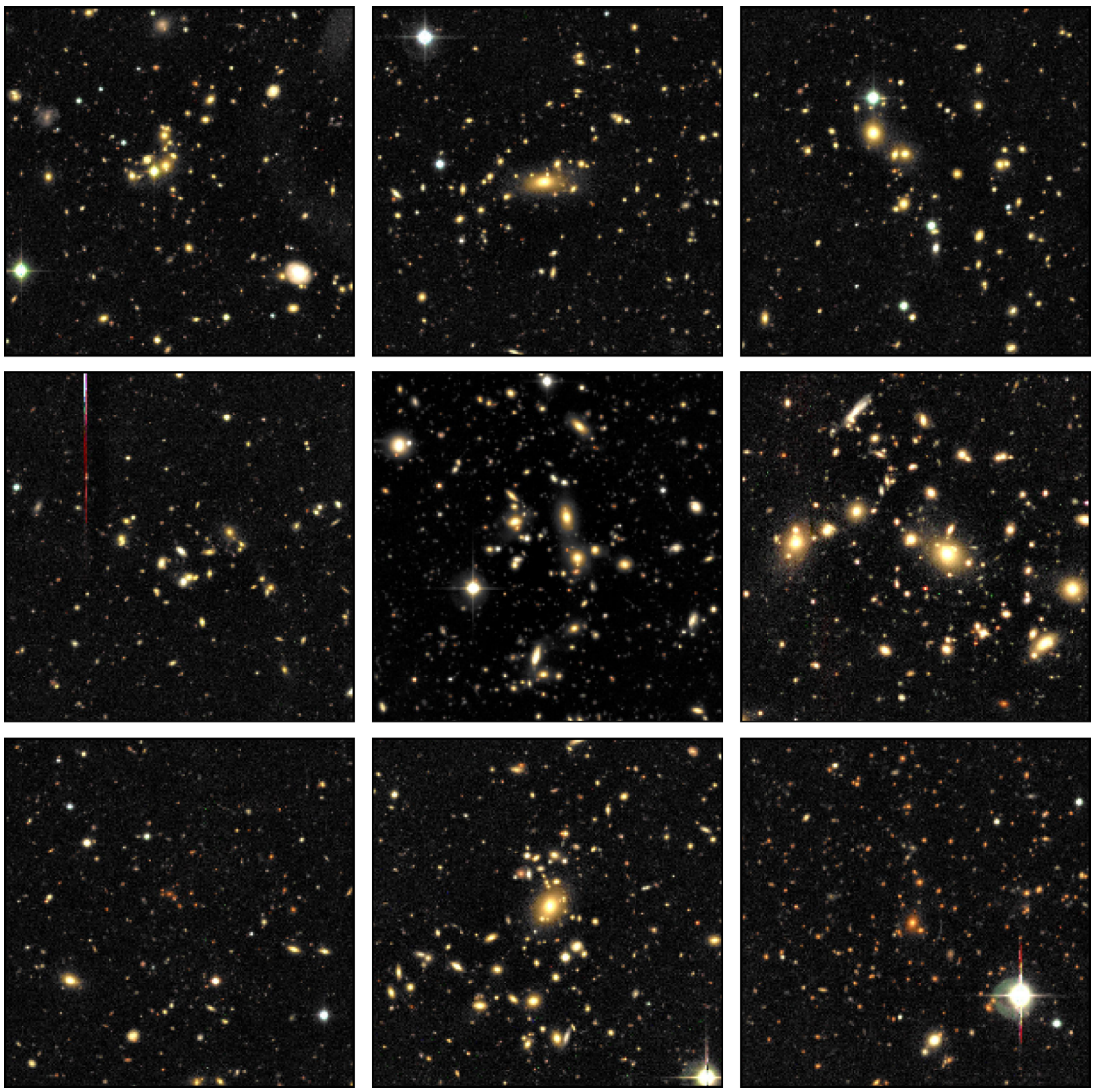

Figure C1. A selection of optically confirmed clusters as imaged by CFHTLenS. False colour composite images are 3 arcmin × 3 arcmin. From left to right and top to bottom, the compilation shows the clusters: XMMXCS J020119.0−064954.6 at $z = 0.33$; XMMXCS J021226.8−053734.6 at $z = 0.31$; XMMXCS J021527.9−053319.2 at $z = 0.28$; XMMXCS J021843.7−053257.7 at $z = 0.40$; XMMXCS J022433.8−041433.7 at $z = 0.39$; and XMMXCS J023142.2−045253.1 at $z = 0.21$. These clusters are included in our sample, flagged either with a 0 or 1 in Table B1. The remaining clusters in our compilation have no measured redshift or temperature and are flagged with a 2 or 3 in Table B1. Continuing onwards these clusters are: XMMXCSJ021517.1−0.60432.8, XMMXCSJ022359.2−083543.4 and XMMXCSJ141446.9+544709.1.

Downloaded from http://mnras.oxfordjournals.org/ at Hiroshima University on December 17, 2015

APPENDIX D: 2D CONTOURS

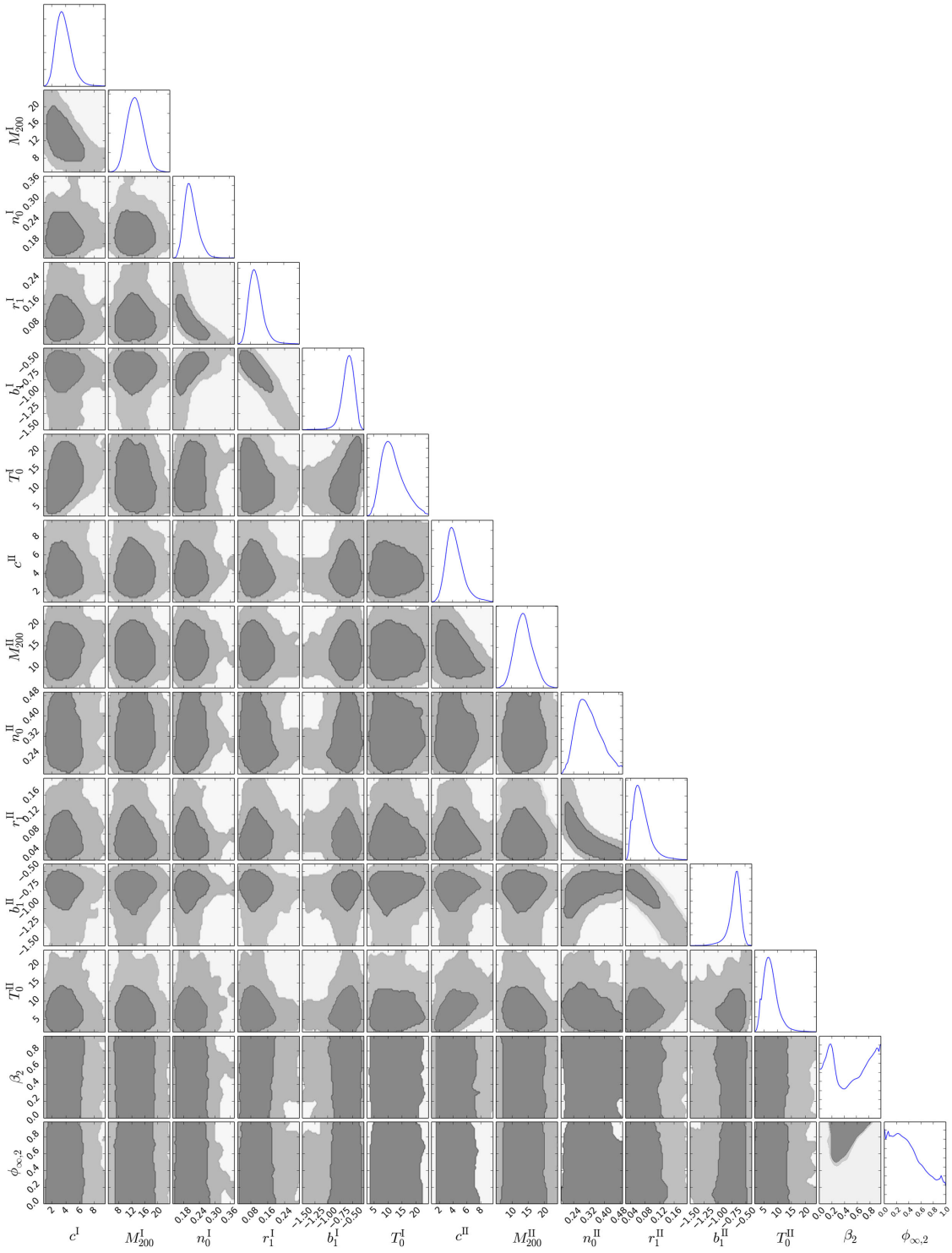

Figure D1. The 95 per cent (dark grey region) and the 99 per cent CL (mid-grey region) 2D marginalized contours for the 14 model parameters $T_0^{\rm I}$ (keV), $n_0^{\rm I}$ ($10^{-2}{\rm cm}^{-3}$), $b_1^{\rm I}$, $r_1^{\rm I}$ (Mpc), $M_{200}^{\rm I}$ ($10^{14}\,{\rm M}_\odot$), $c^{\rm I}$, $T_0^{\rm II}$ (keV), $n_0^{\rm II}$ ($10^{-2}{\rm cm}^{-3}$), $b_1^{\rm II}$, $r_1^{\rm II}$ (Mpc), $M_{200}^{\rm II}$ ($10^{14}\,{\rm M}_\odot$), $c^{\rm II}$, β_2, $\phi_{\infty,2}$ used in our MCMC analysis. The rightmost plots show the 1D likelihood distributions.

This paper has been typeset from a TEX/LATEX file prepared by the author.

Downloaded from http://mnras.oxfordjournals.org/ at Hiroshima University on December 17, 2015